



*NorthWest Research Associates, Inc.*

*P.O. Box 3027 • Bellevue, WA 98009-3027*

*NWRA-CR-99-R203*

*6 October 1999*

# *Dynamical Meteorology of the Equatorial and Extratropical Stratosphere*

*FINAL REPORT*

*for:*

Contract No. NASW-4844

*Prepared by:*

Dr. Timothy J. Dunkerton

Principal Investigator

NorthWest Research Associates, Inc.

*Prepared for:*

National Space and Aeronautics Administration

Atmospheric and Chemistry Modeling and Analysis Program

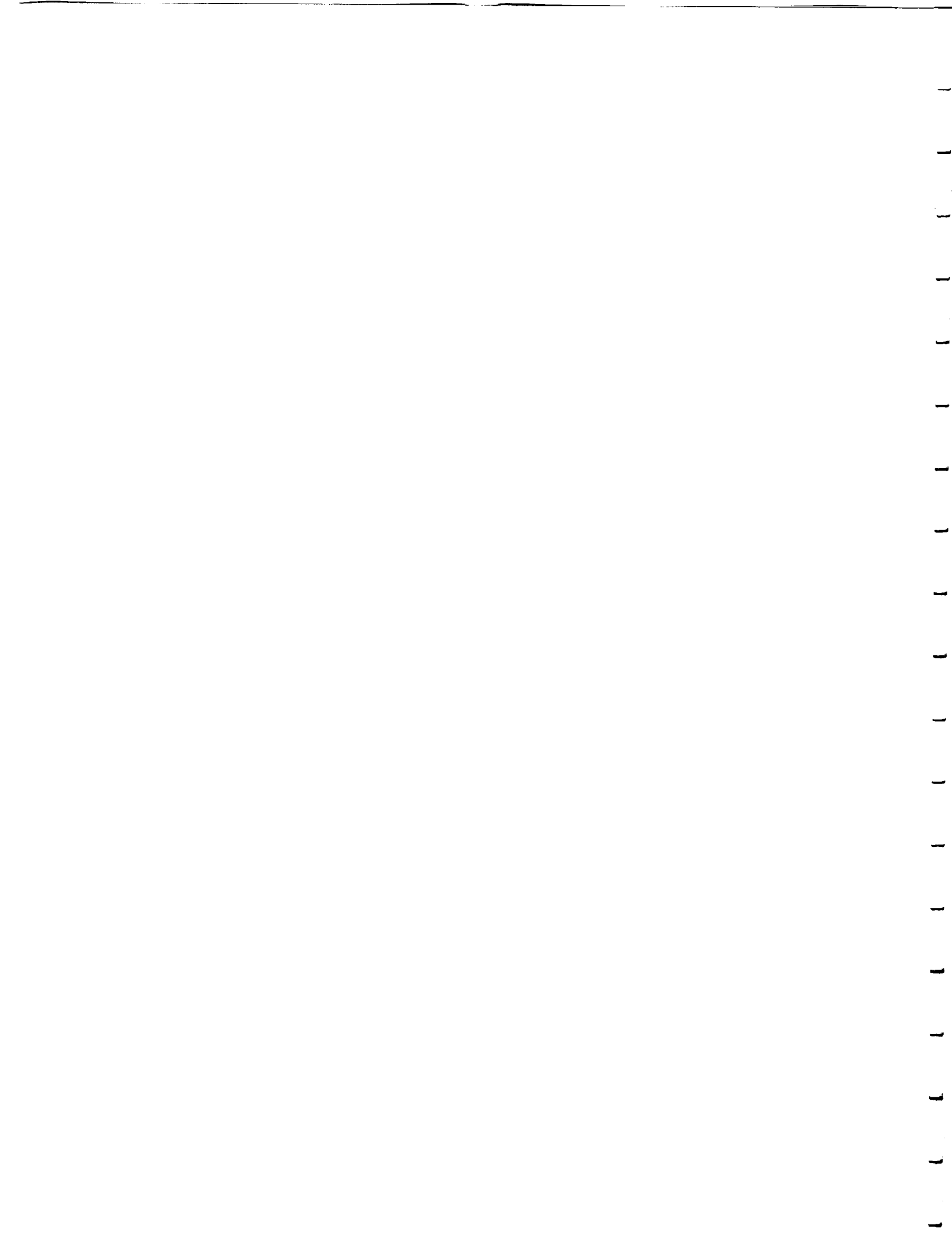


## Table of Contents

### **I. Observational Studies of the Tropical Troposphere**

- (a) Observation of 3-6-Day Meridional Wind Oscillations over the Tropical Pacific, 1973-1992: Horizontal Structure and Propagation
- (b) Evidence of Meridional Motion in the Summer Lower Stratosphere adjacent to Monsoon Regions
- (c) Eastward Propagating -2- to 15-day Equatorial Convection and its Relation to the Tropical Intraseasonal Oscillation

### **II. Observational Studies of the Tropical Stratosphere**

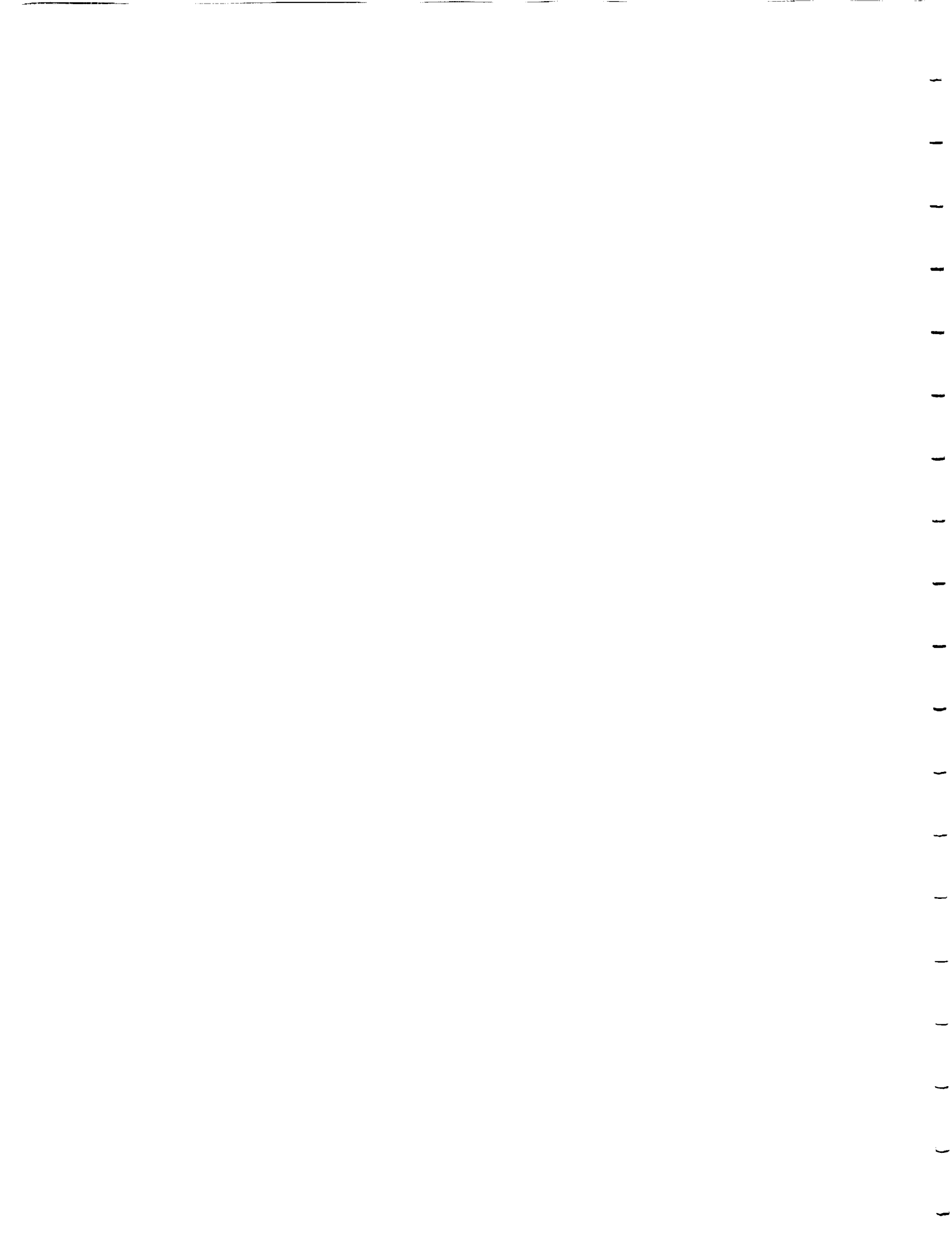
- (a) Mixing Zone in the Tropical Stratosphere above 10 mb
- (b) The Influence of the Quasi-biennial Oscillation on Global Constituent Distributions
- (c) Climatology of the Semiannual Oscillation of the Tropical Middle Atmosphere
- (d) Interaction of the Quasi-biennial Oscillation and Stratopause Semiannual Oscillation
- (e) Estimates of Momentum Flux Associated with Equatorial Kelvin and Gravity Waves

### **III. Observational Studies of the Extratropical Troposphere and Stratosphere**

- (a) Biennial, Quasi-biennial, and decadal Oscillations of Potential Vorticity in the Northern Stratosphere
- (b) Orthogonal Rotation of Spatial Patterns Derived from Singular Value Decomposition Analysis
- (c) Observed Correlations between Winter-Mean Tropospheric and Stratospheric Circulation Anomalies

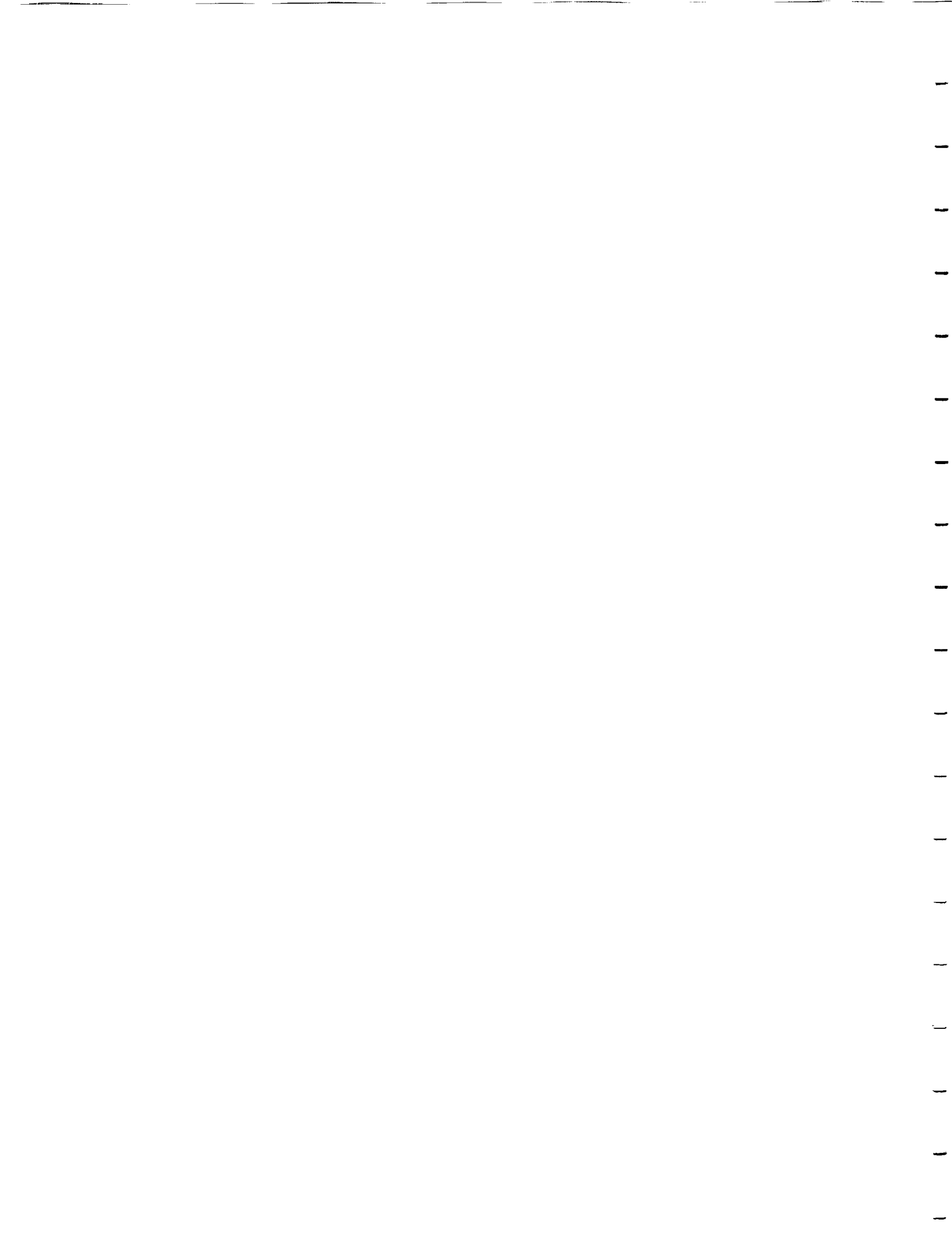
### **IV. Numerical Study of the Quasi-Biennial Oscillation**

- (a) The Role of Gravity Waves in the Quasi-biennial Oscillation





## **I. Observational Studies of the Tropical Troposphere**



## Observation of 3–6-Day Meridional Wind Oscillations over the Tropical Pacific, 1973–1992: Horizontal Structure and Propagation

TIMOTHY J. DUNKERTON AND MARK P. BALDWIN

*Northwest Research Associates, Bellevue, Washington*

(Manuscript received 10 February 1994, in final form 19 September 1994)

### ABSTRACT

Twenty years of rawinsonde data (1973–1992) were examined in conjunction with European Centre for Medium-Range Weather Forecasts (ECMWF) analyses and outgoing longwave radiation (OLR) in 1980–1989 to determine the horizontal structure, propagation, and convective coupling of 3–6-day meridional wind oscillations over the tropical Pacific. Wave properties from ECMWF data, determined by lag correlation with respect to rawinsonde or ECMWF principal components, were consistent with what could be determined from the sparse rawinsonde network alone. Gridded analyses allowed a clearer distinction between equatorially trapped Rossby–gravity waves (RGW) and off-equatorial “tropical-depression” (TD) disturbances, so that the contrasting properties of these waves, including their seasonal and interannual variation, could be studied in better detail. Significant correlations with OLR were found, increasing in magnitude from eastern to western Pacific.

The apparent group propagation of disturbances was equatorward in the western Pacific, eastward across the central and eastern Pacific, and upward–downward out of the 150–300-mb layer. Vertical propagation was evident primarily at higher frequencies, implying that only a fraction of the kinetic energy associated with Rossby–gravity waves in the upper troposphere was involved either in convective coupling to the lower troposphere or vertical momentum transport to the lower stratosphere. It is suggested that in addition to convective and lateral forcings, Rossby–gravity waves are sometimes excited by energetic TD disturbances in the western Pacific.

### 1. Introduction

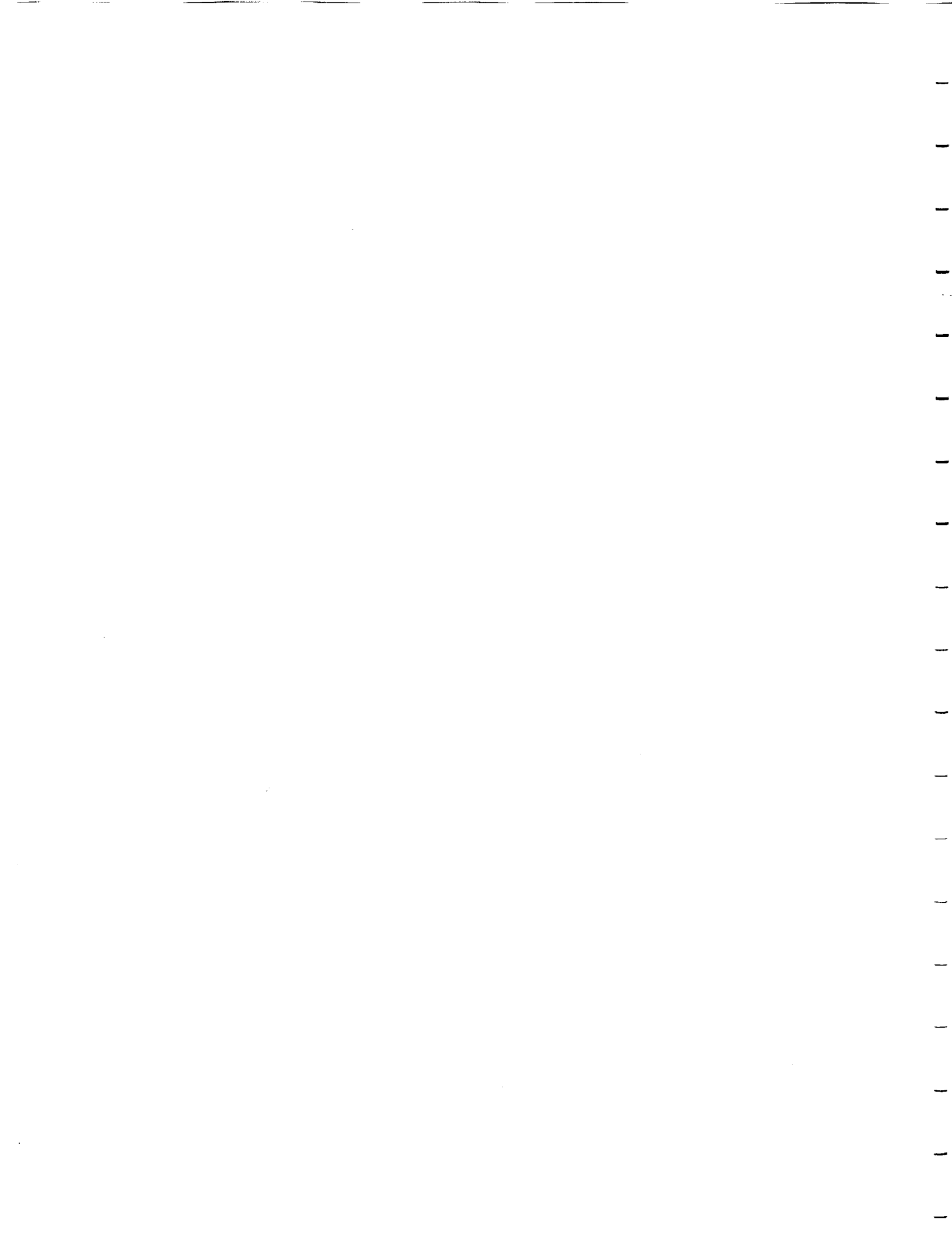
The tropical troposphere contains a complex assortment of meteorological phenomena ranging in horizontal scale from cumulonimbus clouds and mesoscale convective systems, to intraseasonal oscillations and planetary-scale circulations. Of the various phenomena, synoptic-scale disturbances (1500–10 000 km) arguably are the most important because they organize tropical convection and precipitation at shorter scales and comprise the inner scale of planetary circulations. Along the equator, superclusters lie within intraseasonal oscillations (Nakazawa 1988; Mapes and Houze 1993). Tropical convergence zones are stormtracks tracing the locus of deep convection within propagating synoptic-scale waves (Hack et al. 1989; Hess et al. 1993).

Until the early 1980s, knowledge of synoptic-scale phenomena was based on meteorological observations from isolated upper-air stations and a few intensive observing campaigns. Although the major disturbance characteristics were well described in certain regions (Wallace 1971; Yanai 1975), a global perspective was

impossible. Where available, station data were sometimes ambiguous and confusing.

Global analyses—based not only on rawinsonde observations but also satellite-derived temperatures and cloud winds—now reveal the complexity of tropical circulation in more detail. These data afford a better description of horizontal structure and propagation than possible with rawinsonde data alone (Zangvil and Yanai 1980, 1981; Yanai and Lu 1983; Nitta et al. 1985; Nitta and Takayabu 1985; Liebmann and Hendon 1990). In the central and western tropical Pacific, where many of the early rawinsonde studies were concentrated, synoptic-scale waves in the lower troposphere evidently may be classified as “equatorial waves” situated symmetrically or antisymmetrically about the equator (in accord with linear wave theory) and off-equatorial tropical depression (TD) waves or vortical structures akin to the familiar “easterly waves” of early literature (Takayabu and Nitta 1993). Both disturbances regulate, and are in turn influenced by, deep tropical convection at least part of the time. In the central Pacific, equatorial Rossby–gravity waves maximize in northern autumn (Hendon and Liebmann 1991), while TD disturbances prevail farther west, maximizing in northern summer (Takayabu and Nitta 1993). The annual variations are consistent with changes in underlying sea surface temperature (SST) if the waves are coupled to convection and derive en-

Corresponding author address: Dr. Timothy J. Dunkerton, Northwest Research Associates, P.O. Box 3027, Bellevue, WA 98009-3027.



ergy from latent heat release. The importance of convection is suggested by cross-spectrum analysis with cloud observations, analysis of the energy budget and (for Rossby-gravity waves) by inserting a moist equivalent depth in the RGW dispersion relation (Lau and Lau 1990, 1992; Hendon and Liebmann 1991; Takayabu and Nitta 1993). Interannual variations of wave activity are likewise consistent with SST variations where convective coupling occurs.

In addition to convective Rossby-gravity waves and TD disturbances originating in the lower troposphere are shear-modified Rossby-gravity waves attaining largest amplitude in the upper troposphere over the eastern equatorial Pacific (Randel 1992). These waves are not significantly coupled to convection but apparently depend on lateral excitation from baroclinic systems in the midlatitude Southern Hemisphere (see also Zangvil and Yanai 1980, 1981; Magaña and Yanai 1994).

At present, several questions remain unanswered. For example, 1) the relative importance of convective and laterally forced waves in the troposphere and lower stratosphere is unknown; 2) the relation, if any, of upper tropospheric waves to the lower tropical troposphere is unclear; 3) in the lower troposphere, it is uncertain whether equatorial waves and TD disturbances are entirely distinct or evolve continuously from one type to the other as the background environment changes (e.g., from central to western Pacific); 4) seasonal and interannual variations of SST alter the geographical distribution of wave activity, but these variations have not been extensively studied, particularly in data-sparse regions (e.g., eastern Pacific); and 5) when using winds derived entirely from analyses, there is naturally some concern whether observed phenomena are genuine or a model artifact. With the exception of Randel (1992), none of the recent papers used rawinsonde data for validation.<sup>1</sup>

To address these questions, we are investigating available rawinsonde data from the tropical troposphere and lower stratosphere beginning in 1973, together with gridded analyses beginning in 1980. Some preliminary results from rawinsonde data were reported in Dunkerton (1991) for the lower stratosphere throughout the Tropics and in Dunkerton (1993, hereafter D93) for the troposphere and lower stratosphere over the western, central, and southeastern equatorial Pacific. Several results of D93 were consistent with early rawinsonde studies (Yanai and Maruyama 1966; Yanai et al. 1968; Yanai and Hayashi 1969; Nitta 1970) and more recent investigations with analysis data. Four types of meridional wind oscillations were revealed: 1)

a modified Rossby-gravity wave maximizing in upper troposphere (period 5–6 days, zonal wavenumber 4–6), not significantly coupled to the lower troposphere or lower stratosphere; 2) a convectively coupled Rossby-gravity wave maximizing in the central Pacific, lower troposphere (period 4–5 days), but with radiating tail extending vertically into the upper troposphere and lower stratosphere; 3) waves of short zonal scale in the lower troposphere west of the date line, occupying a broad band of frequencies; and 4) stratospheric Rossby-gravity waves (period 3–4 days, zonal wavenumber 3–4). Dominant wave periods and zonal wavelengths were inferred from cross-spectrum analysis of meridional wind. Wavelengths could be estimated only at stations west of the date line near the same latitude (7°–10° N). Cross-equatorial symmetry could be inferred only near the date line.

Seasonal and interannual variations of wave activity were also discussed by D93 and appear consistent with other studies (e.g., Chang and Miller 1977; Yanai and Lu 1983) concerning the effect of El Niño/Southern Oscillation (ENSO) on upper tropospheric waves and with Maruyama (1991) on the role of the stratospheric quasi-biennial oscillation (QBO).

As a continuation of D93, we now discuss the horizontal structure and propagation associated with 3–6-day meridional wind oscillations using gridded analyses in conjunction with rawinsonde data. Similar vertical structures are obtained from both datasets, and significant temporal correlations are found, validating the features observed in gridded data. Section 2 discusses the data analysis and methods, section 3 identifies the dominant vertical and horizontal structures, and section 4 discusses the horizontal wavelength, phase propagation, and apparent group propagation of the various disturbances throughout the Pacific sector. Seasonal and interannual variations are discussed briefly in section 5.

## 2. Data analysis

Rawinsonde data were analyzed at ten stations in the western, central, and southeastern equatorial Pacific (see Table 1 of D93) from a subset of 40+ stations within 10° of the equator identified by Dunkerton (1991) as having copious data in the troposphere and lower stratosphere since 1973. Measurements were typically made once or twice per day (e.g., near 0000 or 1200 UTC) and occasionally at other times, so that binned, interpolated soundings were stored four times daily. Rawinsonde time series extended from 1 January 1973 through 18 April 1992. The quality control, interpolation, and spectral analysis were described in D93. Dominant oscillations were identified from coherence of meridional wind at the same station or between adjacent stations. Examples of coherence spectra and zonal wavelengths in D93 agreed with earlier results based on one or two intensive observing periods (e.g., Yanai et al. 1968).

<sup>1</sup> Analyzed winds in the lower troposphere correlate well with cloud proxy data in regions of convective coupling (Hendon and Liebmann 1991; Takayabu and Nitta 1993).

Rotated principal component analysis was performed in D93 by constructing covariance or correlation matrices within a few "synoptic networks" consisting of stations aligned parallel to the equator in west-central Pacific (from Kota Kinabalu to Tarawa) or stations near the date line on opposite sides of the equator (Majuro, Tarawa, and Funafuti). Cross-spectrum analysis of principal components revealed coherent, westward propagating patterns in agreement with results obtained directly from individual stations. Time histories of their quadrature spectra described seasonal and interannual variations of wave activity.

In this paper, we supplement rawinsonde data with  $2.5^\circ \times 2.5^\circ$  gridded analyses from the European Centre for Medium-Range Weather Forecasts (ECMWF) and outgoing longwave radiation (OLR) datasets. Initialized ECMWF analyses (twice daily) and OLR data (once daily) were obtained for the time period 1 January 1980 to 31 December 1989. There were at most 7306 points of overlap between ECMWF and rawinsonde time series. EOFs obtained from rawinsondes in 1980–1989 were indistinguishable from those obtained from the full record (1973–1992), so the latter were used here.

Our analysis of correlations between rawinsonde and gridded analyses began with individual station time series of meridional wind and principal components derived from the synoptic networks of D93. Point correlations were similar to those determined by Randel (1992). These lay in the range 0.60–0.90 and were highly significant but uninteresting; the spatial patterns were simply bull's eyes centered near the station location with small radius (a few degrees). This comparison established the accuracy of ECMWF anomaly fields, but there are evidently many phenomena passing over individual stations so that the coherence length is quite small when all scales of motion are included. This is a major limitation of one-point correlation analysis in the tropical troposphere.

Correlations between rawinsonde principal components of D93 and ECMWF data were more illuminating, giving significant patterns extending over many days time lag, several tens of degrees longitude, and most latitudes of the tropical belt. Meaningful results could be obtained using extended EOFs from individual stations, even at isolated locations. For this purpose, correlation matrices were constructed at each station on a two-dimensional grid having the vertical coordinate as one direction (at standard pressure levels 850, 700, 500, 400, 300, 250, 200, 150, 100, 70, 50, and 30 mb) and time lag as the other. Meridional wind  $v'$ , zonal wind  $u'$ , and temperature  $T'$  were combined into a single matrix; similar results were obtained from meridional wind alone. This method is a further extension (to many time lags) of "extended, multivariate, rotated principal component analysis" in which spatially gridded data are arrayed at a few time lags (Lau and Lau 1990) or, alternatively, an extension of "singular spec-

trum analysis" of time series (Ghil and Mo 1991) to include a spatial coordinate, several variables, and varimax rotation as well as time lag. As in SSA, the window length is arbitrary; optimum results are obtained if anywhere from one-half to a full cycle of the dominant oscillation fit into the window. (Longer windows produce degenerate EOFs, while shorter windows misrepresent oscillations as a trend.) An increment of one-half day was sufficient for time lags, with maximum lag  $\pm 3$  days. For single-station extended EOFs, the resulting correlation matrix had dimension (13 lags)  $\times$  (3 variables)  $\times$  (12 levels) = 468. Dominant oscillations appeared as a pair of EOFs approximately in quadrature, with coherent principal components. Varimax rotation was used to optimize coherence between rotated PCs, including up to 24 EOFs in the rotation.

As in D93, data were prefiltered to exclude low frequencies. Examples of frequency response using combinations of triangle filters (as in D93) are shown in Figs. 1a, b for highpass and bandpass, respectively. For most of the results shown in this paper, a single highpass filter was applied ( $-.24$  in the notation of D93) with half-power response at about 12 days and nearly full response at higher frequencies. This gave an objective, though imperfect, definition of dominant EOFs. (Filtering did not predetermine the wave period, but more than one disturbance was sometimes found in the same EOF.) Once the dominant wave periods were objectively determined, principal component analysis was repeated with bandpass filters suited to each disturbance. This gave a more accurate definition of wave structure and amplitude variability.

Results did not greatly depend on the choice of filter as long as the lowest frequencies (e.g., Hadley circulation) were excluded, as in D93. Care must be taken when using SSA on prefiltered data since, as shown by Ghil and Mo (1991) even red noise can produce an oscillation. This did not affect any of the structures reported here.

Principal component analysis also used ECMWF data as input. This was done in one of two ways, vertically or horizontally. 1) Meridional wind was arrayed in the longitude–height plane on  $24 \times 7$  grids of length  $60^\circ$  or  $120^\circ$  at standard levels (1000, 850, 700, 500, 300, 200, and 100 mb). The grids were placed at any of 36 starting longitudes ( $10^\circ$  apart) along  $5^\circ$  latitude circles ( $10^\circ\text{S}$ ,  $5^\circ\text{S}$ , equator,  $5^\circ\text{N}$ ,  $10^\circ\text{N}$ ). 2) Meridional wind, zonal wind, and OLR were arrayed in the longitude–latitude plane on  $8 \times 9$  grids of various sizes ( $40^\circ \times 20^\circ$ ,  $40^\circ \times 40^\circ$ , and  $60^\circ \times 60^\circ$ ) at standard pressure levels, starting at any of 36 longitudes as in 1). To check that latitudinal structures were not influenced by sampling, the grids were centered at various latitudes—confirming that rotated EOFs are domain-independent. Results obtained from 2) provided many valuable insights on the dominant patterns of synoptic variability in the tropical troposphere, as well as some useful information on midlatitude baroclinic systems

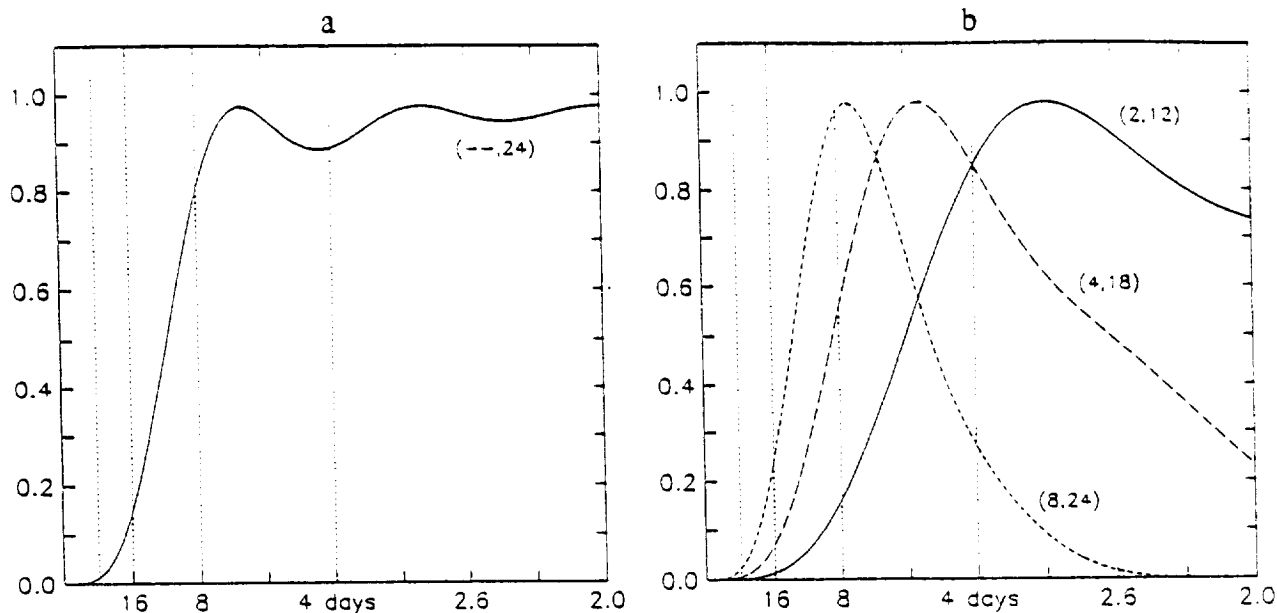


FIG. 1. Response of highpass (a) and bandpass (b) filters used in this study.

penetrating the Tropics. Since it is too extensive to discuss here, this material is reserved for a subsequent manuscript. In this paper we present results obtained in the Pacific sector at 700 mb using  $40^\circ \times 40^\circ$  grids centered on the equator.

### 3. Vertical and horizontal structures

#### a. Rawinsonde observations

Extended EOFs of rawinsonde data ( $v'$ ,  $u'$ , and  $T'$ ) were obtained at the ten stations listed in Table 1 of D93. Several of these were identical in their  $v'$  component to EOFs of  $v'$  alone. Various structures were obtained, including upper-tropospheric waves at 150–300 mb (type A of D93), lower-tropospheric waves (1000–500 mb) with tilted baroclinic structure aloft (type B), and stratospheric Rossby–gravity waves (70–30 mb). These disturbances were characterized by a large meridional wind component. The analysis also revealed Kelvin waves in the stratosphere (for the first time using EOFs) and other tropospheric disturbances involving zonal wind and temperature that may be related to intraseasonal oscillations and the seasonal cycle. Attention is restricted to meridional wind oscillations in the 3–6-day range, concentrating on the troposphere where horizontal structure and propagation could be determined using gridded analyses. Our colorless terminology (A, B) will be used again because, as shown in section 4, these vertical structures sometimes contained a mix of disturbance types.

Examples of type A are shown in Figs. 2a–c. This structure, with maximum  $v'$  at 150–300 mb, was found at each of the ten stations. It was the dominant merid-

ional wind oscillation at central and eastern Pacific stations but of secondary importance in the far western Pacific. The phase relation of meridional ( $v'$ ) and zonal ( $u'$ ) wind (not shown) was as follows. At Atuona, in the southeastern equatorial Pacific,  $u'$  led  $v'$ , consistent with a westward propagating Rossby–gravity wave south of the equator. At Tarawa, in the central equatorial Pacific, the meridional wind had a similar pattern, but  $u'$  was negligible. At Majuro, north of Tarawa,  $u'$  lagged  $v'$ , although the two were not in perfect quadrature, displaying a positive correlation as in D93. Vertical structure evolved gradually toward the western stations so that phase tilts were replaced by an out of phase “first baroclinic mode” (e.g., Koror). All of these structures in central and western Pacific were virtually the same as lag-correlation patterns with respect to the principal components of *spatial* EOFs obtained in D93.

The second EOF pair of meridional wind (type B) displayed a characteristic westward (eastward) tilt with height in upper (lower) troposphere at central and eastern Pacific stations, as shown in Figs. 3a–c (Majuro) and Figs. 4a–c (Atuona). (Westward propagation is assumed in translating the phase delay into a vertical tilt.) The phase relation between zonal and meridional wind switched upon crossing the equator. Likewise, the meridional heat flux switched sign so that the product  $f\overline{v'T'}$  (where  $f$  is the Coriolis parameter and the overbar denotes an average over time lags) was in both hemispheres positive near the tropopause and negative in the lower troposphere. These patterns were consistent with an equatorial wave radiating upward above 200 mb and downward below that level. It may be tempting to discard the B pattern as an artifact of EOF

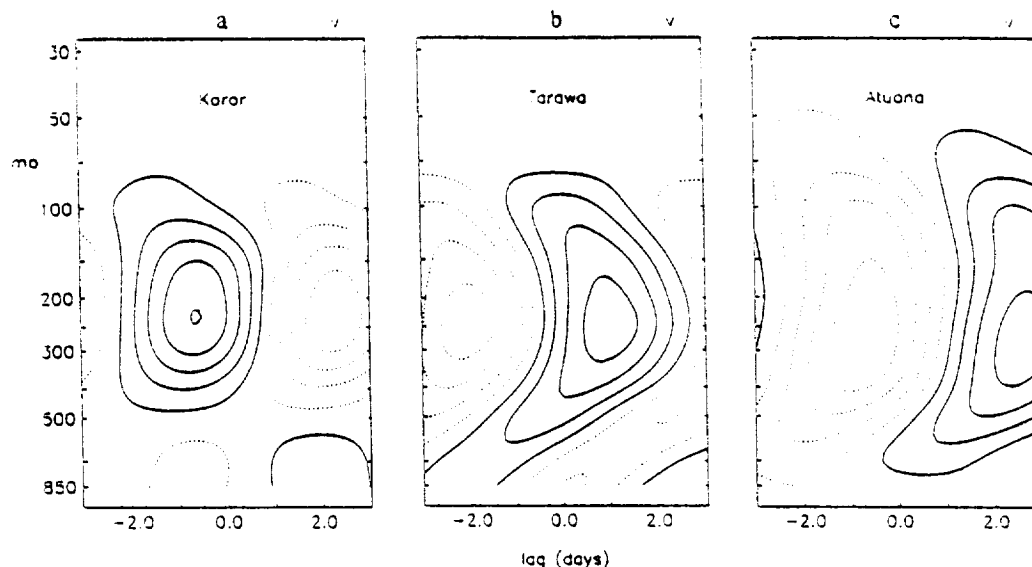


FIG. 2. Meridional wind structure associated with upper troposphere (type A) EOFs at various rawinsonde stations.

analysis given the orthogonality of unrotated EOFs. However, the pattern persists as many EOFs are rotated—reflecting a genuine correlation between the 100-mb level and the lower half of the troposphere (D93). Nearly identical results were obtained when the 150–300-mb layer was omitted.

At Tarawa the meridional wind structure of lower tropospheric waves was similar (Fig. 5c), but zonal wind and temperature (not shown) were negligible. At Truk (Fig. 5b) there was little vertical tilt. In the far western Pacific (Kota Kinabalu, Fig. 5a) there was modest westward tilt over a deep layer and a minor phase reversal in upper troposphere. In this region the order of A and B were reversed, suggesting a strong horizontally divergent component of rawinsonde velocities near the main Hadley cell.

The extended EOF technique gave meaningful results at isolated stations like Atuona (Figs. 2c, 4a–c). The B pattern at this location suggested an unusual, if not bizarre, coupling of lower troposphere and lower stratosphere (Fig. 4a). The interpretation of this pattern was elusive until recently (section 4).

#### b. ECMWF observations

Spatial EOFs of meridional wind were obtained from ECMWF data on various horizontal and vertical grids as described in section 2. Similar vertical structures (A, B) were found as in rawinsonde data; two examples are shown in Figs. 6a, b from the eastern Pacific. These were universal patterns—observed with significant coherence over the three tropical oceans—except for the western Pacific, where the dominant EOF pair displayed westward tilt with height as in Fig. 5a, and the second pair displayed a “first baroclinic mode” structure (not shown).

Figures 7a–c display the lag correlation of ECMWF  $v'$ ,  $u'$ , and  $T'$  with respect to the principal component associated with Fig. 6a (type A). Correlations with respect to that of Fig. 6b are shown in Figs. 8a–c (type B). Zonal wind and temperature perturbations were approximately antisymmetric (not shown). Although the 100-mb data may not be completely reliable as the top-most level of initialized ECMWF data, correlation of meridional wind and temperature clearly suggested an upward flux of wave activity near the tropopause and a downward flux in lower troposphere, as in rawinsonde data. There was an apparent eastward and downward group propagation through the midtroposphere (Liebmann and Hendon 1990).

#### c. Horizontal structures in ECMWF and OLR data

Theoretical equatorial waves have a well-defined horizontal structure and cross-equatorial symmetry. As noted in the Introduction, it is primarily their horizontal structure and propagation that separates equatorially trapped waves from off-equatorial TD disturbances (Lau and Lau 1990, 1992; Takayabu and Nitta 1993) and from eastward traveling midlatitude baroclinic systems. Lau and Lau (1990) used principal component analysis in the horizontal plane to describe TD disturbances. Their method (involving 850-mb vorticity and a few time lags) was well suited for these disturbances since vorticity involves horizontal differentiation (emphasizing smaller scales) but apparently did not yield much useful information on equatorially trapped waves. Takayabu and Nitta (1993) separated the two waves using gridpoint correlation analysis of ECMWF data with respect to GMS equivalent blackbody temperatures (in western and central Pacific during northern summer).



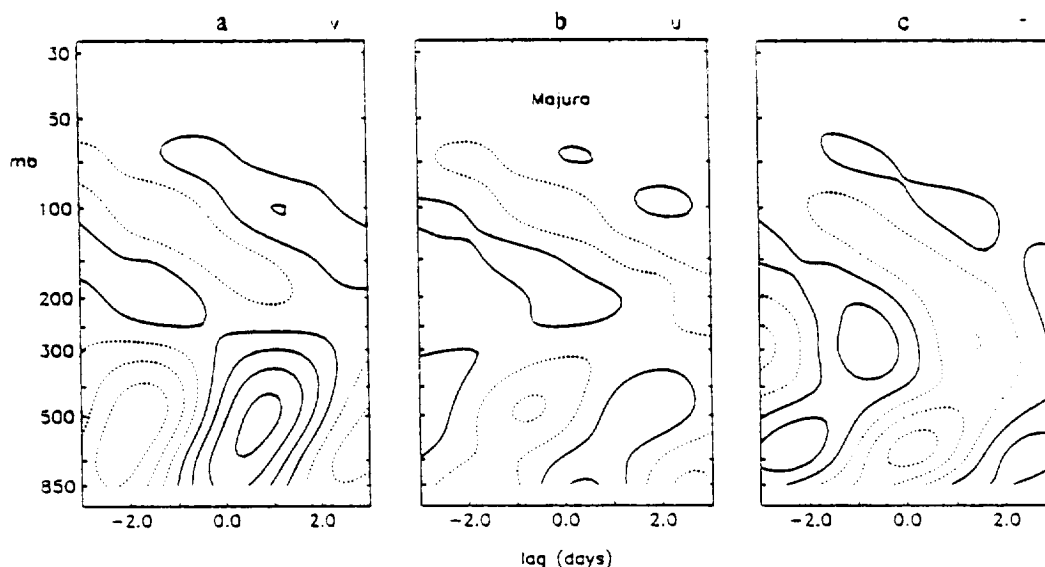


FIG. 3. Structure of lower troposphere (type B) EOF at Majuro. (a) Meridional wind; (b) zonal wind; and (c) temperature.

Wave structures are easily distinguished using the multivariate horizontal EOFs described in section 2 ( $u'$ ,  $v'$ , and OLR). At 700 mb this technique, in contrast to that of Lau and Lau, tended to emphasize Rossby-gravity waves over TD disturbances, except in the western Pacific where TD disturbances attained large amplitude. Four examples of multivariate rotated EOFs are shown in Figs. 9a–d from western to eastern Pacific.

Major variations of wave structure were visible proceeding from western to eastern Pacific. In the west (Fig. 9a) the dominant pattern was centered north of

the equator, with short zonal wavelength, consistent with a vortex train aligned towards the northwest (Lau and Lau 1990). Convection, indicated by the negative OLR anomaly, was closely tied to the cyclonic vortex (Takayabu and Nitta 1993). Near 160° E there was a transition zone where a single EOF pair contained characteristics of both TD and Rossby-gravity waves (Fig. 9b). Note how zonal wavelength in Fig. 9b expands south of the equator, and zonal velocity becomes antisymmetric in the eastern half of the grid. In the central Pacific the disturbance was primarily that of the Rossby-gravity wave (Fig. 9c), centered near the

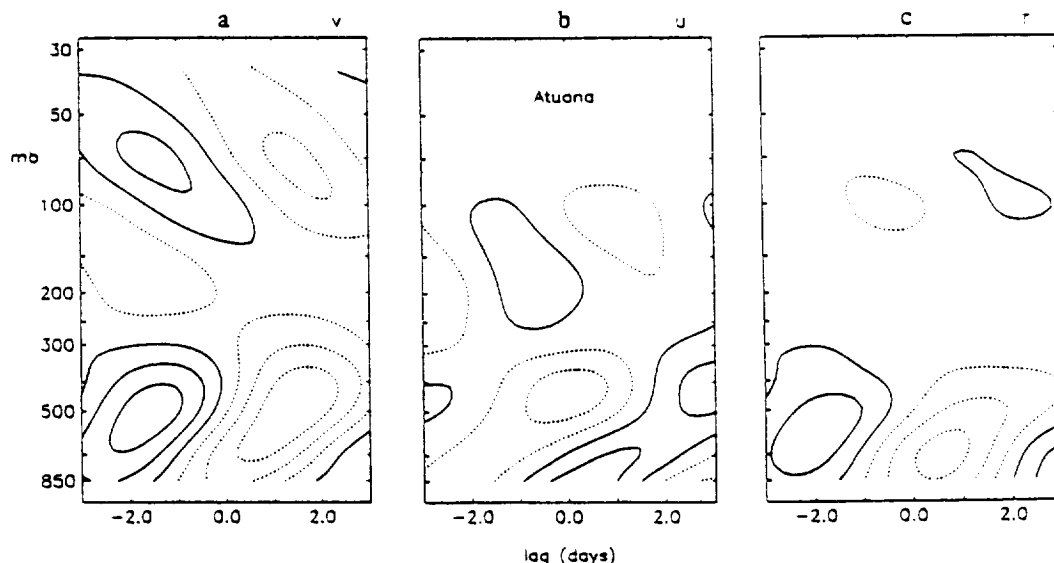


FIG. 4. As in Fig. 3 but for Atuona.

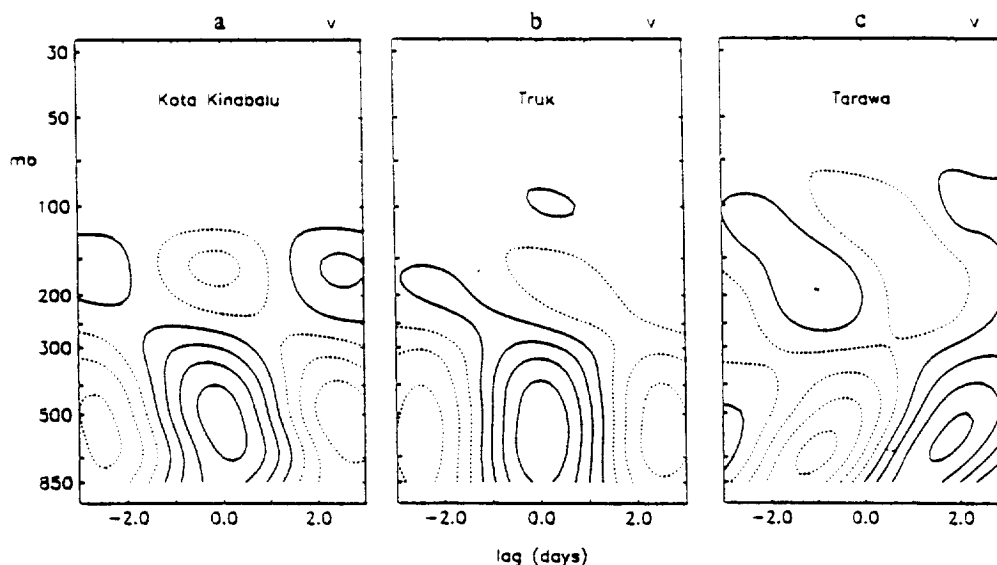


FIG. 5. As in Fig. 2 but for lower troposphere (type B) EOFs.

equator, flanked by remarkable antisymmetric OLR anomalies. In the eastern Pacific the Rossby-gravity structure persisted (Fig. 9d), accompanied by a single, weak lobe of OLR north of the equator. This observation is consistent with a tendency of the intertropical convergence zone (ITCZ) to parallel the equator on the northern side across the Pacific, while the South Pacific convergence Zone (SPCZ) slants southeastward away from the equator (Vincent 1994). East of the date line the SPCZ is too far from the equator to interact with equatorial waves. Figure 9d gives the impression, as it were, of a two-cylinder engine—representing the an-

tisymmetric lobes of convection in Fig. 9c—running on only one cylinder. Disturbances were apparently becoming decoupled from convection in this region as the group propagated eastward. These remarks pertain to the transition of climatological structure from western to eastern Pacific, and not to any particular wave event, although examples of group propagation with structural changes can also be found in the data.

As discussed in the sequel, Rossby-gravity structures were prevalent in the 700-mb analysis throughout the central and eastern Pacific, Atlantic, and Indian Oceans. The TD disturbances were detected not only

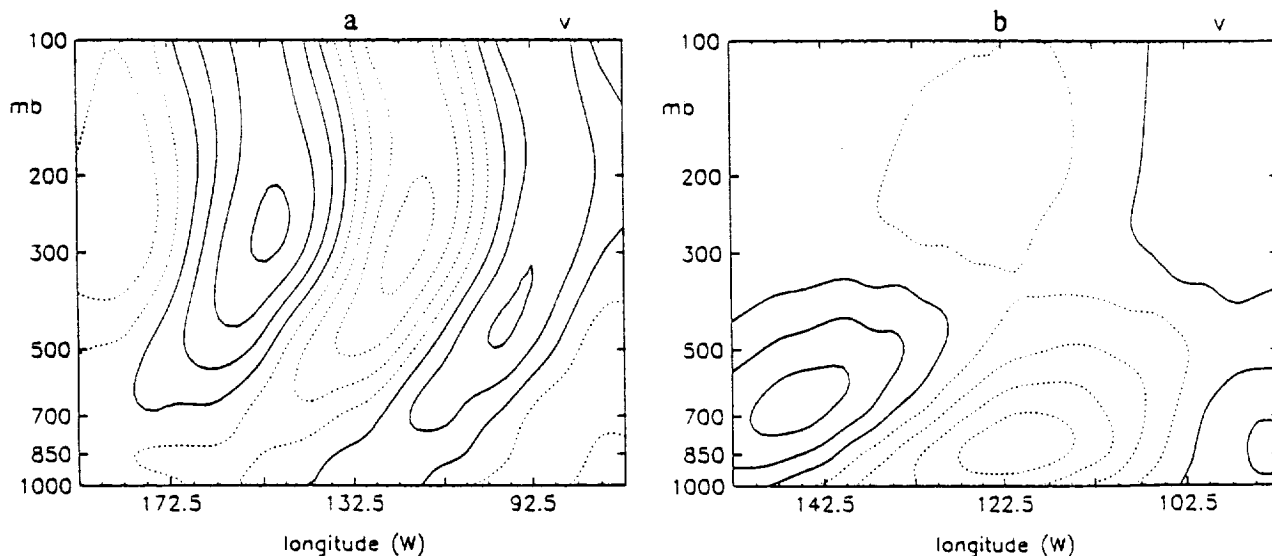


FIG. 6. Longitude-height EOFs of meridional wind from ECMWF data in east-central Pacific. (a) Upper-tropospheric mode at equator; (b) lower-tropospheric mode at 5°S.

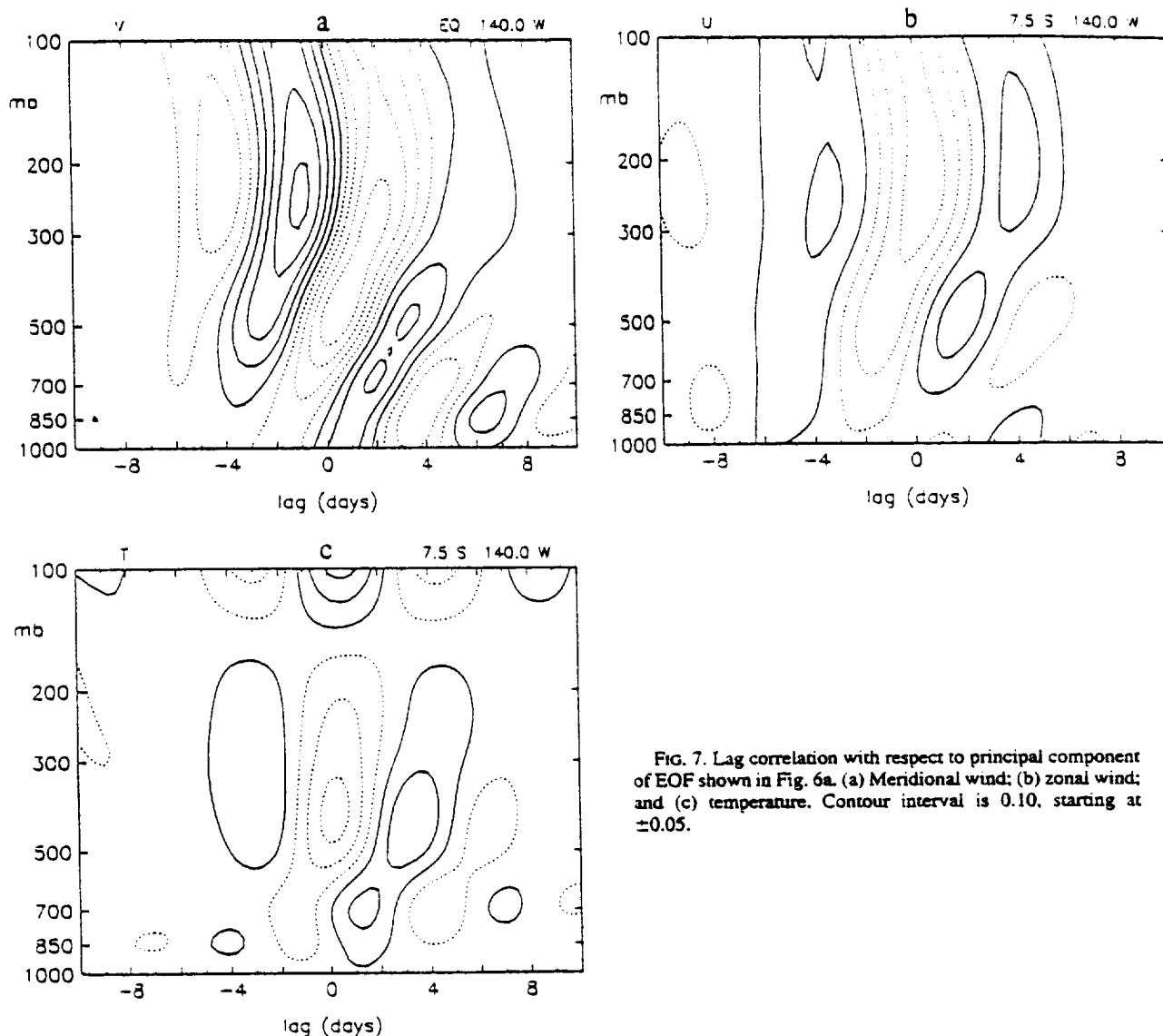


FIG. 7. Lag correlation with respect to principal component of EOF shown in Fig. 6a. (a) Meridional wind; (b) zonal wind; and (c) temperature. Contour interval is 0.10, starting at  $\pm 0.05$ .

in the western Pacific but (with lesser amplitude) in the Atlantic and central American sectors (Lau and Lau 1990). Weak equatorially trapped Rossby waves were found in the Atlantic (Liebmann and Hendon 1990). Subtropical latitudes were dominated by eastward moving baroclinic systems, and some evidence of meridional propagation was seen along the west coast of South America. There were noticeable variations of wave period from one region to the other, even within the same wave type, showing how the local environment is important.

#### 4. Phase and apparent group propagation

##### a. Lag correlation diagrams

Several examples of lag correlation of ECMWF meridional wind with respect to principal compo-

nent time series (PCs) are displayed in Figs. 10a–f. Figures 10a,b show 200–300-mb  $v'$  correlations with respect to rawinsonde type A PCs at Tarawa and Atuona. The dominant wavelength in central Pacific was  $60^{\circ}$ – $80^{\circ}$  (zonal wavenumber 4–6), in agreement with rawinsonde estimates (D93). Apparent group velocity was eastward. The situation at Atuona was rather different (Fig. 10b). The interference pattern at this location was caused by superposition of eastward moving midlatitude baroclinic systems and westward moving equatorial waves. By examining other latitudes, we found that the same reference series that was correlated with westward moving waves at the equator was also correlated with eastward moving waves at  $22.5^{\circ}$  S. Therefore, the type A PC at Atuona contained both types of wave. This is an obvious limitation of sin-

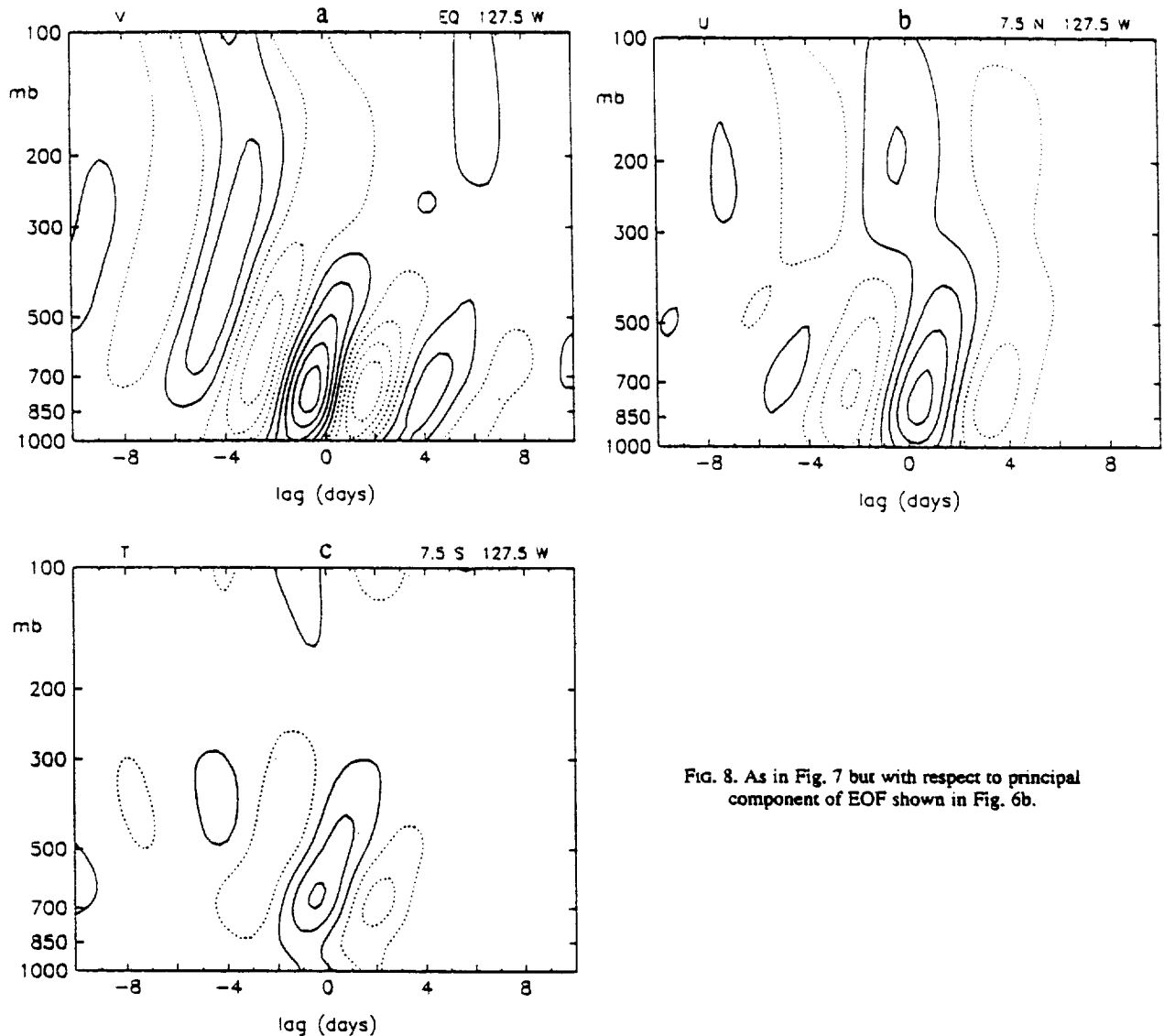


FIG. 8. As in Fig. 7 but with respect to principal component of EOF shown in Fig. 6b.

gle-station EOF analysis since nothing can be inferred about propagation direction.

Correlation with type B gave a significant response in the lower troposphere. In the far western Pacific, zonal wavelengths were shorter by a factor of two (typically  $30^{\circ}$ – $40^{\circ}$ ). Figure 10c shows correlations with respect to type B at Kota Kinabalu. Zonal group velocity was poorly defined, but there was evidence of fast southward group propagation in this region, that is, a lag of 1 or 2 days between the time of maximum activity at  $7.5^{\circ}$ – $15^{\circ}$  N and its appearance near the equator (see discussion surrounding Figs. 13a,d below). Figure 10d shows the correlation with respect to type B at Majuro. In the central Pacific, the pattern mixed together short wavelengths to the west of the date line and longer wavelengths to the east—reminiscent of Nitta's (1970) rawinsonde observa-

tion. In this region type B was probably influenced by TD disturbances, as well as by lower-tropospheric equatorial waves.

The contrast between western and eastern Pacific was obvious using 700-mb ECMWF principal components as the reference series (Figs. 10e,f). Zonal wavelengths were nearly twice as long in eastern Pacific, and the periods were somewhat shorter.

Maximum correlations of ECMWF data with rawinsonde or ECMWF principal components were typically 0.50–0.70, slightly lower than gridpoint correlations mentioned in section 2 but extending over a much larger horizontal area. The percentage of spatially averaged meridional wind variance in the troposphere explained by dominant EOF pairs was typically 10%–30% (D93). Percent variance explained is an ambiguous statistic, reflecting the wave amplitude, spatial ex-

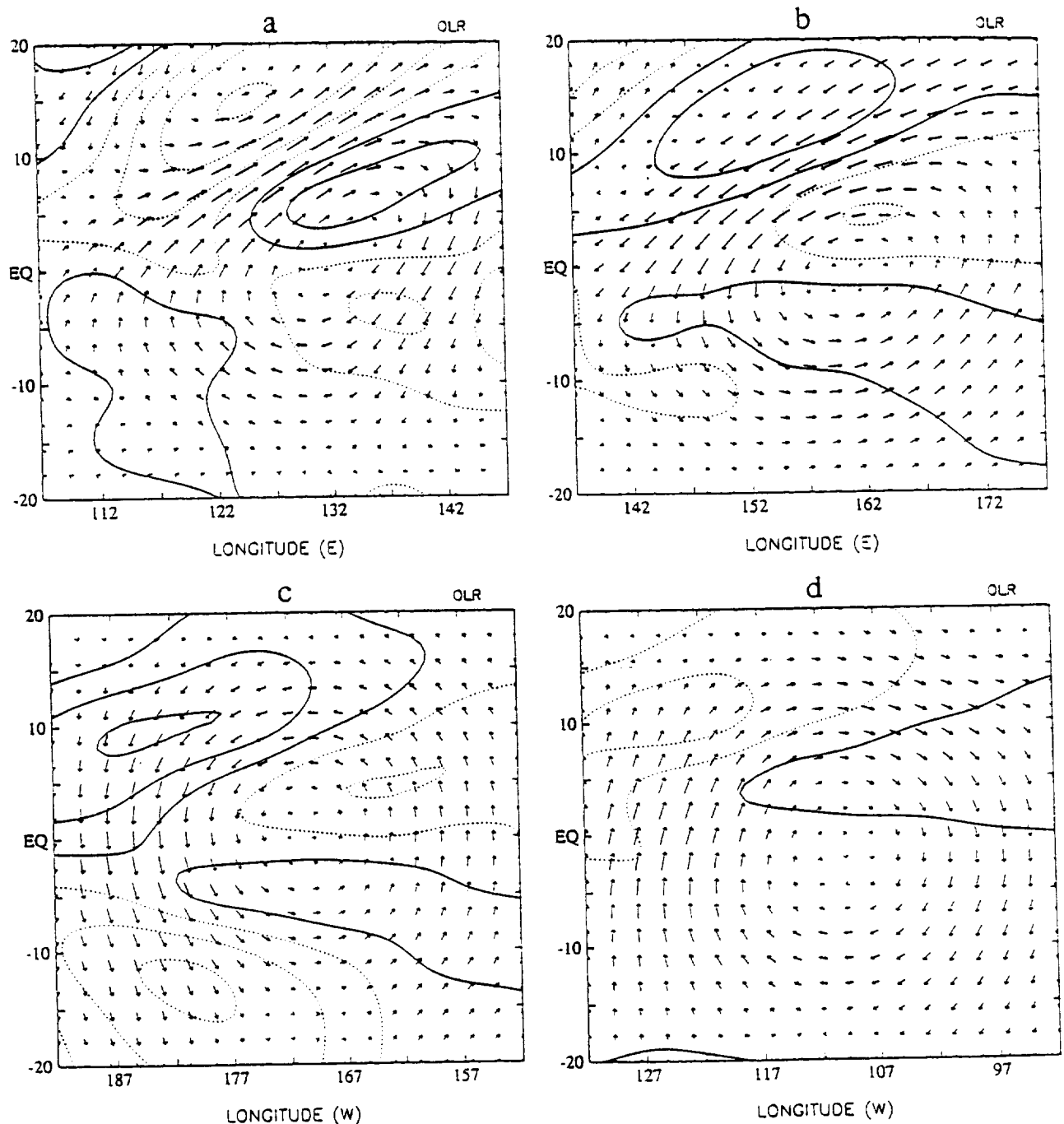


FIG. 9. Multivariate horizontal EOFs from 700-mb ECMWF and OLR data, based on the correlation matrix of horizontal wind components (vectors) and OLR (contours). (a) Far western Pacific; (b) west-central Pacific; (c) east-central Pacific; and (d) far eastern Pacific. Contour interval for OLR is 0.10, starting at  $\pm 0.05$ . The longest vector corresponds to a nondimensional EOF value near 0.6.

tent, and frequency of occurrence relative to other disturbances on the grid. More meaningful is the relative amplitude of waves (compared to the mean flow), which, in the lower troposphere, was generally large in the western Pacific, causing closed vortices to form, while moderate in the central and eastern Pacific, caus-

ing deflection of trade winds  $\sim 45^\circ$  from the prevailing direction.

#### b. Wave parameters

Lag correlations were calculated with respect to ten examples of type A rawinsonde PCs (one from each

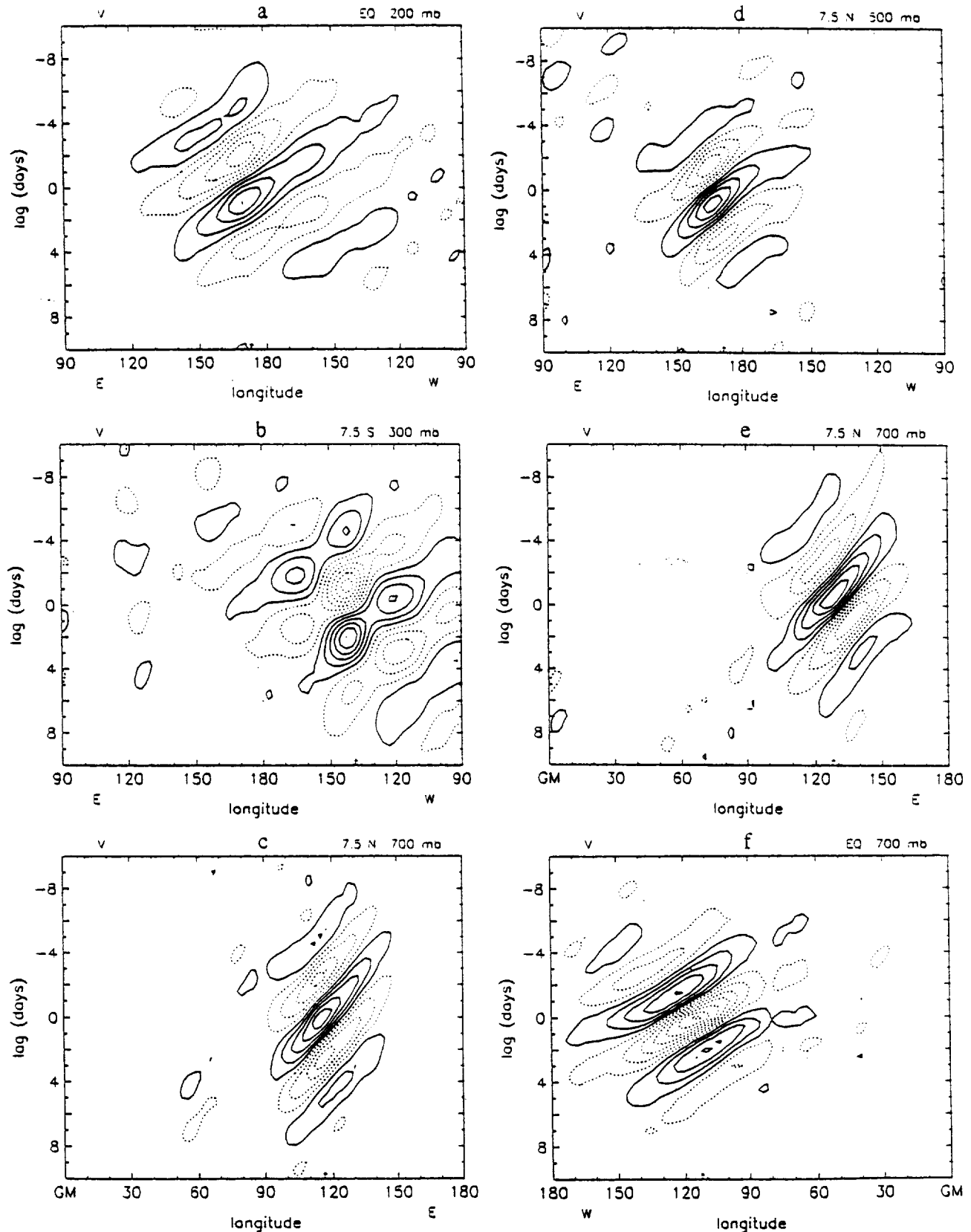


FIG. 10. Lag correlation of meridional wind with respect to principal components of rawinsonde data [(a), (b), (c), (d)] and 700-mb ECMWF and OLR data [(e), (f)]. Arrow at bottom of plot indicates station location or center of ECMWF subgrid. Data from this station (or subgrid) were used to generate the EOF and corresponding principal component time series for lag correlation analysis. Contour interval is 0.10, starting at  $\pm 0.05$ .

station), ten of type B, and 16 examples of 700-mb ECMWF and OLR PCs from western to eastern Pacific (at  $10^\circ$  intervals). Wave parameters were estimated at each pressure level (1000, 850, 700, 500, 300, 200, and 100 mb) at  $15^\circ\text{S}$ ,  $7.5^\circ\text{S}$ , equator,  $7.5^\circ\text{N}$ , and  $15^\circ\text{N}$ . Zonal wavelength, phase speed, apparent group velocity, and wave period were obtained objectively by a simple routine, as illustrated in Fig. 11 using the example from Fig. 10a. Contiguous grid points exceeding a certain threshold (correlation magnitude 0.05) were grouped into clusters, a least-squares fit was obtained (for phase lines) along with a center of mass, and a second least-squares fit was drawn through the centers of mass (for apparent group velocity). Zonal wavelength and wave period were calculated between adjacent phase lines near cluster centers. Examples of zonal wavelength, phase speed, and wave period are shown in Figs. 12a–d.

In Fig. 12a, zonal wavelengths at 850 mb decreased markedly from eastern to western Pacific, as already noted. Immediately west of the date line, wavelengths appeared to decrease gradually, which is somewhat deceptive as the actual transition was more abrupt (e.g., Fig. 10d). There were longer wavelengths (with Rossby–gravity structure) in the Indian Ocean region. Wave periods at 850 mb increased noticeably from eastern to western Pacific (Fig. 12d). The contrast was most apparent in 850-mb phase speed (Fig. 12b). These values are consistent with Liebmann and Hendon (1990).

At 200 mb (Fig. 12c), phase speeds east of the date line separated into two groups (as did zonal wavelength and wave period, not shown): those associated with type A EOFs (maxima near 200 mb, denoted by an  $\times$ ), and type B or 700-mb EOFs (maxima near 700 mb, denoted by a “+” or “ $\Delta$ ”). Two conclusions may be inferred from this analysis: 1) upper- and lower-tropospheric EOFs east of the date line represented distinct phenomena (D93); 2) 700-mb disturbances in this region were coherent with 200 mb  $v'$ , but not at zero lag. Lag correlation diagrams, examples of which are shown in Fig. 13, revealed that lower-tropospheric waves were present at 200 mb in the central Pacific a few days prior to their arrival in the eastern Pacific lower troposphere (Figs. 13c,f). There was a similar delay in the central Pacific with less zonal group propagation (Figs. 13b,e). Waves at 100 mb closely followed those at 200 mb but slightly to the east (not shown). The picture obtained is that of a Rossby–gravity packet in central Pacific entering the eastern Pacific upper troposphere, diverging simultaneously upward to the stratosphere and downward to the lower troposphere. This remarkable observation from ECMWF data may explain the unusual type B correlation pattern in Atuna rawinsonde data (Fig. 4a).

In the far western Pacific, there was little evidence of zonal group propagation but an apparent equatorward propagation of the wave packet (Figs. 13a,d). Given the energetic nature of disturbances in the north-

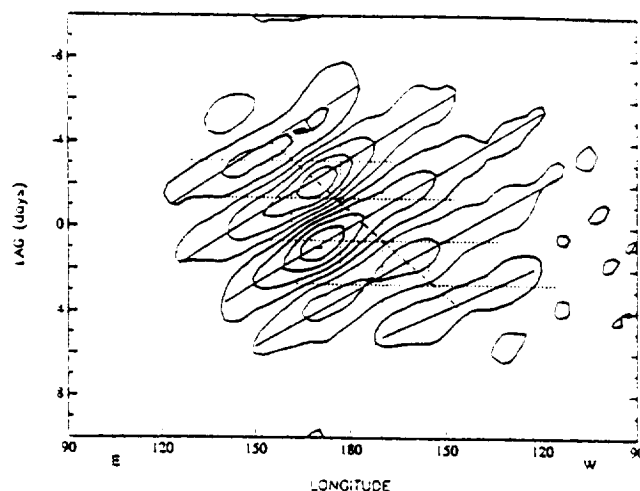


FIG. 11. Lag correlation of meridional wind as in Fig. 10a, illustrating how various wave parameters were determined.

west equatorial Pacific, it would be surprising if Rossby–gravity waves were not excited as result of equatorial penetration of TD disturbances. Examples of this interaction are visible in the data (e.g., November 1981). The modest westward tilt with height of disturbances in this region suggests that if there is a significant projection onto equatorial Rossby–gravity waves, packets of these waves will initially propagate upward into the central Pacific upper troposphere and then diverge along the two ray paths noted above.

### c. EOFs of bandpassed data

The 700-mb multivariate EOFs were also obtained using the bandpass filters shown in Fig. 1b. As noted in section 2, the calculation was performed on a large number of subgrids of the original ECMWF grid to confirm that rotated EOFs were domain independent. The analysis established a clear distinction in each oceanic region between equatorial Rossby–gravity waves and TD disturbances with respect to frequency, zonal wavelength, cross-equatorial symmetry, and horizontal momentum flux. In the tropical Pacific lower troposphere, optimum Rossby–gravity structures were obtained from variance entirely below 5-days period, while TD disturbances were best described from variance in the 6–8-day range. By contrast, Atlantic easterly waves were primarily in the 3–4-day band; Rossby–gravity waves over the Indian Ocean had periods greater than 5 days. Zonal wavelength of TD disturbances was generally much less than that of Rossby–gravity waves. For Rossby–gravity EOFs, the center of meridional wind variance was located, on average, exactly at the equator in the Pacific and Indian Oceans and a few degrees south of the equator in the Atlantic. An advantage of EOF analysis is that we did not demand cross-equatorial symmetry a priori; nev-

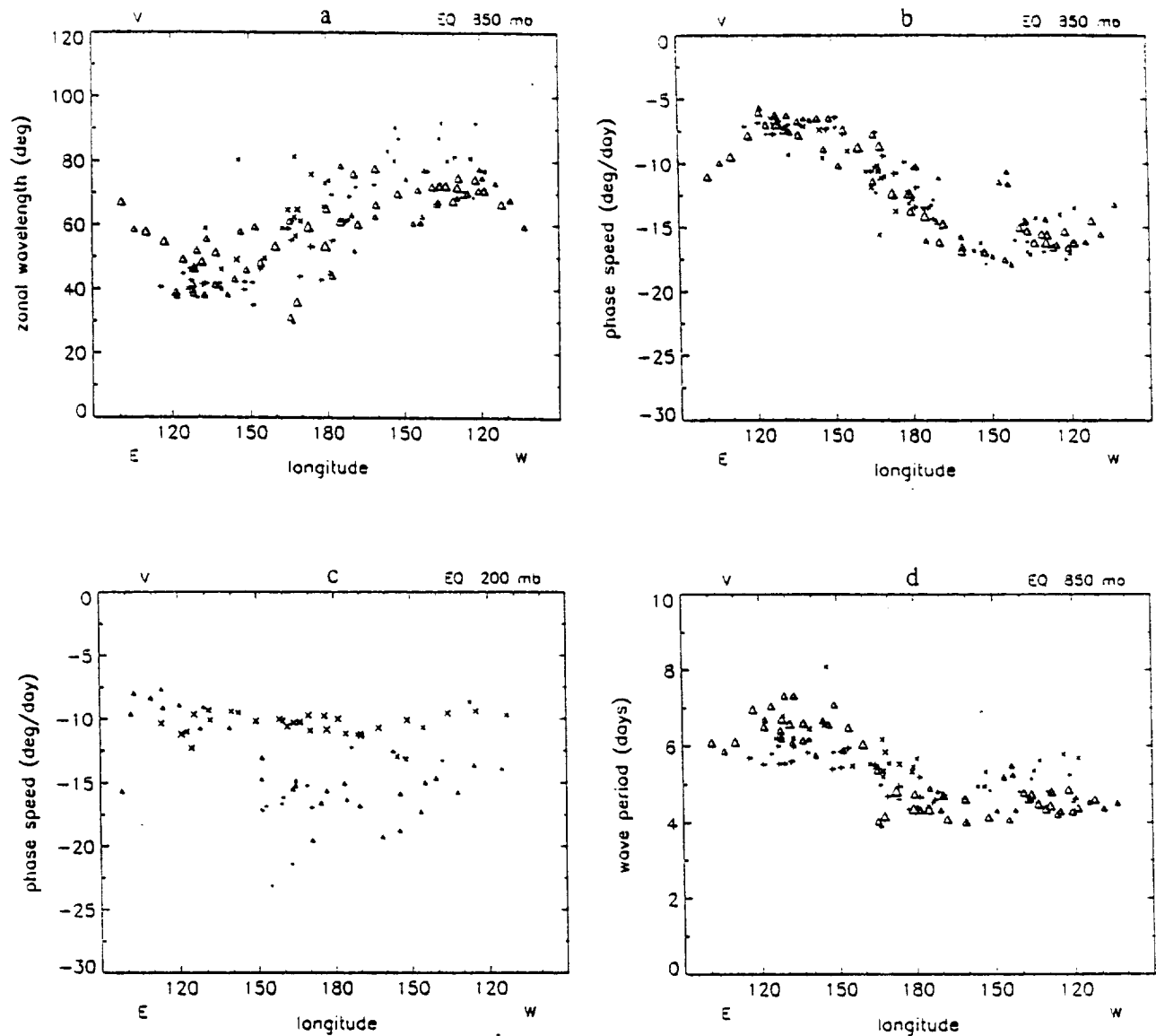


FIG. 12. Wave parameters from lag correlation analysis using principal components as reference series for rawinsonde type A (upper troposphere,  $\times$ ), rawinsonde type B (lower troposphere,  $+$ ), and horizontal EOFs from 700-mb ECMWF and OLR data ( $\Delta$ ). Symbol size is proportional to the average correlation within each cluster of points used to determine wave parameters (see Fig. 11). (a) Zonal wavelength at equator, 850 mb; (b) phase speed at equator, 850 mb; (c) phase speed at equator, 200 mb; and (d) wave period at equator, 850 mb.

ertheless, the expected symmetry was obtained (more or less) at all longitudes. Rossby-gravity EOFs, on average, had a negligible horizontal momentum flux correlation ( $\overline{u'v'} \approx 0$ ). The TD disturbances had a large positive correlation—much larger, in fact, than midlatitude baroclinic waves in the same EOF calculation.

Vector plots of  $(u', v')$  lag correlation were similar to those illustrated by Liebmann and Hendon (1990), Hendon and Liebmann (1991), and Takayabu and Nitta (1993) in the western and central Pacific, so there is no need to show them again here. In the eastern Pa-

cific, the Rossby-gravity structure was like that of the central Pacific, with weak coupling to OLR north of the equator.

### 5. Seasonal and interannual variations

Time series of quadrature power from rawinsonde type B EOFs and 700-mb ECMWF and OLR EOFs are shown in Figs. 14a,b, respectively. The calculation of  $Q(\chi_1, \chi_2)$  between coherent principal components  $\chi_n$  was described in section 5 of D93. One value of  $Q$  was plotted every 32 days and was obtained within a sliding (overlapping) window of length 128 days.



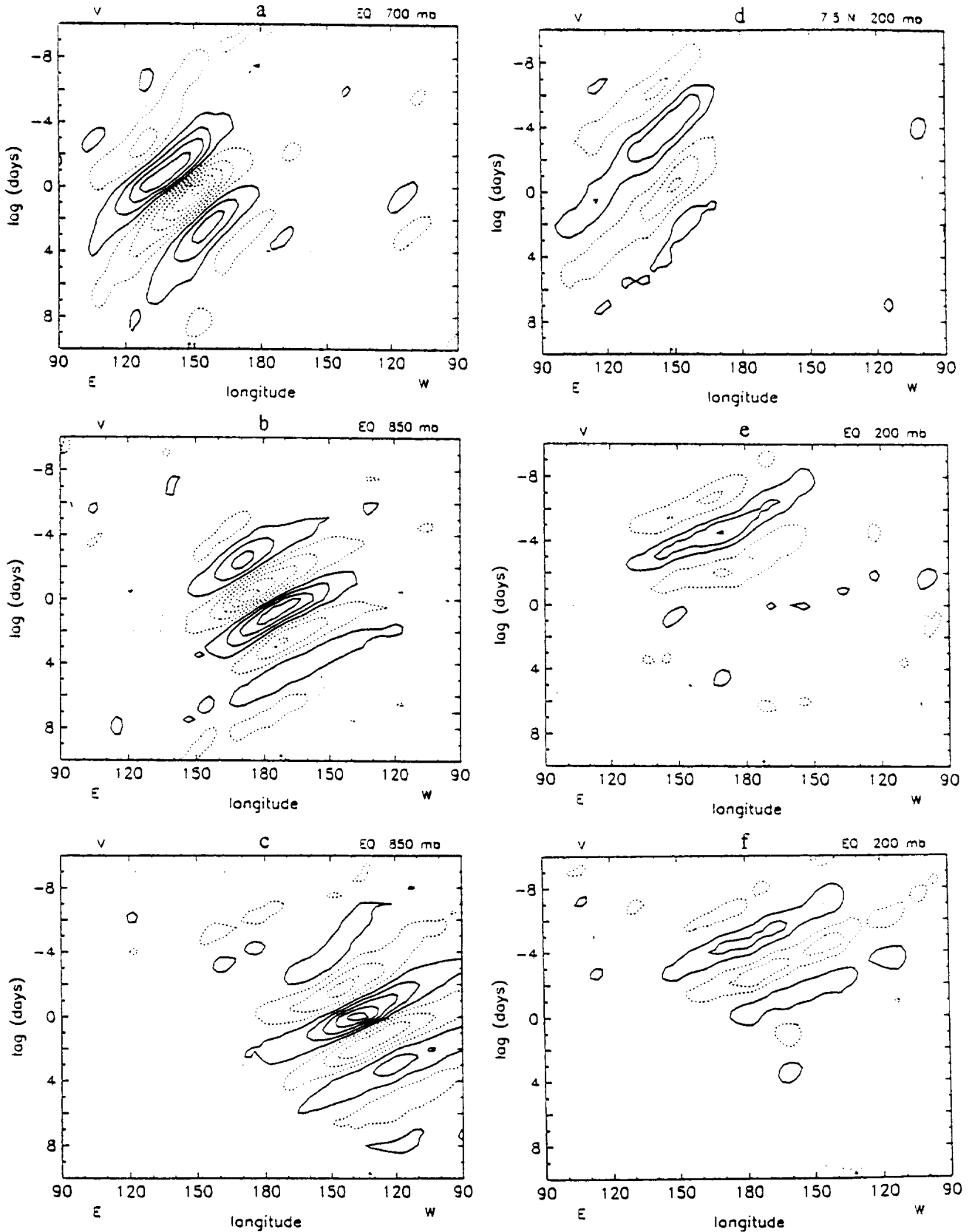


FIG. 13. Lag correlation of meridional wind as in Fig. 10, comparing lower troposphere [(a), (b), (c)] and upper troposphere [(d), (e), (f)] in western [(a), (d)], central [(b), (e)], and eastern [(c), (f)] Pacific. Reference series were obtained from horizontal EOFs of 700-mb ECMWF and OLR data; arrow at bottom of plot indicates the center of ECMWF subgrid used to generate the EOF and corresponding principal component time series. Contour interval is 0.10 in (a), (b), (c), 0.05 in (d), (e), and (f), starting at  $\pm 0.05$ .

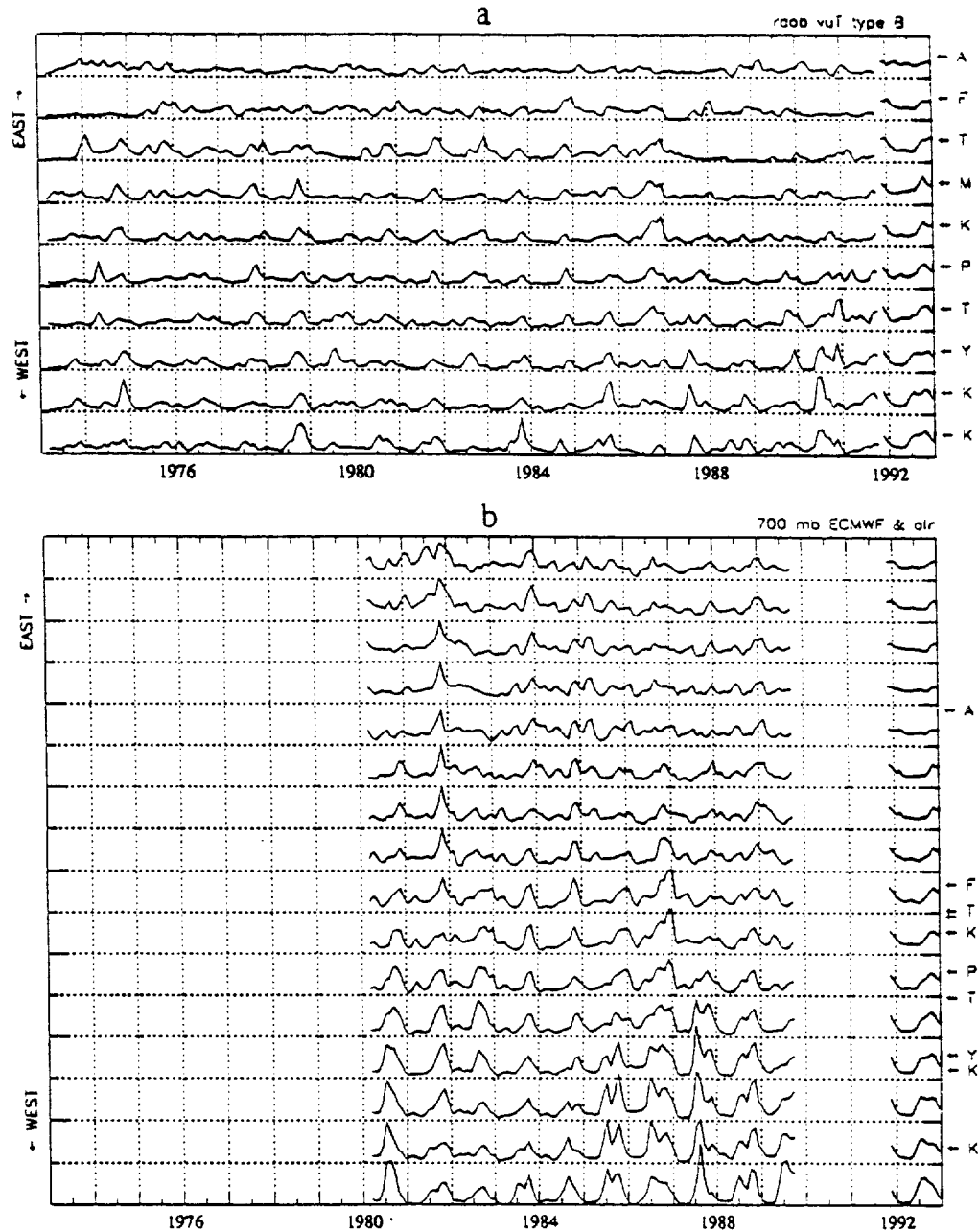


FIG. 14. Time series of quadrature power determined from (a) rawinsonde and (b) 700-mb ECMWF and OLR principal components. Average seasonal cycle is shown at far right (heavy lines). In (a), stations are displayed from western Pacific (bottom) to eastern Pacific (top) as listed in Table 1 of D93. In (b), ECMWF subgrids are displayed from western Pacific (bottom) to eastern Pacific (top) at  $10^\circ$  intervals, beginning at  $107.5^\circ$  E. Station locations are indicated by arrows on the right of (b) for comparison to (a). The date line is near Funafuti (F,  $179.2^\circ$  E).

The average seasonal cycle is also shown (heavy lines). For clarity, the rawinsonde seasonal cycle was magnified by a factor of two, and 1992 was omitted. Although seasonal variations in either dataset were by no means constant from year to year, it is apparent that dominant waves in the lower troposphere maximized in Northern Hemisphere (NH) summer, autumn, and

winter in the western, central, and eastern Pacific, respectively. There was excellent agreement between the two datasets in this respect.

To summarize what has been suggested by earlier authors, the summer maximum in western Pacific is consistent with the time of overall warmest SST, while the autumn maximum in central Pacific reflects the ap-

pearance of twin SST maxima straddling the equator (Hendon and Liebmann 1991). The TD disturbances are strongly coupled to convection (Takayabu and Nitta 1993) but do not require a particular SST pattern. Rossby-gravity waves in the central Pacific are more loosely coupled and apparently prefer off-equatorial SST maxima (Hendon and Liebmann 1991). According to the Sadler et al. (1987) atlas, the SST contrast between the equator and  $\pm 10^\circ$  latitude is strong in NH autumn (NH winter) in central (eastern) Pacific; this may explain the tendency for eastern Pacific waves to maximize a little later than central Pacific waves (Fig. 14b). We note, however, that most of the eastern Pacific activity could be traced back to the central Pacific, in accord with the apparent group propagation discussed in section 4. Thus, in a climatological sense, in situ excitation of convectively coupled Rossby-gravity waves in the eastern Pacific is unlikely when compared to the central Pacific.

Interannual variations are also apparent in Fig. 14. While there was modest agreement between the two datasets during large events (e.g., 1981 and 1986 in central Pacific, 1985 in western Pacific), the rawinsonde series were noisier, and peak to peak climatological variation were smaller, than the ECMWF/OLR series. This is to be expected since the rawinsonde value is a point measurement (as opposed to a spatial PC representing many grid points) and some spatial-temporal smoothing is inherent in the ECMWF analysis scheme.

Takayabu and Nitta (1993) suggested that ENSO modulates the lower-tropospheric waves so that equatorial waves are preferred (relative to TD disturbances) in years of relatively cold equatorial SST, and vice versa, even within the same geographical region. Although there is evidence of interannual variation in Fig. 14, it would be better to document this variability using an *evolutive principal component analysis* in which EOFs change slowly in time (D93) instead of remaining fixed to the climatological structures discussed here.

## 6. Conclusions

Twenty years of rawinsonde data (1973–1992) were examined in conjunction with ECMWF analyses and outgoing longwave radiation (OLR) in 1980–1989 to determine the horizontal structure, propagation, and convective coupling of 3–6-day meridional wind oscillations over the tropical Pacific. Wave properties from ECMWF data were consistent with what could be determined from the sparse rawinsonde network alone. There were significant correlations between the two datasets, using individual station observations or rawinsonde principal components as reference series; the latter gave useful results over a much wider horizontal area. Zonal wavelengths, phase speeds, and wave periods were determined objectively and agreed with previous estimates.

Gridded analyses allowed a clearer distinction between equatorially trapped Rossby-gravity waves and off-equatorial TD disturbances so that the contrasting properties of these waves, including their seasonal and interannual variation, could be studied in better detail. Zonal wavelengths of Rossby-gravity waves east of the date line in the lower troposphere were nearly twice that of TD disturbances in the far western Pacific, and westward phase speeds were larger by a factor of 3. Unlike TD disturbances in other sectors, the western Pacific waves had a relatively long period (6–8 days).

Significant correlations with OLR were found, increasing in magnitude from eastern to western Pacific. In the western Pacific, convection was tightly coupled to the cyclonic vortex of TD disturbances. For 700-mb Rossby-gravity waves in the central Pacific, the convection, by contrast, displayed a remarkable antisymmetric pattern with respect to the equator, consistent with low-level convergence. There was a transition zone in west-central Pacific where disturbances displayed characteristics of both. In the eastern Pacific, only the northern half of the antisymmetric OLR pattern survived and was somewhat weaker. This indicates that, on average, the lower-tropospheric waves were either too weak to organize convection in the southeast equatorial Pacific, or convection was too difficult to establish here due to unfavorable SST.

The apparent group propagation of disturbances was equatorward in the western Pacific, eastward across the central and eastern Pacific, and upward–downward out of the 150–300-mb layer. Vertical propagation was evident mainly at higher frequencies, implying that only a fraction of the kinetic energy associated with Rossby-gravity waves in the upper troposphere was involved either in convective coupling to the lower troposphere or vertical momentum transport to the lower stratosphere. A key result is that even though Rossby-gravity structures dominated the 150–300 layer throughout much of the tropics, their average characteristics (zonal wavelength, phase speed, and wave period) were sufficiently different from faster RGW in the lower troposphere and lower stratosphere so that two or three distinct EOF pairs were required to describe them (D93). Evidently a large component of meridional wind variance near 200 mb—much of it associated with Rossby-gravity waves and following a moist RGW dispersion relation (Randel 1992; Magaña and Yanai 1994)—tended to overwhelm the smaller, faster component responsible for convective coupling and vertical momentum transport. Nevertheless, we found significant correlation to 200 mb a few days *prior* to the arrival of waves in the lower troposphere and lower stratosphere. The vertical group velocity of Rossby-gravity waves is sensitive to intrinsic frequency, which may explain the trapping of lower-frequency waves.

Although our results establish a role for convectively coupled Rossby-gravity waves in the stratosphere, it is doubtful that all stratospheric Rossby-gravity waves are necessarily the result of convection since the B pattern explained only a fraction of stratospheric RGW and their seasonal variations were distinct (D93). Vertical radiation across the tropopause is expected regardless of convective coupling, leaving a role for laterally forced waves in the momentum balance of the lower stratosphere. Further investigation of this matter is desirable but outside the scope of this paper.

It was suggested that in addition to convective and lateral forcings, Rossby-gravity waves could be excited by energetic TD disturbances in the western Pacific. Rossby-gravity packets occasionally emerged eastward from a large TD event in the western Pacific. Although it is expected that individual RGW phases may act to "seed" TD disturbances since the phase propagation is westward (Takayabu and Nitta 1993), the direction of cause and effect is eastward according to linear theory. The observed group propagation was in fact eastward, but we caution that this is an apparent group velocity that, in general, must account for the role of saturation, dissipation, and (possibly) the motion of midlatitude sources.

**Acknowledgments.** The authors thank Harry Hendon for supplying OLR data in a convenient format. This research was supported by the National Aeronautics and Space Administration, Contracts NASW-4508 and NASW-4844, and by the National Science Foundation, Grant ATM-9123797.

#### REFERENCES

- Chang, C.-P., and C. R. Miller III, 1977: Comparison of easterly waves in the tropical Pacific during two contrasting periods of sea surface temperature anomalies. *J. Atmos. Sci.*, **34**, 615-628.
- Dunkerton, T. J., 1991: Intensity variation and coherence of 3-6 day equatorial waves. *Geophys. Res. Lett.*, **18**, 1469-1472.
- , 1993: Observation of 3-6 day meridional wind oscillations over the tropical Pacific, 1973-1992: Vertical structure and interannual variability. *J. Atmos. Sci.*, **50**, 3292-3307.
- Ghil, M., and K. Mo, 1991: Intraseasonal oscillations in the global atmosphere. Part I: Northern Hemisphere and Tropics. *J. Atmos. Sci.*, **48**, 752-779.
- Hack, J. J., W. H. Schubert, D. E. Stevens, and H.-C. Kuo, 1989: Response of the Hadley circulation to convective forcing in the ITCZ. *J. Atmos. Sci.*, **46**, 2957-2973.
- Hendon, H. H., and B. Liebmann, 1991: The structure and annual variation of antisymmetric fluctuations of tropical convection and their association with Rossby-gravity waves. *J. Atmos. Sci.*, **48**, 2127-2140.
- Hess, P. G., D. S. Battisti, and P. J. Rasch, 1993: Maintenance of the intertropical convergence zones and the large-scale tropical circulation on a water-covered earth. *J. Atmos. Sci.*, **50**, 691-713.
- Lau, K.-H., and N.-C. Lau, 1990: Observed structure and propagation characteristics of tropical summertime synoptic scale disturbances. *Mon. Wea. Rev.*, **118**, 1888-1913.
- , and —, 1992: The energetics and propagation dynamics of tropical summertime synoptic-scale disturbances. *Mon. Wea. Rev.*, **120**, 2523-2539.
- Liebmann, B., and H. H. Hendon, 1990: Synoptic-scale disturbances near the equator. *J. Atmos. Sci.*, **47**, 1463-1479.
- Magaña, V., and M. Yanai, 1995: Mixed Rossby-gravity waves triggered by lateral forcing. *J. Atmos. Sci.*, **52**, 1473-1486.
- Mapes, B. E., and R. A. Houze Jr., 1993: Cloud clusters and superclusters over the oceanic warm pool. *Mon. Wea. Rev.*, **121**, 1398-1415.
- Maruyama, T., 1991: Annual variations and QBO-synchronized variations of the equatorial wave intensity in the lower stratosphere at Singapore during 1961-1989. *J. Meteor. Soc. Japan*, **69**, 219-232.
- Nakazawa, T., 1988: Tropical super clusters within intraseasonal variations over the western Pacific. *J. Meteor. Soc. Japan*, **66**, 823-839.
- Nitta, T., 1970: Statistical study of tropospheric wave disturbances in the tropical Pacific region. *J. Meteor. Soc. Japan*, **48**, 47-59.
- , and Y. Takayabu, 1985: Global analysis of the lower tropospheric disturbances in the tropics during the northern summer of the FGGE year. Part II: Regional characteristics of the disturbances. *Pure and Appl. Geophys.*, **123**, 272-292.
- , Y. Nakagomi, Y. Suzuki, N. Hasegawa, and A. Kadokura, 1985: Global analysis of the lower tropospheric disturbances in the tropics during the northern summer of the FGGE year. Part I: Global features of the disturbances. *J. Meteor. Soc. Japan*, **63**, 1-19.
- Randel, W. J., 1992: Upper tropospheric equatorial waves in ECMWF analyses. *Quart. J. Roy. Meteor. Soc.*, **118**, 365-394.
- Sadler, J. C., M. A. Lander, A. M. Hori, and L. K. Oda, 1987: Tropical Marine Climatic Atlas, Vol. II: Pacific Ocean. Department of Meteorology, University of Hawaii Rep. UHMET 87-02.
- Takayabu, Y. N., and T. Nitta, 1993: 3-5 day period disturbances coupled with convection over the tropical Pacific ocean. *J. Meteor. Soc. Japan*, **71**, 221-246.
- Vincent, D. G., 1994: The South Pacific Convergence Zone (SPCZ): A review. *Mon. Wea. Rev.*, **122**, 1949-1970.
- Wallace, J. M., 1971: Spectral studies of tropospheric wave disturbances in the tropical western Pacific. *Rev. Geophys. Space Phys.*, **9**, 557-612.
- Yanai, M., 1975: Tropical meteorology. *Rev. Geophys. Space Phys.*, **13**, 685-710, 800-808.
- , and T. Maruyama, 1966: Stratospheric wave disturbances propagating over the equatorial Pacific. *J. Meteor. Soc. Japan*, **44**, 291-294.
- , and Y. Hayashi, 1969: Large-scale equatorial waves penetrating from the upper troposphere into the lower stratosphere. *J. Meteor. Soc. Japan*, **47**, 167-182.
- , and M.-M. Lu, 1983: Equatorially trapped waves at the 200-mb level and their association with meridional convergence of wave energy flux. *J. Atmos. Sci.*, **40**, 2785-2803.
- , T. Maruyama, T. Nitta, and Y. Hayashi, 1968: Power spectra of large-scale disturbances over the tropical Pacific. *J. Meteor. Soc. Japan*, **46**, 308-323.
- Zangvil, A., and M. Yanai, 1980: Upper tropospheric waves in the tropics, Part I: Dynamical analysis in the wavenumber-frequency domain. *J. Atmos. Sci.*, **37**, 283-298.
- , and —, 1981: Upper tropospheric waves in the tropics, Part II: Association with clouds in the wavenumber-frequency domain. *J. Atmos. Sci.*, **38**, 939-953.

# Evidence of meridional motion in the summer lower stratosphere adjacent to monsoon regions

Timothy J. Dunkerton

Northwest Research Associates, Bellevue, Washington

**Abstract.** Twenty-one years of rawinsonde data were used together with 8 years of uninitialized European Centre for Medium-Range Weather Forecasts (ECMWF) analyses to describe the climatological structure of large-scale circulations adjacent to monsoon regions in northern and southern hemisphere summers. In the upper troposphere and lower stratosphere, equatorward and poleward motions occur on the eastern and western sides of monsoon regions, respectively. It is shown that significant meridional velocities ( $>1 \text{ ms}^{-1}$ ) penetrate the lower stratosphere up to a maximum height of 50–30 mbar. Largest meridional velocities are observed in connection with the Asian monsoon in northern summer. Although evanescent in height, these motions are relatively important for horizontal transport of constituents in the summer lower stratosphere, when planetary waves are otherwise small. Asian and Mexican monsoons in this season are displaced sufficiently far from the equator, in close proximity to the tropopause break, to have a significant role in stratosphere–troposphere (S/T) exchange. The companion paper by Chen (1995) provides evidence of irreversible S/T exchange in the “upper middle world” during northern summer.

## 1. Introduction

Large changes of circulation, cloudiness, and precipitation accompany the seasonal march of the tropical and subtropical troposphere. These variations are especially prominent over the eastern hemisphere (attributed to African, Asian, and Australian monsoons) and Americas. Although complex in detail, and varying somewhat from year to year, the seasonal cycle follows a predictable course. Deep convection and rainfall occur in the summer hemisphere, attracted to the warmest land surfaces and sea surface temperature. Tropospheric circulations provide moisture for convection and are in turn driven by latent heat release. The upper tropospheric response is approximately opposite that near the surface, containing a significant cross-equatorial divergent flow, as well as rotational circulations in the subtropics adjacent to the convection. Mid-latitude jet streams are enhanced locally as part of the rotational response, with meridional transport into jet entry regions and away from jet exit regions.

Although monsoon circulations have been described in many textbooks, relatively little attention has been given to the structure of climatological circulation in the upper troposphere and lower stratosphere. For reasons that are not entirely clear, we find numerous illustrations of 200 mbar circulation in the literature, as if this level adequately described the upper tropospheric flow. Among mandatory rawinsonde levels, the 200 mbar level contains the maximum zonal wind of midlatitude jets ( $u$ ), and largest zonally averaged meridional wind at the equator ( $\bar{v}$ ); this level also provides a qualitatively correct picture of the rotational response to tropical convection. However, the magnitude of response in northern summer is generally largest in the 200–100 mbar layer, especially over Asia, and is best illustrated using 150 or 100 mbar data.

Copyright 1995 by the American Geophysical Union.

Paper number 95JD01263.  
0148-0227/95/95JD-01263\$05.00

Circulation patterns of the subtropical upper troposphere are visible in the lower stratosphere during summer, decaying rapidly with height. These circulations are able to transport constituents horizontally in the lowest layers of the stratosphere, as illustrated, for example, in the poleward dispersal of volcanic aerosol following the eruption of Mount Pinatubo [Trepte *et al.*, 1993]. Although summer monsoon circulations and quasistationary waves are evanescent in height (significant only up to approximately 20–25-km altitude), they are primarily responsible for lateral mixing of the lower stratosphere in this season, when planetary waves are otherwise small.

In a companion paper, Chen [1995] emphasizes for the first time the role of summer monsoon circulations in stratosphere–troposphere (S/T) exchange. Chen finds that isentropic mixing and S/T exchange in the “upper middle world” are significant in northern summer, in connection with Asian and Mexican monsoons. Extending the terminology of Hoskins [1991], the upper (lower) “middle world” contains surfaces of constant potential temperature  $\theta$  intersecting the tropopause above (below) the jet maximum.

The purpose of this paper is to describe the climatological circulation of the upper troposphere and lower stratosphere at the solstices, emphasizing the penetration of monsoon circulations and quasistationary waves into the lower stratosphere in the northern hemisphere during summer. Rawinsonde data for 1973–1993 are compared to analyses obtained from the European Centre for Medium-Range Weather Forecasts (ECMWF) in 1985–1992 (the data and analysis methods are described in section 2). The upward penetration is more dramatic in northern summer (section 3) and displaced farther from the equator, in comparison to southern summer (section 4). Variability of monthly means is discussed briefly in section 5.

## 2. Data Analysis

Rawinsonde wind and temperature data for January 1, 1973, through November 6, 1993, were used in this study. Mandatory

level data were subject to quality control and linearly interpolated to 4 times daily as described by Dunkerton [1993]. The mandatory levels are 1000, 850, 700, 500, 400, 300, 250, 200, 150, 100, 70, 50, 30, 20, and 10 mbar. For monthly means, a minimum of eight soundings per month were required. For each station's climatology, a minimum of four Januarys, four Februarys, etc., were needed in order to be included in the analysis. Stations selected for study met one of two criteria: (1) having a minimum of 90,000 data records (one record is equivalent to wind or temperature data reported at a single pressure level), or (2) having a minimum of 45,000 data records and more records than any adjacent station in a  $10^\circ \times 2^\circ$  grid box. At least 1000 wind observations at the 200 mbar level were required in either case. Altogether, 971 stations were selected in this time period. Most were in the first category; all stations in this category were used regardless of station density.

Rawinsonde analyses were constructed by mapping station climatologies onto a  $10^\circ \times 2^\circ$  grid using Barnes' algorithm [Daley, 1991] with anisotropic weight function  $\exp -r$ , where  $r^2 = (x/L_x)^2 + (y/L_y)^2$ . The eccentricity of ellipse  $R_f = L_x/L_y$  was determined for a particular variable  $f (= u, v, T)$  by the ratio of rms latitudinal gradient to rms zonal gradient, using uninitialized ECMWF climatological data as a guide, such that  $1 \leq R_f \leq 5$ . The area of ellipse  $\pi L_x L_y$  was held constant, equal to that of a circle with radius  $6^\circ$  at the equator. This value gave a reasonable compromise between analysis coverage (requiring large radius) and small-scale structure (requiring small radius). To compensate for station density, the weight function at a particular station was reduced by a factor equal to the number of adjacent stations within a normalized distance  $r = 1$ . Two iterations were applied after the first guess. The choice of weight function and other nuances are unimportant for analysis near stations since the iteration is guaranteed to converge to the station values at their respective locations. Analysis between stations is more realistic with anisotropic weighting, particularly for zonal wind and temperature which have strong latitudinal gradients near jet streams. This procedure gave good overall agreement with ECMWF climatology, except for slightly smoother fields. In regions where no stations were nearby, such that the sum of all weights fell below some threshold, rawinsonde analysis values were discarded. Latitude-height cross sections integrated over a range of longitudes are therefore incomplete if analysis values are "missing." This problem is unavoidable in certain regions, such as the eastern Pacific and southern midlatitudes, but does not affect any of the conclusions in this paper.

Uninitialized ECMWF analyses on a  $2.5^\circ \times 2.5^\circ$  grid were obtained as monthly means for 1985–1992 and averaged to yield climatological fields for each level and month. Identical mandatory levels were used except for 20 mbar which was unavailable. Stratospheric analyses prior to June 1986 were discarded for reasons explained by Trenberth [1992]. Comparison with climatologies derived from initialized ECMWF fields for 1980–1989 showed good agreement, although the uninitialized fields had slightly more variance at the smallest horizontal scales.

When comparing rawinsonde and ECMWF climatological analyses, recall that rawinsonde analyses were formed from station climatologies, regardless of when a particular station was in operation, whereas ECMWF climatologies were obtained from twice-daily analyses using a subset of these stations (and others) at any one time, together with other input data such as aircraft reports, satellite radiances, and cloud winds.

Because of possible trends in the data, as well as different sampling times, observational input and analysis techniques, exact agreement between rawinsonde and ECMWF climatologies should not be expected. For the purposes of this paper, they agree well and may be used interchangeably.

### 3. Climatology: Northern Summer

#### 3.1. Regions of Strong Meridional Flow

Figures 1 and 2 show the zonal and meridional components of velocity at 150 mbar for July, derived from ECMWF analyses for 1985–1992. In the summer hemisphere we notice two concentrated positive  $v$  maxima over western North America and eastern Mediterranean. Comparable values are attained in June and August. In June, another positive maximum is located off northwestern Africa. This feature is reduced by midsummer, as upper level easterlies encroach from the east. Negative values of meridional wind appear over eastern North America and China, complementing the poleward flow. These circulations are part of the Mexican and Asian summer monsoons, respectively, if the term "monsoon" can be used broadly to include quasistationary waves adjacent to convectively active regions. Closer inspection of Figure 2 indicates equatorward flow east of the Caspian Sea and weak poleward flow over western India. The latter occurs at the western edge of the moist Indian monsoon. As shown in section 5, this feature is quite variable from year to year. Most of the poleward diversion of mass occurs west of the Arabian peninsula, around a secondary anticyclone west of the main Tibetan anticyclone (cf. Plate III of Ramage [1971]). This concentrated maximum over the eastern Mediterranean is a robust feature of the northern summer circulation [Oort, 1983, p. 121].

The zonal component at 150 mbar for July is shown in Figure 1 from ECMWF data. Each of the positive  $u$  anomalies in Figure 2 coincides with a local acceleration of the zonal component  $u$ , including the anomaly north of India. Relatively strong speeds are attained over the Caspian Sea ( $\sim 25 \text{ ms}^{-1}$ ), although these values are weak compared to those of northern winter or southern hemisphere. The overall weakness of northern summer jets is important for isentropic mixing in the upper troposphere as discussed in section 6.

The meridional component of velocity derived from rawinsondes in 1973–1993 (not shown) is very similar to that of Figure 2. All of the features identified in Figure 2 are present. The weak poleward flow north of India in Figure 2 appears as a weakly negative local maximum. Strong positive anomalies over western North America and eastern Mediterranean are similar to those derived from ECMWF data. Examples of station climatologies near  $v$  extrema of Figure 2 are shown in Figures 3a–3e. Maximum poleward flow over the eastern Mediterranean exceeds  $12 \text{ ms}^{-1}$  in summer. Stations in the vicinity of this spatial maximum have their temporal maximum  $v$  at 150 mbar in June, July, or August. It is worth noting that the tropical easterly jet attains its maximum value over southern India at the 100 mbar level. The relatively high altitude of upper tropospheric circulations induced by the Asian monsoon suggests that Asia is the most important region for isentropic mixing and S/T exchange in northern summer [Trepte et al., 1993; Chen et al., 1994; Chen, 1995].

Of the stations shown in Figure 3, the largest stratospheric meridional winds are observed at Ankara, typical of the eastern Mediterranean. Whether the observed values at other locations are significantly large depends on the context and rel-

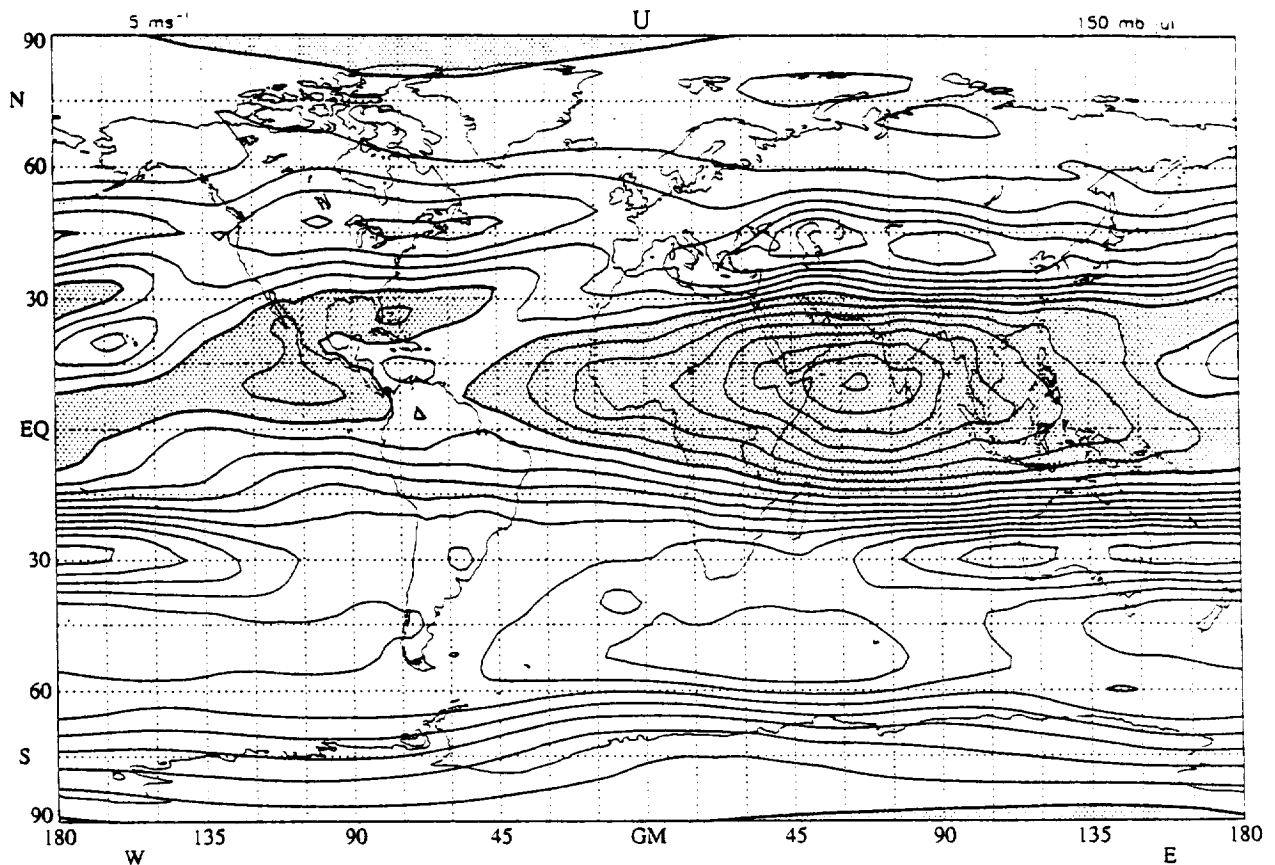


Figure 1. Zonal velocity at 150 mbar for July, derived from ECMWF data. Contour interval  $5 \text{ ms}^{-1}$ , with easterlies shaded.

active magnitude of  $u$ . Any of the local extrema of 70 mbar  $v$  (approximately  $1\text{--}3 \text{ ms}^{-1}$ ) are large compared to the zonally averaged, seasonally varying diabatic circulation at this altitude. They are also large compared to induced QBO circulations in the tropical lower stratosphere. Over North America,  $u$  and  $v$  are both smaller than over Asia, so the deflection of wind from a purely zonal direction is comparable in the two regions.

### 3.2. Asian and African Monsoons

Cross sections of zonal and meridional velocity from ECMWF data, averaged over  $16^{\circ}\text{--}46^{\circ}\text{E}$ , are shown in Figures 4a and 4b. Among the four regions of large  $v$  in Figure 2, this sector and its complement over China display the greatest penetration of meridional motions into the summer lower stratosphere. The region of maximum meridional flow at 150 mbar is slightly equatorward of the local jet maximum. The meridional component terminates abruptly poleward of  $45^{\circ}\text{N}$ . Most of the climatological northward motion at 150 mbar simply provides mass to the accelerating jet stream. Convergence of meridional velocity in this region ( $\sim 4.5 \times 10^{-6} \text{ s}^{-1}$ ) agrees well with the divergence of zonal current ( $\sim 3.9 \times 10^{-6} \text{ s}^{-1}$ ). The jet is quite narrow and pushed well poleward of its winter position; its maximum coincides with the tropopause break in this sector. The zero-wind line meanders upward through the region of largest meridional velocity before turning poleward in the lower stratosphere. We observe strong easterlies over the northern tropics in upper troposphere, extending into the southern tropics (causing a semiannual oscil-

lation, which will be discussed elsewhere). Weak surface westerlies appear north of the equator, separated from very weak westerlies in summer midlatitudes.

The profile of meridional velocity (Figure 4b) should not be confused with the Hadley circulation, although the southward (northward) Hadley flow is evident at the equator in the upper (lower) troposphere. The apparent meridional cell at  $30^{\circ}\text{N}$  is actually a quasihorizontal rotational circulation, so this feature must be compensated on the same pressure level by opposing equatorward flow at some other longitude. According to Figure 2, the return flow at 150 mbar occurs in a broad region from China eastward to the central Pacific. Much of it is concentrated over eastern China. Cross sections of ECMWF meridional flow in this region indicate that maximum negative  $v$  is located south of the jet core, with significant penetration into the lower stratosphere (not shown). As in west Asia, the zero-wind line is close to the latitude of maximum meridional velocity. Southward flow at the equator is considerably stronger in east Asia, approaching  $-7 \text{ ms}^{-1}$ . This agrees, for example, with the climatology of  $v$  at Singapore. The jet core and tropopause break are located at approximately the same latitude as on the western side of the monsoon region. Temperature in the interior of the troposphere has a local maximum at  $30\text{--}40^{\circ}\text{N}$ , coincident with zero vertical shear as required by thermal wind balance.

Cross sections of rawinsonde meridional velocity for 1973–1993 are shown in Figures 5a and 5b for western and eastern sides, respectively, of the Asian summer monsoon. Although

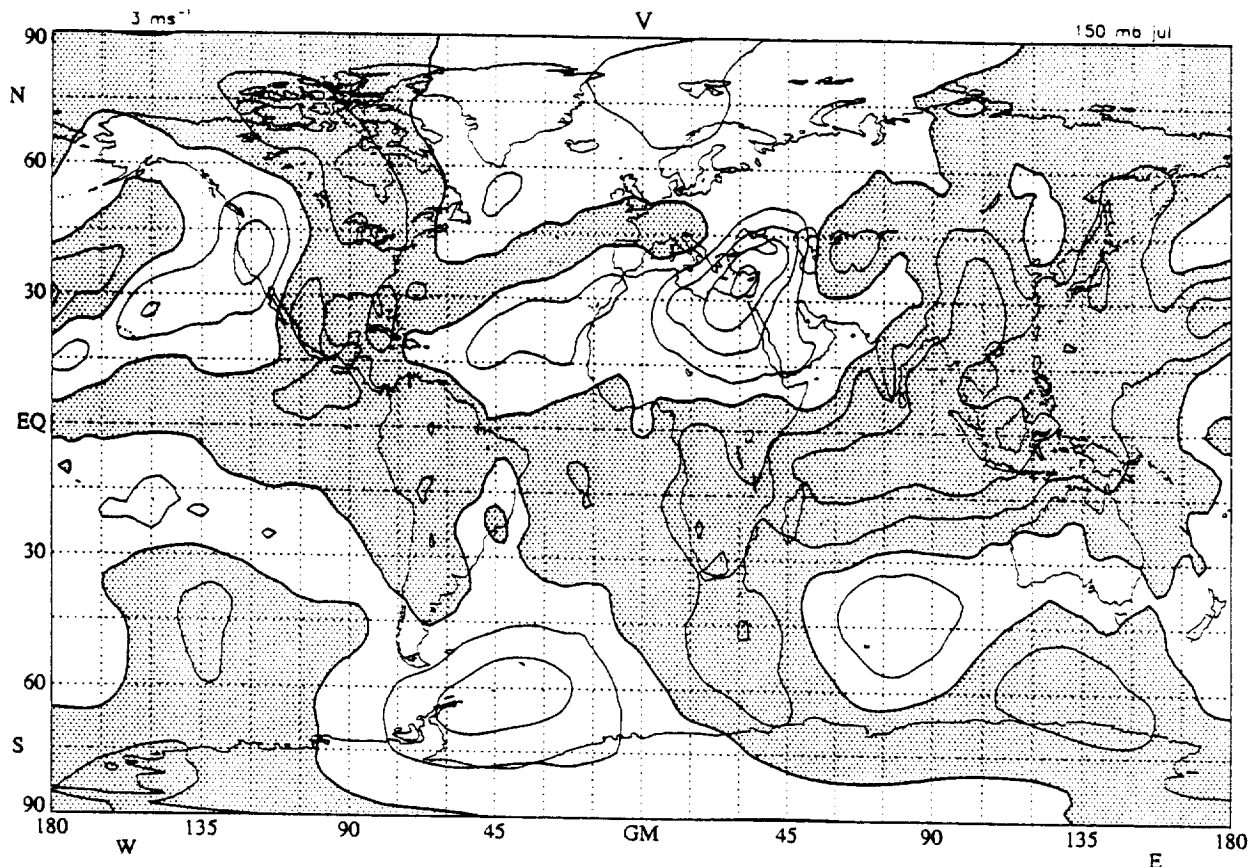


Figure 2. Meridional velocity at 150 mbar for July, derived from ECMWF data. Contour interval  $3 \text{ ms}^{-1}$ , with negative (southward) values shaded, zero contour heavy.

the data coverage at other latitudes is incomplete as noted in section 2, our main conclusions from ECMWF data are confirmed, including the stratospheric penetration. A much longer data record was used in Figure 5, providing a more stable estimate of meridional motion in the summer lower stratosphere. It is only in these two regions that the climatological meridional velocities at 70 mbar exceed  $\pm 3 \text{ ms}^{-1}$ . Zonal variations of 70 mbar zonal wind are induced by the rotational circulation at this level: for example, stronger tropical easterlies are found south of India ( $-12 \text{ ms}^{-1}$ ), compared to the western hemisphere at this latitude ( $-6 \text{ ms}^{-1}$ ).

When averaged over the entire Asian monsoon region, the meridional wind shown in Figure 6 is obtained (from ECMWF data). This sector is sufficiently wide to encompass most of the rotational circulation in upper troposphere, leaving a fairly accurate picture of the eastern hemisphere's divergent Hadley circulation. Maximum divergent flow occurs in the 150–200 mbar layer, decaying more rapidly with height than the rotational circulations that penetrate the lower stratosphere. Weak meridional cells of reversed sign are visible on either side.

During early summer there is some meridional transport over northwestern Africa (see Figure 3c) with a split zonal jet. In the north Atlantic, jet entry and exit regions occur side-by-side. ECMWF and rawinsonde  $v$  at 70–100 mbar are approximately  $1\text{--}2 \text{ ms}^{-1}$  but closer to the equator, as is the tropopause break.

### 3.3. Mexican Monsoon

Horizontal circulations associated with the Mexican monsoon and quasistationary anticyclone over North America also

penetrate the lower stratosphere during northern summer. ECMWF  $v$  at 70–100 mbar are approximately  $1\text{--}2 \text{ ms}^{-1}$  on both sides of the continent (not shown); similar values are observed in rawinsonde data (see Figure 3d and 3e). Southward flow at 150 mbar prevails over eastern North America and western Atlantic, but is smaller and less concentrated than its poleward counterpart over western North America. Jet velocities are considerably weaker than over Asia, so the relative magnitude of  $v$  is about the same in both regions.

Streamlines of horizontal wind form nearly closed circulations centered about the zero-wind line at 150 and 70 mbar, as shown in Figures 7 and 8, respectively. The streamlines are displayed in such a way as to approximate the streamfunction in regions where the flow is horizontally nondivergent. At 150 mbar, streamlines gently spiral outward due to horizontal divergence. In northern summer, one of these cells is centered over northwestern Mexico, associated with the Mexican monsoon, and a pair of cells are located over Iran and Tibet, associated with the Asian monsoon. Anticyclonic circulations at 70 mbar are slightly poleward of those at 150 mbar, by about  $8^{\circ}\text{--}12^{\circ}$ , consistent with a poleward displacement of zero-wind line in the latitude height cross section (e.g., Figure 4a). Weak convergence is evident in the anticyclones. Zonal variation of tropical easterlies can also be seen.

## 4. Climatology: Southern Summer

Meridional velocity at 150 mbar in January is largely antisymmetric about the equator, as shown in Figure 10. This situation contrasts with that of northern summer. The ten-



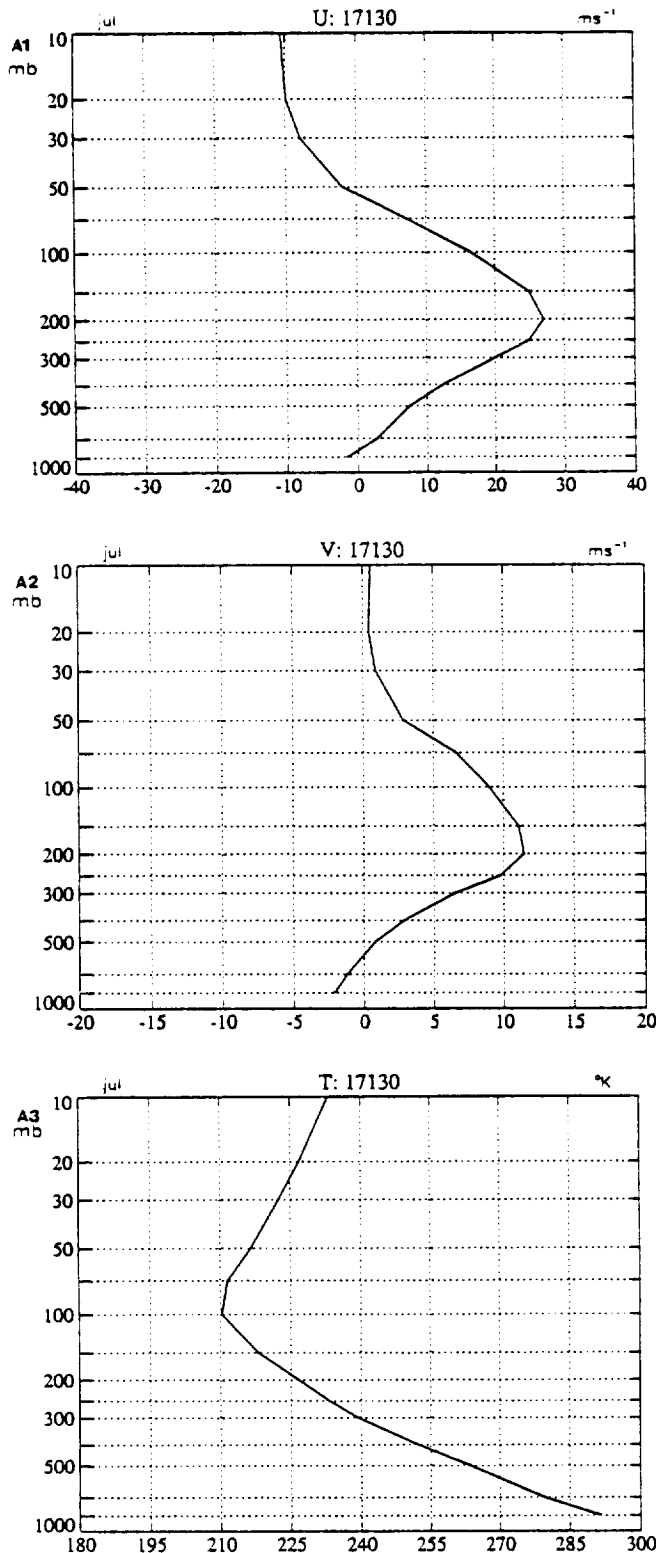


**Figure 3.** Climatological profiles of zonal wind, meridional wind, and temperature at rawinsonde stations during northern summer (June or July): (a) Ankara (40.0°N, 32.9°E), (b) Chengdu (30.7°N, 104.0°E), (c) Santa Cruz de Tenerife (28.5°N, 16.3°W), (d) Nashville (36.1°N, 86.7°W), and (e) Oakland (37.8°N, 122.2°W). Data are displayed at mandatory pressure levels only.

dency of deep convection to overlap the equator in southern summer, rather than being displaced well off the equator as in northern summer, causes the different circulation response in the two seasons. There are six potentially interesting regions of large meridional transport in the southern summer hemisphere. These are related to zonal variations of the zonal velocity component as shown in Figure 9. Rawinsonde analyses agree well, both with regard to the magnitude and location of significant anomalies (not shown). The corresponding maps for December and February are similar.

Cross sections were examined in each of the six regions. As might be inferred from comparison of Figures 9 and 10,  $v$  extrema are well removed from the jet maxima and tropopause breaks, by as much as 25°–40° latitude, except for the "eastern Australia" sector. An example of transport by the Australian monsoon circulation was discussed by *Danielsen* [1993]. Lower stratospheric  $v$  are comparable to or less than that associated with the Mexican monsoon in northern summer (not shown). The rotational circulations are also of limited horizontal extent compared to the massive Asian monsoon. Although some isentropic mixing of the southern tropical lower stratosphere seems possible in December, January, and February (DJF), significant S/T exchange is less likely in this hemisphere and season [Chen, 1995].

Upward penetration of  $v$  is slightly greater on the opposite (winter) side of the equator, but zonal jets near 30°N are considerably stronger and more concentrated than in summer (Figure 9). According to Chen, S/T exchange in the upper middle world is insignificant in either winter hemisphere, due to the strong gradient of potential vorticity associated with enhanced, concentrated zonal jets. Chen's results and ours highlight the importance of monsoon circulations and quasi-stationary waves during northern summer as discussed in the previous section.

## 5. Variability of Monthly Means

Monsoon circulations and quasistationary waves are not identical to those of the climatology in any particular year [Webster and Yang, 1992]. Interannual variations occur, some of which may be attributable to or interact with remote phenomena such as the El Niño/Southern Oscillation (ENSO) and Eurasian snow cover [Nigam, 1994]. Nor are these circulations steady for an entire season. Intraseasonal oscillations, monsoon breaks, and transient synoptic-scale disturbances cause significant day-to-day variability. The role of eddies on shorter timescales than seasonal is essential to isentropic mixing and the potential vorticity balance of the upper troposphere (section 6).

It was noted in Section 3 that the maximum poleward flow over the eastern Mediterranean occurs in each northern summer, while greater variability is observed north of India. Figure 11a shows the variability of ECMWF  $v$  at 150 mbar in July, averaged over 20°–45°N. This band encompasses the centers of maximum  $|v|$  over Asia and North America. In some years, there is a secondary maximum  $v$  near 75°E (1986, 1987, 1989, 1991) while in other years, broad regions of positive and negative  $v$  occur adjacent to one another (1985, 1988, 1992). These differences are attributable to intraseasonal as well as interannual variability, since August monthly means sometimes differ from those of July in the same year.

Variance of monthly mean  $v$  has several individual maxima from Europe eastward to the Pacific, each with rms magnitude

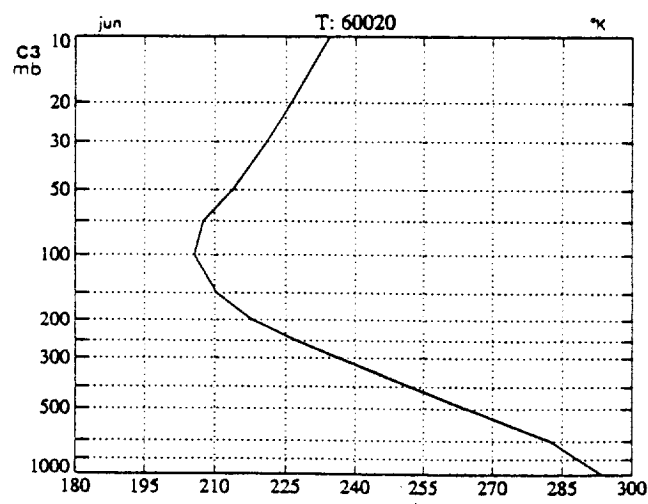
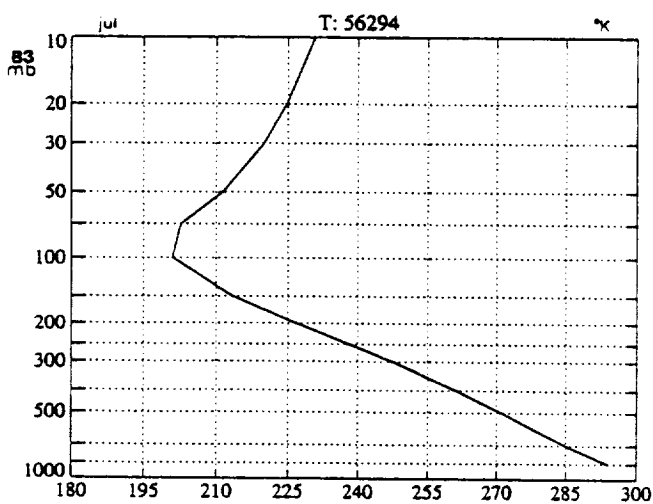
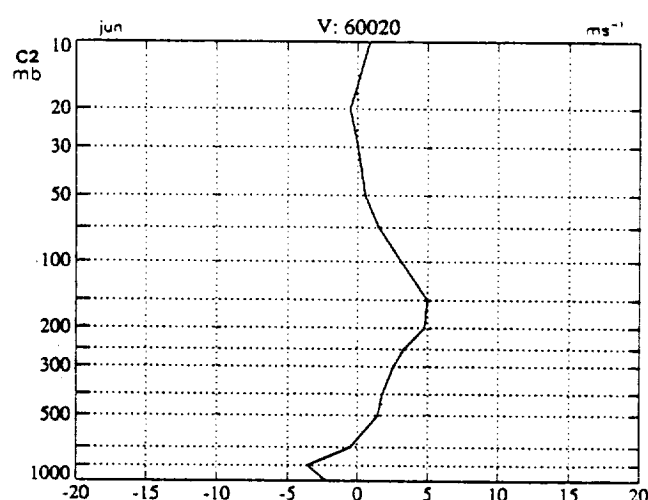
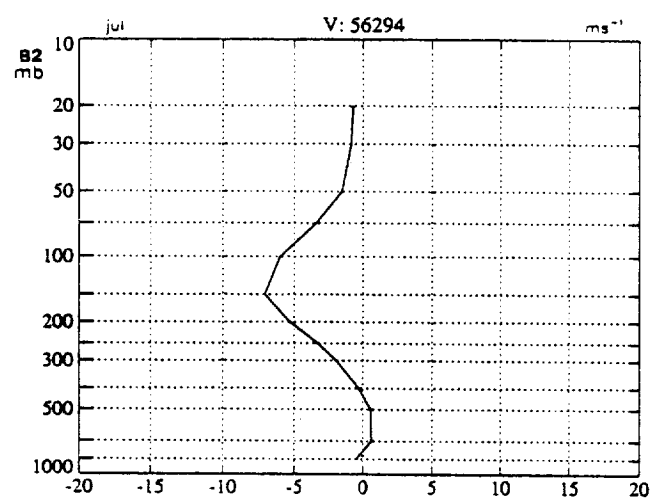
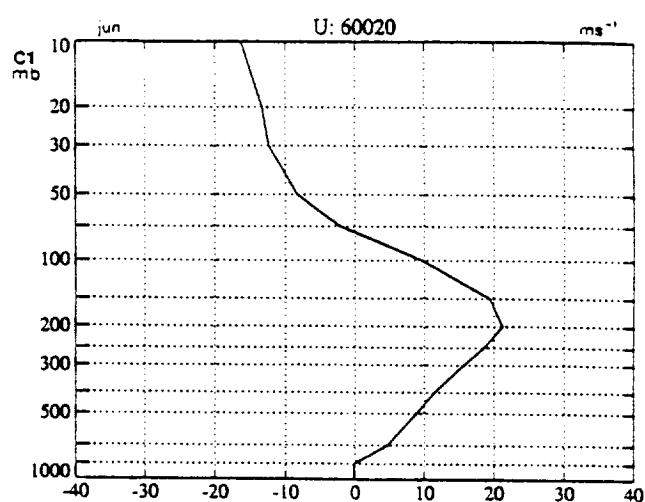
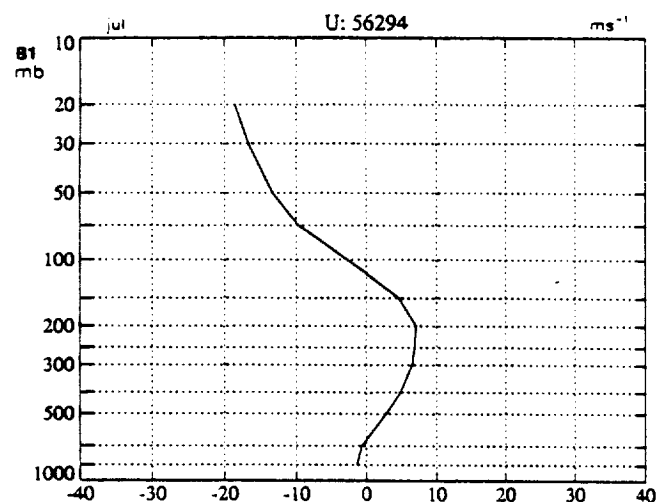


Figure 3b. Chengdu (30.7°N, 104.0°E)

Figure 3c. Santa Cruz de Tenerife (28.5°N, 16.3°W)

$\sim 4 \text{ ms}^{-1}$  (not shown). This is small compared to the climatological extrema at 150 mbar, but large within regions of smaller  $v$ , as in central Asia. We infer that climatological motions dominate meridional transport near their extrema, but inter-annual and intraseasonal variations are relatively important in central Asia and elsewhere, attaining a magnitude comparable to the climatology. Anomaly maps suggest that the variability

over central Asia is part of a well-defined teleconnection pattern extending over this region with zonal wavelength  $\sim 50^\circ$ – $60^\circ$ .

Figure 11b shows the variability of monthly mean ECMWF  $v$  at 70 mbar. Climatological extrema are apparent, and there is evidence of the same variation over central Asia as in Figure 11a (e.g., 1989). The impression gained is that these variations

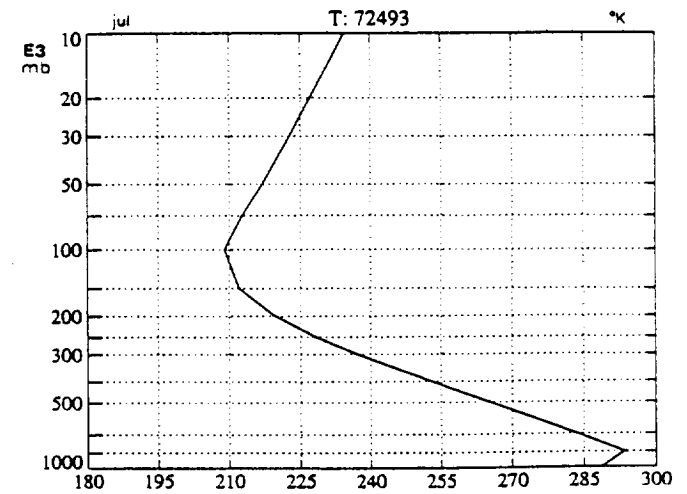
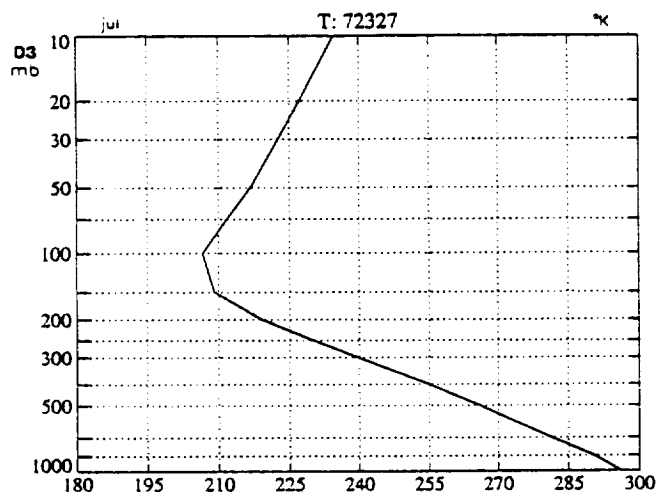
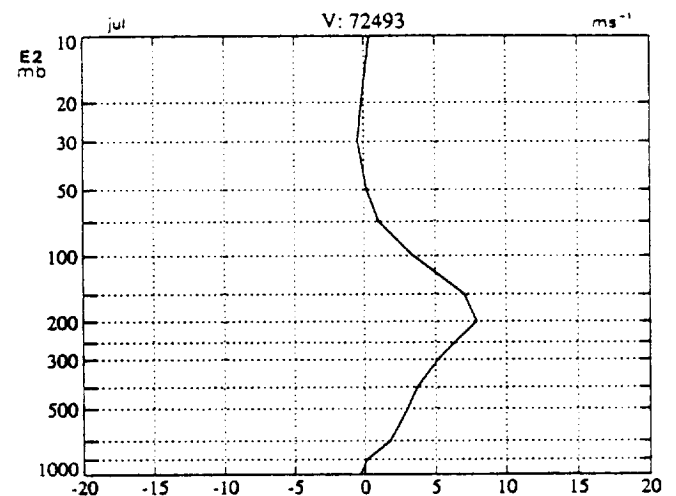
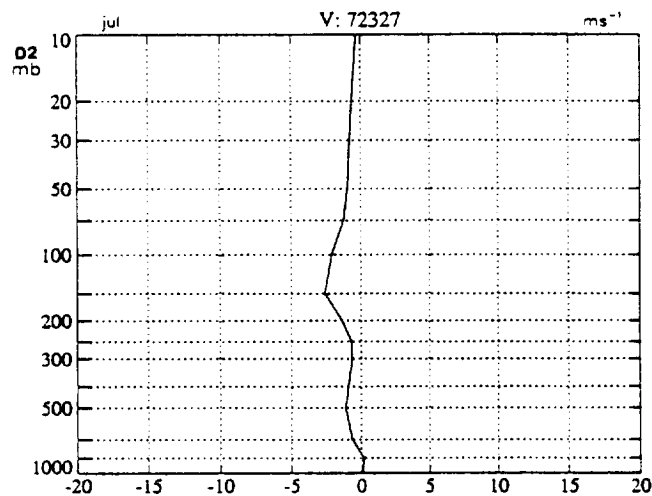
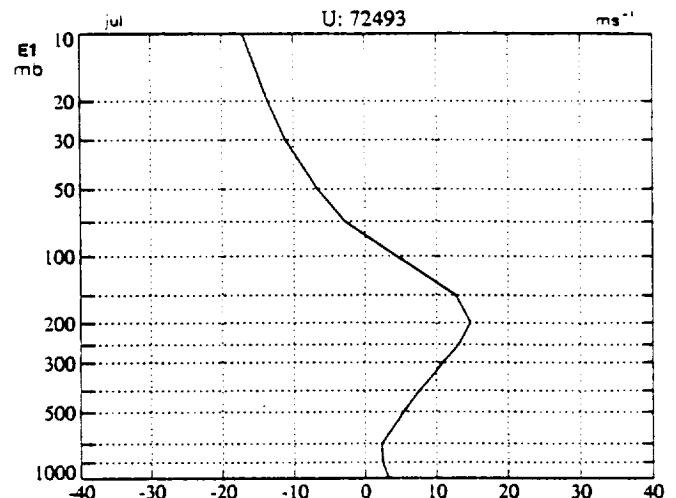
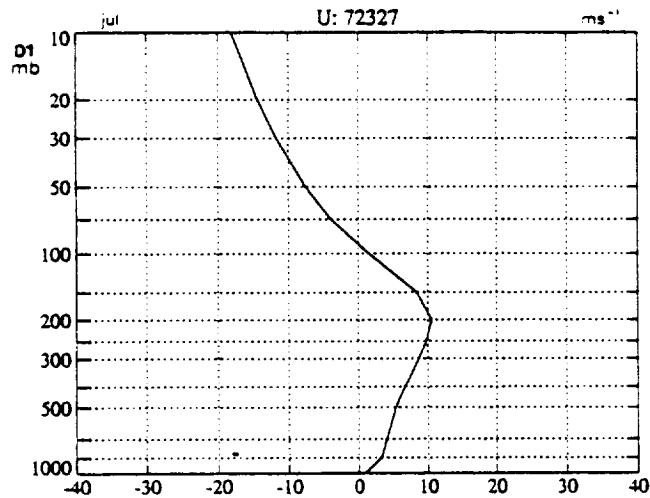


Figure 3d. Nashville (36.1°N, 86.7°W)

Figure 3e. Oakland (37.8°N, 122.2°W)

from climatology decay more rapidly with height than the climatological features, possibly due to their shorter zonal scale.

## 6. Discussion

The nearly closed anticyclonic circulations of northern summer may be likened to critical layer "cat's-eyes" associated with quasistationary Rossby waves encountering a zero-wind

line in the upper troposphere and lower stratosphere. Significant meridional parcel displacements occur in a developing critical layer because disturbances with  $\bar{u} = c$ , by definition, are stationary with respect to the fluid. Adiabatic mixing is expected within a Rossby wave critical layer, particularly if the isentropic potential vorticity (PV) gradient is weak. An example is the stratospheric "surf zone" [McIntyre and Palmer, 1984].

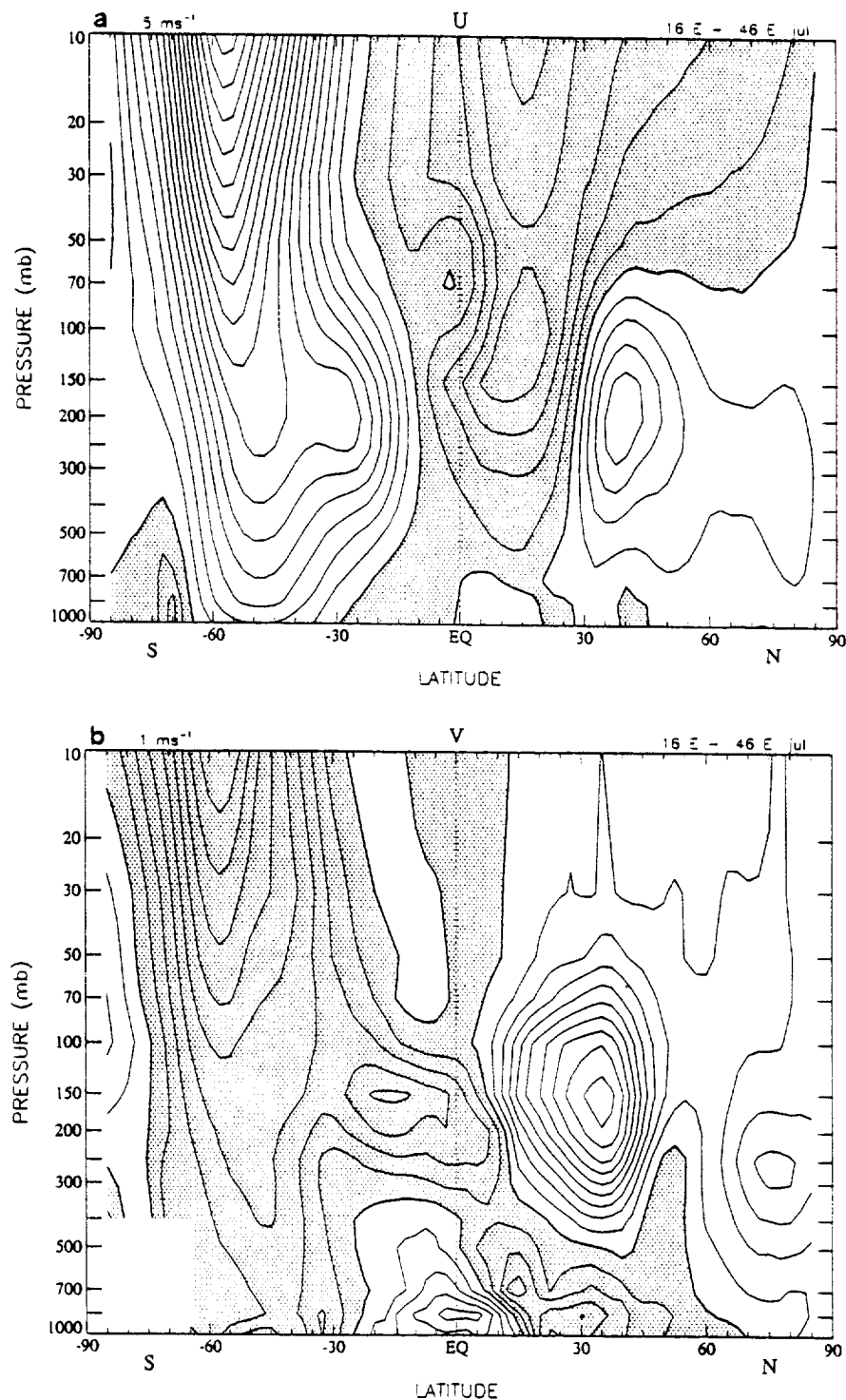


**Figure 4.** Latitude height cross sections of ECMWF (a) zonal and (b) meridional velocity for July, averaged over 16°–46°E, from ECMWF data. Contour interval 3 ms<sup>-1</sup> in (a), 1 ms<sup>-1</sup> in (b), negative values shaded.

Although important for transport, climatological monsoon circulations cannot cause isentropic mixing or S/T exchange by themselves. By definition, these circulations (including the resolved climatological PV, and conserved tracers advected by the climatological flow) undergo a steady oscillation with the seasonal cycle. Nonconservation of PV, either of coarse-grained PV due to unresolved motions, or of exact PV due to diabatic heating and molecular diffusion, is essential for irre-

versible mixing and S/T exchange. Transient eddies, even if resolved by the data, are an unresolved part of the climatology.

Three classes of transient large-scale motion are potentially important to augment the mean transport illustrated in this paper, leading to irreversible mixing and S/T exchange. (1) Fluctuations in the intensity of quasistationary monsoon circulations, along with slowly moving intraseasonal oscillations, stationary orographic waves and low-frequency variability will

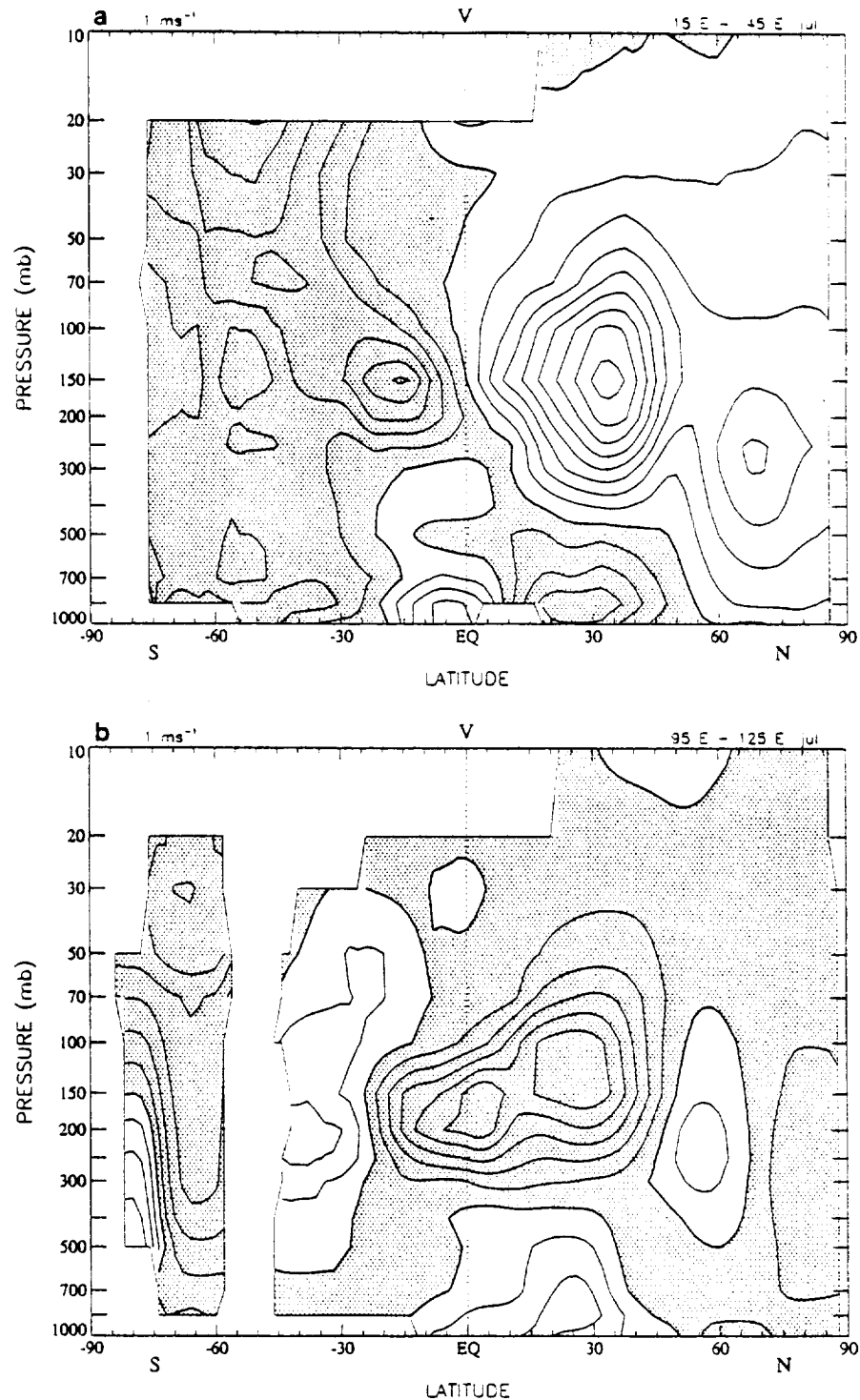


**Figure 5.** Cross sections of rawinsonde meridional velocity for July, averaged over (a) 15°–45°E; (b) 95°–125°E. Contour interval 1 ms<sup>-1</sup>.

contribute to parcel dispersion in the vicinity of climatological anticyclones that straddle the zero-wind line. The role of large-scale circulations was emphasized in the companion paper by Chen as the primary means of S/T exchange in northern summer. (2) Eastward propagating baroclinic waves originating poleward of the jet axis have critical layers in the range 5–10 ms<sup>-1</sup> and may contribute to mixing equatorward or poleward of the jet maximum. It is interesting to note that in the case of a weak jet, the critical level of eastward propagating distur-

bances crosses the tropopause break. This is unlikely for stationary waves, since the zero-wind line crosses the tropical tropopause before turning poleward. Critical layers nevertheless have finite width, so mixing caused by stationary as well as eastward propagating waves may be enhanced in the tropopause break in relatively weak zonal flow. Baroclinic systems contribute to S/T exchange in the lower middle world [Chen, 1995], where  $\theta$ -surfaces descend beneath the jet maximum. (3) Westward propagating disturbances of tropical origin are im-

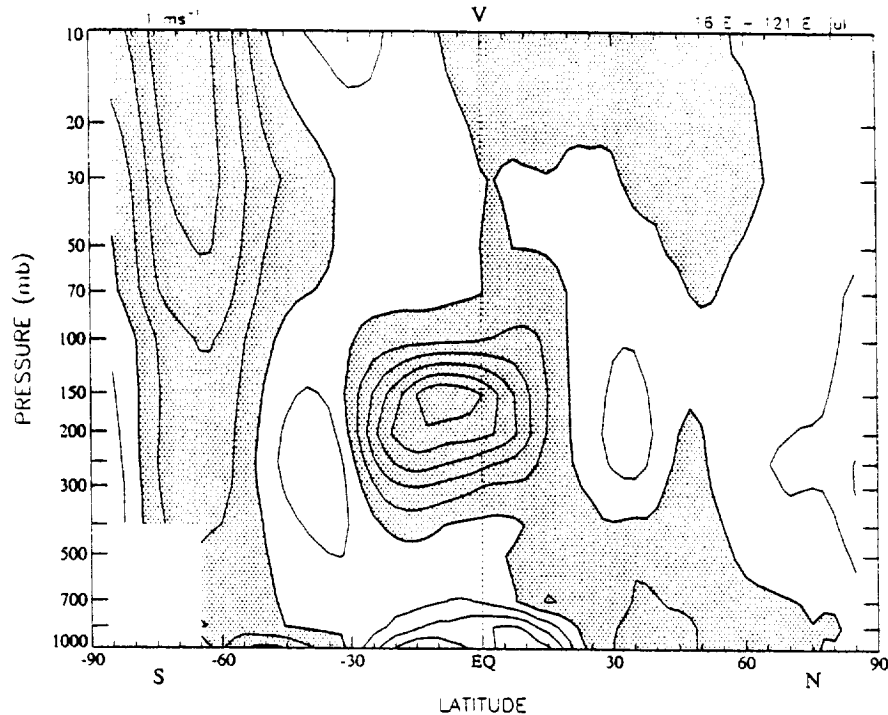


**Figure 6.** Cross section of ECMWF meridional velocity for July, averaged over 16°–121°E. Contour interval 1 ms<sup>-1</sup>.

portant equatorward of the jet maximum, being responsible for daily fluctuations of tropical motions, cloudiness, or precipitation, and contributing to isentropic and diapycnal mixing within the tropics. Of the three classes, these waves seem least likely to be involved in S/T exchange in the upper middle world. Tropical waves penetrating the lower stratosphere may contribute to isentropic mixing as observed within the first few weeks following major eruptions of tropical volcanoes.

A schematic illustration of transport in the vicinity of the jet axis and tropopause break is shown in Figure 12, representing the western side of the monsoon region. The situation portrayed is typical of northern summer, with large meridional velocities near the jet core. For the eastern side of the monsoon, the sign of mean meridional velocity (large arrow at 30°N) should be reversed. The zonal wind, tropopause, isentropic slopes, and Hadley cell are typical of the entire Asian monsoon region (16°E–121°E, July). In the upper troposphere, mean meridional motions associated with rotational circulations transport air into (out of) the jet stream on the western (eastern) side. Isentropic mixing is attributable to eddies with critical layers above, beside, or below the jet maximum. Mixing is enhanced in a relatively weak jet, when PV gradients are small (ineffective barrier) and critical layers relatively wide. Significant S/T exchange is possible across the tropopause break. By contrast, a strong jet suppresses mixing across its center due to the effective PV barrier [Chen, 1995] and discourages critical layer mixing for quasistationary or eastward propagating disturbances having zonal phase speeds in the observed range.

Apart from radiative heating, irreversible transport across  $\theta$ -surfaces is attributable to small-scale motions such as breaking gravity or inertia-gravity waves, Kelvin-Helmholtz instabilities, and latent heat release in deep moist convection. These processes act on timescales that are rapid compared to transient large-scale motions. Radiative heating operates on a

comparable timescale and has been implicated in S/T exchange [Lamarque and Hess, 1994].

## 7. Conclusion

Twenty-one years of rawinsonde data were used together with 8 years of uninitialized ECMWF analyses to describe the climatological structure of large-scale circulations adjacent to monsoon regions in northern and southern hemisphere summers. In the upper troposphere and lower stratosphere, equatorward and poleward motions occur on the eastern and western sides of monsoon regions, respectively. It was shown that significant meridional velocities ( $>1 \text{ ms}^{-1}$ ) penetrate the lower stratosphere up to a maximum height of 50–30 mbar. Largest meridional velocities are observed in connection with the Asian monsoon in northern summer. Although evanescent in height, these motions are relatively important for horizontal transport of constituents in the summer lower stratosphere, when planetary waves are otherwise small. The role of monsoon circulations in the poleward dispersal of tropical volcanic aerosol in the lower stratosphere was noted by Trepte *et al.* [1993].

Asian and Mexican monsoons in this season are displaced sufficiently far from the equator, in close proximity to the tropopause break, to have a significant role in stratosphere-troposphere (S/T) exchange. The companion paper by Chen [1995] provides evidence of irreversible S/T exchange in the “upper middle world” during northern summer.

Climatological circulations are expected to play a major role in lower stratospheric transport in all seasons and S/T exchange in northern summer. Irreversible mixing is attributable to eddies and (ultimately) nonconservation of potential vorticity. Considerably more work must be done to interpret isentropic mixing and S/T exchange, as well as their seasonal and interannual variability. Calculations such as those of Hoerling *et*

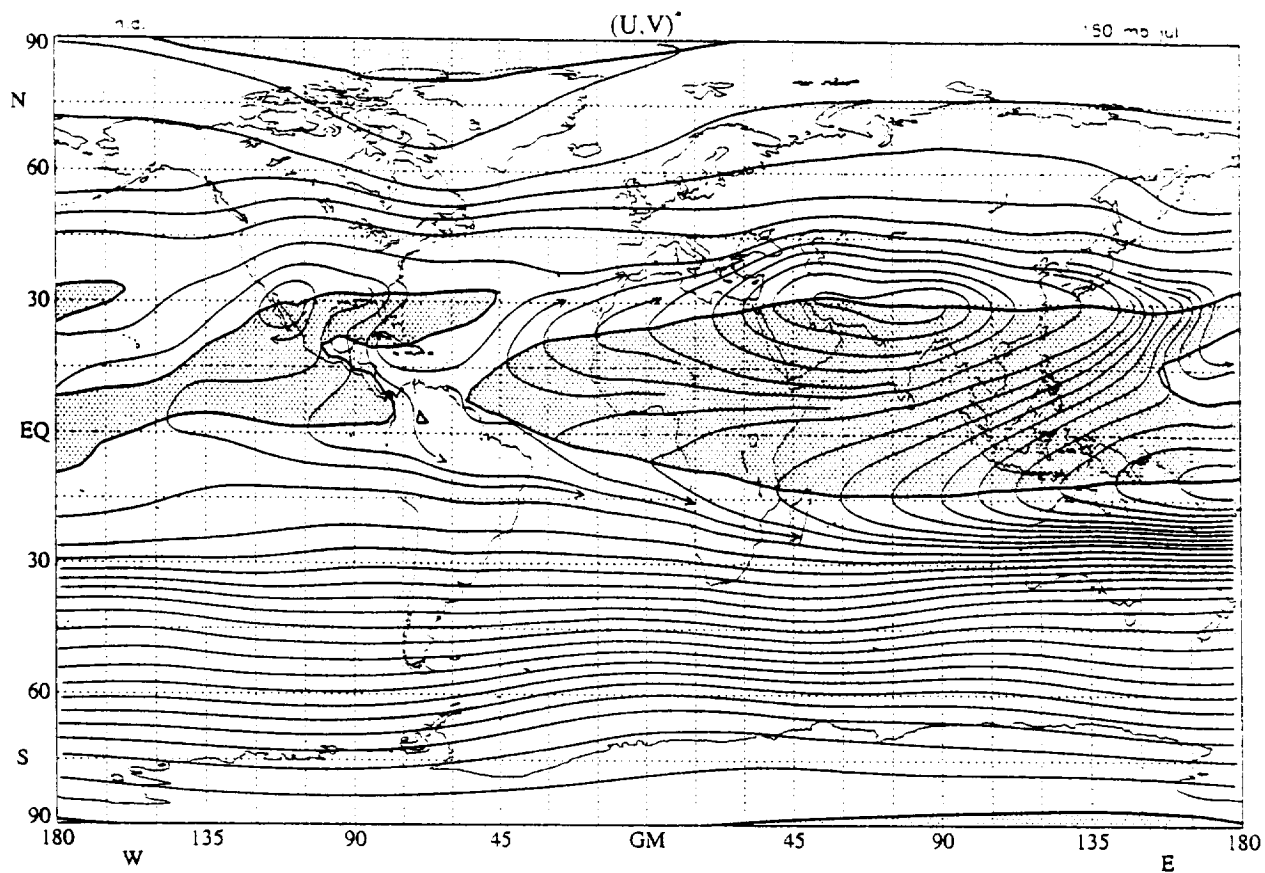


Figure 7. ECMWF streamlines at 150 mbar for July, with zero-wind line superposed. easterlies shaded.

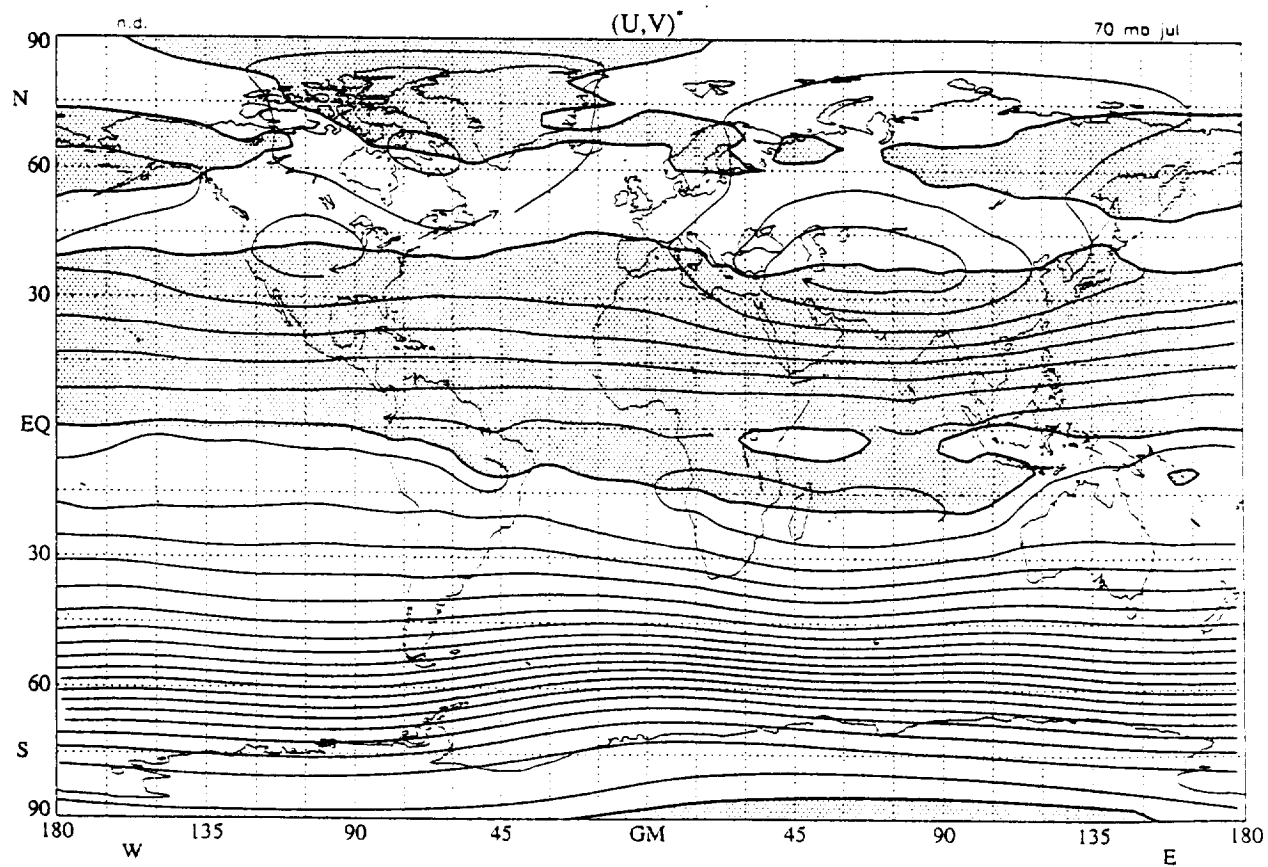


Figure 8. As in Figure 7, but at 70 mbar.

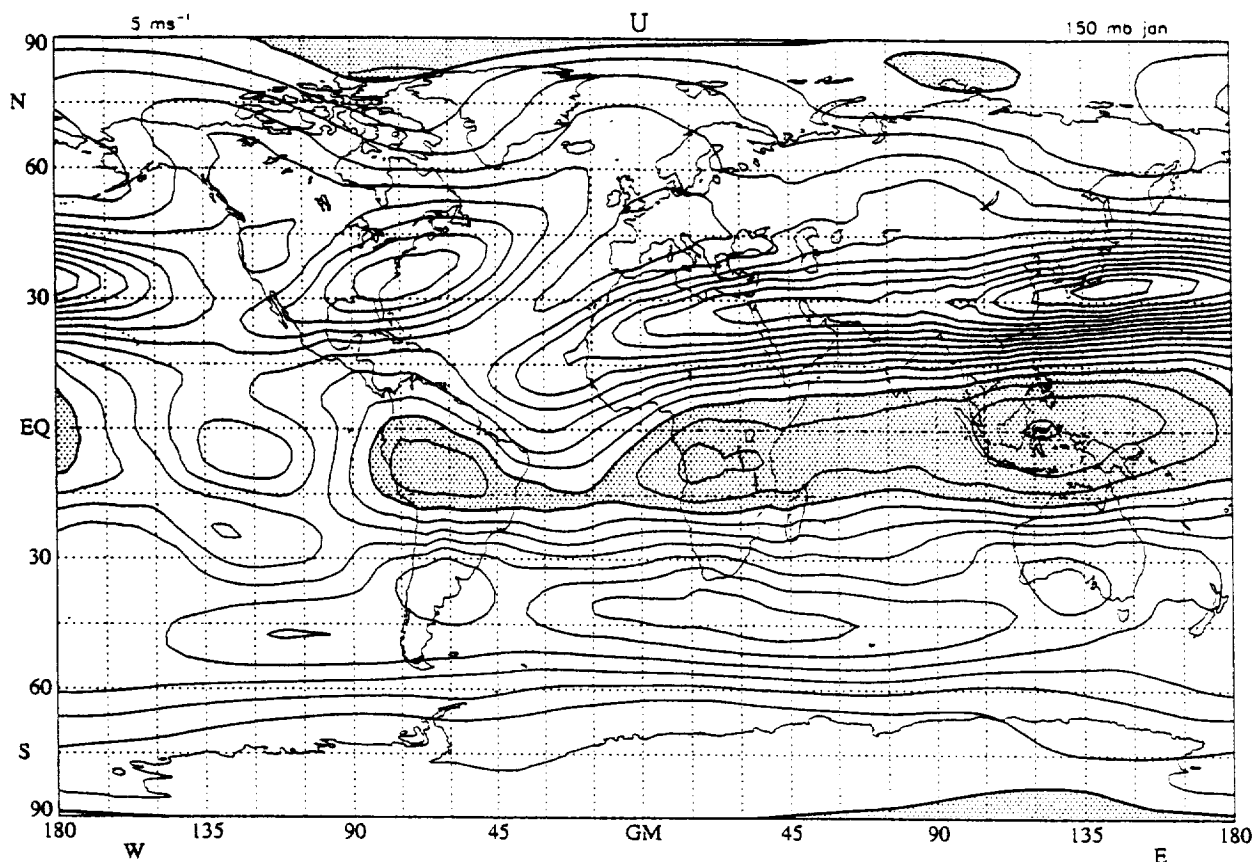


Figure 9. ECMWF zonal velocity at 150 mbar as in Figure 2, but for January.

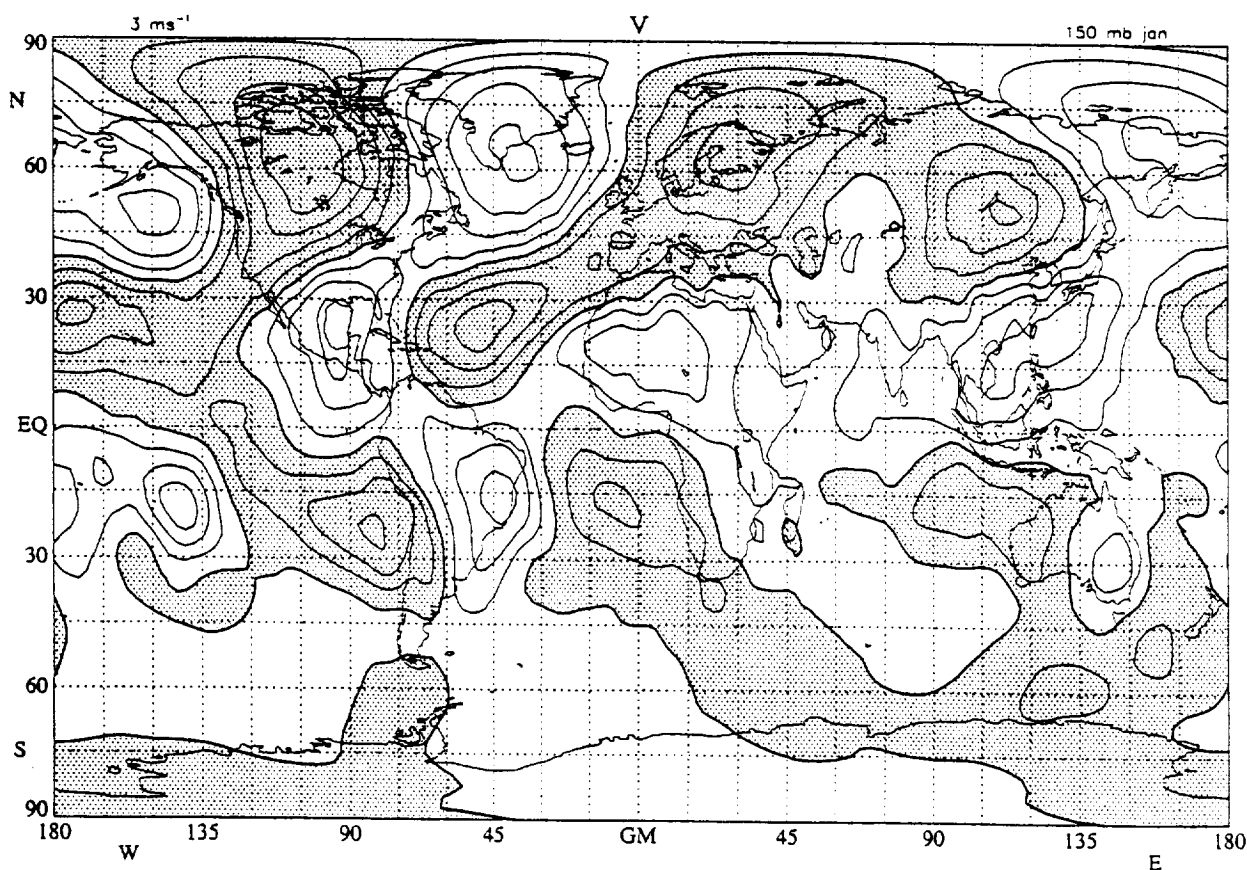


Figure 10. ECMWF meridional velocity at 150 mbar as in Figure 1, but for January.



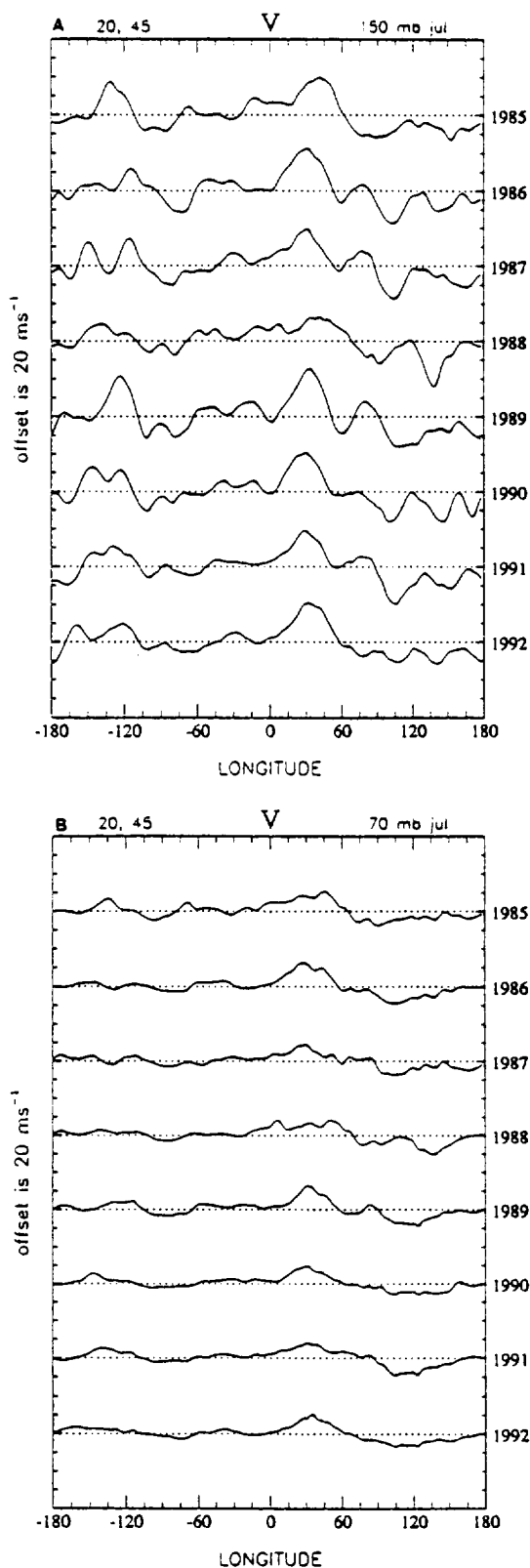


Figure 11. Variations of ECMWF monthly mean  $v$  in July, averaged over  $20^{\circ}$ – $45^{\circ}$ N. (a) 150 mbar; (b) 70 mbar.

*al.* [1993] have helped to quantify S/T exchange in extratropical latitudes. Further study of large-scale adiabatic processes that lead to S/T exchange would be valuable.

As noted by *Chen* [1995], S/T exchange associated with

Asian and Mexican monsoons is a two-way process, with tracers entering the extratropical stratosphere from the upper tropical troposphere and vice versa. The ultimate fate of tracers entering the lower stratosphere, to be sure, is also affected by diabatic descent at higher latitudes. Thus it is unclear whether monsoon transport is very important for the injection of CFCs and chemistry of the ozone layer. This transport seems more important in the vicinity of the tropopause: a region coming under scrutiny for possible effects of supersonic and subsonic aviation on stratospheric chemistry. The residence time of trace constituents and pollutants in the lower stratosphere is determined by transport processes [*Douglass et al.*, 1991] which are poorly understood or difficult to quantify. Hydration of the stratospheric middle world is apparently possible due to S/T exchange in midlatitudes (A. E. Dessler *et al.*, Mechanisms controlling water vapor in the lower stratosphere: A tale of two stratospheres, submitted to *Journal of Geophysical Research*, 1995). Transport of dehydrated stratospheric air into the tropical upper troposphere may prove important to the radiative balance of this region and terrestrial climate.

Of interest to this paper is the Rossby wave excitation and propagation associated with monsoon circulations. The summer stratosphere is relatively undisturbed because quasistationary Rossby waves require westerlies for vertical propagation [*Charney and Drazin*, 1961]. Rotational monsoon circulations and midlatitude anticyclones in summer are therefore unable to significantly influence the stratosphere above  $\sim 25$  km. The magnitude of evanescent meridional motion in the lower stratosphere is nevertheless large compared to the diabatic circulation in this region. Although such motion is essentially rotational and therefore vanishes identically in the zonal mean, its local effect on constituent transport is relatively important within the summer hemisphere, as observations of volcanic aerosol [*Trepte et al.*, 1993] and semi-Lagrangian calculations of isentropic mixing [*Chen et al.*, 1994; *Chen*, 1995] attest.

These observations invite further theoretical study of monsoon circulations and Rossby wave propagation. The role of combined latitudinal and vertical shear in Rossby wave critical layer dynamics and the nonlinear advection of angular momentum and PV caused by rotational and divergent circulations must be taken into account in order to understand the response in the upper troposphere and lower stratosphere. Nonlinear dynamics is likely to be important for the evolution of secondary vortices, such as that over the Arabian peninsula in northern summer. This feature is responsible for the extreme values of meridional velocity over the eastern Mediterranean. According to Figure 7 of *Ting* [1994], the linear response to diabatic heating explains the overall structure of Asian monsoon circulation in the upper troposphere, but stationary nonlinearity has a significant effect in certain regions, such as central Asia. Monsoon circulations over Mexico during northern summer and over South America, Africa, and Australia during southern summer illustrate flow patterns associated with more localized distributions of diabatic heating, in contrast to those associated with the massive Asian monsoon and zonally elongated intertropical convergence zones.

**Acknowledgments.** The assistance of Mark Baldwin in unpacking ECMWF data was appreciated. Discussions with Ping Chen helped shape the ideas of section 6, and provided a stimulus for timely publication of these observations. This research was supported by the National Aeronautics and Space Administration, Contract NASW-4844, and by the National Science Foundation, Grant ATM-9123797.

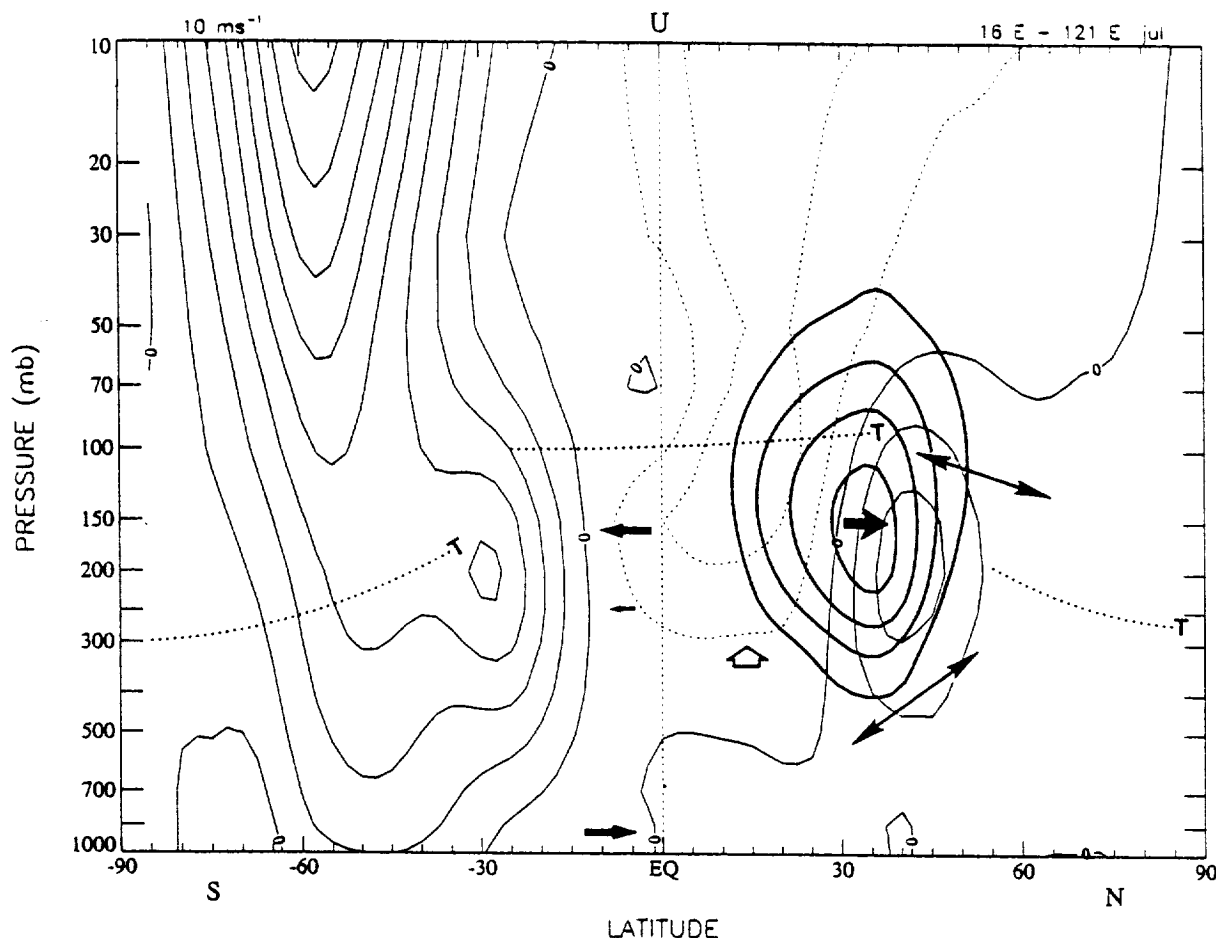


**Figure 12.** Schematic diagram of meridional transport and mixing adjacent to monsoon regions in northern summer, superposed on contours of zonal wind (interval  $10 \text{ ms}^{-1}$ ). Heavy contours (interval  $2 \text{ ms}^{-1}$ ) and one-way bold arrows indicate climatological meridional transport; two-way arrows illustrate mixing along isentropic surfaces. The large bold arrow at  $30^\circ\text{N}$  represents the western side of the Asian monsoon. Its direction should be reversed for the eastern side, where  $v$  is opposite and slightly smaller. Tropopause is shown (heavy dotted line, "T") and zero-wind line is labeled "0".

## References

- Charney, J. G., and P. G. Drazin, Propagation of planetary scale disturbances from the lower into the upper atmosphere, *J. Geophys. Res.*, **66**, 83–109, 1961.
- Chen, P., Isentropic cross-tropopause mass exchange in the extratropics, *J. Geophys. Res.*, this issue, 1995.
- Chen, P., J. R. Holton, A. O'Neill, and R. Swinbank, Isentropic mass exchange between the tropics and extratropics in the stratosphere, *J. Atmos. Sci.*, **51**, 3006–3018, 1994.
- Daley, R., *Atmospheric Data Analysis*, 457 pp., Cambridge University Press, New York, 1991.
- Danielsen, E. F., In situ evidence of rapid, vertical, irreversible transport of lower tropospheric air into the lower tropical stratosphere by convective cloud turrets and by larger-scale upwelling in tropical cyclones, *J. Geophys. Res.*, **98**, 8665–8681, 1993.
- Douglass, A. R., M. A. Carroll, W. B. DeMore, J. R. Holton, I. S. A. Isaksen, H. S. Johnston, and M. K. W. Ko, The atmosphere effects of stratospheric aircraft: A current consensus, *NASA Ref. Publ.*, **1251**, 1–39, 1991.
- Dunkerton, T. J., Observation of 3–6 day meridional wind oscillations over the tropical Pacific, 1973–1992: Vertical structure and interannual variability, *J. Atmos. Sci.*, **50**, 3292–3307, 1993.
- Hoerling, M. P., T. K. Schaack, and A. J. Lenzen, A global analysis of stratospheric-tropospheric exchange during northern winter, *Mon. Weather Rev.*, **121**, 162–172, 1993.
- Hoskins, B. J., Towards a PV- $\theta$  view of the general circulation, *Tellus* **43A**, 27–35, 1991.
- Lamarque, J.-F., and P. G. Hess, Cross-tropopause mass exchange and potential vorticity budget in a simulated tropopause folding, *J. Atmos. Sci.*, **51**, 2246–2269, 1994.
- McIntyre, M. E., and T. N. Palmer, The 'surf zone' in the stratosphere, *J. Atmos. Terr. Phys.*, **46**, 825–849, 1984.
- Nigam, S., On the dynamical basis for the Asian summer monsoon rainfall—El Niño relationship, *J. Clim.*, **7**, 1750–1771, 1994.
- Oort, A. H., Global atmospheric circulation statistics, 1958–1973, *NOAA Prof. Pap.*, **14**, 1–180, U.S. Government Printing Office, 1983.
- Ramage, C. S., *Monsoon Meteorology*, Academic, San Diego, Calif., 1971.
- Ting, M., Maintenance of northern summer stationary waves in a GCM, *J. Atmos. Sci.*, **51**, 3286–3308, 1994.
- Trenberth, K. E., Global analyses from ECMWF and atlas of 1000 to 10 mb circulation statistics, *NCAR Tech. Note, NCAR/TN-373+STR*, Natl. Cent. for Atmos. Res. Boulder, Colo., 1992.
- Trepte, C. R., R. E. Veiga, and M. P. McCormick, The poleward dispersal of Mount Pinatubo volcanic aerosol, *J. Geophys. Res.*, **98**, 18,563–18,573, 1993.
- Webster, P. J., and S. Yang, Monsoon and ENSO: Selectively interactive systems, *Q. J. R. Meteorol. Soc.*, **118**, 877–926, 1992.
- T. J. Dunkerton, Northwest Research Associates, P.O. Box 3027, Bellevue, WA 98009. (e-mail: tim@nwra.com)

(Received December 12, 1994; revised April 12, 1995; accepted April 12, 1995.)

# Eastward propagating ~2- to 15-day equatorial convection and its relation to the tropical intraseasonal oscillation

Timothy J. Dunkerton and Francis X. Crum

Northwest Research Associates, Bellevue, Washington

**Abstract.** Anomalies of outgoing longwave radiation (OLR) in 1980–1989 were examined in a narrow latitude band about the equator to elucidate the propagation and interaction of tropical intraseasonal oscillations (TIOs) and synoptic-scale convective activity. Hovmöller diagrams of OLR data reconstructed from two frequency bands (corresponding to periods of ~30–60 days and ~2–15 days, respectively) revealed a clear distinction between the phase speed of eastward moving TIOs ( $3\text{--}7\text{ m s}^{-1}$ ) and that of eastward synoptic-scale convection ( $10\text{--}13\text{ m s}^{-1}$ ). Coherent propagation of TIOs from the Indian to the western Pacific Oceans was often observed with temporary diminution of amplitude over the maritime continent. Propagation of high-frequency anomalies was generally confined to an individual basin. Dominance of eastward propagating synoptic-scale convection in the equatorial zone contrasts sharply with the westward propagation of off-equatorial convergence zones. Interaction between the TIO and high-frequency activity resolved by daily OLR was visible as a modest enhancement of eastward synoptic-scale events (and of high-frequency activity in general) during the convectively active phase of the TIO.

## 1. Introduction

The tropical intraseasonal oscillation (TIO) is an important source of variability in the Earth's atmosphere. Since its discovery by Madden and Julian [1971, 1972] and a related observation of slow Kelvin waves at 100 mbar by Parker [1973], this phenomenon has received considerable attention. Intraseasonal (~30- to 60-day) oscillations were found in various data sets, including rawinsonde zonal wind, outgoing longwave radiation (OLR), analyzed velocity potential, and stream function [e.g., Madden and Julian, 1971; Weickmann, 1983; Lau and Chan, 1985; Knutson and Weickmann, 1987]. Eastward propagating circulation anomalies are apparently coupled to regions of eastward propagating equatorial convection [Rui and Wang, 1990]. Convection anomalies attain largest amplitude over the Indian and western Pacific Oceans. Circulation anomalies extend farther east, possibly all around the equator [Knutson and Weickmann, 1987; Hendon and Salby, 1994]. There are demonstrated or postulated relationships between the TIO and monsoons [Hendon and Liebmann, 1990], tropical cyclones [Liebmann et al., 1994], El Niño/Southern Oscillation (ENSO) [Lau and Lim, 1986], and extratropical latitudes [Liebmann and Hartmann, 1984; Lau and Phillips, 1986]. Observational aspects of the TIO were recently reviewed by Madden and Julian [1994].

All of this literature may lead us to suppose that the TIO is a prominent feature in observations of tropical convection in the eastern hemisphere. In fact, the TIO is not obvious without temporal filtering of the data. Its discovery, after all, is relatively recent in the history of tropical meteorology. In unfiltered data the TIO is obscured by convection on shorter spatial and temporal scales. Figure 1 displays a 10-year record of near-equatorial daily OLR for 1980–1989 (low OLR only), on

which our remaining discussion is based. Considerable evidence of eastward propagating convection is seen at all longitudes, but this activity occurs on timescales much shorter than intraseasonal. As will be shown later, the phase speed of high-frequency activity is distinct from that of the TIO. That zonal propagation of convection resolved by daily OLR is mainly eastward near the equator contrasts sharply with off-equatorial convergence zones, where propagation of synoptic-scale convection is westward owing to tropical depression disturbances and Rossby-gravity waves [Lau and Lau, 1990, 1992; Hendon and Liebmann, 1991; Takayabu and Nitta, 1993; Dunkerton and Baldwin, 1994].

Upon closer examination, broad clumps of enhanced convection appear in Figure 1, such as around April 1980, April 1982, and January 1988, also propagating eastward but at a slower rate than the high-frequency activity. With appropriate time filtering, these events prove to be quite common but are somewhat variable from year to year. They correspond to the convectively active phase of the TIO.

The TIO's convection does not consist of a single huge cloud cluster. Instead, several smaller clusters are embedded within the convectively active phase of the TIO [Nakazawa, 1988]. On the synoptic scale, many of these equatorial clusters propagate eastward at a rate similar to that of propagating clusters during the inactive phase of TIO. The term "supercluster" (or supercloud cluster) has been applied to clusters having horizontal scales of 2000–4000 km and timescales, broadly speaking, of the order of ~2–15 days [Hayashi and Sumi, 1986; Nakazawa, 1988; Lau et al., 1991; Sui and Lau, 1992]. Superclusters are thought to be networks of mesoscale convective complexes that are so gregarious as to become spatially and temporally interconnected [Mapes and Houze, 1993]. They are one of perhaps several forms of synoptic-scale cloud organization in the tropics. Analogous to the TIO, synoptic-scale activity forms a spatial-temporal envelope for rapidly evolving mesoscale cloud clusters, many of which propagate westward [Nakazawa, 1988;

Copyright 1995 by the American Geophysical Union.

Paper number 95JD02678.  
0148-0227/95/95JD-02678\$05.00

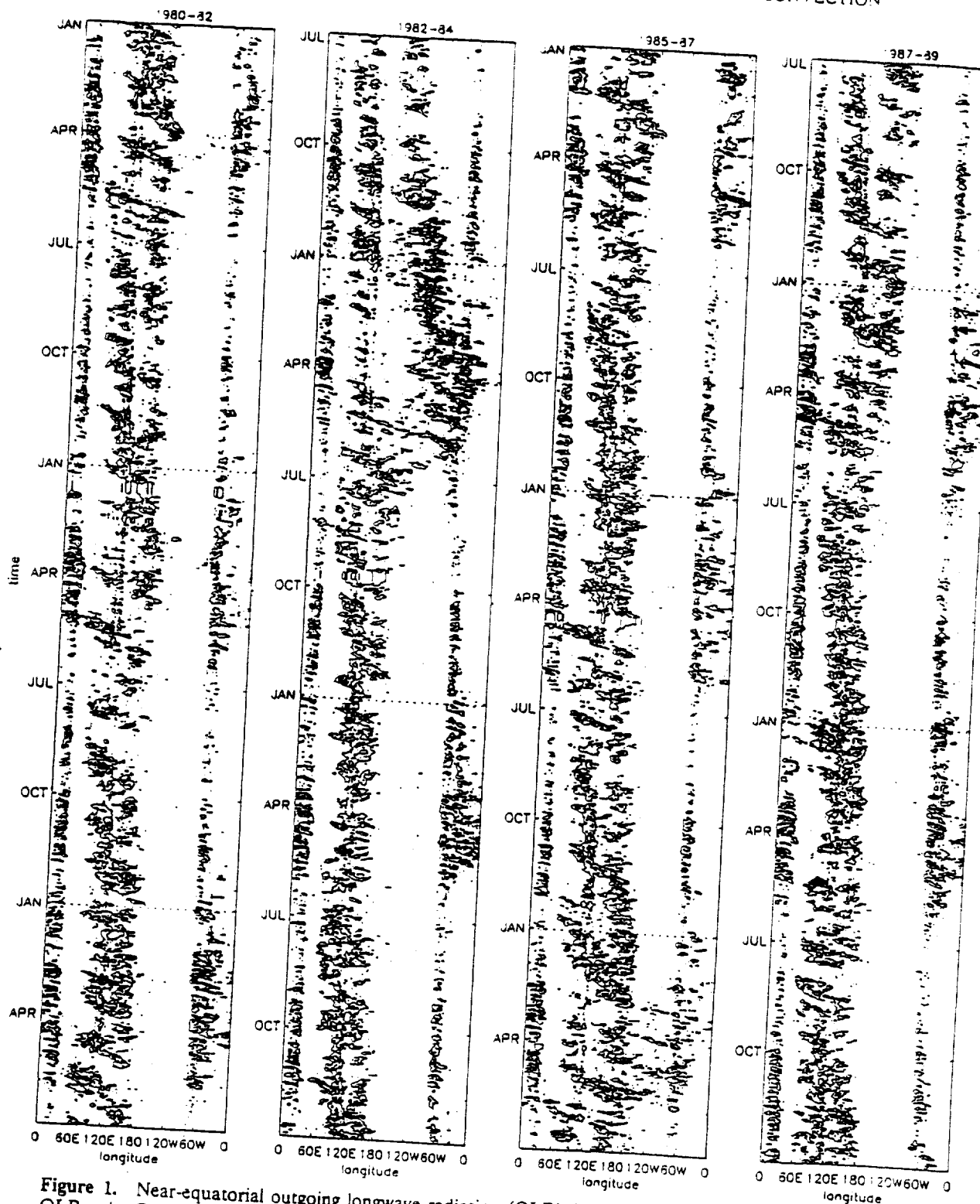


Figure 1. Near-equatorial outgoing longwave radiation (OLR) ( $2.5^{\circ}\text{S}$ – $2.5^{\circ}\text{N}$ ) for 1980–1989, showing low OLR only. Contours are 120, 160, and  $200 \text{ W m}^{-2}$ .

Lau et al., 1991; Hendon and Liebmann, 1994]. The daily OLR obtained from polar orbiting satellites cannot resolve the inner scale of synoptic activity, as the cloud imagery can, but is apparently adequate for the envelope of mesoscale convection. According to Figure 1, the synoptic-scale organization of equatorial convection is at least as important as that of the TIO.

In this paper we examine further the morphology of east-

ward propagating synoptic-scale convection near the equator and its relation to the TIO, extending the earlier discussions by Nakazawa [1986a, b]. In the first paper, Nakazawa examined OLR in the First Global Atmospheric Research Program (GARP) Global Experiment (FGGE) year (1979), investigating the role of short-period fluctuations within intraseasonal oscillations. In the second paper he used eight years of OLR

data (1975–1983 excluding 1978), documenting the behavior of low- and high-frequency convection without discussing in detail the morphology of these disturbances and their relationship. Our analysis extends these studies using 10 years of OLR data beginning in 1980. We show Hovmöller diagrams of OLR data reconstructed from the respective frequency bands (corresponding to periods of  $\sim 30$ –60 and  $\sim 2$ –15 days) to elucidate their episodic behavior and relationship in physical space. By examining eastward and westward propagating components of daily OLR separately, a spectrum of phase speeds is obtained for synoptic-scale convection events during this time period. For eastward propagating disturbances, the spectrum is sharply peaked at  $10$ – $13 \text{ m s}^{-1}$ .

## 2. Data Analysis

We used daily OLR data for 1980–1989 on a  $2.5^\circ \times 2.5^\circ$  latitude-longitude grid. To focus clearly on the latitudes of eastward propagating convection and to avoid regions of westward propagating activity in off-equatorial convergence zones, OLR data were averaged from  $2.5^\circ\text{S}$  to  $2.5^\circ\text{N}$ . Discussion is therefore limited to the zonal component of propagation along the equator, although it is recognized from Madden and Julian [1994] that a meridional component of propagation is sometimes observed. For OLR spectra (but not Hovmöller diagrams), the annual cycle was removed by calculating the mean and first three harmonics of the 10-year average annual cycle and subtracting them from the total field. Statistical significance of peaks was assessed by computing red noise spectra from the data following Gilman *et al.* [1963] and considering the signal-to-noise background power ratio as a chi-square random variable with  $2M$  degrees of freedom, where  $M$  is the number of points in the periodogram smoother. Two temporal filters were designed to separate low- and high-frequency variability associated with TIO and synoptic scales, respectively.

On the high-frequency end, spectra of daily OLR are limited to periods greater than 2 days. There is no meteorologically significant reason to exclude the shorter periods characteristic of mesoscale convection, but only the envelope of mesoscale activity is described by daily OLR. For our purpose, OLR is useful because the planetary- and synoptic-scale organization of convection is revealed. It should be kept in mind that “high-frequency OLR” here refers to disturbances in daily OLR obtained from polar-orbiting satellites, with a minimum resolvable period of 2 days.

## 3. Results

### 3.1. OLR Spectra

Average spectra of near-equatorial OLR in longitude sectors representing the Indian and western Pacific Oceans are shown in Figures 2a and 2b, respectively. The combined spectrum of both regions, including the maritime continent lying in between, is shown in Figure 2c. The OLR spectra are generally featureless except for a TIO peak near 40 days, a dip in the spectrum near 15 days, and broad power extending down to at least 3 days. The TIO is relatively more important over the Indian Ocean. This region has a shallow minimum near 15 days and broad ledge of power from 3 to 15 days. Over the western Pacific the TIO peak is again evident but weaker. A minimum near 15 days is not seen except with respect to the red noise curves. It is unclear where to divide the western Pacific spectrum, but this is not crucial to our analysis. Several sharp peaks

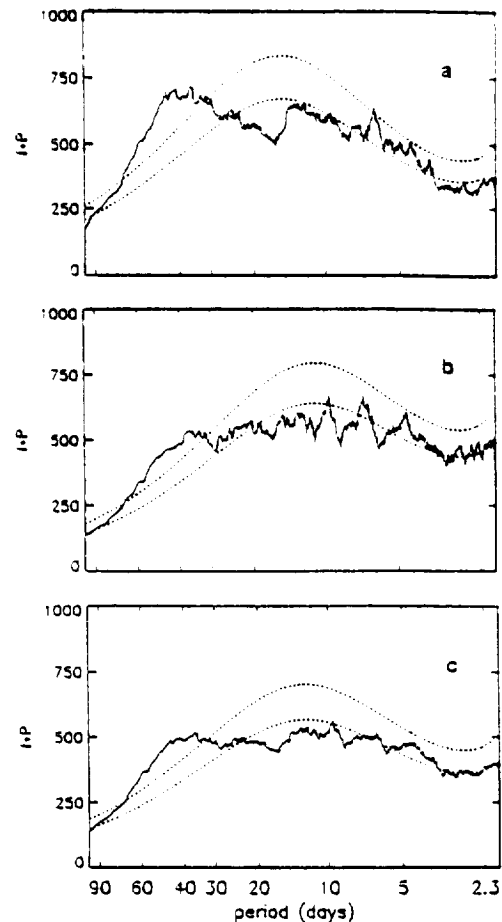


Figure 2. Frequency spectra of near-equatorial OLR over (a) Indian Ocean ( $60^\circ$ – $97.5^\circ\text{E}$ ); (b) western Pacific Ocean ( $135^\circ$ – $162.5^\circ\text{E}$ ); and (c) combination of both regions, including maritime continent ( $60^\circ$ – $162.5^\circ\text{E}$ ). Red noise spectra are shown together with 95% confidence level (dashed lines). Note that spectra are weighted by frequency and plotted as a function of log frequency.

emerge at 5–10 days. Spectra at individual longitudes have peaks like these extending above the red noise curves, similar over a narrow band of longitudes ( $\sim 15^\circ$ ). Some of these peaks may represent important phenomena at particular longitudes, but this is unclear. Rather than trying to explain individual peaks below 15 days, we incorporate them simultaneously into a broad high-frequency band.

On the basis of average spectra shown in Figure 2, temporal filters were used to separate intraseasonal variability from convective activity on  $\sim 2$ - to 15-day timescales. A band-pass filter was designed to capture intraseasonal variance with half-power points at 30 and 60 days. High-frequency variations were obtained from a high-pass filter with half-power point at 15 days. There was essentially no overlap in the response of the two filters.

### 3.2. Filtered Data

Figure 3 shows a Hovmöller diagram of  $\sim 30$ - to 60-day band-passed anomalies. Eastward propagating anomalies are now obvious (unlike in Figure 1), mainly over the Indian and western Pacific Oceans, with phase speeds of  $3$ – $7 \text{ m s}^{-1}$ . A typical phase speed is  $360^\circ$  per 90 days ( $\sim 5 \text{ m s}^{-1}$ ), which would correspond to a wavenumber 2 disturbance if the con-

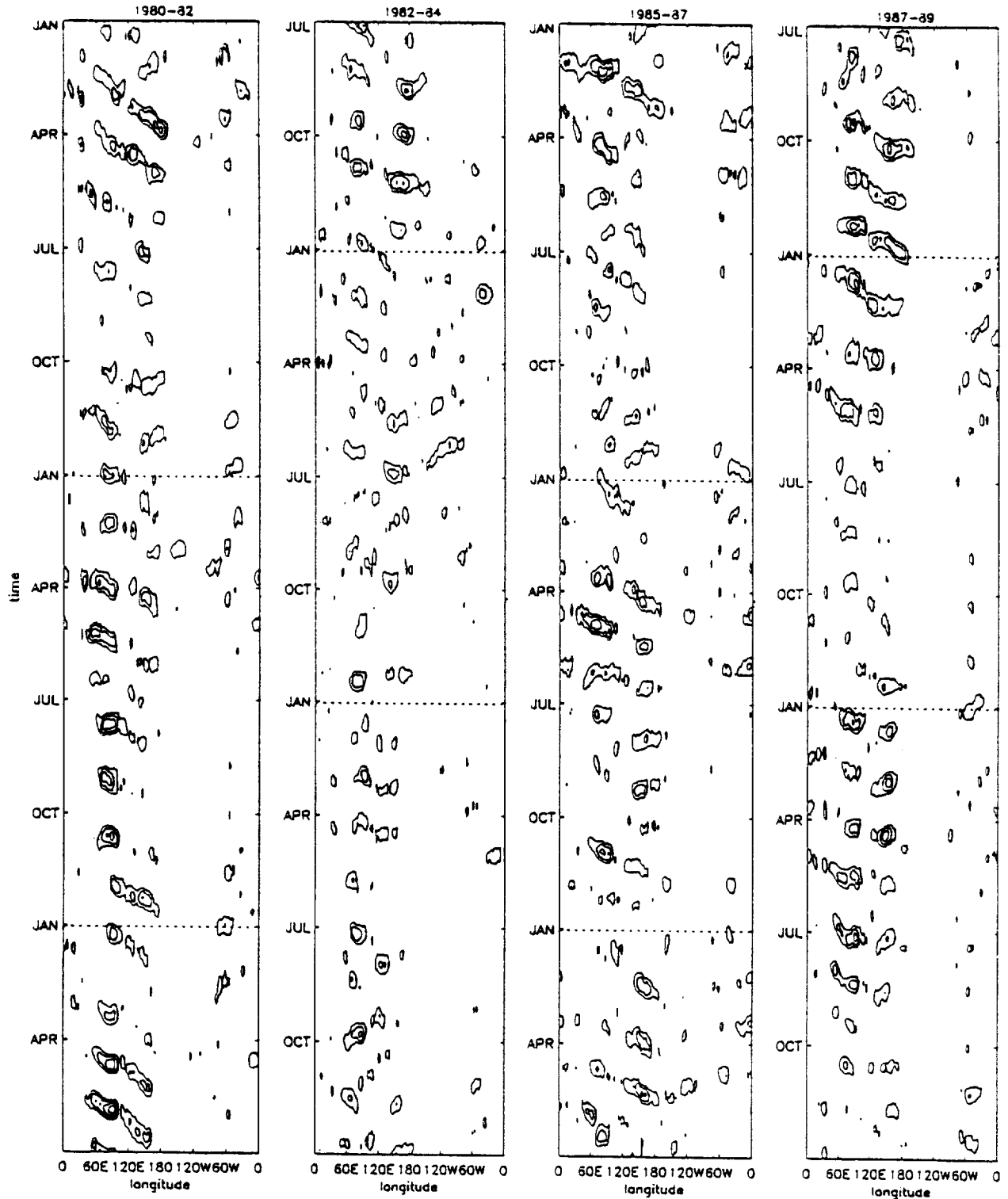


Figure 3. Near-equatorial anomalously low OLR in the tropical intraseasonal oscillation (TIO) frequency band ( $\sim 30$ – $60$  days). Contour interval is  $10 \text{ W m}^{-2}$ , beginning at  $-10 \text{ W m}^{-2}$ .

vective anomaly were to propagate all the way around the equator. The zonal width of coherent negative anomalies, indicative of the convectively active regions, is typically  $40^\circ$ – $50^\circ$ . Zonal extent of the active phase is smaller than what one might infer from a space-time spectrum of OLR, which is dominated by planetary wavenumbers. The distance traversed by the active region in a lifecycle is larger, typically  $60^\circ$ – $150^\circ$ . Ampli-

tudes weaken over the maritime continent, but stronger TIOs seem coherent between the two ocean basins. Such events reappear in the western Pacific soon after their apparent termination in the eastern Indian Ocean.

TIO events are more prominent over the Indian Ocean, as suggested by the spectra. Their eastward propagation is apparent within this region, more so than in the western Pacific.

Events in the western Pacific sometimes propagate eastward with equal clarity but often appear as a "blob" following an event in the Indian Ocean (e.g., the sequence in 1989). On a few occasions, westward propagation is observed. The timing of events in the western Pacific Ocean opposes the idea of a seesaw of convection between the Indian and western Pacific Oceans, because events in the western Pacific occur prior to the minimum of activity in the Indian Ocean. Intraseasonal variability of OLR is best interpreted in terms of coherent propagation from one ocean basin to the other, with amplitude temporarily diminished over the maritime continent.

There is large annual and interannual variation of the TIO. Anomalies are often strongest and most coherently propagating during the northern winter and spring, but weaker and/or less coherently propagating in the summer and fall. This is not true in every year: the annual variability is complex, as described by Madden [1986]. Results of Hendon and Liebmann [1994] suggest opposite seasonal variations of the TIO in convergence zones north and south of the equator [see Madden and Julian, 1994, and references therein]. Effects of the 1982–1983 and 1986–1987 ENSO events are apparent as an eastward shift of TIO convection closer to, but not east of, the dateline. As discussed in section 3.4, TIO events east of the dateline in early 1983 may be defined in terms of the ~30- to 60-day amplitude envelope of high-frequency convection, rather than of the ~30- to 60-day convection itself.

High-frequency (~2- to 15-day) anomalies are shown in Figure 4. Eastward propagating features over the Indian and western Pacific Oceans are obvious throughout the record, along with less frequent episodes of westward propagation (e.g., mid-1983). Eastward phase speeds are ~10–13 m s<sup>-1</sup>, faster than those of the TIO. Because of their faster propagation, only a few high-frequency events extend through an entire life cycle of the TIO. More commonly, an event in one phase of the TIO over the Indian Ocean terminates and is replaced by a new event in the western Pacific when the TIO arrives there. The zonal width of coherent negative anomalies is 15°–40°, considerably less than the distance traversed in a typical sequence of events (40°–150°). A similar amplitude gap is apparent over the maritime continent with coherent propagation on either side. Eastward propagating synoptic-scale clusters are occasionally seen over the equatorial Atlantic Ocean and Africa, where the convective TIO is relatively weak or absent.

As in the TIO band, annual variability of high-frequency convection is complex. More coherent behavior is suggested in the first half of the calendar year (March–July, in most of the years), but exceptions are found (as in October 1987). Interannual variability is strongly influenced by the two ENSO events during which anomalies have significant amplitude and coherent propagation east of the dateline.

By "coherent propagation" of high-frequency activity we are referring to the tendency of eastward propagating negative OLR anomalies to occur in colinear fashion along a line  $x - ct = \text{const}$ , where the phase speed  $c$  at the equator has a positive bias for synoptic-scale convection. These events are seldom defined by a single continuous cluster, since on closer inspection, propagating clusters are usually broken into segments along such a line. The daily OLR data, in any case, do not resolve fine structure such as mesoscale convective complexes and individual clouds. A simple mathematical transform introduced in the next subsection easily identifies coherently propagating groups of synoptic-scale cloud clusters.

The predominance of eastward over westward convection

was clearly seen in the space-time spectrum of near-equatorial OLR (not shown). Activity in the TIO frequency band comprises mainly low zonal wavenumbers 1–6, while the high-frequency band contains significant power at wavenumbers 2–10, centered in a range of phase speeds 10–22 m s<sup>-1</sup>. It is important to note that for near-equatorial OLR, eastward propagating activity is much larger than westward propagating activity, not only in the TIO band but at higher frequencies as well, consistent with the fine structure displayed in Figures 1 and 4. This statement does not apply to mesoscale convection unresolved by daily OLR, for which westward propagation is considerably more important.

### 3.3. Equatorial Convection Events

To investigate the episodic nature of high-frequency convection events, a simple transform was applied to the ~2- to 15-day near-equatorial OLR:

$$F(x, t, c) = \int_{t-\Delta t}^{t+\Delta t} f(x - ct', t') dt'$$

where  $\Delta t = \Delta x/c$  and  $\Delta x$  is the half width of a longitude sector. For the two ocean basins of interest, we set  $x = 90^\circ\text{E}$  or  $150^\circ\text{E}$ , and  $\Delta x = 30^\circ$ . This transform was actually applied to a subset of OLR data reconstructed from the eastward (or westward) propagating components of the space-time spectrum with periods below 15 days. Isolation of the eastward component is justifiable because of its dominance over the westward component and from our observation (based on the space-time spectrum) that the standing component of near-equatorial OLR is small. Over the oceans the eastward and westward components of OLR correspond mainly to propagating events, rather than standing oscillations of convection. This is not to deny the existence of standing oscillations over land or local flare-ups of convection that inevitably occur at various times and places. Westward events can be found in Figure 1 but are relatively small, and large events are rare.

Figures 5a, 5b, and 5c show the raw OLR data (low OLR only), ~2- to 15-day filtered data, and eastward ~2- to 15-day data, respectively, for a 90-day segment early in the record. Westward ~2- to 15-day data for the same time period are shown in Figure 5d. Superimposed are the active phases of ~30- to 60-day TIO signal (shading) and dominant phase speeds for individual high-frequency events (thick sloping lines). These events were defined in the convectively active period by searching for periods of large negative OLR anomaly along a line  $x - ct = \text{const}$ ; a dominant phase speed  $c$  was then selected from within the range  $\pm 1\text{--}50 \text{ m s}^{-1}$ . There were a few cases where multiple phase speeds occurred simultaneously; for simplicity, only one value of  $c$  from each 3-day interval was retained in the analysis. After exploring various thresholds, a minimum value of  $300 \text{ W m}^{-2}$  was selected for the integrated amplitude of each event, corresponding to an average grid point OLR anomaly of  $-12 \text{ W m}^{-2}$ . This threshold captured most of the propagating events visible in the data but was large enough to avoid random alignments of insignificant clusters.

The phase speed transform provides a useful phenomenological description of the propagation of high-frequency clusters, including events lying off-center to one side or the other of  $90^\circ\text{E}$  or  $150^\circ\text{E}$ . As seen in Figure 5b, there is considerable variation of OLR along the cluster track, much of which is

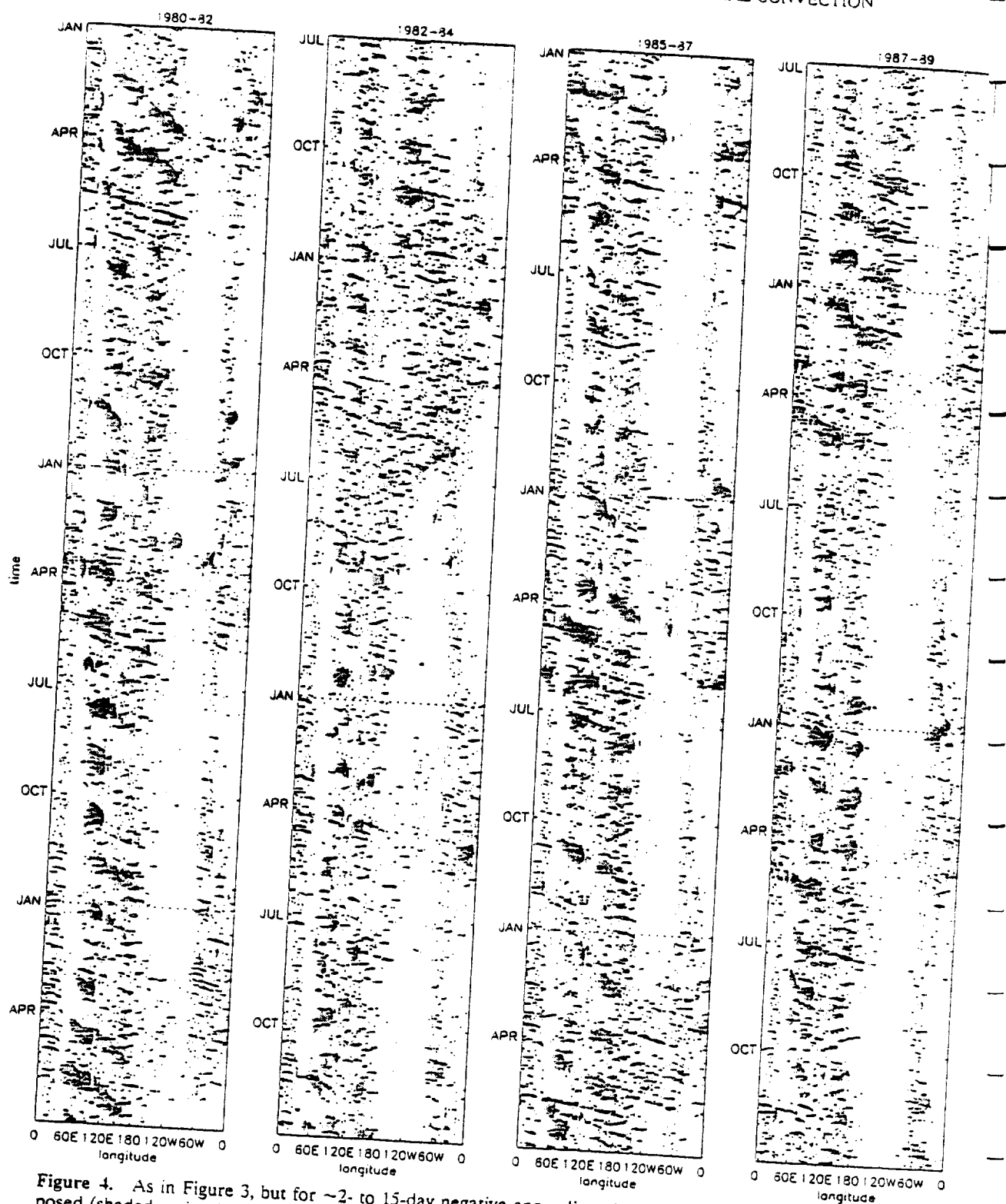


Figure 4. As in Figure 3, but for  $\sim 2$ - to 15-day negative anomalies with TIO events of Figure 3 superimposed (shaded regions). Contour interval is as in Figure 3.

eliminated when plotting eastward data (Figure 5c). Propagating clusters are usually large enough to be visible in the raw data (Figure 5a) but are obscured by TIO events and climatological convection.

The time period chosen for display in Figure 5 contains an interesting variety of behavior, including a well-defined TIO event with weak high-frequency events (first half) and a weak

TIO with strong and unusually coherent eastward high-frequency events (second half). Many events satisfied our minimum amplitude criterion: Altogether, the 10-year OLR record gave 324 eastward events in the Indian Ocean and 312 eastward events in the western Pacific Ocean, of which only about 49 could be described as reasonably coherent between the two oceans. Thus the majority of high-frequency events did



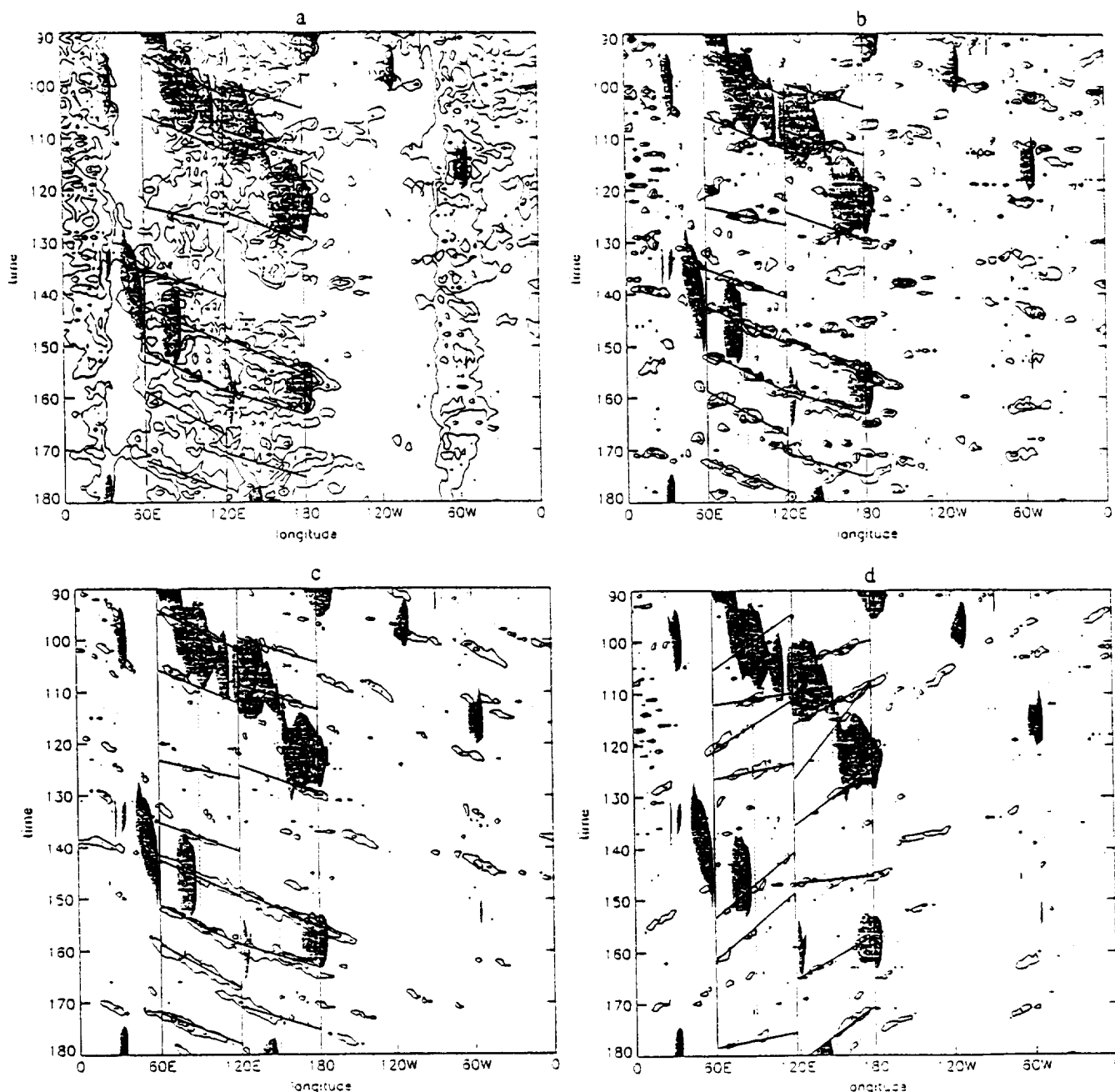


**Figure 5.** Low or anomalously low OLR in early 1980 for (a) total field (contours 120, 160, 200, and 240  $\text{W m}^{-2}$ ); (b) ~2- to 15-day negative anomalies; (c) eastward component of ~2- to 15-day anomalies; and (d) westward component of ~2- to 15-day anomalies. Eastward events derived from Figure 5c are superimposed as thick sloping lines in Figures 5a, 5b, and 5c; westward events derived from Figure 5d are superimposed in Figure 5d. TIO events are superimposed (shaded regions) as in Figure 4. Contour interval in Figures 5b–5d is  $10 \text{ W m}^{-2}$ , beginning at  $-10 \text{ W m}^{-2}$ .

not span an entire region, nor did they cross the maritime continent. Westward events were slightly less numerous and generally much smaller.

The cumulative amplitude of OLR events as a function of phase speed is shown in Figures 6a and 6b for the Indian and western Pacific Oceans, respectively. Strictly speaking, this is a spectrum of finite amplitude events (with unique phase speed assigned to each event), not a spectrum of phase speeds obtained from the continuous space-time spectrum, although the two would agree qualitatively since most of the high-frequency

OLR power lay in the range  $10\text{--}22 \text{ m s}^{-1}$  as noted earlier. The eastward component in Figure 6 has a much larger amplitude, particularly over the Indian Ocean, with most events in the range  $5\text{--}20 \text{ m s}^{-1}$  and a sharp peak at  $10\text{--}13 \text{ m s}^{-1}$ . Evidently, the phase speed transform is biased toward the low end of dominant phase speeds suggested by the space-time spectrum. The westward component maximizes at a smaller absolute speed of about  $-8 \text{ m s}^{-1}$ . The shaded area of the histogram refers to the active phase of the TIO, as discussed in the next subsection. The minimum phase speed resolved by high-

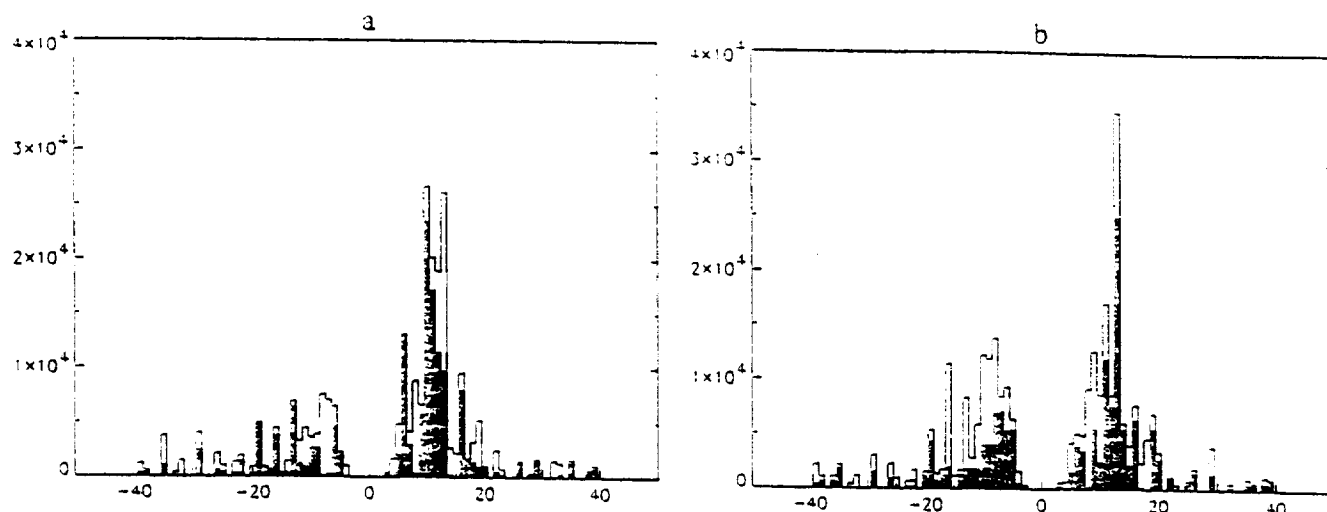


Figure 6. Histogram of event amplitudes (integrated over longitude, in units of watts per square meter; see text for explanation) as a function of dominant phase speed  $c$  (in meters per second) for (a) Indian Ocean and (b) western Pacific Ocean. Shading refers to active phase of the TIO.

frequency OLR is that corresponding to a wavelength of  $5^{\circ}$ – $30^{\circ}$  and a period of 15 days, or  $0.4$ – $2.4 \text{ m s}^{-1}$ , well below the observed falloff of amplitude in Figure 6.

The seasonal variation in each basin is shown in Figure 7 for eastward and westward events; the dominance of eastward over westward propagation is again seen. High-frequency activity is largest in northern spring-summer, with a hint of semi-annual variation (from western Pacific). Interestingly, this season contains the majority of easterly and westerly quasi-biennial oscillation (QBO) phase onsets in the equatorial lower stratosphere [Dunkerton, 1990]. Also, Maruyama [1991] found enhanced 70-mbar Kelvin-wave activity in northern hemisphere spring. Kelvin waves in the lower stratosphere are responsible, in part, for the westerly acceleration phase of the QBO. These waves are thought to have planetary scales and phase speeds of  $20$ – $30 \text{ m s}^{-1}$  [Wallace and Kousky, 1968], longer and faster than the synoptic-scale convective activity described here. Whether stratospheric Kelvin waves originate in these eastward propagating equatorial convection events is unclear. The two could not remain in phase for very long because of the mismatch in propagation speed. Nonnegligible

power exists in equatorial OLR, however, at wavenumbers and frequencies characteristic of Kelvin waves in the stratosphere.

Gravity waves excited within the envelope of convective activity may also transmit the seasonal variation of equatorial convection to the stratospheric QBO. Although such waves would have a wide range of positive and negative phase speeds, selective filtering in descending QBO shear zones would produce a net body force and help account for the required QBO acceleration [Pfister *et al.*, 1993]. The level of gravity-wave activity relevant to the QBO would of course be determined by convection at all longitudes, in addition to events comprising Figure 7. We observe from Figure 1 that equatorial convection in the western hemisphere also maximizes around northern spring equinox [Mitchell and Wallace, 1992].

### 3.4. Relation to the TIO

The relation between high-frequency ( $\sim 2$ - to 15-day) anomalies and ( $\sim 30$ - to 60-day) TIOs is now examined to determine if strong high-frequency events cluster during periods of strong low-frequency activity. There is no mathematical reason why this need be so. If different parts of the frequency spectrum are noninteracting, episodes of high- and low-frequency convection would be uncorrelated. To address this question, two methods were employed.

First, each high-frequency event defined in the preceding subsection was split into active and inactive TIO categories by summing amplitudes in the two phases of TIO separately. This was done by integrating along the line of dominant phase speed in each high-frequency event. Such a line would generally intersect regions of positive and negative TIO anomaly. The assignment of negative and positive  $\sim 30$ - to 60-day OLR anomalies to the active and inactive phases, respectively, of TIO is arbitrary, but each has a roughly equal probability of occurrence in the time series at any grid point. From Figure 4 it seems that no obvious relation exists between the high-frequency events and TIO anomalies, and Figure 5 provides a good example of noninteraction. However, a hint of scale interaction is evident when the entire data are examined. The shaded region of Figure 6 corresponds to the convectively active phase of the TIO, which explains  $\sim 60\%$  of the eastward event amplitudes. This would imply enhancement of eastward

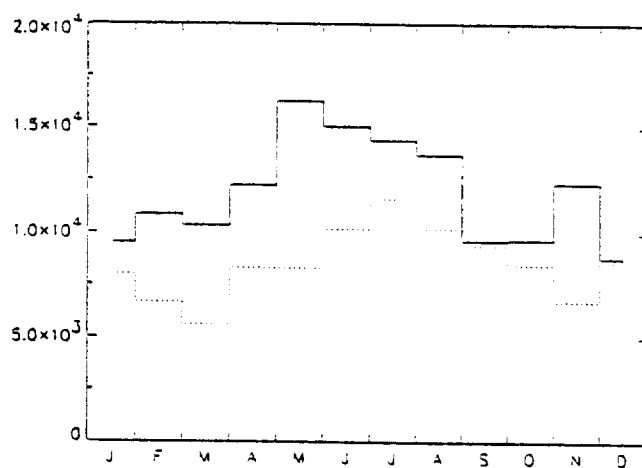


Figure 7. Histogram of event amplitudes as a function of month for eastward (solid) and westward (dashed) events.

high-frequency events by no more than 50% in the active phase of TIO, a result comparable to that inferred by *Hendon and Liebmann* [1994] for synoptic-scale convection during "windowed" time series corresponding to the most significant episodes of the TIO. Some of our best events fall outside the active phase of the ~30- to 60-day TIO, so this result is not surprising.

Second, the ~30- to 60-day envelope of ~2- to 15-day OLR variance was calculated by applying the TIO band-pass filter to the absolute value of high-frequency activity. Results of this calculation were quite noisy, but demonstrated on many occasions a good correspondence between the envelope of high-frequency and band-passed TIO. A nonzero correlation must exist, if for no other reason than that inactive periods of TIO are sometimes devoid of convection, so that high- and low-frequency activity are both suppressed. However, we also observe a slight enhancement of high-frequency activity during the active phase of TIO.

An intriguing observation is that the ~30- to 60-day envelope of high-frequency activity sometimes suggests eastward group propagation at a speed equal to that of the TIO itself, even though the "linear TIO" (defined by the ~30- to 60-day component of convection) is entirely absent, as in the eastern Pacific during early 1983. There is evidently some process that causes eastward group propagation of high-frequency activity that does not require a ~30- to 60-day OLR signal to exist.

On the other hand, the ~30- to 60-day OLR signal does not require high-frequency activity on synoptic scales as resolved by daily OLR (Figure 4). It is therefore unnecessary to suppose that synoptic-scale activity or superclusters are essential to the TIO. The role of superclusters in the cloud hierarchy suggested by *Nakazawa* [1988], while relevant in some TIO events, is not relevant to all, nor is the eastward propagation of synoptic-scale activity confined to the active phase of the TIO.

Modulation of convection at shorter spatial and temporal scales is nevertheless an important and perhaps essential feature of the TIO. Cloud imagery shows that the envelope of mesoscale convection is strongly enhanced during the active phase of the TIO [*Hendon and Liebmann*, 1994]. This effect might appear in daily OLR, unrealistically, as a large contiguous region of convection not punctuated by synoptic-scale activity.

Our observations and those of *Nakazawa* [1988] and *Hendon and Liebmann* [1994] suggest an alternative definition of the convective TIO, consisting of groups of enhanced synoptic-scale and/or mesoscale convection, with individual elements in each group propagating eastward or westward along the equator. The ~30- to 60-day OLR signal mainly represents an ensemble of convection on shorter spatial and temporal scales. Whether the group propagation of wave packets in off-equatorial convergence zones similarly corresponds to the eastward propagation of low-frequency convection in these regions, as conjectured by *Liebmann and Hendon* [1990], remains to be seen.

#### 4. Conclusions

Anomalies of outgoing longwave radiation (OLR) in 1980–1989 were examined in a narrow latitude band about the equator to elucidate the propagation and interaction of tropical intraseasonal oscillations (TIOs) and synoptic-scale convective activity. The latter includes superclusters, which were previously thought to play an important role in the TIO.

Hovmöller diagrams of OLR data reconstructed from two frequency bands (corresponding to periods of ~30–60 and ~2–15 days, respectively) revealed a clear distinction between the phase speed of eastward moving TIOs ( $3\text{--}7\text{ m s}^{-1}$ ) and that of eastward synoptic-scale convection ( $10\text{--}15\text{ m s}^{-1}$ ). Coherent propagation of TIOs from the Indian to the western Pacific Oceans was often observed with diminution of amplitude over the maritime continent, presumably owing to the strong diurnal cycle there [*Hendon and Woodberry*, 1993]. Propagation of high-frequency anomalies was generally confined to an individual basin, although coherent anomalies were sometimes found to propagate through both regions. Dominance of eastward propagating synoptic-scale convection in the equatorial zone contrasts sharply with the westward propagation of synoptic-scale convection in off-equatorial convergence zones.

Interaction between the TIO and high-frequency activity resolved by daily OLR was visible as a modest enhancement of eastward synoptic-scale events (and of high-frequency activity in general) during the convectively active phase of the TIO. This effect did not occur in every TIO event, and many eastward propagating synoptic-scale events were seen during the inactive phase of the TIO. It is therefore unnecessary to regard the synoptic activity or superclusters as essential to, or uniquely associated with, the convectively active phase of the TIO. Nevertheless, modulation of convection on shorter spatial and temporal scales is an important and perhaps essential feature of the tropical intraseasonal oscillation. Cloud imagery shows that mesoscale activity is strongly enhanced in the active phase of the TIO [*Hendon and Liebmann*, 1994]. The mechanism is unknown but presumably involves the large-scale circulation associated with the TIO.

Given the prominence of synoptic-scale and mesoscale activity in equatorial convection, what is important to the TIO's large-scale circulation is not the enhancement of a large contiguous region of convection in the active phase, but the ~30- to 60-day enhancement of high-frequency convective activity on shorter spatial and temporal scales. Either scenario leads to enhanced precipitation and latent heat release when averaged over the active phase of the TIO, because there are no "negative clouds." Although clear-sky conditions exist here and there within the envelope of convective activity, a net positive heating remains when averaged over the active phase of a TIO event. Detailed observations of convection highlight the importance of the second mechanism. A potential feedback therefore exists between the large-scale circulation induced by the envelope of synoptic-scale and mesoscale convection, and the effect of this circulation on the development of convective elements making up the envelope.

This survey of equatorial OLR invites further study using cloud imagery in order to elucidate the propagation and interaction of equatorial convection at various spatial and temporal scales. An example described by *Hendon and Liebmann* [1994, Figure 9] provides a striking illustration of scale interaction involving the TIO and mesoscale convection. It would be interesting to explore these interactions with a longer record and also to consider in more detail the role of synoptic-scale cloud organization, particularly during times of strong, coherent eastward propagation. Further examination of these events in conjunction with circulation data may shed light on the mechanisms of Kelvin wave excitation in the troposphere, the seasonal variation of these waves, and the effects on the stratospheric QBO.

**Acknowledgments.** The authors appreciate the advice of Jerry Ziemke and Xinhua Cheng and thank Harry Hendon for providing the OLR data in a convenient format. This research was supported by the National Science Foundation, grants ATM-9123797 and ATM-9213437, and by the National Aeronautics and Space Administration, contract NASW-4844.

## References

- Dunkerton, T. J., Annual variation of deseasonalized mean flow acceleration in the equatorial lower stratosphere, *J. Meteorol. Soc. Jpn.*, **68**, 499–508, 1990.
- Dunkerton, T. J., and M. P. Baldwin, Observation of 3–6 day meridional wind oscillations over the tropical Pacific, 1973–1992: Horizontal structure and propagation, *J. Atmos. Sci.*, **52**, 1585–1601, 1994.
- Gilman, D. L., F. J. Fuglister, and J. M. Mitchell Jr., On the power spectrum of “red noise,” *J. Atmos. Sci.*, **20**, 182–184, 1963.
- Hayashi, Y.-Y., and A. Sumi, The 30–40 day oscillations simulated in an “aqua-planet” model, *J. Meteorol. Soc. Jpn.*, **64**, 451–467, 1986.
- Hendon, H. H., and B. Liebmann, The intraseasonal (30–50 day) oscillation of the Australian summer monsoon, *J. Atmos. Sci.*, **47**, 2909–2923, 1990.
- Hendon, H. H., and B. Liebmann, The structure and annual variation of antisymmetric fluctuations of tropical convection and their association with Rossby-gravity waves, *J. Atmos. Sci.*, **48**, 2127–2140, 1991.
- Hendon, H. H., and B. Liebmann, Organization of convection within the Madden-Julian oscillation, *J. Geophys. Res.*, **99**, 8073–8084, 1994.
- Hendon, H. H., and M. L. Salby, The life cycle of the Madden-Julian oscillation, *J. Atmos. Sci.*, **51**, 2225–2237, 1994.
- Hendon, H. H., and K. Woodberry, The diurnal cycle of tropical convection, *J. Geophys. Res.*, **98**, 16,623–16,637, 1993.
- Knutson, T. R., and K. M. Weickmann, 30–60 day atmospheric oscillations: Composite life cycles of convection and circulation anomalies, *Mon. Weather Rev.*, **115**, 1407–1436, 1987.
- Lau, K.-M., and P. H. Chan, Aspects of the 40–50 day oscillation during the northern winter as inferred from outgoing longwave radiation, *Mon. Weather Rev.*, **113**, 1889–1909, 1985.
- Lau, K.-H., and N.-C. Lau, Observed structure and propagation characteristics of tropical summertime synoptic-scale disturbances, *Mon. Weather Rev.*, **118**, 1888–1913, 1990.
- Lau, K.-H., and N.-C. Lau, The energetics and propagation dynamics of tropical summertime synoptic-scale disturbances, *Mon. Weather Rev.*, **120**, 2523–2539, 1992.
- Lau, K.-M., and H. Lim, The 40–50 day oscillation and El Niño/Southern Oscillation: A new perspective, *Bull. Am. Meteorol. Soc.*, **67**, 533–534, 1986.
- Lau, K.-M., and T. J. Phillips, Coherent fluctuations of extratropical geopotential height and tropical convection in intraseasonal timescales, *J. Atmos. Sci.*, **43**, 1164–1181, 1986.
- Lau, K.-M., T. Nakazawa, and C. H. Sui, Observations of cloud cluster hierarchies over the tropical western Pacific, *J. Geophys. Res.*, **96**, 3197–3208, 1991.
- Liebmann, B., and D. L. Hartmann, An observational study of tropical-midlatitude interaction on intraseasonal timescales during winter, *J. Atmos. Sci.*, **41**, 3333–3350, 1984.
- Liebmann, B., and H. H. Hendon, Synoptic-scale disturbances near the equator, *J. Atmos. Sci.*, **47**, 1463–1479, 1990.
- Liebmann, B., H. H. Hendon, and J. D. Glick, The relationship between tropical cyclones of the western Pacific and Indian Oceans and the Madden-Julian oscillation, *J. Meteorol. Soc. Jpn.*, **72**, 401–411, 1994.
- Madden, R. A., Seasonal variations of the 40–50 day oscillation in the tropics, *J. Atmos. Sci.*, **43**, 3138–3158, 1986.
- Madden, R. A., and P. R. Julian, Detection of a 40–50 day oscillation in the zonal wind in the tropical Pacific, *J. Atmos. Sci.*, **28**, 702–708, 1971.
- Madden, R. A., and P. R. Julian, Description of global-scale circulation cells in the tropics with a 40–50 day period, *J. Atmos. Sci.*, **29**, 1109–1123, 1972.
- Madden, R. A., and P. R. Julian, Observations of the 40–50 day tropical oscillation: A review, *Mon. Weather Rev.*, **122**, 814–837, 1994.
- Mapes, B. E., and R. A. Houze Jr., Cloud clusters and superclusters over the oceanic warm pool, *Mon. Weather Rev.*, **121**, 1398–1415, 1993.
- Maryama, T., Annual variations and QBO-synchronized variations of the equatorial wave intensity in the lower stratosphere at Singapore during 1961–1989, *J. Meteorol. Soc. Jpn.*, **69**, 219–232, 1991.
- Mitchell, T. P., and J. M. Wallace, The annual cycle in equatorial convection and sea surface temperature, *J. Clim.*, **5**, 1140–1156, 1992.
- Nakazawa, T., Intraseasonal variations of OLR in the tropics during the FGGE year, *J. Meteorol. Soc. Jpn.*, **64**, 17–34, 1986a.
- Nakazawa, T., Mean features of 30–60 day variations as inferred from 8-year OLR data, *J. Meteorol. Soc. Jpn.*, **64**, 777–786, 1986b.
- Nakazawa, T., Tropical super clusters within intraseasonal variations over the western Pacific, *J. Meteorol. Soc. Jpn.*, **66**, 823–839, 1988.
- Parker, D. E., Equatorial Kelvin waves at 100 millibars, *Q. J. R. Meteorol. Soc.*, **99**, 116–129, 1973.
- Pfister, L., K. R. Chan, T. P. Bui, S. Bowen, M. Legg, B. Gary, K. Kelly, M. Proffitt, and W. Starr, Gravity waves generated by a tropical cyclone during the STEP tropical field program: A case study, *J. Geophys. Res.*, **98**, 8611–8638, 1993.
- Rui, H., and B. Wang, Development characteristics and dynamic structure of tropical intraseasonal convection anomalies, *J. Atmos. Sci.*, **47**, 357–379, 1990.
- Sui, C.-H., and K.-M. Lau, Multiscale phenomena in the tropical atmosphere over the western Pacific, *Mon. Weather Rev.*, **120**, 407–430, 1992.
- Takayabu, Y. N., and T. Nitta, 3–5 day period disturbances coupled with convection over the tropical Pacific ocean, *J. Meteorol. Soc. Jpn.*, **71**, 221–246, 1993.
- Wallace, J. M., and V. E. Kousky, Observational evidence of Kelvin waves in the tropical stratosphere, *J. Atmos. Sci.*, **25**, 900–907, 1968.
- Weickmann, K. M., Intraseasonal circulation and outgoing longwave radiation modes during northern hemisphere winter, *Mon. Weather Rev.*, **111**, 1838–1858, 1983.

F. X. Crum and T. J. Dunkerton, Northwest Research Associates, P. O. Box 3027, Bellevue, WA 98009. (e-mail: tim@nwra.com; crum@persephone.gsfc.nasa.gov)

(Received March 3, 1994; revised August 24, 1995; accepted August 28, 1995.)

## **II. Observational Studies of the Tropical Stratosphere**



# Mixing zone in the tropical stratosphere above 10 mb

Timothy J. Dunkerton and Donal J. O'Sullivan

Northwest Research Associates, Bellevue, Washington

**Abstract.** Observations of trace constituents obtained from the Upper Atmosphere Research Satellite in late winter 1991/92 reveal a zone of quasi-horizontal stirring in the tropical stratosphere above 10 mb, equatorward of the subtropical jet. This mixing region was separated from the midlatitude surf zone by a strong gradient of potential vorticity and tracer along the jet axis. The jet and accompanying gradients are climatological features. Mixing equatorward of the jet evidently depends on the phase of the quasi-biennial oscillation.

## Introduction

The distribution of long-lived trace constituents in the middle atmosphere is affected by quasi-horizontal stirring due to planetary Rossby waves and instabilities resulting from these waves. Preferred regions of mixing include the 'surf zone' in the midlatitude winter stratosphere [McIntyre and Palmer, 1984], the polar winter mesosphere [Dunkerton and Delisi, 1985], and the lowermost stratosphere in all seasons [Chen, 1995; Dunkerton, 1995; Holton et al., 1995]. Steep horizontal gradients of potential vorticity and trace constituents are observed at the lateral boundaries of mixing regions. In this letter we describe another region of stirring, the northern tropical stratosphere above 10 mb, as observed by instruments aboard the Upper Atmosphere Research Satellite (UARS) in late winter 1991/92.

## Data Analysis

Several UARS constituents were examined, including water vapor ( $\text{H}_2\text{O}$ ) from the Microwave Limb Sounder (MLS) version 3 [Barath et al., 1993; Waters et al., 1993] and nitrous oxide ( $\text{N}_2\text{O}$ ) from the Cryogenic Limb Array Etalon Spectrometer (CLAES) version 7 [Roche et al., 1993]. Features described in this letter were observed in other UARS constituents as well, but could be seen more clearly in some tracers than in others, depending on the background distribution. Level 3AT data, consisting of soundings along the orbital track, were interpolated to a longitude-latitude grid using 4 consecutive days of data as input. The weight function was an elliptical gaussian with major axis aligned in the zonal direction. Assigning a relatively small radius of influence ( $3^\circ \times 1^\circ$ ) to this function, comparable to the distance between soundings, strong tracer gradients

were preserved, as well as in the original data. A disadvantage of this method is that any rapidly evolving ( $< 4$ -day) disturbances are aliased into spurious features with short longitudinal scale. Aliasing was insignificant in the examples shown, but small-scale features in our tracer figures should be viewed with caution. This simple procedure captured the slow evolution of tracers affected by quasi-stationary planetary waves, and was entirely adequate for zonally averaged latitude-height cross sections. Circulation data were obtained from the United Kingdom Meteorological Office (UKMO) analyses [Swinbank and O'Neill, 1994], and the state of the quasi-biennial oscillation (QBO) at the equator was determined using rawinsonde data from Singapore ( $1.4^\circ\text{N}$ ,  $104.0^\circ\text{E}$ ).

## Results

Figure 1 displays the mean zonal wind at 4.6 mb for UARS day 50-650 beginning in November 1991. The first northern winter, occurring in a deep easterly phase of the QBO ( $\sim 70$ -15 mb), experienced stronger wave activity and a more disturbed vortex than the second winter, occurring in a deep westerly phase. Aside from differences in timing, the mean flow evolution was qualitatively similar in the two winters. Breakdown of mid-winter westerlies led to the formation of a detached subtropical westerly jet near  $30^\circ\text{N}$ . This jet is commonly observed in late northern winter [Randel, 1992] persisting for one or two months after the transition to easterlies at higher latitudes.

To illustrate the relation between the subtropical jet and quasi-horizontal stirring, we focus on the second half of February and first half of March 1992, UARS days 160-185, indicated at the top of Fig. 1 by a bold line. Figures 2a,b show latitude-height cross sections of MLS  $\text{H}_2\text{O}$  and CLAES  $\text{N}_2\text{O}$ , respectively, averaged over this time interval. Figure 3 shows the corresponding latitude-height cross section of mean zonal wind, from UKMO analyses. The axis of the subtropical jet is indicated by a bold curve in each of the figures, and a few isopleths of  $\text{N}_2\text{O}$  are superposed in Fig. 3. Both constituents display an unusual 'staircase' pattern in the latitude-height plane (highlighted in yellow). This complicated pattern can be separated into individual features and interpreted, tentatively, as follows: 1) In the upper stratosphere south of the equator, tracer isopleths are pushed upward due to Brewer-Dobson upwelling. 2) In the upper stratosphere north of the equator, between 10 and 2.2 mb, there is a region of weak tracer gradient due to quasi-horizontal stirring (as shown below). 3) Near the tropical stratopause there

Copyright 1996 by the American Geophysical Union.

Paper number 96GL02302

0094-8534/96/96GL-02302\$05.00

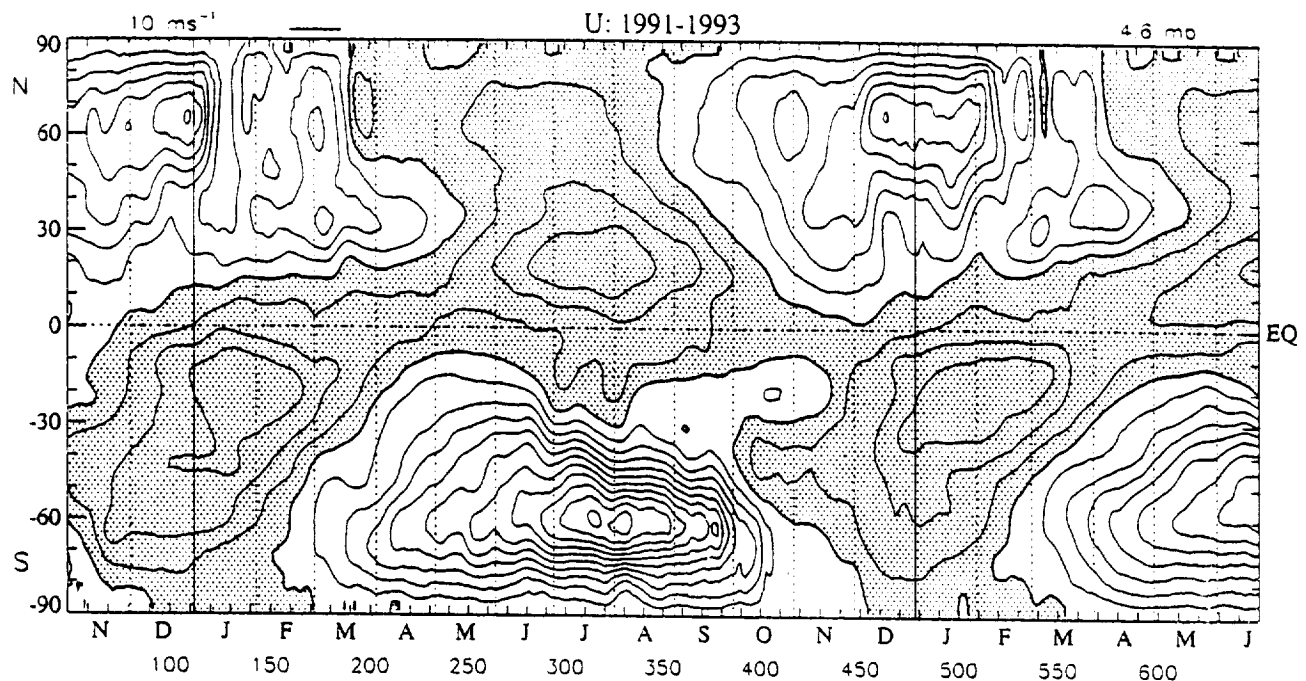


Figure 1. Latitude-time cross section of mean zonal wind at 4.6 mb, from UKMO analyses. Contour interval  $10 \text{ ms}^{-1}$ , easterlies are shaded.

is a double-peak structure associated with the onset of the semiannual oscillation (SAO) west phase. 4) In the tropical middle stratosphere, there is another double-peak structure associated with the onset of the QBO west phase. This feature is visible as a weak depression of tracer isopleths on the equator accompanied by tracer anomalies on either side, the one on the north side being especially prominent in  $\text{N}_2\text{O}$ . 5) There is a strong horizontal gradient of tracer along the axis of the subtropical jet, extending from the middle stratosphere, where the gradient is visible in both tracers, to the upper stratosphere, where the gradient is evident only in  $\text{H}_2\text{O}$ . Lack of a strong gradient in  $\text{N}_2\text{O}$  is attributable to the small amount and/or weak background gradient of this constituent in the upper stratosphere. 6) Tracer isopleths in the midlatitude Northern hemisphere stratosphere are quasi-horizontal, extending across the region of weak mean zonal wind, i.e., the surf zone. 7) A modest horizontal gradient of  $\text{N}_2\text{O}$  at 46–22 mb, but not of  $\text{H}_2\text{O}$ , coincides with the axis of a weak polar night jet near  $60^\circ\text{N}$ .

Comparing Fig. 2 with a cross section one year later, in the opposite phase of the QBO, we find several similarities and differences. There is a strong gradient of tracer coincident with the subtropical jet, flat isopleths of tracer across the midlatitude surf zone, and a modest  $\text{N}_2\text{O}$  gradient approaching polar latitudes (not shown). The SAO double peak is also apparent. On the other hand, there is less evidence of Brewer-Dobson upwelling south of the equator, no hint of QBO anomaly in the middle stratosphere, and no evidence of quasi-horizontal stirring in the upper half of the tropical stratosphere.

The QBO evidently affects the distribution of conserved tracers in four ways. 1) QBO circulation cells

in the tropics advect tracers horizontally and vertically in the latitude-height plane. 2) The QBO zonal wind anomaly determines whether planetary Rossby waves can enter the tropical stratosphere from the winter hemisphere. 3) The equatorial QBO affects the polar vortex and planetary-wave flux in the northern winter stratosphere, thereby indirectly influencing the amount of wave activity that can enter the tropics, and 4) the strength and southern extent of the Brewer-Dobson circulation.

We note incidentally that UKMO analyses underestimated the onset of the QBO west phase in early 1992 relative to that of Singapore. While there is a suggestion in Fig. 3 of westerly vertical shear at the equator above 22 mb, Singapore winds revealed a much stronger shear with absolute westerlies maximizing at almost  $20 \text{ ms}^{-1}$ . The reason for this discrepancy is unknown.

The latitude-height cross sections of tracer and mean zonal wind in Figs. 2,3 are representative of shorter intervals within this time period. Figure 4 displays a horizontal map of CLAES  $\text{N}_2\text{O}$  and UKMO zonal wind for UARS days 180–183 at the 4.6 mb level. There was a significant planetary-wave event in March 1992, leading to the breakdown of a remnant vortex and final transition to summer easterlies at higher latitudes. This event was underway during the time period shown, but unfortunately, the north-viewing yaw period of UARS ended on day 194.

In Fig. 4, a strong tracer gradient just north of the equator bifurcates into two strong gradients near the dateline; the northern one links up with the subtropical jet and closely follows the jet axis as it meanders through the Western hemisphere and extends into midlatitudes in the Eastern hemisphere. The flow is dominated by wavenumber 1, but higher wavenumbers



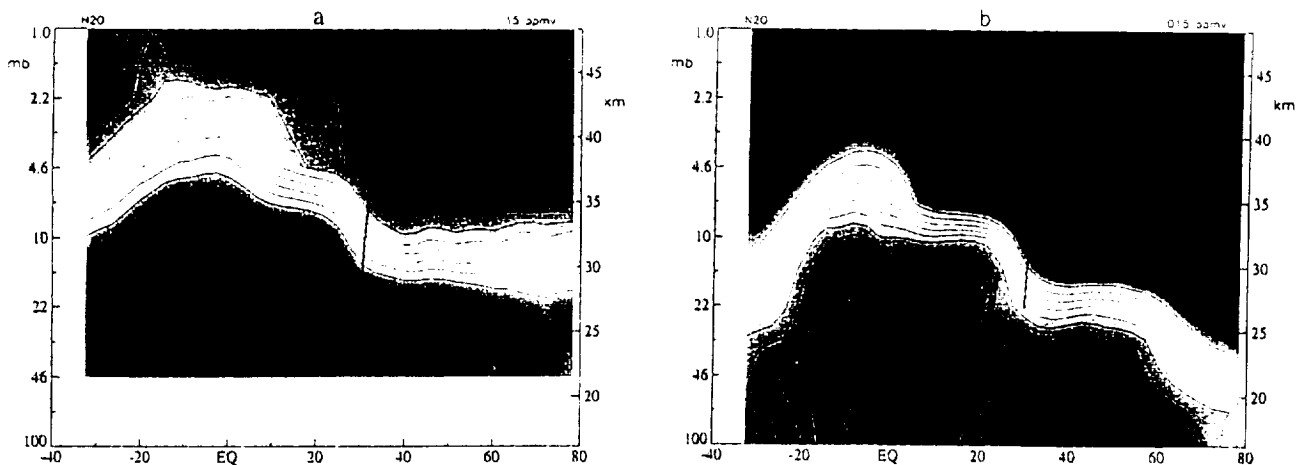


**Figure 2.** Latitude-height cross sections of (a) MLS  $\text{H}_2\text{O}$ , and (b) CLAES  $\text{N}_2\text{O}$ , averaged over UARS day 160-185. Contour interval is 0.15 ppmv in (a), starting at 3.8 ppmv (dark blue); 0.015 ppmv in (b), starting at 0.015 ppmv.

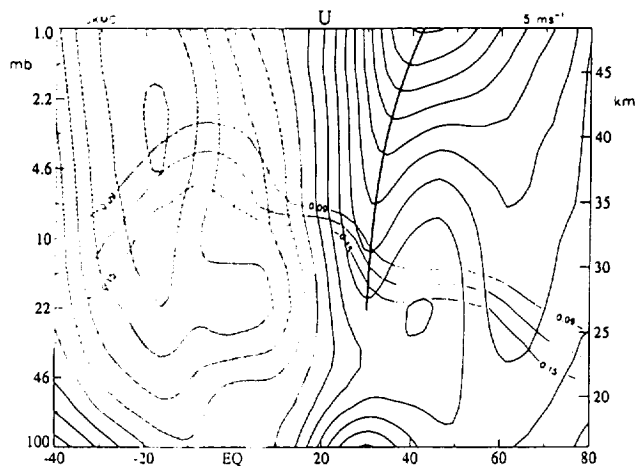


**Figure 3.** Latitude-height cross section of mean zonal wind, from UKMO analyses, averaged over UARS day 160-185. Contour interval  $5 \text{ ms}^{-1}$ , easterlies are shaded. A few isopleths of  $\text{N}_2\text{O}$  are also shown (thin lines).

develop in the Western hemisphere inside the tropical mixing region. A sequence of maps around this time suggests that the apparent flux of high  $\text{N}_2\text{O}$  concentrations into the Northern hemisphere is occurring in two branches: one near the dateline, and another near  $90^\circ\text{W}$ . Spontaneous formation of higher wavenumbers was observed in nonlinear simulations of a Rossby-wave critical layer [Salby *et al*, 1990].

What is remarkable about this picture, in contrast to the usual midlatitude surf zone, is that the narrow mixing region occurs equatorward of the subtropical jet, rather than poleward of it, and is dynamically separated from the midlatitude mixing region. In effect, one can imagine that the subtropical jet has split the surf zone into two parts: a midlatitude part and a tropical part. The tropical mixing zone is isolated from the midlatitude surf zone at most longitudes, except over east Asia and the west Pacific. Meridional displace-

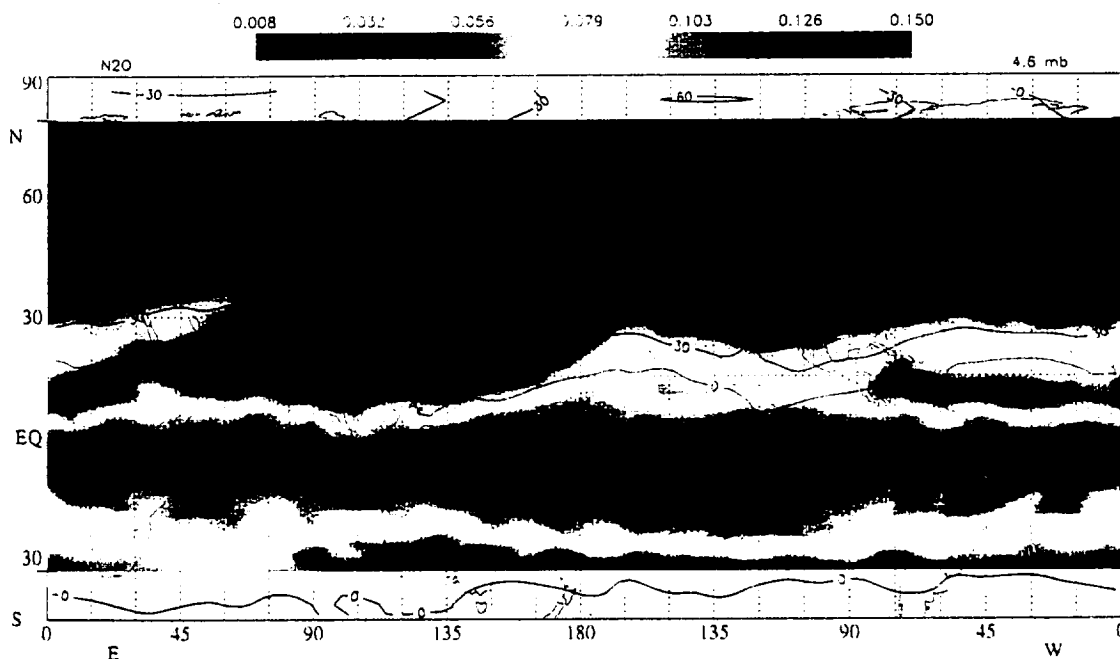


**Figure 4.** Horizontal map of CLAES  $\text{N}_2\text{O}$  and UKMO zonal wind at 4.6 mb, averaged over UARS day 180-183. Units: ppmv ( $\text{N}_2\text{O}$ ) and  $\text{ms}^{-1}$  (zonal wind).

ment of air parcels is reduced in the jet core, so that mixing is inhibited there. Mixing is encouraged where parcel displacements are large, i.e., approaching a critical layer. This interpretation is supported by Fig. 3, showing that the zero-wind line intersects the tropical mixing zone above 10 mb. The subtropical jet and accompanying PV/tracer gradients are most likely the result of i) Coriolis torques due to a mean meridional circulation extending outside the region of wave driving to the north, and ii) mixing on either side of the jet maximum.

## Conclusion

UARS observations suggest that the so-called subtropical transport 'barrier', evident at lower levels in volcanic aerosol and trace constituents [e.g., Trepte and Hitchman, 1992; Randel et al., 1994] extends to higher altitudes and represents not only the equatorward boundary of the midlatitude surf zone but also the poleward boundary of an intermittent mixing zone in the tropical upper stratosphere. Although this region is not as isolated from midlatitude disturbances as at lower levels, the subtropical jet separates the intermittent tropical mixing from the more pervasive stirring in the midlatitude surf zone. Except where the subtropical gradient is breached, there is tendency for the tropical stratosphere to remain isolated even at higher levels. During the west phase of the QBO, a strong tracer gradient also develops at the equator, which marks the southern boundary of the tropical mixing zone.

Strong PV/tracer gradients often coincide with westerly jets in the atmosphere and ocean because Rossby-wave and instability critical levels cannot exist near a westerly maximum. Propagating Rossby waves must have negative intrinsic phase speed and therefore cannot have a critical level near the center of a westerly jet. Barotropic and baroclinic instabilities must have a critical level in a region of reversed potential vorticity gradient, which can only occur in the flanks of a westerly jet. Mixing is therefore inhibited near the jet core, but as long as the maximum wind is not too strong, Rossby waves can propagate across the jet and break in regions of weaker mean flow.

Tracer gradients are necessarily the result of Rossby wavebreaking. A strong, zonally symmetric  $\text{N}_2\text{O}$  gradient at the southern boundary of the domain in Fig. 4 suggests a possible role for differential mixing at subtropical latitudes of the summer hemisphere, in addition to a 'leftover' effect of wavebreaking from the previous winter. Further study is necessary to determine the relative importance of these effects.

**Acknowledgments.** This research was supported by the National Aeronautics and Space Administration, Contracts NASW-4844 and NAS5-32862, and by the National Science Foundation, Grant ATM-9301105.

## References

- Barath, F.T., and Co-authors. The Upper Atmosphere Research Satellite Microwave Limb Sounder instrument. *J. Geophys. Res.*, **98**, 10,751-10,762, 1993.
- Chen, P. Isentropic cross-tropopause mass exchange in the extratropics. *J. Geophys. Res.*, **100**, 16,661-16,673, 1994.
- Dunkerton, T.J., Evidence of meridional motion in the summer lower stratosphere adjacent to monsoon regions. *J. Geophys. Res.*, **100**, 16,675-16,688, 1995.
- Dunkerton, T.J., and D.P. Delisi. The subtropical mesospheric jet observed by the Nimbus 7 Limb Infrared Monitor of the Stratosphere. *J. Geophys. Res.*, **90**, 10,681-10,692, 1985.
- Holton, J.R., P.H. Haynes, M.E. McIntyre, A.R. Douglass, R.B. Rood, and L. Pfister. Stratosphere-troposphere exchange. *Rev. Geophys.*, **33**, 403-439, 1995.
- McIntyre, M.E., and T.N. Palmer. The 'surf zone' in the stratosphere. *J. Atmos. Terr. Phys.*, **46**, 825-849, 1984.
- Randel, W.J., Global Atmospheric Circulation Statistics, 1000-1 mb. NCAR Tech. Note (NCAR/TN-366+STR), Boulder, CO, 1992.
- Randel, W.J., B.A. Boville, J.C. Gille, P.L. Bailey, S.T. Massie, J.B. Kumer, J.L. Mergenthaler, and A.E. Roche. Simulation of stratospheric  $\text{N}_2\text{O}$  in the NCAR CCM2: comparison with CLAES data and global budget analyses. *J. Atmos. Sci.*, **51**, 2834-2845, 1994.
- Roche, A.E., J.B. Kumer, J.L. Mergenthaler, G.A. Ely, W.G. Uplinger, J.F. Potter, T.C. James and L.W. Sterritt. The Cryogenic Limb Array Etalon Spectrometer (CLAES) on UARS: experiment description and performance. *J. Geophys. Res.*, **98**, 10,763-10,776, 1993.
- Salby, M.L., D. O'Sullivan, R.R. Garcia, and P. Callaghan. Air motions accompanying the development of a planetary wave critical layer. *J. Atmos. Sci.*, **47**, 1179-1204, 1990.
- Swinbank, R. and A. O'Neill. A stratosphere-troposphere data assimilation system. *Mon. Wea. Rev.*, **122**, 686-702, 1994.
- Trepte, C.R., and M.H. Hitchman. The stratospheric tropical circulation deduced from aerosol satellite data. *Nature*, **355**, 626-628, 1992.
- Waters, J.W., L. Froidevaux, W.G. Read, G.L. Manney, L.S. Elson, D.A. Flower, R.F. Jarnot, and R.S. Harwood. Stratospheric  $\text{ClO}$  and ozone from the Microwave Limb Sounder on the Upper Atmosphere Research Satellite. *Nature*, **362**, 597-602, 1993.

T. J. Dunkerton and D. J. O'Sullivan, Northwest Research Associates, P.O. Box 3027, Bellevue, WA 98009.  
e-mail: tim@nwra.com; donal@nwra.com

(received May 8, 1996; revised June 25, 1996;  
accepted June 28, 1996.)

# The influence of the quasi-biennial oscillation on global constituent distributions

Donal O'Sullivan and Timothy J. Dunkerton

Northwest Research Associates, Bellevue, Washington

**Abstract.** Long-lived stratospheric constituents observed by the Upper Atmosphere Research Satellite are compared between late northern winters 1991-1992 and 1992-1993. The phase of the quasi-biennial oscillation (QBO) was such that the equatorial zonal wind was easterly (westerly) in the lower stratosphere during the first (second) winter. In the tropics, winter-to-winter differences in the latitude-height distribution of zonally averaged  $N_2O$  and  $H_2O$  are associated with differences in large-scale upwelling, the QBO's mean meridional circulations, and lateral mixing by incident extratropical Rossby waves. In the extratropics, significant differences in zonally averaged  $N_2O$  and  $H_2O$  are also found which are believed to represent the extratropical constituent QBO. The transport processes creating the extratropical constituent QBO are tentatively identified: In the winter extratropics, QBO modulation of the residual circulation appears to dominate in the upper stratosphere, while QBO-modulated Rossby-wave isentropic mixing dominates below about 10 mbar. Analysis of Rossby waves at low latitudes, as deduced from isobaric constituent distribution maps, suggests that the meridional distribution of Rossby wave breaking depends on the tropical zonal winds. Easterly QBO winds prevent Rossby-wave radiation into the tropics, so that a strong constituent concentration gradient is generated in the winter subtropics. Westerly QBO winds allow some wave radiation into the tropics, accompanied by isentropic mixing in the winter subtropics, cross-equatorial propagation, and occasional mixing in the summer subtropics. These effects depend on altitude and appear to vary in accord with the descending phases of the QBO.

## 1. Introduction

In the tropics, the zonal mean distribution of long-lived constituents is dramatically altered by the annual cycle, the semiannual oscillation (SAO), and the quasi-biennial oscillation (QBO) [Gray and Pyle, 1986; Zawodny and McCormick, 1991; Trepte and Hitchman, 1992; Hasebe, 1994; Hitchman et al., 1994]. The mean meridional circulations associated with these oscillations have upwelling/downwelling in conjunction with easterly/westerly shear layers on the equator. Thus, for example, a westerly SAO shear zone produces a double peak of methane mixing ratio in the upper stratosphere during springtime [Gray and Pyle, 1986].

Quasi-biennial variability in constituents or circulation is not nearly as dominant in the extratropics as it is in the tropics, because of the larger interannual, seasonal, and shorter-term variability present there. Nevertheless, the interaction of the QBO with the northern hemisphere extratropics has been documented in both circulation and long-lived constituents: the most active

seasons for QBO-extratropical interaction appear to be winter and spring.

The interaction of the QBO and extratropical circulation was first documented by Holton and Tan [1980, 1982] who found a robust correlation between the phase of the QBO at 50 mbar and the geopotential height in the north polar region. The relation is such that the December-February polar night jet is stronger during winters when the QBO phase at 50 mbar is westerly. Such QBO-correlated interannual variability of the polar vortex strength is now known as the extratropical QBO. The coupling of the winter extratropical circulation to the QBO apparently occurs through QBO modulation of extratropical Rossby-wave activity, as there is greater Eliassen-Palm flux convergence at middle and high latitudes throughout the stratosphere in the easterly QBO winter composite [Dunkerton and Baldwin, 1991; Baldwin and Dunkerton, 1991; Baldwin and Tung, 1994]. This tendency has also been simulated in numerical models [O'Sullivan and Salby, 1990; Dameris and Ebel, 1990; Holton and Austin, 1991; O'Sullivan and Young, 1992; O'Sullivan and Dunkerton, 1994; Butchart and Austin, 1996; Chen, 1996]. Such results imply that extratropical transport of constituents should be modulated by the phase of the QBO, as suggested by Tung and Yang [1994a, b] and Hess and O'Sullivan [1995].

Copyright 1997 by the American Geophysical Union.

Paper number 97JD01689.  
0148-0227/97/97JD-01689\$09.00

Thus the QBO affects tracer transport not only in the tropics but also throughout the winter middle atmosphere. The QBO signal in total ozone has been described using data from the satellite-borne total ozone mapping spectrometer (TOMS) [Bowman, 1989; *Last et al.*, 1989; *Chandra and Stolarski*, 1991; *Randel and Cobb*, 1994; *Tung and Yang*, 1994a]. These data show the dominant influence of the QBO in the tropics where the total ozone anomaly is approximately in phase with the equatorial 30-mbar zonal wind. They also depict an off-equatorial total ozone anomaly which develops in both northern and southern hemispheres during the local winter-spring season, with amplitude and sign depending on the QBO's phase. This seasonally synchronized subtropical and extratropical QBO signal in total ozone maximizes at  $\sim 30^\circ$ - $40^\circ$  latitude, and again at the pole, and is out of phase with the tropical anomaly [e.g., *Randel and Cobb*, 1994, Figure 11].

Studies using vertically integrated total ozone cannot reveal details of the extratropical QBO's vertical structure, however. *Randel and Wu* [1996] used stratospheric aerosol and gas experiment (SAGE) ozone and nitrogen dioxide (over the range  $\pm 60^\circ$  latitude with 1-km vertical resolution) and stressed the importance of the extratropical ozone QBO at middle stratospheric levels (above 30 mbar) in addition to the larger signal at lower levels (below 30 mbar). The extratropical QBO for different constituents depends greatly on the constituent's mean distribution, as this is the basic distribution that the QBO-modulated transport acts upon. Thus to isolate the extratropical QBO signal in constituent transport ideally requires multiyear data sets with vertical and global coverage of constituents which are long-lived at middle and lower stratospheric levels. Unfortunately, such data sets will not be available in the foreseeable future. The Upper Atmosphere Research Satellite (UARS) Halogen Occultation Experiment (HALOE) data may prove useful for this purpose, but the infrequent horizontal sampling by HALOE (about 30 profiles daily) limits its value for studying eddy transport processes.

In this paper, as an alternative to a long-term climatological study, we compare long-lived constituent distributions observed by UARS during its first two northern winters. We note the fortuitous phasing of the QBO, which switched phase by approximately  $180^\circ$  between winters, from a deep easterly QBO phase during the first winter to a deep westerly phase during the second. It is notable that the winter-mean extratropical circulations seen during these two northern winters were similar to the extratropical circulations observed for easterly and westerly QBO composites described above. Thus it is reasonable to suppose that the constituent transport seen during these two winters is also representative of a multiyear QBO composite and that the constituent's winter-to-winter difference is representative of the constituent's extratropical QBO signal. The objectives of this paper are to analyze the UARS observations of long-lived stratospheric constituents in order to determine the QBO's influence on global constituent distributions and to clarify how

the QBO modulates transport processes in the tropics and winter hemisphere.

## 2. Data

The UARS constituents chosen for this study are nitrous oxide ( $N_2O$ ) observed by the cryogenic limb array etalon spectrometer (CLAES) instrument [*Roche et al.*, 1993; *Roche et al.*, 1996] and water vapor ( $H_2O$ ) observed by the Microwave Limb Sounder (MLS) instrument [*Barath et al.*, 1993; *Waters et al.*, 1993; *Lahoz et al.*, 1996]. Level 3AT data, consisting of soundings along the orbital track, were used. The CLAES data have a vertical resolution of 2.5 km, while MLS data have about 6-km spacing.

$N_2O$  and  $H_2O$  are long-lived constituents in the stratosphere [*Andrews et al.*, 1987, Figure 9.2].  $N_2O$  is destroyed through photolysis and has a lifetime of greater than a year at 10 mbar, and which increases rapidly at lower levels.  $H_2O$  is created in the stratosphere from methane oxidation and therefore has a lifetime similar to methane's of about 3 years at 10 mbar and which increases rapidly below. Methane's longer lifetime allows this constituent to act as a source of  $H_2O$  in the extratropical upper stratosphere, providing a background concentration gradient that mixing processes can deform. On the other hand,  $N_2O$ 's shorter lifetime in this region results in nearly homogenized, very low mixing ratio values.

The UARS orbit allows coverage of the stratosphere between  $35^\circ S$  (N) and  $80^\circ N$  (S) during a northward (southward) viewing yaw period. Maps of the L3AT data were made by interpolating to a latitude-longitude grid using data from three consecutive days and an elliptical Gaussian weight function with major axis aligned in the zonal direction, as described by *Dunkerton and O'Sullivan* [1996]. These mappings take advantage of the CLAES and MLS instrument's frequent sampling, providing over 1200 vertical profiles per day. Such mappings capture the slowly evolving features and are particularly successful at lower latitudes where wind speeds are relatively weak. Comparison of maps for successive days shows that most significant features at low latitudes are slow moving and are well represented.

## 3. Comparison of the First Two Northern Winters of UARS

### 3.1. Zonal Wind

The evolution of the stratosphere's zonal mean wind at 10 mbar over the first two years of UARS is shown in Figure 1, using United Kingdom Meteorological Office (UKMO) assimilated winds [*Swinbank and O'Neill*, 1994a]. The polar vortex was relatively disturbed during the first winter when the QBO phase was easterly over a deep layer from 60 mbar to near 15 mbar (Figure 2a), while it was relatively quiet during the second winter [*Manney et al.*, 1994, 1995] when the QBO was westerly over a deep layer (from 70 to above 10 mbar). Comparing the two northern winters shows that the polar vortex broke down earlier in 1991-1992 than the fol-

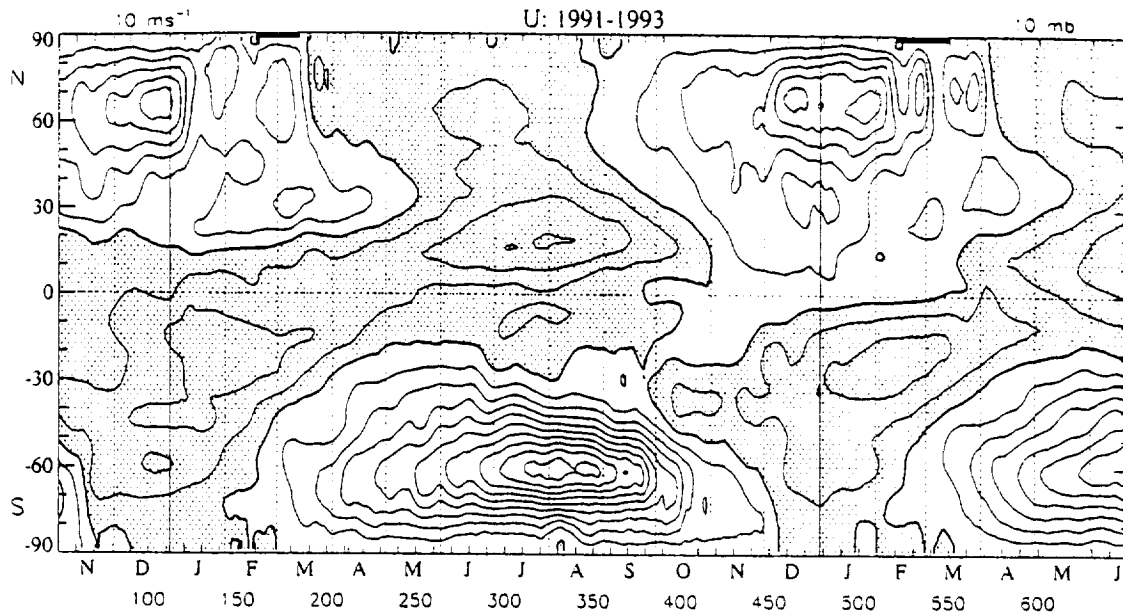


Figure 1. Latitude-time cross section of mean zonal wind at 10 mbar, from United Kingdom Meteorological Office (UKMO) analyses. Contour interval is  $5 \text{ m s}^{-1}$ , and easterlies are shaded. The bold bars indicate the duration of the northward viewing yaw periods discussed here.

lowing year. In 1991-1992 the vortex broke down in mid-January, whereas in the following year it survived until the beginning of March.

Although the UKMO assimilation provides a good representation of the QBO at most times when compared with Singapore rawinsonde data (Figure 2a) [Naujokat, 1986], there is a discrepancy at the 10-mbar level during the first UARS winter, with the onset of the westerly phase at 10 mbar occurring 10 months later in the UKMO analyses than in Singapore rawinsonde observations (Figure 2a), occurring in September 1992 versus November 1991, respectively [Swbank and O'Neill, 1994b]. The UARS high resolution Doppler imager (HRDI) instrument [Ortland *et al.*, 1996, Figure 11] provides independent zonal wind observations and indicates that zonal mean westerly winds near 10 mbar first appear during April 1992. At other times, there is much better agreement between Singapore, UKMO, and HRDI zonal wind observations.

Figure 2b shows the 1992 minus 1993 difference in the zonal mean wind averaged over the months of January, February and March. This corresponds to an "easterly minus westerly" QBO phase difference and shows the dipole pattern associated with Holton and Tan's [1980] extratropical QBO [Baldwin and Dunkerton, 1991, Figure 3]. The corresponding difference in geopotential height at 10 mbar (not shown) also gave a pattern similar to that of Holton and Tan [1980] (and Dunkerton and Baldwin [1991]). These results suggest that the QBO is responsible for the extratropical circulation differences between the two northern winters. In the following we will refer to the differing extratropical circulation as the extratropical QBO's dynamical signal. It is, in any case, the signature of a relatively "active" versus "inactive" winter in the northern hemisphere stratosphere.

### 3.2. CLAES Nitrous Oxide Distributions

To compare the distribution of long-lived constituents between the first two northern winters, we are limited to the time periods when the UARS instruments were northward viewing. This occurred from early December to mid-January and again from mid-February to mid-March of both winters. Unfortunately, only a few days of data are available from the CLAES instrument for the first time period during the winter of 1991-1992, so we concentrate on a year-to-year comparison of constituents during the mid-February to mid-March yaw period. Plate 1 shows the zonal mean  $\text{N}_2\text{O}$  mixing ratio cross section averaged over mid-February to mid-March for both years, along with their difference. The bold horizontal line in the tropics indicates the 27-km ( $\sim 20$  mbar) level which approximately marks the aerosol cloud top in early 1992 [Lambert *et al.*, 1993]. Both winters show the extratropical surf zone between about  $20^\circ$  and  $60^\circ\text{N}$  as a region of nearly horizontal isopleths. The polar vortex is evident north of about  $60^\circ\text{N}$  in the lower stratosphere as a region of lower  $\text{N}_2\text{O}$  mixing ratio. Both years also show displacement of isopleths due to tropical upwelling and winter extratropical downwelling characteristic of the large-scale Brewer-Dobson circulation. The elevated maximum  $\text{N}_2\text{O}$  mixing ratio in the tropics between 30 and 50 mbar (Plate 1a) is probably an artifact introduced by the Mount Pinatubo aerosol cloud, since the major source of stratospheric  $\text{N}_2\text{O}$  is ground-level emissions from microbiological activity followed by tropical ascent into the stratosphere. At this time the Pinatubo aerosol cloud was dense below about 30 mbar ( $\sim 26$  km) within about  $20^\circ$  of the equator [Grant *et al.*, 1994], so  $\text{N}_2\text{O}$  values in this region may not be accurate. It is unlikely that aerosol lofting could explain the constituent pattern outside of

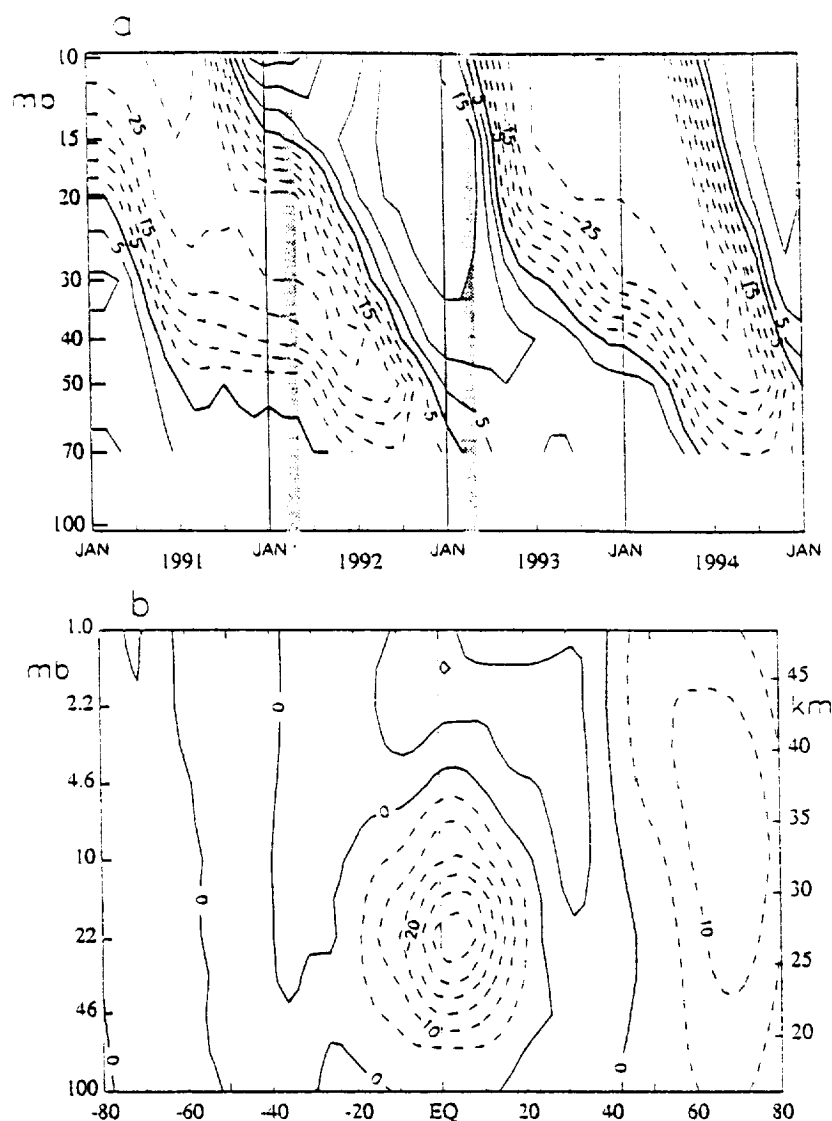


Figure 2. (a) Monthly mean zonal winds at Singapore ( $1^{\circ}\text{N}$ ,  $104^{\circ}\text{E}$ ). Contour interval is  $5 \text{ m s}^{-1}$  and easterlies are shown by dashed lines. Shading denotes the time periods discussed in this paper. (b) Latitude-height cross-section of the 1992 minus 1993 mean zonal wind difference, averaged over January through March, from UKMO analyses.

the equatorial lower stratosphere, however. As noted by Dunkerton and Delisi [1991] in their study of the time period after El Chichon, it is difficult for aerosols to have much direct, long-lasting impact on the mean meridional circulation because (1) the aerosol tends to settle into a shallow layer, implying a small geopotential perturbation for a typical temperature anomaly, and (2) the aerosol spreads horizontally, reducing the latitudinal gradient of heating (which is one of two terms driving the mean meridional circulation). Furthermore, (3) aerosol-induced lofting is accompanied by ozone reduction, which has a buffering effect on the mean meridional circulation [Kinne *et al.*, 1992]. Finally, (4) the magnitude and even the sign of heating rate above an aerosol cloud is not known, so that little can be said about the direct effect of aerosols above the aerosol cloud.

Analysis of CLAES  $\text{N}_2\text{O}$  during January–March 1992 suggests the following. The structure of the tropical

maximum (mixing ratio greater than 240 parts per billion by volume (ppbv)) is consistent with transport by the QBO mean meridional circulation as discussed by Trepte and Hitchman [1992], given that the QBO zonal wind has a westerly shear layer near 15 mbar according to the Singapore rawinsonde record (Figure 2a). Strong meridional gradients of  $\text{N}_2\text{O}$  develop about the equator near  $20^{\circ}\text{N}$  or  $20^{\circ}\text{S}$  latitude, partly attributable to meridional outflow away from the equator below the westerly shear layer, as discussed by Trepte and Hitchman. Strong vertical gradient of  $\text{N}_2\text{O}$  mixing ratio occurs just above 15 mbar at the equator due to the QBO mean meridional circulation's downwelling in the westerly shear zone.

The marked asymmetry of  $\text{N}_2\text{O}$  mixing ratio about the equator at and above 15 mbar is, however, a major difference between this pattern and the canonical QBO-induced aerosol pattern discussed by Trepte and Hitchman [1992]. Transport by the QBO's mean merid-

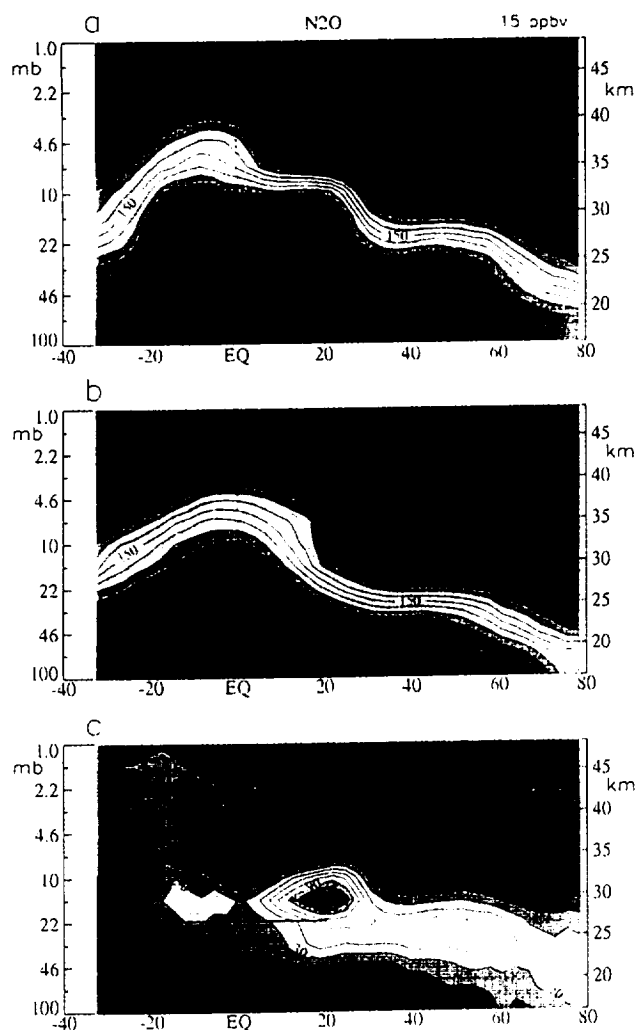


**Plate 1.** Latitude-height cross-sections of CLAES  $\text{N}_2\text{O}$ , averaged over UARS days (a) 160-185 (February 18-March 14, 1992); (b) 520-550 (February 12-March 14, 1993); and (c) the difference (a) minus (b). Contour interval is 15 ppbv in Plates 1a-1c with the darkest blue representing 0-15 ppbv in Plate 1a and Plate 1b. In Plate 1c negative values are shown by dashed contours, and the bold line denotes the zero isopleth. In the tropics a solid horizontal line indicates 27-km altitude, indicating the approximate top of the Mount Pinatubo aerosol cloud in early 1992.

ional circulations alone would produce a pattern symmetric about the equator. This difference could be due to the different season examined here (late winter) compared with Trepte and Hitchman's cases, which were from early October and early November (see their Figure 3). In our case, the upwelling Brewer-Dobson circulation has become stronger in the summer hemisphere subtropics, tending to elevate the mixing ratio isopleths near  $10^\circ$ - $20^\circ\text{S}$ . Grant *et al.* [1996] similarly show equatorial asymmetry about the equator for constituent distributions below 30 km during winter and summer due to seasonally varying upwelling. A second difference is the presence of a strong flux of Rossby-wave activity toward the tropics from the winter extratropics. The propagation and breakdown of these waves, approach-

ing the equator at a particular altitude, depends on the phase of the QBO at that altitude as discussed in section 3.4. A third factor to consider is that the altitude range studied by Trepte and Hitchman was lower than our region of interest, since aerosol concentration is very low above about 30 km.

A year later, in January-March 1993, the QBO has evolved to a nearly opposite phase, with a rapidly descending easterly shear layer near 10 mbar and weaker westerly shear mainly below 50 mbar (Figure 2a). The zonal mean  $\text{N}_2\text{O}$  mixing ratio pattern (Plate 1b) is very different from a year earlier (Plate 1a) at low latitudes, having weaker meridional gradients flanking a central, nearly equatorial peak. The easterly shear layer and upwelling at the equator are centered near 10 mbar, where the mixing ratio isopleths show a more pronounced upward displacement than is seen at altitudes above or below. The asymmetry of the mixing ratio pattern about the equator, above 50 mbar, is mainly due to a stronger meridional gradient in the winter subtropics. This represents the equatorward edge of the winter midlatitude surf zone as it encroaches on the tropics [Grant *et al.*, 1996]. The strongest meridional gradient in the winter subtropics slopes upward and equatorward from  $\sim 20^\circ\text{N}$  at 30-40 mbar to  $\sim 10^\circ\text{N}$  at 10 mbar. Above 10 mbar the strongest gradient again occurs at  $\sim 20^\circ\text{N}$ . This is consistent with HRDI wind observations for March 1993 [Ortland *et al.*, 1996] showing equatorial easterlies reaching to near  $20^\circ\text{N}$  above 10 mbar, while westerlies occur below, approximately the reverse of the zonal wind configuration a year earlier. Isobaric synoptic maps of constituent mixing ratios are presented in section 3.4 to help distinguish the transport effects of mean motions from those of eddy mixing.

Comparing the two winters'  $\text{N}_2\text{O}$  distributions indicates that greater large-scale tropical upwelling occurred in February-March 1992 than in February-March 1993. This is indicated in the 1992 minus 1993 mixing ratio difference (Plate 1c) by a positive anomaly in the summer hemisphere's low latitudes above 50 mbar. Similarly, the mixing ratio difference in the winter extratropical upper stratosphere suggests that greater downwelling occurred in 1992, creating the negative difference in the winter extratropics between 30 and 40 km. In the extratropics below 10 mbar, however, it appears that enhanced meridional mixing by Rossby waves during February-March 1992 was the dominant effect. Such differences in long-lived constituent distributions are consistent with the dynamical differences between the two winters. During the 1991-1992 (easterly QBO phase) winter, the more disturbed extratropical circulation would result in a strengthened Brewer-Dobson circulation and greater Rossby-wave mixing compared with the less disturbed 1992-1993 (westerly QBO phase) winter.

### 3.3. MLS Water Vapor Distributions

In this section we look at water vapor, an independently observed long-lived constituent observed by MLS, for comparison with  $\text{N}_2\text{O}$ . Plates 2a,b present zonal mean MLS  $\text{H}_2\text{O}$  mixing ratio cross sections for

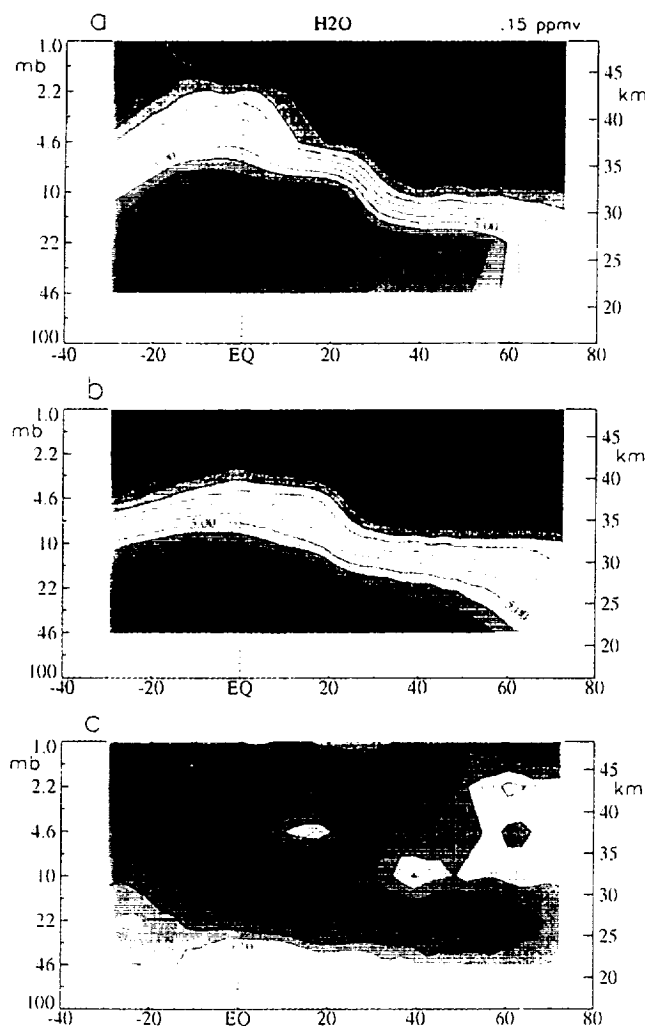


**Plate 2.** Latitude-height cross sections as in Plate 1 except for MLS  $\text{H}_2\text{O}$ . Contour interval is 0.15 ppmv in Plates 2a-2c, with the darkest blue representing 3.65-3.8 ppmv in Plate 2a and Plate 2b.

the mid-February to mid-March yaw periods of 1992 and 1993, respectively.

There is a strong similarity between the  $\text{H}_2\text{O}$  and  $\text{N}_2\text{O}$  mixing ratio patterns, allowing for their approximately inverted source/sink distribution with height and the poorer vertical resolution of MLS relative to CLAES. Plate 2a shows the stronger tropical upwelling with strong meridional gradients near  $\sim 25^\circ\text{N}$  and  $20^\circ\text{S}$ , the tropical mixing zone above 10 mbar, downwelling in the winter extratropics and especially within the polar vortex, and the winter midlatitude surf zone. The lower vertical resolution of MLS does not permit the sharp vertical gradient near 10 mbar and  $0^\circ$ - $20^\circ\text{N}$  to be resolved as well as by CLAES, however. Methane oxidation increases  $\text{H}_2\text{O}$  mixing ratios with height in the upper stratosphere, so that  $\text{H}_2\text{O}$  shows strong gradients in this region, whereas the  $\text{N}_2\text{O}$  has been mostly destroyed and therefore appears nearly constant. Thus the  $\text{H}_2\text{O}$  mixing ratio (Plates 2a and 2b) highlights the meridional gradient near 5 mbar and  $35^\circ\text{N}$  much more clearly than the  $\text{N}_2\text{O}$  mixing ratio (Plates 1a and 1b).

The  $\text{H}_2\text{O}$  mixing ratio from 1993 similarly compares well with the  $\text{N}_2\text{O}$  mixing ratio. The main difference between the two constituent distributions is that the  $\text{H}_2\text{O}$  mixing ratio gradients are more uniformly distributed over the domain, although the meridional gradient at the subtropical jet is still clearly evident from  $\sim 20^\circ\text{N}$  near 22 mbar to  $30^\circ\text{N}$  near 2.2 mbar (Plate 2b). The 1992 minus 1993 difference (Plate 2c) bears a strong similarity to that of the  $\text{N}_2\text{O}$  mixing ratio (Plate 1c), apart from a sign change. The agreement between  $\text{N}_2\text{O}$  and  $\text{H}_2\text{O}$  is remarkable, considering the instrument and species lifetime differences, and increases our confidence in the accuracy of the observations.

As with  $\text{N}_2\text{O}$ , the main features in the winter difference plot can be attributed to transport processes. The tropical mixing zone above 10 mbar in February-March 1992 results in a positive maximum in the  $\text{H}_2\text{O}$  mixing ratio difference near  $0^\circ$ - $20^\circ\text{N}$ . Large-scale tropical upwelling, cross-equatorial transport and winter extratropical downwelling above 10 mbar are stronger during the first winter than the second, causing the large region of negative  $\text{H}_2\text{O}$  differences in the tropics and summer low latitudes, with positive difference above 10-15 mbar in the winter extratropics north of about  $40^\circ\text{N}$ . Below 10-15 mbar, for example, at 22 mbar, in the extratropics the negative  $\text{H}_2\text{O}$  difference reflects stronger surf zone meridional transport in the first winter. Thus comparing the February-March period between these winters suggests that meridional mixing dominates the zonal mean  $\text{H}_2\text{O}$  mixing ratio tendency below 10-15 mbar while Brewer-Dobson advection dominates above. The longer lifetime of  $\text{H}_2\text{O}$  in the middle and upper stratosphere allows the 1992 minus 1993  $\text{H}_2\text{O}$  mixing ratio difference to be seen better in the upper stratosphere than was the case with  $\text{N}_2\text{O}$ . Otherwise, despite minor differences, the  $\text{H}_2\text{O}$  mixing ratio winter difference (Plate 2c) resembles the  $\text{N}_2\text{O}$  difference with sign reversed.

### 3.4. Rossby Wave-Induced Mixing

The striking winter-to-winter variability seen in the zonal mean constituent distribution at low northern latitudes, mirrored in the strong, equatorially asymmetric difference anomaly (Plate 1c and 2c), suggests that QBO-dependent Rossby-wave transport is active in shaping the distributions. To illustrate the importance of Rossby-wave mixing for trace constituent differences between easterly and westerly QBO phase, and their dependence on altitude, we present a few maps of CLAES  $\text{N}_2\text{O}$  in the time periods of interest. Plates 3a and 3b show the distribution of  $\text{N}_2\text{O}$  in early 1992 (UARS days 165-168; February 23-26) at 4.6 and 14.7 mbar, respectively, while Plates 4a and 4b show the corresponding distribution at these altitudes in early 1993 (UARS days 528-530; February 20-23). The days selected from each winter are representative of their yaw periods, and the features we discuss are also evident on other days of each yaw period. One feature immediately apparent is the larger  $\text{N}_2\text{O}$  concentration throughout the tropics in the first winter at 14.7 mbar. This may indicate en-



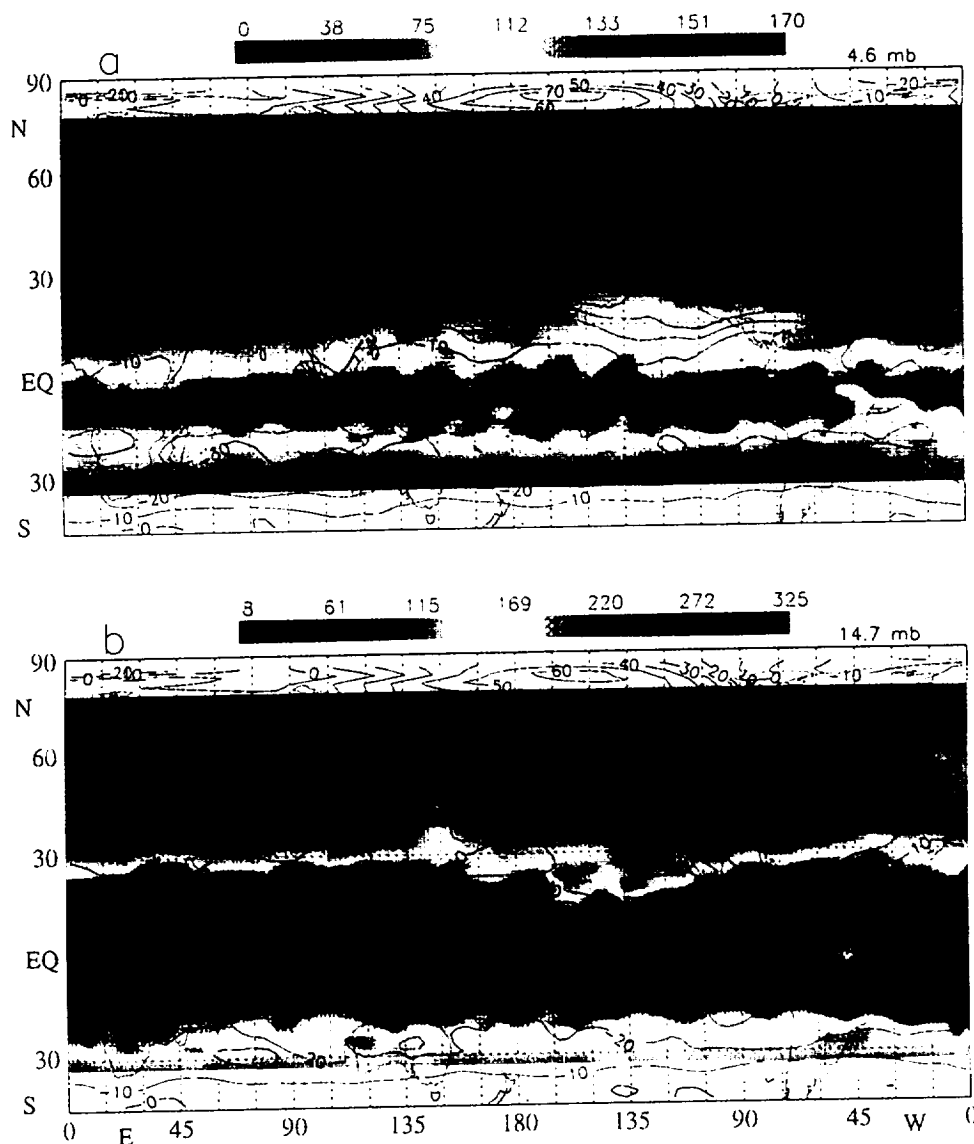
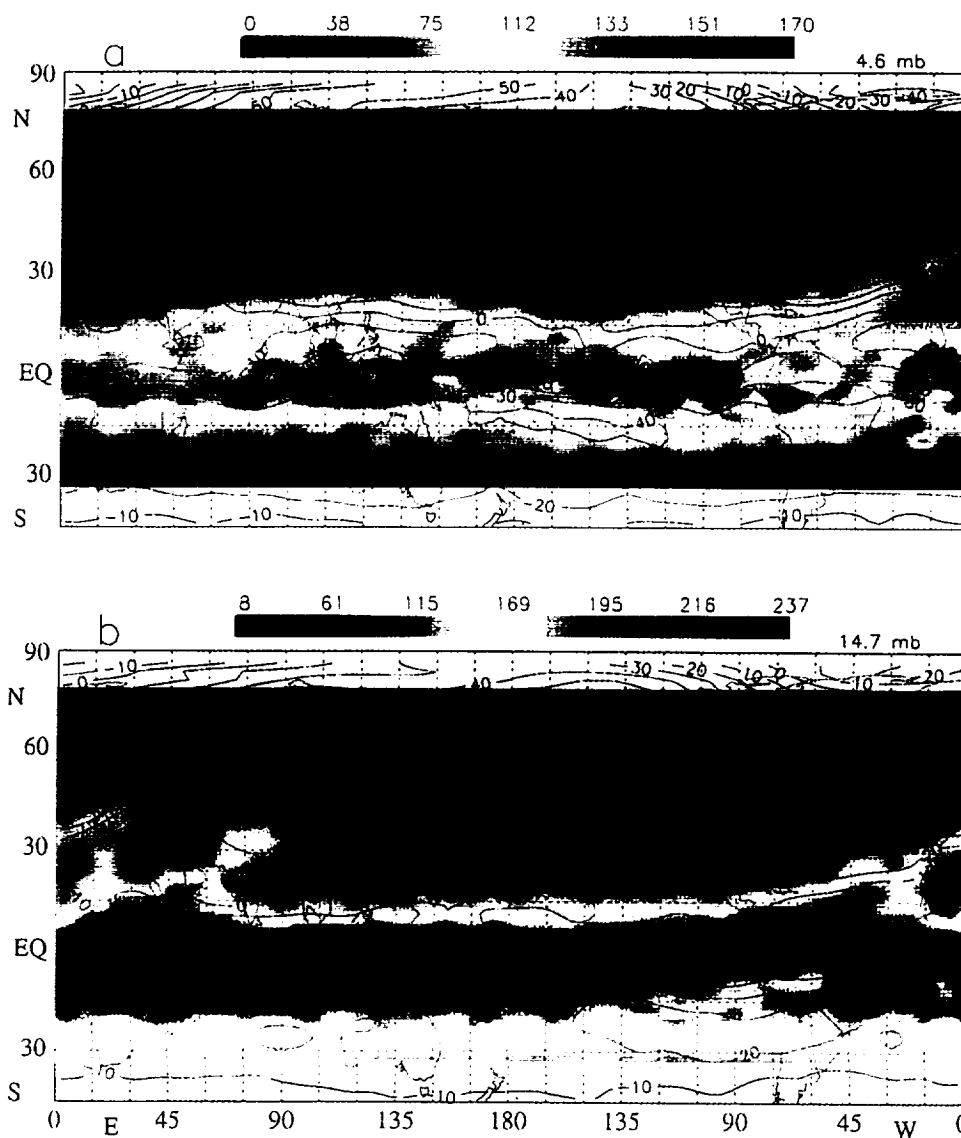


Plate 3. Horizontal map of CLAES N<sub>2</sub>O mixing ratio (ppbv) and UKMO zonal wind ( $\text{m s}^{-1}$ ) averaged over UARS day 165-168 (February 23-26, 1992) at (a) 4.6 mbar, and (b) 14.7 mbar.

hanced Brewer-Dobson upwelling, as noted above, since the pattern of increased N<sub>2</sub>O in Plate 3b is almost zonally symmetric and unperturbed by Rossby waves. Note that the same color scheme is used in Plates 3a and 4a (4.6 mbar) but that the scheme is altered between Plates 3b and 4b (14.7 mbar) due to the different tropical N<sub>2</sub>O concentrations seen at that level in each winter. Several other features in these maps comparing the two years cannot be explained solely in terms of mean meridional transport, however. The data suggest that Rossby-wave propagation and breaking, as modulated locally by the QBO, plays a significant role in shaping the distribution of long-lived constituents in the tropics and subtropics (where our color scheme displays the greatest contrast). In particular, the intensity and location of maximum horizontal N<sub>2</sub>O gradient, and the latitude of maximum N<sub>2</sub>O concentration, differ significantly between the two winters in a manner consistent with the action of laterally propagating Rossby waves

and a local modulation of their propagation and breaking by the QBO winds.

During January-March 1992, Rossby waves are seen to transport N<sub>2</sub>O-depleted air quasi-horizontally closer to the equator above about 10 mbar, creating a tropical mixing zone between the equator and 20°N. Isobaric maps of N<sub>2</sub>O above 10 mbar show that N<sub>2</sub>O is transported to about 10°N on day 165 (Plate 3a) and to about 5°N by day 180 [see Dunkerton and O'Sullivan, 1996, Figure 4]. Below 10 mbar, such maps show quasi-stationary Rossby-wave radiation to be nearly completely blocked at about 20°N throughout February and March (Plate 3b). This is presumably due to the QBO zonal wind, which is westerly above 10-15 mbar and easterly below (Figure 2a). Winds observed by HRDI during March 1992 also show strong tropical easterlies below about 10 mbar reaching to about 20°N, while above 10 mbar (to at least 2 mbar) there are weak easterly or westerly zonal mean winds between the equator



**Plate 4.** Horizontal map of CLAES  $\text{N}_2\text{O}$  mixing ratio (ppbv) and UKMO zonal wind ( $\text{m s}^{-1}$ ) averaged over UARS day 528-530 (February 20-23, 1993) at (a) 4.6 mbar, and (b) 14.7 mbar. Note the altered color scale between Plate 3b and Plate 4b.

and the extratropical westerly jet (Figure 3a and *Ortland et al.* [1996, Figure 12a]). One effect of Rossby-wave mixing at low latitudes above 10 mbar is the dissipation of the QBO mean meridional circulation-induced peak near  $20^\circ\text{N}$ . The equatorward transport and mixing above 10 mbar during February and March was discussed by *Dunkerton and O'Sullivan* [1996].

Examination of isobaric maps of  $\text{N}_2\text{O}$  mixing ratio during late February 1993 indicates that Rossby waves penetrate closer to the equator below 10 mbar, to about  $10^\circ\text{N}$  at least, with some evidence of propagation across to the summer hemisphere (e.g., Plate 4b shows the 15-mbar level) while their transport signature is largely confined poleward of  $\sim 15^\circ$ - $20^\circ\text{N}$  above 10 mbar (Plate 4a). Such behavior is consistent with linear Rossby-wave theory, which permits the equatorward radiating Rossby waves to propagate until they reach their critical latitude ( $\bar{u} = c \sim 0$  in this case). During February and

March 1993, QBO easterlies should block equatorward radiating Rossby waves near  $\sim 20^\circ\text{N}$  above 10 mbar, (e.g., Figure 3a). Below 10 mbar at this time, however, zonal winds at low latitudes remain weakly westerly in the lower stratosphere according to UKMO wind analyses (not shown) or HRDI observations (Figure 3b). This allows the possibility of Rossby-wave radiation from extratropical westerlies to reach the equator and summer hemisphere [*Chen*, 1996; *O'Sullivan*, 1997].

The propagation of Rossby waves and their irreversible effect on the distribution of a long-lived tracer evidently depend on the local wind distribution as modulated by the QBO. A "westerly over easterly" zonal wind pattern (as occurred in the first UARS winter) allows the possibility of wave propagation into the equatorial zone in the upper, but not lower, levels, while an "easterly over westerly" pattern (as developed in the second winter) prevents equatorial penetration at up-

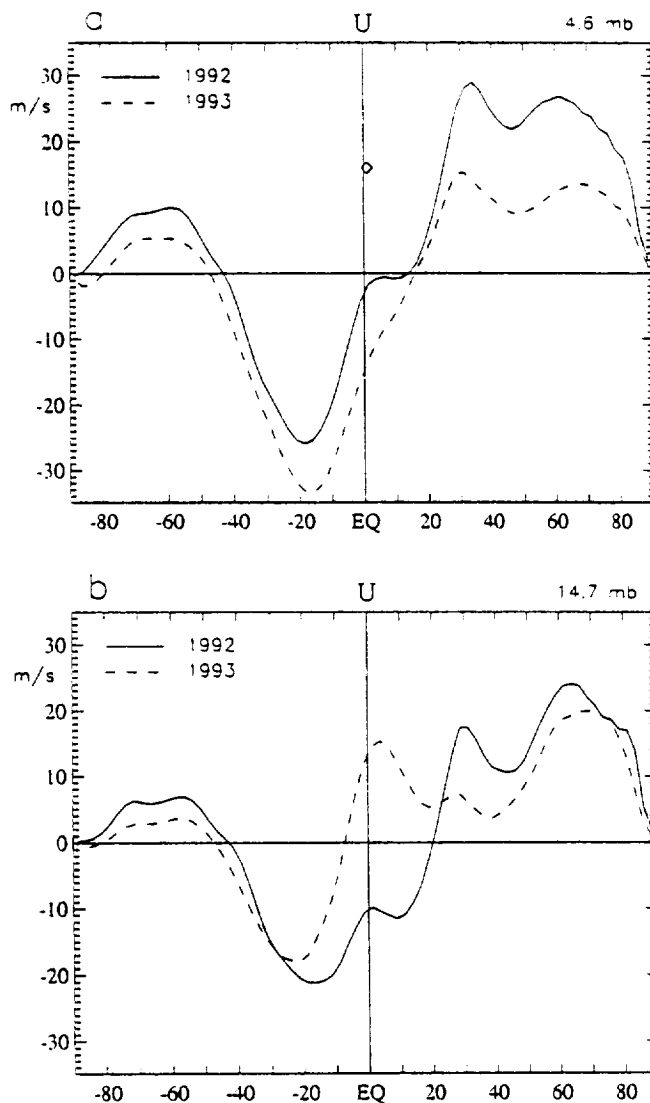


**Figure 3.** Meridional profile of zonal mean wind at (a) 4.6 mbar, and (b) 14.7 mbar, averaged over the two yaw periods. Winds are from UKMO analyses poleward of  $30^\circ$  and HRDI equatorward of  $16^\circ$ , with a linear transition between. The corresponding 1992 Singapore zonal wind observation in Figure 3a is shown by the diamond.

per levels while allowing a modest amount of isentropic mixing at lower levels of the tropics. The strength and location of the subtropical tracer "barrier" therefore depends on the ability of Rossby waves to penetrate the tropics, irrespective of any remote effect of the QBO on extratropical waves. Not surprisingly, at any given altitude this barrier (e.g., in the region  $\sim 10^\circ$ – $25^\circ$ N) was more diffuse when tropical winds were westerly compared with when they were easterly. Thus, at 4.6 mbar a sharper subtropical gradient is visible in Plate 3b than in Plate 4b, while at 14.7 mbar the subtropical gradient is sharper in Plate 3b than in Plate 4b. Dunkerton and O'Sullivan [1996] showed, however, that in the first UARS late winter, the subtropical tracer gradient coincided with the axis of a climatological subtropical jet. The jet axis and tracer gradient tilted poleward with height in the upper stratosphere. There was a second

tracer gradient at the equator, associated with QBO westerlies that formed around this time. These features are visible in Plate 3a.

In general, the apparent subtropical "transport barrier" can be viewed as the lateral terminus of a mixing zone. However, there may be more than one reason for such a terminal latitude to appear in the tracer data. On the one hand, Rossby-wave mixing tends to be suppressed in a westerly jet core for reasons discussed by Dunkerton and O'Sullivan [1996]. On the other hand, a critical latitude (i.e., critical level where intrinsic phase speed goes to zero) acts as a barrier to mixing because propagation, hence breaking, is precluded beyond this point, or more precisely, beyond the edge of the critical layer. In the first case, mixing does not occur because a critical latitude cannot exist at the jet core for waves able to propagate on the jet, so that mixing is discouraged at the center of the jet. In the second case, mixing does not occur because further wave propagation is precluded by the presence of a critical latitude. The common thread is that significant mixing occurs only in a region of breaking waves, i.e., a critical layer. For quasi-stationary waves which dominate the winter middle atmosphere, the breaking region or "surf zone" occurs poleward of the zero-wind line in a region of relatively weak winds, and is bounded to the north and south either by a westerly jet(s) (equatorial, subtropical, and/or polar) or a region of strong easterlies in which such waves cannot propagate at all.

The tracer distribution in the tropical and subtropical upper stratosphere in the first UARS late winter may be explained in terms of the first mechanism, due to the subtropical westerly jet and formation of QBO westerlies over the equator. At lower levels in the first winter and at upper levels in the second winter, the second mechanism seems more relevant on account of QBO easterlies at the respective altitudes. Latitudinal profiles of mean zonal wind for the two yaw periods in 1992 and 1993 are shown in Figure 3 as obtained from HRDI and UKMO data, together with the point measurement at Singapore. At the upper level in 1992 (Figure 3a), a new westerly jet is beginning to develop near the equator, but the actual maximum value is just shy of zero, unlike the situation at Singapore where typical QBO westerlies have already been attained. There is evidently some zonal variation in the onset of QBO westerlies, such that westerlies first appear near the maritime continent, in the region south-southwest of the Aleutian anticyclone, into which positive potential vorticity (PV) is advected by the prevailing anticyclonic flow. Westerlies are associated with the southern flank of an extrusion of high-PV air and are therefore expected to form in this region as a result of planetary wave breaking. At the upper level in 1993, zonal winds are easterly south of about  $15^\circ$ N, and the subtropical jet is weaker than in 1992. (These results agree with Figure 2b. However, the polar night jet in Figure 2b (January–March average) is weaker in 1992, as expected of the Holton–Tan oscillation, whereas in Figure 3a the jet speed, averaged over the yaw period (mid-February to mid-March), is stronger in 1992. Compared with Figure 1, the polar

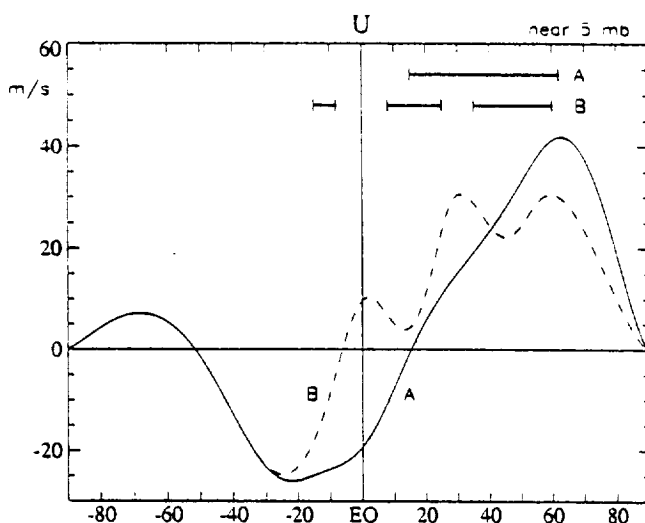


**Figure 4.** Schematic of the meridional profile of zonal mean wind in the upper stratosphere during late winter, when the quasi-biennial oscillation's phase in the lower stratosphere is westerly (letter A) or easterly (letter B). (Note that the QBO reverses phase between the lower and upper stratosphere.) The solid horizontal lines indicate the extent of distinct meridional mixing zones which may form during late winter (see text for details).

night jet reappeared during the yaw period in late winter 1992, but in 1993, winds were actually at a local minimum during this time. Thus the apparent QBO anomaly in high latitudes in Figure 3a is simply due to the timing of planetary wave events and does not indicate the true extratropical QBO shown in Figure 2b.) At the lower level in 1992 (Figure 3b), the QBO was westerly in 1993, while in 1992 the QBO was easterly, and a new westerly jet was beginning to emerge.

The ability of Rossby waves to penetrate the tropics differs significantly between the two periods shown in Figure 3, at both levels. At the upper level in 1992, stationary waves can radiate across the equator at certain longitudes (e.g., near Singapore), and slowly westward propagating waves can reach the equator at all longitudes. In 1993, all such waves are excluded from the tropics. (The Singapore zonal wind at 35 km in 1993 is  $-18 \text{ m s}^{-1}$  in good agreement with HRDI,  $-15 \text{ m s}^{-1}$ , and there is no evidence of significant zonal asymmetry at this time.) At the lower level the difference in wave propagation is more dramatic, but wave amplitudes at this altitude should be smaller, on average, due to the density effect.

Figure 4 summarizes schematically the contrasting situations observed at upper levels in early 1992 and 1993, which may be taken to represent opposing phases of the tropical QBO in the upper stratosphere in late winter. QBO easterlies at lower levels are accompanied by the formation of QBO westerlies at upper levels. In this case, indicated by letter B, the extratropical QBO signal is such that midlatitude planetary wave activity is enhanced, the polar night jet is weakened, a more pronounced subtropical jet forms, and Rossby waves

are able to penetrate the tropics at upper levels. The midlatitude surf zone is divided in half by the subtropical jet, and mixing extends to the equator, the "tropical mixing zone" of Dunkerton and O'Sullivan [1996]. In the opposite phase of the QBO, indicated by letter A, planetary wave activity is diminished somewhat by QBO westerlies at lower levels, etc., and propagation of quasi-stationary waves into the tropics at upper levels is entirely prevented by QBO easterlies. In the latter time and place, surf-zone mixing ends close to the zero-wind line. In reality, it is possible that westward moving disturbances are excited in the breaking zone of quasi-stationary waves [Polvani et al., 1995; O'Sullivan and Chen, 1996], which may lead to minor mixing equatorward of the zero-wind line, or wherever such waves encounter their critical latitude. The main mixing zones in the upper stratosphere for each winter are indicated in Figure 4 by bold lines. Also included is a mixing zone at low latitudes in the summer hemisphere which can form when the equatorial wind is westerly [O'Sullivan, 1997].

#### 4. Conclusions

We have compared the distribution of long-lived stratospheric constituents in the first two northern winters (1991-1992 and 1992-1993) observed by the UARS satellite. In the tropics, these winters were characterized by opposite QBO phases: A deep layer of easterlies dominated the lower stratosphere with westerlies above about 10 mbar during the first winter, and zonal winds were westerly throughout the lower stratosphere during the second winter with easterlies above about 10 mbar.

The behavior of the extratropical circulation during these two northern winters was consistent with the extratropical QBO [Holton and Tan, 1980, 1982] whereby the polar vortex is more disturbed and weaker during winters with easterly QBO rather than westerly QBO phase at 40 mbar. This is seen in the January-March average zonal mean wind (Figure 2b) and in 10-mbar geopotential height. It is reasonable, then, to expect that the distribution of long-lived constituents during these two northern winters should also be representative of their QBO composites, if enough years of data were available to obtain such composites.

The main objective of this paper has been to compare the late winter distribution of long-lived constituents, CLAES  $\text{N}_2\text{O}$  and MLS  $\text{H}_2\text{O}$ , between two northern winters with opposite QBO phase in order to reveal how the QBO may be influencing their distribution globally. From the comparison of winters it is concluded that long-lived constituents are affected by the QBO throughout the tropics and winter hemisphere. The winter-to-winter difference of these two independently observed constituents shows a similar mixing ratio pattern, as would be expected if the difference were due to differing transport between winters.

Comparison of the two winters (Plates 1 and 2) shows that transport by mean meridional circulations is affected by the QBO both locally and globally. The local redistribution by the QBO's mean meridional cir-

ulation has been previously studied and is evident regardless of season because it is the dominant source of transport variability in the tropics. During the first winter, having a deep easterly QBO phase below about 10 mbar, both  $\text{N}_2\text{O}$  and  $\text{H}_2\text{O}$  (zonally averaged) show a region of weak mixing ratio gradient within about  $20^\circ$  of the equator, at altitudes up to about 10 mbar, flanked by strong meridional gradients. The second winter, in contrast, had westerly QBO phase below 10 mbar and shows a narrower, peaked zonal mean mixing ratio distribution centered near the equator with much weaker meridional mixing ratio gradients along its flanks.

The QBO also modulates the large-scale Brewer-Dobson circulation and its associated transport via the extratropical QBO, since the strength of the Brewer-Dobson circulation is closely coupled to the intensity of extratropical Rossby waves. The differing strengths of Brewer-Dobson circulation between winters can be seen in Plates 1 and 2. The circulation is stronger in the more active first winter than in the second. The ascending branch, occurring mainly in the summer subtropics (see Figure 17 of Dunkerton [1989]), is stronger in the first winter and elevates mixing ratio isopleths to higher altitudes than the following winter. This is best seen above 10 mbar where the circulation and its winter-to-winter difference are strongest. Variations in the strength of the large-scale meridional circulation are also seen in its descending branch at winter high latitudes, particularly in the upper stratosphere. Plate 2 shows that mixing ratio isopleths at high latitudes in the upper stratosphere are drawn to lower altitudes during the more active first winter, hence the positive  $\text{H}_2\text{O}$  mixing ratio difference above about 15 mbar in the middle and high latitudes (Plate 2c). These effects of the Brewer-Dobson circulation strength are not so evident in  $\text{N}_2\text{O}$  (Plate 1) as they are in  $\text{H}_2\text{O}$  because  $\text{N}_2\text{O}$ 's shorter chemical lifetime in the upper stratosphere reduces its interannual variability there, relative to that seen in  $\text{H}_2\text{O}$ .

QBO modulation of extratropical Rossby-wave activity implies that an extratropical QBO signal also exists in isentropic Rossby-wave transport. The observations presented here appear to confirm this, showing greater quasi-horizontal constituent mixing occurring at latitudes poleward of  $\sim 30^\circ\text{N}$  in the middle and lower stratosphere below 10 mbar during the first, more dynamically active winter. This causes the positive (negative) difference anomaly in Plate 1c (Plate 2c) in the winter extratropics below about 10 mbar. An alternative explanation for the distribution difference, in terms of different mean vertical transport between winters, seems unlikely, as it would create an extratropical difference having the same sign at all altitudes, given that the vertical gradients of the background constituent mixing ratio do not change sign with height. The quasi-biennial variability of the Brewer-Dobson circulation may explain the constituent variation in the middle and high-latitude upper stratosphere above 10 mbar, however. At an intermediate height, near 10 to 15 mbar, the mean and eddy transport effects apparently cancel for these constituents.

Randel and Wu [1996] examined the vertical structure of the extratropical QBO in using SAGE II ozone. Employing a seasonally varying regression between global ozone and QBO wind, they extracted QBO anomalies during January-March. Aside from the expected tropical ozone QBO anomalies, the regressed anomalies were large only in the winter hemisphere (see their Figure 10). The extratropical ozone anomalies are similar to the long-lived constituent anomalies seen here in latitudinal range but occur at different altitudes. They show two extratropical anomalies, near 10-20 mbar and near 50 mbar, of the same sign, and extending from about  $20^\circ\text{N}$  to  $60^\circ\text{N}$ , the limit of their data. They attribute the lower extratropical anomaly to vertical displacement, based on the background ozone distribution, while the middle stratospheric anomaly's origin is unknown. The different structure of their extratropical ozone QBO from that seen here in  $\text{N}_2\text{O}$  and  $\text{H}_2\text{O}$  is not surprising, given the very different species lifetimes and background mixing ratios. Ozone has a much weaker meridional mixing ratio gradient in the stratosphere, reducing the effect of isentropic mixing relative to that of  $\text{N}_2\text{O}$  and  $\text{H}_2\text{O}$ .

Finally, the most prominent winter-to-winter differences in  $\text{N}_2\text{O}$  occur between the equator and  $\sim 30^\circ\text{N}$  and are attributed to the effect of the QBO winds on wave breaking equatorward of  $30^\circ\text{N}$ , as discussed in section 3.4. The frequent sampling of the CLAES and MLS instruments allow "synoptic" maps of  $\text{N}_2\text{O}$  and  $\text{H}_2\text{O}$  to be made, clearly showing that Rossby-wave breaking in the winter low latitudes is influenced by the QBO phase. Plates 3 and 4 show that Rossby waves penetrate closer to the equator when the QBO winds are westerly rather than easterly. Partly as a consequence of this, there is also a weaker constituent mixing ratio gradient between the tropics and extratropics when the QBO winds are westerly rather than easterly. This relationship is consistent with results from numerical modeling of tracer transport under such circumstances [O'Sullivan and Chen, 1996]. Thus the distribution of mixing ratio in the tropics appears to be affected by the breaking of Rossby waves incident from the winter hemisphere. In fact, there appears to be evidence of such waves propagating across the equator at 15 mbar during the westerly QBO phase of the second winter. As discussed by O'Sullivan [1997], such waves will not break in the QBO westerlies but will instead break on reaching a critical latitude in the summer subtropics. The constituent maps, as well as the zonal mean winter-to-winter differences, support the conclusion that QBO modulation of Rossby-wave transport plays an important role, along with QBO modulated mean meridional transport, in forming the seasonally synchronized, off-equatorial QBO in long-lived constituents.

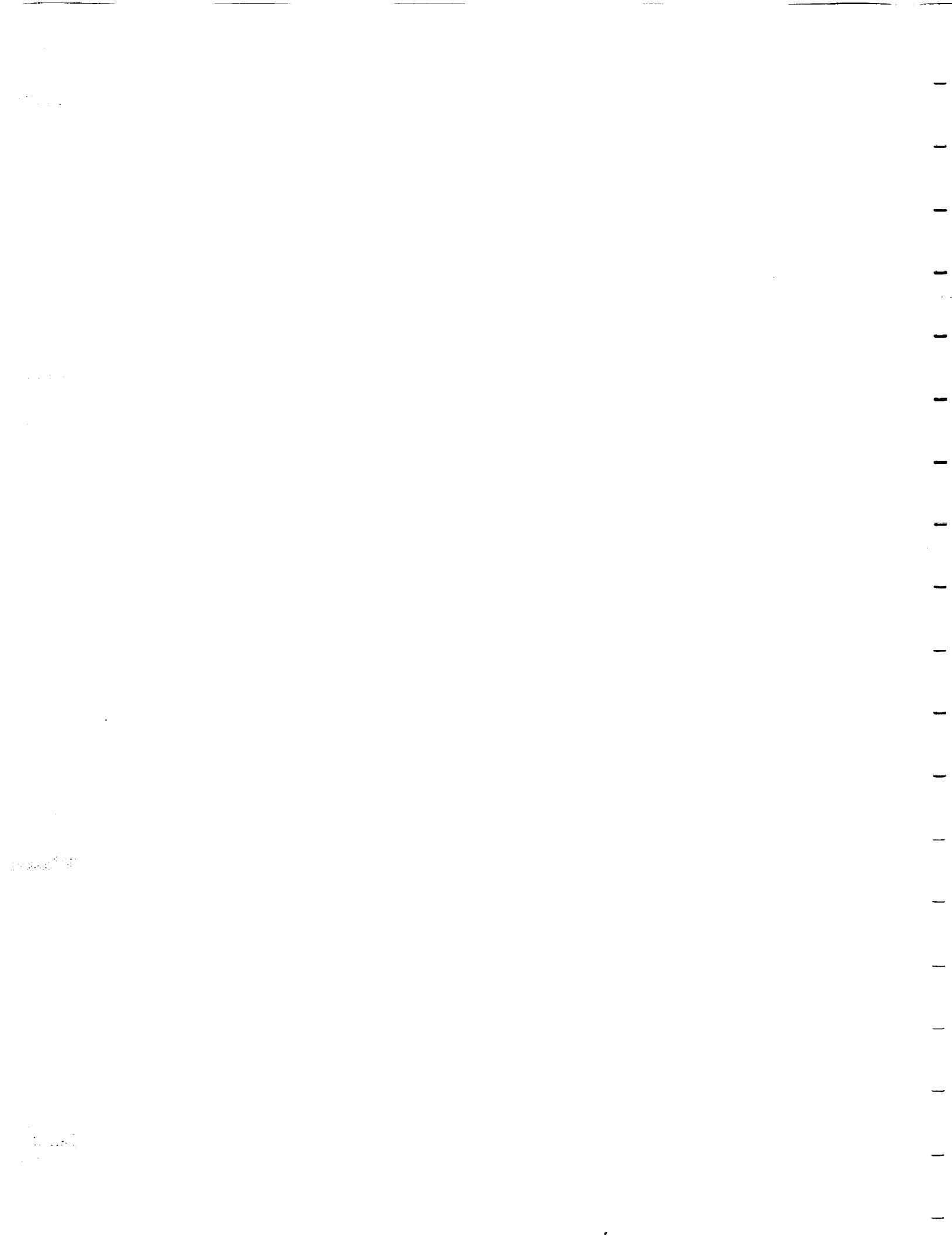
**Acknowledgments.** This research was supported by National Science Foundation grant ATM-9634394 and by National Aeronautics and Space Administration contracts NAS5-32862 and NASW-4844. We are grateful to D. Ortland for providing HRDI data and to B. Naujokat for providing Singapore rawinsonde data.

## References

- Andrews, D. G., J. R. Holton, and C. B. Leovy, *Middle Atmosphere Dynamics*, 489 pp., Academic, San Diego, Calif., 1987.
- Baldwin, M. P., and T. J. Dunkerton, Quasi-biennial oscillation above 10 mb, *Geophys. Res. Lett.*, **18**, 1205-1208, 1991.
- Baldwin, M. P., and K. K. Tung, Extratropical QBO signals in angular momentum and wave forcing, *Geophys. Res. Lett.*, **21**, 2717-2720, 1994.
- Barath, F. T., et al., The Upper Atmosphere Research Satellite Microwave Limb Sounder instrument, *J. Geophys. Res.*, **98**, 10,751-10,762, 1993.
- Bowman, K. P., Global patterns of the quasi-biennial oscillation in total ozone, *J. Atmos. Sci.*, **46**, 3328-3343, 1989.
- Butchart, N., and J. Austin, On the relationship between the quasi-biennial oscillation, total chlorine and the severity of the antarctic ozone hole, *Q. J. R. Meteorol. Soc.*, **122**, 183-218, 1996.
- Chandra, S., and R. S. Stolarski, Recent trends in stratospheric total ozone: Implications of dynamical and El Chichon perturbations, *Geophys. Res. Lett.*, **18**, 2277-2280, 1991.
- Chen, P., The influences of zonal flow on wave breaking and tropical-extratropical interaction in the lower stratosphere, *J. Atmos. Sci.*, **53**, 2379-2392, 1996.
- Dameris, M., and A. Ebel, The quasi-biennial oscillation and major stratospheric warmings: A three-dimensional model study, *Ann. Geophys.*, **8**, 79-86, 1990.
- Dunkerton, T. J., Nonlinear Hadley circulation driven by asymmetric differential heating, *J. Atmos. Sci.*, **46**, 956-974, 1989.
- Dunkerton, T. J., and D. P. Delisi, Anomalous temperature and zonal wind in the tropical upper stratosphere, 1982/83, *J. Geophys. Res.*, **96**, 22,631-22,641, 1991.
- Dunkerton, T. J., and M. P. Baldwin, Quasi-biennial modulation of planetary wave fluxes in the northern hemisphere winter, *J. Atmos. Sci.*, **48**, 1043-1061, 1991.
- Dunkerton, T. J., and D. O'Sullivan, Mixing zone in the tropical middle stratosphere above 10 mb, *Geophys. Res. Lett.*, **23**, 2497-2500, 1996.
- Grant, W. B., et al., Aerosol-associated changes in tropical stratospheric ozone following the eruption of Mount Pinatubo, *J. Geophys. Res.*, **99**, 8197-8211, 1994.
- Grant, W. B., E. V. Browell, C. S. Long, L. L. Stowe, R. G. Grainger, and A. Lambert, Use of volcanic aerosols to study the tropical stratospheric reservoir, *J. Geophys. Res.*, **101**, 3973-3988, 1996.
- Gray, L. J., and J. A. Pyle, The semi-annual oscillation and equatorial tracer distributions, *Q. J. R. Meteorol. Soc.*, **112**, 387-407, 1986.
- Hasebe, F., Quasi-biennial oscillations of ozone and diabatic circulation in the equatorial stratosphere, *J. Atmos. Sci.*, **51**, 729-745, 1994.
- Hess, P. G., and D. O'Sullivan, A three dimensional modeling study of the extra-tropical quasi-biennial oscillation in ozone, *J. Atmos. Sci.*, **52**, 1539-1554, 1995.
- Hitchman, M., M. McKay, and C. R. Trepte, A climatology of stratospheric aerosol, *J. Geophys. Res.*, **99**, 20,689-20,700, 1994.
- Holton, J. R., and J. Austin, The influence of the equatorial QBO on sudden stratospheric warmings, *J. Atmos. Sci.*, **48**, 607-618, 1991.
- Holton, J. R., and H.-C. Tan, The influence of the equatorial quasi-biennial oscillation on the global circulation at 50 mb, *J. Atmos. Sci.*, **37**, 2200-2208, 1980.
- Holton, J. R., and H.-C. Tan, The quasi-biennial oscillation in the Northern Hemisphere lower stratosphere, *J. Meteorol. Soc. Jpn.*, **60**, 140-148, 1982.
- Kinne, S., O. B. Toon, and M. J. Prather, Buffering of stratospheric circulation by changing amounts of tropical ozone: A Pinatubo case study, *Geophys. Res. Lett.*, **19**, 1927-1930, 1992.
- Lahoz, W. A., et al., Validation of UARS microwave limb sounder 183 GHz H<sub>2</sub>O measurements, *J. Geophys. Res.*, **101**, 10,129-10,149, 1996.
- Lambert, A., R. G. Grainger, J. J. Remedios, C. D. Rodgers, M. Corney and F. W. Taylor, Measurements of the evolution of the Mount Pinatubo aerosol cloud by ISAMS, *Geophys. Res. Lett.*, **20**, 1287-1290, 1993.
- Lait, L. R., M. R. Schoeberl, and P. A. Newman, Quasi-biennial modulation of the Antarctic ozone depletion, *J. Geophys. Res.*, **94**, 11,559-11,571, 1989.
- Manney, G. L., R. W. Zurek, M. E. Gelman, A. J. Miller, and R. Nagatani, The anomalous Arctic lower stratospheric polar vortex of 1992-1993, *Geophys. Res. Lett.*, **21**, 2405-2408, 1994.
- Manney, G. L., L. Froidevaux, J. W. Waters and R. W. Zurek, Evolution of microwave limb sounder ozone and the polar vortex during winter, *J. Geophys. Res.*, **100**, 2953-2972, 1995.
- Naujokat, B., An update of the observed quasi-biennial oscillation of the stratospheric winds over the tropics, *J. Atmos. Sci.*, **43**, 1873-1877, 1986.
- Ortland, D. A., W. R. Skinner, P. B. Hays, M. D. Burrage, R. S. Lieberman, A. R. Marshall, and D. A. Gell, Measurements of stratospheric winds by the high-resolution Doppler imager, *J. Geophys. Res.*, **101**, 10,351-10,363, 1996.
- O'Sullivan, D., The interaction of extratropical Rossby waves with westerly quasi-biennial oscillation winds, *J. Geophys. Res.*, in press, 1997.
- O'Sullivan, D. and P. Chen, Modeling the quasi-biennial oscillation's influence on isentropic tracer transport in the subtropics, *J. Geophys. Res.*, **101**, 6811-6822, 1996.
- O'Sullivan, D. and T. J. Dunkerton, Seasonal development of the extratropical QBO in a numerical model of the middle atmosphere, *J. Atmos. Sci.*, **51**, 3706-3721, 1994.
- O'Sullivan, D. and M. L. Salby, Coupling of the tropical and extratropical circulations in the stratosphere through planetary wave transport, *J. Atmos. Sci.*, **47**, 650-673, 1990.
- O'Sullivan, D. and R. E. Young, Modeling the quasi-biennial oscillation's effect on the winter stratospheric circulation, *J. Atmos. Sci.*, **49**, 2437-2448, 1992.
- Polvani, L. M., D. W. Waugh, and R. A. Plumb, On the subtropical edge of the stratospheric surf zone, *J. Atmos. Sci.*, **52**, 1288-1309, 1995.
- Randel, W. J., and J. B. Cobb, Coherent variations of monthly mean column ozone and lower stratospheric temperature, *J. Geophys. Res.*, **99**, 5433-5447, 1994.
- Randel, W. J., and F. Wu, Isolation of the ozone QBO in SAGE II data by singular value decomposition, *J. Atmos. Sci.*, **53**, 2546-2559, 1996.
- Roche, A. E., J. B. Kumer, J. L. Mergenthaler, G. A. Ely, W. G. Uplinger, J. F. Potter, T. C. James and L. W. Sterritt, The cryogenic limb array etalon spectrometer (CLAES) on UARS: Experiment description and performance, *J. Geophys. Res.*, **98**, 10,763-10,776, 1993.
- Roche, A. E., et al., Validation of CH<sub>4</sub> and N<sub>2</sub>O measurements by the cryogenic limb array etalon spectrometer instrument on the upper atmosphere research satellite, *J. Geophys. Res.*, **101**, 9679-9710, 1996.
- Swinbank, R., and A. O'Neill, A stratosphere-troposphere data assimilation system, *Mon. Wea. Rev.*, **122**, 686-702, 1994a.
- Swinbank, R., and A. O'Neill, Quasi-biennial and semian-

- nual oscillations in equatorial wind fields constructed by data assimilation, *Geophys. Res. Lett.*, **21**, 2099-2102, 1994b.
- Trepte, C. R., and M. H. Hitchman, The tropical stratospheric circulation deduced from satellite aerosol data, *Nature*, **355**, 626-628, 1992.
- Tung, K.K., and H. Yang, Global QBO in circulation and ozone. Part I: Reexamination of observational evidence, *J. Atmos. Sci.*, **51**, 2699-2707, 1994a.
- Tung, K.K., and H. Yang, Global QBO in circulation and ozone. Part II: A simple mechanistic model, *J. Atmos. Sci.*, **51**, 2708-2721, 1994b.
- Waters, J. W., L. Froidevaux, W. G. Read, G. L. Manney, L. S. Elson, D. A. Flower, R. F. Jarnot, and R. S. Harwood, Stratospheric ClO and ozone from the Microwave Limb Sounder on the Upper Atmosphere Research Satellite, *Nature*, **362**, 597-602, 1993.
- Zawodny, J. M. and M. P. McCormick, Stratospheric Aerosol and Gas Experiment II measurements of the quasi-biennial oscillations in ozone and nitrogen dioxide, *J. Geophys. Res.*, **96**, 9371-9377, 1991.
- 
- D. O'Sullivan and T. J. Dunkerton, Northwest Research Associates, Inc., P.O. Box 3027, Bellevue, WA 98009-3027. (e-mail: donal@nwra.com, tim@nwra.com)

(Received March 6, 1997; revised May 21, 1997; accepted June 5, 1997.)





# Climatology of the semiannual oscillation of the tropical middle atmosphere

Rolando R. Garcia,<sup>1</sup> Timothy J. Dunkerton,<sup>2</sup> Ruth S. Lieberman,<sup>3</sup> and Robert A. Vincent<sup>4</sup>

**Abstract.** We have used a variety of satellite, ground-based, and in situ observations to construct a climatology of the semiannual oscillation (SAO) of the tropical middle atmosphere. The sources of data include rocketsonde observations of winds and temperature, MF radar wind observations, and observations of winds and temperatures made from space by the High Resolution Doppler Imager (HRDI) and the Solar Mesosphere Explorer (SME). These data sets provide a generally consistent picture of the SAO, of the relationship between its stratospheric and mesospheric manifestations, and of its apparent modulation by the stratospheric quasi-biennial oscillation (QBO). In agreement with earlier studies, we find that the first cycle of the stratospheric SAO (which begins with the stratopause easterly phase in northern winter) is stronger than the second cycle (beginning with the easterly phase in southern winter). Similar behavior is apparent in the mesosphere, where the easterly phase is stronger during the first cycle than during the second cycle. HRDI and MF radar are capable of observing the seasonal cycle well into the lower thermosphere. Data from these two sources indicate that a strong SAO is present up to about 90 km, giving way above this altitude to time mean easterly winds with a weak semiannual variation. Between 105 and 110 km, HRDI data indicate the presence of a westerly wind layer with almost no seasonal variation. Apparent modulation of the stratospheric SAO by the QBO is found in rocketsonde data, while HRDI and MF radar observations suggest a correlation between the QBO and the easterly phase of the mesospheric SAO. We discuss the implications of these observations for the wave processes that drive the SAO.

## 1. Introduction

The existence of a semiannual oscillation (SAO) in the tropical stratosphere was first documented by Reed [1962], who examined the seasonal evolution of tropical temperatures in the lower stratosphere and noted the presence of a semiannual wave above 50 mbar. Further work by Reed [1966] using rocketsonde observations showed that an SAO in zonal wind extended throughout the upper stratosphere and the lower mesosphere, and that the semiannual wind harmonic peaked near the stratopause (~50 km).

Reed's [1962, 1966] original description of the tropical SAO has been validated by many subsequent investigations [e.g., Angell and Korshover, 1970; Belmont *et al.*, 1974, 1975; Cole and Cantor, 1975, 1978; Hopkins, 1975]. These and other studies employed observations of winds and temperature obtained from the Meteorological Rocket Network (MRN) to define the meridional structure of the SAO in the upper stratosphere and lower mesosphere. Above 65 km, occasional rocket observations, together with meteor radar measurements, indicate that the SAO is present throughout the mesosphere [Groves, 1972; Cole and Kantor, 1978]. Hirota [1978] used a combination of routine and occasional rocket observations from Ascension Island to show that the SAO in fact consists of two oscillations with amplitude maxima near the stratopause and mesopause, and an amplitude minimum near 64 km. The phase of the zonal wind varies more or less smoothly throughout this range of altitude and is such that the behavior at the stratopause is nearly out of phase with that at the mesopause. Hirota's findings were confirmed by Hamilton [1982], who found similar amplitude and phase behavior in data from Kwajalein Island.

With the advent of satellite observations it has been possible to obtain a more complete description of the

<sup>1</sup>National Center for Atmospheric Research, Boulder, Colorado.

<sup>2</sup>NorthWest Research Associates, Inc., Bellevue, Washington.

<sup>3</sup>Space Physics Research Laboratory, University of Michigan, Ann Arbor.

<sup>4</sup>Department of Physics and Mathematical Physics, University of Adelaide, South Australia, Australia.

spatial structure of the oscillation, especially in the stratosphere and the lowest 10 to 15 km of the mesosphere [e.g., Fritz, 1974; Barnett, 1974; Hitchman and Leovy, 1986; Delisi and Dunkerton, 1988a; Garcia and Clancy, 1990]. The work of Hitchman and Leovy and of Delisi and Dunkerton has emphasized the seasonal evolution of the SAO. In particular, Delisi and Dunkerton [1988b] have shown that the stratospheric SAO exhibits a seasonal asymmetry such that the "first cycle" (which begins with the easterly phase in northern hemisphere winter) is stronger than the "second cycle" (beginning with the easterly phase in southern hemisphere winter) and that the asymmetry is due to differences in extratropical planetary wave forcing, which is stronger in northern winter than in southern winter.

The mesospheric SAO is much less well documented than the stratospheric oscillation. As opposed to the routine rocketsonde observations of the MRN, rocket observations of the upper mesosphere have been too infrequent and discontinuous to define a true climatology or to document interannual variability. This situation has been changing due to the increasing availability of satellite and ground-based measurements covering the entire mesosphere. The purpose of this paper is to review several of these data sources in order to construct a more detailed picture of the SAO in the stratosphere and mesosphere, its interannual variability, and its connection with the quasi-biennial oscillation of the stratosphere.

## 2. Data Sources

Four sets of data are used in the analyses presented in this paper:

1. Wind and temperature measurements made by sounding rockets from the islands of Ascension and Kwajalein. Some of these data have been used in the past to document the SAO in the stratosphere and mesosphere. Here we examine observations below 65 km, which are available between 1969 and 1987, as well as occasional measurements extending to 84 km.

2. MF radar observations from Christmas Island between 68 and 96 km for the years 1990-1995.

3. Observations of stratospheric temperature made by the Solar Mesosphere Explorer satellite (SME) during the period 1982-1986. SME data were analyzed originally over the altitude range 55-90 km [Clancy and Rusch, 1989], but they have been reanalyzed recently extending the coverage down to 40 km.

4. Wind measurements made by the High Resolution Doppler Imager (HRDI), on board the Upper Atmosphere Research Satellite (UARS). This instrument provides direct observations of winds by two different techniques, covering the altitude ranges 10-40 km and 65-110 km.

Each of these data sets is described in detail in the following subsections.

### 2.1. Rocketsonde Winds and Temperature

Data from the historical Meteorological Rocketsonde Network were obtained from a variety of sources and processed at NorthWest Research Associates to form monthly means of zonal wind and temperature at each station. Measurements were binned into 0.2 scale height ( $\sim 1.4$  km) intervals, and the binned soundings were averaged together for each month. Rocket soundings usually include a partially overlapping, contemporaneous rawinsonde profile. After binning, rocketsonde and rawinsonde data were blended using a linear ramp in the height interval 3.7-4.7 scale heights (26-33 km).

Rocketsonde observations at Ascension and Kwajalein have been made at various local times, but they tend to cluster in the early afternoon at both stations. As a result, averaging of the available observations does not guarantee that contamination by the diurnal tide has been removed. This is unlikely to be a problem below about 80 km, where the diurnal tidal signal is relatively small, but conclusions based on data above this altitude must be treated with caution.

Two sets of figures were prepared from these data. Routine MRN observations were used to construct altitude versus time contour plots for the islands of Kwajalein ( $8.7^\circ\text{N}$ ,  $167.7^\circ\text{W}$ ) and Ascension ( $7.6^\circ\text{S}$ ,  $14.4^\circ\text{W}$ ), covering the period 1969-1987 and the altitude range 0-63 km. Prior to plotting, the data were smoothed by taking the following "square" average over altitude and time:

$$\bar{x}_{i,j} = \frac{1}{16} \left[ 8x_{i,j} + \sum x_{i',j'} \right] \quad (1)$$

where  $i$  denotes altitude,  $j$  denotes time, and the summation extends over all points adjacent to  $i, j$ .

The second set of figures depicts the climatological composite seasonal cycle at Kwajalein and Ascension. These seasonal cycles were obtained by averaging the data for all Januaries, Februaries, etc. In addition to the usual MRN observations, occasional observations extending up to 84 km were used to prepare the climatological composites. Data above 65 km are available for relatively short periods in the early 1970s at Ascension Island and the middle 1970s at Kwajalein; additional observations covering a few months in the 1980s are also available at both stations [see Dunkerton and Delisi, this issue]. The data used to construct the composite seasonal cycles were smoothed vertically with four passes of a 1-2-1 smoother and temporally retaining only the time mean, annual harmonic, semiannual harmonic, and one-half of the ternary harmonic.

### 2.2. Christmas Island MF Radar Winds

Mesospheric winds were measured with an MF partial reflection radar located on Christmas Island ( $2^\circ\text{N}$ ,  $157^\circ\text{W}$ ) during the period January 1990 to April 1995. The radar operates at 1.98 MHz using a spaced-antenna system. It can operate unattended and, in principle, can make observations continuously with a time resolu-

tion of 2 min. In practice, wind measurements are only possible when suitable echoes are present. Useful observations can be made over the range 60–100 km during the day; at night, the lower limit of this range moves to about 80 km due to insufficient ionization at lower altitudes [Vincent and Lesicar, 1991]. These limitations are unimportant for the purposes of this study, which is concerned with the seasonal variation of the zonal mean winds. Above 80 km contamination of the zonal mean by the diurnal tide is effectively removed by averaging data taken throughout the day. Below 80 km this is not possible because nighttime data are often unavailable; however, the amplitude of the diurnal tide contribution to the zonal wind at these altitudes is small [Lieberman and Hays, 1994]. The daily averaged Christmas Island data discussed here are plotted after application of a frequency-domain, low-pass filter with a 20-day cutoff. Otherwise, the data represent the “raw” mesospheric winds, without removal of either the time mean or the annual cycle. The data shown in this paper cover the altitude range 68–96 km, with vertical resolution of about 4 km.

### 2.3. HRDI Zonal Winds

The High Resolution Doppler Imager (HRDI) on board the Upper Atmosphere Research Satellite was designed to measure daytime winds in the stratosphere (10–40 km) and in the mesosphere and lower thermosphere (50–115 km). Because measurement errors are large in the lower mesosphere and also above 110 km, we restrict the data reviewed in this paper to the altitude ranges 10–40 km and 65–110 km. The measurement techniques are discussed by Hays *et al.* [1993]. Details of the retrieval procedure, sources of errors, and comparisons with correlative measurements are addressed by Ortland *et al.* [1996] for the stratospheric observations and by Burrage *et al.* [1996a] for measurements in the mesosphere and lower thermosphere. UARS orbits the Earth about 15 times per day, sampling each latitude circle at roughly the same local time on a given day. The precession of the orbit shifts the local time of the observing points by about 20 min from one day to the next. Over the course of 36 days, roughly 12 local daytime hours are sampled by HRDI. From November 1991 to April 1994, HRDI generally viewed the mesosphere every other day, 15 orbits per day. Following April 1994, HRDI viewed the mesosphere daily but only during 7 orbits per day.

For this study we have selected HRDI winds for the period of greatest continuity, from August 1992 through April 1995. To study the behavior of the equatorial SAO, each day's winds within 5° of the equator are binned and averaged around a latitude circle. Because the measurements are made at the same local time, both the zonal mean and the migrating diurnal and semidiurnal tides contribute to the zonal average. The data presented in this paper are 30-day means of the daily zonal averages. Although this process nearly averages out the

semidiurnal tide, the diurnal tide cannot be fully eliminated by averaging HRDI daytime winds. However, estimates of the diurnal zonal winds made by Lieberman and Hays [1994] indicate that, near the equator, the amplitude of the diurnal tide is at most 20% of the zonal mean winds at 95 km and less than 5% below 85 km. For this reason, we present HRDI observations with no processing other than 30-day averaging of the zonal means. Although averaging will reduce aliasing by the diurnal tide, depending on the phase of the latter with respect to the range of local times observed during the averaging period, the possibility of tidal contamination must be borne in mind when examining HRDI data above 85 km.

### 2.4. SME Temperatures

The ultraviolet spectrometer (UVS) on the Solar Mesosphere Explorer satellite obtained profiles of Rayleigh scattered solar irradiance, from which mesospheric temperature profiles can be derived [Clancy and Rusch, 1989]. The original analysis of Clancy and Rusch used observations at ultraviolet wavelengths exclusively; this limited the coverage to the altitude range 60–92 km. The upper limit of this range is determined by the signal-to-noise ratio of the radiance profiles, which decreases with the atmospheric density; the lower limit is set by ozone absorption in the Hartley band, which becomes important below 60 km. Clancy *et al.* [1994] have reanalyzed the SME data using near ultraviolet and visible wavelengths, which extends the altitude coverage down to 40 km with vertical resolution of 4 km. These extended range observations are available from 1983 to 1986, although coverage is not complete in 1986. For the altitude range 60–92 km, observations are available from 1982 through 1986. The reanalysis also corrects a systematic error of about –5 K near 60 km in the temperature profiles reported by Clancy and Rusch [1989]. The error has been eliminated by restricting the wavelengths used for the temperature retrieval in the lower mesosphere to those unaffected by ozone absorption. In this paper, we use the reanalyzed SME temperature profiles tabulated by Clancy *et al.* [1994].

Because of the low signal-to-noise ratio of individual radiance profiles, SME temperature retrievals are summed into monthly averages to obtain satisfactory signal-to-noise ratios over the entire altitude range. The monthly average temperature profiles have estimated inversion errors of  $\pm 2$  K below 80 km, increasing to  $\pm 10$  K at the uppermost level (92 km). Uncertainties in the altitude registration contribute an additional  $\pm 2$  K error to the retrieved temperatures. In addition, SME observations do not provide uniform coverage in longitude but are available only over widely separated longitude sectors [Clancy *et al.*, 1994, Figure 2]. Therefore, SME temperature profiles do not represent true zonal averages, although the monthly averaging procedure should greatly reduce the contribution of longitu-

dinal asymmetries, with the possible exception of the diurnal tide, since SME observations are made at constant local times. The problem of tidal contamination is likely to be most acute above about 80 km, where the diurnal temperature tide in the tropics becomes large.

### 3. Annual Composite SAO

#### 3.1. Zonal Wind

Rocketsonde observations of the seasonal behavior of the zonal wind at Kwajalein and Ascension islands are shown in Figure 1. A semiannual oscillation is evident at most altitudes. The first cycle of the stratospheric SAO (beginning with the stratopause easterlies in January) is much stronger than the second cycle at Ascension Island ( $\sim 90 \text{ m s}^{-1}$  versus  $\sim 30 \text{ m s}^{-1}$  peak-to-peak); at Kwajalein Island, the second cycle ( $\sim 50 \text{ m s}^{-1}$ ) is actually stronger than the first ( $\sim 30 \text{ m s}^{-1}$ ), but the difference is much smaller than at Ascension.

*Delisi and Dunkerton* [1988b] noted that the first cycle of the stratospheric SAO is usually stronger than the second cycle. They attributed this seasonal asymmetry to stronger dynamical forcing in northern winter, which produces stronger tropical easterlies and sets the stage for a strong westerly phase immediately following the strong easterly phase. This description refers to the SAO at the equator and is inferred by interpolation of the data from Ascension and Kwajalein. When the data for each station are considered separately, the stronger westerly phase follows the stronger easterly phase, and easterly phases are always stronger

in local summer. However, the first easterly phase at Ascension is by far the strongest, and it is followed by the strongest westerly phase, yielding a stronger first cycle when Ascension and Kwajalein data are interpolated to the equator. Routine direct observations of the zonal wind at the equator were not available prior to HRDI. Even HRDI data do not cover the peak of the stratopause SAO. Nonetheless, a latitude-time cross-section of HRDI zonal winds at 40 km (Figure 4a), discussed below, is consistent with the behavior inferred from interpolation of near-equatorial station data.

The climatologies at both Ascension and Kwajalein display time-mean westerlies in the lower mesosphere, between about 55 and 70 km. The flow at these altitudes is in superrotation most of the year (to conserve angular momentum, an air parcel at rest on the equator would accelerate to only  $\sim 10 \text{ m s}^{-1}$  upon displacement to the latitude of each of the stations). In the upper mesosphere, rocket observations are sparse compared to lower levels, but the overall picture of the mesopause SAO is consistent with the other measurements discussed in this paper [see also *Hirota*, 1978, 1980; *Hamilton*, 1982]. Easterly phases of the mesospheric SAO lie almost directly above westerly extrema of the stratospheric SAO. This behavior was modeled by *Dunkerton* [1982] and attributed to vertically propagating gravity and ultrafast Kelvin waves. Time-mean easterlies exist in the upper mesosphere; absolute westerlies at these altitudes are weak or nonexistent. The first mesospheric SAO easterly phase is clearly stronger than the second at Ascension Island. At Kwajalein,

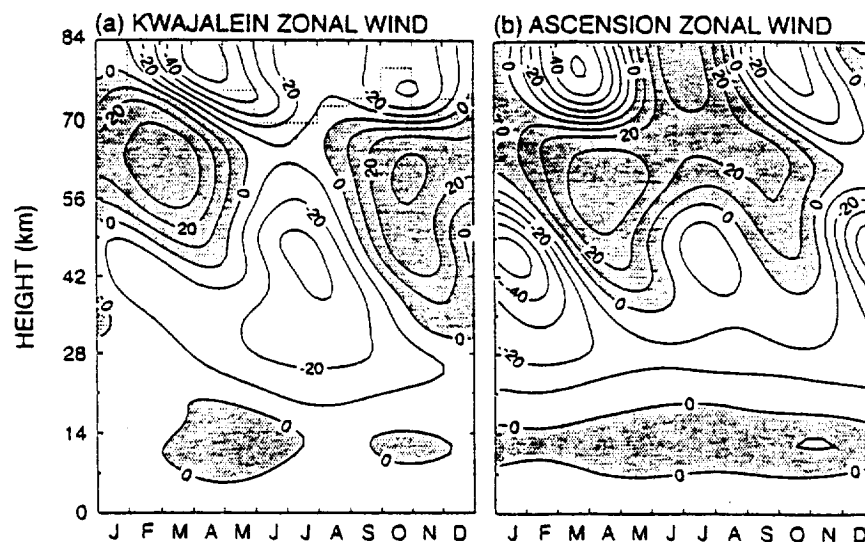


Figure 1. Composite seasonal cycle of the zonal wind derived from rocketsonde data for (a) Kwajalein Island ( $8.7^{\circ}\text{N}$ ,  $167.7^{\circ}\text{W}$ ) and (b) Ascension Island ( $7.6^{\circ}\text{S}$ ,  $14.4^{\circ}\text{W}$ ). The contour interval is  $10 \text{ m s}^{-1}$ . Data for times and altitudes demarcated by the dashed line in Figure 1a were extrapolated from lower levels and interpolated between available times.

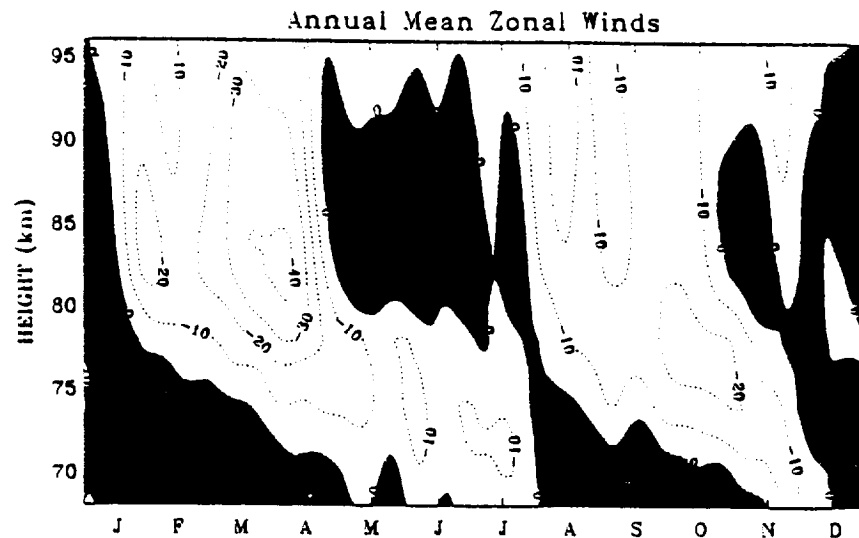


Figure 2. Composite seasonal cycle of the zonal wind in the upper mesosphere/lower thermosphere obtained with the MF radar at Christmas Island. The contour interval is  $10 \text{ m s}^{-1}$ .

there are no observations above 70 km during much of the year, but the available data are consistent with the behavior at Ascension.

In a Fourier decomposition (not shown), the phase of the annual cycle varies rather little with height and is approximately antisymmetric about the equator (i.e., the annual cycle at Ascension is out of phase with that at Kwajalein). The phase of the semiannual harmonic reverses between the stratopause and mesopause and is approximately symmetric about the equator (Ascension in phase with Kwajalein.) The semiannual harmonic has a node at  $\sim 65 \text{ km}$ . The amplitude of the semiannual harmonic at the stratopause is stronger at Ascension, i.e., south of the equator [Belmont *et al.*, 1974; Hirota, 1980; Ortland *et al.*, 1996].

These rocketsonde results can be compared with MF radar and HRDI observations, which extend throughout the upper mesosphere and into the lower thermosphere. Figures 2 and 3 show seasonal composites derived from the Christmas Island MF radar and from HRDI data, respectively. The overall behavior of the seasonal cycle in figures 2 and 3 is in remarkably good agreement with the rocket data of Figure 1. In each data set, there are time mean westerlies up to about 70 km, which give way to time-mean easterlies above that altitude. A large semiannual cycle is present throughout the upper stratosphere and mesosphere. Below 75 km, maximum westerly winds occur just before the equinoxes, reaching speeds of  $30\text{--}40 \text{ m s}^{-1}$  in the HRDI climatology, although only about  $10 \text{ m s}^{-1}$  in the radar data. These westerlies are continuous with the westerly phase at stratopause level, which attains its maximum amplitude just after the equinoxes. The continuity of the westerly phase between 70 km and 35–40 km can be seen clearly by comparing the evolution of the wind in Figure 1 with that depicted in Figures 2 and 3. The HRDI data reveal a semiannual cycle at all altitudes below about 100 km.

In the upper mesosphere, maximum easterly winds develop shortly before the equinoxes near 80 km in both the radar and HRDI data. These easterly maxima are separated by periods of weaker westerly winds, peaking near 85 km. The behavior is similar to that at Ascension Island shown in Figure 1. At Kwajalein, there is insufficient data to confirm the presence of westerlies in the upper mesosphere. The semiannual oscillation in the upper mesosphere is clearly out of phase with that in the stratosphere and lower mesosphere: westerlies occur at the solstice, when easterlies peak near the stratopause, while easterlies dominate the equinoxes, when the stratopause westerlies are strongest.

No rocketsonde observations are available above 84 km, but data from the MF radar and from HRDI offer a consistent picture. Above about 90 km, the zonal winds are easterly at nearly all times and exhibit a weak semiannual oscillation in phase with that at the mesopause. Maximum velocities obtained by HRDI are again larger than those measured by the MF radar. For example, near 95 km HRDI winds reach  $-20$  to  $-30 \text{ m s}^{-1}$ , while

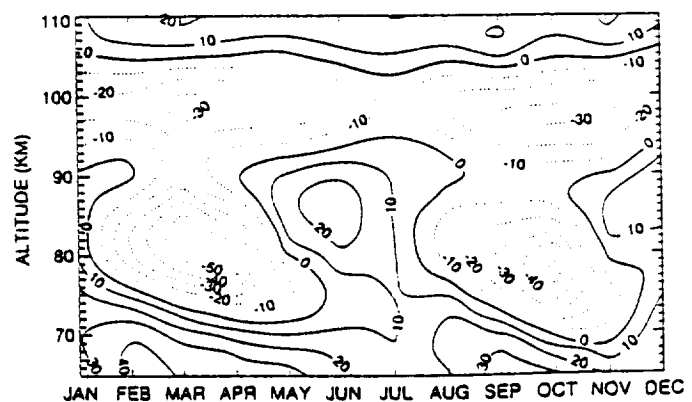


Figure 3. As in Figure 2, but for data from the High Resolution Doppler Imager (HRDI) extending to 110 km.

radar winds are usually no stronger than  $-10$  to  $-15$   $\text{m s}^{-1}$ . The presence of easterlies above 90 km is to some extent the result of deposition of easterly momentum by the diurnal tide which is rapidly damped in this region [Lieberman and Hays, 1994]. Above 95 km, data are available only from HRDI. These show that easterly winds peak slightly above 95 km and give way to westerlies at 105 km. This westerly regime shows little seasonal variability, so the time mean flow of about  $15$   $\text{m s}^{-1}$  is representative of conditions throughout most of the year. The behavior above about 85 km must be interpreted with caution, since at these altitudes contamination by the diurnal tide is likely to be significant. In particular, it is likely that the semiannual cycle peaking near 98 km is due in part to aliasing by the diurnal tide, whose amplitude is known to exhibit a strong semiannual variation [Burrage et al., 1995; Lieberman, 1996].

Both radar and HRDI observations indicate that the mesospheric SAO exhibits seasonal asymmetry. This is most evident near the peak of the oscillation around 80–85 km. The easterly maximum in the first cycle of the oscillation (April) is considerably stronger than the easterly maximum in the second cycle (October). The peak values are  $-50$   $\text{m s}^{-1}$  in the first cycle versus  $-40$   $\text{m s}^{-1}$  in the second cycle according to HRDI data, and  $-40$   $\text{m s}^{-1}$  versus  $-20$   $\text{m s}^{-1}$  according to the MF radar. On the other hand, the radar data do not show any appreciable difference between the westerly maxima in the first and second cycles; in the HRDI observations, the second westerly maximum (beginning in southern hemisphere winter, i.e., in June) actually appears somewhat stronger than the first.

In general, although HRDI and MF radar data are in good qualitative agreement, the composite SAO derived from MF radar measurements is weaker than that observed by HRDI. The reason for this discrepancy is not clear, but it cannot be attributed to the different averaging periods from which the annual composites are derived since the difference is present throughout the period (1992–1995) when MF and HRDI observations overlap (not shown). Burrage et al. [1996a] have examined in some detail the differences between HRDI and MF radar observations. They point out that HRDI wind magnitudes are in good agreement with correlative rocket and meteor radar observations, and especially with measurements made from UARS by the Wind Imaging Interferometer (WINDII), which has a sampling pattern similar to HRDI's. Although they do not pinpoint a specific cause, Burrage et al. suggest several mechanisms that could cause the MF radar technique to underestimate the wind by as much as 50%.

Figure 4 shows the HRDI composite monthly and zonally averaged zonal wind as a function of latitude at 40 and 80 km. At 40 km (Figure 4a) the seasonal cycle is dominated by the annual component at extratropical latitudes; semiannual behavior is seen clearly only within  $20^\circ$  of the equator. At the equator, the first

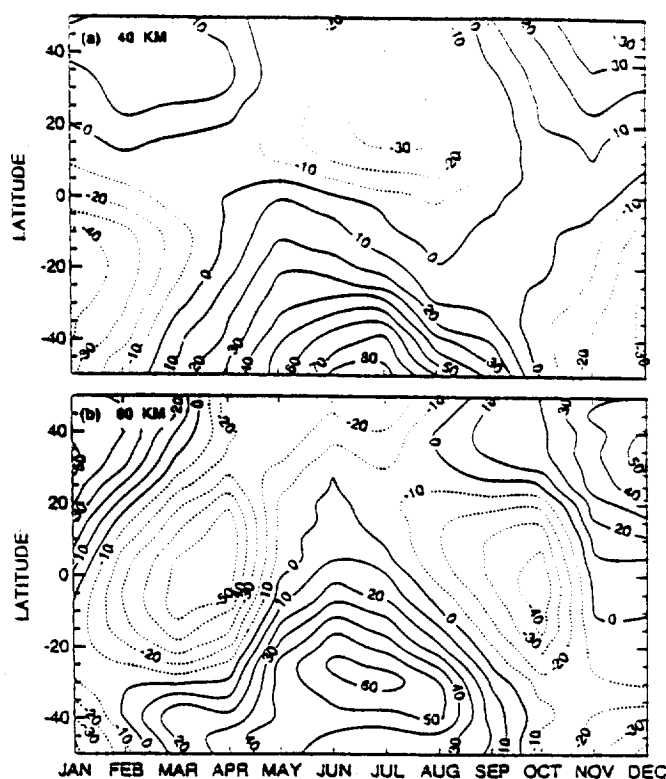


Figure 4. Meridional structure of the composite seasonal cycle at (a) 40 km and (b) 80 km derived from HRDI data. The contour interval is  $10$   $\text{m s}^{-1}$ .

easterly cycle is stronger than the second, apparently as a result of cross-equatorial advection of mean easterly winds from southern hemisphere summer. The westerly phases of the first and second cycles have comparable amplitudes. However, at the latitudes of Ascension and Kwajalein islands ( $7.6^\circ\text{S}$  and  $8.7^\circ\text{N}$ , respectively) the easterly phase corresponding to local summer is always stronger and it is followed by the stronger westerly phase. This behavior is entirely consistent with that inferred from the rocketsonde station data (Figure 1).

Near the mesopause (Figure 4b), the semiannual oscillation maximizes at low latitudes, giving way to an annual variation at midlatitudes characterized by winter westerlies and summer easterlies. The mesospheric winter westerlies peak at relatively low latitudes ( $\sim 30^\circ$ ), consistent with the behavior found by Dunkerton and Delisi [1985a], who referred to this configuration as the "subtropical mesospheric jet." The easterly phase of the SAO is more equatorially confined and more nearly symmetric about the equator, while the westerlies appear as extensions of the midlatitude winter westerlies. This is also the case at 85 km, the altitude where the SAO westerlies reach their peak (not shown).

### 3.2. Temperature

Figure 5 shows the seasonal cycle of temperature departures from the annual mean derived from rocketsonde observations at Kwajalein and Ascension islands. Rocketsonde temperature data are insufficient to describe the seasonal variation above 60 km. At lower altitudes

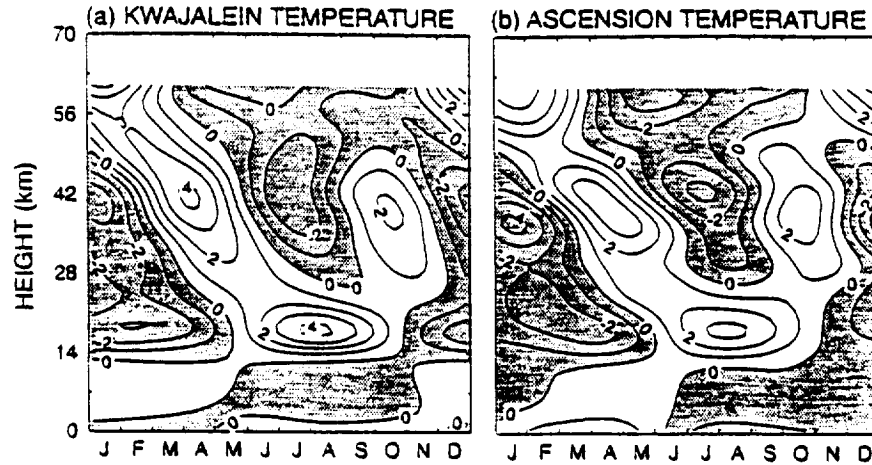


Figure 5. As in Figure 1, but for temperature. The contour interval is 1 K.

titudes, the rocketsonde data show a dominant annual cycle near the tropopause, with peak-to-peak variation of 6–8 K and warmest temperatures in northern summer [see also Reed and Vlcek, 1969; van Loon and Jenne, 1970]. This annual variation has been attributed by Yulaeva *et al.*, [1994] to variations in the strength of the global circulation driven by planetary wave dissipation in the stratosphere.

Between 30 and 60 km, the predominant seasonal variation is semiannual. Comparison with Figure 1 indicates that warm anomalies coincide with the regions of descending westerly vertical shear associated with the zonal wind SAO, while cold anomalies occur below or slightly ahead of maximum easterlies, in the region of easterly shear. These relationships imply that the wind and temperature fields associated with the SAO are in approximate geostrophic balance [Andrews *et al.*, 1987]. In the stratosphere, the first cycle of the temperature SAO is stronger than the second cycle. There is also evidence of a strong first cycle in the lower mesosphere preceding the corresponding pair of stratospheric SAO anomalies by ~2–3 months.

Figure 6 shows SME observations of equatorial temperature between 40 and 92 km, which overlap the rocketsonde data in the upper stratosphere and lower mesosphere. In the region of overlap (40–60 km) there is good overall agreement between the SME and the rocketsonde data. For example, the successive warm and cold anomalies that peak near 40 km in the rocketsonde observations are also present in the SME composite, although the SME amplitudes are somewhat larger and the timing of the maximum anomalies can differ by as much as a month. In the lower mesosphere there is also general agreement between the two sets of data, although there are again differences in detail. The SME data confirms the suggestion found in the rocket observations of a stronger first cycle in the lower mesosphere.

In the upper mesosphere the SME data indicate a very large SAO in temperature, with peak-to-peak vari-

ation of over 25 K near 90 km. There is also some suggestion of a seasonal asymmetry at altitudes above 80 km. However, contrary to what is found in the stratosphere and lower mesosphere, the second cycle appears to be somewhat stronger than the first. Both the amplitude of the SAO and its seasonal asymmetry raise questions about the accuracy of SME temperature data at these altitudes. The very large amplitude of the SAO between 80 and 92 km does not appear to be consistent with the shear of the zonal wind in either the radar or the HRDI data shown in Figures 2 and 3.

Figure 7 compares the vertical shear of the zonal wind,  $\bar{u}_z$ , computed from the HRDI data with the vertical shear estimated from the SME temperature anomalies under the assumption of geostrophic balance,

$$\bar{u}_{gz} = \frac{aR}{2\Omega H} \cdot \frac{T}{L^2} \quad (2)$$

where  $a$  is the radius of the Earth,  $R$  is the gas constant,

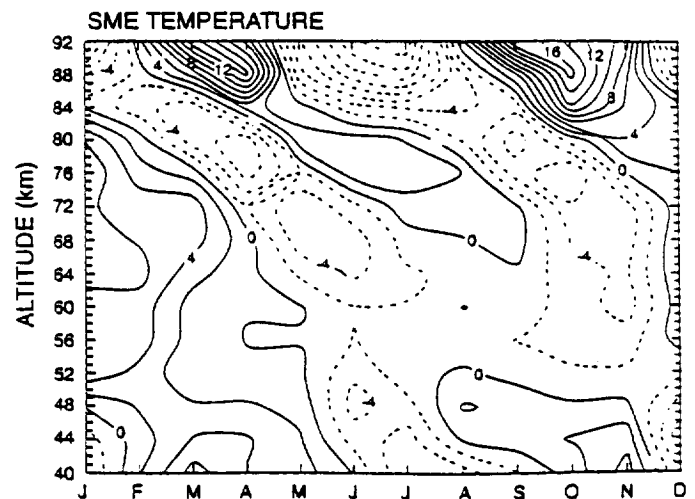


Figure 6. Composite seasonal cycle of temperature between 40 and 92 km observed by the Solar Mesosphere Explorer (SME). The contour interval is 2 K.



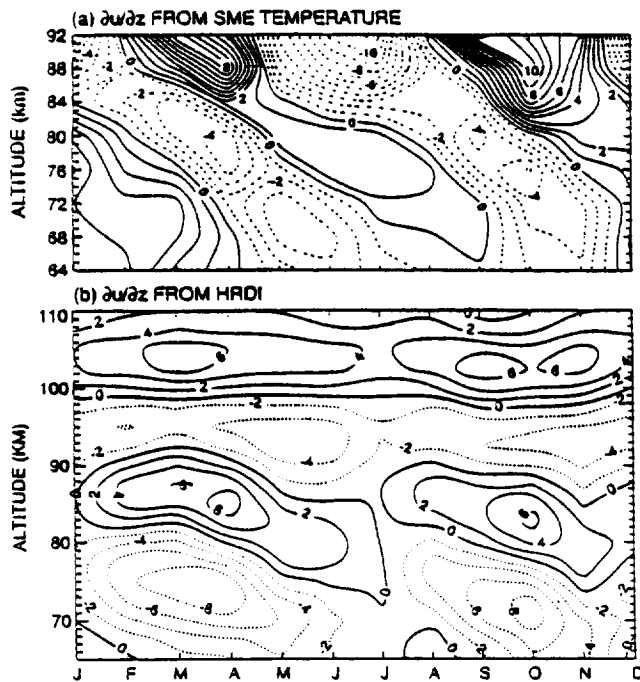


Figure 7. Annual cycle of the vertical shear of the zonal wind derived from (a) SME temperature data assuming geostrophic balance and (b) HRDI wind data. The contour interval is  $1 \text{ m s}^{-1} \text{ km}^{-1}$  in Figure 7a and  $2 \text{ m s}^{-1} \text{ km}^{-1}$  in Figure 7b.

$\Omega$  is the Earth's rotational frequency,  $H$  is the atmospheric scale height (taken to be 7 km), and  $L$  is the meridional scale of the oscillation [see, e.g., Garcia and Clancy, 1990]. The estimates of  $\bar{u}_{gz}$  shown in Figure 7a assume  $L=15^\circ$ . Below 80 km there is reasonable agreement between  $\bar{u}_{gz}$  from SME and  $\bar{u}_z$  from HRDI data (Figure 7b), although the latter is considerably stronger than the former. Above 80–85 km, larger differences between  $\bar{u}_{gz}$  and  $\bar{u}_z$  are apparent. The shear inferred from SME temperatures becomes very large above 85 km, and even its sign often does not agree with the sign of the shear computed from HRDI winds. The discrepancy in magnitude would have been even larger had  $\bar{u}_z$  been computed from Christmas Island radar winds since, as noted previously, the latter are generally weaker than those obtained from HRDI. Adopting a larger value for the meridional scale,  $L$ , in the upper mesosphere [Hitchman and Leovy, 1986] would have alleviated this problem, but it would not have reconciled the differences in sign.

Garcia and Clancy [1990] have argued that the SME temperatures above 80 km could be influenced by the presence of the diurnal tide, since SME measurements are made at constant local time, and the tidal temperature signal is large at the equator. Thus semiannual variations in the amplitude of the diurnal temperature tide could be misinterpreted as being part of the SAO in zonal mean temperature. This suggestion has been questioned by Clancy et al. [1994], who note that current numerical models do not predict significant seasonal variability in tidal amplitudes and that a very

strong SAO in temperature is also present in SME data at  $\pm 15^\circ$ , where models indicate that the tidal temperature signal should vanish. On the other hand, the recent studies of Lieberman and Hays [1994] and Burrage et al. [1995] document a large seasonal variation in the amplitude of the diurnal tide and in the tide-induced acceleration of the zonal wind. The seasonal variation is such that tidal amplitudes are about a factor of two stronger near the equinoxes than during the solstices. These results are consistent with earlier work by Vincent and Ball [1981] and Vincent et al. [1989]. Although a definitive statement cannot be made at this time, the available evidence suggests that the very large temperature SAO seen by SME in the upper mesosphere is at least in part the result of contamination by the seasonal variation in the amplitude of the diurnal tide, as originally suggested by Garcia and Clancy.

#### 4. Interannual Variability

A time-height cross section of rocketsonde zonal wind for the period 1969 to 1987 is shown in Figure 8 for Kwajalein Island. Figure 8 may be divided into four layers: a quiescent troposphere and lowermost stratosphere ( $\sim 0$ –20 km), the quasi-biennial oscillation (QBO) ( $\sim 20$ –35 km), the stratopause SAO ( $\sim 35$ –55 km), and a layer of time-mean westerlies above  $\sim 55$  km. The QBO at Kwajalein is weaker than at the equator [Dunkerton and

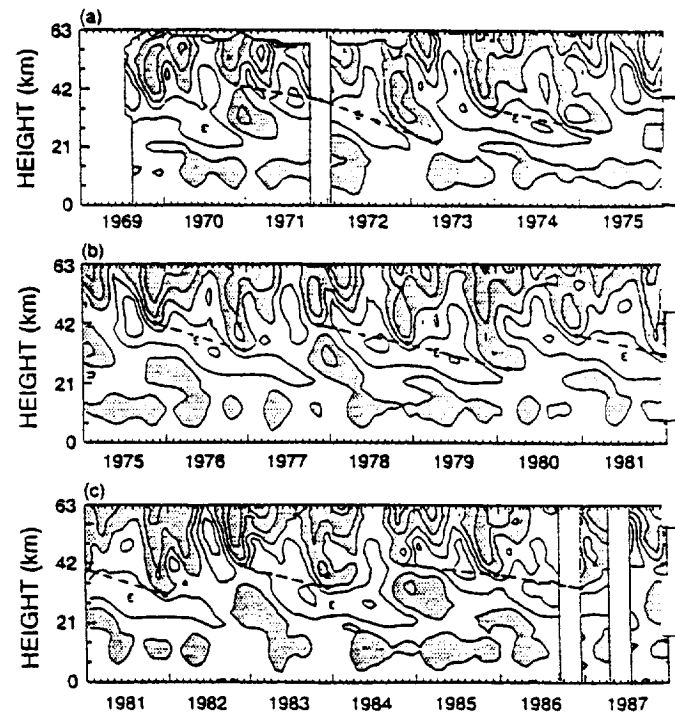


Figure 8. Rocketsonde observations of zonal wind at Kwajalein Island over the period 1969–1987. The contour interval is  $20 \text{ m s}^{-1}$ ; regions of westerly winds are shaded. The dots denote the altitude of maximum descent of the second-cycle westerly phase; they are joined by dashed lines to help visualize the relationship with the underlying QBO winds.



*Delisi*, 1985b; Naujokat, 1986], particularly the west phase of the QBO, which is narrow in latitude. Absolute westerlies in the QBO region, visible mainly during local winter at each station, are evidently due to the annual cycle as much as to the QBO itself.

Interannual variability of the stratospheric SAO is complex. This region is influenced remotely by extratropical wave driving, the tropical QBO, and volcanic eruptions. Warming events in northern polar winter dictate the timing of onsets in the first stratospheric SAO phase [*Delisi and Dunkerton*, 1988b]. *Wallace* [1973] and *Dunkerton and Delisi* [this issue] have noted that QBO modulation of the SAO below the stratopause is visible as a systematic tendency for SAO westerly phases to descend lower as the QBO westerly phase wanes. On closer examination, this effect is observed mainly in the second westerly phase at Kwajalein (Figure 8) and in the first westerly phase at Ascension (not shown); the first westerly phase at Kwajalein and the second westerly phase at Ascension do not exhibit any apparent QBO influence. Note that it is the altitude of maximum descent, and not the strength, of SAO westerly phases in the stratosphere that appears to be modulated by the QBO. At both stations, the SAO westerly phase affected by the QBO is the westerly phase that descends farthest in a climatological sense (compare Figures 1 and 2).

Substantial interannual variability is also found in the mesospheric SAO. Figure 9 shows HRDI observations for 1992-95 over the altitude ranges 65-110 km and 10-40 km. As noted in a recent study by *Burrage et al.* [1996b], there is a striking variation in the strength of the mesopause easterly phase, which appears to be correlated with the stratospheric QBO. Figure 9a shows very strong mesopause easterlies of about  $-80 \text{ m s}^{-1}$  during the first SAO cycle of 1993 and the first cycle of 1995. QBO westerlies were present in the middle stratosphere (25-30 km) during each of these periods (Figure 9b). On the other hand, when QBO easterlies prevail in the middle stratosphere, the easterly phase of the mesospheric SAO is much weaker (e.g., winds of  $-30$  to  $-40 \text{ m s}^{-1}$  in the second cycle of 1993 and both cycles of 1994). The mesopause westerlies exhibit much less interannual variability, with no clear correlation with the phase of the stratospheric QBO.

Christmas Island radar winds for the period 1990-1995 are shown in Figure 10. As was the case for the composite seasonal cycle, SAO winds measured by the Christmas Island radar are generally weaker than those observed by HRDI. Nevertheless, their interannual variation, including the apparent correlation with the QBO, is consistent with that seen in the HRDI data. Note, in particular, the strong easterly phases during the first cycles of 1993 and 1995, with weaker easterly phases in the second half of 1993 and all of 1994. However, the Christmas Island data for 1990 and 1991 do not show a clear correlation with the phase of the QBO. For example, the QBO phase was westerly during the second

SAO cycle of 1990 (see below), but the easterly phase of the SAO during that cycle were weak.

The relationship between the Christmas Island winds and the stratospheric QBO can be seen more clearly in Figure 11, which displays the radar winds at 84 km together with the strongest westerly and easterly winds found in the 10-70 mbar (19-32 km) layer of the stratosphere. The stratospheric winds were obtained from the climatology compiled by the Free University of Berlin, which (for the period in question) is based on Singapore ( $\sim 1.4^\circ\text{N}$ ) radiosonde observations. The strong SAO easterly cycles of 1993 and 1995 occurred during periods when deep westerlies were present in the 10-70 mbar layer, as indicated by the small magnitude of the strongest easterlies. However, the second easterly cycle of 1990 was weak, although it coincided with a period of deep QBO westerlies; the first easterly cycles of 1990 and 1991, which occurred in the presence of strong stratospheric easterlies, were fairly strong, although not as much as those that occurred during the deep QBO westerlies of 1993 and 1995. *Burrage et al.* [1996b] have analyzed HRDI and Christmas Island data and attributed the correlation between stratospheric and mesospheric winds to filtering of gravity wave fluxes

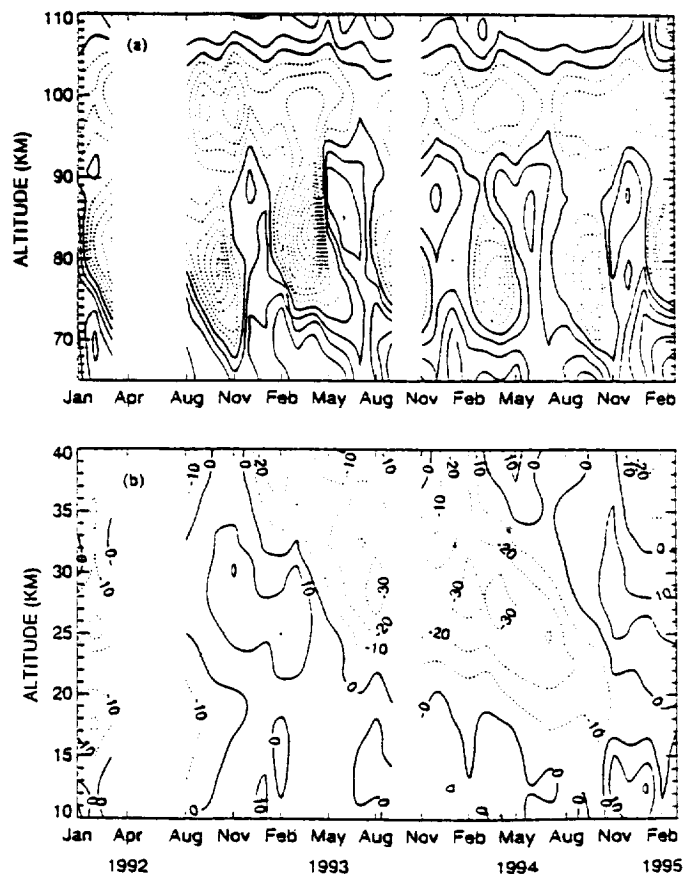


Figure 9. HRDI observations of zonal wind for the period January 1992 to April 1995 over the altitude ranges (a) 65-110 km and (b) 10-40 km. The contour interval is  $10 \text{ m s}^{-1}$ .

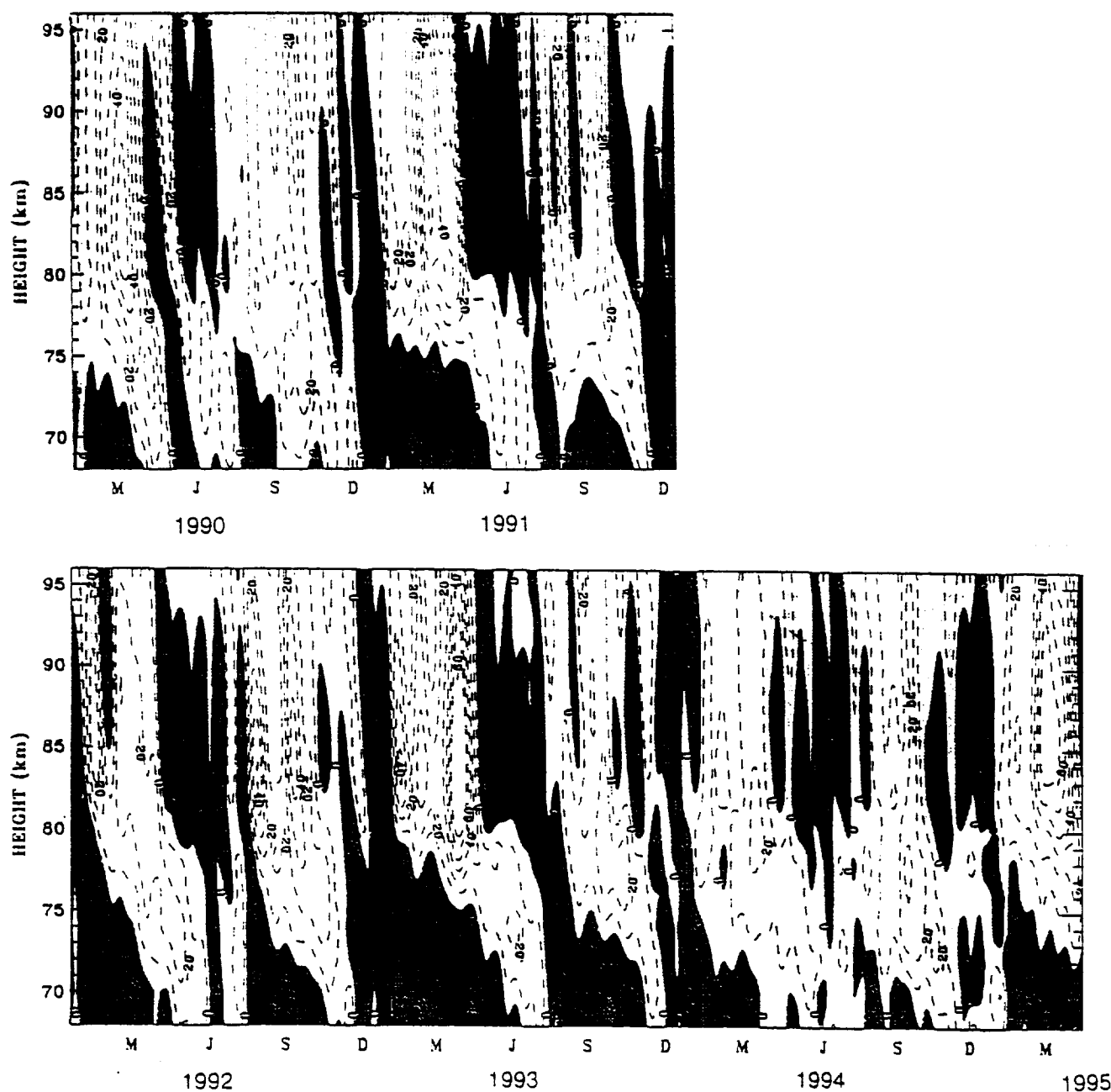


Figure 10. MF radar observations of zonal wind at Christmas Island for the period January 1990 to April 1995. The contour interval is  $10 \text{ m s}^{-1}$ .

emanating from the troposphere by the stratospheric QBO. We discuss this question in section 5.

Shorter-term variability is also evident in the Christmas Island winds (Figure 10). This behavior has been ascribed by Eckermann and Vincent [1994] to modulation of the flux of wave activity emanating from the troposphere. Eckermann and Vincent suggest that the modulation arises from fluctuations in convection associated with the passage of 40–60 day oscillations [Madden and Julian, 1972] in the tropical Pacific Ocean.

## 5. Summary and Discussion

We have used rocketsonde, MF radar and satellite observations to document the behavior of the tropi-

cal semiannual oscillation from the middle stratosphere through the lower thermosphere. Rocketsonde observations, which usually include a partially overlapping rawinsonde profile, cover the altitude range 0–63 km routinely, and 0–84 km occasionally. MF radar data are available in the upper mesosphere and lower thermosphere (68–96 km), as are temperature observations from the Solar Mesosphere Explorer (64–92 km). Data from the High Resolution Doppler Imager extend the range of observations to very high altitudes (65–110 km). The combination of these data sources provides a comprehensive view of the tropical SAO throughout the entire range of altitudes where it dominates the seasonal cycle.

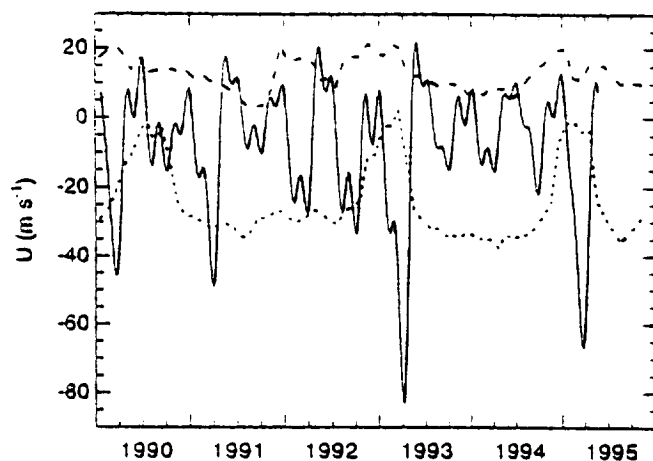


**Figure 11.** Comparison of Christmas Island radar winds at 84 km (solid line) with the strongest westerly (long-dashed) and easterly (short-dashed) Singapore radiosonde winds in the layer 10–70 mbar. The Singapore wind data were kindly provided by S. Pawson, Stratospheric Research Group, Free University of Berlin. The Christmas Island winds have been treated with a 60-day cutoff, low-pass filter to remove the strong intraseasonal variations seen in Figure 10.

Our main findings can be summarized as follows:

1. Rocketsonde, radar, HRDI, and SME data are generally consistent, especially in the stratosphere and lower mesosphere. They show a strong SAO in the upper stratosphere, peaking near the stratopause, where the annual-mean flow is easterly. The semiannual cycle decreases in amplitude in the lower mesosphere, with a minimum near 65 km. In the layer between about 55 and 70 km the time-mean flow is westerly; in fact, the westerlies in this layer are interrupted only by brief intervals of easterly flow near the solstices. Above 65 km, the SAO amplitude increases to a second maximum near the mesopause, where the easterly phase is considerably stronger than the westerly phase and, consequently, the time-mean flow is easterly. Above about 90 km, MF radar and HRDI data indicate easterly flow throughout the year, with only a weak semiannual variation. Altitudes above 100 km are observed only by HRDI; these data show an almost steady westerly flow throughout the year above about 105 km.

2. The SAO exhibits seasonal asymmetry in both the stratosphere and mesosphere, as first noted by *Delisi and Dunkerton* [1988b]. In the stratosphere, interpolation of rocketsonde observations from the islands of Kwajalein (8.7°N) and Ascension (7.6°S) yields a stronger first cycle at the equator. Routine observations of the zonal wind near the equatorial stratopause do not exist. However, HRDI data at 40 km (the level closest to the stratopause observed by HRDI) are consistent with the behavior interpolated from the rocketsonde stations. In the mesosphere, both HRDI and MF radar observations indicate that the easterly phase dur-

ing the first cycle is considerably stronger than its counterpart during the second cycle. Differences between the westerly phases in the first and second cycles are much smaller. A similar seasonal asymmetry is apparent in SME temperature data, as noted earlier by *Garcia and Clancy* [1990]. Positive and negative deviations from the annual mean temperature accompany the descent of westerly and easterly shear zones, as expected from geostrophic balance; these temperature anomalies are stronger during the first cycle than during the second cycle throughout the mesosphere.

3. Both HRDI and MF radar data show that the easterly phase of the mesospheric SAO experiences large interannual variations. As first noted by *Burrage et al.* [1996b], these variations often correlate with the behavior of the stratospheric QBO. Our analysis suggests that the easterly phase of the mesospheric SAO is usually much stronger when deep QBO westerlies are present in the middle stratosphere than during the QBO easterly phase. This relationship holds uniformly throughout the period (1992–1995) of HRDI observations, but when MF radar data from 1990 and 1991 are examined, exceptions to that rule are found. In particular, the second easterly cycle of 1990 was not strong, even though it coincided with a period of deep QBO westerlies in the stratosphere (compare Figures 9 and 11). Mesospheric westerlies do not show marked interannual variability, nor do they appear to be correlated with the QBO. The stratopause easterly phase is unaffected by the QBO, but the stratospheric SAO westerlies do show an apparent QBO modulation. The SAO westerly phase descends farther in the middle stratosphere as the QBO westerlies decay in the lower stratosphere. This effect is observed clearly only in the first westerly phase at Ascension, and in the second westerly phase at Kwajalein [*Dunkerton and Delisi*, this issue].

It is interesting to speculate on the implications of our findings for the wave processes that drive the SAO. As noted above, rocketsonde observations show that the stratopause SAO is seasonally asymmetric, with a much stronger first cycle at Ascension and a slightly stronger second cycle at Kwajalein. The data from these stations suggest that the west phase of the stratopause SAO is also asymmetric about the equator: westerlies descend farther on the south side of the equator in northern spring and on the north side of the equator in northern autumn. This observation indirectly supports the idea that small-scale gravity waves (horizontal wavelength of order 100 km) play an important role in the descent of SAO westerlies [*Hitchman and Leovy*, 1988]. Wave driving due to planetary Kelvin waves is symmetric about the equator, assuming latitudinal shear is zero, and would in any case tend to symmetrize the flow about the equator [*Holton*, 1979]. Stronger westerlies may be due to enhanced gravity-wave transmission in local summer [*Delisi and Dunkerton*, 1988a] and/or stronger excitation of gravity waves by tropical convection at this time of the year [*Allen and Vincent*, 1995].

The modulation of the stratospheric SAO westerlies by the QBO further supports the role of small-scale gravity waves having a range of phase speeds roughly comparable to the range of QBO winds. Westerly (eastward propagating) waves of moderate phase speed ( $15\text{--}30\text{ m s}^{-1}$ ) are strongly absorbed in QBO westerlies but are free to propagate vertically in QBO easterlies. Fast planetary Kelvin waves also experience absorption in QBO westerlies [Dunkerton, 1979]. However, a recent calculation of equatorial wave spectra by Bergman and Salby [1994] indicates that only about 40% of the Eliassen-Palm flux in vertically propagating waves is carried by planetary-scale Kelvin, Rossby, and Rossby-gravity modes. The remaining 60% of their resolved flux is due to all other waves, including intermediate-scale Kelvin waves, and intermediate- and small-scale inertia-gravity waves with phase speeds in the range  $\sim 15\text{--}60\text{ m s}^{-1}$ . Waves with phase speeds in the lower half of this range are expected to be important in the momentum balance of the QBO [Dunkerton, this issue], and they may influence the stratospheric SAO insofar as their vertical propagation is significantly modulated by the phase of the QBO.

Burrage *et al.* [1995] and Lieberman [1996] have shown that the amplitude of the diurnal tide observed by HRDI is almost a factor of 2 larger during 1992 and early 1993, and again in early 1995, than at other times. Lieberman has also shown that the easterly driving associated with the tide varies accordingly, reaching particularly large values ( $\sim 16\text{ m s}^{-1}\text{ d}^{-1}$  at 97 km) in late 1992 and early 1993. It is tempting to suggest that interannual variations in easterly driving by the diurnal tide are responsible for the variability of the easterly phase of the mesospheric SAO illustrated in Figures 9–11. However, forcing by the diurnal tide is strongest near 100 km; at 85 km, it decreases to  $\sim 4\text{ m s}^{-1}\text{ d}^{-1}$  even in late 1992 and early 1993, and it all but vanishes at  $\sim 80\text{ km}$  in all years. Therefore it appears unlikely that tidal driving alone can account for the interannual variability of the mesospheric SAO easterlies.

Burrage *et al.* [1996b] have argued instead that small-scale gravity waves may play a role in the mesospheric SAO. They support their conclusion with the results of the numerical model described by Mengel *et al.* [1995], which produces quasi-biennial behavior in the mesosphere as a result of filtering of the imposed gravity wave spectrum by the stratospheric QBO. Although the resemblance between these model results and the observations displayed in our Figures 9–11 is only qualitative, it does suggest that filtering of small-scale gravity waves is a plausible mechanism whereby the QBO can influence the mesospheric SAO.

Another possibility is raised by the work of Sassi and Garcia [1994], who have argued that intermediate-scale (zonal wavenumbers 5–25) Kelvin and inertia-gravity waves may contribute a significant fraction of the momentum required to drive the SAO. The typical phase speeds of these waves are  $\pm 30\text{--}60\text{ m s}^{-1}$ , which suggests an explanation for our finding that the easterly phase of

the mesospheric SAO appears to be strongly modulated by the QBO, while the westerly phase is unaffected. The amplitude distribution of QBO winds is asymmetric about zero velocity, i.e., easterly winds are twice as strong as westerlies (peak easterlies of about  $-30\text{ m s}^{-1}$  versus maximum westerlies of  $15\text{ m s}^{-1}$ , compare Figure 9b). Therefore, waves with phase speeds in the  $-30$  to  $-60\text{ m s}^{-1}$  range should be dissipated strongly or even absorbed during the QBO easterly phase, but they could propagate readily to higher altitudes during the westerly phase. On the other hand, waves with phase speeds of  $+30$  to  $+60\text{ m s}^{-1}$  should be affected to a much lesser degree by the phase of the QBO, since their intrinsic frequency is relatively high even during the westerly phase.

Any attempt at explaining the interannual variation of the mesospheric SAO must be accompanied by a note of caution at present. The relationship between strong easterly phases in the mesosphere and the prevalence of QBO westerlies in the stratosphere is striking during the HRDI period of observations (1992–1995) but less evident when Christmas Island radar winds for 1990–1991 are examined (compare Figure 11). Thus observations of the mesospheric SAO spanning several more cycles of the QBO are likely to be necessary before any conclusive statements can be made about the relationship between the two. Such considerations underline the importance of continuing long-term observations of the upper mesosphere and lower thermosphere.

Finally, the observation of a westerly wind layer by HRDI above 105 km deserves a brief comment. Insofar as the HRDI measurements represent a true zonal mean wind, the atmosphere at these levels is in superrotation, which implies the existence of a westerly momentum source. As noted earlier HRDI zonal winds above 85 km cannot be taken at face value because of the possibility of contamination by the diurnal tide. Nevertheless, the recent work of Lieberman and Riggan [this issue] suggests that a such a westerly wind layer may be the result of momentum deposition by ultrafast Kelvin waves.

**Acknowledgments.** We would like to thank Don Delis and Lloyd Lowe for their help in processing the rocketsonde data, and the HRDI science team for their efforts in processing and validating HRDI wind observations. Steven Pawson of the Stratospheric Research Group at the Free University of Berlin, kindly provided data on the equatorial QBO. Operation of the Christmas Island radar is supported by the Australian Research Council. T.J.D.'s research was supported by the National Aeronautics and Space Administration, under contract NASW-4844, and by the National Science Foundation, under grant ATM-9500613. R.R.G. was supported in part by NASA grant L99120C. The National Center for Atmospheric Research is Sponsored by the National Science Foundation.

## References

- Allen, S.J., and R.A. Vincent, Gravity wave activity in the lower atmosphere: Seasonal and latitudinal variations, *J. Geophys. Res.*, 100, 1327–1350, 1995.

- Andrews, D.G., J.R. Holton, and C.B. Leovy, *Middle Atmosphere Dynamics*, 489 pp., Academic, Orlando, Fla., 1987.
- Angell, J.K., and J. Korshover, Quasi-biennial, annual, and semiannual zonal wind and temperature harmonic amplitudes and phases in the stratosphere and low mesosphere of the northern hemisphere, *J. Geophys. Res.*, **75**, 543-550, 1970.
- Barnett, J.J., The mean meridional temperature behavior of the stratosphere from November 1970 to November 1971 derived from measurements by the Selective Chopper Radiometer on Nimbus 4, *Q. J. R. Meteorol. Soc.*, **100**, 505-530, 1974.
- Belmont, A.D., D.G. Dartt, and G.D. Nastrom, Periodic variations in stratospheric zonal wind from 20-65 km, at 80N to 70S, *Q. J. R. Meteorol. Soc.*, **100**, 203-211, 1974.
- Belmont, A.D., D.G. Dartt, and G.D. Nastrom, Variations of stratospheric zonal winds, 20-65 km, 1961-1971, *J. Appl. Meteorol.*, **14**, 585-594, 1975.
- Bergman, J.W., and M.L. Salby, Equatorial wave activity derived from fluctuations in observed convection, *J. Atmos. Sci.*, **51**, 3791-3806, 1994.
- Burrage, M.D., M.E. Hagan, W.R. Skinner, D.L. Wu, and P.B. Hays, Long-term variability in the solar diurnal tide observed by HRDI and simulated by the GSWM, *Geophys. Res. Lett.*, **22**, 2641-2644, 1995.
- Burrage, M. D., et al., Validation of mesosphere and lower thermosphere winds from the High Resolution Doppler Imager on UARS, *J. Geophys. Res.*, **101**, 10365-10392, 1996a.
- Burrage, M. D., R. A. Vincent, H. G. Mayr, W. R. Skinner, N. F. Arnold, and P. B. Hays, Long term variability in the equatorial mesosphere and lower thermosphere zonal winds, *J. Geophys. Res.*, **101**, 12847-12854, 1996b.
- Clancy, R.T., and D.W. Rusch, Climatology and trends of mesospheric (55-90 km) temperatures based upon 1982-1986 SME limb scattering profiles, *J. Geophys. Res.*, **94**, 3377-3393, 1989.
- Clancy, R.T., D.W. Rusch, and M.T. Callan, Temperature minima in the average vertical structure of the mesosphere (70-80 km) from analysis of 40 to 92 km SME global temperature profiles, *J. Geophys. Res.*, **99**, 19001-19020, 1994.
- Cole, A.E., and A.J. Cantor, Tropical atmospheres, 0 to 90 km, project 8624, *Tech. Rep. AFRL-TR-75-0527*, Aeron. Lab., Air Force Cambridge Res. Lab., Hanscom, Mass., 1975.
- Cole, A.E., and A.J. Cantor, Air Force reference atmospheres, project 6670, *Tech. Rep. AFGL-TR-78-0051*, Meteorol. Div., Air Force Geophys. Lab., Hanscom, Mass., 1978.
- Delisi, D.P., and T.J. Dunkerton, Equatorial semiannual oscillation in zonally averaged temperature observed by the Nimbus 7 SAMS and LIMS, *J. Geophys. Res.*, **93**, 3899-3904, 1988a.
- Delisi, D.P., and T.J. Dunkerton, Seasonal variation of the semiannual oscillation, *J. Atmos. Sci.*, **45**, 2772-2787, 1988b.
- Dunkerton, T.J., On the role of the Kelvin wave in the westerly phase of the semiannual zonal wind oscillation, *J. Atmos. Sci.*, **36**, 32-41, 1979.
- Dunkerton, T.J., Theory of the mesopause semiannual oscillation, *J. Atmos. Sci.*, **39**, 2681-2690, 1982.
- Dunkerton, T.J., The role of gravity waves in the quasi-biennial oscillation, *J. Geophys. Res.*, this issue.
- Dunkerton, T.J., and D.P. Delisi, The subtropical mesospheric jet observed by the Nimbus 7 Limb Infrared Monitor of the Stratosphere, *J. Geophys. Res.*, **90**, 10681-10692, 1985a.
- Dunkerton, T.J., and D.P. Delisi, Climatology of the equatorial lower stratosphere, *J. Atmos. Sci.*, **42**, 376-396, 1985b.
- Dunkerton, T.J., and D.P. Delisi, Anomalous temperature and zonal wind in the tropical upper stratosphere, 1982/1983, *J. Geophys. Res.*, **96**, 22631-22641, 1991.
- Dunkerton, T.J., and D.P. Delisi, Interaction of quasi-biennial oscillation and stratopause semiannual oscillation, *J. Geophys. Res.*, this issue.
- Eckermann, S.D., and R.A. Vincent, First observations of intraseasonal oscillations in the equatorial mesosphere and lower thermosphere, *Geophys. Res. Lett.*, **21**, 265-268, 1994.
- Fritz, S., On the causes of the annual and semi-annual variations in radiance (or temperature) from the tropical stratopause, *J. Atmos. Sci.*, **31**, 813-822, 1974.
- Garcia, R.R., and R.T. Clancy, Seasonal variation in equatorial mesospheric temperatures observed by SME, *J. Atmos. Sci.*, **47**, 1666-1673, 1990.
- Groves, G.V., Annual and semiannual zonal wind components and corresponding temperature and density variations, 60-130 km, *Planet. Space Phys.*, **20**, 2099-2112, 1972.
- Hamilton, K., Rocketsonde observations of the mesospheric semiannual oscillation at Kwajalein, *Atmos.-Ocean*, **20**, 281-286, 1982.
- Hays, P.B., V.J. Abreu, M.E. Dobbs, D.A. Gell, H.J. Grassl, and W.R. Skinner, The High-Resolution Doppler Imager on the Upper Atmosphere Research Satellite, *J. Geophys. Res.*, **98**, 10713-10723, 1993.
- Hirota, I., Equatorial waves in the upper stratosphere and mesosphere in relation to the semi-annual oscillation of the zonal wind, *J. Atmos. Sci.*, **35**, 714-722, 1978.
- Hirota, I., Observational evidence of the semiannual oscillation in the tropical middle atmosphere: A review, *Pure Appl. Geophys.*, **118**, 217-238, 1980.
- Hitchman, M.H., and C.B. Leovy, Evolution of the zonal mean state in the equatorial middle atmosphere during October 1978-May 1979, *J. Atmos. Sci.*, **43**, 3159-3176, 1986.
- Hitchman, M.H., and C.B. Leovy, Estimation of Kelvin wave contribution to the semiannual oscillation, *J. Atmos. Sci.*, **45**, 1462-1475, 1988.
- Holton, J.R., Equatorial wave-mean flow interaction: A numerical study of the role of latitudinal shear, *J. Atmos. Sci.*, **36**, 1030-1040, 1979.
- Hopkins, R.H., Evidence of polar-tropical coupling in upper stratosphere zonal wind anomalies, *J. Atmos. Sci.*, **32**, 712-719, 1975.
- Lieberman R.S. and P.B. Hays, An estimate of the momentum deposition in the lower thermosphere by the observed diurnal tide, *J. Atmos. Sci.*, **51**, 3094-3105, 1994.
- Lieberman, R.S., Long-term variations of zonal mean winds and (1,1) driving in the equatorial lower thermosphere, *J. Atmos. Solar-Terr. Phys.*, in press, 1997.
- Lieberman, R.S. and D. Riggan, High-Resolution Doppler Imager observations of Kelvin waves in the equatorial mesosphere and lower thermosphere, *J. Geophys. Res.*, this issue.
- Madden, R.A., and P.R. Julian, Description of global-scale circulation cells in the tropics with a 40-50 day period, *J. Atmos. Sci.*, **29**, 1109-1123, 1972.
- Mengel, J.H., H.G. Mayr, K.L. Chan, C.O. Hines, C.A. Reddy, N.F. Arnold and H.S. Potter, Equatorial oscillations in the middle atmosphere generated by small-scale gravity waves, *Geophys. Res. Lett.*, **22**, 3027-3033, 1995.
- Nastrom, G.D., and A.D. Belmont, Periodic variations in stratospheric-mesospheric temperature from 20-65 km at 80N to 30S, *J. Atmos. Sci.*, **32**, 1715-1722, 1975.

- Naujokat, B., An update of the observed quasi-biennial oscillation of the stratospheric winds over the tropics, *J. Atmos. Sci.*, **43**, 1873-1877, 1986.
- Ortland, D. A., W. R. Skinner, P. B. Hays, Burrage, M. D., R. S. Lieberman, A. R. Marshall and D. A. Gell, Measurements of stratospheric winds by the High Resolution Doppler Imager, *J. Geophys. Res.*, **101**, 10351-10363, 1996.
- Reed, R.J., Some features of the annual temperature regime in the tropical stratosphere, *Mon. Weather Rev.*, **90**, 211-215, 1962.
- Reed, R.J., Zonal wind behavior in the equatorial stratosphere and lower mesosphere, *J. Geophys. Res.*, **71**, 4223-4233, 1966.
- Reed, R.J., and C.L. Vilek, The annual temperature variation in the lower tropical stratosphere, *J. Atmos. Sci.*, **26**, 163-167, 1969.
- Sassi, F. and R.R. Garcia, A one-dimensional model of the semiannual oscillation driven by convectively forced gravity waves, *J. Atmos. Sci.*, **51**, 3167-3182, 1994.
- van Loon, H., and R.L. Jenne, The annual wave in the temperature of the low stratosphere, *J. Atmos. Sci.*, **27**, 701-705, 1970.
- Vincent, R.A., and S.M. Ball, Mesospheric winds at low- and mid-latitudes in the southern hemisphere. *Geophys. Res. Lett.*, **86**, 9159-9169, 1981.
- Vincent, R.A., and D. Lesicar, Dynamics of the equatorial mesosphere: First results with a new generation partial reflection radar, *Geophys. Res. Lett.*, **18**, 825-828, 1991.
- Vincent, R.A., T. Tsuda, and S. Kato, Asymmetries in mesospheric tidal structure, *J. Atmos. Terr. Phys.*, **51**, 609-616, 1989.
- Wallace, J.M., General circulation of the tropical lower-stratosphere, *Rev. Geophys.*, **11**, 191-222, 1973.
- Yulaeva, E., J.R. Holton, and J.M. Wallace, On the cause of the annual cycle in tropical lower-stratospheric temperatures, *J. Atmos. Sci.*, **51**, 169-174, 1994.

---

T.J. Dunkerton, NorthWest Research Associates, P.O. Box 3027, Bellevue, WA 98009. (e-mail: tim@nwra.com)

R.R. Garcia, NCAR, P.O. Box 3000, 1850 Table Mesa Dr., Boulder, CO 80307-3000. (e-mail: rgarcia@ncar.ucar.edu)

R.S. Lieberman, Space Physics Research Laboratory, University of Michigan, Ann Arbor, MI 48109. (e-mail: lieberman@sprlj.sprl.umich.edu)

R.A. Vincent, Department of Physics and Mathematical Physics, University of Adelaide, Adelaide, S.A. 5001, Australia. (e-mail: rvincent@physics.adelaide.edu.au)

(Received April 22, 1996; revised October 7, 1996; accepted January 19, 1997.)

# Interaction of the quasi-biennial oscillation and stratopause semiannual oscillation

Timothy J. Dunkerton and Donald P. Delisi

Northwest Research Associates, Bellevue, Washington

**Abstract.** Analysis of rawinsonde and rocketsonde data at Ascension Island (7.6°S, 14.4°W) and Kwajalein (8.7°N, 167°E) in 1962–1991 suggests that the quasi-biennial oscillation (QBO) in the middle stratosphere is synchronized with the seasonal cycle and that descending westerly phases of the stratopause semiannual oscillation (SAO) are strongly influenced by the underlying QBO. The effect of the seasonal cycle on the QBO in the middle stratosphere is revealed in two, perhaps unrelated, observations: first, a tendency for deseasonalized QBO westerly maxima to occur in local winter (or to avoid local summer); second, a smooth, uninterrupted connection between descending SAO westerly shear zones and the formation of a new QBO westerly shear zone aloft. The timing of deseasonalized QBO westerly maxima in the middle stratosphere allows a simple composite of 2- and 3-year cycles to be constructed from the data, illustrating the effect of the QBO on descending westerly phases of the stratopause SAO.

## 1. Introduction

The quasi-biennial oscillation (QBO) of the equatorial stratosphere is so named because the average period of the oscillation is slightly longer than 2 years. Almost 20 cycles have been observed since rawinsonde data first became available in the early 1950s; the average period is now 28.4 months. Individual cycles range from ~22 to 36 months, i.e., from about 2 to 3 years.

The prefix “quasi” would apply equally well to an oscillation with continuously variable period, or an oscillation consisting of discrete periods (e.g., 24 months, with a few 30- or 36-month cycles) strung together in some regular or irregular fashion. The period of the QBO is customarily measured at mandatory rawinsonde pressure levels, e.g., 50, 30, or 10 mbar [Dunkerton and Delisi, 1985; Angell, 1986; Naujokat, 1986; Dunkerton, 1990]. This approach, based on one-dimensional time series, leads to the conclusion that the QBO period is variable, tending to form a continuous distribution as time progresses. Exact synchronization with the seasonal cycle is not observed, although as noted by Dunkerton [1990], the deseasonalized mean flow acceleration, distribution of phase onsets, and period of the QBO evidently depend on the time of year. This dependence on the seasonal cycle is due, in part, to a pronounced tendency for descending QBO easterlies to “stall” near 30 mbar between July and February [Naujokat, 1986]. Modulation of the QBO by the seasonal cycle can be distinguished from exact synchronization, which would produce one or more delta functions in the distribution of onset times. Both types of behavior were simulated in a QBO model [Dunkerton, 1990].

It was suggested by Lindzen and Holton [1968, p. 1101], however, that the QBO in the middle stratosphere is “synchronized” with the semiannual oscillation (SAO). Onset of QBO westerlies, in particular, is tied to the westerly phase of the SAO, and therefore “the appearance of successive westerly regimes at 30 km tends to be a multiple of 6 months” [Lindzen and Holton, 1968, p. 1106]. Using nearly four decades of raw-

insonde data, Dunkerton [1990] found that QBO onsets at 10 mbar are modulated by the semiannual cycle, while onsets at 50 mbar display an annual variation. The comments of Lindzen and Holton, based on a combination of rawinsonde and rocketsonde data extending to higher altitudes, seem to imply a stronger synchronization than found at constant pressure levels by Dunkerton. It is noteworthy that the QBO attains maximum amplitude at or above the 10 mbar level [Hamilton, 1981] so rawinsondes alone cannot describe the entire phenomenon. Moreover, there is no reason to insist that the initiation of a new QBO phase, or maximum anomaly amplitude, should necessarily occur at the same pressure level in every cycle. Lindzen and Holton’s observations may therefore be compatible with Dunkerton’s analysis, but it is unclear whether the data displayed in their Figure 6 (1962–1966) are representative of a longer time series. Another complication is that rocketsonde data used in the top part of their figure were obtained several degrees from the equator, and the seasonal cycle was not removed.

The purpose of this paper is to examine a longer time series of rawinsonde and rocketsonde data at Ascension Island (7.6°S, 14.4°W) and Kwajalein (8.7°N, 167°E), extending from 1962 to 1991. Our results demonstrate that Lindzen and Holton’s [1968] comments are generally valid at these off-equatorial locations during the time period analyzed. We also find that QBO westerly maxima tend to occur in local winter (or to avoid local summer) even when the seasonal cycle is removed from the data. Using deseasonalized westerly maxima to delimit QBO cycles, most of the deseasonalized QBO periods can be approximated by cycles of 24 or 36-month duration, with perhaps one or two 30-month cycles. This observation can be used to construct composite QBO cycles of 2 or 3 year’s duration, illustrating more succinctly the seasonal synchronization of QBO onsets and extrema in the middle stratosphere and the effect of the QBO on descending westerly phases of the SAO.

## 2. Data Analysis

Data from the historical rocketsonde network were obtained from a variety of sources and processed to form monthly means

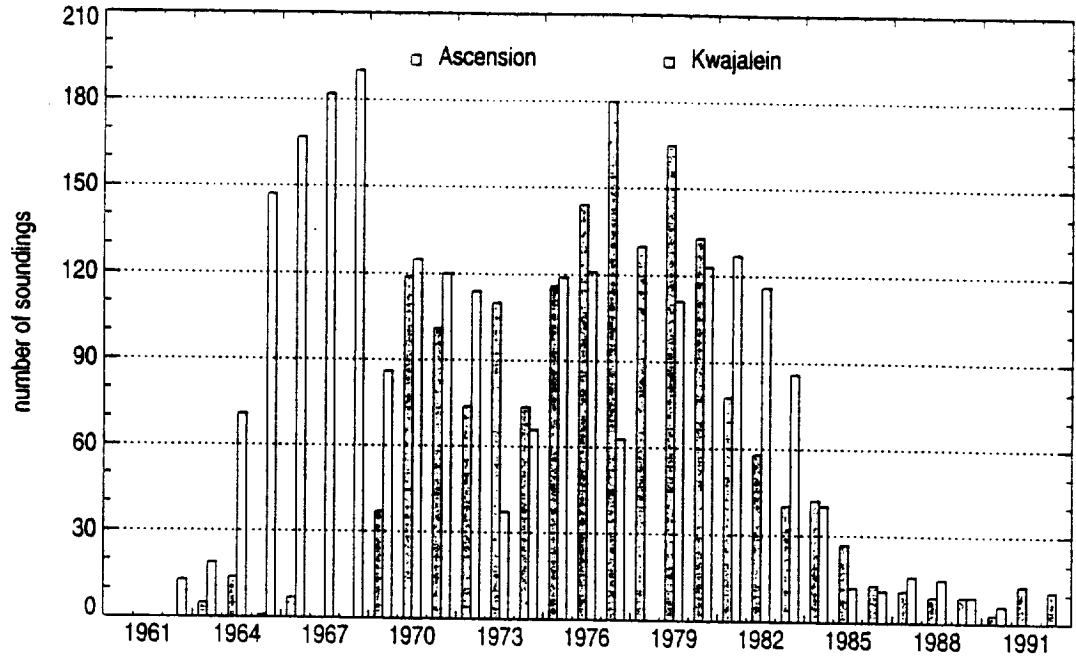


Figure 1. Number of rocketsonde observations per year at Ascension and Kwajalein.

of zonal wind at each station. Measurements were binned into 0.2 scale-height intervals (approximately 1.4 km, using a nominal pressure scale height of 7 km). The binned soundings were averaged together in each month, and a minimum of  $M$  soundings were required per month. Satisfactory results were obtained with  $M = 1$ , although "monthly mean" data are noisy, due to insufficient soundings, near the endpoints of the time period. The number of soundings per year at Ascension and Kwajalein is shown in Figure 1.

Rocket soundings usually include a partially overlapping, contemporaneous rawinsonde profile. After binning, rocketsonde and rawinsonde data were blended using a linear ramp in the height interval 3.7–4.7 scale heights. Starting at 3.7 scale heights, rawinsonde data were tapered to zero at 4.7 scale heights, and starting at 4.7 scale heights, rocketsonde data were tapered to zero at 3.7 scale heights, such that their combined weights equaled unity at each level in this height interval. The climatological seasonal cycle was obtained by averaging all months individually. Data were deseasonalized by removing the climatological seasonal cycle at each station from the respective time series. For clarity of presentation, blended data were smoothed once according to

$$\bar{u}_{j,k} = \frac{\sum_{p=-1}^{+1} \sum_{q=-1}^{+1} u_{j+p,k+q} w_{j+p,k+q} + 7u_{j,k}}{\sum_{p=-1}^{+1} \sum_{q=-1}^{+1} w_{j+p,k+q} + 7} \quad (1)$$

where

$$w_{j,k} = \begin{cases} 1 & \text{if } u_{j,k} \text{ exists} \\ 0 & \text{otherwise.} \end{cases} \quad (2)$$

### 3. Results

Figures 2a–2g show time-height cross sections of monthly mean zonal wind at Ascension and Kwajalein. Several quanti-

ties are displayed: (1) deseasonalized westerlies equal to  $20 \text{ ms}^{-1}$  (thick solid contours); (2) deseasonalized easterlies equal to  $-20 \text{ ms}^{-1}$  (thin solid contours); (3) zonal wind with seasonal cycle included: (mostly westerly) winds  $> -5 \text{ ms}^{-1}$  (light shading); thin dotted contours in the shaded region indicate westerlies at 15 and  $35 \text{ ms}^{-1}$ ; (4) zonal wind with seasonal cycle included: (weak easterly) winds in the range  $-15$  to  $-5 \text{ ms}^{-1}$  (dark shading); (5) zonal wind with seasonal cycle included: (strong easterly) winds  $< -15 \text{ ms}^{-1}$  (unshaded); thin dotted contours in the unshaded region indicate easterlies at  $-35$  and  $-55 \text{ ms}^{-1}$ ; (6) regions where the shear-zone parameter  $R > 1$  (see below), indicative of descending shear zones (diagonal lines). Blank regions indicate missing data. The definition of  $R$  is

$$R = \text{sgn}(\bar{u}_z \cdot \bar{u}_t) \sqrt{\left(\frac{\bar{u}_z}{\sigma_z}\right)^2 + \left(\frac{\bar{u}_t}{\sigma_t}\right)^2} \quad (3)$$

where  $\bar{u}$  is the mean zonal wind with seasonal cycle included,  $\bar{u}_z$  and  $\bar{u}_t$  are vertical shear and mean flow acceleration, respectively;  $\sigma_z$  and  $\sigma_t$  are the standard deviations of these quantities over the entire grid.  $R$  is a measure of shear-zone strength that gives equal emphasis to vertical shear and mean flow acceleration and is independent of the plot aspect ratio. Large positive  $R$  indicates shear-zone descent, since

$$\left(\frac{dz}{dt}\right)_a = -\frac{\bar{u}_t}{\bar{u}_z} \quad (4)$$

Figure 2 shows that weak easterlies (dark shading) often run through the center of descending SAO/QBO shear zones at Ascension and Kwajalein.

#### 3.1. Deseasonalized QBO Westerly Maxima

Westerly shear zones in the QBO descend faster than easterly shear zones, on the average, so that QBO westerly regimes are short-lived in the middle stratosphere, and it is relatively easy to determine the time of maximum deseasonalized westerlies (inside the thick solid contours). At Ascension the



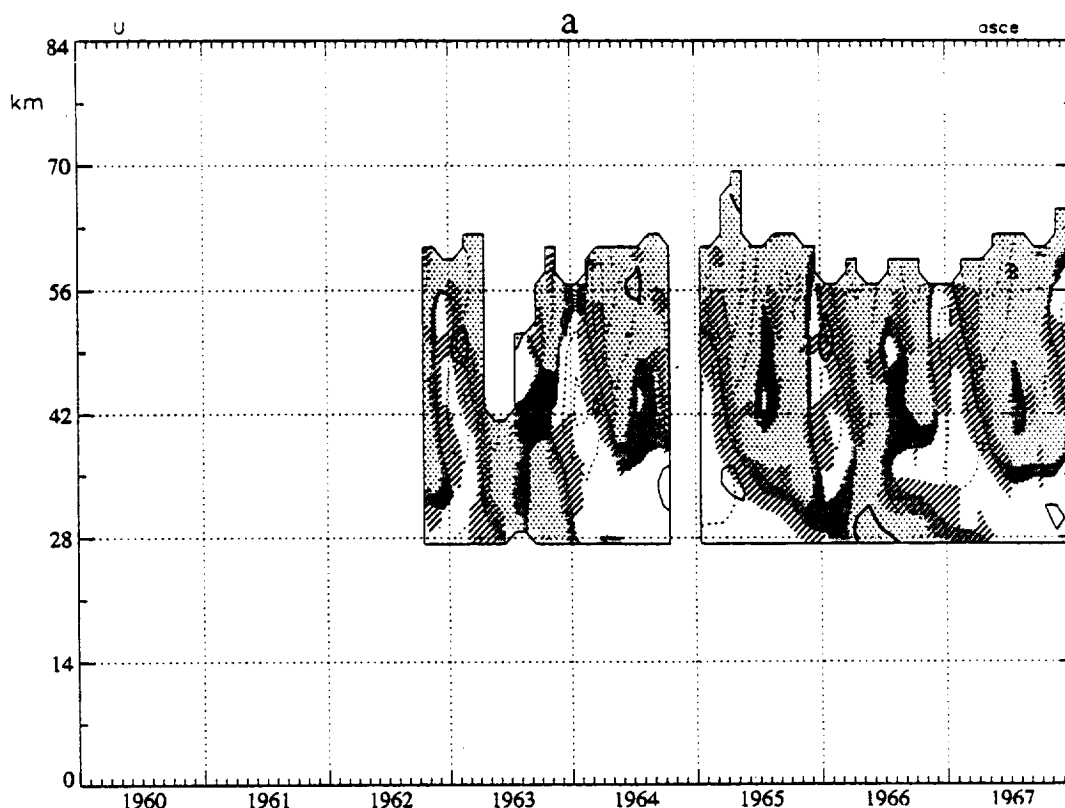


Figure 2. Time-height cross sections of monthly mean zonal wind at (a, b, d, f) Ascension and (c, e, g) Kwajalein. Deseasonalized winds equal to  $20 \text{ ms}^{-1}$  are shown by thick solid contours; deseasonalized winds equal to  $-20 \text{ ms}^{-1}$  are shown by thin solid contours. Light shading indicates winds (with seasonal cycle included) greater than  $-5 \text{ ms}^{-1}$ , i.e., westerlies or very weak easterlies. Thin dotted contours in the shaded region indicate westerlies at  $15$  and  $35 \text{ ms}^{-1}$ . Dark shading indicates winds (with seasonal cycle included) between  $-15$  and  $-5 \text{ ms}^{-1}$ . Easterly winds (with seasonal cycle included) less than  $-15 \text{ ms}^{-1}$  are unshaded. Thin dotted contours in the unshaded region indicate easterlies at  $-35$  and  $-55 \text{ ms}^{-1}$ . Diagonal lines indicate regions where the shear-zone parameter  $R$  is greater than 1 (see text). Altitude is approximate using a nominal pressure scale height of 7 km.

deseasonalized QBO westerly maxima are located around 3.5–5 scale heights (25–35 km) and tend to occur in the middle of a calendar year. Such was the case in 1966, 1969, 1971, 1975, 1980, and 1985. Westerlies were probably a bit early in 1973 (a data gap) and slightly late in 1982 and 1987. (It would be more accurate to say that westerlies in 1982 and 1987 were early, by 6–9 months, due to unusually fast shear-zone descent.) At Ascension it is safe to conclude that in the time period shown, deseasonalized QBO westerly maxima tend to prefer local winter (i.e., northern hemisphere summer) or to avoid local summer (i.e., northern hemisphere winter).

At Kwajalein the deseasonalized QBO westerly maxima prefer northern winter, in contrast to Ascension. Such was the case at the beginning of 1971, 1973, 1975, 1978, 1980, and 1983. Westerlies were slightly late in 1985 and slightly early at the end of 1987. At Kwajalein also, it is safe to conclude that in the time period shown, deseasonalized QBO westerly maxima tend to prefer local winter (i.e., northern hemisphere winter) or to avoid local summer (i.e., northern hemisphere summer). The same is evidently true of deseasonalized QBO easterly minima.

Comparing the two stations when simultaneous data are available, the deseasonalized westerly maxima at Ascension often lag those at Kwajalein by several ( $\leq 6$ ) months, as in 1971, probably 1973, 1975, and 1980. In 1982 the maximum at Ascension preceded that at Kwajalein, while in 1985 and 1987, the maxima near 28 km were nearly coincident.

All of the deseasonalized QBO westerly maxima occur inside a westerly regime of the QBO defined by the total zonal wind (with seasonal cycle included) indicated by light shading. The annual cycle has a dramatic effect on QBO westerly regimes in the layer  $\sim 21$ –35 km, often splitting them in half about local summer. Such was the case at Ascension in early 1966, 1975, 1980, and 1988, and at Kwajalein in the middle of 1971, 1975, 1977, 1980, 1982, 1985, and 1987.

The tendency for deseasonalized QBO westerly maxima in the middle stratosphere to occur at the same time of year is useful for constructing 2- and 3-year composite QBOs (section 3.3).

### 3.2. Descending QBO Westerly Shear Zones

The “synchronization” observed by Lindzen and Holton [1968] describes how a new westerly shear zone of the QBO is triggered by a descending westerly shear zone of the stratospheric SAO. According to Figure 2, at Ascension there is indeed a spectacular and generally reliable connection between descending westerly shear zones of the SAO and QBO in the 28–56 km layer. Here, it is always the westerly acceleration phase of the “first” SAO cycle in a calendar year that connects to a new QBO westerly shear zone. This is not surprising, since at Ascension, the first SAO cycle is stronger than the second cycle, on the average, and SAO westerlies descend farther into the stratosphere in the first cycle [Garcia *et al.*, this issue] (see

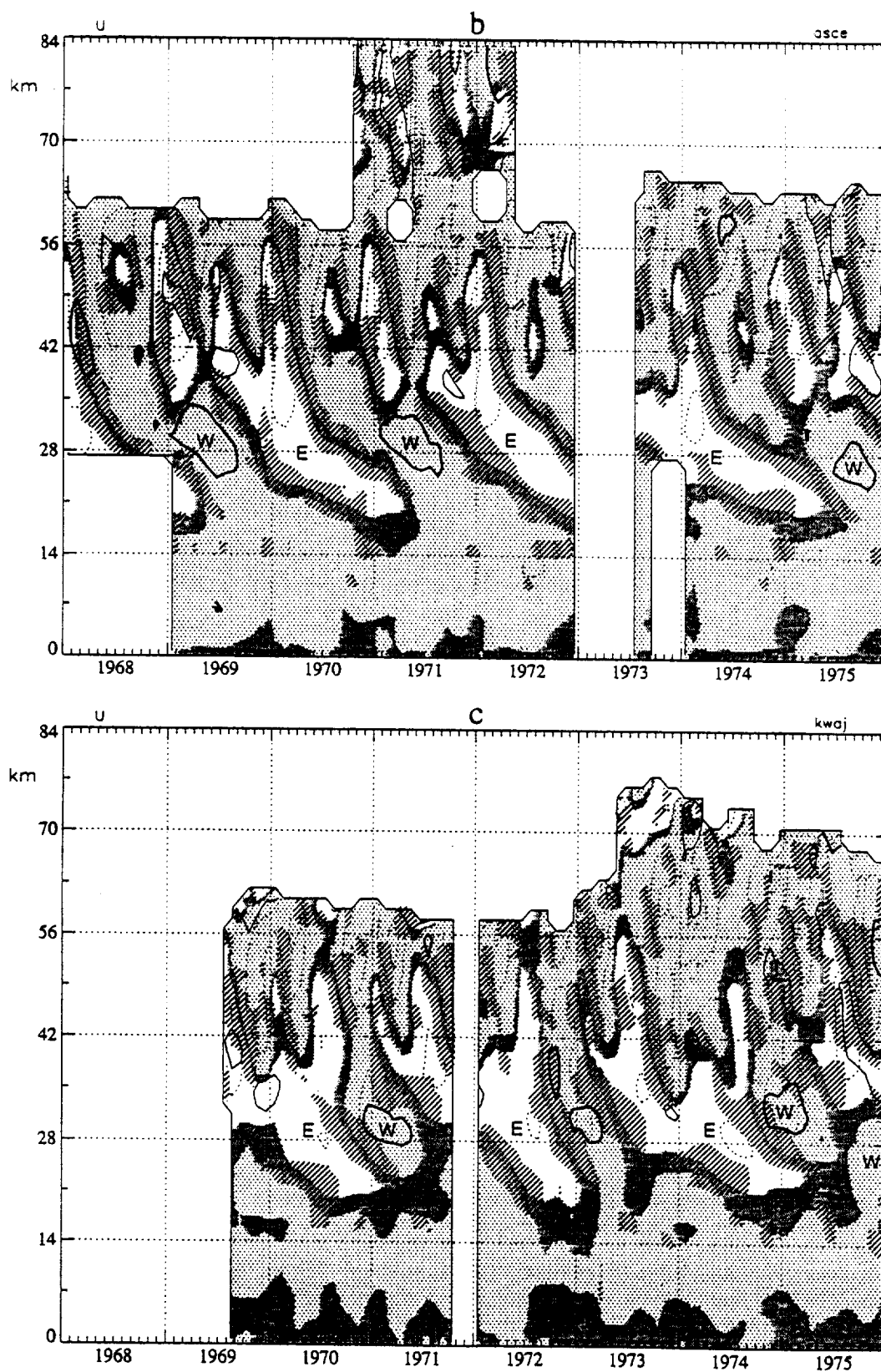


Figure 2. (continued)

also section 3.3). On closer inspection the Ascension data suggest two distinct patterns of connection. The more common pattern is for SAO westerlies to descend in what might be called "year 0" (1965, 1968, 1970, 1972, 1974, probably 1977,

1979, and 1984) and to initiate a new QBO westerly regime then, but the deseasonalized QBO westerly maximum near 28 km is delayed until the following "year 1" (1966, 1969, 1971, probably 1973, 1975, possibly 1978, 1980, and 1985). A less

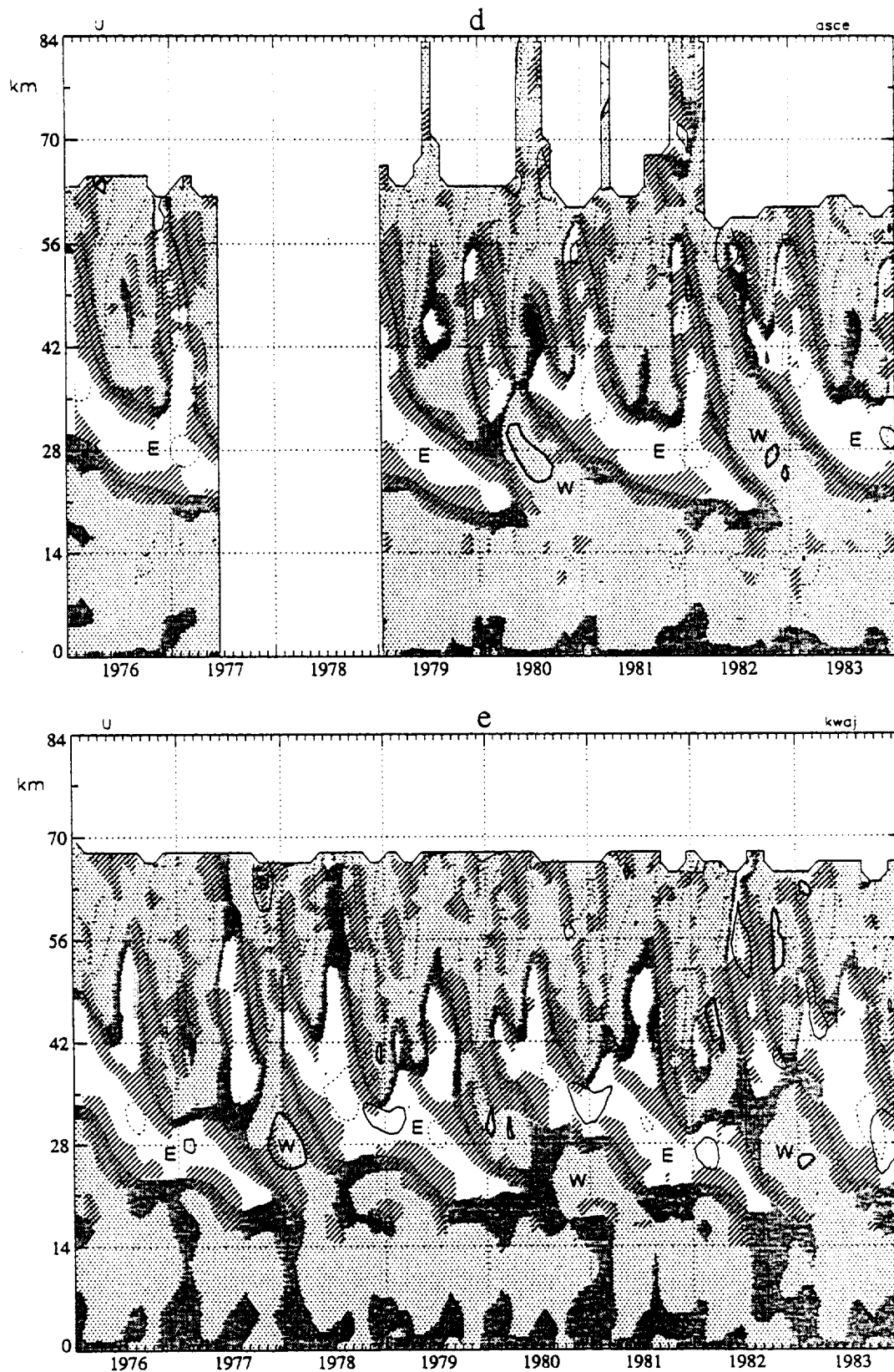


Figure 2. (continued)

common pattern is for the QBO westerly onset and maximum to occur in the same year (1982, 1987, and probably 1963) when the westerly shear zone descends unusually fast (possibly due to the enhanced Kelvin-wave activity found by Maruyama

[1991, 1994] and Sato and Dunkerton [this issue]). There is apparently no relation, however, between the type of SAO/QBO connection pattern and the period of the next QBO cycle. Faster descent of QBO westerlies does not guarantee a

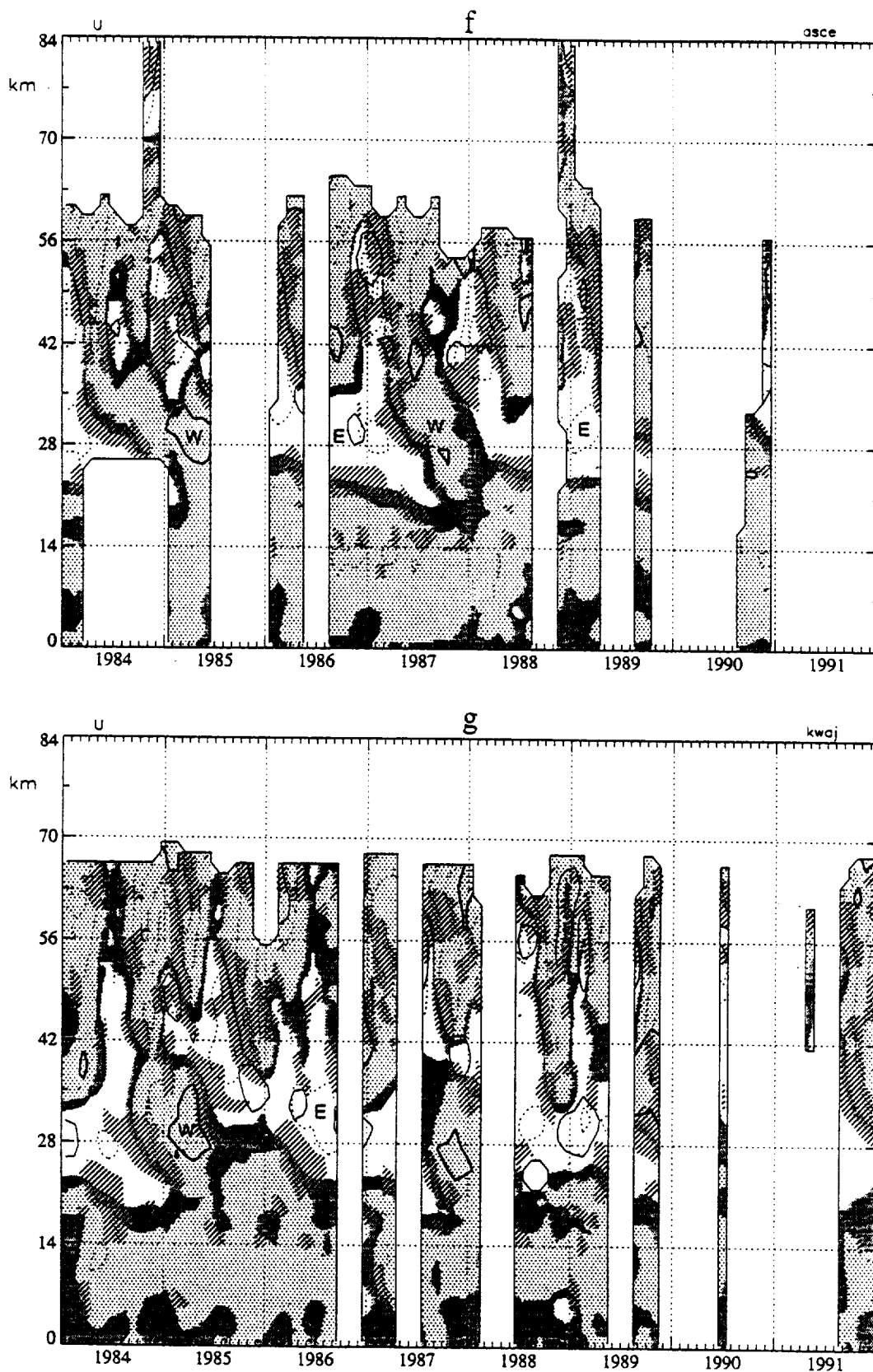


Figure 2. (continued)

short QBO cycle, because the total period is also determined by the rate of QBO easterly shear-zone descent, which varies considerably [Dunkerton and Delisi, 1985; Dunkerton, 1990].

At Kwajalein, the situation is more complicated. Generally

speaking, a new westerly phase of the QBO defined in terms of the total zonal wind (with seasonal cycle included) connects to the "second" SAO cycle in a calendar year, rather than to the first cycle as at Ascension. This also is not surprising, since at

Kwajalein, the second cycle is slightly stronger than the first, and SAO westerlies descend farther in the second cycle [Garcia *et al.*, this issue] (see also section 3.3). The seasonal variation is stronger at Ascension, so that interpolated equatorial data display the same variation as at Ascension, consistent with balanced winds derived from satellite data [see Delisi and Dunkerton, 1988]. On the other hand, there are several occasions when the region of large shear-zone parameter  $R > 1$  connects back to the first SAO cycle, despite the fact that QBO westerlies connect to the second cycle. Such was the case in 1970, 1974, 1976, 1979, and 1981. (Note that a contiguous region of large  $R$  has the same sign of shear and acceleration throughout; for example, the above mentioned times correspond to westerly shear and acceleration lying atop the QBO easterly phase.) In some years (e.g., 1972, 1976, 1981, 1991) the region of large shear parameter connects to the second cycle, a situation which can occur only if the SAO westerly onset precedes that of the QBO (since positive  $R$  indicates a descending shear zone). In 1984 there was apparently no connection to the SAO, and in later years, the data are scarce and quite noisy.

It is interesting to consider what is happening at Kwajalein when the region of large shear-zone parameter  $R$  "bridges the gap" across northern hemisphere summer even though the westerlies themselves do not connect. Development of climatological easterlies in northern hemisphere summer evidently disrupts the connection between SAO and QBO westerlies without erasing the strong westerly shear zone formed during the first SAO cycle. The annual cycle of zonal wind is due primarily to horizontal advection of angular momentum by the mean meridional circulation and is characterized by relatively weak vertical shear and acceleration, compared to that associated with the westerly SAO and QBO.  $R$  therefore tends to emphasize the SAO and QBO, so that a similar pattern is found at the two stations.

There is evidently a wave transport process common to both stations (e.g., Kelvin wave, mean-flow interaction) causing QBO westerly shear zones to form at the same time, despite the cross-equatorial asymmetry introduced by the annual cycle. The QBO and climatological SAO are not exactly symmetric about the equator, however [Garcia *et al.*, this issue] (see also section 3.3). Differences of mean-flow evolution between the two stations may indicate that some aspects of wave transport are sensitive to local conditions (e.g., gravity wave, mean-flow interaction).

Regions of strong easterly shear and acceleration are also apparent in Figure 2, but the connection between SAO and QBO, if any, is difficult to ascertain. Dunkerton [1990] found that easterly onsets at 10 mbar are modulated by the seasonal cycle, perhaps due to the modulation of onsets at 50 mbar. Periods of stalled easterly descent during northern hemisphere winter are visible at lower levels of the QBO, especially at Kwajalein.

### 3.3. Composite 2- and 3-year QBOs

The preceding discussion emphasizes the role of the seasonal cycle in determining the onset of QBO westerly phases and the timing of deseasonalized QBO westerly maxima in the middle stratosphere. The data also reveal an effect of the QBO on descending westerly phases of the SAO, vividly displayed in Figure 6 of Lindzen and Holton [1968]: SAO westerlies descend farther into the middle stratosphere as the westerly phase of the QBO wanes in the lowermost stratosphere. This

behavior is apparent in Figure 2 (some good examples are 1973–1974 at Kwajalein and 1980–1981 at both stations [see also Garcia *et al.*, this issue] and was partially explained by Dunkerton [1979] as being due to the effect of the westerly QBO on Kelvin-wave transport. The QBO also modulates gravity-wave transport [Dunkerton, this issue], which is important in the SAO [Hitchman and Leovy, 1988].

Another view of this phenomenon is obtained by constructing composites of two- and three-year QBOs, taking advantage of the observation in Figure 2 that deseasonalized QBO westerly maxima in the middle stratosphere are approximately synchronized with the seasonal cycle. Using deseasonalized westerly maxima at Kwajalein, together with Ascension Island data in time periods not covered at Kwajalein, we partitioned all of the observed QBO cycles into 2- or 3-year categories as follows: "2-year" cycles: 1969–1970, 1971–1972, 1973–1974, 1978–1979, 1983–1984, 1988–1989; "3-year" cycles: 1963–1965, 1966–1968, 1975–1977, 1980–1982, 1985–1987. In most cases this selection put deseasonalized QBO westerly maxima in the first year of the composite. In a few cases it may have been better to allow for 30-month cycles, for example, to account for the early arrival of QBO westerlies at Ascension at the end of 1982 and 1987. Nevertheless, we rounded each cycle to the nearest integral number of years (guided by Kwajalein data) in order to maximize the number of cycles in each composite. This compromise is not meant to suggest that 30-month cycles are unimportant but rather that the data record is too short to account for them.

Figure 3 shows 2- and 3-year composite QBOs at each station together with the climatological seasonal cycle derived from all years. Composite QBOs were derived using the total zonal wind (with seasonal cycle included) and display the effect of the QBO on descending westerly phases of the SAO. This effect is clearly seen in the 3-year composite, especially in the first (second) SAO cycle at Ascension (Kwajalein), i.e., the SAO westerly phase that normally descends farther at each station. The other SAO westerly phase is also influenced by the QBO but descends only about as far as the westerly phase immediately preceding it.

The fundamental difference between two- and three-year composite QBOs is the descending easterly phase, which is slower in the 3-year composite and contains an additional "ledge," or stall, just above 21 km (especially at Kwajalein). The different rate of easterly shear-zone descent can be detected at both stations in the first year of the composite, as well as in later years, suggesting a variation of QBO forcing on a longer timescale than the QBO itself. The QBO period is known to vary on a decadal timescale [Dunkerton and Delisi, 1985].

Another difference involves the onset of the new QBO westerly phase in the middle stratosphere. In the 2-year composite at Ascension the first SAO westerly phase in year 2 triggers a new QBO westerly phase. Similarly, in the 2-year composite at Kwajalein the second SAO westerly phase in year 2 is connected to a new QBO westerly phase, and there is evidence of a weak "bridge" to the first SAO cycle where  $R > 1$  (diagonal lines) in the middle of year 2. We can unambiguously identify the start of a new QBO westerly phase, because its descent to the lower stratosphere is uninterrupted. On the other hand, the 3-year composites indicate that a new westerly shear zone forms in the middle stratosphere during year 2 but stalls. At Ascension this stall occurs at the base of the first and second SAO cycles in year 2, while at Kwajalein, it occurs at the base

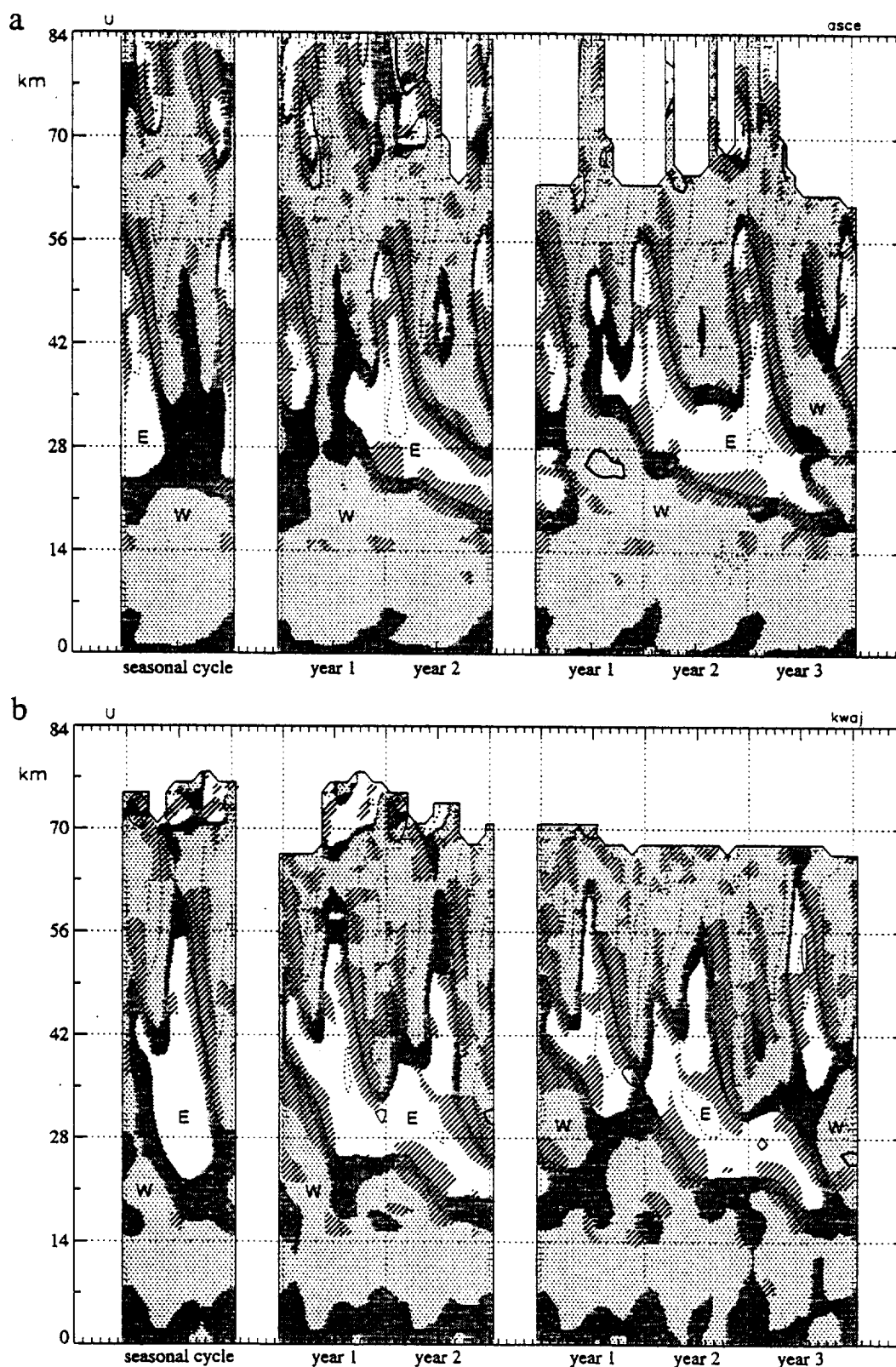


Figure 3. Composite 2- and 3-year quasi-biennial oscillations at (a) Ascension and (b) Kwajalein, together with the climatological seasonal cycle, displayed as in Figure 2. Vertical dotted lines correspond to January 1 in each case.

of the second cycle in year 2 and of the first cycle in year 3. At Ascension the stalled westerly shear zone seems disconnected from the onset of the true QBO westerly phase, which is triggered by the first SAO cycle in year 3. At Kwajalein the

shear zone forms a little later, and there is a weak connection to the QBO onset.

The impression gained in the middle stratosphere is that a new westerly phase of the QBO tries to form in the middle of

year 2 in the 3-year composite but does not immediately initiate westerly shear-zone descent. This event may be likened to a "false start" of the QBO that either has no connection to the true onset of the next QBO westerly phase or represents an onset that will be delayed, partially interrupted by the annual cycle in year 3.

Descent of the new westerly phase in the 3-year composite is also delayed by the slower descent of QBO easterlies at lower levels and (as a result) a slower decay of westerlies in the lowermost stratosphere. Continuous descent of the new QBO westerly shear zone from the middle stratosphere begins in the last year of all composites, as westerlies in the lowermost stratosphere come to an end. It is clear that a new westerly shear zone can form in the middle stratosphere prior to the complete decay of QBO westerlies in the lowermost stratosphere but cannot descend into the lower stratosphere until the old westerlies decay. This observation suggests that (1) the phase speeds of westerly waves responsible for formation of a new shear zone in the middle stratosphere exceed the maximum speed of westerly winds in the lower stratosphere and (2) additional waves, with slower phase speed and/or slower vertical group velocity, are necessary for final descent of QBO westerlies.

Examples of stalled westerly onsets in the middle stratosphere are found in several "3-year" cycles in Figure 2 (e.g., 1967, 1976, 1981), demonstrating that this behavior is not an artifact of the compositing procedure. A characteristic feature of premature onsets is for two adjacent westerly phases of the SAO to be linked together at their base. It should be noted in this context that our distinction between SAO and QBO westerlies is somewhat artificial; near-equatorial westerlies are produced by vertical transport of momentum due to a continuous spectrum of waves. Formation of SAO and QBO westerlies therefore may be viewed as part of a single process. The only fundamental difference between the stratopause SAO and QBO is that the former is controlled by a "pacemaker" due to horizontal advection of angular momentum by the seasonally varying diabatic circulation [Dunkerton, 1991]. The downward extent of the SAO's synchronizing influence on the QBO, on the other hand, is confined to the middle stratosphere and is ineffective at lower levels.

Regions of strong shear and acceleration ( $R > 1$ ) associated with the easterly phase of the SAO are also modulated by the QBO, although the effect is not so dramatic nor as convincing as in the SAO westerly phase. This is to be expected since the SAO easterly phase is due primarily to horizontal advection rather than vertical wave propagation.

#### 4. Conclusion

Analysis of rawinsonde and rocketsonde data at Ascension Island (7.6°S, 14.4°W) and Kwajalein (8.7°N, 167°E) in 1962–1991 suggests that the quasi-biennial oscillation (QBO) in the middle stratosphere is synchronized with the seasonal cycle and that descending westerly phases of the stratopause semi-annual oscillation (SAO) are strongly influenced by the underlying QBO. The effect of the seasonal cycle on the QBO in the middle stratosphere is revealed in two, perhaps unrelated, observations: first, a tendency for deseasonalized QBO westerly maxima to occur in local winter (or to avoid local summer); second, a smooth, uninterrupted connection between descending SAO westerly shear zones and the formation of a new QBO westerly shear zone aloft. The timing of deseasonalized QBO

westerly maxima in the middle stratosphere allows a simple composite of 2- and 3-year cycles to be constructed from the data, illustrating the effect of the QBO on descending westerly phases of the stratopause SAO.

Given the fact that QBO westerly maxima do not always occur at the same time with respect to the westerly onset initiated by the SAO (section 2.2), these two aspects of seasonal synchronization may be distinct. Formation of a new westerly shear zone clearly involves vertical transport of momentum by wave motions [Lindzen and Holton, 1968], but the timing of QBO westerly maxima is also influenced by other factors, such as horizontal advection of angular momentum by the mean meridional circulation. In the westerly phase, horizontal advection translates the equatorial angular momentum maximum into the winter hemisphere in a manner consistent with observations. The easterly phase has a small angular momentum gradient and is affected by horizontal advection to a much lesser degree [Dunkerton, 1991]. We cannot rule out the possibility that differences of wave transport at the two stations may also affect the timing of QBO extrema.

The relation of SAO and QBO westerly onsets prompts two questions: first, whether a downward influence of the SAO on the QBO is consistent with the theory of the QBO; second, whether synchronization in the middle stratosphere has any effect on the QBO as a whole. In the Lindzen and Holton [1968] theory, downward influence is mathematically possible because the absorption of a continuous spectrum of gravity waves at critical levels is equivalent to downward advection [Dunkerton, this issue]. In the Holton and Lindzen [1972] theory, on the other hand, downward influence cannot occur apart from a small diffusion term [Plumb, 1977] due to the assumed discrete spectrum of absorbed waves. The real world is closer to the Lindzen and Holton (1968) model except that waves are absorbed prior to their critical levels [Dunkerton, this issue]. Therefore downward influence is possible due to wavedriving alone. The QBO-induced mean meridional circulation also causes downward advection of westerly shear [Dunkerton, 1991].

Concerning the impact of synchronization on the QBO as a whole, it is clear that the total QBO period is controlled by a number of factors in addition to the initial impulse provided by the SAO. Descending easterlies, in particular, are quite erratic and strongly modulated by the seasonal cycle throughout their descent. The seasonal cycle affects the QBO in the lower stratosphere [Dunkerton, 1990; Kinnersley and Pawson, 1996] in a manner distinct from its effect in the middle stratosphere. Long-term variations of QBO forcing are also possible, e.g., due to El Niño-Southern Oscillation [Maruyama and Tsunetaka, 1988]. Synchronization in the middle stratosphere constrains the timing of QBO phases and onsets in this region but does little to determine whether the next onset will occur two, two and a half, or three years later. Thus, although we have shown that the onset of a new QBO cycle is synchronized with the seasonal cycle, such information is insufficient to predict how long this QBO cycle will last, or in which year the next cycle will begin. To understand an entire QBO cycle requires knowledge of dynamical mechanisms relevant to the mean flow evolution throughout the cycle.

Variations of shear-zone descent occurring from one cycle to the next reconcile the observation of synchronization in the middle stratosphere with the analysis of QBO period on constant pressure levels [Dunkerton, 1990], suggesting that the QBO is modulated but not exactly synchronized by the sea-



sonal cycle. It should be noted that the SAO itself is not exactly synchronized, due to interannual variability in the winter hemisphere [Delisi and Dunkerton, 1988]. Therefore exact synchronization of the QBO is not expected in the middle stratosphere.

Unfortunately, no rocketsonde data are available on the equator, and rocketsondes are no longer used for routine measurements of the middle atmosphere. It is possible that due to their limited time span, our data may not be representative of a longer time series. Also, because these data were obtained at two stations off the equator, it is uncertain to what extent our conclusions apply at the equator, or which of the stations more closely represents the equatorial flow. While QBOs at each station share much in common, the synchronization and modulation effects emphasized in this paper differ somewhat between the two stations, because annual and semiannual cycles are not symmetric about the equator [Garcia *et al.*, this issue].

The historical record describing this multifaceted relationship between the QBO and the seasonal cycle underscores the need for reliable, long-term measurements of wind in the equatorial middle atmosphere. By all appearances the rocketsonde data will never be extended in time. Satellite observations with global coverage [e.g., Orland *et al.*, 1996] are well suited to describe these oscillations (and any longitudinal asymmetry) and will eventually lead to a better understanding of dynamical mechanisms involved in seasonal modulation or synchronization of the QBO. Fine vertical resolution will, of course, be required to adequately represent descending shear zones in the SAO and QBO.

**Acknowledgments.** The authors thank Donal O'Sullivan for helpful discussion and Lloyd Lowe for programming assistance. This research was supported by the National Aeronautics and Space Administration, contract NASW-4844, the National Science Foundation, grant ATM-9500613, and NWRA IR&D.

## References

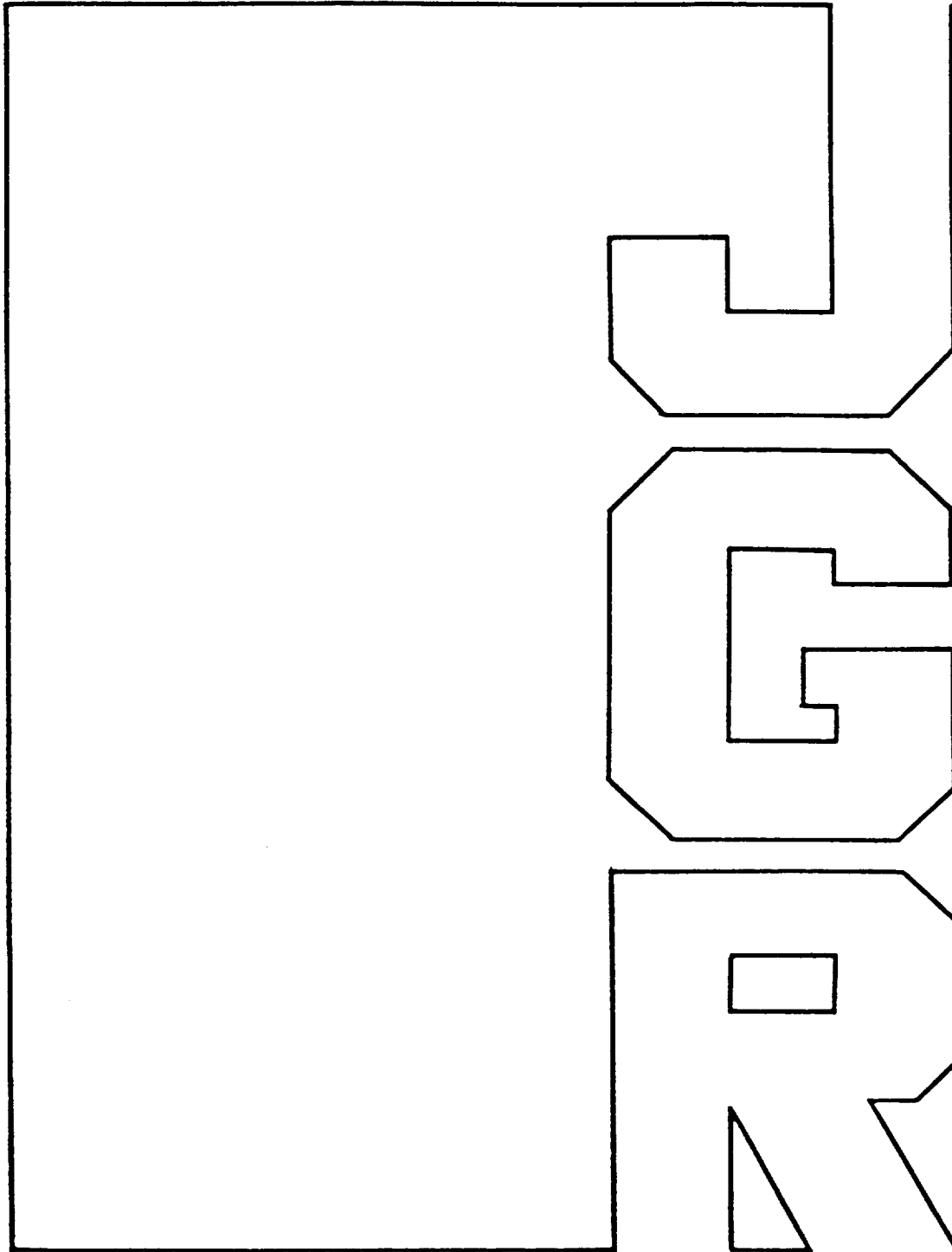
- Angell, J. K., On the variation in period and amplitude of the quasi-biennial oscillation in the equatorial stratosphere, 1951–85, *Mon. Weather Rev.*, **114**, 2272–2278, 1986.
- Delisi, D. P., and T. J. Dunkerton, Seasonal variation of the semiannual oscillation, *J. Atmos. Sci.*, **45**, 2772–2787, 1988.
- Dunkerton, T. J., On the role of the Kelvin wave in the westerly phase of the semiannual zonal wind oscillation, *J. Atmos. Sci.*, **36**, 32–41, 1979.
- Dunkerton, T. J., Annual variation of deseasonalized mean flow acceleration in the equatorial lower stratosphere, *J. Meteorol. Soc. Jpn.*, **68**, 499–508, 1990.
- Dunkerton, T. J., Nonlinear propagation of zonal winds in an atmosphere with Newtonian cooling and equatorial wavelike driving, *J. Atmos. Sci.*, **48**, 236–263, 1991.
- Dunkerton, T. J., Role of gravity waves in the quasi-biennial oscillation, *J. Geophys. Res.*, this issue.
- Dunkerton, T. J., and D. P. Delisi, Climatology of the equatorial lower stratosphere, *J. Atmos. Sci.*, **42**, 376–396, 1985.
- Garcia, R. R., T. J. Dunkerton, R. S. Lieberman, and R. A. Vincent, Climatology of the semiannual oscillation of the tropical middle atmosphere, *J. Geophys. Res.*, this issue.
- Hamilton, K., The vertical structure of the quasi-biennial oscillation: Observations and theory, *Atmos. Ocean*, **19**, 236–250, 1981.
- Hitchman, M. H., and C. B. Leovy, Estimation of the Kelvin wave contribution to the semiannual oscillation, *J. Atmos. Sci.*, **45**, 1462–1475, 1988.
- Holton, J. R., and R. S. Lindzen, An updated theory for the quasi-biennial cycle of the tropical stratosphere, *J. Atmos. Sci.*, **29**, 1076–1080, 1972.
- Kinnersley, J. S., and S. Pawson, The descent rates of the shear zones of the equatorial QBO, *J. Atmos. Sci.*, **53**, 1937–1949, 1996.
- Lindzen, R. S., and J. R. Holton, A theory of the quasi-biennial oscillation, *J. Atmos. Sci.*, **25**, 1095–1107, 1968.
- Maruyama, T., Annual variations and QBO-synchronized variations of the equatorial wave intensity in the lower stratosphere at Singapore during 1961–1989, *J. Meteorol. Soc. Jpn.*, **69**, 219–232, 1991.
- Maruyama, T., Upward transport of westerly momentum due to disturbances of the equatorial lower stratosphere in the period range of about 2 days—A Singapore data analysis for 1983–1993, *J. Meteorol. Soc. Jpn.*, **72**, 423–432, 1994.
- Maruyama, T., and Y. Tsuneoka, Anomalous short duration of the easterly wind phase of QBO at 50 hPa in 1987 and its relation with an El Niño event, *J. Meteorol. Soc. Jpn.*, **69**, 219–232, 1988.
- Naujokat, B., An update of the observed quasi-biennial oscillation of the stratospheric winds over the tropics, *J. Atmos. Sci.*, **43**, 1873–1877, 1986.
- Orland, D. A., W. R. Skinner, P. B. Hays, M. D. Burrage, R. S. Lieberman, A. R. Marshall, and D. A. Gell, Measurements of stratospheric winds by the high resolution Doppler imager, *J. Geophys. Res.*, **101**, 10,351–10,363, 1996.
- Plumb, R. A., The interaction of two internal waves with the mean flow: Implications for the theory of the quasi-biennial oscillation, *J. Atmos. Sci.*, **34**, 1847–1858, 1977.
- Sato, K., and T. J. Dunkerton, Estimates of momentum flux associated with equatorial Kelvin and gravity waves, *J. Geophys. Res.*, this issue.
- D. P. Delisi and T. J. Dunkerton, Northwest Research Associates, P. O. Box 3027, Bellevue, WA 98009. (e-mail:tim@nwra.com)

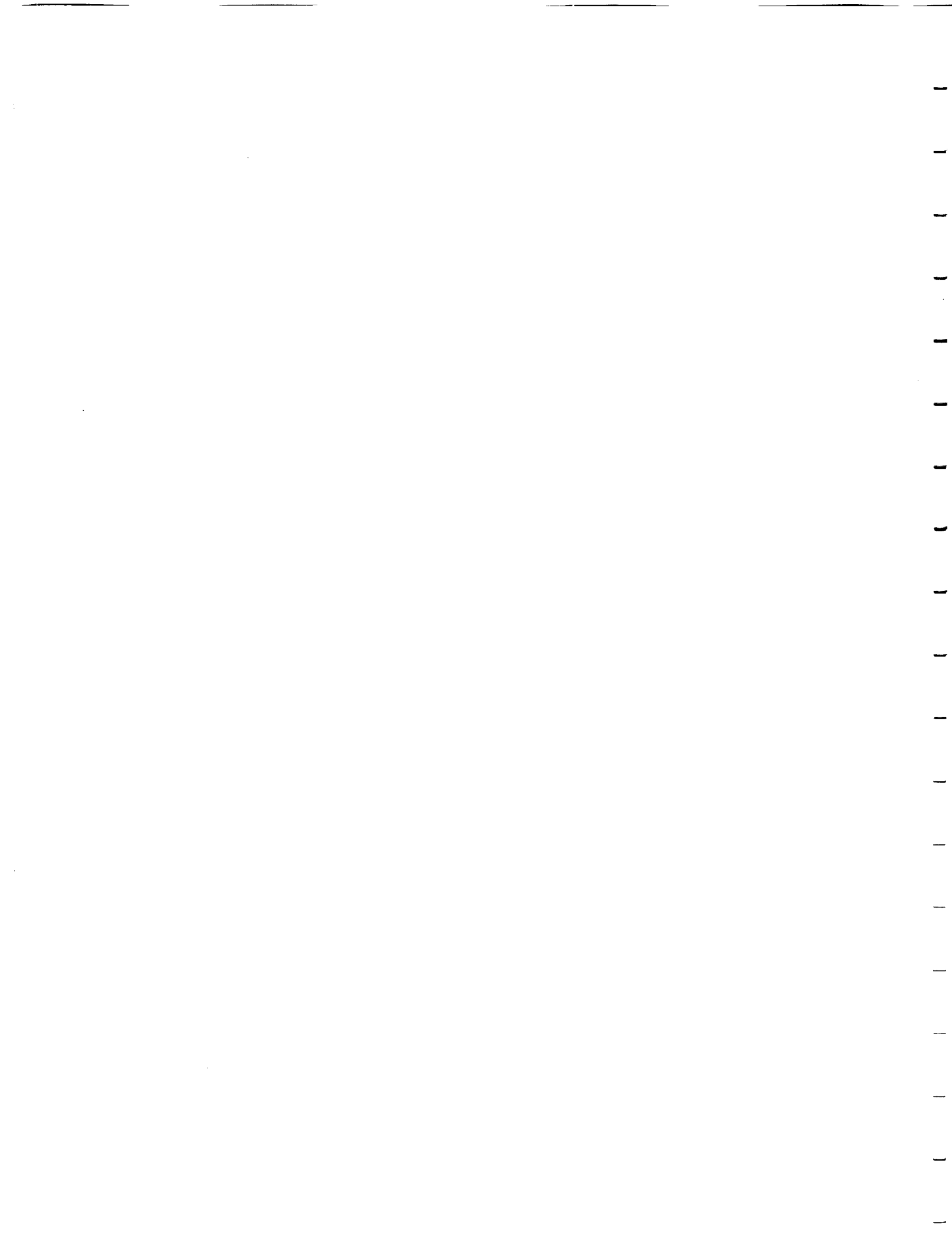
(Received June 3, 1996; revised November 20, 1996; accepted November 23, 1996.)



# Estimates of momentum flux associated with equatorial Kelvin and gravity waves

Kaoru Sato, Timothy J. Dunkerton





# Estimates of momentum flux associated with equatorial Kelvin and gravity waves

Kaoru Sato

Department of Geophysics, Kyoto University, Kyoto, Japan

Timothy J. Dunkerton

Northwest Research Associates, Bellevue, Washington

**Abstract.** A new indirect method is proposed to estimate momentum flux based on the theory of slowly varying gravity waves and equatorial waves in vertical shear by Dunkerton [this issue] which explains the discovery by Sato *et al.* [1994] that the cospectra of temperature and zonal wind fluctuations at Singapore (1.4°N, 104.0°E) are synchronized with the quasi-biennial oscillation (QBO) of mean zonal wind in the stratosphere. The indirect estimates obtained from cospectra correspond to the summation of absolute values of momentum flux associated with each wave, whereas direct estimates from quadrature spectra give the summation of momentum flux. An analysis was made for twice daily rawinsonde data at Singapore. The direct estimate for Kelvin waves (5–20 day components) is  $2\text{--}9 \times 10^{-3} \text{ m}^2 \text{ s}^{-2}$  and accords with the indirect estimate to within the estimation error. This result supports the validity of the indirect method. Although the indirect estimate depends on an assumed wave structure, large values of momentum flux are obtained for all possible equatorial modes having short periods (1–3 days). The indirect estimate for westerly shear is  $20\text{--}60 \times 10^{-3} \text{ m}^2 \text{ s}^{-2}$  based on the theory of two-dimensional gravity waves, while the direct estimate is only  $0\text{--}4 \times 10^{-3} \text{ m}^2 \text{ s}^{-2}$ . The reduction of indirect estimate under the assumption of equatorial waves is about 30–70%. The discrepancy between direct and indirect estimates indicates a large cancelation of positive and negative momentum fluxes. This is the case also for easterly shear. The indirect estimate for westerly shear is almost twice as large as that for easterly shear. The characteristics of waves near the source in the troposphere are thought to be independent of the QBO in the stratosphere, so that the difference in wave activity should be attributed to the differing characteristics of wave propagation under the strong QBO shear. Several possible explanations are discussed. Parameters such as phase velocity and zonal wavelength are estimated from the ratio of potential to kinetic energies assuming that the 1–3 day components are due to equatorial waves. The estimates in this paper were made assuming that the observed frequencies are actual ground-based wave frequencies. If there is aliasing from higher frequencies than 1 day, the actual momentum fluxes can be significantly larger than the estimated values.

## 1. Introduction

Many theoretical and observational studies show that gravity waves play an important role in the global atmospheric circulation, redistributing momentum in the atmosphere through their generation, propagation, and breaking. The majority of studies have emphasized the role of gravity waves in the global circulation of middle- and high-latitude regions. However, we also expect energetic gravity waves associated with vigorous convection in the equatorial region. Such gravity waves may be important for the mechanism of the quasi-biennial oscillation (QBO) of mean zonal wind in the equatorial lower stratosphere as suggested by theoretical studies (see Dunkerton [this issue] for a review).

Observational evidence that gravity waves are important in the equatorial region, in addition to large-scale Kelvin and Rossby gravity waves, has been reported in several recent stud-

ies. Tsuda *et al.* [1994a, b] conducted a pioneering observational campaign for 24 days in Watukosek, Indonesia (7.6°S, 112.7°E), using 100 rawinsondes with vertical resolution of 150 m. Gravity waves having a vertical wavelength of 2–2.5 km and a period of about 2 days were detected in the time sequence of wind and temperature profiles. Wave propagation was eastward in the westerly shear phase of the QBO. Recently, Takayabu *et al.* [1996] examined westward propagating quasi-2-day modes in convective activity using various high-resolution data such as infrared equivalent black body temperature ( $T_{\text{BB}}$ ) during the intensive observation period (IOP) of the Tropical Ocean Global Atmosphere/Coupled Ocean-Atmosphere Response Experiment (TOGA/COARE) campaign. Clear inertio-gravity wave-like signals propagating upward and downward from a ~175 hPa level were detected in composite time-height sections of horizontal winds from radiosonde observations with a reference of the quasi-2-day mode observed in  $T_{\text{BB}}$ .

The importance of gravity waves in the tropics was also shown by Allen and Vincent [1995], who examined gravity wave

Copyright 1997 by the American Geophysical Union.

Paper number 96JD02514.  
0148-0227/97/96JD-02514\$09.00

activity as a function of latitude for the range of 12°S–68°S, using rawinsonde data with high vertical resolution of 50 m, at 18 stations in Australia. The gravity wave energy increased monotonically approaching the equator, which is especially clear in summer. Such a latitudinal variation is not clear in the northern hemisphere winter as shown by *Kitamura and Hirota* [1989] using operational rawinsonde data over Japan (27°N–45°N). In their study, gravity wave energy maximized instead near the subtropical westerly jet. *Ogino et al.* [1995] examined radiosondes launched at a research vessel over a period of about 1 month during the IOP of TOGA/COARE campaign, covering a latitude range of 14°S–25°N. The energy of wave components with vertical wavelengths of 2–3 km was estimated from 112 observations in the equatorial region of 5°N–5°S and is consistent with an extrapolation of the latitudinal variation of gravity wave energy shown by *Allen and Vincent*.

Year-to-year variation of short-period (1–3 day) waves near the equator was examined using rawinsonde data at Singapore over the 10 years 1984–1993 by *Maruyama* [1994] and *Sato et al.* [1994] independently. *Maruyama* estimated momentum flux from the covariance of zonal wind and temperature tendency. He found that the momentum flux associated with short-period waves varies in a synchronized manner with the QBO and the magnitude of the flux is comparable to that of long-period (7.4–32 days) Kelvin waves. (Owing to a typographical error, the momentum fluxes are smaller than that shown in Figures 7 and 8 of *Maruyama* [1994] by exactly 1 order of magnitude (*T. Maruyama*, personal communication, 1996).) On the other hand, *Sato et al.* [1994] (hereinafter referred to as S94) showed year-to-year variations of spectral characteristics of horizontal wind and temperature fluctuations in the period range 1–20 days. Figure 1 shows power and cross spectra of temperature ( $T$ ) and zonal wind ( $u$ ) fluctuations averaged over the height region 20–25 km, in energy or flux content form, as a function of time as obtained by S94. A low-pass filter with cutoff of 6 months was applied in order to display the relation with the QBO more clearly. As mentioned in S94, dominant peaks in the power spectra of  $T$  and  $u$  are observed in the short-period range of 1–3 days during both phases of the QBO and around 10-day period in the westerly shear phase of the QBO. The latter peak corresponds to Kelvin waves, which have been examined in previous studies. Temperature spectral densities in the short-period range are large also in the easterly shear phase compared with those at longer periods, indicating that the activity of short-period waves is large in both phases of the QBO.

A mysterious feature, which was emphasized and discussed in S94, is the clear synchronization of cospectra  $C_{Tu}(\omega)$  (Figure 1c) with the QBO observed in the whole range of frequencies. Positive and negative values appear alternately in the westerly and easterly shear phases, respectively, although the negative values around 10-day period are weak. Such variation was not observed in the cross spectra of meridional wind and temperature fluctuations. The variation of cospectra of  $T$  and  $u$  components cannot be explained by the previous theory of equatorial waves in a uniform background wind [*Matsuno*, 1966]. According to the theory the cospectra should be almost zero, and quadrature spectra of  $T$  and  $u$  components  $Q_{Tu}(\omega)$  should have significant values proportional to  $-u'w'$  as described by *Maruyama* [1991, 1994], where  $w$  is the vertical wind component. In fact, large negative values are observed in  $Q_{Tu}(\omega)$ , as shown in Figure 1d, around 10 days corresponding

to the positive  $\overline{u'w'}$  associated with Kelvin waves, consistent with the result of *Maruyama* [1994].

*Dunkerton* [1995] (hereinafter referred to as D95) analyzed theoretically and numerically the covariance of horizontal wind and temperature for two-dimensional (plane) gravity waves in a background wind having vertical shear. The theory has been extended to three-dimensional equatorial waves (*T.J. Dunkerton*, manuscript in preparation, 1997, hereafter referred to as D97). For slowly varying, steady, conservative, incompressible waves, the covariance of zonal wind and temperature is proportional to the vertical shear and vertical flux of horizontal momentum, or radiation stress. The sign of the covariance is determined by the vertical shear, independent of the horizontal and vertical direction of gravity wave propagation, which is qualitatively consistent with the observation shown in Figure 1c.

In this paper, we examine in detail the relation between cospectra (of  $T$  and  $u$ ) and the vertical shear of the mean zonal wind, using rawinsonde data at Singapore, to evaluate *Dunkerton's* (D95, D97) theory quantitatively (section 2). In section 3 we introduce a new method of momentum flux estimation from cross spectra (both cospectra and quadrature spectra) of  $T$  and  $u$  components, which provides positive and negative momentum fluxes separately. Such method of estimation is particularly important for short-period gravity waves which can propagate in any direction. Quantitative analysis is made for the momentum flux using Singapore data, and the results are assured by clarifying the observational error in the estimates. Further discussion is given in section 4. Summary and concluding remarks are made in section 5.

## 2. Comparison of Vertical Shear and Zonal Heat Flux

According to D95, the covariance of  $T$  and  $u$  components of slowly varying two-dimensional gravity waves acquires a significant value when the background wind  $U$  varies rapidly over a scale height:

For upward energy propagation

$$\overline{u'T'} = + \frac{N\bar{T}}{2gk\bar{c}} \overline{u'w'} U_z, \quad (1)$$

For downward energy propagation

$$\overline{u'T'} = - \frac{N\bar{T}}{2gk\bar{c}} \overline{u'w'} U_z, \quad (2)$$

where  $N$  is the Brunt-Väisälä frequency,  $g$  is the acceleration of gravity,  $k$  is the horizontal wavenumber which is taken to be positive without loss of generality,  $\bar{T}$  is the background temperature, and  $\bar{c}$  is the intrinsic phase velocity. It is convenient to express (1) and (2) with

$$\overline{u'T'} = \frac{N\bar{T}}{2gk|\bar{c}|} |\overline{u'w'}| U_z, \quad (3)$$

since  $\overline{w'\phi'} = \bar{c}\overline{u'w'}$  and the direction of vertical energy propagation is determined by  $w'\phi'$ , where  $\phi'$  is the geopotential perturbation. It is worth noting that  $\overline{u'T'}$  is proportional to  $U_z$ . The sign is determined only by the vertical shear and is independent of the direction of horizontal and vertical propagation. Thus the vertical shear of the mean wind is a key parameter to explain the covariance of  $u$  and  $T$ . The extended theory of slowly varying equatorial waves (D97) shows that the

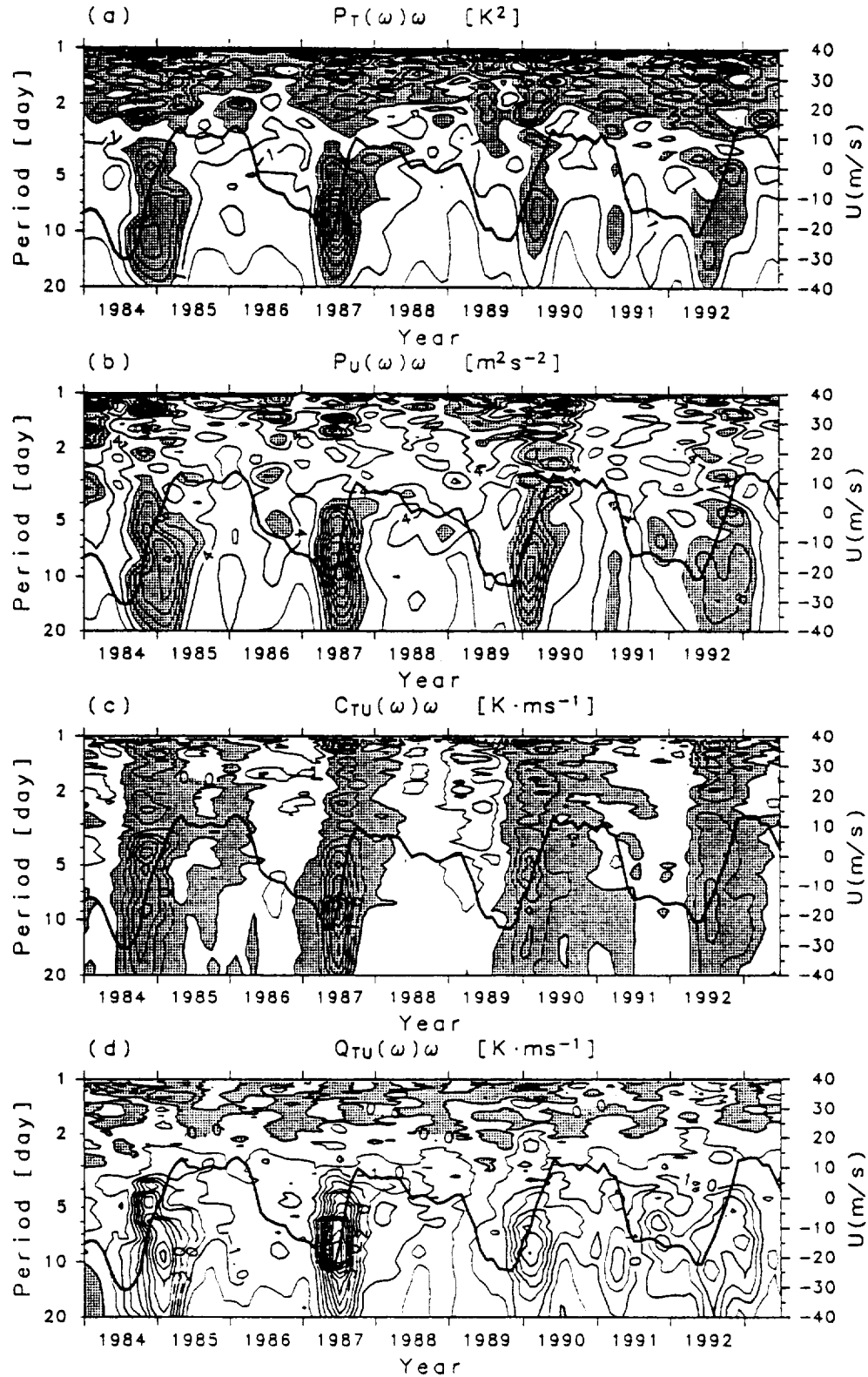


**Figure 1.** Dynamic power spectra of (a) temperature fluctuations  $T$  and (b) zonal wind fluctuations  $u$  in energy content form for 1984–1993, averaged over the height range 20–25 km at Singapore. (c) Cospectra and (d) quadrature spectra of  $T$  and  $u$  are also shown in flux content form. Temporal smoothing was applied using a lowpass filter with cutoff of 6 months in order to display the relation with the QBO more clearly. Thick solid curves show the monthly mean zonal wind averaged over the same height range; the scale is shown on the right axis. Contour intervals are  $0.5 K^2$  in Figure 1a,  $2 m^2 s^{-2}$  in Figure 1b, and  $0.5 K m s^{-1}$  in Figures 1c and 1d. Shading indicates values larger than  $1.5 K^2$  in Figure 1a, larger than  $6 m^2 s^{-2}$  in Figure 1b, and positive values in Figures 1c and 1d.

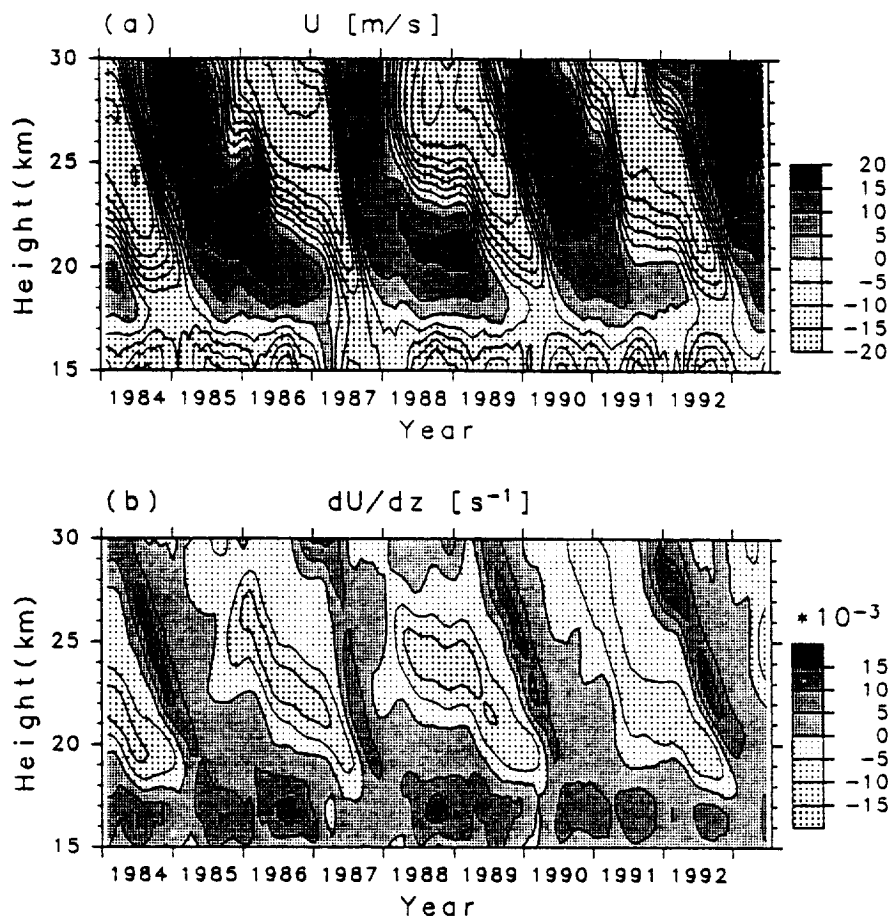


**Figure 2.** Time-height sections of (a) monthly mean zonal wind and (b) its vertical shear at Singapore. Contour intervals are  $5 \text{ m s}^{-1}$  in Figure 2a and  $5 \times 10^{-3} \text{ s}^{-1}$  in Figure 2b. Temporal and vertical smoothing was applied with low-pass filters having cutoff lengths of 6 months and 3 km, respectively.

relation of the covariance and vertical shear does not change significantly except for the numerical factor in the denominator on the right-hand side of (3).

The time evolution of monthly mean zonal wind over the 10 years 1984–1993 is shown in Figure 2a as a function of height. Four cycles of the QBO are seen. The vertical shear obtained from Figure 2a is shown in Figure 2b. The tropopause is usually located around 17 km, varying annually with an amplitude of about 1 km (not shown). Large shears are observed in the lower stratosphere in the QBO transition zones from westerly wind to easterly and from easterly wind to westerly, i.e., along zero contours of the mean zonal wind. Another region of large vertical shear is observed near the tropopause where easterly winds in the troposphere change to westerly in the stratosphere. The easterly phase below 20 km continues for only one-fourth or one-fifth of the QBO cycles, which is short compared with the duration of the easterly phase above.

Subsequent sections are devoted mainly to the lower stratosphere above 20 km where the QBO is clearly seen in the vertical shear. We define three periods of large westerly (positive) shear as A (from the beginning of 1984 to the middle of 1985), B (from the beginning to the end of 1987), and C (from the beginning of 1992 to the beginning of 1993); and three periods of large easterly (negative) shear as a (from the beginning of 1986 to the middle of 1987), b (from the beginning of 1988 to the beginning of 1990), and c (from the end of 1990 to

the end of 1992). Another period of large westerly shear from the middle of 1989 to the middle of 1990 is not examined because of the large percentage of missing data (see S94). The durations of easterly shear periods are 1.5 to 2 times longer than those of westerly shear periods, corresponding to the different descent rates of westerly and easterly phases of the QBO. An interesting point is that there is not a large difference in the strength of vertical shear between easterly and westerly shear periods. It should be noted that the shears in periods B and c are relatively weak.

The covariance of  $T$  and  $u$  components ( $C_{Tu} \equiv \overline{T'u'}$ ) having a range of frequencies from  $\omega_1$  to  $\omega_2$  is obtained by integrating spectra over the range

$$C_{Tu} = \int_{\omega_1}^{\omega_2} C_{Tu}(\omega) d\omega, \quad (4)$$

where  $\omega$  is ground-based frequency. Similarly, we can define  $Q_{Tu}$  as an integration of quadrature spectra over the same frequencies:

$$Q_{Tu} = \int_{\omega_1}^{\omega_2} Q_{Tu}(\omega) d\omega \approx \frac{1}{|\omega_0|} \frac{\partial \overline{T'}}{\partial t} u', \quad (5)$$

where  $\omega_0$  is the central (ground-based) frequency of the inte-

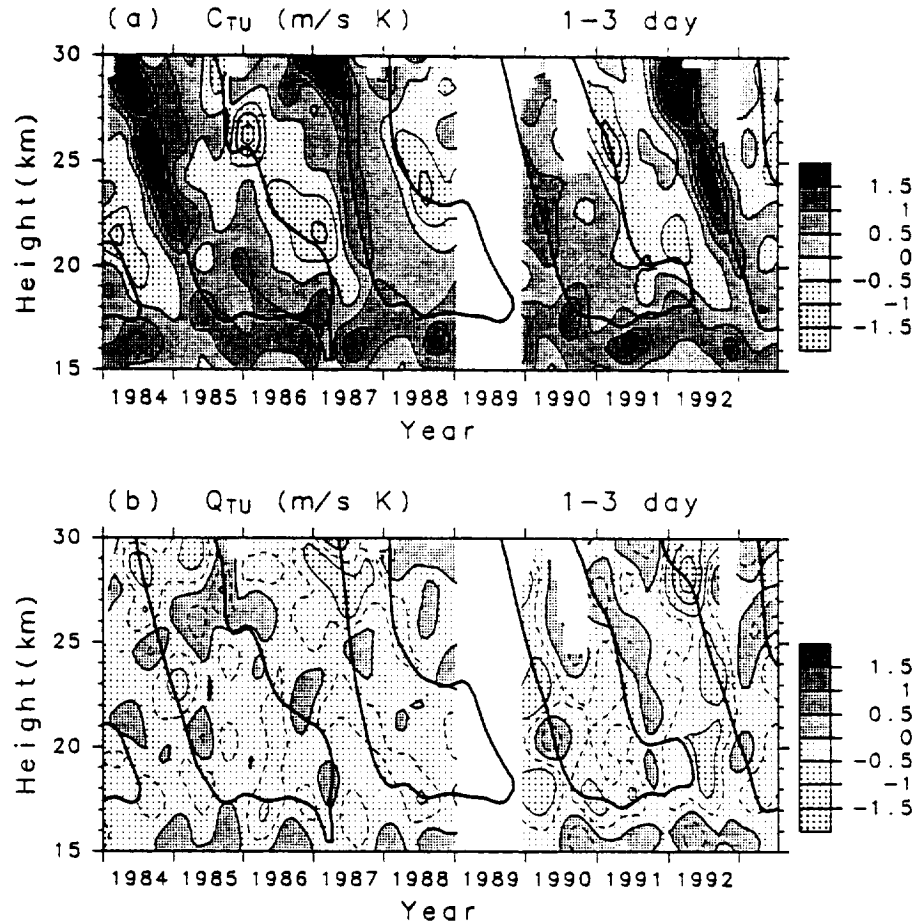


**Figure 3.** Time height sections of (a) cospectra of temperature and zonal wind components  $C_{Tu}$  and (b) that of quadrature spectra  $Q_{Tu}$  integrated over the period range of 1–3 days. Thick curves indicate zero contours of the monthly mean zonal wind shown in Figure 2. Contour intervals are  $0.5 \text{ K m s}^{-1}$ . Dashed curves in Figure 3b are the contours of  $0.25$  and  $-0.25 \text{ K m s}^{-1}$ . Filters used for smoothing are the same as those for Figure 2.

gration range. From the thermodynamic equation,  $Q_{Tu}$  is related to total momentum flux:

$$Q_{Tu} \sim -\text{sgn}(\omega_0) \frac{\bar{T} N^2}{g \bar{\omega}} \overline{u'w'}, \quad (6)$$

where  $\bar{\omega}$  is the intrinsic frequency of waves having the central frequency  $\omega_0$ .

### 2.1. The 1–3 Day Components

Figure 3a shows a time-height section of  $C_{Tu}$  for 1–3 day wave components, which are considered to be due mainly to gravity waves. Blank regions indicate where an estimate could not be made due to a large number of missing values. Large positive and negative values are observed along westerly and easterly shear zones, respectively, which is qualitatively consistent with the theory of D95. It is interesting that there seems to be a good quantitative correspondence as well, although the magnitude of  $C_{Tu}$  should depend on  $u'w'$  as well as  $U_z$ . Large (small) values are observed in strong (weak) shear at periods A, C, a and b (B and c).

To see the details of the correlation, a scatter diagram was made (Figure 4) using data from the cross sections of  $C_{Tu}$  and the vertical shear of mean zonal wind. Clear linear distribution is seen in regions of positive and negative vertical shear. The

number of events having positive (negative)  $C_{Tu}$  in negative (positive) shear is small, especially when the shear is strong. This fact supports the theory of D95.

The gradient of the linear distribution in positive shear seems larger than that in negative shear. Thin straight lines are the result of a least squares fit in the respective regions. The slopes of the lines differ by a factor of about 2.5. If we ignore the Doppler shift of wave frequency by the mean wind, the slope is proportional to momentum fluxes according to (3). Thus the difference suggests that the momentum flux of 1–3 day waves is larger in westerly shear than in easterly shear. The difference in momentum fluxes between westerly and easterly shear periods will be quantitatively discussed in section 4.3 showing their vertical profiles.

The time-height section of  $Q_{Tu}$  for 1–3 day components is shown in Figure 3b. It is obvious that  $Q_{Tu}$  values are small compared with  $C_{Tu}$  (Figure 3a). However, since the variation of  $Q_{Tu}$  observed in Figure 3 is slightly larger than the error in  $Q_{Tu}$  (and  $C_{Tu}$  also) which is about  $0.2 \text{ m s}^{-1} \text{ K}$  as estimated later, some qualitative discussion of  $Q_{Tu}$  is possible.

The  $Q_{Tu}$  observed in Figure 3 is biased toward negative values over the whole region, indicating the relative dominance of eastward propagating waves, and is consistent with the results of Maruyama [1994]. The bias may be due to selective

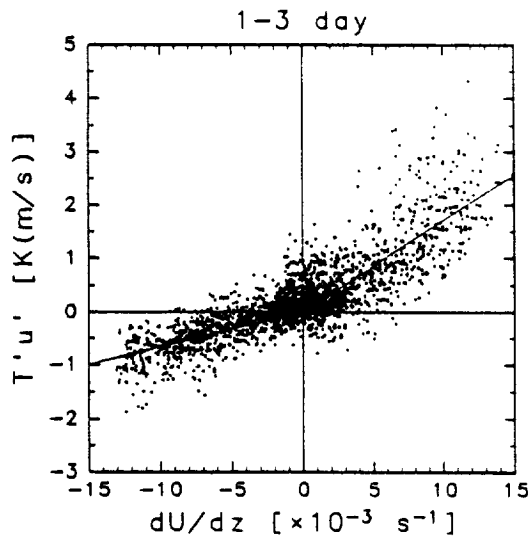


Figure 4. Scatter diagram of vertical shear ( $dU/dz$ ) versus covariance of temperature and zonal wind ( $T'u'$ ) of 1-3 day components.

transmission in easterly winds of the upper troposphere, which inhibit the vertical propagation of gravity waves having westward phase speed. If the wave sources are below 15 km, this speculation is consistent with the observation in Figure 3b that

the percentage of time with positive  $Q_{Tu}$  is 45% at 15 km, decreases with height, and becomes only 2% at 18 km. Another explanation is that the distribution of phase velocities of gravity waves generated by convection in the easterly tropospheric wind may be biased toward eastward waves [Pfister *et al.*, 1993].

It is important that positive values of  $Q_{Tu}$  are seen in places of Figure 3. This feature suggests the existence of at least two kinds of short-period waves having positive and negative momentum fluxes. Systematic positive areas above easterly shear zones may be explained also by the shielding of eastward propagating waves due to westerly winds below the shear zone. A comprehensive discussion of this point will be made based on the results of momentum flux estimation in section 3.

## 2.2. The 5-20 Day Components

An integration over the period range of 5-20 days gives  $C_{Tu}$  and  $Q_{Tu}$  for long-period Kelvin waves. Results are shown in Figures 5a and 5b for  $C_{Tu}$  and  $Q_{Tu}$ , respectively. As reported by Maruyama [1994],  $Q_{Tu}$  values are largely negative along westerly shear in the lower stratosphere, corresponding to positive  $u'w'$  due to Kelvin waves. Large values are also observed in the profile of  $C_{Tu}$  along westerly shear. The sign is positive, which is consistent with the theory of D95. On the other hand, negative  $C_{Tu}$  values along easterly shear are very weak compared with positive values along westerly shear, even though the strength of easterly shear is almost the same as that of westerly shear, as already mentioned. According to the theory of

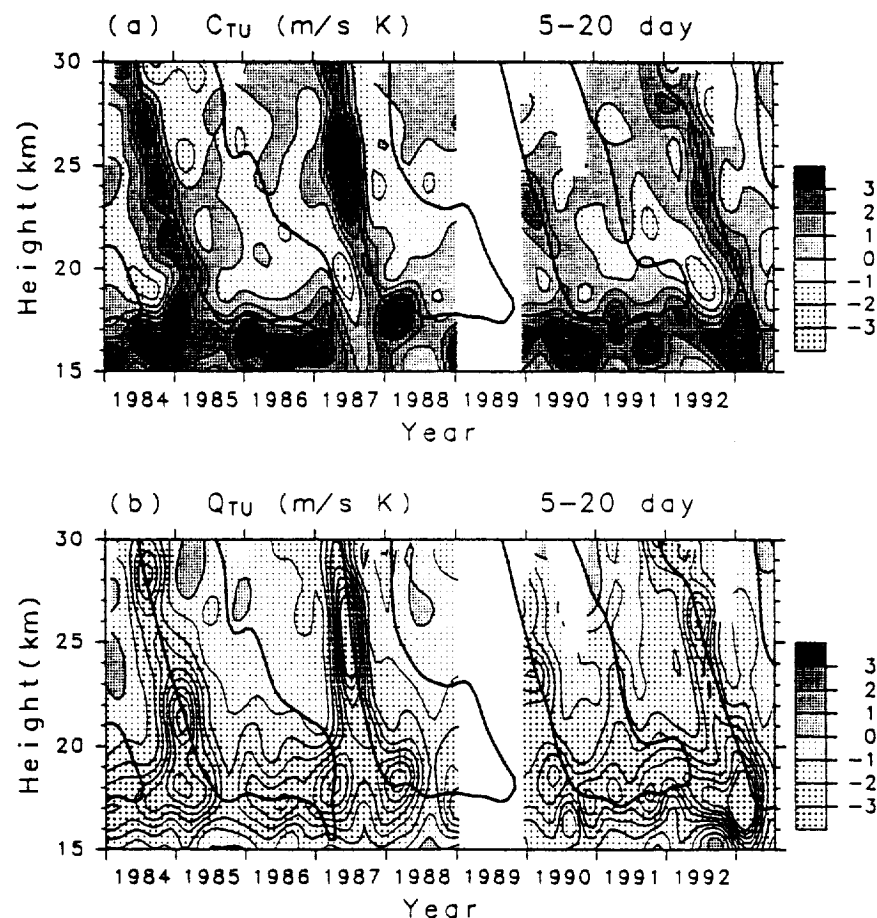


Figure 5. Integrated cospectra and quadrature spectra as in Figure 3 but for the period range 5-20 days. Contour interval is  $1 \text{ K m s}^{-1}$ .



D95, small values of cospectra mean that amplitudes of individual wave components in the period range of 5–20 days are very small.

Also interesting is the feature near the tropopause where large positive values of  $C_{Tu}$  and negative values of  $Q_{Tu}$  are continuously observed. Tsuda *et al.* [1994a] reported slow Kelvin waves which are dominant around the tropopause and modulate the tropopause height. Figure 5 suggests that such Kelvin waves are common. It is likely that the dominance of Kelvin waves is related to the long duration of westerly wind above the tropopause (around 20 km).

Figure 6 shows a scatter diagram for 5–20 day components in the 20–30 km height region. The values of  $C_{Tu}$  in positive shear are mostly positive and linearly proportional to the shear. The correlation, however, is not high compared with that of 1–3 day components (Figure 4), indicating that the variation of Kelvin wave activity is larger. A bias of  $C_{Tu}$  toward negative values in negative shear is unclear. Solid straight lines show the result of a least squares fit. The ratio of slopes for positive versus negative shear is larger than 7. Thus it is suggested that long-period wave activity in easterly shear is less than in westerly shear by about 1 order of magnitude.

It was found from the analysis in this section that most features of  $C_{Tu}$  are consistent with the theory of gravity or equatorial waves in vertical shear [D95, D97], and it was suggested that  $C_{Tu}$  includes important information on the wave characteristics. Therefore, we use this theory to estimate momentum flux quantitatively in section 3.

### 3. Estimates of $\overline{u'w'}$ Based on Cross Spectra of $T$ and $u$

#### 3.1. Methods of Direct and Indirect Estimation

Using (3) and (6), we can make two kinds of estimates of momentum flux under the assumption of two-dimensional gravity waves.

The first is a direct method from quadrature spectra of  $T$  and  $u$  fluctuations:

$$\overline{u'w'} = -\frac{g}{\bar{T}N^2} \int_{\omega_1}^{\omega_2} Q_{Tu}(\omega) \omega d\omega, \quad (7)$$

where  $\omega_1$  and  $\omega_2$  are lower and upper limits of the frequency range that we are interested in. The Doppler effect of mean wind is ignored, since the mean wind around the large shear is weak. We use 220K for  $\bar{T}$  and 5 min for the Brunt-Väisälä period as typical values in the lower stratosphere. The direct estimate of  $\overline{u'w'}$  is composed of positive  $(\overline{u'w'})_+$  and negative  $(\overline{u'w'})_-$  momentum fluxes:

$$\overline{u'w'} = (\overline{u'w'})_+ + (\overline{u'w'})_-. \quad (8)$$

Observations suggest that the short-period waves propagate energy predominantly upward in the equatorial lower stratosphere [e.g., Tsuda *et al.*, 1994; Maruyama, 1994; S94]. Thus, if we assume that the waves are mainly propagating upward,  $(\overline{u'w'})_+$  and  $(\overline{u'w'})_-$  are due to eastward and westward propagating waves, respectively. It is also possible that the cancellation is partly due to reflected waves propagating downward [D95].

The second is an indirect method from cospectra of  $T$  and  $u$  fluctuations:

$$|\overline{u'w'}| = \frac{2g}{N\bar{T}U_z} \int_{\omega_1}^{\omega_2} C_{Tu}(\omega) \omega d\omega. \quad (9)$$

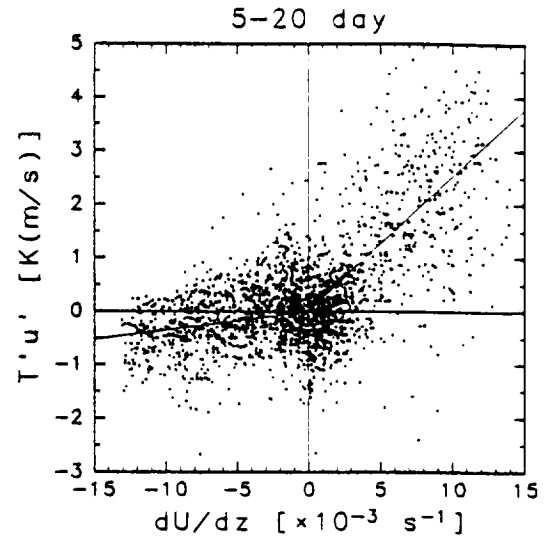


Figure 6. As in Figure 4, but for 5–20 day components.

under the assumption that the disturbances are due to two-dimensional gravity waves. The factor on the right hand side of (9) must be modified for equatorial waves as noted in section 2. The indirect estimate of  $|\overline{u'w'}|$  is the sum of absolute values of  $\overline{u'w'}$  of all waves having a frequency in the particular range which we considered:

$$|\overline{u'w'}| = |(\overline{u'w'})_+| + |(\overline{u'w'})_-|. \quad (10)$$

Therefore, using (8) and (10), we can obtain  $(\overline{u'w'})_+$  and  $(\overline{u'w'})_-$  separately.

It should be noted that the indirect estimate of momentum flux from  $C_{Tu}$  is possible only when the wind shear is large and when the mean wind is sufficiently weak not to cause severe Doppler effect. For this paper, we made direct and indirect estimates when the strength of wind shear  $|U_z|$  is larger than  $5 \times 10^{-3} \text{ s}^{-1}$  and that of mean zonal wind  $|U|$  is smaller than  $5 \text{ m s}^{-1}$  for the positive shear periods (A, B, and C) and negative shear periods (a, b, and c). Four frequency bands were examined, corresponding to 1–3 day, 3–5 day, 5–20 day, and 1–20 day periods.

Ignoring the Doppler effect by the mean wind may cause uncertainty for the momentum flux estimate, but it is probably not severe. For example, the most severe error caused by the mean wind of  $5 \text{ m s}^{-1}$  for waves with a period of 1.5 day and a zonal wavelength of 3000 km, which is a typical value as shown later, is only a few tens percent, so that the uncertainty in the value averaged over each shear period would be negligible. The validity of the assumption of two-dimensional gravity waves is discussed later.

#### 3.2. Accuracy of Momentum Flux Estimates

Before discussing the estimates of momentum flux, the observational error is considered. Here we use the notation of error( $A$ ) as the error in a physical quantity  $A$ .

The observational error of temperature and winds depends on the method and performance of the device used for rawinsonde observations at Singapore and is not easy to evaluate. However, we can estimate the error roughly from the observational data. As mentioned in S94, clear wave-like structures observed in a time-height section of high-pass filtered  $T$  and  $u$  components have amplitudes of about 1 K and  $2 \text{ m s}^{-1}$ , re-

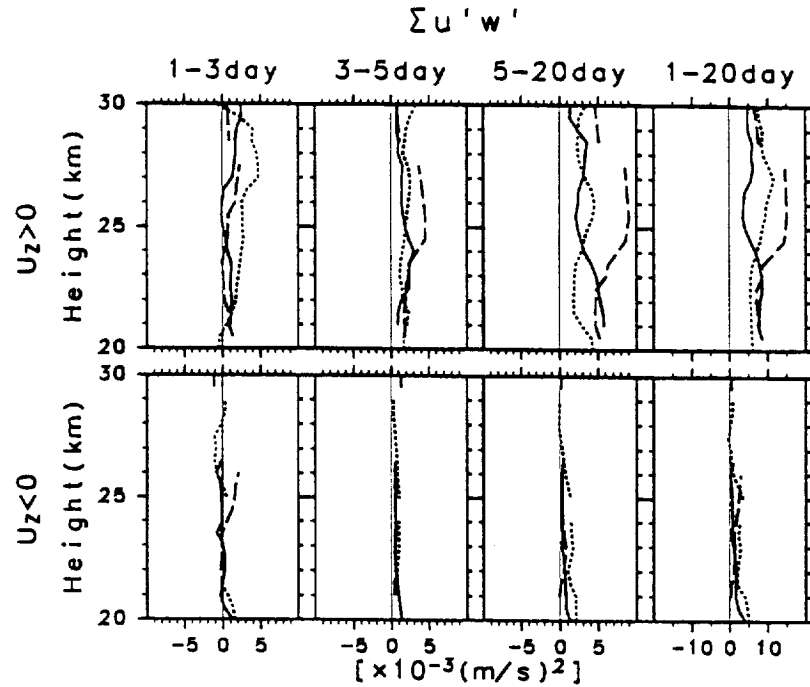


Figure 7. Direct estimate of momentum flux  $\overline{u'w'}$  as a function of height for period ranges of 1–3 days, 3–5 days, 5–20 days, and 1–20 days, during time periods when the vertical shear is (top) greater than  $5 \times 10^{-3} \text{ s}^{-1}$  and (bottom) less than  $-5 \times 10^{-3} \text{ s}^{-1}$ . Solid, long-dashed, and short-dashed curves in the top (bottom) figures are estimates in time periods A (a), B (b), and C (c), respectively.

spectively. The error in the original data is considered to be almost the same as that of the high-pass filtered profiles and is safely assumed to be no more than 0.5 K for  $\text{error}[T]$  and  $1 \text{ m s}^{-1}$  for  $\text{error}[u]$  (i.e., one-half of the wave amplitude).

Further, it is safely assumed that the observational errors in  $T$  and  $u$  are independent of time, and there is no correlation between the errors. Since the frequency spectrum of such errors is white, the error in  $Q_{Tu}$  (and  $C_{Tu}$ ) is

$$\text{error}[Q_{Tu}] = \text{error}[C_{Tu}] = \sigma_T \frac{\text{error}[u]}{\sqrt{n_s}} + \sigma_u \frac{\text{error}[T]}{\sqrt{n_s}} + \frac{\text{error}[u]\text{error}[T]}{n_s}, \quad (11)$$

where  $\sigma_T$  and  $\sigma_u$  are square roots of the variance of  $T$  and  $u$  fluctuations having frequencies in the integrated range, respectively, and  $n_s$  is the number of integrated spectral points. The last term on the right-hand side of (11) can be ignored when  $n_s$  is sufficiently large.

For 1–3 day (5–20 day) components,  $\sigma_T$  and  $\sigma_u$  are about 1.5 K (2 K) and  $2.5 \text{ m s}^{-1}$  ( $5 \text{ m s}^{-1}$ ), respectively, and  $n_s$  is 120 (28) for the spectra calculated using a window of 3 months. Since the average in each of the large shear periods was made for at least 6 months,  $n_s$  should be doubled, i.e., 240 for 1–3 day components and 56 for 5–20 day components. Using these values, we obtain  $\text{error}[Q_{Tu}]$  and  $\text{error}[C_{Tu}]$  of  $0.2 \text{ K m s}^{-1}$  for 1–3 day components and  $0.6 \text{ K m s}^{-1}$  for 5–20 day components.

The observational errors in momentum flux obtained by the direct and indirect methods are estimated from the values of  $\text{error}[Q_{Tu}]$  and  $\text{error}[C_{Tu}]$ :

$$\text{error}[\overline{u'w'}] \sim \frac{g\omega_0}{TN^2} \text{error}[Q_{Tu}], \quad (12)$$

$$\text{error}[|\overline{u'w'}|] \sim \frac{2g\omega_0}{NTU_z} \text{error}[C_{Tu}], \quad (13)$$

where  $\omega_0$  is the central frequency of the integration range. As a result, we obtained almost the same values of error for 1–3 day and 5–20 day components:

$$\text{error}[\overline{u'w'}] = 5-8 \times 10^{-4} \text{ m}^2 \text{ s}^{-2}, \quad (14)$$

for direct estimates, and

$$\text{error}[|\overline{u'w'}|] = 4-8 \times 10^{-3} \text{ m}^2 \text{ s}^{-2} \quad (15)$$

$$|U_z| = 5 \times 10^{-3} \text{ s}^{-1},$$

$$\text{error}[\overline{u'w'}] = 2-4 \times 10^{-3} \text{ m}^2 \text{ s}^{-2} \quad (16)$$

$$|U_z| = 10 \times 10^{-3} \text{ s}^{-1},$$

for indirect estimates. It should be noted again that the estimated errors are the largest (i.e., most pessimistic) estimates and hence the real accuracy must be better than this at lower levels where missing data are few. At upper levels, however, the error may be larger because the percentage of missing data becomes larger [S94]. The error of indirect estimates assuming equatorial waves is modified corresponding to the modification— for (9).

### 3.3. Results of Direct Estimation

Direct estimates of  $\overline{u'w'}$  were obtained from quadrature— spectra using (7). Profiles of momentum flux were averaged

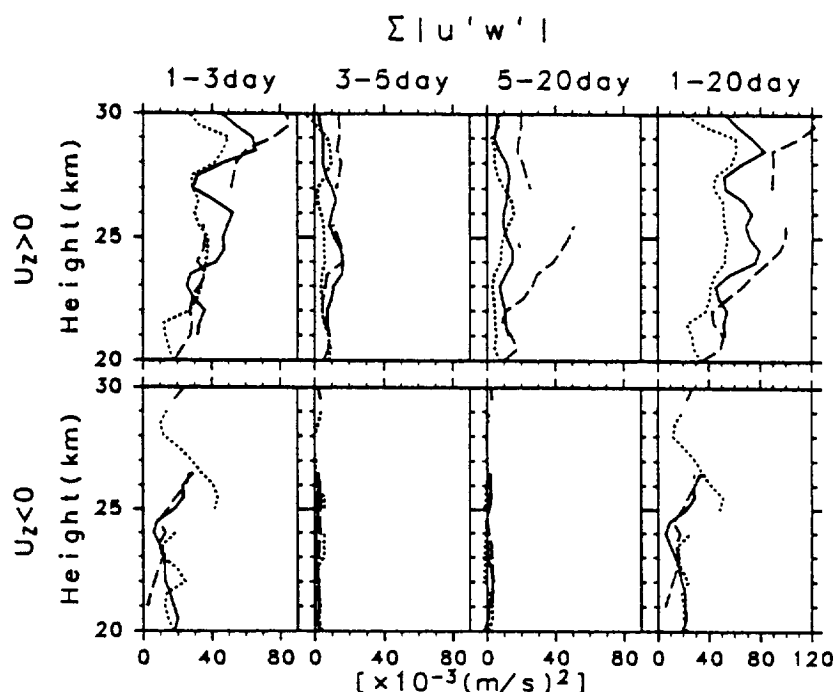


Figure 8. As in Figure 7, but for the indirect estimate of momentum flux  $|\overline{u'w'}|$ .

over each of positive shear periods (A, B, and C) and negative shear periods (a, b, and c). The mean values of  $\overline{u'w'}$  are plotted separately for 1–3 day, 3–5 day, 5–20 day, and 1–20 day components in Figure 7 as a function of height. Different line styles show different time periods. The reader is cautioned that the vertical profiles of  $\overline{u'w'}$  were obtained for periods of large shear, and the time of observation depends on altitude (see Figure 2). Therefore the displayed vertical profiles of momentum flux do not provide the wave drag from its convergence.

For westerly shear ( $U_z > 0$ ), values of  $\overline{u'w'}$  are biased toward positive in all frequency ranges. The momentum flux associated with 1–3 day components is about  $0.5 \times 10^{-3} \text{ m}^2 \text{ s}^{-2}$ , and tends to increase with height from  $1 \times 10^{-3} \text{ m}^2 \text{ s}^{-2}$  at 22 km to  $3 \times 10^{-3} \text{ m}^2 \text{ s}^{-2}$  at 28 km, on average. The estimate is meaningful because the average values are larger than the error estimated in the previous section.

The momentum flux for long-period (5–20 day) Kelvin waves in westerly shear is  $2.9 \times 10^{-3} \text{ m}^2 \text{ s}^{-2}$ . These values are a little smaller than the estimate from previous observational studies of  $\sim 6 \times 10^{-3} \text{ m}^2 \text{ s}^{-2}$  [e.g., Andrews *et al.*, 1987]. It should be noted, however, that the quadrature spectra due to Kelvin waves in Figure 1 is spread over a wide range of periods extending from about 20 days to 3 days. It may be better to examine the sum of 3–5 day and 5–20 day components, which is  $4\text{--}12 \times 10^{-3} \text{ m}^2 \text{ s}^{-2}$  and comparable to previous studies.

The total momentum flux in westerly shear associated with 1–20 day components is about  $4\text{--}15 \times 10^{-3} \text{ m}^2 \text{ s}^{-2}$ . The contribution by long-period Kelvin waves is largest, and the momentum flux due to 1–3 day components is about half as large.

On the other hand, the momentum flux in easterly shear is generally small compared with that in westerly shear. For 5–20 day components, positive bias due to Kelvin waves around the tropopause is observed at lower levels and the momentum flux is comparable to the error above 26 km. The momentum flux associated with 1–3 day components is weakly negative above 26 km, corresponding to systematic positive values of  $Q_{Tu}$

around easterly shear observed in Figure 3, although the momentum flux below is distributed around zero. The total momentum flux in easterly shear for 1–20 day components is about  $2\text{--}6 \times 10^{-3} \text{ m}^2 \text{ s}^{-2}$  at lower levels, decreasing with height and almost zero at upper levels.

### 3.4. Results of Indirect Estimation

The results from indirect estimation of momentum flux using (9) are summarized in Figure 8 in the same manner as the direct estimate (Figure 7). The indirect estimates should accord with those of the direct estimation if momentum fluxes associated with waves in the period range are of one sign.

First, let us examine the results for 5–20 day components in westerly shear, in which we expect dominance of long-period Kelvin waves. The vertical profiles of indirect estimates in Figure 7 are similar to those of direct estimates, although the indirect estimates of momentum flux ( $3\text{--}50 \times 10^{-3} \text{ m}^2 \text{ s}^{-2}$ ) are larger than the direct estimates ( $2\text{--}9 \times 10^{-3} \text{ m}^2 \text{ s}^{-2}$ ).

According to the extended theory for equatorial waves [D97], the factor in (9) is  $3/2$  instead of 2 if the disturbances are due to Kelvin waves. Thus the indirect estimate for 5–20 day components is likely to be overestimated by a factor of  $3/2$ . This modification makes the indirect estimates almost consistent with results from the direct method, except for period B (long-dashed curves) which has significantly larger values compared with the other two periods A and C. The large amplitudes for period B suggest that nonlinear effects such as “saturation” are not negligible [D95]. In such cases, the covariance of  $T$  and  $u$  components can be larger than expected from (3). Figure 9 shows the modified profiles of indirect estimates for periods A and C (thin curves). Direct estimates for the same time periods are plotted by thick curves for comparison. The difference between modified indirect estimates and direct estimates for A and C profiles is  $0\text{--}4 \times 10^{-3} \text{ m}^2 \text{ s}^{-2}$ , which is within the estimation error of the indirect method. The consistency between the results of direct and indirect estimation

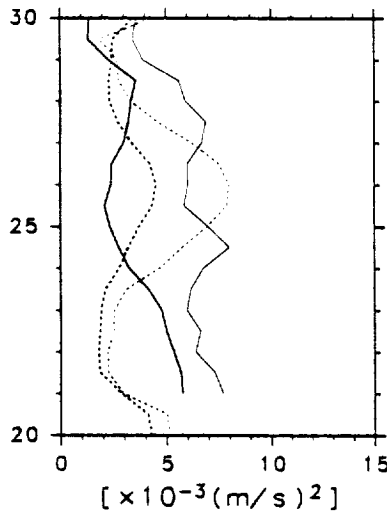


**Figure 9.** Vertical profiles of indirect estimates of momentum flux for 5–20 day components in time periods A (solid) and C (dashed) based on the theory of equatorial Kelvin waves (thin curves). The direct estimates of momentum flux for the same time periods and wave components are shown by thick curves for comparison.

for long-period Kelvin waves supports the validity of the indirect method.

The most important feature in Figure 8 is that the indirect estimates of the momentum flux associated with short-period (1–3 day) components are significantly large and occupy the largest portion of the total (1–20 day) momentum flux in both westerly and easterly shears. The magnitude of indirect estimates of momentum flux due to 1–3 day components in westerly shear is about  $20 \times 10^{-3} \text{ m}^2 \text{ s}^{-2}$  at 21 km, increases with height, and becomes  $50 \times 10^{-3} \text{ m}^2 \text{ s}^{-2}$  at 30 km, which is almost 10 times larger than the direct estimates of  $0.5 \times 10^{-3} \text{ m}^2 \text{ s}^{-2}$ . This fact indicates that 1–3 day components are composed of at least two kinds of waves having positive and negative momentum fluxes and that large momentum fluxes associated with the waves are cancelled in the sum. Assuming that short-period waves propagate mainly upward, the momentum flux of waves in one direction (eastward or westward) must be almost one-half of the indirect estimate, and significantly larger than the momentum flux due to long-period Kelvin waves. The difference between the three periods of A, B, and C is small, reflecting the high correlation of  $C_{\tau u}$  and vertical shear observed in Figure 4.

In easterly shear, the 1–3 day components are dominant again. The momentum fluxes are  $7\text{--}30 \times 10^{-3} \text{ m}^2 \text{ s}^{-2}$  which are nearly half of those in westerly shears. The difference in momentum fluxes affects largely the difference in the gradient of the distribution between westerly and easterly shear periods in the scatter diagram of Figure 4. The indirect estimates are much larger than the direct estimates which are smaller than  $3 \times 10^{-3} \text{ m}^2 \text{ s}^{-2}$ , suggesting that the large cancellation between positive and negative momentum fluxes occurs also in easterly shear. This is consistent with the  $Q_{\tau u}$  profile, in which the sign changes around the large shear as discussed in section 2.1. On the other hand, indirect estimates for 3–5 and 5–20 day components are small, consistent with the direct estimates. This fact means that the amplitudes of individual longer-period waves in easterly shear is small at the equator.

### 3.5. Possibility of Equatorially Trapped Waves for 1–3 Day Components

In section 3.4 we assumed that 1–3 day components are due to two-dimensional gravity waves. This assumption may be valid near source regions, i.e., at lower levels in the stratosphere, where the horizontal (in particular, the meridional) expanse of wave packets is too small to feel the beta effect of the earth rotation. It is likely, however, that as the waves propagate upward, their localized structure disappears and the waves acquire the structure of equatorially trapped modes. Thus, in this section we consider the possibility of equatorial waves for 1–3 day components and examine the modification of indirect momentum flux estimate.

An important quantity to examine the structure of equatorially trapped waves is the ratio of potential energy (PE) and kinetic energy (KE), which depends on the mode index  $n$  characterizing the meridional structure, the nondimensional zonal wavenumber  $k^* (= ky_0)$ , and the nondimensional wave frequency  $\omega^* (= \omega/\beta y_0)$ , where  $y_0 (= \sqrt{N/|m|\beta})$  is the latitudinal scale factor and  $\beta = 2.283 \times 10^{-11} \text{ m}^{-1} \text{ s}^{-1}$  at the equator. Figure 10a shows the dispersion curves for odd IGW modes ( $n = 1, 3, 5, \dots$ ) and Kelvin modes ( $n = -1$ ) which have a nonzero  $u$  component at the equator (i.e., at Singapore). The dispersion relation is

$$\omega^{*2} - \frac{k^*}{\omega^*} - k^{*2} = 2n + 1 \quad (17)$$

The upper limit of  $\omega^* \sim 4$  in Figure 10a corresponds to a minimum vertical wavelength of 2 km for the central frequency  $(1.5 \text{ days})^{-1}$  in the period range of 1–3 days, which is detectable by routine rawinsonde observations in the lower stratosphere with vertical resolution of about 1 km. At the equator, assuming that latitudinal shear is  $O(y)$ , the ratio ( $R$ ) of PE to zonal KE (i.e., the contribution to KE by  $u$  component) is

$$R = \frac{\text{PE}}{\text{zonal KE}} = \frac{\phi'^2/N^2}{\phi'^2/c^2} \sim \frac{m^2 \omega^2}{N^2 k^2} = \frac{\omega^{*2}}{k^{*2}}, \quad (18)$$

where  $m$  is vertical wavenumber. Figure 10b shows  $R$ , which is 1 for Kelvin waves and larger than 1 for IGWs. It should also be noted that for two-dimensional hydrostatic gravity waves,

$$\text{PE/KE} \sim 1. \quad (19)$$

Figure 10c shows the correction factor  $C$  which is used to obtain an indirect estimate of momentum flux for equatorial waves  $[u'w']_{\text{eq}}$  from our earlier estimate under the assumption of two-dimensional gravity waves  $[u'w']_{2\text{-dim}}$ :

$$[u'w']_{\text{eq}} = C [u'w']_{2\text{-dim}}, \quad (20)$$

where

$$C = \frac{1}{2} \left[ \left( 1 - \frac{k^{*2}}{4|\omega^*|W_g^*} \right) \frac{\omega^*}{k^*} \right]^{-1} \quad (21)$$

and

$$W_g^* = \frac{\omega^*(\omega^{*2} + k^{*2} + k^*/\omega^*)}{2\omega^{*2} + k^*/\omega^*}. \quad (22)$$

is the nondimensional vertical group velocity [D97]. The correction factor  $C$  is smaller than 1 for all equatorial Kelvin and inertia-gravity waves. For the equatorial inertia-gravity waves, the correction factor  $C$  decreases as  $R$  increases for one mode.

Thus the momentum flux obtained under the assumption of two-dimensional gravity waves in the previous section may be overestimated. However, it is shown in the following that the modification is too small to affect our conclusion that there is a large cancellation of positive and negative momentum fluxes for 1–3 day components.

Figures 11 and 12 show the zonal KE ( $\overline{u'^2}$ ) and PE ( $((T'g/TN)^2)$ ), respectively (divided by density), in the same manner as Figures 7 and 8. The contribution of meridional wind component to KE ( $\overline{v'^2}$ ; meridional KE divided by density) is shown in Figure 13.

In westerly shear ( $\bar{U}_z > 0$ ), PE is larger than zonal KE for 1–3 day components below 25 km, which is consistent with the characteristics of equatorial inertia-gravity waves with odd  $n$ . It should be noted that meridional KE is as large as zonal KE in this height region and that total KE (zonal KE plus meridional KE) is comparable to PE. It is possible that the meridional KE is due to Rossby gravity waves or other modes with even  $n$ . However, if we take into account that the height region is near the source of the waves, there is another possibility that the zonal KE and meridional KE belong to the same disturbances whose wave vector has both zonal and meridional components. In fact, wave-like structure is sometimes observed in the meridional wind component in the lower stratosphere below 25 km (see Figure 4b of S94). The equipartition of PE and total KE in this height region is consistent with the assumption of two-dimensional gravity waves used in the momentum flux estimation in section 3.4.

Such waves having a meridional component of the wave vector would propagate outward from the equator, refract back and forth in the equatorial waveguide [e.g., Gill, 1982] while propagating upward, so that zonally oriented equatorial modes would form in the upper region. This scenario is consistent with the fact that zonal KE is larger than meridional KE above 25 km. It is important that the zonal KE is almost equal to PE for 1–3 day components above 25 km. This is again consistent with the assumption of zonally oriented plane gravity waves used for momentum flux estimation in the previous section. However, it is also the case for equatorial Kelvin waves (see Figure 10b).

Let us consider the hypothesis that the 1–3 day waves are composed only of equatorial Kelvin waves. In this case, the momentum flux obtained from two-dimensional gravity wave theory is overestimated by a factor of  $\frac{1}{2}$  as for long-period Kelvin waves. Using the value of  $50 \times 10^{-3} \text{ m}^2 \text{ s}^{-2}$  above 25 km in Figure 8, we obtain a (modified) indirect estimate of  $33 \times 10^{-3} \text{ m}^2 \text{ s}^{-2}$ . However, this value is still much larger than the direct estimate of  $\sim 2 \times 10^{-3} \text{ m}^2 \text{ s}^{-2}$  shown in Figure 7 which is independent of wave characteristics. Thus the indirect estimate cannot be explained by Kelvin waves alone, and we need to consider the coexistence of other kinds of waves.

It is worth noting that radiative damping can modify the ratio of PE and KE of waves. According to equatorial wave theory, Kelvin waves should have equal PE and zonal KE. This is the case for long-period Kelvin waves below 24 km (see Figures 12 and 11). However, KE is larger than PE above 24 km. The reduced PE is likely due to radiative damping. The maximum reduction seems about 50%. Such damping may occur also for 1–3 day components but is probably smaller.

Let us consider another hypothesis that the 1–3 day waves are composed of an equatorial wave having  $R$  of 2, assuming 50% reduction of PE by radiative damping so as to obtain the minimum, i.e., most severe correction factor  $C$ . Possible modes

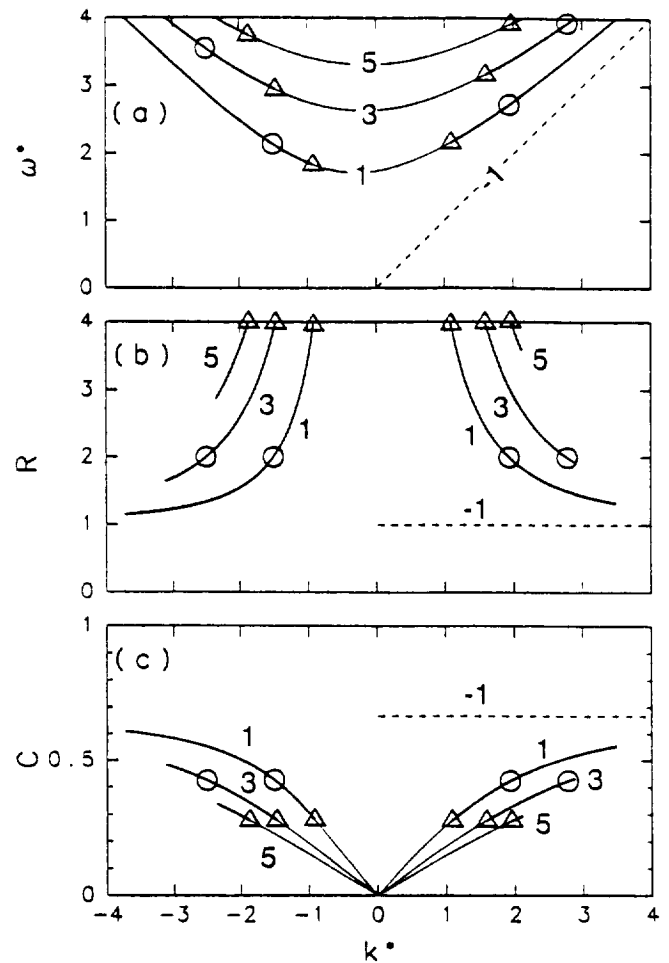


**Figure 10.** (a) Dispersion curves of odd modes of equatorial inertia-gravity waves (solid curves) and Kelvin wave (dashed line). Horizontal and vertical axes show nondimensional zonal wavenumber and frequency. (b) The ratio of potential energy to kinetic energy ( $R$ ). (c) Correction factor ( $C$ ) to obtain indirect estimates of momentum flux from the estimate based on two-dimensional gravity wave theory. Open circles and triangles are modes having  $R$  of 2 and 4, respectively. Thick curves show the inertia-gravity modes with  $R$  smaller than 4 for observed 1–3 day components.

are denoted by open circles, and the correction factor  $C$  is about 0.42. Thus the indirect estimate of momentum flux above 25 km is about  $20 \times 10^{-3} \text{ m}^2 \text{ s}^{-2}$  which is still much larger than the direct estimate of  $\sim 2 \times 10^{-3} \text{ m}^2 \text{ s}^{-2}$ .

In easterly shear, zonal KE is relatively large for the period range of 5–20 days and 1–3 days. The zonal KE for 5–20 days is slightly larger than PE as seen in westerly shear. Judging by the dominance of zonal KE at long periods, the 5–20 day components are likely due to Kelvin waves which leak through the westerly wind below. The 1–3 day components have PE about twice as large as zonal KE, independent of height. Considering the most severe reduction (50%) by radiative damping again, we can assume that 1–3 day components are due to inertia-gravity waves at upper levels,  $R$  of which is 4. The corresponding correction factor  $C$  is 0.28 (denoted by triangles in Figure 10). The momentum flux modified under the assumption of equatorial inertia-gravity waves is then  $2\text{--}8 \times 10^{-3} \text{ m}^2$

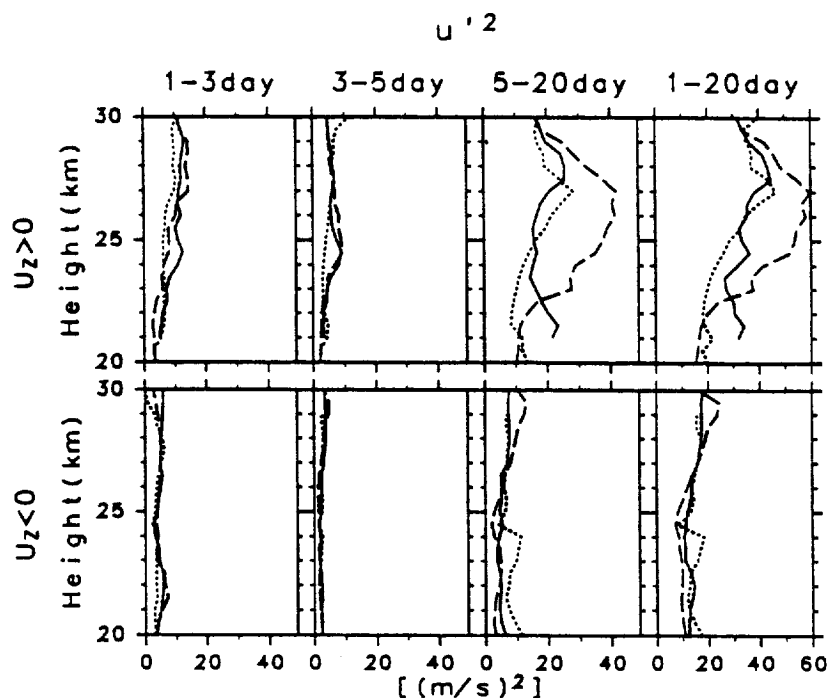


Figure 11. As in Figure 7, but for the kinetic energy (divided by density) due to zonal wind component.

$s^{-2}$ , which is still considerably larger than the direct estimate (note that the direct estimate is small compared to the error). It is also worth noting that meridional KE is large even at upper levels, in particular for 1-3 and 3-5 day components. This feature corresponds to the dominance of Rossby gravity waves along easterly shear zones shown by S94.

From the discussion above, it is concluded that we cannot

explain the difference between direct and indirect estimates of momentum flux for 1-3 day components in both easterly and westerly shears without taking into consideration the coexistence of multiple waves having positive and negative momentum fluxes. This conclusion is also supported by  $Q_{\tau u}$  showing a complicated distribution of positive and negative values in the time-height section of Figure 3.

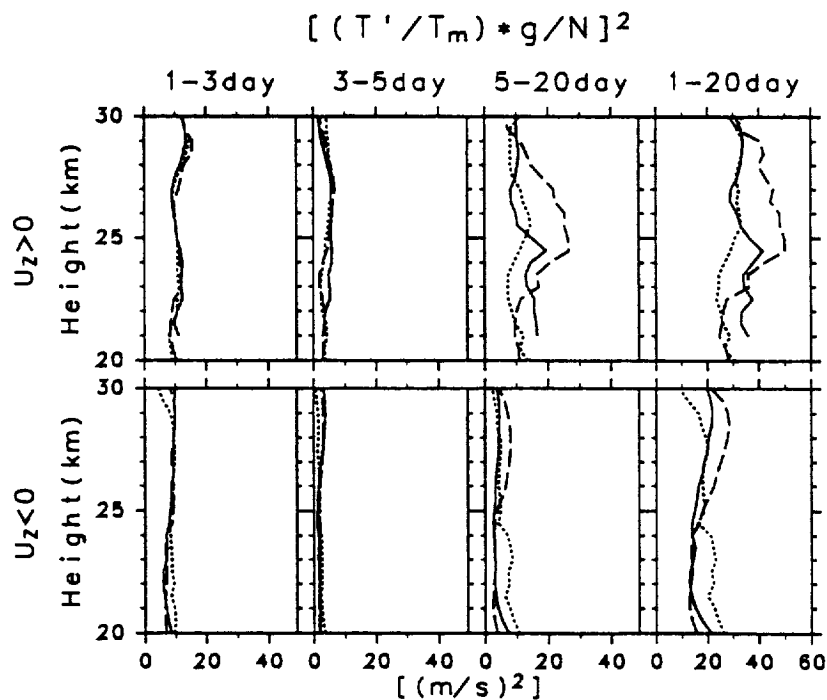


Figure 12. As in Figure 7, but for the potential energy (divided by density).

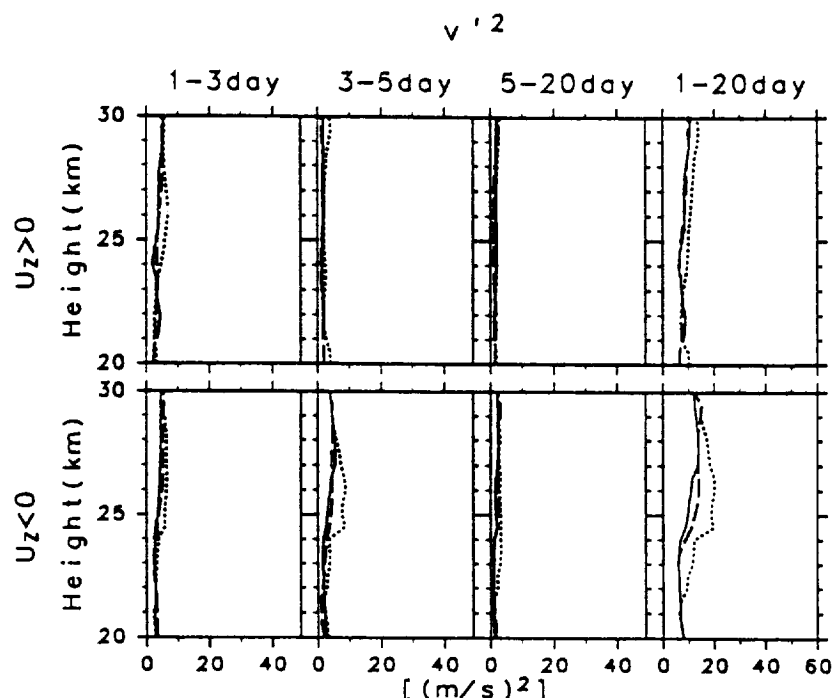


Figure 13. As in Figure 7, but the kinetic energy (divided by density) due to meridional wind component.

## 4. Discussion

### 4.1. Difference Between Easterly and Westerly Shears

It was shown in the previous section that there are some differences in wave characteristics for 1–3 day components between easterly and westerly shears. The indirect estimate of momentum flux was larger in westerly shear than in easterly shear. The ratio of potential energy to kinetic energy is smaller in westerly shear than in easterly shear. If wave spectra in the source region (i.e., troposphere) are independent of the QBO in the lower stratosphere, the differences that depend on the QBO must be attributed to propagation in the lower stratosphere below QBO shear zones, assuming that the waves are mainly propagating energy upward. Several possible explanations are listed below.

First, there may be asymmetry in the phase velocity spectra of short-period waves emerging from the troposphere. Since the easterly (westerly) wind below the westerly (easterly) shear inhibits upward propagation of westward (eastward) waves, the dominance of wave activity in westerly shear may be due to dominance of eastward waves in the source spectra. This is likely because the mean wind in the upper troposphere is easterly in convective regions such as the Maritime Continent (see Figure 2). The “topographic” effect of convection in an easterly mean wind will generate a phase velocity spectrum biased toward eastward waves [e.g., Pfister *et al.*, 1993]. Even if eastward and westward gravity waves are generated equally at some lower levels in the troposphere, gravity waves with westward phase velocities comparable to the easterly wind in the upper troposphere cannot propagate to the tropopause.

Second, differences may be due to an asymmetric manifold of equatorial waves, i.e., the asymmetry of dispersion curves around  $k^* = 0$  (see Figure 10). If 1–3 day components are due mainly to equatorial waves, the characteristics of propagation can be asymmetric even if the QBO of mean zonal wind is symmetric. An extreme case is that of Kelvin waves below

$\omega^* \approx 2$  (for 5–20 day components): there is no “anti-Kelvin” wave, or westward mirror image of this mode, on the dispersion diagram.

Third, the QBO of mean zonal wind is itself asymmetric as seen in Figure 2. Even if gravity wave spectra were symmetric at the tropopause, the characteristics of propagation would be different below easterly and westerly shears because of the asymmetry of the QBO. Gravity waves may partly contribute to the asymmetry of the QBO, but there are other processes, e.g., asymmetric acceleration by Kelvin and Rossby gravity waves, and the induced mean meridional circulation [Dunkerton, 1991].

### 4.2. Parameters of Possible Equatorial Waves for 1–3 Day Components

Although it was shown in section 3 that 1–3 day components are likely composed of a mixture of various waves, it would be useful to infer wave parameters of possible modes even roughly. Taking the central frequency of  $(1.5 \text{ days})^{-1}$  as a typical frequency for the 1–3 day wave components, the dispersion curves are examined. As described in the following, there are at least three criteria which should be satisfied by the waves observed around the shear region.

First, from the definition of  $\omega^*$  as described in section 3.5, it is found that the maximum  $\omega^*$  is determined by the minimum observable vertical wavelength. Since the vertical resolution of rawinsonde observation is about 1 km, the minimum observable vertical wavelength is about 2 km (ignoring the aliasing of waves with shorter vertical wavelengths). Thus the maximum  $\omega^*$  is about 4 for all equatorial wave modes.

Second, the minimum  $\omega^*$  is determined by the maximum  $R$ , i.e., the ratio of PE to zonal KE, since  $R$  increases as  $\omega^*$  decreases for each mode (see Figures 10a and 10b). The maximum  $R$  found from Figures 11 and 12 is 1 and 2 for westerly and easterly shear, respectively. Assuming 50% reduction due to radiative damping as discussed in section 3.5, the maximum

**Table 1.** Parameters of Possible Equatorial Waves for Observed 1–3 Day Components in Westerly Shear

Mode	$c$ , $\text{m s}^{-1}$	$\lambda_z$ , km	$\lambda_y$ , km	$y_0$ , $\times 10^3$ km
$n = -1$ Kelvin waves	$>6.7$	$>870$	$>2.0$	$>550$
$n = 1$ eastward IGW	7.7–19.6	1000–2500	2.0–4.2	550–790
$n = 3$ eastward IGW	9.4	1200	2.0	550
$n = 1$ westward IGW	–25 to –31.8	3200–4100	5.7–6.7	920–1010

The zonal phase velocity, zonal wavelength, vertical wavelength, latitudinal scale factor are denoted by  $c$ ,  $\lambda_z$ ,  $\lambda_y$ , and  $y_0$ , respectively. IGW, inertia-gravity waves.

$R$  is taken to be 2 and 4 for respective shears. The minimum  $\omega^*$  for each mode is denoted by open circles for westerly shear and open triangles for easterly shear in Figure 10. The thick curves in Figure 10 indicate possible waves satisfying both the first and second criteria.

Further, we can give the third criterion in terms of the mean wind. If the waves around the westerly and easterly shear come from the lower levels, their phase velocities must be out of the range of the mean wind below the shear; otherwise the waves would encounter their critical levels before reaching the shear zones. The underlying wind is about  $-25$  to  $-5 \text{ m s}^{-1}$  for westerly shear and  $-5$  to  $+15 \text{ m s}^{-1}$  for easterly shear (see Figure 2a). If we take the damping below the critical levels into account, the phase velocity range of observable waves may be more narrowed.

The possible waves satisfying these three criteria are eastward  $n = -1$  modes ( $c > 6.7 \text{ m s}^{-1}$ ), eastward  $n = 1$  modes ( $c = 7.7\text{--}19.6 \text{ m s}^{-1}$ ), eastward  $n = 3$  modes ( $c = 9.4 \text{ m s}^{-1}$ ), and westward  $n = 1$  modes ( $c = -31.8$  to  $-25 \text{ m s}^{-1}$ ) for westerly shear. As for the easterly shear, they are eastward  $n = -1$  modes ( $c > 15 \text{ m s}^{-1}$ ), eastward  $n = 1$  modes ( $c = 15\text{--}44.1 \text{ m s}^{-1}$ ), eastward  $n = 3$  modes ( $c = 15\text{--}20.6 \text{ m s}^{-1}$ ), westward  $n = 1$  modes ( $c = -61.8$  to  $-7.2 \text{ m s}^{-1}$ ), westward  $n = 3$  modes ( $c = -23.8$  to  $-8.6 \text{ m s}^{-1}$ ) and westward  $n = 5$  modes ( $c = -14.7$  to  $-11.7 \text{ m s}^{-1}$ ). Westward  $n = 3$  modes cannot propagate through the mean wind below westerly shear, although some waves of  $n = 3$  satisfy the first and second criteria. This is also the case for eastward  $n = 5$  modes in the easterly shear. Parameters of the possible equatorial waves are summarized in Tables 1 and 2 for westerly and easterly shear, respectively.

The momentum flux estimated in this paper is the value at the equator. Since the QBO is a phenomena having the latitudinal half width of  $25^\circ$ , the latitudinal scale factor  $y_0$  listed in Tables 1 and 2 that corresponds to the  $e$ -folding latitude of wave amplitude is important when we consider the mean wind acceleration by convergence of momentum fluxes associated with the waves. The factor  $y_0$  is proportional to the square root of the vertical wavelength and independent of the wave frequency. The possible equatorial modes for short-period waves except for  $n = -1$  modes (short-period Kelvin waves) have shorter vertical wavelengths and hence smaller meridional extent than long-period Kelvin waves with typical vertical wavelengths of  $10\text{--}15 \text{ km}$  [e.g., Andrews *et al.*, 1987] corresponding to  $y_0$  of  $940\text{--}1210 \text{ km}$ . The possible short-period Kelvin waves have a wide range of vertical wavelengths and meridional extent which can be either larger or smaller than those of long-period Kelvin waves.

#### 4.3. Aliasing of Waves With Periods Shorter Than 1 Day

The direct and indirect estimates of momentum flux were made under an assumption that the observed frequency is the actual ground-based frequency of the waves. Since the rawinsonde observation is made only twice a day, aliasing of waves with periods shorter than 1 day is possible. The degree of aliasing in the spectra depends on the spectral shape; blue spectra cause significant aliasing, for instance. The spectra at periods shorter than 1 day may be speculated by extrapolation of the observed spectra to higher frequencies. The cospectra in Figure 1c that were used for indirect estimate of momentum flux have larger values at shorter periods. Taking into consideration that the spectra were plotted in flux content form, the spectral shape seems nearly white. The power spectra of Figures 1a and 1b also suggest enhanced activity in 1–2 day range, which could well be due to wave motions aliased from higher frequencies. In fact, there is observational evidence of higher-frequency gravity waves associated with convection [e.g., Sato, 1993; Pfister *et al.*, 1993; Sato *et al.*, 1995; Alexander and Pfister, 1995]. The direct and indirect estimates of momentum flux are proportional to  $\omega$ . The aliased higher-frequency waves can have significant momentum fluxes, although they may have smaller amplitudes than waves with periods longer than 1 day. Therefore the true values can be significantly larger than the estimates given here.

#### 5. Summary

A new indirect method was used to estimate momentum flux from cospectra of temperature and zonal wind fluctuations based on the theory of two-dimensional (plane) gravity waves and three-dimensional equatorial waves in vertical shear [Dunkerton, 1995, manuscript in preparation, 1997]. This method provides the summation of absolute values of momentum flux associated with each wave. Comparing to direct estimates of total momentum flux from the quadrature spectra, we can estimate positive and negative momentum fluxes separately. An analysis was made of rawinsonde data at Singapore over 10 years. The validity of this method was reinforced by the observation of an approximately linear relationship between the cospectrum and vertical shear, and relatively few events of positive (negative) covariance of  $T$  and  $u$  components in negative (positive) vertical shear. Estimation of observational error was made to evaluate the derived momentum fluxes quantitatively.

The direct and indirect estimates for 5–20 day components in westerly shear, thought to be attributable to eastward propagating equatorial Kelvin waves, are in accord with one another to within the observational error, except for the 1987 case when Kelvin waves had such a large amplitude that we could not ignore the nonlinear effect. The direct estimates of

**Table 2.** Same as Table 1 but for Easterly Shear

Mode	$c$ , $\text{m s}^{-1}$	$\lambda_z$ , km	$\lambda_y$ , km	$y_0$ , $\times 10^3$ km
$n = -1$ Kelvin waves	$>15$	$>1900$	$>2.7$	$>820$
$n = 1$ eastward IGW	15–44.1	1900–5700	3.4–6.6	710–970
$n = 3$ eastward IGW	15–20.6	1900–2700	2.6–3.1	630–660
$n = 1$ westward IGW	–7.2 to –61.8	930–8000	2.0–9.3	550–1180
$n = 3$ westward IGW	–8.6 to –23.8	1100–3100	2.0–3.6	550–730
$n = 5$ westward IGW	–11.7 to –14.7	1500–1900	2.0–2.2	550–570



momentum flux, which are more accurate than the indirect estimates, are  $2-9 \times 10^{-3} \text{ m}^2 \text{ s}^{-2}$ , consistent with previous observational studies. Indirect as well as direct estimates in easterly shear are small, indicating the absence of long-period waves.

This method is effective in particular for short-period (1-3 day) disturbances because these waves can propagate both eastward and westward. The results for short-period waves are summarized as follows.

1. The indirect estimates of momentum flux under the assumption of two-dimensional gravity waves are  $20-60 \times 10^{-3} \text{ m}^2 \text{ s}^{-2}$  for westerly shear and  $7-30 \times 10^{-3} \text{ m}^2 \text{ s}^{-2}$  for easterly shear. The estimated values become smaller by about 30-70% when three-dimensional equatorial modes are assumed.

2. The direct estimates of momentum flux, which are independent of wave structure, are  $0-5 \times 10^{-3} \text{ m}^2 \text{ s}^{-2}$  for westerly shear and  $-1 \text{ to } +2 \times 10^{-3} \text{ m}^2 \text{ s}^{-2}$  for easterly shear.

3. The indirect estimates are always much larger than the direct estimates, indicating that there is a large cancelation of positive and negative momentum fluxes. If waves are mainly propagating energy upward, then eastward and westward waves must coexist, with approximately equal and opposite fluxes. It is also possible that the cancelation is partly due to reflected waves.

4. The momentum flux in one direction (approximately one-half of the total indirect estimate) is at least 3 times larger than that of long-period Kelvin waves in westerly shear.

5. There are some differences in wave characteristics between westerly and easterly shear. The ratio of potential and kinetic energy is smaller in westerly shear than in easterly shear. The indirect estimate of momentum flux, indicating wave activity, is about twice as large in westerly shear as in easterly shear.

Possible explanations for the difference between easterly and westerly shear were discussed. Wave parameters were inferred from the ratio of potential and kinetic energies and the mean wind below the shears, assuming that the short-period waves are composed of equatorial modes. The effects of aliasing, from components with periods shorter than 1 day, on the momentum flux estimation was also discussed. If there is the aliasing, the actual momentum fluxes can be significantly larger than estimated in this paper assuming that the observed frequencies are actual ground-based wave frequencies.

Singapore is located where vigorous convection is observed [e.g., Bergman and Salby, 1994]. The characteristics of waves near their source region may be localized, although waves in the middle and upper stratosphere possibly attain a modal, equatorially trapped structure. Further analysis is necessary using observational data at other locations near and off the equator to identify the short-period waves more precisely and to determine whether they display similar characteristics elsewhere.

**Acknowledgments.** The authors wish to thank Toru Sato for discussion on the estimation of observational error in the momentum flux. Thanks are extended to James R. Holton, M. Joan Alexander, and anonymous reviewers for constructive comments. This research was supported, in part by the Grant-in-Aid for Encouragement of Young Scientists (A) 07740384 of the Ministry of Education, Science and Culture, Japan (K.S.), by the National Science Foundation, grant ATM-9500613, and the National Aeronautics and Space Administration, contract NASW-844 (T.J.D.).

## References

- Alexander, M. J., and L. Pfister, Gravity wave momentum flux in the lower stratosphere over convection, *Geophys. Res. Lett.*, 22, 2029-2032, 1995.
- Allen, S. J., and R. A. Vincent, Gravity wave activity in the lower atmosphere: Seasonal and latitudinal variations, *J. Geophys. Res.*, 100, 1327-1350, 1995.
- Andrews, D. G., J. R. Holton, and C. B. Leovy, *Middle Atmosphere Dynamics*, 489 pp., Academic, San Diego, Calif., 1987.
- Bergman, L. W., and M. L. Salby, Equatorial wave activity derived from fluctuations in observed convection, *J. Atmos. Sci.*, 51, 3791-3806, 1994.
- Dunkerton, T. J., Nonlinear propagation of zonal winds in an atmosphere with Newtonian cooling and equatorial wave driving, *J. Atmos. Sci.*, 48, 236-263, 1991.
- Dunkerton, T. J., Horizontal buoyancy flux of internal gravity waves in vertical shear, *J. Meteorol. Soc. Jpn.*, 73, 747-755, 1995.
- Dunkerton, T. J., The role of gravity waves in the quasi-biennial oscillation, *J. Geophys. Res.*, this issue.
- Gill, A. E., *Atmosphere-Ocean Dynamics*, 662 pp., Academic, San Diego, Calif., 1982.
- Kitamura, Y., and I. Hirota, Small-scale disturbances in the lower stratosphere revealed by daily rawin sonde observations, *J. Meteorol. Soc. Jpn.*, 67, 817-831, 1989.
- Maruyama, T., Annual and QBO-synchronized variations of lower-stratospheric equatorial wave activity over Singapore during 1961-1989, *J. Meteorol. Soc. Jpn.*, 69, 219-232, 1991.
- Maruyama, T., Upward transport of westerly momentum due to disturbances of the equatorial lower stratosphere in the period range about 2 days—A Singapore data analysis for 1983-1993, *J. Meteorol. Soc. Jpn.*, 72, 423-432, 1994.
- Matsuno, T., Quasi-geostrophic motions in the equatorial area, *J. Meteorol. Soc. Jpn.*, 44, 25-43, 1966.
- Ogino, S., M. D. Yamanaka, and S. Fukao, Meridional variation of lower stratospheric gravity wave activity: A quick look at Hakuho-Marui J-COARE cruise rawinsonde data, *J. Meteorol. Soc. Jpn.*, 73, 407-413, 1995.
- Pfister, L., K. R. Chan, T. P. Bui, S. Bowen, M. Legg, B. Gary, K. Kelly, M. Proffitt, and W. Starr, Gravity waves generated by a tropical cyclone during the STEP tropical field program: A case study, *J. Geophys. Res.*, 98, 8611-8638, 1993.
- Sato, K., Small-scale wind disturbances observed by the MU radar during the passage of Typhoon Kelly, *J. Atmos. Sci.*, 50, 518-537, 1993.
- Sato, K., F. Hasegawa, and I. Hirota, Short-period disturbances in the equatorial lower stratosphere, *J. Meteorol. Soc. Jpn.*, 72, 423-432, 1994.
- Sato, K., H. Hashiguchi, and S. Fukao, Gravity waves and turbulence associated with cumulus convection observed with the UHF/VHF clear-air Doppler radars, *J. Geophys. Res.*, 100, 7111-7119, 1995.
- Takayabu, Y. N., K.-M. Lau, and C.-H. Sui, Observation of quasi two-day wave during TOGA COARE, *Mon. Weather Rev.*, 124, 1892-1913, 1996.
- Tsuda, T., Y. Murayama, H. Wiryosumarto, S. W. B. Harijono, and S. Kato, Radiosonde observations of equatorial atmosphere dynamics over Indonesia, 1. Equatorial waves and diurnal tides, *J. Geophys. Res.*, 99, 10,491-10,506, 1994a.
- Tsuda, T., Y. Murayama, H. Wiryosumarto, S. W. B. Harijono, and S. Kato, Radiosonde observations of equatorial atmosphere dynamics over Indonesia, 2. Characteristics of gravity waves, *J. Geophys. Res.*, 99, 10,507-10,516, 1994b.
- T. J. Dunkerton, Northwest Research Associates, P.O. Box 3027, Bellevue, WA 98009. (e-mail: tim@nwra.com)
- K. Sato, Department of Geophysics, Kyoto University, Kyoto 606-01, Japan. (e-mail: sato@kugi.kyoto-u.ac.jp)

(Received April 9, 1996; revised July 31, 1996; accepted July 31, 1996.)

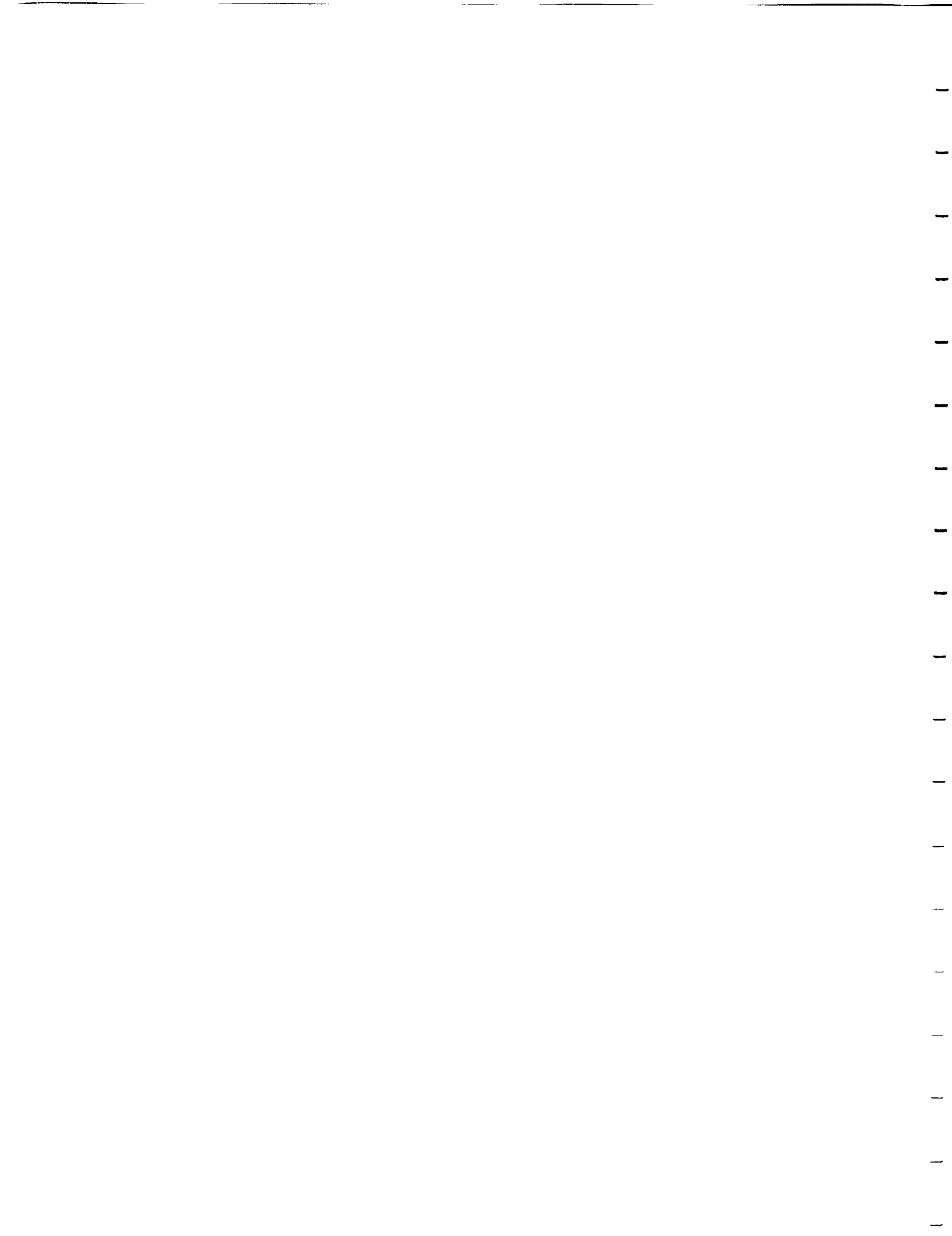
100

100

100

100

**III. Observational Studies of the ExtraTropical  
Troposphere and Stratosphere**



# Biennial, quasi-biennial, and decadal oscillations of potential vorticity in the northern stratosphere

Mark P. Baldwin and Timothy J. Dunkerton

Northwest Research Associates, Bellevue, Washington

**Abstract.** Seasonal and interannual variations of the northern hemisphere stratosphere on the 600 K isentropic surface (20–35 hPa) are investigated by using observations for 1964–1996. An area diagnostic is defined in terms of Ertel's potential vorticity (PV), which measures the area enclosed by PV contours as a function of equivalent latitude and is not tied to the spherical coordinate system. Data from all seasons are examined for oscillations with periods of 6 months to more than a decade. Spectral analysis of PV at equivalent latitudes from 20°N to the pole reveals several possible signals: (1) In addition to the well-known annual cycle of the polar vortex there is a striking semiannual oscillation of PV in middle equivalent latitudes. At 34°–53°N the semiannual oscillation is larger than the annual cycle. This oscillation arises from the formation of a surf zone in winter, due to planetary wave breaking, superposed on the annual cycle. (2) A signal associated with the quasi-biennial oscillation (QBO) of the equatorial stratosphere, with average period slightly less than 30 months, is strongest at low equivalent latitudes and is apparent in middle equivalent latitudes up to 67°N. Through interaction with the annual cycle, oscillations with periods of 20.2 and 8.5 months are generated. These three spectral peaks at approximately 30, 20, and 8.5 months have been observed in ozone and wind data and are seen here, for the first time, in PV. (3) At middle to high equivalent latitudes, on the other hand, we observe biennial and associated 8-month oscillations related to the occurrence of stratospheric warmings and strong, undisturbed vortices in midwinter to late winter. The data record is remarkable in that, at high equivalent latitudes, strong and weak polar vortices alternated from year to year, producing the biennial signal and a significant negative lag-1-year autocorrelation. The addition of an 8-month harmonic generates a much better fit to the sharp late winter anomalies. (4) South of 60°N a spectral peak at 10.6 years is observed, with the clearest signal near 20°N. This spectral peak may be caused by the solar cycle, or it may arise through interaction of biennial and quasi-biennial oscillations.

## 1. Introduction

On timescales ranging from intraseasonal to interannual the stratospheric polar vortex is influenced by several factors: e.g., the propagation and breakdown of planetary waves originating in the troposphere, low-frequency tropospheric circulation anomalies, the seasonal cycle of diabatic heating and cooling in the stratosphere, the equatorial quasi-biennial oscillation (QBO), volcanic eruptions, El Niño/Southern Oscillation (ENSO), and decadal variations possibly associated with the solar cycle.

A concise description of the stratospheric flow and its seasonal and interannual variability can be obtained in terms of Ertel's potential vorticity (PV). In this study, we use daily maps of PV on the 600 K isentropic surface to characterize the polar vortex and to examine the data for regular and nearly regular oscillations. PV is a quasi-conservative tracer of air motion along isentropic surfaces. Following McIntyre and Palmer

[1983, 1984], the high Richardson number approximation to Ertel's PV is used:

$$P = -g(\zeta + f)\partial\theta/\partial p$$

The relative vorticity,  $\zeta$ , is computed on constant pressure surfaces, and  $\partial\theta/\partial p$  is static stability. Hereafter,  $P$  is scaled by the climatological value of static stability (defined by using the lapse rate of the U.S. Standard Atmosphere, as in Dunkerton and Delisi [1986]), and has units  $s^{-1}$ .

McIntyre and Palmer [1983, 1984] showed that isentropic maps of Ertel's PV are a fundamental, simple, and useful way of viewing dynamical processes in the northern winter stratosphere. They showed that during winter the extratropical middle stratosphere can be divided into two regions, the "main vortex" and the "surf zone." The main vortex consists of a region of high PV inside a band of steep PV gradients, while the surrounding surf zone is characterized by relatively low PV and weak gradients.

Butchart and Remsberg [1986] showed that the seasonal evolution of the stratosphere could be visualized by plotting the fractional area of the hemisphere enclosed by PV contours. In effect, PV is rearranged to be zonally symmetric, and latitudinal variations of the vortex can be displayed as PV versus

equivalent latitude. Their "area diagnostic" concisely showed the evolution of the vortex/surf zone structure for the 1978–1979 winter. The area coordinate avoids the distraction of accounting for reversible wave-mean flow interactions when the polar vortex is temporarily displaced from the pole or distorted without changing size. Baldwin and Holton [1988] used the area diagnostic to examine the climatology and variability of the northern stratospheric vortex for 19 winters. Similar calculations during the initial period of the Upper Atmosphere Research Satellite (UARS) were reported by Zurek *et al.* [1996].

## 2. Data and Processing

Our data consist of daily National Centers for Environmental Prediction (NCEP, formerly the National Meteorological Center, or NMC) 1200 UTC heights and temperatures. For the period January 1, 1964 to September 23, 1978, these data are available north of 18°N at the levels 1000, 850, 700, 500, 400, 300, 250, 200, 150, 100, 70, 50, 30, and 10 hPa. After that date the coverage became global, and the levels 5, 2, and 1 hPa were added. The data set is archived on a  $5^\circ \times 4^\circ$  longitude/latitude grid for the period January 1, 1964 to May 11, 1996. For this study the period May 12, 1964 to May 11, 1996 was used. Discarding the initial period (January 1, 1964 to May 11, 1964) leaves exactly 32 years of data with endpoints in late spring. By using an even number of years one of the spectral frequencies (*viz.*, the sixteenth harmonic) corresponds to a period of exactly 2 years. The data were subject to quality control to remove erroneous grids. Single missing levels were vertically interpolated. All remaining missing data were linearly interpolated in time. Horizontal wind components were calculated by using the linear balance method [Robinson, 1986; Hitchman *et al.*, 1987; Randel, 1987].

Ertel's PV was then calculated on the 600 K potential temperature surface, typically found between 20 and 35 hPa, with lowest pressures occurring during the winter. The 600 K surface was chosen because it is near, but below, the 10 hPa uppermost data level for the early years. From daily maps of PV, Butchart and Remsberg's [1986] area diagnostic was calculated for the region including equivalent latitudes between 20°N and the pole. On each day the area diagnostic was computed by integrating the area inside PV contours, giving area as a function of PV value. This calculation is somewhat sensitive to the grid resolution of the data as well as the spacing of PV contours. To achieve sufficient accuracy, PV fields were interpolated, by using cubic splines, to a  $2^\circ \times 1^\circ$  longitude/latitude grid, and a spacing of  $2.5 \times 10^{-5} \text{ s}^{-1}$  was used (190 contour values). The PV data were transformed onto a grid of 66 evenly spaced points in  $\sin(\text{equivalent colatitude})$  from 0.0 to 0.65, corresponding to 90.0°–20.5°N. This latitudinal coordinate is linearly proportional to area on the sphere. The result of the transformation is an array of PV values on a grid of 11,688 days by 66 equivalent latitudes. All of the calculations are based on this equivalent latitude grid. For brevity we use "latitude" to refer to "equivalent latitude." Similarly, the "pole" refers to the "equivalent north pole." Subsequently, the data were 10-day low-pass filtered. Spectral calculations were performed by sampling time series every 5 days, and 50 points at the beginning and end of each time series were linearly tapered to zero. The results are insensitive to taper width, because the endpoints are in May, a time of small interannual variability in the northern stratosphere.

For time series analysis the QBO is represented by monthly means of Singapore zonal wind at 40 hPa. The solar cycle time series consists of observed monthly mean values of 10.7-cm solar flux, smoothed with a 13-month running mean.

## 3. Results

A climatology of the area diagnostic was constructed by averaging over each calendar day and then smoothing the daily average with a 90-day low-pass filter (this process is equivalent to keeping about four harmonics of the annual cycle). The filter cutoff was sharp enough so that periods of 6 months and longer were nearly unaffected by the smoothing. The smoothed climatology captures the essential features of an unsmoothed climatology while eliminating noise. Figure 1a shows the climatological average of the area diagnostic for 32 years of data on the 600 K surface. For clarity, two annual cycles are shown. The dominant feature is the polar vortex (shaded for values greater than  $1.3 \times 10^{-4} \text{ s}^{-1}$ ) which develops rapidly in autumn and, on average, dissipates even more quickly in spring. This climatology presents a picture consistent with the concepts of wave breaking and vortex/surf zone regions proposed by McIntyre and Palmer [1983, 1984]. In their conceptual model, breaking planetary waves erode the vortex at its periphery, stripping off high-PV air and irreversibly mixing it into the surrounding surf zone (which extends southward beyond the lowest latitudes shown here). This situation contrasts with that obtained from a zonally symmetric general circulation model of the middle atmosphere [Butchart and Remsberg, 1986, Figure 6] in which the evolution of the vortex is nearly symmetric about a midwinter PV maximum.

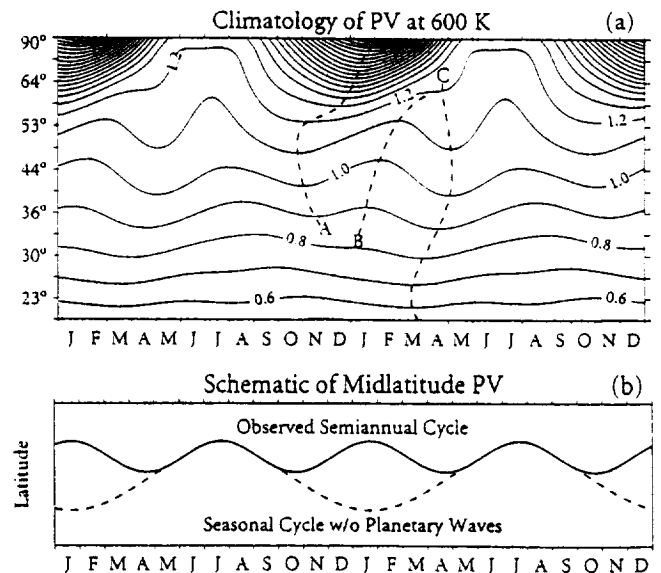


Figure 1. (a) The 32-year climatology of the potential vorticity area diagnostic on the 600 K isentropic surface, smoothed with 90-day low-pass filter. For clarity, two seasonal cycles are shown. The contour labels are scaled by  $1.0 \times 10^{-4} \text{ s}^{-1}$ . Values greater than  $1.3 \times 10^{-4} \text{ s}^{-1}$  are shaded. The heavy dashed lines A, B, and C follow local maxima and minima; see text for details. (b) Idealized schematic illustration of midlatitude PV contours. The solid curve represents the observed PV climatology, typical of the  $1.0 \times 10^{-4} \text{ s}^{-1}$  contour in Figure 1a. The dashed segments describe a hypothetical seasonal cycle in the absence of planetary waves.

Since the PV climatology is the average of discrete events that occur at different times for different years, the effect is to dull the distinction between the polar vortex and surrounding surf zone, but the basic features of PV evolution can be traced through the climatological seasonal cycle. In autumn, PV values increase at latitudes north of 30°N, consistent with Butchart and Remsberg's zonally symmetric model, which has virtually no annual cycle at 30°N. The increase of PV is halted in midlatitudes during late October and early November. Butchart and Remsberg's data for the 1978–1979 winter (their Figure 4) show essentially the same feature. During autumn, upward propagating planetary waves are not focused into the polar cap but begin to define the vortex edge at lower latitudes by mixing PV there, subsequently involving higher PV contours at higher latitudes as the winter season progresses. Figure 4 of Butchart and Remsberg [1986] clearly shows how, during late autumn, the outer edge of the region of tight PV gradients initially defines the vortex boundary at low latitudes and the boundary is found at successively higher values of PV at later times. At the edge of the shaded region the vortex has already begun shrinking during December, but at the center of the vortex the highest PV values are not attained until early February.

In Figure 1a the heavy dashed line A traces the time at which PV values stop increasing at each equivalent latitude. The region between lines A and B defines the period in which midlatitude PV decreases with time. This process may be seen as a tightening of PV gradients at the vortex edge in Butchart and Remsberg's data for the 1978–1979 winter and in other years shown by Baldwin and Holton [1988]. In midlatitudes the process of wave breaking and vortex erosion substantially alters the predominantly annual cycle that would be observed in a zonally symmetric atmosphere. Butchart and Remsberg's [1986] Figure 7 illustrates the mean PV value between 20°N and the pole for both the real atmosphere and a zonally symmetric model. They concluded that the effect of planetary waves is to reduce the average PV north of 20°N after the vortex is established in autumn. In individual years this process is not necessarily continuous, as is implied by the climatology, but intermittent. Each wave breaking episode reduces the average PV, presumably by mixing with the region south of 20°N. Diabatic effects attempt to restore the PV distribution to an undisturbed state. Potential vorticity increases with time between B and C, and at lower latitudes the very gradual increase of PV beginning in autumn ends along line C.

The entire region between lines A and C may be interpreted as an effect of breaking planetary waves which act initially to reduce PV values during the erosion process. Before and after this period the midlatitude region is much closer to an axisymmetric structure simulated in the absence of planetary waves. A striking result of the erosion process may be seen near 45°N on the  $1.0 \times 10^{-4} \text{ s}^{-1}$  contour. Instead of an annual cycle in PV, the dominant component is a semiannual cycle, produced by the signature of vortex erosion superposed on the annual cycle. This concept is illustrated schematically in Figure 1b, showing the observed semiannual cycle of the  $1.0 \times 10^{-4} \text{ s}^{-1}$  contour from Figure 1a and an annual cycle that would presumably occur in the absence of waves. In this schematic, formation of the surf zone decreases PV values during midwinter. Outside this time period the distribution of PV is near its undisturbed state. We note, however, that in Figure 1a the timing of largest deviation from an annual cycle depends on latitude,

with maximum deviations occurring later for higher PV contours.

The effect of planetary waves is not restricted to surf zone breaking and erosion, since the dynamical transport of these waves also maintains a departure from radiative equilibrium at the winter pole and induces a mean meridional circulation of global scale. Such effects are implicit in the temporal evolution of potential vorticity, but a detailed analysis of the PV balance is beyond the scope of this paper. One feature, highlighted in a recent paper by Dunkerton and O'Sullivan [1996], is the formation of a detached subtropical jet in late northern winter. This feature is evident in Figure 1a as a band of enhanced PV gradient, which might otherwise be interpreted as a region of suppressed lateral mixing. Although mixing is indeed suppressed here, the formation of the jet in the first place involves westerly accelerations that cannot be attributed solely to Rossby wave drag.

Time series of the area diagnostic at each equivalent latitude were examined for regular or quasi-regular oscillations. Potential vorticity time series at representative latitudes are shown in Figure 2. For clarity the time series were 90-day low-pass filtered and deseasoned (by subtracting the climatology). Deviations north of 62°N are much larger than those to the south. The largest deviations at northern latitudes occur during winter and early spring (the vertical lines indicate each January 1). Large positive and negative deviations are common. Low wintertime PV values in high latitudes tend to be mirrored as high values at lower latitudes (e.g., January 1969) and vice versa (e.g., January 1996). At low latitudes after 1980 the QBO is easily seen.

Figure 3 illustrates the resulting power spectrum at 17 equivalent latitudes (every fourth value) for periods of 5 months and greater. For this calculation the data were 10-day low-pass filtered but not deseasoned, and for clarity, individual spectra were normalized to the same maximum value. At high latitudes the annual cycle of the polar vortex is dominant and can be seen at other latitudes as well. There is, however, a minimum near 40°–50°N where the annual cycle is small. As suggested by Figure 1, the semiannual period dominates in midlatitudes. Note that the spectral power is not concentrated at exactly 12 and 6 months but also involves adjacent spectral points (e.g., 11.6 and 12.4 months). The addition of adjacent harmonics allows for low-frequency modulation of the annual and semiannual cycles. At the lowest latitudes a 29.5-month (QBO period) oscillation has more spectral power than either the annual or semiannual cycles.

To examine the data for oscillations other than the large annual and semiannual cycles, the climatology shown in Figure 1a was subtracted from the daily values of area diagnostic. By removing the annual cycle, spectral power at 12- and 6-month periods is reduced to near zero. However, moderate spectral power can remain at periods very close to the annual cycle. To eliminate the annual spectral band in its entirety, the data were notch filtered at 11–13 months by using a narrow band-pass filter. As is shown in Figure 4, most of the remaining spectral power is found at frequencies associated with a biennial oscillation, the QBO, and a decadal oscillation. Each of these oscillations and the associated spectral peaks is discussed below.

### 3.1. Quasi-Biennial Oscillation and Related Harmonics

As was noted by Gray and Dunkerton [1990], the interaction of the annual and QBO frequencies can generate new har-

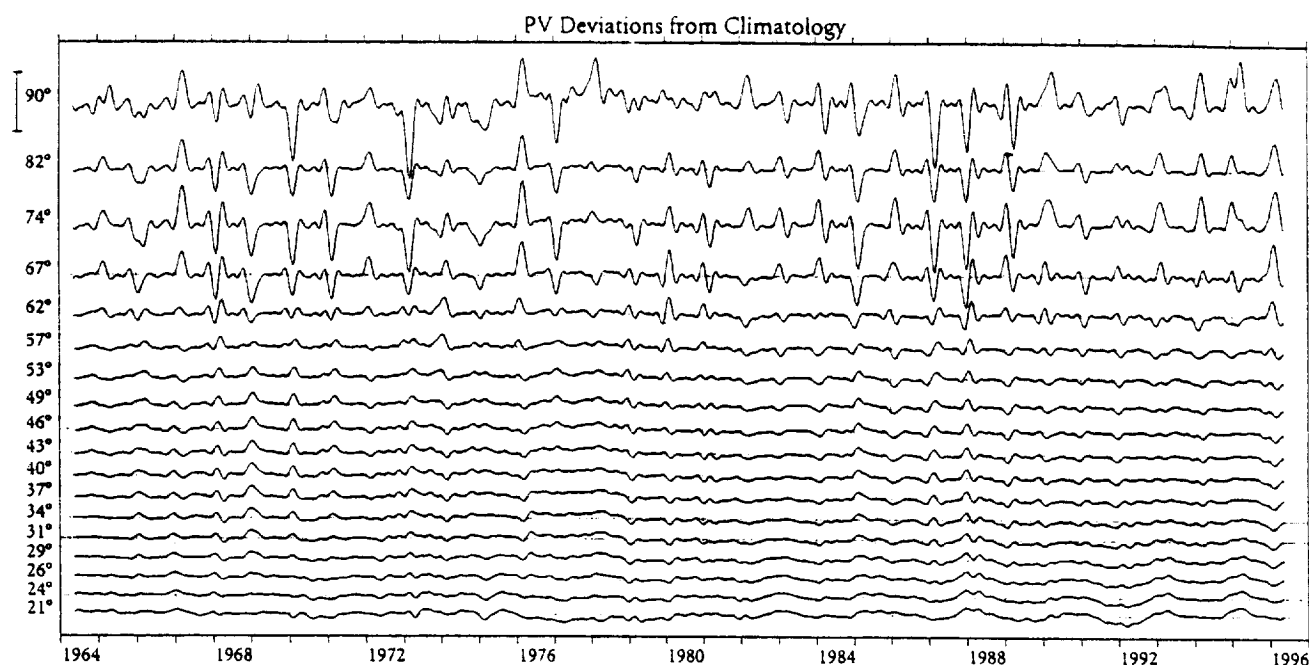


Figure 2. Time series of PV at equivalent latitudes from 21° to 90°N. The data were deseasoned by subtracting the climatology of Figure 1a and were smoothed with a 90-day low-pass filter. The vertical axis is linear in  $\sin(\text{equivalent colatitude})$  and the vertical scale is the same for all equivalent latitudes. The scale bar at the left edge of the figure indicates a range of  $1.0 \times 10^{-4} \text{ s}^{-1}$ .

monics with frequencies equal to their sum or difference. In spectra of ozone [Tung and Yang, 1994a], angular momentum, and Eliassen-Palm (EP) flux divergence [Baldwin and Tung, 1994] the QBO was found to exhibit a three-peak (~30-, 20-, and 8.6-month periods) spectrum through its interaction with the annual cycle.

The period of the QBO varies, averaging 28.7 months during 1964–1995. The best fit to the Singapore 40-hPa wind is obtained with a 28.7-month harmonic (yielding a correlation of 0.71). However, no single harmonic can fit the QBO's variable period. In a 32-year data set the closest discrete harmonics to the QBO are at 32.0, 29.5, and 27.4 months. The power spectrum of Singapore 40-hPa zonal wind is shown in Figure 6a and is essentially the same as that shown by Tung and Yang [1994a] for Singapore 30-hPa wind. There is modest power at 32 months, with a peak at 29.5, and nearly as much power at 27.4 months.

In Figure 4 the three-peak spectrum of the QBO can be seen in potential vorticity. The 29.5-month peak is clearly visible at most latitudes south of 67°N but is weak at the pole. The 20.2-month peak is evident south of 53°N, and the 8.5-month peak is present between 57° and 67°N.

A complementary view of the spectral peaks is obtained by correlating the PV area diagnostic at each equivalent latitude with best fit harmonics having periods identical to those used in the spectral analysis. Each best fit harmonic is obtained by retaining only a single sinusoidal harmonic (e.g., 24 months) from the PV data at each equivalent latitude. Figure 5 illustrates these correlations, which tend to accent regions of low total variance (e.g., low latitudes) while suppressing regions of high variance such as the north pole. The 29.5- and 20.2-month peaks are clearly visible, while an 8.5-month correlation is present but not well defined. This diagram reinforces

the view obtained from spectral analysis. In general, correlations greater than 0.10 seem to correspond to the spectral peaks visible in Figure 4. Peak correlations south of 30°N for the 29.5-month harmonic exceed 0.45, while correlations above 0.10 extend north to 67°N. The latitudinal extent of the 20.2-month harmonic in Figure 5 is similar to that of the spectra in Figure 4; there is a band of correlations greater than 0.10 extending over the subtropics and midlatitudes. Correlations with the 8.5-month harmonic exceed 0.10 only near 65°–75°N. The latitudes of maximum 29.5- and 20.2-month correlation are similar, while the 8.5-month correlation is observed only in the northernmost range of the 29.5-month harmonic. Thus the regions affected by the 20.2- and 8.5-month oscillations are distinct in the correlation plot.

To explore further the 29.5- and 20.2-month oscillations, the time series at 23°N was filtered to include only the QBO frequency band. The data were reconstructed with a narrow 1-2-1 band-pass filter, retaining the central harmonic (in this case, 29.5 months) plus half the adjacent harmonics (32.0 and 27.4 months). Figure 6b illustrates these narrow band-pass data in comparison with 90-day low-pass-filtered, deseasoned data and monthly mean Singapore 40-hPa zonal wind. The inclusion of harmonics adjacent to 29.5 months allows some variation of the amplitude of the signal, with the greatest amplitude obtained during the 1980s. Comparison of the data with the reconstructed (gray) curve shows that the best fit is obtained during the later years. The poor fit in early years results from the variable period of the QBO and the smaller amplitude of the QBO resolved by NCEP data during this time. Until about 1980 the amplitude of the QBO in PV is small but discernible. In the second half of the data set it is prominent. The change in character of the data coincides with the use of satellites for operational NCEP data in the late 1970s. Com-



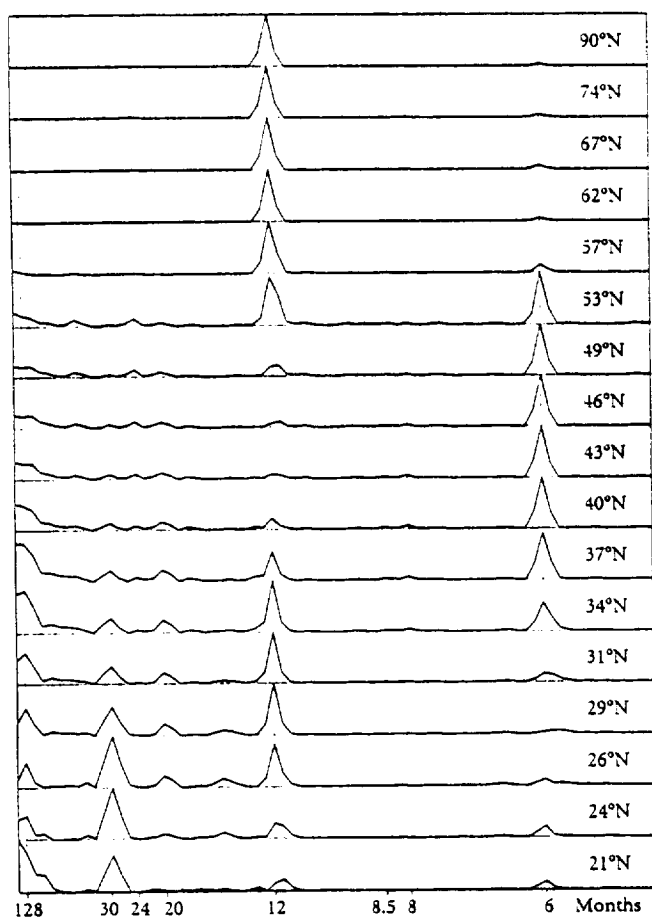


Figure 3. Power spectra of PV at equivalent latitudes from 21° to 90°N. Vertical gray lines indicate 128-, 29.5-, 24.0-, 20.2-, 8.53-, 8.0-, and 6.0-month periods. The vertical scale for each time was adjusted so that the maximum value at each latitude is the same.

paring the Singapore 40-hPa wind to the PV data shows a reasonable match of maxima and minima (the correlation between Singapore wind and PV at 23°N is 0.46 for the first 16 years and 0.60 for the second 16 years). The gray curve superposed on the Singapore wind is a reconstruction of the Singapore wind using a 1-2-1 filter centered on 29.5 months. The reconstruction does not provide a good fit during all years because the period of the reconstructed curve is so narrowly defined. The poor fit during early years can also be traced to 1972–1976 when the QBO period was 24 months.

In Figure 6c the solid curve is a reconstruction using the same method as that in Figure 6b, except that the 20.2-month band is added (again using 1-2-1 weighting surrounding the central harmonic). The correlation is increased only modestly from 0.65 to 0.70. In Figure 6d an improved fit has been obtained by dividing the record into two parts, retaining the 30- and 20.2-month spectral bands. The correlations for the respective periods are 0.46 and 0.73.

### 3.2. Biennial Oscillation and Related Harmonics

A spectral peak at 24 months is prominent in the power spectra (Figure 4) north of 66°N and also from 37° to 57°N. This peak is negligible at intermediate latitudes with a node at 62°N. Correlations of best fit harmonics with the data (Figure

5) show values of at least 0.10 over the entire range of latitudes except for a minimum near 62°N. A purely biennial oscillation, when modulated by the annual cycle, is expected to produce a third oscillation with a period of 8 months, in a manner similar to the three-peak QBO. In Figure 5 the 8-month spectral peak is pronounced only between 53° and 67°N and appears weakly in midlatitudes. A biennial oscillation was noted in singular spectrum analysis of the first (latitude-height) empirical orthogonal function (EOF) of northern hemisphere stratospheric temperature by Dunkerton and Baldwin [1992], while Salby [1995] and Salby *et al.* [1997] found a biennial spectral peak in 30-hPa north polar temperatures.

To examine the fit of a 24-month oscillation to high-latitude PV, data at 79°N were reconstructed by using the method in Figure 6, but with harmonics centered at 24 months (Figure 7a). The deseasoned PV shows only modest deviations from climatology except during the time period late December through April. The large deviations may be either positive (representing exceptionally strong vortices in cold, undisturbed years) or negative (representing major warmings). Examining these late winter anomalies in all years reveals that many of the spikes align with the reconstructed curve (gray line), especially in 1971–1991. The earlier and later years tend neither to contribute to this effect nor to oppose it. The reconstructed curve reflects this tendency, with a larger amplitude during the middle years. On average, the extrema in the

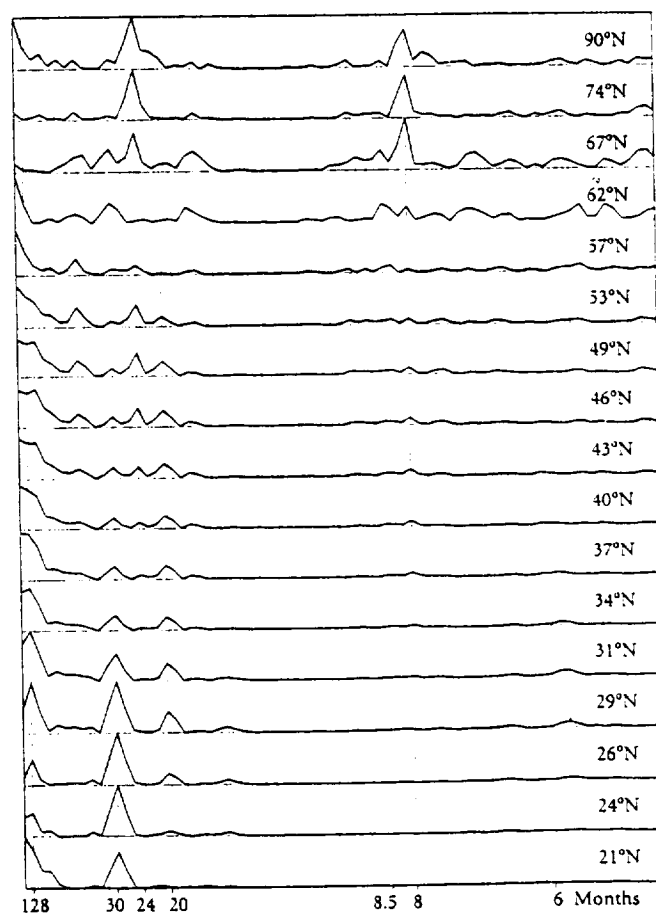


Figure 4. As in Figure 3, but for deseasoned data obtained by subtracting the climatology of Figure 1a and notch filtered to remove the 11- to 13-month band.

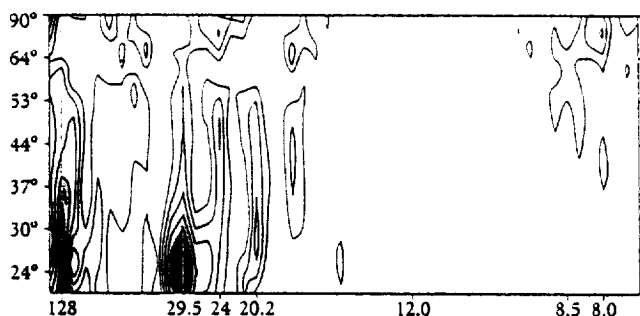


Figure 5. Correlation between PV time series and best fit harmonics. For each period the best fit harmonics are calculated by using a single sinusoidal harmonic that retains only that period (e.g., 24 months). The contour interval is 0.1, and the minimum contour is 0.1. Prior to the calculation, PV data at each equivalent latitude were deseasoned (by subtracting the climatology) and smoothed with a 10-day low-pass filter.

reconstructed curve are located in late February, coinciding with the maximum climatological variance in PV (not shown). The correlation between the reconstructed curve and the 90-day low-pass-filtered data is 0.33.

At high latitudes in Figures 4 and 5, both 24- and 8-month peaks are prominent. Figure 7b shows a reconstruction of the data at 79°N using both 24- and 8-month oscillations. The amplitude and phase of the 8-month oscillation are such that the 8-month harmonic adds constructively to the 24-month extrema and sharpens the fit to the late winter anomalies. The correlation with the data improves from 0.33 to 0.45 with the addition of the 8-month harmonic.

Since the biennial oscillation is nearly as prominent in midlatitudes, the same curve fit was performed for data at 48°N (Figure 7c). Here the amplitude of PV anomalies is much smaller (the vertical scale in Figure 7c is only 15% of that in Figure 7b), and late winter anomalies are less distinct. There are several years in which the sign of the anomaly does not change sign from the previous year. However, during each year the midlatitude anomalies tend to be of opposite sign to the polar anomalies. The correlation between time series at 48°N and 79°N is -0.56. The reconstructed curve in Figure 7c is almost exactly out of phase with that of Figure 7a. The negative correlation between high latitudes and midlatitudes represents a compensating effect consistent with McIntyre and Palmer's vortex/surf zone conceptual model as well as Butchart and Remsberg's observation that as high-PV air is mixed out of the vortex, PV values in the surf zone increase.

To isolate the nature and timing of the biennial signal, PV data for the north pole were high-pass filtered to remove low-frequency variability with timescales longer than the QBO and smoothed with a 3-month running mean. Figure 8a shows the resulting time series, with vertical lines on each January 1. Although some winter/spring periods have both positive and negative anomalies (which tend to cancel), typically each period can be represented by the 90-day mean centered on March 1. Not all winters match the alternating biennial pattern, but most of the large anomalies fit a pattern of strong vortices during even years and weak vortices during odd years. Of the 26 winters displaying a large PV anomaly in excess of about  $2 \times 10^{-5}$  in Figure 7a, most even years contained a large positive anomaly (strong vortex) in midwinter or late winter,

while most odd years contained a large negative anomaly (weak vortex) in midwinter or late winter.

To illustrate the importance of late winter anomalies, the PV values from Figure 8a (90-day means centered on March 1) were used to construct annual spikes with 90-day width centered on March 1 (Figure 8b). Data outside each 90-day interval were set to zero. The resulting power spectrum (Figure 8c) shows pronounced 24- and 8-month peaks and looks very similar to the 90°N panel in Figure 4. Smaller spectral peaks

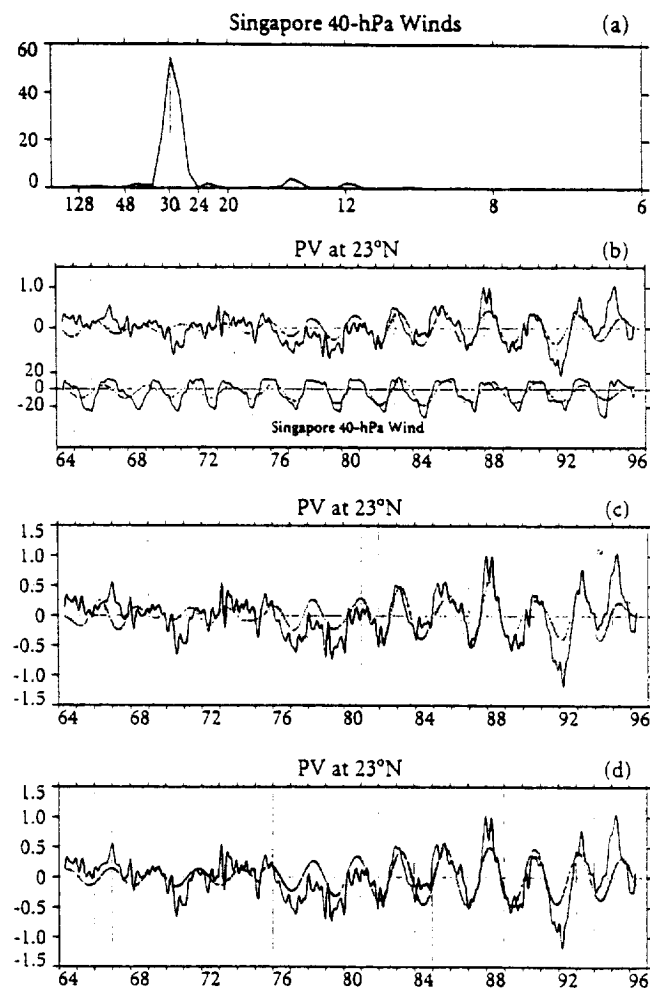


Figure 6. (a) Power spectrum of monthly mean Singapore 40-hPa wind. The vertical gray line indicates a 29.5-month period. (b) The 90-day low-pass filtered PV at 23°N (solid line) and reconstruction of the data using a 1-2-1 weighted spectral band centered on the 29.5-month harmonic (gray line). The vertical gray lines indicate January 1 of each year (1964-1996). The PV labels on the vertical axis are scaled by  $10^5$ . The correlation coefficient between the two series is 0.65. The lower curve is the observed monthly mean Singapore 40-hPa wind, and the gray curve is a reconstruction using a 1-2-1 weighted spectral band centered on the 29.5-month harmonic. (c) The 90-day low-pass filtered PV at 23°N (solid line) and reconstruction of the data using 1-2-1 weighted spectral bands centered on both 29.5- and 20.2-month harmonics (gray line). The labels on the vertical axis are scaled by  $10^5$ . The correlation is 0.70. (d) As is Figure 6c, but with reconstructions performed separately for 1964-1975 and 1975-1996. The correlations for the respective periods are 0.46 and 0.73.

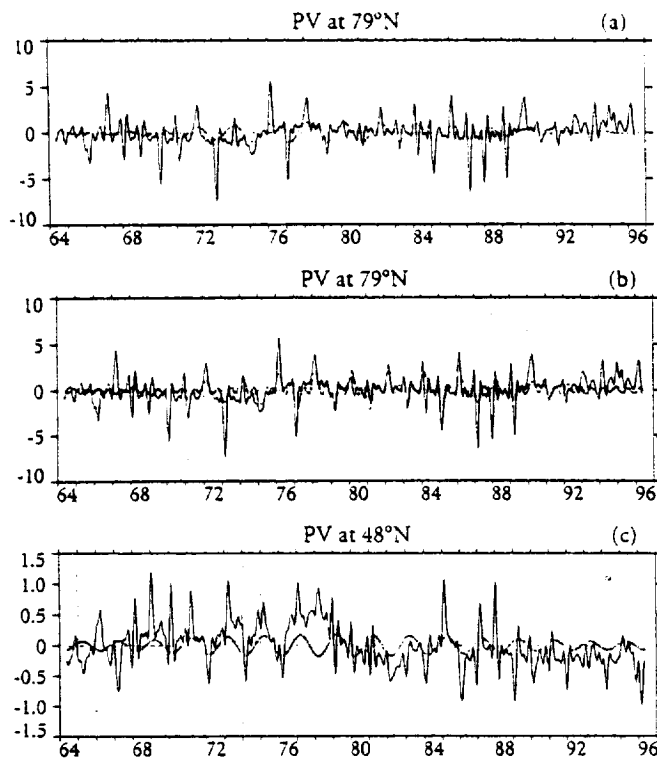


Figure 7. (a) The 90-day low-pass PV at 79°N (solid line) and reconstruction using a single 1-2-1 weighted spectral band centered on the 24-month harmonic (gray line). The vertical lines indicate January 1 of each year (1964–1996). The labels on the vertical axis are scaled by  $10^5$ . The correlation coefficient between the two series is 0.33. (b) As in Figure 7a, but with 8.0-month band included. The correlation is 0.45. (c) As in Figure 7a except at 48°N. The correlation coefficient is 0.24.

associated with the QBO (29.5, 20.2, and 8.5 months) are also evident, and the spectrum is symmetric about 12 months.

How unusual is the biennial spectral peak seen in the high-latitude PV data? To estimate the probability of the biennial oscillation occurring by chance, we first created, for each equivalent latitude, a time series of 3-month running means centered on March 1. From these time series we obtained values of the biennial spectral power at each equivalent latitude. We then performed two Monte Carlo tests. In the first test we assumed that the annual observations are independent, and we simulated the time series with random normal deviates. Using 10,000 time series, we obtained a distribution of biennial spectral power that can be expected if the annually sampled data are independent. We found that the biennial spectral peak observed for equivalent latitudes 68°–74°N can be expected by chance less than 1% of the time.

However, the data are not independent. The lag-1-year autocorrelation of the PV data within the polar cap is negative, ranging from -0.22 to -0.37. We performed a Monte Carlo test similar to that described above, but we constrained the random time series to have a lag-one-year autocorrelation between -0.25 and -0.35. With this constraint it is easier to obtain strong biennial variability; the biennial spectral peak between 67° and 76°N can be expected by chance less than 5% of the time.

A strong autocorrelation is a necessary, but not sufficient, condition to produce a biennial spectral peak. For example, a

very high autocorrelation would result from an alternating pattern in 16 winters, skipping one winter, then alternating in 15 winters again. Because the phase of the biennial oscillation in this hypothetical example switches sign in the center of the time series, the biennial power is near zero when calculated over the entire record at once, but the lag-1-year autocorrelation remains significantly negative. Since there is nothing special about even or odd years as far as the atmosphere is concerned, the more significant aspect of our north polar obser-

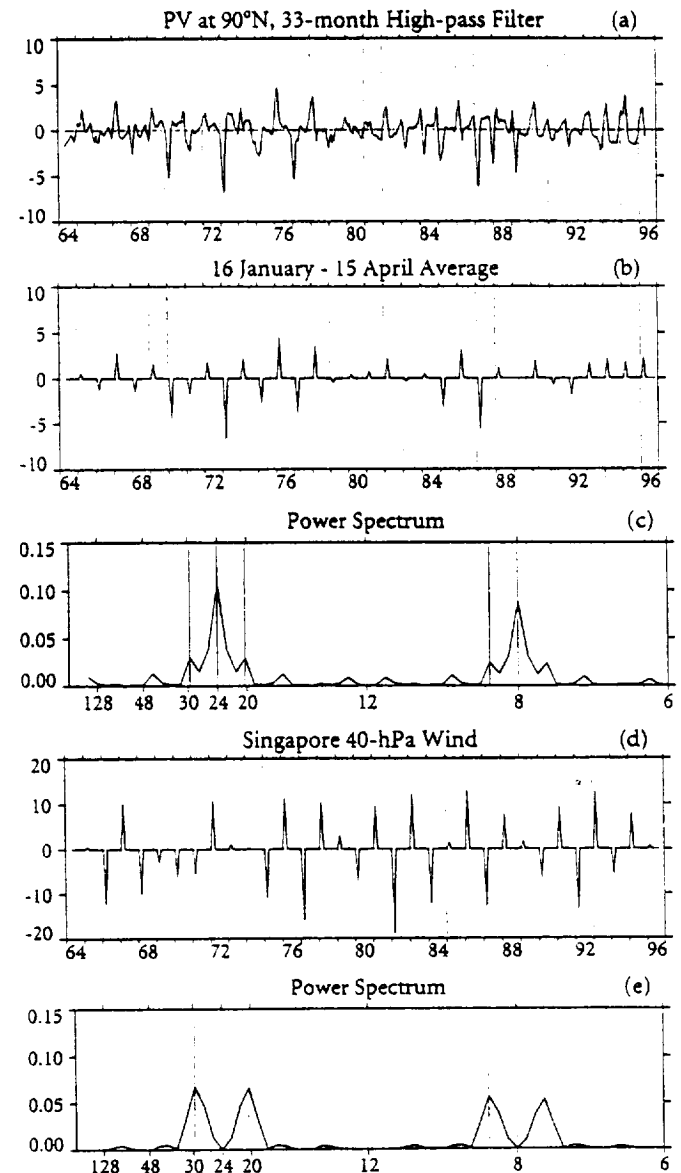


Figure 8. (a) PV time series at 90°N equivalent latitude, high-pass filtered to include periods of less than 33 months and smoothed with a 3-month running mean. The vertical lines indicate January 1 of each year (1964–1996). Labels on the vertical axis are scaled by  $10^5$ . (b) The value on each March 1 (January 16 to April 15 average) taken from Figure 8a, defining a 90-day spike. Data are set to zero at all other times. (c) Power spectrum obtained from north polar PV in Figure 8b. The time series was normalized to unit variance. (d) As in Figure 8b, but with data values taken from a 90-day running mean of Singapore 40-hPa wind centered on March 1. (e) Power spectrum obtained from annually sampled Singapore wind in Figure 8d.

variations is the large negative lag-1-year autocorrelation and accompanying tendency for vortex anomalies to alternate sign from one year to the next. This behavior can produce biennial power during relatively short time periods.

If we substitute the spikes in Figure 8b with 90-day running mean Singapore 40-hPa wind data (sampled on March 1) and repeat the analysis, the spectral signature shows only peaks on either side of 24 and 8 months (Figures 8d and 8e); biennial power is negligible. Evidently, something in addition to the equatorial QBO is responsible for PV variability in late winter at high latitudes. Since we are not aware of any mechanism that could link even-numbered years decades apart, we cannot rule out the possibility that the persistence of the biennial signal is largely due to chance and that it is a feature of this particular data record. It was shown by Dunkerton and Baldwin [1992] that in February the north polar temperature in the lower stratosphere is correlated not with the QBO per se, but with a modulated signal consisting of the product of a decadal time series and sign of the QBO (Labitzke and van Loon, 1988). The influence of the QBO on north polar temperature in late winter varies on a decadal timescale. It was also shown empirically by Dunkerton and Baldwin [1992] that a biennial time series, acting in combination with quasi-biennial variations, could produce the observed decadal modulation.

### 3.3. Decadal Oscillation

At latitudes south of 60°N in Figure 4 a spectral peak centered broadly on 128 months (10.6 years) emerges, suggestive of the 11-year solar cycle. A solar cycle signal in the stratosphere would be expected at low, rather than high, latitudes as a result of solar heating effects. Van Loon and Labitzke [1990] found that midlatitude to low-latitude geopotential variability at 30 hPa correlated well with the solar cycle during all months of the year. The relationship between PV at 20°N and the observed 10.7 cm solar flux is shown in Figure 9a. The correlation of PV data with the solar flux is -0.24 and is compromised somewhat by the large-amplitude QBO in the second half of the data. A slightly better correlation (-0.35) is obtained if the PV data are lagged by 1 year. The lower solid curve in Figure 9a is a reconstruction using the 128-month band, yielding a correlation of 0.52. Although low-latitude PV varies on a decadal timescale, its relation to the solar cycle is less convincing, especially considering that the data record includes only three solar cycles.

Figure 9b shows the power spectrum of the solar 10.7-cm flux time series. Although a spectral peak appears at 128 months, there is considerable power at adjacent periods (192 and 96 months). This spectrum looks similar to that of PV at latitudes south of 35°N (Figure 4).

As an alternative to the solar cycle hypothesis we note the possibility that the observed 128-month spectral peak may be the result of interaction between quasi-biennial and biennial oscillations, in the same way that an annually modulated QBO produces 20.2- and 8.6-month peaks. For a "QBO  $\times$  biennial" oscillation, the resulting spectral peaks occur at 128 and 13 months. Figure 9c illustrates the power spectrum resulting from the QBO (reconstructed by using a 1-2-1 weighting of the frequencies centered on 29.5 months) multiplied by a purely biennial sinusoidal harmonic. The power spectrum shows peaks at both 13 and 128 months. In the data a 13-month peak would be difficult to extract, since it would probably be weak in comparison with the annual cycle.

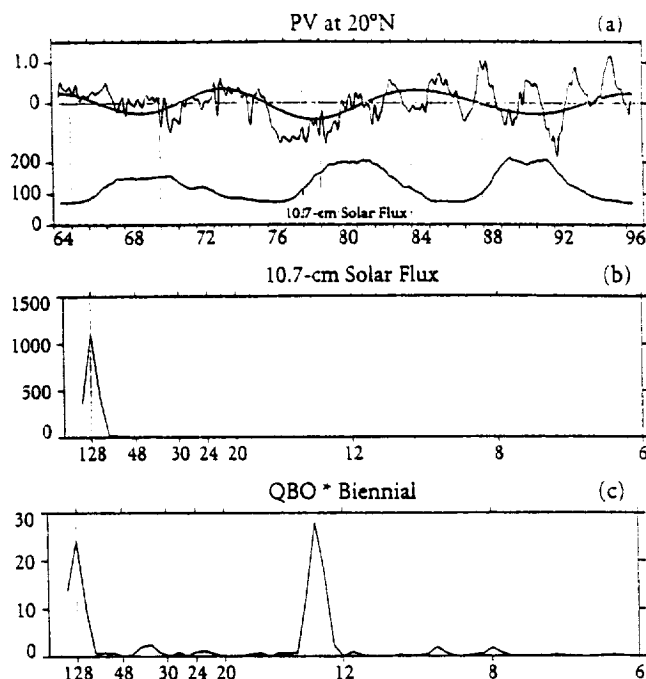


Figure 9. (a) The 90-day low-pass filtered PV at 20°N (solid line) and reconstruction of the data using a 1-2-1 weighted spectral band centered on the 128.5-month harmonic (gray curve). The vertical lines indicate January 1 of each year (1964–1996). Labels on the vertical axis are scaled by  $10^3$ . The correlation coefficient between the two series is 0.65. The lower curve is a 13-month running mean of observed 10.7-cm solar flux. (b) Power spectrum of solar flux. (c) Power spectrum of the product of a biennial sinusoid and observed quasi-biennial signals.

If the 128-month peak results from interaction between the QBO and biennial components, one might expect the decadal variation to be found where both the QBO and biennial components are seen. Figure 6 shows that this is generally true. The QBO is visible from 20° to 67°N, while the biennial component is seen from 20° to 58°N and again north of 64°N. The location and size of the correlations for the 128-month harmonic are similar to those of the QBO. The 24-month harmonic overlaps this latitudinal band but is strongest in mid-latitudes and high latitudes.

## 4. Conclusion

Spectral and correlation analysis of a PV area diagnostic for 32 years of data on the 600 K isentropic surface reveal annual and semiannual cycles, a biennial oscillation, a quasi-biennial oscillation, and a decadal oscillation similar to the solar cycle. Additional harmonics result from modulation of biennial and quasi-biennial oscillations by the annual cycle. It is remarkable that the data show few other spectral peaks or noise. The PV-area diagnostic provides a powerful tool, averaging data along PV contours rather than latitude circles. As was shown by Butchart and Remsberg [1986], a clearer picture of the dynamics is obtained.

At high latitudes the annual cycle is the dominant mode of variability, representing the annual formation and dissipation of the polar vortex. In midlatitudes a semiannual oscillation is more pronounced. The semiannual oscillation arises from the

formation and dissipation of a vortex/surf zone structure, superposed on the annual cycle. This process, due to breaking planetary waves, causes a wintertime reversal of the formation of moderately high PV that would be expected in the absence of planetary waves and their attendant erosion of the polar vortex. Although a double annual temperature maximum has been observed, due to summer solar heating and winter wave driving of poleward and downward flow, this is the first observation of a semiannual cycle in PV.

Extratropical effects of the equatorial QBO have been observed [Holton and Tan, 1980, 1982; Dunkerton and Baldwin, 1991; Baldwin and Dunkerton, 1991] and modeled [O'Sullivan and Dunkerton, 1994] to occur during the extended winter season. A preference for winter is consistent with the hypothesis that quasi-stationary planetary waves, which propagate vertically only at this time of year, are essential to the QBO's influence on the polar vortex. As a result the QBO signal in extratropical latitudes is modulated by the annual cycle to produce 20-month and 8.5-month harmonics, as found by Tung and Yang [1994a, b] and Baldwin and Tung [1994] who observed a three-peak QBO spectrum in ozone and angular momentum, respectively, using data from all seasons. Seasonal synchronization is also observed in the subtropical ozone QBO, as was noted by Gray and Dunkerton [1990] and others. Our PV area diagnostic confirms the three-peak QBO signature for the region outside the polar vortex. The QBO is seen up to approximately 67°N, but only weakly at the pole, possibly as a result of the large variance there. A related 20.2-month signal is also seen over nearly the same latitudes, while an 8.5-month signal is observed only in the range 57°–67°N. At low latitudes the QBO spectral peak is stronger than the annual cycle.

The existence of a biennial polar oscillation is not well documented but has been noted in an EOF analysis of zonal mean stratospheric temperature by Dunkerton and Baldwin [1992] and in north pole temperature by Salby [1995] and Salby *et al.* [1997]. A biennial oscillation of PV is found at high latitudes and in midlatitudes with opposite phase. An 8-month oscillation is seen at similar latitudes, generated through interaction of 24- and 12-month signals. These spectral peaks describe well the late winter anomalies of PV, representing the signatures of major warmings and, in the opposite sense, strong vortices in cold, undisturbed winters.

The interannual variability of PV in the polar cap is well represented by 3-month means centered on March 1. If the 32 years of observations are assumed to be independent, the biennial spectral peak can be expected to occur by chance less than 1% of the time. However, the state of the polar vortex does not appear to be independent of the previous year's state. The lag-1-year autocorrelation within the polar vortex is near -0.3 and likely reflects the influence of the QBO, which usually changes sign from year to year. If the lag-1-year autocorrelation is assumed to be -0.3, the probability of obtaining the observed biennial spectral peak is slightly less than 5% within the polar cap. Beyond the influence of the QBO, which is incapable of generating a purely biennial signal, there exists the possibility that the subtropical flow anomalies persist long enough to influence the formation of the polar vortex during the following autumn and winter.

An intriguing possibility for the maintenance of a biennial signal was suggested recently by R.K. Scott and P.H. Haynes (Internal variability of the extratropical stratospheric circula-

tion: The interannual flywheel, submitted to *Quarterly Journal of the Royal Meteorological Society*, 1997). In a mechanistic primitive equation model of the stratosphere they note the possibility that zonal wind anomalies in the subtropics can persist through the summer and affect the formation of the polar vortex during the following autumn, in a manner similar to the extratropical influence of the QBO. In their model a biennial oscillation is observed, even with no interannual variability in wave forcing or imposed QBO. In preliminary calculations with observational data we find that at low latitudes to midlatitudes, 600-K PV during the summer and autumn is positively correlated with values from the previous winter, consistent with the idea that winter anomalies may persist long enough to affect the development of the vortex during the following autumn and winter. However, the effect is difficult to distinguish from that of the QBO.

Finally, a decadal spectral peak is apparent, especially at low latitudes, where stratospheric ozone heating is modulated by the solar cycle [Haigh, 1996]. The observed 128-month component of PV at 20°N shows reasonable agreement with the solar 10.7-cm flux time series; a better fit is obtained when the solar cycle leads the data by almost 1 year. An alternative explanation for the 128-month oscillation is that it arises through interaction of QBO and biennial modes. Such an interaction can produce spectral power at 128 months. The latitudes at which the quasi-biennial, biennial, and decadal oscillations occur are similar, although biennial power is found mainly at mid- to high latitudes. By similar reasoning a biennial signal can be produced through interaction of quasi-biennial and decadal signals.

This study was conducted by using operational NCEP analyses. There have been numerous changes over the decades in the quantity of input data and analysis schemes. In recognition of these inconsistencies the NCEP data are now being reanalyzed with a single, consistent method. The use of the reanalyzed data could significantly affect some of the results shown here, for example, the magnitude of a low-latitude QBO signal, which is clear only after satellite observations began during the 1970s. It is also possible that some of the observed low-frequency variability at all latitudes originates from changes in the input data (depending, for example, on whether satellite data were available) and analysis scheme. Further investigation of interannual variability in the reanalyzed data is therefore desirable.

The present study did not address possible tropospheric forcing. Baldwin *et al.* [1994] found that a tropospheric mode related to the North Atlantic Oscillation was strongly linked to stratospheric wind and geopotential. In preliminary work we find that a similar tropospheric mode can account for much of the polar variability after the regular oscillations have been removed. However, this mode does not exhibit a biennial spectral peak, and further study is warranted.

**Acknowledgments.** We thank Steve Pawson for helpful comments on the manuscript. This research was supported by the National Science Foundation, grants ATM-9303068, ATM-9405448, ATM-9500613, and ATM-9708026, and by the National Aeronautics and Space Administration, contract NASW-4844.

## References

- Baldwin, M.P., and T.J. Dunkerton, Quasi-biennial oscillation above 10 mb, *Geophys. Res. Lett.*, 18, 1205–1208, 1991.
- Baldwin, M.P., and J.R. Holton, Climatology of the stratospheric polar

- vortex and planetary wave breaking, *J. Atmos. Sci.*, 45, 1123–1142, 1988.
- Baldwin, M.P., and K.-K. Tung, Extra-tropical QBO signals in angular momentum and wave forcing, *Geophys. Res. Lett.*, 21, 2717–2720, 1994.
- Baldwin, M.P., X. Cheng, and T.J. Dunkerton, Observed correlation between winter-mean tropospheric and stratospheric anomalies, *Geophys. Res. Lett.*, 21, 114–1144, 1994.
- Butchart, N., and E.E. Remsberg, The area of the stratospheric polar vortex as a diagnostic for tracer transport on an isentropic surface, *J. Atmos. Sci.*, 43, 1319–1339, 1986.
- Dunkerton, T.J., and M.P. Baldwin, Quasi-biennial modulation of planetary-wave fluxes in the Northern Hemisphere winter, *J. Atmos. Sci.*, 48, 1043–1061, 1991.
- Dunkerton, T.J., and M.P. Baldwin, Modes of interannual variability in the stratosphere, *Geophys. Res. Lett.*, 19, 49–52, 1992.
- Dunkerton, T.J., and D.P. Delisi, Evolution of potential vorticity in the winter stratosphere of January–February 1979, *J. Geophys. Res.*, 91, 1199–1208, 1986.
- Dunkerton, T.J., and D.J. O'Sullivan, Mixing zone in the tropical stratosphere above 10 mb, *Geophys. Res. Lett.*, 23, 2497–2500, 1996.
- Gray, L.J., and T.J. Dunkerton, The role of the seasonal cycle in the quasi-biennial oscillation of ozone, *J. Atmos. Sci.*, 47, 2429–2452, 1990.
- Haigh, J.D., The impact of solar variability on climate, *Science*, 272, 981–984, 1996.
- Hitchman, M.H., C.B. Leovy, J.C. Gille, and P.L. Bailey, Quasi-stationary zonally asymmetric circulations in the equatorial lower mesosphere, *J. Atmos. Sci.*, 44, 2219–2236, 1987.
- Holton, J.R., and H.-C. Tan, The influence of the equatorial quasi-biennial oscillation on the global circulation at 50 mb, *J. Atmos. Sci.*, 37, 2200–2208, 1980.
- Holton, J.R., and H.-C. Tan, The quasi-biennial oscillation in the Northern Hemisphere lower stratosphere, *J. Meteorol. Soc. Jpn.*, 60, 140–148, 1982.
- Labitzke, K., and H. van Loon, Association between the 11-year solar cycle, the QBO and the atmosphere. Part I: The troposphere and stratosphere in the northern hemisphere in winter, *J. Atmos. Terr. Phys.*, 50, 197–206, 1988.
- McIntyre, M.E., and T.N. Palmer, Breaking planetary waves in the stratosphere, *Nature*, 305, 593–600, 1983.
- McIntyre, M.E., and T.N. Palmer, The 'surf zone' in the stratosphere, *J. Atmos. Terr. Phys.*, 46, 825–849, 1984.
- O'Sullivan, D.J., and T.J. Dunkerton, Seasonal development of the extratropical QBO in a numerical model of the middle atmosphere, *J. Atmos. Sci.*, 51, 3706–3721, 1994.
- Randel, W.J., The evaluation of winds from geopotential height data in the stratosphere, *J. Atmos. Sci.*, 44, 3097–3120, 1987.
- Robinson, W., The application of quasi-geostrophic Eliassen-Palm flux to the analysis of stratospheric data, *J. Atmos. Sci.*, 43, 1017–1023, 1986.
- Salby, M.L., Evidence of solar variability in the atmosphere: Its significance and relationship to terrestrial variability, in *The Solar Cycle Variation of the Stratosphere. A STEP Working Group 5 Report*, 16 pp., edited by L. Hood, Lunar and Planetary Laboratory, Department of Planetary Sciences, University of Arizona, 1995.
- Salby, M.L., P. Callaghan, and D. Shea, Interdependence of the tropical and extratropical QBO: Relationship to the solar cycle vs. a biennial oscillation in the stratosphere, *J. Geophys. Res.*, in press, 1997.
- Tung, K.-K., and H. Yang, Global QBO in circulation and ozone, Part I: Reexamination of observational evidence, *J. Atmos. Sci.*, 51, 2699–2707, 1994a.
- Tung, K.-K., and H. Yang, Global QBO in circulation and ozone, Part II: A simple mechanistic model, *J. Atmos. Sci.*, 51, 2708–2721, 1994b.
- van Loon, H., and K. Labitzke, Association between the 11-year solar cycle and the atmosphere. Part IV: The stratosphere, not grouped by the phase of the QBO, *J. Clim.*, 3, 827–837, 1990.
- Zurek, R.W., G.L. Manney, A.J. Miller, M.E. Gelman, and R.M. Nagatani, Interannual variability of the north polar vortex in the lower stratosphere during the UARS mission, *Geophys. Res. Lett.*, 23, 289–292, 1996.

---

M.P. Baldwin and T.J. Dunkerton, Northwest Research Associates, PO Box 3027, Bellevue, WA, 98009-3027. (e-mail: mark@nwra.com, tim@nwra.com)

(Received December 11, 1996; revised July 11, 1997; accepted July 22, 1997.)

## Orthogonal Rotation of Spatial Patterns Derived from Singular Value Decomposition Analysis

XINHUA CHENG AND TIMOTHY J. DUNKERTON

*Northwest Research Associates, Bellevue, Washington*

(Manuscript received 23 May 1994, in final form 20 March 1995)

### ABSTRACT

Singular value decomposition (SVD) analysis is frequently used to identify pairs of spatial patterns whose time series are characterized by maximum temporal covariance. It tends to compress complicated temporal covariance between two fields into a relatively few pairs of spatial patterns by maximizing temporal covariance explained by each pair of spatial patterns while constraining them to be spatially orthogonal to the preceding ones of the same field. The resulting singular vectors are sometimes complicated and difficult to interpret physically. This paper introduces a method, an extension of SVD analysis, which linearly transforms a subset of total singular vectors into a set of alternative solutions using a varimax rotation. The linear transformation (known as "rotation"), weighting singular vectors by the square roots of the corresponding singular values, emphasizes geographical regions characterized by the strongest relationships between two fields, so that spatial patterns corresponding to rotated singular vectors are more spatially localized. Several examples are shown to illustrate the effectiveness of the rotation in isolating coupled modes of variability inherent in meteorological datasets.

### 1. Introduction

The representation of spatial patterns of meteorological variables in terms of empirical orthogonal functions (EOFs), known as principal component analysis (PCA), has been used with increasing frequency in atmospheric science since its introduction several decades ago (Lorenz 1956). This analysis technique enables one to describe a multidimensional meteorological field with a relatively small number of spatial patterns that account for large fractions of variance of the field. Similar analysis techniques such as canonical correlation analysis (CCA) and singular value decomposition (SVD) analysis that identify pairs of spatial patterns from two data fields are also becoming popular. Singular value decomposition, in general, is a basic matrix operation in linear algebra, whereas the SVD analysis discussed in the present study refers to the technique that isolates pairs of spatial patterns and their associated time series by performing singular value decomposition on the temporal covariance matrix between two data fields. Both CCA and SVD are generalizations of PCA analysis, designed for a single data field, to two data fields and identify linear combinations of variables (or spatial patterns) in two fields that are most strongly related to each other. The main difference between CCA and SVD is that CCA identifies

spatial patterns by maximizing the temporal correlation between two data fields, whereas SVD maximizes the temporal covariance between two data fields. In an unpublished paper dated in 1982, K. E. Muller at the University of North Carolina proposed to use SVD analysis as an alternative to CCA because it utilizes the information on the variance in the fields under consideration, whereas this information is obscured in CCA. Recently, Bretherton et al. (1992) gave an extensive review of these analysis techniques.

Spatial patterns (or EOFs) derived from PCA are constrained to be both spatially and temporally orthogonal to one another so that they can be the most efficient patterns for explaining the temporal variance integrated over the entire analysis domain. However, the spatial orthogonality is sometimes a strong and undesirable constraint imposed on EOFs. As a result, EOFs are subject to a number of inherent problems such as domain dependence, sampling variability and inaccurate representation of the real physical relationship in the input data (Richman 1986). Linear transformation (or rotation) of a subset of leading EOFs, known as rotated PCA, is often used to obtain spatial patterns that are more physically meaningful and statistically robust. Due to the similarity between the optimization criteria in PCA and SVD analysis, spatial patterns derived from SVD analysis also suffer from the same problem as unrotated EOFs, especially when the relationships between two fields involve a spatial scale much smaller than the analysis domains. Experience based on rotated PCA suggests that SVD analysis should be considered

Corresponding author address: Dr. Xinhua Cheng, Northwest Research Associates, P.O. Box 3027, Bellevue, WA 98009-3027.





as the first step in identifying coupled modes of variability within two fields by reducing the original fields into a small number of pairs of linearly independent components. Then the initial solutions can be linearly transformed subject to certain constraints to yield alternative solutions that may be more physically interpretable. In a study designed to document the relationships between extratropical sea surface temperature and the 700-hPa height field, Lanzante (1984) tried to rotate the spatial patterns derived from the SVD analysis between anomalies in the two fields using the varimax method. However, his approach is not appropriate because the rotation included only a subset of spatial patterns belonging to one of the two fields that he analyzed. Hence, it is not clear whether the geographical regions that are most strongly correlated within the two fields are emphasized in the results. There are also studies (Cliff and Krus 1976; Reynolds and Jackosfsky 1981) that attempt to rotate canonical variates to enhance the interpretability of results obtained from CCA. The rotation was based on a subset of unweighted canonical coefficients.

The purpose of this paper is to present a new method that yields alternative solutions by orthogonally rotating the spatial patterns derived from SVD analysis. The outline of the paper is as follows. Section 2 introduces mathematical formulations of SVD analysis and of the orthogonal rotation. Section 3 provides several examples to illustrate the effectiveness of the rotation in the diagnosis of coupled modes of variability inherent in meteorological datasets. Conclusions are presented in the last section.

## 2. Formulation

In this section, we will propose a method that relaxes the spatial orthogonality constraint imposed on spatial patterns derived from SVD analysis. To facilitate our presentation of the method, the discussion of SVD analysis in Bretherton et al. (1992) is summarized in the following subsection.

### a. SVD analysis

The problem of isolating a pair of spatial patterns whose temporal covariance is maximized between two data fields can be formulated mathematically as follows. Consider a "left" data field  $\mathbf{S}(x, t)$  that consists of  $T$  observations, each of which has  $N_x$  grid points, and a "right" data field  $\mathbf{Z}(y, t)$  that contains the same number of maps, each of which has  $N_y$  grid points. These two data fields can be viewed as  $N_x$  by  $T$  and  $N_y$  by  $T$  matrices, respectively. We want to determine a set of  $N_x$ -dimensional orthogonal vectors  $\mathbf{p}_k$  ( $k = 1, \dots, N_x$ ) for  $\mathbf{S}(x, t)$  and a set of  $N_y$ -dimensional orthogonal vectors  $\mathbf{q}_k$  ( $k = 1, \dots, N_y$ ) for  $\mathbf{Z}(y, t)$  so that covariance between projections of  $\mathbf{S}(x, t)$  on  $\mathbf{p}_k$  and projections of  $\mathbf{Z}(y, t)$  on  $\mathbf{q}_k$

$$\frac{1}{T} (\mathbf{p}_k^T \mathbf{S}) (\mathbf{q}_k^T \mathbf{Z})^T \quad (1)$$

is maximized subject to the conditions

$$\mathbf{p}_k^T \mathbf{p}_k = 1 \quad \text{and} \quad \mathbf{q}_k^T \mathbf{q}_k = 1. \quad (2)$$

The maximization of covariance between  $\mathbf{S}(x, t)$  and  $\mathbf{Z}(y, t)$  is a variational problem that leads to the equation

$$\mathbf{p}_k^T \mathbf{C}_{xz} \mathbf{q}_k = \sigma_k, \quad (3)$$

where  $\mathbf{C}_{xz} = 1/T \mathbf{S} \mathbf{Z}^T$  is an  $N_x$  by  $N_y$  temporal covariance matrix and  $\sigma_k$  is a Lagrange multiplier that measures covariance between the two fields for the  $k$ th mode. In matrix form (3) becomes

$$\mathbf{C}_{xz} = \mathbf{P} \mathbf{\Sigma} \mathbf{Q}^T, \quad (4)$$

where  $\mathbf{\Sigma}$  is an  $N_x$  by  $N_y$  matrix whose elements equal zero except for the first  $R$  [ $R \leq \min(N_x, N_y)$ ] diagonal elements ( $\sigma_k$ ), and  $\mathbf{P} = (\mathbf{p}_1 | \dots | \mathbf{p}_{N_x})$  and  $\mathbf{Q} = (\mathbf{q}_1 | \dots | \mathbf{q}_{N_y})$  are respective  $N_x$  by  $N_x$  and  $N_y$  by  $N_y$  orthogonal matrices, which satisfy

$$\mathbf{P}^T \mathbf{P} = \mathbf{I} \quad \text{and} \quad \mathbf{Q}^T \mathbf{Q} = \mathbf{I}. \quad (5)$$

Equation (4) is a fundamental matrix operation known as singular value decomposition in linear algebra and can be computed numerically with an efficient algorithm available in most linear algebra software packages. From now on, the Lagrange multipliers  $\sigma_k$ , the nonzero diagonal elements in  $\mathbf{\Sigma}$ , are recognized as the singular values, which are ranked in descending order  $\sigma_1 \geq \sigma_2 \geq \dots \geq \sigma_R \geq 0$ . Vectors  $\mathbf{p}_k$  and  $\mathbf{q}_k$  are referred to as the associated left and right singular vectors, respectively.

Having defined the matrices  $\mathbf{P}$  and  $\mathbf{Q}$  uniquely, we can decompose the data fields  $\mathbf{S}(x, t)$  and  $\mathbf{Z}(y, t)$  as follows:

$$\mathbf{S}(x, t) = \mathbf{P}(x) \mathbf{A}^T(t) \quad (6a)$$

$$\mathbf{Z}(y, t) = \mathbf{Q}(y) \mathbf{B}^T(t), \quad (6b)$$

where  $\mathbf{A}$  and  $\mathbf{B}$  are respective  $T$  by  $N_x$  and  $T$  by  $N_y$  matrices. Column vectors in  $\mathbf{A}$  and  $\mathbf{B}$  are time series of expansion coefficients that are defined by projecting the left (right) field onto the left (right) singular vectors. A pair of singular vectors, together with the associated time series define a *mode* in the SVD analysis. A time series contains temporal variations of the corresponding singular vectors and has the unit of the field it represents. Hence, temporal covariance between the two fields can be expressed in terms of the time series by substituting of (6) into (4)

$$\frac{1}{T} \mathbf{A}^T \mathbf{B} = \mathbf{\Sigma}. \quad (7)$$

That is, a time series of the left field is correlated only with the time series of the same mode in the right field.

Singular vectors represent the solutions to the problem of maximizing temporal covariance between two data fields. They are defined in such a way that the temporal covariance between the associated time series is always positive. As evident in (7), the covariance explained by a pair of singular vectors ( $\mathbf{p}_k, \mathbf{q}_k$ ) is  $\sigma_k$  and the total covariance between the two fields is equal to the trace of  $\Sigma$ . Therefore, the relative importance of a SVD mode can be measured in terms of covariance fraction (CF),<sup>1</sup> which is defined as

$$CF_k = \frac{\sigma_k}{\sum_{i=1}^R \sigma_i} \quad (8)$$

The two important properties associated with SVD results are that singular vectors are orthogonal to one another within each field as evident in (5) and that the associated time series of expansion coefficients are orthogonal between the two fields as evident in (7) (i.e., the  $k$ th column time series in  $\mathbf{A}$  is correlated only with the  $k$ th column time series in  $\mathbf{B}$ ). The latter relationship is useful in establishing one-to-one relationships between two fields, whereas the former is often considered as a strong and undesirable constraint unless one wants to describe as much as possible of the covariance between two fields with as small as possible a number of SVD modes.

#### b. Rotated SVD analysis

To obtain objective solutions that are more spatially localized, we orthogonally rotate a loading matrix that includes a subset of the total singular vectors. The loading matrix is constructed by combining the left and right singular vectors into a single column vector, in a manner similar to that used in multivariate PCA (i.e., Kutzbach 1967; Weare 1987; Wang 1992), and weighting the vector by the square root of the corresponding singular value

$$\mathbf{L} = \begin{pmatrix} \mathbf{P} \\ \mathbf{Q} \end{pmatrix} \Sigma^{1/2} = \begin{pmatrix} p_1^{(1)} & p_2^{(1)} & \dots & p_N^{(1)} \\ \vdots & \vdots & \dots & \vdots \\ p_1^{(N_1)} & p_2^{(N_1)} & \dots & p_N^{(N_1)} \\ q_1^{(1)} & q_2^{(1)} & \dots & q_N^{(1)} \\ \vdots & \vdots & \dots & \vdots \\ q_1^{(N_2)} & q_2^{(N_2)} & \dots & q_N^{(N_2)} \end{pmatrix} \times \begin{pmatrix} \sqrt{\sigma_1} & & & \\ & \sqrt{\sigma_2} & & \\ & & \ddots & \\ & & & \sqrt{\sigma_N} \end{pmatrix}, \quad (9)$$

<sup>1</sup> To be consistent with PCA and rotated PCA, we use covariance fraction as a measure of relative importance of SVD modes. Bretherton et al. (1992) used squared covariance fraction (SCF) as the measure because the total squared covariance in  $\mathbf{C}_{12}$  is an invariant in SVD analysis.

where  $\hat{\mathbf{P}}$  and  $\hat{\mathbf{Q}}$  are the respective truncated left and right singular vector matrices, which contain only the  $N$  leading SVD modes, and  $\hat{\Sigma}^{1/2}$  is an  $N$  by  $N$  diagonal matrix whose diagonal elements are the square roots of the  $N$  leading singular values. Hence,  $\hat{\mathbf{L}}$  is an  $N_1 + N_2$  by  $N$  matrix, which can be imagined as  $N_1 + N_2$  vectors in  $N$ -dimensional space. In the present study, the rotation is carried out by varimax orthogonal rotation, where the orthogonal rotation refers to the transformation matrix,  $\mathbf{U}$ , which transforms the loading matrix through orthogonal rotation of the  $N_1 + N_2$  vectors in  $N$ -dimensional space. The reason for choosing varimax rotation is because it is one of the widely used rotation methods and produces "realistic" spatial patterns.

Varimax rotation simplifies the column structures of the loading matrix  $\hat{\mathbf{L}}$  by maximizing the total variance of the squared column loadings [e.g., Eq. (20) in Richman (1986)], which is known as the simplicity criterion and will be referred to as the localization criterion in the following discussion. As a result, simplified structures tend to have column loadings biased toward either large or zero values. Weighting the left and right singular vectors by the square roots of the corresponding singular values creates spatial patterns that have large amplitude in the regions where the temporal covariance between the fields is large. Hence, the rotated spatial patterns should be easier to interpret than their unrotated counterparts. The column vectors in  $\hat{\mathbf{L}}$  are orthogonally rotated in an  $N$ -dimensional space to achieve the localization criterion. Once the rotation is done, an orthonormal transformation matrix  $\mathbf{U}$  is defined uniquely, which, in turn, determines the rotated loading matrix

$$\mathbf{L}^* = \hat{\mathbf{L}}\mathbf{U}, \quad (10)$$

where  $\mathbf{U}$  is an  $N$  by  $N$  square matrix and satisfies  $\mathbf{U}^T\mathbf{U} = \mathbf{U}\mathbf{U}^T = \mathbf{I}$ . The rotated left and right singular vectors can be obtained by substituting (9) into (10)

$$\mathbf{P}^* = \hat{\mathbf{P}}\hat{\Sigma}^{1/2}\mathbf{U}\mathbf{W}_l^{-1} \quad (11a)$$

$$\mathbf{Q}^* = \hat{\mathbf{Q}}\hat{\Sigma}^{1/2}\mathbf{U}\mathbf{W}_r^{-1}, \quad (11b)$$

where  $\mathbf{W}_l$  and  $\mathbf{W}_r$  are both  $N$  by  $N$  diagonal matrices that normalize the column vectors in  $\mathbf{P}^*$  and  $\mathbf{Q}^*$  to unit vectors, respectively. By requiring the amount of variance explained by the  $N$  leading SVD modes in each field to remain the same after the rotation, time series of expansion coefficients associated with the rotated singular vectors can be determined using linear regression:

$$\mathbf{A}^* = \hat{\mathbf{A}}\hat{\Sigma}^{-1/2}\mathbf{U}\mathbf{W}_l, \quad (12a)$$

$$\mathbf{B}^* = \hat{\mathbf{B}}\hat{\Sigma}^{-1/2}\mathbf{U}\mathbf{W}_r, \quad (12b)$$

where  $\hat{\mathbf{A}}$  and  $\hat{\mathbf{B}}$  are both  $T$  by  $N$  matrices, containing the first  $N$  columns of matrices  $\mathbf{A}$  and  $\mathbf{B}$ , respectively. The time series in matrices  $\mathbf{A}^*$  and  $\mathbf{B}^*$  represent the time variations of the corresponding rotated singular

vectors and have the units of the corresponding fields. It is worth noting that (12) is an efficient way to compute the rotated time series.

It is easy to verify that the product of  $\mathbf{P}^* \mathbf{T} \mathbf{P}^*$  or  $\mathbf{Q}^* \mathbf{T} \mathbf{Q}^*$  is no longer a diagonal matrix. Therefore, the spatial orthogonality imposed on the singular vectors is relaxed by the rotation. On the other hand, one can show that temporal covariance between the rotated time series remains orthogonal:

$$\frac{1}{T} \mathbf{A}^* \mathbf{T} \mathbf{B}^* = \Sigma^*, \quad (13)$$

where  $\Sigma^* = \mathbf{W}_l \mathbf{W}_r$  is an  $N$  by  $N$  diagonal matrix because  $\mathbf{W}_l$  and  $\mathbf{W}_r$  are both  $N$  by  $N$  diagonal matrices. Because the loading matrix  $\mathbf{L}$  is orthogonally rotated, the amount of covariance retained in the matrix remains the same. Therefore, the trace of matrix  $\Sigma^*$  is equal to that of  $\Sigma$ . Since the rotated time series are temporally orthogonal, the fractions of covariance that they account for are additive. In analogy with (8), one can show that the covariance fraction explained by a pair of rotated singular vectors ( $\mathbf{p}_k^*$ ,  $\mathbf{q}_k^*$ ) is

$$CF_k^* = \frac{\sigma_k^*}{\sum_{l=1} \sigma_l}, \quad (14)$$

where  $\sigma_k^*$  is the  $k$ th diagonal element of matrix  $\Sigma^*$ .

Once the time series associated with the rotated singular vectors are obtained, one can compute heterogeneous regression maps. If  $a_k^*(t)$  and  $b_k^*(t)$  are the time series associated with  $\mathbf{p}_k^*$  and  $\mathbf{q}_k^*$ , respectively, one can show that the left and right heterogeneous regression maps are proportional to the corresponding rotated singular vectors:

$$\text{reg}[\mathbf{S}(x, t), b_k^*(t)] = (\sigma_k^* / \langle b_k^{*2}(t) \rangle^{1/2}) \mathbf{p}_k^* \quad (15a)$$

$$\text{reg}[\mathbf{Z}(y, t), a_k^*(t)] = (\sigma_k^* / \langle a_k^{*2}(t) \rangle^{1/2}) \mathbf{q}_k^*, \quad (15b)$$

where  $\langle f(t) \rangle$  denotes the time average of a time series  $f(t)$ . The heterogeneous regression maps of the  $k$ th SVD mode indicate how well the anomaly pattern in the left (right) field is related to the  $k$ th singular vector of the right (left) field. Anomaly amplitude in the maps reflects the strength of the coupling between the two fields, which can be considered as the response of left (right) field to a one-standard-deviation anomaly in the right (left) field. If the data fields have been normalized, (15) represents the respective left and right heterogeneous correlation maps. One can also verify that the  $k$ th left (right) homogeneous regression map is not proportional to  $\mathbf{p}_k^*$  ( $\mathbf{q}_k^*$ ).

If the left field  $\mathbf{S}(x, t)$  and the right field  $\mathbf{Z}(y, t)$  are identical, the left singular vectors will be the same as the right ones. Hence, (4) becomes PCA: the singular values are equal to eigenvalues and the singular vectors are the EOFs. It is easy to show, in this case, that the sim-

ilarity (variance of squared loadings) of a loading vector in  $\mathbf{L}$  is equal to that of the PC loadings (the EOF weighted by the square root of the corresponding eigenvalue). Therefore, varimax rotation of the two loading matrices will yield the same transformation matrix  $\mathbf{U}$ , which indicates the rotated SVD analysis is equivalent to rotated PCA. In this case, the rotated SVD analysis produces identical left and right spatial patterns and they are equal to those obtained from rotated PCA. Equations (8) and (14) can be interpreted as the fraction of the variance explained by unrotated and rotated PCs, respectively. The left and right heterogeneous regression maps defined in (15) are identical and are equal to the regression maps based on the rotated PCs.

An important question concerning the rotation is to determine the proper number of pairs of singular vectors to be retained in the analysis. The number of SVD modes to retain in the rotation depends upon the data being analyzed. Because of its similarity with respect to rotated PCA, experience based on rotated PCA also applies to rotated SVD analysis. Many techniques have been devised to serve as guidelines in determining the optimal number of EOFs to rotate [e.g., the scree test (Cattell 1966), eigenvalue separation test (North et al. 1982) and the Rule  $N$  test (Preisendorfer 1988)]. Richman and Lamb (1987) and O'Lenic and Livezey (1988) demonstrated rotated patterns resulting from inappropriate choices of truncation point. In practice, one should experiment with a number of truncation points. On the other hand, rotating a small number of singular vectors tends to blend together patterns that are really discrete due to the lack of degrees of freedom. On the other hand, if the number of retained singular vectors exceeds the number of degree of freedom in the data, the dynamical structure in the data will be over-resolved and as a consequence, the resulting patterns will tend to be monopoles. Rotated patterns of physical interest should be the ones that are stable within a fairly wide range of truncation points. In this range, rotation is capable of separating the mixture of patterns evident on the unrotated SVD maps to reveal localized features and the resulting patterns are quite insensitive to the number of SVD modes retained.

### 3. Examples

In this section, we will present some examples that illustrate the effectiveness of the rotated SVD analysis in identifying physical meaningful patterns. The datasets used in the first three examples are the Northern Hemisphere wintertime anomalies of sea level pressure (SLP) and 500- and 500-hPa height fields, derived from National Meteorological Center (NMC) final analyses. The anomaly fields are archived on a 445-point polar stereographic grid that covers the Northern Hemisphere north of 20°N. The data used in the last example are the European Centre for Medium-Range Weather Fore-

cast (ECMWF) 200-hPa uninitialized wind analyses on a  $2.5^\circ$  by  $2.5^\circ$  latitude-longitude grid for the period 1985–93. Our SVD analyses are based on the temporal covariance matrix.

#### a. Vertical structure of low-frequency variability

There have been many studies (i.e., Kutzbach 1970; Wallace and Gutzler 1981; Horel 1981; Esbensen 1984; Barnston and Livezey 1987; Kushnir and Wallace 1989) using PCA to document atmospheric low-frequency variability at a given vertical level such as the sea level, 700 or 500 hPa. In general, spatial patterns of the leading EOFs of low-frequency variability tend to be hemispheric in extent, difficult to interpret dynamically, and not very robust from a statistical point of view. Upon rotation of the leading PCs, several statistically robust, spatially localized patterns, the Pacific/North American (PNA) pattern (Wallace and Gutzler 1981) and the North Atlantic Oscillation (NAO) (Walker and Bliss 1932) emerge among the leading modes in terms of the explained variance. Hsu and Wallace (1985) showed that the prominent low-frequency patterns are characterized by structures that are to first-order equivalent barotropic, but exhibit slight westward tilts with height in the lower troposphere.

Our SVD analysis of the low-frequency variability in the lower troposphere is based on 10-day low-pass-filtered SLP and 500-hPa height anomalies sampled at 5-day intervals (2, 7 December, . . . , 25 February) for 48 December–February winters from January 1946 through February 1993. The rotation is carried out retaining the first 15 SVD pairs. The results for the leading rotated SVD modes are quite robust as the truncation is varied. For example, the pattern correlation between the PNA pattern shown in Fig. 2c and the corresponding one obtained from the analysis with the first 10 and 20 SVD pairs retained is 0.98 and 0.99, respectively. Figure 1 shows the percentage of the total hemispherically integrated temporal covariance explained by the 15 leading pairs of unrotated (crosses) and rotated (asterisks) singular vectors. The 15 pairs of singular vectors together account for 82.2% of the total covariance between the two fields. The rotation does not affect the amount of covariance accounted for by the singular vectors retained in the analysis but changes the distribution of the covariance among them. In general, the leading rotated solutions fall short of the unrotated ones with respect to the fraction of the covariance explained. However, it should be emphasized that rotated solutions are optimized for explaining covariance concentrated in a few regions rather than for explaining as much as possible of the covariance integrated over the whole domain.

Figure 2 shows the spatial patterns of unrotated singular vectors for SLP and 500-hPa height fields. The singular vectors are scaled so that they can be consid-

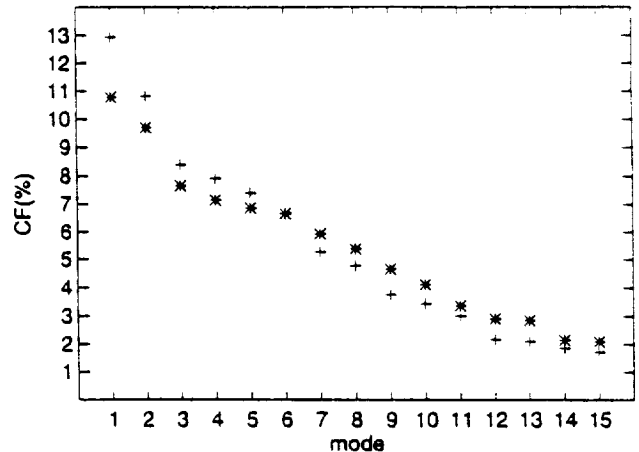
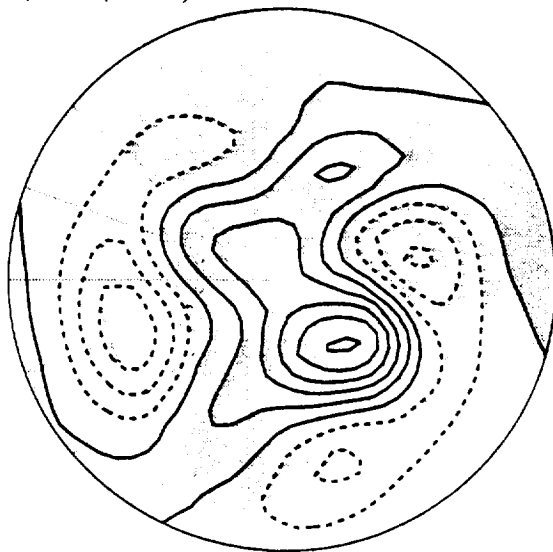


FIG. 1. Percentage of the hemispherically integrated covariance fraction associated with the first 15 pairs of unrotated (crosses) and rotated (asterisks) singular vectors based on the 10-day low-pass-filtered SLP and 500-hPa height fields for 48 winter seasons from January 1946 through February 1993.

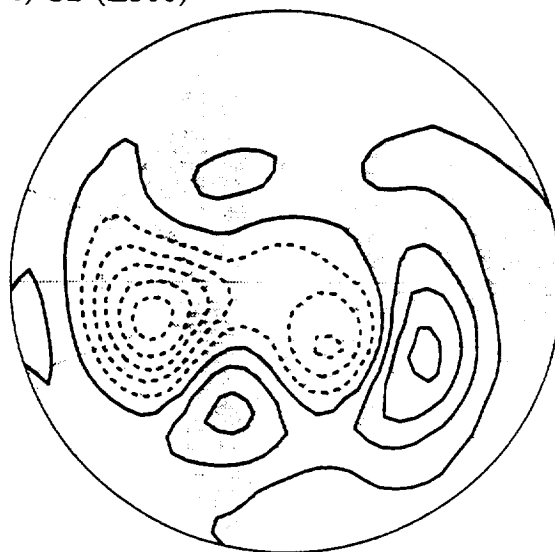
ered as regression maps of the field, obtained by regressing the field with the normalized time series associated with the pairing singular vector of the other field. The two leading singular vectors at the 500 hPa bear a close resemblance to the EOFs of the 10-day low-pass-filtered 500-hPa height field shown in Cheng and Wallace (1993). The two pairs of singular vectors contain elements of the PNA, NAO, and the North Pacific Oscillation (NPO) (Walker and Bliss 1932; Rogers 1981) patterns. In particular, the NAO and NPO appear convoluted in the second singular vector, and the NAO seems to be split between the first two singular vectors. The spatial patterns of the higher SVD modes (not shown) tend to be more hemispheric in extent and smaller in scale.

Figure 3 shows the first two pairs of rotated singular vectors, scaled in a manner similar to those in Fig. 2. It is evident that the spatial patterns exhibit more regional structures than the unrotated ones. Comparing the first pair of rotated singular vectors with results of earlier studies, it is evident that they correspond to the NAO, which is characterized by a seesaw in the SLP between Iceland and the Azores as emphasized by van Loon and Rogers (1978). The poleward center of action at the 500-hPa level is located about  $20^\circ$  of longitude to the west of its counterpart at sea level, implying the existence of low-level horizontal temperature advection. The second pair corresponds to the PNA pattern, which exhibits only a slightly westward tilt with height. The time series associated with the SLP and 500-hPa spatial patterns of the two rotated SVD modes exhibit temporal correlations of 0.94 and 0.90, respectively. The results based on rotated SVD analysis are, in general, consistent with those obtained by Hsu and Wallace (1985), whose analysis was based on lin-

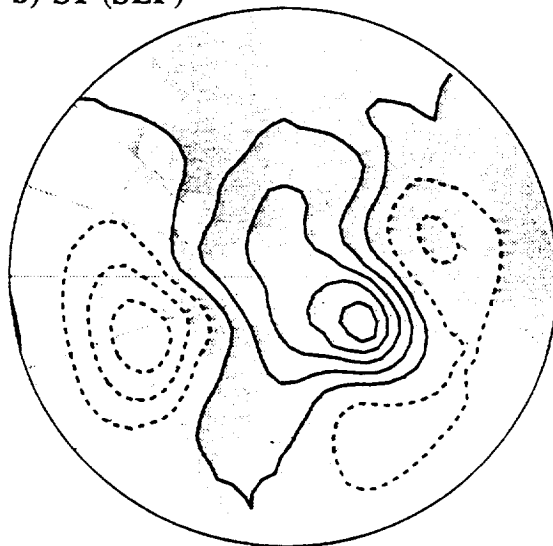
a) S1 (Z500)



c) S2 (Z500)



b) S1 (SLP)



d) S2 (SLP)

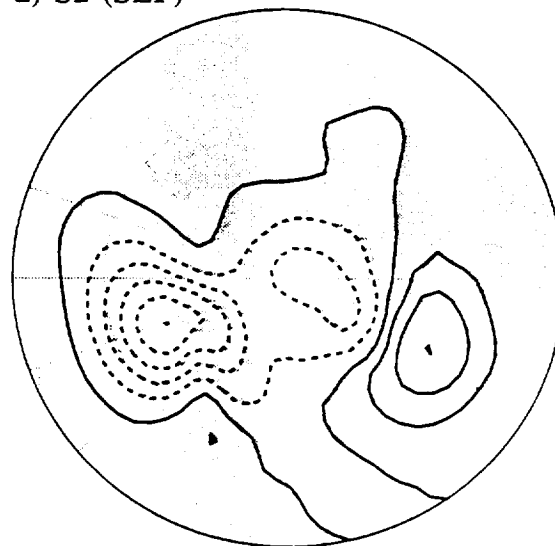


FIG. 2. Heterogeneous regression maps for the first (left column) and second (right column) unrotated SVD modes based on the 10-day low-pass-filtered SLP and 500-hPa height anomaly fields. Contour intervals are 20 m for the 500-hPa patterns (top panels) and 2 hPa for the SLP patterns (lower panels); negative contours are dashed.

ear correlations of 500-hPa height with rotated principal components of the SLP field.

The rotated singular vectors are linear combinations of the unrotated vectors. Table 1 shows the weights for the first six of the 15 unrotated singular vectors that are linearly combined to yield the rotated solutions. Because singular vectors of the left and right fields are rotated together, the weights apply to both fields. It is evident that the first rotated singular vector is closely related to the four leading unrotated ones, while the second rotated singular vector is determined predomi-

nantly by the second, first, fourth, and fifth unrotated ones, etc.

#### *b. Vertical structure of high-frequency variability*

High-frequency fluctuations in the lower troposphere are dominated by synoptic-scale migrating disturbances with periods shorter than a week, referred to as baroclinic waves. Studies (i.e., Blackmon et al. 1984; Nakamura and Wallace 1990) based on one-point correlation analysis reveal that the high-frequency fluctu-

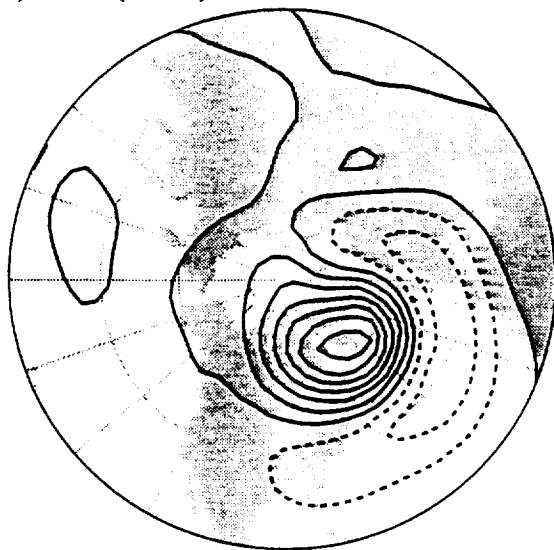
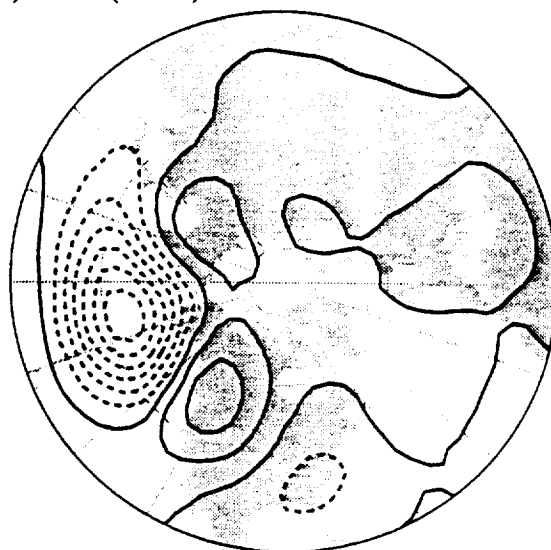
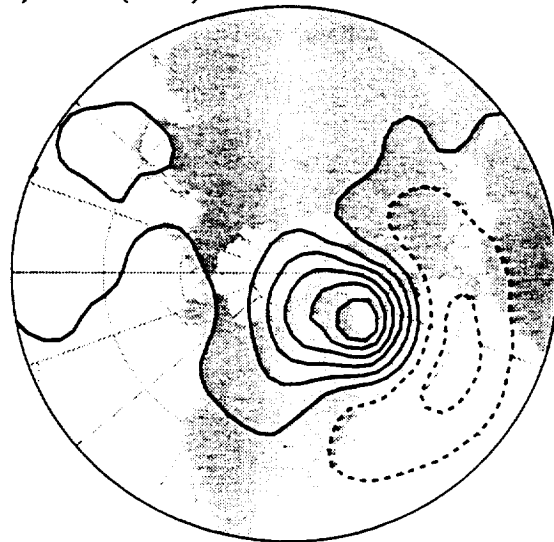
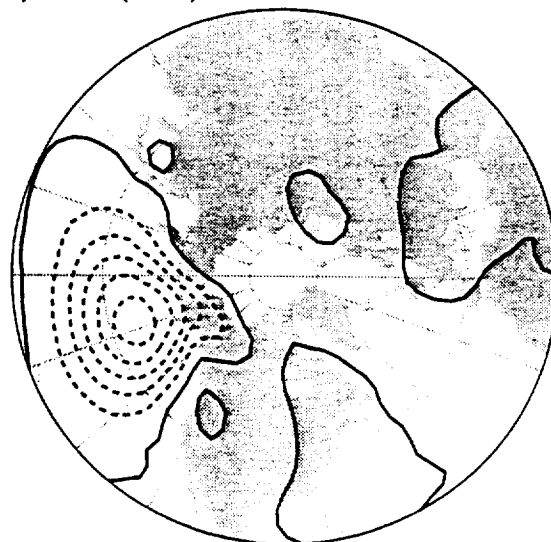
**a) RS1 (Z500)****c) RS2 (Z500)****b) RS1 (SLP)****d) RS2 (SLP)**

FIG. 3. As in Fig. 2 but for the two leading rotated SVD modes.

ations are mainly concentrated over the midlatitude oceans in form of zonally oriented wavetrains. The two localized wavetrains, in which disturbances appear to be temporally uncorrelated with one another, are characterized by meridionally elongated anomalies that tilt westward with height. Rotated PCA can reproduce the localized horizontal structures of the baroclinic waves (not shown), whereas unrotated PCA blends the two regional storm tracks together as a single east-west-oriented wavetrain that involves a much larger span of longitude and is less physically interpretable (not shown).

Our SVD analysis of the high-frequency variability in the lower troposphere is based on 3–7-day bandpass-filtered SLP and 500-hPa height anomaly fields for 13 December–February winters from 1 December 1980 through 28 February 1993. Figure 4 shows the pair of the leading singular vectors derived from the SVD analysis of the bandpass-filtered fields, scaled in a manner analogous to Fig. 2. The spatial patterns exhibit structures of zonally oriented wavetrains with westward tilts between the earth's surface and the 500-hPa level. The second pair of singular vectors (not shown) resembles the first pair but is shifted 90° in phase. These

TABLE 1. Weights for the first 6 of the 15 unrotated singular vectors that are linearly combined to yield rotated singular vectors in the rotated SVD analysis of the 10-day low-pass filtered SLP and 500-hPa height anomaly fields. The weights are defined as the elements in the orthonormal transformation matrix  $U$ .

Rotated SVD	Unrotated SVD					
	1	2	3	4	5	6
1	0.76	-0.28	-0.47	-0.22	0.10	0.06
2	0.47	0.60	0.16	0.43	-0.37	-0.03
3	-0.02	-0.52	0.05	0.46	-0.27	0.48
4	0.02	0.04	-0.09	0.53	0.78	-0.13

two leading SVD modes explain 8% and 7% of the total covariance between the bandpass-filtered fields, respectively. They closely resemble the leading unrotated EOFs of the corresponding fields in which the Atlantic and Pacific storm tracks are blended together to form a single unrealistically long storm track. The reason for that is (once again) the maximal covariance property attempting to force as much covariance onto a single vector, merging unique physical identities.

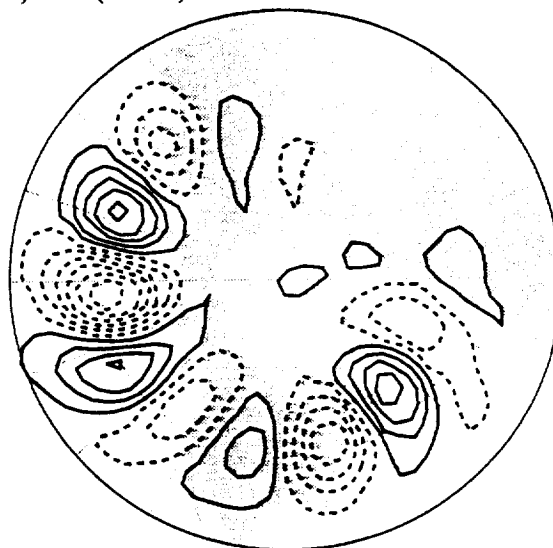
Rotated SVD analysis was applied to a subset of the leading singular vectors of the bandpass-filtered fields. We found that the spatial patterns of the rotated singular vectors are not sensitive to the number of singular vectors included in the rotation as long as the number is larger than four. The first four rotated SVD modes obtained by rotating the first 10 pairs of singular vectors each explain about 7% of the total covariance. Figure 5 shows the first and third pairs of the rotated singular vectors, scaled in a manner similar to Fig. 2. The first and second pairs of the rotated singular vectors exhibit similar wavetrain patterns but have a  $90^\circ$  phase shift. It is readily apparent that the two of them, taken together, represent a wavetrain over the North Pacific with a wavelength of  $\sim 50^\circ$  of longitude and an arbitrary longitudinal phase. The third and fourth pairs, taken together, represent a similar wavetrain over the North Atlantic. It is evident that the rotated singular vectors bear close resemblance to the observed baroclinic wave structures over the North Pacific and the North Atlantic storm tracks.

### c. Coupling between the troposphere and stratosphere

We next present some results showing dynamical link between the troposphere and stratosphere based on rotated SVD analysis of 27 December–February winters of 50- and 500-hPa unfiltered height anomaly fields from 1 January 1964 through 24 February 1990. Spatial patterns of the unrotated singular vectors (not shown) are quite complicated and difficult to interpret physically, especially for the higher SVD modes. Varimax rotation of the 15 leading pairs of the singular vectors simplifies the spatial patterns so that they are more

amenable to physical interpretation. Some of the well-known extratropical tropospheric circulation patterns exhibit strong correlations with features in the lower stratosphere. The strongest relationships between the two fields do not appear in the simultaneous correlations but in the correlations when the 500-hPa field leads the 50-hPa field by four days, consistent with the concept of upward propagation of wave energy. Figure 6 shows the two most prominent coupled modes of variability between the two fields, which account for

### a) S1 (Z500)



### b) S1 (SLP)

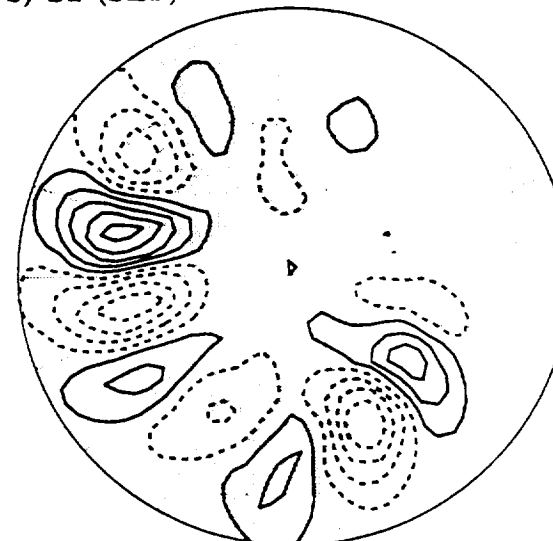


FIG. 4. Spatial patterns of the leading unrotated SVD mode based on the 3–7-day bandpass filtered SLP and 500-hPa height anomaly fields for 13 winter seasons 1 December 1980 through 28 February 1993. Contour intervals are 6 m for the 500-hPa pattern (a) and 0.6 hPa for the SLP pattern (b); negative contours are dashed.

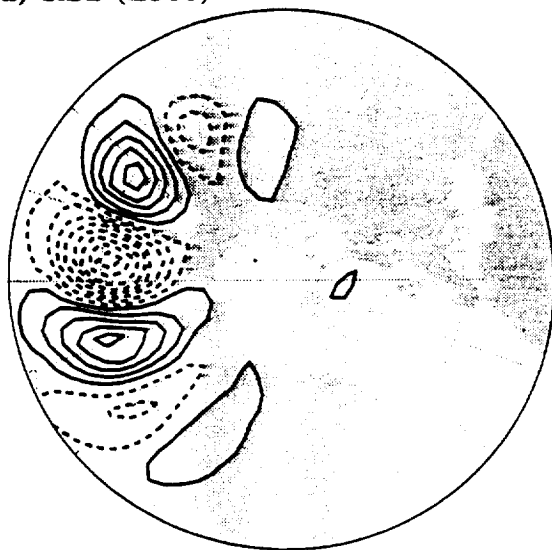
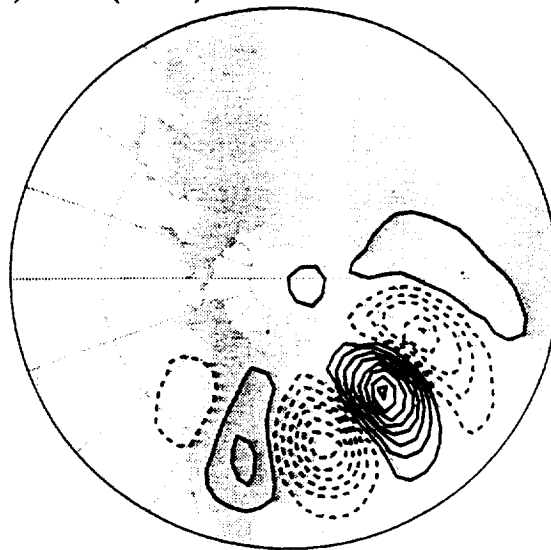
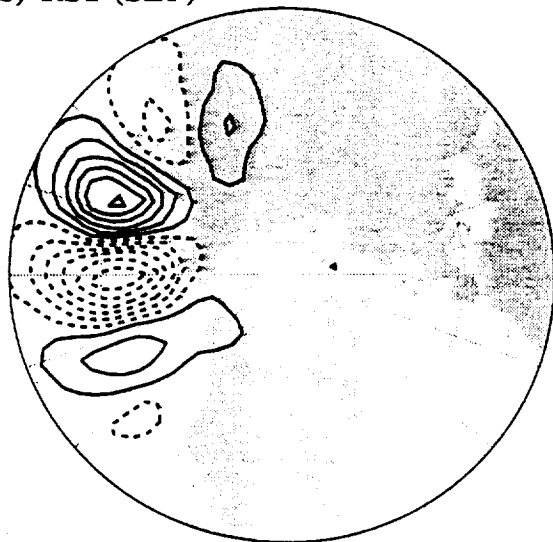
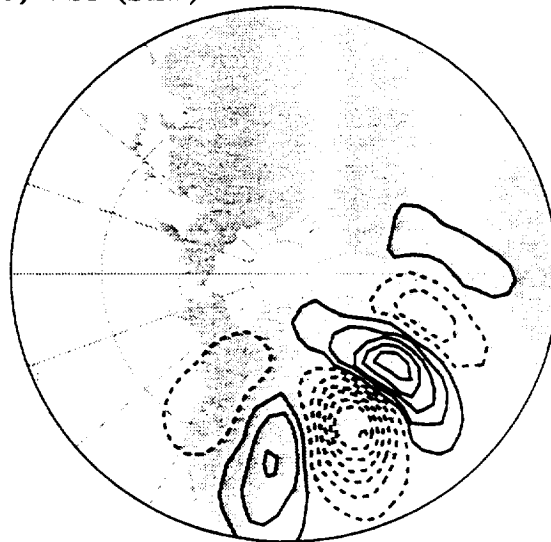
**a) RS1 (Z500)****c) RS3 (Z500)****b) RS1 (SLP)****d) RS3 (SLP)**

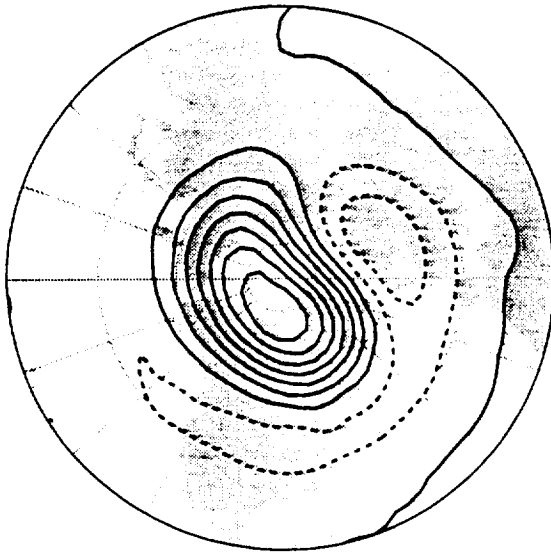
FIG. 5. Spatial patterns of the first (left column) and third (right column) rotated SVD modes based on the 3–7-day bandpass filtered SLP and 500-hPa height anomaly fields. Contour intervals are 6 m for the 500-hPa patterns (top panels) and 0.6 hPa for the SLP patterns (lower panels); negative contours are dashed.

18.4% and 16.4% of the total covariance between the two fields, respectively. The first mode (Figs. 6a,b) is characterized by a dipole over the North Atlantic resembling the NAO and a weaker anomalous center of action over eastern Siberia at the 500-hPa level, and a zonally symmetric structure centered near the North Pole at the 50-hPa level. The two patterns exhibit a temporal correlation of 0.58. The second mode (Figs. 6c,d) exhibits a stronger temporal correlation of 0.64 and is characterized by a strong anomaly over Alaska

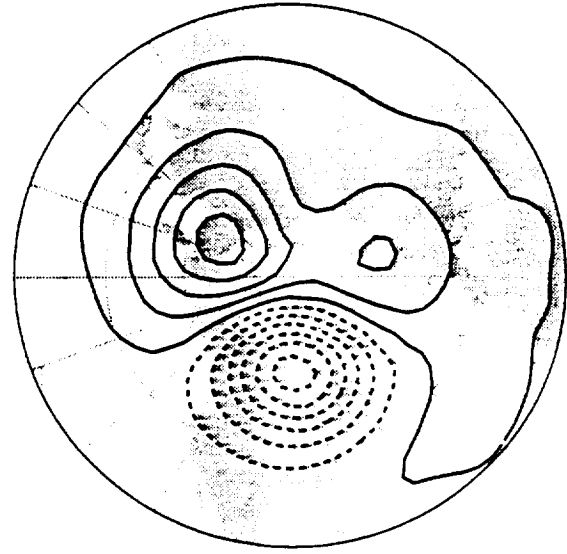
in the middle troposphere and a large-scale disturbance that combines features of wavenumbers 1 and 2 in the lower stratosphere. In both modes the stratospheric patterns exhibit a higher concentration of variance in the lowest zonal wavenumbers (0, 1, and 2), in agreement with Charney and Drazin (1961). The time series associated with the 500-hPa maps shown in Figs. 6b and 6d are characterized by strong positive skewness, +0.32 and +0.40, respectively, indicative of blocking activity in high latitudes (Knox and Hay 1985).



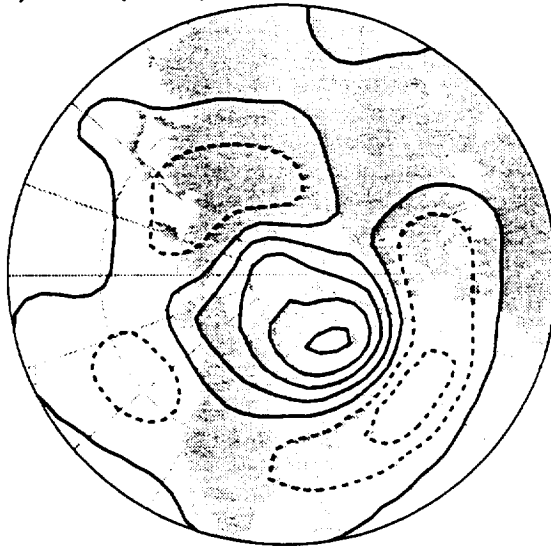
a) RS1 (Z50)



c) RS2 (Z50)



b) RS1 (Z500)



d) RS2 (Z500)

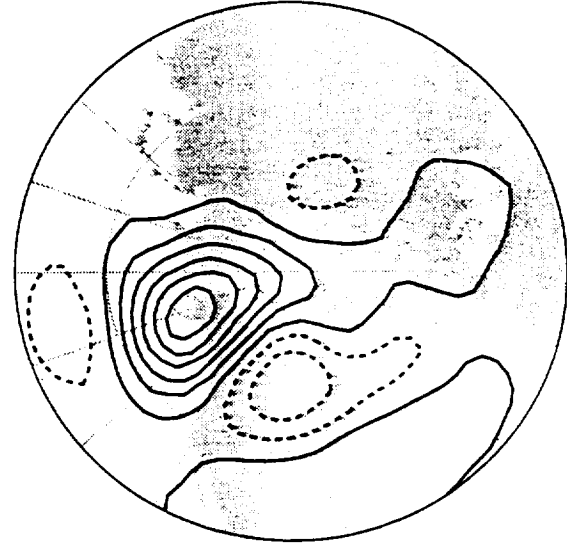


FIG. 6. Spatial patterns for the first (left column) and second (right column) rotated SVD modes based on 50- and 500-hPa height anomalies for 27 winters 1 January 1964 through 24 February 1990 with the 500-hPa field leading the 50-hPa field by four days. Contour intervals are 30 m for the 50-hPa maps (top panels) and 15 m for the 500-hPa maps (lower panels); negative contours are dashed.

#### d. Patterns derived from two linearly related fields

Newman and Sardeshmukh (1994) questioned whether SVD analysis is capable of isolating a linear relationship between two fields. Their argument can be summarized as follows. Assuming the two data fields  $\mathbf{Z}(y, t)$  and  $\mathbf{S}(x, t)$  as defined in section 2a have a linear relationship  $\mathbf{Z} = \mathbf{L}\mathbf{S}$ , where  $\mathbf{L}$  is a linear operator, the question is whether SVD is able to identify pairs of singular vectors that satisfy  $\mathbf{q}_k \propto \mathbf{L}\mathbf{p}_k$ . Using (6) and (7), one can show that sin-

gular vectors obtained from SVD analysis satisfy  $\mathbf{Q}\Sigma = 1/\mathbf{TLP}(\mathbf{A}^T\mathbf{A})$ . Similarly, the rotated singular vectors satisfy  $\mathbf{Q}^*\Sigma^* = 1/\mathbf{TLP}^*(\mathbf{A}^{*T}\mathbf{A}^*)$ , according to (11) and (12). A perfect linear relation requires the matrices  $\mathbf{A}^T\mathbf{A}$  and  $\mathbf{A}^{*T}\mathbf{A}^*$  to be diagonal. In general, this is not true because neither time series in  $\mathbf{A}$  or  $\mathbf{A}^*$  are mutually orthogonal. The question is whether any physical interpretation of results from rotated SVD analysis is justified. To address this question, we perform rotated SVD analysis between relative vorticity ( $\zeta$ ) and streamfunction ( $\psi$ )

fields. Because the two fields have the linear relationship  $\zeta = \nabla^2 \psi$ , we want to examine whether the resulting singular vectors associated with the  $\zeta$  and  $\psi$  fields can be related through the linear operator  $\nabla^2$  and whether the singular vectors are of any physical meaning.

The  $\zeta$  and  $\psi$  fields were derived from the ECMWF 200-hPa wind. Pentad (five-day mean) wind was computed in a manner similar to Lau et al. (1994). The climatological annual cycle was then computed and removed to obtain the anomaly wind. The pentad relative vorticity,  $\zeta$ , was calculated from the anomaly wind and the pentad streamfunction,  $\psi$ , was determined as  $\nabla^{-2} \zeta$ . The  $\zeta$  and  $\psi$  fields were then weighted by the square root of cosine latitude. Our analysis was performed for the November–March season (270 pentads in each field) on a reduced  $10^\circ \times 5^\circ$  global grid. Lau et al. (1994) reported that removal of the zonal mean component provides a better separation between tropical and extratropical modes in their rotated PCA of the  $\psi$  field. Hence, our analysis was performed on the zonally asymmetric components of the  $\zeta$  and  $\psi$  fields.

Unrotated singular vectors (not shown) exhibit spatial patterns that tend to be global in extent, indicative of possible mixing among different circulation modes. We performed rotated SVD analysis by retaining the five leading SVD pairs. Figure 7 shows the rotated singular vectors of the  $\psi$  and  $\zeta$  fields for the first three modes. For the sake of comparison, the  $\zeta$  singular vectors shown in Fig. 7 have been converted into streamfunctions ( $\psi_\zeta$ ) using inverse Laplacian transform. The reason for keeping the first five SVD pairs in the rotation is that the associated covariance fraction exhibits a large gap between the fifth and sixth SVD pairs. We also performed the analysis by retaining the ten leading SVD pairs and the first three rotated SVD modes obtained from this rotation were essentially the same as those shown in Fig. 7.

Because time series in  $\mathbf{A}^*$  are not mutually orthogonal, the rotated SVD analysis does not recover the exact linear relationship between the  $\psi$  and  $\zeta$  fields. The difference between the  $\psi$  and  $\psi_\zeta$  patterns shown in Fig. 7 is reflected in the anomaly amplitude and the structure with small spatial scales. Nevertheless, the corresponding  $\psi$  and  $\psi_\zeta$  patterns bear strong resemblance to each other, with pattern correlations of 0.96, 0.97, and 0.96, respectively. Their associated time series exhibit temporal correlations of 0.92, 0.97, and 0.93, respectively. The strong resemblance between the corresponding  $\psi$  and  $\psi_\zeta$  patterns is due to the fact that the matrix  $\mathbf{A}^* \mathbf{A}^*$  is diagonally dominant: the values of diagonal elements are at least an order of magnitude larger than those of off-diagonal elements. The same is true for other examples presented in this paper.

The first two modes are primarily characterized by quadrupole structures straddling the equator over the Pacific and Indian Oceans, with approximately  $90^\circ$  phase shift from one mode to the other. The two modes

account for 4.9% and 4.1% of the total covariance between the  $\psi$  and  $\zeta$  fields, respectively. The associated time series are dominated by strong interannual variability similar to that of the El Niño/Southern Oscillation (ENSO). It appears that the two modes together represent an atmospheric response due to the eastward displacement of tropical heating associated with ENSO events such as the one that occurred during 1986/87. The circulation pattern associated with the second mode is generally observed during ENSO years (Mo and Kousky 1993; Lau et al. 1994). The third mode, which accounts for 4.1% of the total covariance, exhibits a circulation pattern in the extratropical region of the Northern Hemisphere. The spatial pattern, which is mainly confined in the region of the North Pacific and North America, bears strong resemblance to the PNA pattern (Wallace and Gutzler 1981). The spatial patterns associated with the three rotated SVD modes can be identified among the prominent modes of variability in rotated PCA based on either the  $\psi$  or  $\zeta$  field.

#### 4. Conclusions

As an extension of conventional SVD analysis, we have described an analysis procedure that yields a set of alternative solutions. The unrotated singular vectors can be viewed as initial solutions of the coupled modes of variability within two data fields. However, spatial patterns of unrotated singular vectors are often difficult to interpret physically and less statistically robust. These disadvantages are the consequence of the optimization criterion in SVD analysis, which seeks pairs of singular vectors that maximize the temporal covariance between two data fields while constraining the singular vectors to be temporally and spatially orthogonal as defined in (5) and (7).

Upon orthogonally rotating a subset of total singular vectors subject to certain constraints, we are able to relax the spatial orthogonality constraint imposed on the singular vectors while retaining the temporal orthogonality inherent in the associated time series. As a result, the spatial patterns of the rotated singular vectors are free to assume the form of "teleconnection" patterns with widely separated centers of action, or monopoles with only a single region of high correlation, as evident in the examples presented in this study. Although the rotated singular vectors of each field are no longer spatially orthogonal to one another, a rotated singular vector of the left field is temporally correlated with only a single rotated singular vector of the right field. This property of rotated SVD analysis allows us to more clearly identify coupled modes of variability inherent in two data fields. Analogous to the relationship between conventional PCA and SVD analysis, one can show that rotated PCA is in fact a special case of rotated SVD analysis in which the left field is identical to the right field.

Because SVD analysis is based on datasets with a finite number of temporal realizations, the results are

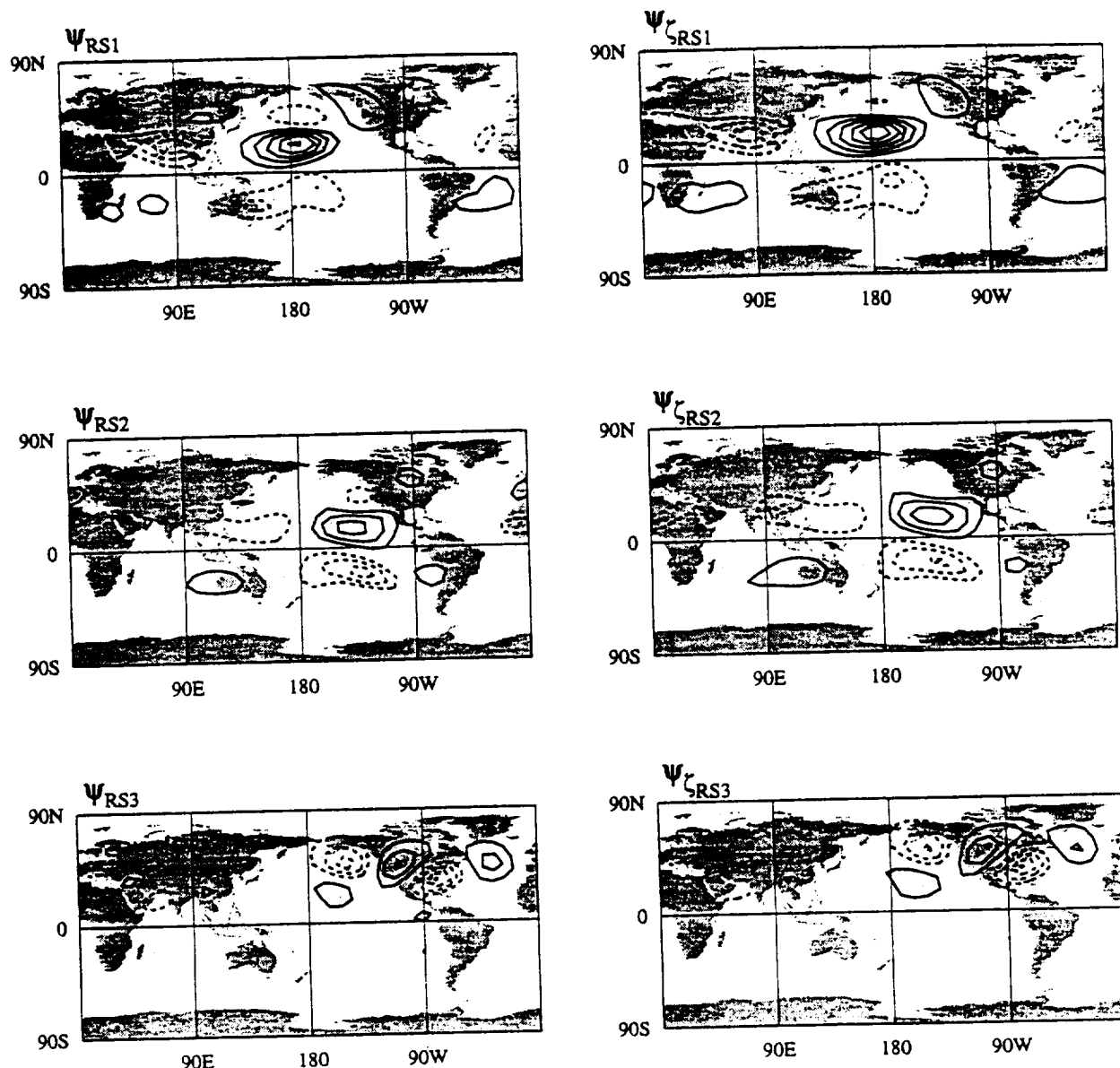


FIG. 7. The three leading rotated SVD modes obtained from the analysis based on the zonally asymmetric components of 200-hPa streamfunction ( $\psi$ ) and vorticity ( $\zeta$ ) for nine winters (November–March) from January 1985 through December 1993. Left: streamfunction patterns for singular vectors of the  $\psi$  field. Right: streamfunction patterns calculated from the corresponding singular vectors of the  $\zeta$  field. Contour interval is  $2 \times 10^6 \text{ m}^2 \text{ s}^{-1}$ ; negative contours are dashed. The zero contour is removed for clarity.

subject to sampling variability. Using the same linear analysis technique as the one employed by North et al. (1982) in analyzing shifts in eigenvalues and eigenvectors due to small sampling perturbations, one can show that the rule of thumb for PCA can also be applied to SVD analysis. In other words, when sampling error in a singular value is comparable to the distance from the singular value to a nearby singular value, the corresponding singular vectors will be subject to large sampling variability. By comparing the robustness of unrotated and rotated PC patterns based on randomly generated synthetic data, Richman (1986) concluded

that rotated solutions are less sensitive to sampling fluctuations than the unrotated ones. Cheng et al. (1995) examined robustness of unrotated and rotated PCs based on 10-day low-pass-filtered 500-hPa height fields and found that loading vectors of the prominent rotated PCs, which closely resemble the rotated SVD patterns shown in Figs. 3a and 3c, are statistically more robust than their unrotated counterparts. They can be robust even when the unrotated ones are completely degenerate.

Despite that rotated SVD does not recover the *exact* linear relationship between two fields, we have shown in

the last example that this analysis technique is able to recover the linear relationship between the  $\psi$  or  $\zeta$  fields to a large degree and the results are of physical meaning. CCA does not have such a problem since canonical variates (time series) are mutually orthogonal within each field as well as between two fields. However, CCA has the same drawback; namely, the resulting spatial patterns (canonical coefficients) are often quite complex and difficult to interpret. To increase interpretability of CCA results, Cliff and Krus (1976) proposed orthogonal rotation of canonical solutions based on unweighted canonical coefficients, but at the price of losing the orthogonality between canonical variates of two fields. Since the purpose of such an analysis is to identify coupled modes of variability between two fields, it is reasonable to determine the rotation based on the patterns of *heterogeneous* correlation (weighted singular vectors) rather than the patterns of *homogeneous* correlation (unweighted singular vectors). We applied CCA to the datasets used in example 3a and found that the result tends to blend different regional patterns (not shown). Utilizing the rotation procedure proposed in this study, we obtain a result similar to that of rotated SVD shown in Fig. 3. Therefore, the rotation procedure outlined in this paper may also be useful in CCA.

**Acknowledgments.** The authors thank Profs. C. S. Bretherton and J. M. Wallace for examining an early version of the manuscript and offering helpful comments. One of us (XC) is indebted to Prof. J. M. Wallace for bringing SVD analysis technique to his attention, which has led to this study. We also thank Dr. Steve Cherry at NCAR for sharing the paper by Dr. Muller with us. Dr. Matthew Newman and an anonymous reviewer offered valuable comments. This research was supported by the National Aeronautics and Space Administration Contract NASW-4844 and the National Science Foundation Grant ATM-9123797.

#### REFERENCES

- Barnston, A., and R. E. Livezey, 1987: Classification, seasonality and persistence of low-frequency circulation patterns. *Mon. Wea. Rev.*, **115**, 1083–1126.
- Blackmon, M. L., Y.-H. Lee, and J. M. Wallace, 1984: Horizontal structure of 500-mb height fluctuations with long, intermediate and short time scales. *J. Atmos. Sci.*, **41**, 961–979.
- Bretherton, C. S., C. Smith, and J. M. Wallace, 1992: An intercomparison of methods for finding coupled patterns in climate data. *J. Climate*, **5**, 541–560.
- Cattell, R. B., 1966: The scree test for number of factors. *Multivar. Behav. Res.*, **1**, 245–276.
- Charney, J. G., and P. J. Drazin, 1961: Propagation of planetary-scale disturbances from the lower into the upper atmosphere. *J. Geophys. Res.*, **66**, 83–109.
- Cheng, X., and J. M. Wallace, 1993: Cluster analysis of the Northern Hemisphere wintertime 500-hPa height field: Spatial patterns. *J. Atmos. Sci.*, **50**, 2674–2695.
- , G. Nitsche, and J. M. Wallace, 1995: Robustness of low-frequency circulation patterns derived from EOF and rotated EOF analyses. *J. Climate*, **8**, 1709–1713.
- Cliff, N., and D. J. Krus, 1976: Interpretation of canonical analysis: Rotated vs. unrotated solutions. *Psychometrika*, **41**, 35–42.
- Esbensen, S. K., 1984: A comparison of intermonthly and interannual teleconnections in the 700-mb geopotential height field during the Northern Hemisphere winter. *Mon. Wea. Rev.*, **112**, 2016–2032.
- Horel, J. D., 1981: A rotated principal component analysis of the interannual variability of the Northern Hemisphere 500-mb height field. *Mon. Wea. Rev.*, **109**, 2080–2092.
- Hsu, H., and J. M. Wallace, 1985: Vertical structure of wintertime teleconnection patterns. *J. Atmos. Sci.*, **42**, 1963–1710.
- Knox, J. L., and J. E. Hay, 1985: Blocking signatures in the Northern Hemisphere: Frequency distribution and interpretation. *J. Climatol.*, **5**, 1–16.
- Kushnir, Y., and J. M. Wallace, 1989: Low-frequency variability in the Northern Hemisphere winter: Geographical distribution, structure and time-scale dependence. *J. Atmos. Sci.*, **46**, 3122–3142.
- Kutzbach, J. E., 1967: Empirical eigenvectors of sea level pressure, surface temperature, and precipitation complexes over North America. *J. Appl. Meteor.*, **6**, 791–802.
- , 1970: Large-scale features of monthly mean Northern Hemisphere anomaly maps of sea-level pressure. *Mon. Wea. Rev.*, **98**, 708–716.
- Lanzante, J. R., 1984: A rotated eigenanalysis of the correlation between 700-mb heights and sea surface temperatures in the Pacific and Atlantic. *Mon. Wea. Rev.*, **112**, 2270–2280.
- Lau, K.-M., P.-J. Sheu, and I.-S. Kang, 1994: Multiscale low-frequency circulation modes in the global atmosphere. *J. Atmos. Sci.*, **51**, 1169–1193.
- Lorenz, E. N., 1956: Empirical orthogonal functions and statistical weather prediction. Sci. Rep. No. 1, Statist. Forecasting Proj., Dept. Meteor., MIT, 49 pp.
- Mo, K. C., and V. E. Kousky, 1993: Further analysis of the relationship between circulation anomaly patterns and tropical convection. *J. Geophys. Res.*, **98**, 5103–5113.
- Nakamura, H., and J. M. Wallace, 1990: Observed changes in baroclinic wave activity during the life cycles of low-frequency circulation anomalies. *J. Atmos. Sci.*, **47**, 1100–1116.
- Newman, M., and P. D. Sardeshmukh, 1994: A caveat concerning singular value decomposition. *J. Climate*, **8**, 352–360.
- North, G. R., T. L. Bell, R. F. Cahalan, and F. J. Moeng, 1982: Sampling errors in the estimation of empirical orthogonal functions. *Mon. Wea. Rev.*, **110**, 699–706.
- O'Lenic, E. A., and R. E. Livezey, 1988: Practical considerations in the use of rotated principal component analysis (RPCA) in diagnostic studies of upper-air height fields. *Mon. Wea. Rev.*, **116**, 1682–1689.
- Preisendorfer, R. W., 1988: *Principle Component Analysis in Meteorology and Oceanography*. Elsevier, 425 pp.
- Reynolds, T. J., and E. F. Jackosky, 1981: Interpreting canonical analysis: The use of orthogonal transformations. *Educ. Psychol. Meas.*, **41**, 35–42.
- Richman, M. B., 1986: Rotation of principal components. *J. Climatol.*, **6**, 293–335.
- , and P. J. Lamb, 1987: Patterns analysis of growing seasons precipitation in southern Canada. *Atmos.-Ocean*, **25**, 137–158.
- Rogers, J. C., 1981: The North Pacific oscillation. *J. Climatol.*, **1**, 39–57.
- van Loon, H., and J. C. Rogers, 1978: The seesaw in winter temperatures between Greenland and northern Europe. Part I: General description. *Mon. Wea. Rev.*, **106**, 296–310.
- Walker, J. M., and E. M. Bliss, 1932: World Weather V. *Mem. Roy. Meteor. Soc.*, **4**, 53–84.
- Wallace, J. M., and D. S. Gutzler, 1981: Teleconnections in the geopotential height field during Northern Hemisphere winter. *Mon. Wea. Rev.*, **109**, 784–812.
- Wang, B., 1992: The vertical structure and development of the ENSO anomaly mode during 1979–1989. *J. Atmos. Sci.*, **49**, 689–712.
- Weare, B. C., 1987: Relationships between monthly precipitation and SST variations in the tropical Pacific region. *Mon. Wea. Rev.*, **115**, 2687–2698.

## Observed correlations between winter-mean tropospheric and stratospheric circulation anomalies

Mark P. Baldwin, Xinhua Cheng, and Timothy J. Dunkerton

Northwest Research Associates, Bellevue, Washington

**Abstract.** It is shown that interannual variability of the northern winter stratospheric flow in 1964-1993 was closely linked to large-scale circulation anomalies in the middle troposphere. Of the known tropospheric teleconnection patterns, the one having the strongest relation to the DJF zonal-mean stratospheric flow was the North Atlantic Oscillation (NAO). Singular value decomposition between the 500 and 50-hPa geopotential heights produced a 500-hPa structure containing elements of the NAO pattern, but including an anomaly in eastern Siberia. During this time period, the correlation of NAO-related modes to the polar lower stratosphere exceeded that of the equatorial quasi-biennial oscillation.

### Introduction

On interannual timescales, the wintertime stratospheric circulation is influenced in several ways. One of the strongest influences is the quasi-biennial oscillation of the equatorial lower stratosphere (QBO), with variable period averaging about 28 months [Holton and Tan, 1980; Holton and Tan, 1982; Baldwin and Dunkerton, 1991; Dunkerton and Baldwin, 1991]. There is a stronger polar vortex during the west 40-hPa QBO phase, and a weaker vortex (and greater likelihood of sudden warmings) during the east phase. The mechanism involves a modulation of the waveguide for upward propagating planetary-scale waves. The QBO's influence has been confirmed in modeling studies [e.g. O'Sullivan and Young, 1992; O'Sullivan and Dunkerton, 1994].

Since planetary waves are essential to stratospheric variability, interannual variations of tropospheric forcing are potentially important; e.g., those associated with the El Niño/Southern Oscillation (ENSO). Stratospheric effects of ENSO were investigated by several authors. Due to a coincidence of ENSO and QBO phases, Wallace and Chang [1982] and van Loon and Labitzke [1987] found that the influence of the QBO and ENSO were apparently similar, with warm ENSO events resulting in a weaker, more disturbed polar vortex. Using several partitioning schemes to minimize overlap with the QBO, Hamilton [1993] found however that ENSO's

influence was moderate compared to that of the QBO, and not statistically significant.

In a related study, Baldwin and O'Sullivan [1994] examined the stratosphere's observed relationship with three tropospheric modes of variability that are influenced, in part, by ENSO. Using principal-component time series corresponding to the Pacific/North American (PNA), Western Pacific Oscillation (WPO), and the Tropical/Northern Hemisphere (TNH) patterns, Baldwin and O'Sullivan found no significant effect on the strength of the polar vortex, although waves 1 and 2 were modulated at the 50-hPa level.

In this paper we investigate the possibility that interannual variability of other tropospheric circulation patterns (beside PNA, WPO, and TNH) unrelated to either ENSO or the QBO may modulate the strength of the stratospheric polar vortex. In particular, we examine the North Atlantic Oscillation (NAO) and related patterns and use singular-value decomposition (SVD) to find the strongest association between height field and mean zonal wind anomalies in the troposphere and lower stratosphere.

### Data Analysis

Our dataset consisted of daily (12Z) National Meteorological Center (NMC) height fields for the period 1/1/64-5/8/93. These data were available north of 18°N at the standard levels 1000, 850, 700, 500, 400, 300, 250, 200, 150, 100, 70, 50, 30, and 10 hPa. EOFs were calculated from 30 years of December-February (DJF) average 500-hPa geopotential using the covariance matrix. The leading modes were obtained with varimax rotation using a 317-point, polar stereographic grid which corresponds approximately to 6° latitude horizontal resolution. SVD analysis was carried out between the 500 and 50-hPa height fields using a similar polar stereographic grid or, alternatively, using 500 hPa geopotential and 1000-10 hPa mean zonal wind as input.

### Results

Applying varimax rotation to EOFs of the temporal covariance matrix of the DJF 500-hPa height field gave structures corresponding closely to the PNA, NAO, and WPO patterns of Wallace and Gutzler [1981] and Kushnir and Wallace (1989). Figure 1 shows the second mode, which resembled the NAO and accounted for 14.3% of the variance in the 30-year dataset. This mode

Copyright 1994 by the American Geophysical Union.

Paper number 94GL01010  
0094-8534/94/94GL-01010\$03.00

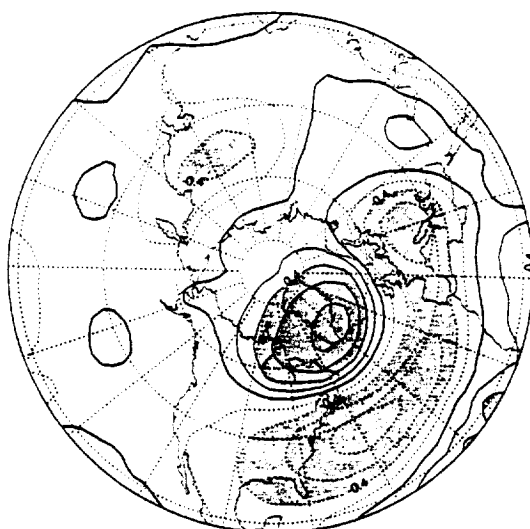


**Figure 1.** The second rotated EOF of the temporal covariance matrix of 500 hPa geopotential based on winter (DJF-average) data for the years 1964–93. 10 modes were included in the varimax rotation. The value at each grid point is the correlation between the principal-component time series and the geopotential anomalies at that point. Contour interval 0.2; negative values dashed.

was characterized by a north-south dipole in the North Atlantic, with a center near Greenland and a longitudinally broad anomaly stretching from Europe to the West Atlantic near 40°N. A third feature over eastern Siberia was somewhat weaker. The Siberian center was less prominent in a longer dataset (1946–93) than in the 30-year dataset used here. This mode does not appear to be influenced by ENSO. The correlation between its principal component and winter-mean Tahiti–Darwin sea level pressure anomalies is .07.

When we correlated the principal-component time series of the NAO-like mode of Figure 1 with the mean zonal wind, the result was a strong north-south dipole extending at least through 10 hPa (Figure 2). Near 50–60°N, correlations greater than 0.6 extended up through 70 hPa, but values decreased to less than 0.4 by 10 hPa.

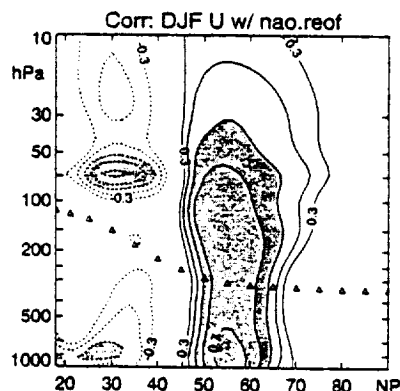


**Figure 2.** Correlation between the principal component of the NAO-like EOF (Figure 1) and the DJF mean zonal wind. Triangles represent the approximate wintertime tropopause. Contour interval 0.1, beginning at  $\pm 0.3$ .

The stratospheric dipole was a fundamental mode of variability, appearing as the leading mode (accounting for 70% of the interannual variance) in an EOF analysis of the mean zonal wind [Dunkerton and Baldwin, 1992].

A more direct approach to investigate tropospheric links with the stratosphere employs SVD analysis, e.g., of the covariance matrix between 500 and 50-hPa geopotential height [Cheng, 1993]. This method identifies pairs of spatial patterns that most efficiently explain the temporal covariance between two fields [Bretherton *et al.*, 1992]. The 500-hPa height pattern of the leading SVD mode is shown in Figure 3a. Features of this pattern were broadly similar to the NAO-like mode, but differed in several ways. 1) The South Atlantic anomaly was longitudinally more confined, with a single center near the Atlantic coast of Europe. 2) The Siberian center was more prominent. 3) The Greenland center was located farther west, north of Labrador, and extended farther over the polar cap. 4) Circular symmetry, about a vortex center displaced toward Greenland, was more

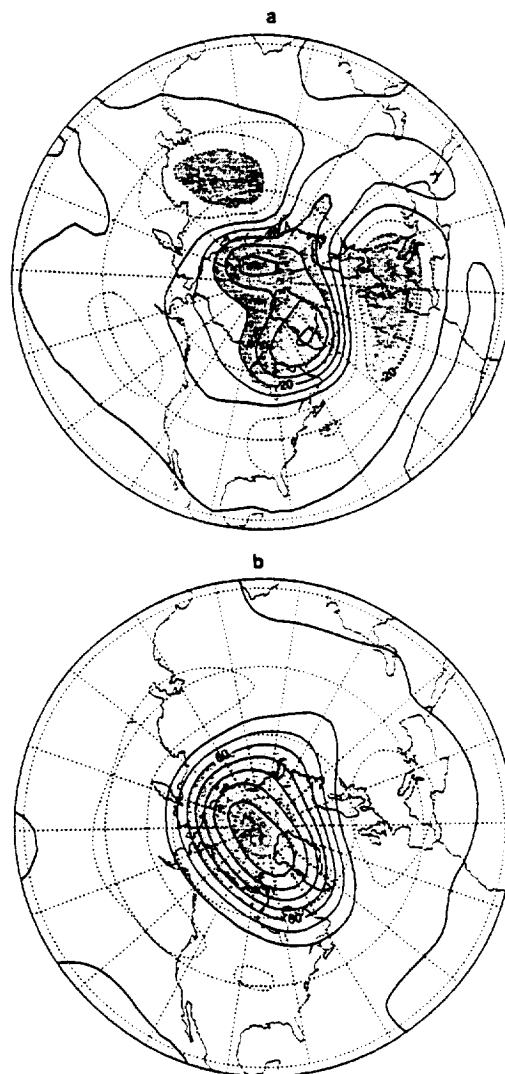


**Figure 3.** The leading mode (heterogeneous regression map) from SVD analysis between DJF 500 and 50-hPa height fields. (a) 500 hPa (contour interval 10 m); (b) 50 hPa (contour interval 30 m).

pronounced. The corresponding stratospheric anomaly (Figure 3b) was centered near the pole. When we performed SVD between the 500-hPa height field and the mean zonal wind, the resulting pattern (Figure 4) was similar to that of Figure 2, but with higher correlations exceeding 0.9 in the lower stratosphere and 0.6 at 10 hPa. The 500-hPa structure (not shown) was similar to Figure 3a.

The 500-hPa SVD pattern indicates that the troposphere-stratosphere link was not just a simple manifestation of the NAO pattern with its north-south 'seesaw' over the North Atlantic, but also involved an anomaly over eastern Siberia. In order to highlight these regional aspects, time series were constructed based on pairs of grid points, in a manner similar to *Wallace and Gutzler's* [1981] definitions of the WPO and other patterns. We defined a North Atlantic index (NA) as the difference between normalized geopotential anomalies at 62°N, 80°W and 46°N, 20°W. A cross-polar index (XP) was defined similarly, using 62°N, 80°W and 58°N, 100°E. Although the correlation between the indices was 0.86, they appeared to represent two distinct aspects of a troposphere-stratosphere link. Figure 5a illustrates the correlation between the NA index and the mean zonal wind. Correlations in the northern half of the stratospheric dipole far exceeded those using the principal component of the NAO-like mode (Figure 1) and nearly matched those of the leading SVD mode (Figure 4). Correlations with the NA index at 60°N exceeded 0.6 from the surface through 10 hPa.

Correlations between the XP index and the mean zonal wind (Figure 5b) were slightly higher than correlations using the NA index, and exceeded those of the 500-hPa SVD mode above 50 hPa. Overall, the correlations using gridpoint-based indices were similar, as expected from the high correlation between the two indices. By comparison a QBO index, defined as the 40-hPa Singapore wind, was not as highly correlated with the mean zonal wind as the NA index, the XP index, or the leading SVD mode (Figure 5c). Correlations did not exceed 0.6 anywhere in the diagram, and

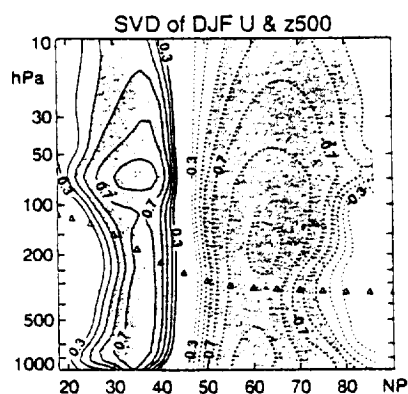


**Figure 4.** Heterogeneous correlation between 500 hPa principal component and mean zonal wind, from SVD analysis using 500 hPa geopotential and 1000-10 hPa mean zonal wind as input.

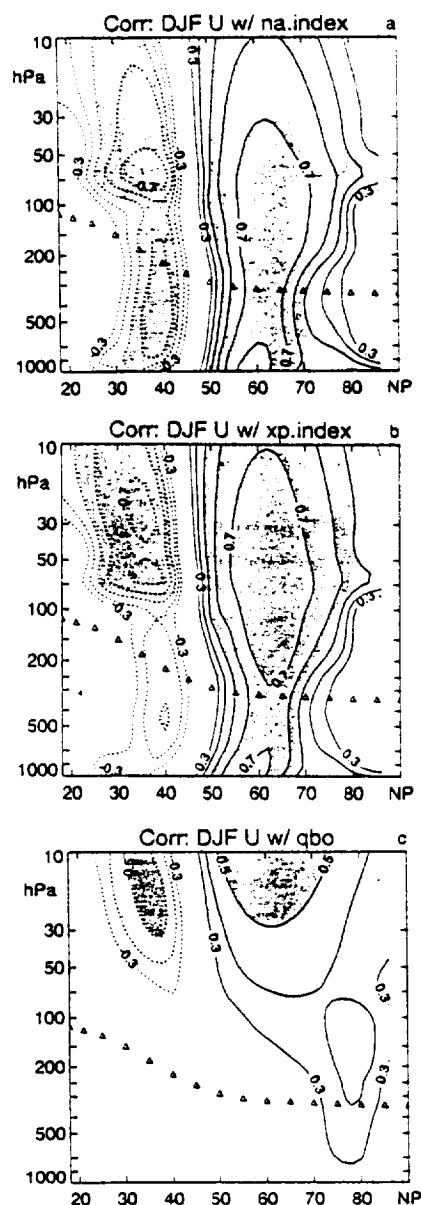


**Figure 5.** Correlation of mean zonal wind with (a) NA index, (b) XP index, and (c) the 40 hPa Singapore QBO. See text for definition of indices.

diminished greatly upon entering the troposphere. Unlike the tropospheric indices, however, the effect of the QBO increased with height in the stratosphere.

## Conclusion

A pattern resembling the North Atlantic Oscillation (NAO) was strongly correlated with the zonal-mean stratospheric polar vortex in 1964-1993. This structure, best represented as the 500-hPa SVD mode in Figure 3a, had prominent anomalies in eastern Siberia and eastern Atlantic, opposing a main center north of Labrador. The pattern displayed a large degree of circular symmetry about a central point displaced toward Greenland. This displacement off the pole seems important, as it may result in a wave-1 anomaly which could act to force the stratosphere from below. Inter-

estingly there were two parts of the tropospheric pattern (NA, XP). Either by itself was sufficient to generate high correlations with the stratosphere, yet both appeared as a single mode in SVD analysis. This suggests that combinations of tropospheric teleconnection patterns are essential to stratospheric interannual variability; e.g., cross-polar excitation of wave 1 combined with blocking over Greenland. Alternatively, part of the tropospheric pattern may represent downward influence from the stratosphere. Analysis of daily data (to be reported elsewhere) indicates however that the strongest lag correlations within most SVD patterns occur when the troposphere leads the stratosphere by a few days – suggesting that the direction of cause-and-effect is for the most part upward.

**Acknowledgments.** This research was supported by the National Aeronautics and Space Administration, Contracts NASW-4508 and NASW-4844, and by the National Science Foundation, Grants ATM-9013280, ATM-9123797, and ATM-9303068. Partial computing support was provided by the University of Alaska Southeast.

## References

- Baldwin, M. P. and T. J. Dunkerton, Quasi-biennial oscillation above 10 mb. *Geophys. Res. Lett.*, **18**, 1205-1208, 1991.
- Baldwin, M. P., and D. O'Sullivan, Stratospheric effects of ENSO-related tropospheric circulation anomalies. *J. Climate*, **7**, in press, 1994.
- Bretherton, C. S., C. Smith, and J. M. Wallace, An intercomparison of methods for finding coupled patterns in climate data. *J. Climate*, **5**, 541-560, 1992.
- Cheng, X., Linear and nonlinear aspects of the northern hemisphere wintertime variability in the 500 hPa height field. Ph.D. dissertation, Univ. of Washington, 180 pp., 1993.
- Dunkerton, T. J. and M. P. Baldwin, Quasi-biennial modulation of planetary wave fluxes in the northern hemisphere winter. *J. Atmos. Sci.*, **48**, 1043-1061, 1991.
- Dunkerton, T. J. and M. P. Baldwin, Modes of interannual variability in the stratosphere. *Geophys. Res. Lett.*, **19**, 49-52, 1992.
- Hamilton, K., An examination of observed southern oscillation effects in the northern hemisphere stratosphere. *J. Atmos. Sci.*, **11**, 3468-3473, 1993a.
- Holton, J. R. and H.-C. Tan, The influence of the equatorial quasi-biennial oscillation on the global circulation at 50 mb. *J. Atmos. Sci.*, **37**, 2200-2208, 1980.
- Holton, J. R. and H.-C. Tan, The quasi-biennial oscillation in the Northern Hemisphere lower stratosphere. *J. Met. Soc. Japan*, **60**, 140-148, 1982.
- Kushnir, Y., and J. M. Wallace, Low-frequency variability in the northern hemisphere winter: geographical distribution, structure and time-scale dependence. *J. Atmos. Sci.*, **46**, 3122-3142, 1989.
- O'Sullivan, D. J., and T. J. Dunkerton, Seasonal development of the extratropical quasi-biennial oscillation in a numerical model of the middle atmosphere. *J. Atmos. Sci.* in press.
- O'Sullivan, D. J., and R. E. Young, Modeling the quasi-biennial oscillation's effect on the winter stratospheric circulation. *J. Atmos. Sci.*, **49**, 2437-2448, 1992.
- van Loon, H. and K. Labitzke, The southern oscillation. Part V: The anomalies in the lower stratosphere of the northern hemisphere in winter and a comparison with the quasi-biennial oscillation. *Mon. Weather Rev.*, **115**, 357-369, 1987.
- Wallace, J. M. and D. S. Gutzler, Teleconnections in the geopotential height field during the northern hemisphere winter. *Mon. Weather Rev.*, **109**, 784-812, 1981.
- Wallace, J. M. and F.-C. Chang, Interannual variability of the wintertime polar vortex in the northern hemisphere middle stratosphere, *J. Meteor. Soc. Japan*, **60**, 149-155, 1982.

M. P. Baldwin, X. Cheng, and T. J. Dunkerton,  
Northwest Research Associates, P.O. Box 3027, Bellevue,  
WA 98009. Email: mark@nwra.com; xinhua@nwra.com;  
tim@nwra.com

(received February 14, 1994; revised April 11, 1994;  
accepted April 18, 1994.)



# **IV. Numerical Study of the Quasi-Biennial Oscillation**



# The role of gravity waves in the quasi-biennial oscillation

Timothy J. Dunkerton

Northwest Research Associates, Bellevue, Washington

**Abstract.** The role of gravity wave momentum transport in the quasi-biennial oscillation (QBO) is investigated using a two-dimensional numerical model. In order to obtain an oscillation with realistic vertical structure and period, vertical momentum transport in addition to that of large-scale, long-period Kelvin and Rossby-gravity waves is necessary. The total wave flux required for the QBO is sensitive to the rate of upwelling, due to the Brewer-Dobson circulation, which can be estimated from the observed ascent of water vapor anomalies in the tropical lower stratosphere. Although mesoscale gravity waves contribute to mean flow acceleration, it is unlikely that the momentum flux in these waves is adequate for the QBO, especially if their spectrum is shifted toward westerly phase speeds. Short-period Kelvin and inertia-gravity waves at planetary and intermediate scales also transport momentum. Numerical results suggest that the flux in all vertically propagating waves (planetary-scale equatorial modes, intermediate inertia-gravity waves, and mesoscale gravity waves), in combination, is sufficient to obtain a QBO with realistic Brewer-Dobson upwelling if the total wave flux is 2–4 times as large as that of the observed large-scale, long-period Kelvin and Rossby-gravity waves. Lateral propagation of Rossby waves from the winter hemisphere is unnecessary in this case, although it may be important in the upper and lowermost levels of the QBO and subtropics.

## 1. Introduction

The quasi-biennial oscillation (QBO) of the tropical lower stratosphere is arguably one of the best examples of wave, mean-flow interaction in the Earth's atmosphere. It is thought that large-scale (10,000–40,000 km) long-period ( $\sim 4$ –15 day) Kelvin and Rossby-gravity waves drive the QBO, in part, as suggested by Holton and Lindzen [1972, hereinafter referred to as HL72] who simulated the oscillation in a one-dimensional model. Their work was motivated by the discovery of equatorial waves in rawinsonde data [Yanai and Maruyama, 1966; Wallace and Kousky, 1968] and a theoretical explanation of the QBO advanced by Lindzen and Holton [1968, hereinafter referred to as LH68]. It was later suggested that additional wave transport may be necessary [Lindzen and Tsay, 1975; Andrews and McIntyre, 1976]. The momentum deficit anticipated by those authors became more significant when Dunkerton [1991a, hereinafter referred to as D91] showed that the fluxes of HL72 are inadequate if sustained upwelling is present [Brewer, 1949; Dobson, 1956; Dunkerton, 1978]. The rate of upwelling is thought to be comparable, but opposite in sign, to the descent of QBO shear zones. If a model is able to generate a realistic QBO without upwelling (as in HL72, or Dunkerton [1985, hereinafter referred to as D85]), then in order to achieve the same QBO with upwelling, it is necessary to multiply wave fluxes by at least a factor of 2 [Gray and Pyle, 1989; D91; Kinnersley and Pawson, 1995]. The Rossby-gravity flux of HL72 was larger than observed, by a factor of  $\sim 2$ –4. Descent of QBO easterlies therefore cannot be obtained with Rossby-gravity waves alone [Takahashi and Boville, 1992], and there is a similar (though less severe) problem explaining the descent of westerlies with only long-period Kelvin waves.

Given a wide spectrum of motions excited in the tropical

troposphere by convection, lateral forcing, and other mechanisms, it is likely that waves exist besides those discovered by Yanai and Maruyama [1966] and Wallace and Kousky [1968]. With their source primarily in the underlying troposphere these additional waves transport momentum upward and may play a role in the QBO [Lindzen and Tsay, 1975; Cadet and Teitelbaum, 1979]. Recent observational and theoretical studies reinforce this idea. Using rawinsonde data from Singapore, Maruyama [1994] estimated that short-period ( $\sim 1$ –3 days) disturbances transport zonal momentum vertically at a rate comparable to that of long-period (7.4–32 day) Kelvin waves. Sato *et al.* [1994] also examined these data, observing a significant cospectrum of zonal wind and temperature. Interestingly, the cospectrum of short-period disturbances alternates sign with the QBO. An interpretation of their result is that both eastward and westward waves are present, interacting with QBO shear zones [Dunkerton, 1995]. Substantial power and momentum flux evidently exist at higher frequencies and some of this variance is resolved in twice-daily rawinsonde data [Sato and Dunkerton, this issue]. It is likely that disturbances with even shorter periods and smaller horizontal scales are also present. Using cloud imagery, Bergman and Salby [1994] estimated theoretical wave spectra due to tropical convection with periods  $T \geq 6$  hours and zonal wavenumbers  $s \leq 256$ . Their calculations suggest that the total vertical Eliassen-Palm flux in all waves is  $\sim 2.5$  times as large as that of planetary-scale equatorial modes alone (Kelvin, Rossby, and Rossby-gravity waves). Using ER-2 data, Pfister *et al.* [1993a, b] derived a phase-speed spectrum of gravity waves originating in mesoscale convective complexes. Their estimates of momentum flux suggest that mesoscale gravity waves contribute 10–20% of the observed QBO accelerations.

It is reasonable to inquire whether enough momentum transport can be found in all vertically propagating waves collectively, sufficient to drive the QBO in spite of Brewer-Dobson upwelling. Intermediate inertia-gravity and mesoscale

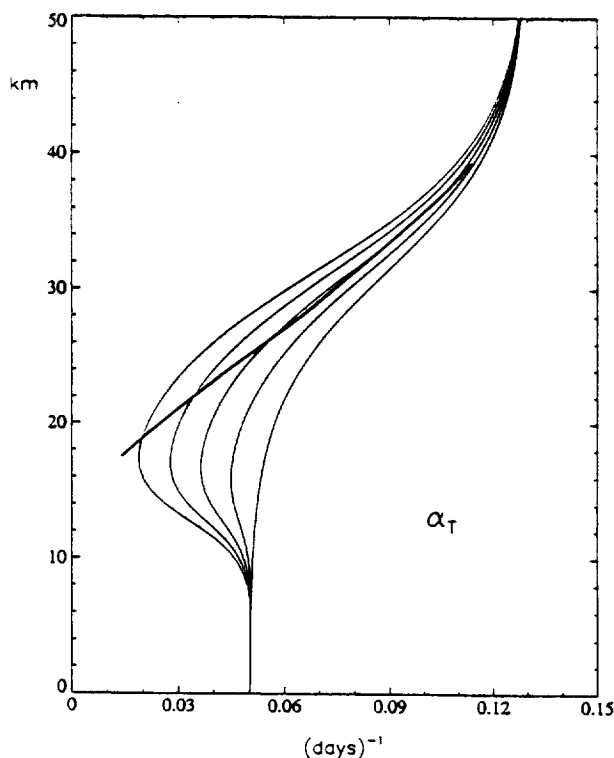


Figure 1. Vertical profiles of radiative relaxation rate (thin lines) and globally averaged  $\alpha_T$  estimated from a radiative code (thick line). The middle curve was used in this study.

gravity waves, in this case, are essential for realistic descent of QBO shear zones. An alternative explanation for the QBO easterly phase is that laterally propagating planetary Rossby waves from the winter stratosphere enter the tropics and decelerate the zonal wind there [Andrews and McIntyre, 1976; Dunkerton, 1983]. While some evidence of this effect can be found in the middle and upper stratosphere, the lower stratosphere appears rather protected from intrusion by extratropical planetary waves. A semipermeable barrier to isentropic transport of trace constituents is observed in the subtropical lower stratosphere above  $\sim 20$  km [King *et al.*, 1991; Murphy *et al.*, 1993; Grant *et al.*, 1994; Randel *et al.*, 1994; Waugh, 1996; Dunkerton and O'Sullivan, 1996]. Remarkable persistence of QBO westerlies at 50 mb attests to the dynamical isolation of the equatorial lower stratosphere [Dunkerton and Delisi, 1985; Naujokat, 1986]. The dependence of planetary-wave propagation on subtropical zonal wind was discussed by Chen [1995]. These observations imply that for transport of chemical constituents the tropical lower stratosphere is somewhat like a "pipe" [Plumb, 1996] unexposed to vigorous isentropic mixing with midlatitude air. The apparent upwelling of water vapor anomalies in the equatorial lower stratosphere is consistent with tropical confinement [Mote *et al.*, 1995, 1996] and provides a uniquely valuable estimate of residual vertical velocity. From the apparent upwelling it is possible to estimate the total Eliassen-Palm flux required to generate a realistic QBO due to vertically propagating waves.

The purpose of this paper is to review the observational evidence of tropical upwelling and gravity waves in the equatorial lower stratosphere, and (in the context of a two-dimensional model) to demonstrate how the equatorial QBO can be simulated realistically when the total wave flux is sub-

stantially larger than in HL72. While it is impossible to assign momentum fluxes to the entire wave spectrum precisely, it is worthwhile to determine the total flux required for the QBO as a function of upwelling rate. Unlike in previous simulations of the QBO [Gray and Pyle, 1989; D91; Kinnersley and Pawson, 1995] fluxes due to long-period equatorial waves will not be increased in order to obtain an oscillation. Kelvin and Rossby-gravity fluxes instead will be held close to their observed values, and additional waves (including a continuous spectrum of gravity waves) will be superposed. This approach, incidentally, yields a more realistic QBO structure than in D91. Treatment of the continuous spectrum begins with the parameterization of LH68, discussing various aspects and shortcomings of their scheme and assessing its accuracy by comparison with line-by-line calculations of wave-induced acceleration. The QBO is simulated in a two-dimensional model (1) using the LH68 scheme to represent all fluxes except those of long-period Kelvin and Rossby-gravity waves and (2) using an alternative model in which intermediate waves are represented explicitly and the LH68 formula used only for mesoscale gravity waves. The scale-dependent damping of QBO temperature perturbations is examined with a radiative code. Finally, a one-dimensional model of the QBO is formulated from the two-dimensional results using a simple regression for vertical velocity and effective  $\beta$ . The one-dimensional model provides an economical way to determine the total wave flux required for a realistic QBO as a function of upwelling rate.

The two-dimensional numerical model and theoretical formulation of equatorial-wave and gravity-wave transport are discussed in section 2, along with the parameterization of extratropical body forces that are essential to tropical upwelling. The observed upwelling and wave fluxes are examined in section 3; this information is central to the paper, as it provides (for the first time) a preliminary basis for numerical simulation of the actual QBO. Results of the two-dimensional and one-dimensional models are presented in sections 4 and 5, respectively.

## 2. Theoretical Formulation

### 2.1. Numerical Model

The numerical model used here is an improved version of model II of D91. The model domain extends from pole to pole and from 0 to 84 km with 97 equally spaced grid points in sine-latitude and altitude. Latitudinal spacing of grid points is variable, reaching a minimum  $\Delta\theta \sim 1.2^\circ$  at the equator. The vertical grid spacing is uniformly  $\Delta z = 875$  m. The time step is 8640 s. Gradient balance was assumed [Stevens, 1983], rather than geostrophic balance as in D91, requiring minor changes in the residual stream function equation. Another modification is that the local contribution to static stability  $\bar{\phi}_{zz}$  is now included, which is important in the tropical upper troposphere.

### 2.2. Radiative Heating

Radiative heating of the middle atmosphere was represented in either of two ways: (1) as thermal relaxation to radiatively determined temperatures  $\bar{T}^E(y, z, t)$  or (2) using Shine's [1987] MIDRAD algorithm. Solstitial profiles of  $\bar{T}^E$  were obtained from Shine's paper, corresponding to temperatures achieved during a seasonal cycle without dynamical heat fluxes. Some arbitrary analytic profiles of radiative relaxation rate  $\alpha_T$  are shown in Figure 1, together with a globally averaged relaxation profile derived from MIDRAD, obtained by adding a small temperature perturbation to the whole vertical

column (0–84 km). The middle curve of Figure 1 was used for thermal relaxation rate in all simulations, except those using MIDRAD, described in this paper. The maximum radiative damping time is about 30 days at the tropical tropopause, much shorter than the timescale for radiation to space [Dickinson, 1973; Fels, 1982; Gille and Lyjak, 1986] indicated by the thick curve in the figure. The vertical scale dependence of radiative damping [Fels, 1982] cannot be ignored in this region, where annual cycle and QBO produce shallow temperature signals [Yulaeva et al., 1994]. For equatorial waves, scale-dependent radiative damping was determined by an analytic fit to the Fels [1982] damping rate  $\alpha_T(m, z)$  as done previously by Hamilton [1981], Vijayan and Reddy [1994], D85, and D91. Radiative heating of the troposphere was accomplished by relaxation to observed temperatures, with uniform rate 0.05 per day. Heating rates near the tropopause were merged smoothly between 300 and 100 mbar to avoid discontinuities.

### 2.3. Cumulus Heating

Following Held and Hou [1980] and later authors [Lindzen and Hou, 1988; Plumb and Hou, 1992], cumulus heating in the model was represented as relaxation to a specified equilibrium profile  $\bar{T}_c^E(y)$ . To achieve realistic mass flux, the rate coefficient was set at 0.5 per day, constant up to 250 mbar, and decreasing linearly to zero at 100 mbar.  $\bar{T}_c^E(y)$  was assumed independent of height and written as the sum of first and second Legendre polynomials with amplitude  $T_1$ ,  $T_2$ , respectively. The symmetric part was held fixed, while the antisymmetric part varied annually. In simulations reported here,  $(T_1, T_2) = (12.5, 26)$  K, respectively. This combination gave good overall agreement with observations according to six criteria: latitude of the Intertropical Convergence Zone, Hadley mass flux, meridional velocity in the upper troposphere, zonal and vertical velocity at the tropopause, and ratio of winter to summer cells. Cumulus heating was applied over a wide latitudinal range determined interactively by a Gaussian with  $e$ -folding scale  $23^\circ$ , centered on the latitude of maximum upwelling at the top of the boundary layer. Narrower distributions were attempted, with less satisfactory results. The simulated Hadley cell is quite realistic, as shown in Figure 2b for northern winter solstice.

### 2.4. Equatorial-Wave Transport

Large-scale equatorial waves were parameterized as in D85. For each wave, the latitudinally integrated vertical component of Eliassen-Palm flux is determined by an equation of the form

$$B(z) = B(z_0) \exp [(z - z_0)/H - P(z)] \quad (1a)$$

$$P(z) = \int_{z_0}^z D(z') dz' \quad (1b)$$

where  $D(z)$  is the dissipation rate ( $m^{-1}$ ). Steady waves are assumed in (1a) and (1b), slowly varying in height. The wave-induced mean flow acceleration is of the form

$$\bar{u}_t = a(\xi) D(z) B(z_0) \exp [(z - z_0)/H - P(z)] / y_0 \quad (2)$$

where  $a(\xi)$  is a nondimensional acceleration profile [Andrews and McIntyre, 1976], normalized such that  $\int_{-\infty}^{\infty} a(\xi) d\xi = 1$ , and  $\xi = y/y_0$ , i.e., dimensional latitude divided by the meridional scale of the wave  $y_0$ . Profiles of  $a(\xi)$  for Kelvin and Rossby-gravity waves were given in D85. The quantity  $B(z_0)$  is

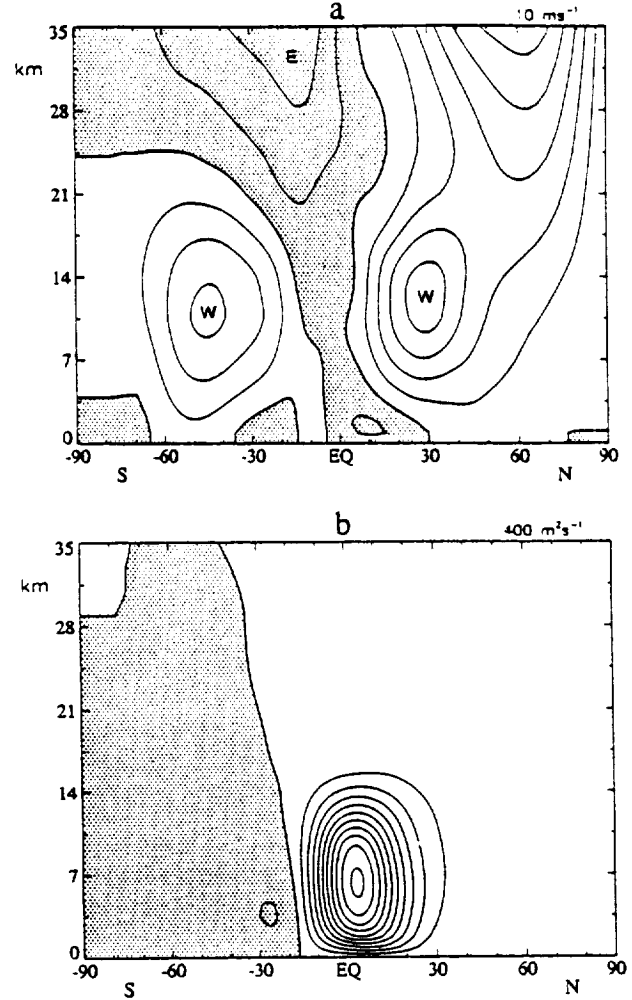


Figure 2. (a) Mean zonal wind at northern winter solstice from control run. Contours:  $10 \text{ ms}^{-1}$ , with easterlies shaded. (b) Residual mass stream function. Contours:  $400 \text{ m}^2 \text{ s}^{-1}$ , with negative values shaded.

related to the local vertical component of Eliassen-Palm flux  $F_{(z)}$  as

$$B(z_0) = \int_{-\infty}^{\infty} F_{(z)} dy = F_{(z)}(\xi_{\max}, z_0) y_{00} / b(\xi_{\max}) \quad (3)$$

where  $b(\xi)$  is a nondimensional profile of  $F_{(z)}$ , normalized such that  $\int_{-\infty}^{\infty} b(\xi) d\xi = 1$ ,  $y_{00}$  is the meridional scale at  $z_0$ , and  $\xi_{\max}$  is the nondimensional latitude of maximum  $F_{(z)}$ .

### 2.5. Gravity-Wave Transport

While any combination of vertically propagating waves can be represented using the formalism described above, it is cumbersome to do so as the number of waves becomes very large. Saravanan [1990] stored 40,000 values of the integrand of (1b) in a lookup table so that one-dimensional model simulations could be performed economically with 200 different values of  $c$ . Saravanan used only a single zonal wavenumber for all waves. It would be desirable, as an alternative, to represent at least part of the observed wave spectrum as a continuum of phase speeds, with momentum flux at any level determined by

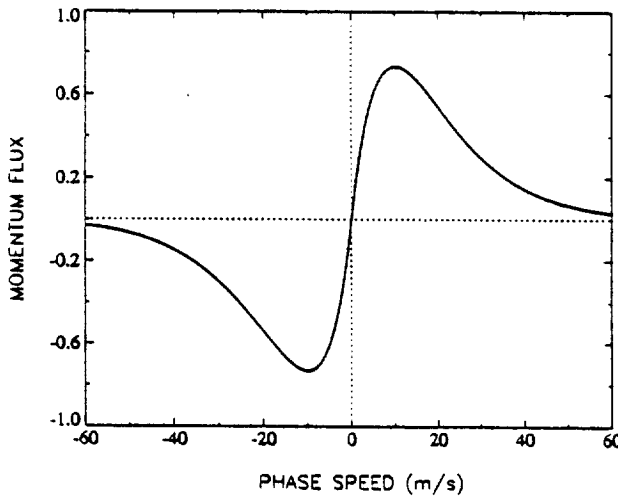


Figure 3. Nondimensional phase-speed spectrum of internal gravity waves used in the model.

$$\rho_0^*(z) B(z) = \int_{-\infty}^{\infty} \mathcal{B}(c, z) dc \quad (4)$$

where  $\rho_0^* = \exp - (z - z_0)/H$  is the nondimensional density profile. Unfortunately, even if  $\mathcal{B}(c, z)$  is known (e.g., from (1)), it is difficult to evaluate this integral. Some approximation must be made.

One approximation leads to a simple result. If it is assumed that waves are steady and conservative beneath their critical level, and completely absorbed at that level, the wave-induced acceleration is

$$\frac{\partial \bar{u}}{\partial t} = |\mathcal{B}_0(\bar{u})| \cdot \bar{u}_z \exp [(z - z_0)/H]. \quad (5)$$

as shown in the Appendix. This representation of gravity waves is actually the centerpiece of *Lindzen and Holton's* [1968] theory of the QBO. It is interesting that the mathematical form of (5) is similar to downward advection, for as shown by D91, additional fluxes are needed to overcome upward advection at the equator due to the Brewer-Dobson circulation.

All waves experience breaking or dissipation before reaching their critical level; the wave driving implied by (5) is therefore somewhat inaccurate. The magnitude of the error depends on the assumed wave spectrum and damping mechanism(s) and must be determined in each case. To illustrate the nature of the error, line-by-line calculations of wave driving using the exact formula (4) were performed and the results compared with those of (5). The phase-speed spectrum was chosen to be reasonably consistent with *Pfister et al.* [1993a] and *Bergman and Salby* [1994]:

$$\mathcal{B}_0(c) = \frac{B_0}{2c_1} \frac{|c|}{c_1} \exp - \frac{|c|}{c_1} \quad (6)$$

with  $c_1 = 10 \text{ ms}^{-1}$ , as shown in Figure 3. For simplicity the flux was distributed evenly among 12 zonal wavenumbers ( $s = 1, 2, 4, 8, 16, \dots, 1024, 2048$ ) using the same phase-speed spectrum (6) at each wavenumber. The spectrum was truncated at  $\pm 60 \text{ ms}^{-1}$  since adding faster waves had little effect on the total acceleration, due to the assumed spectrum (6). Scale-dependent radiative damping was used as in (A12). For this

calculation there were 541 vertical grid points (0–84 km) and  $\Delta c = 0.1 \text{ ms}^{-1}$  (600 waves). An example is shown in Figure 4 (eastward waves only) for a typical shear zone at the equator. Similar results were obtained in other wind profiles, or with diffusive damping added.

The acceleration according to (5) shown in Figure 4 onsets abruptly at the level where the mean flow turns eastward (close to the level of maximum shear) and decays more gradually above [*Leroy and Ingersoll*, 1995]. Exact and approximate profiles agree fairly well. The exact acceleration illustrates the consequences of neglecting wave absorption away from critical levels. There is positive acceleration well above and somewhat below the level of maximum shear. Acceleration below the shear zone is due mainly to absorption of waves with critical levels in the flow; acceleration above is due almost entirely to absorption of waves without critical levels. Agreement with (5) is therefore somewhat fortuitous. The formula of LH68 attributes acceleration entirely to waves with critical levels, and places it too high in the shear zone. The true acceleration due to these waves is located at a slightly lower altitude, but when the acceleration induced by waves without critical levels is added, the total acceleration maximizes at an altitude close to that implied by (5).

Considering the expense of line-by-line calculations, compared with that of (5), the agreement between the two is sufficiently good to incorporate (5) in a numerical model of the QBO as a way to supplement large-scale wave fluxes. Experiments in sections 4 and 5 used the LH68 formula in conjunction with equatorial wave driving as described above. This is an economical method, adequate for our QBO model but not for the middle atmosphere as a whole. A major limitation is that

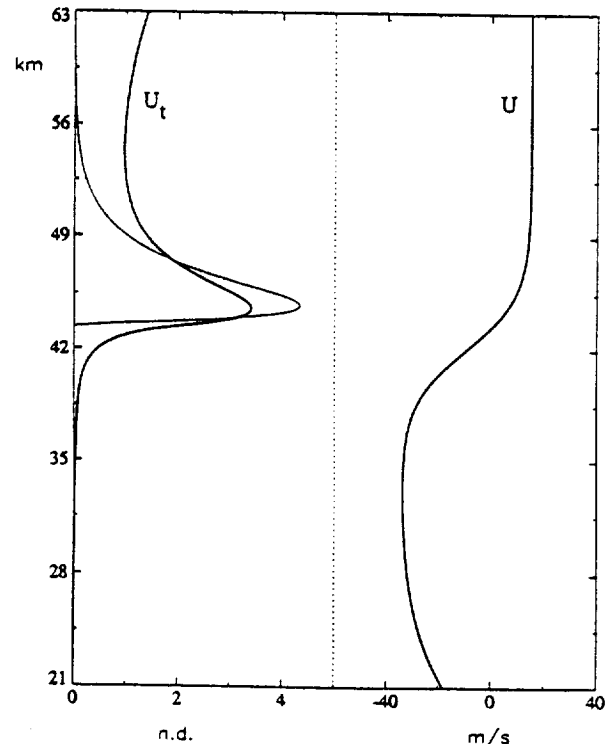


Figure 4. Nondimensional mean-flow acceleration due to a spectrum of vertically propagating internal gravity waves (eastward only), comparing line-by-line calculation (thick line) and LH68 formula (thin line). Profile of mean zonal wind at right.

(5) cannot create shear zones where none exist. Initial formation of a QBO shear zone is due to discrete (damped) equatorial waves and overlying semiannual oscillation (SAO). The spontaneous formation of vertical shear is a desirable property of spectral parameterizations [e.g., Mengel *et al.*, 1995] and is obtained in line-by-line calculations of wave-induced acceleration. A generalized version of the LH68 formula, taking into account absorption beneath the critical level, is derived in the Appendix.

## 2.6. Unresolved Body Forces

Without extratropical forces, upwelling in the tropical lower stratosphere is weak (D91) and temperatures unrealistically warm [Kinnersley and Pawson, 1995]. In D91, one-way relaxation of westerly zonal winds greater than  $25 \text{ ms}^{-1}$  generated an extratropical force, since maximum QBO westerlies are less than  $25 \text{ ms}^{-1}$ . This method unfortunately could not represent extratropical forces in weaker westerlies, or in easterly winds.

A two-step procedure was devised in order to obtain realistic body forces away from the equator. A control run was performed first without equatorial waves or QBO. The control run included frictional relaxation to the observed winds  $\bar{u}^M$  (a blend of the European Center for Medium-Range Weather Forecasts (ECMWF) and COSPAR International Reference Atmosphere (CIRA) 1986 monthly mean climatologies):

$$\frac{\partial \bar{u}}{\partial t} = \alpha_{M0} [\bar{u}^M(y, z, t) - \bar{u}(y, z, t)] + \dots$$

$$= G(y, z, t) + \dots \quad (\text{control run}) \quad (7)$$

regardless of the magnitude or sign of  $\bar{u}$ . Climatological winds near the equator were altered to match rocketsonde data below 63 km and high-resolution Doppler imager (HRDI) data above 63 km [Garcia *et al.*, 1996]. The friction parameter  $\alpha_{M0}$  was adjusted to produce realistic upwelling in the tropical lower stratosphere. Good results were obtained with  $\alpha_{M0}$  in the range 0.1–0.2 per day (Figure 2a). Relaxation to observed winds allowed a more sophisticated parameterization of transport by extratropical Rossby waves, gravity waves, and instabilities [Hitchman and Brasseur, 1988; Garcia, 1991; Kinnersley, 1995]. All subsequent runs with the same thermodynamic parameterization used the body force from a control run  $G(y, z, t)$  multiplied by a mask  $f_m$  to exclude forces in the tropical lower stratosphere:

$$\frac{\partial \bar{u}}{\partial t} = G(y, z, t) \cdot f_m(y, z) + \dots$$

$$= G_m(y, z, t) + \dots \quad (\text{subsequent runs}) \quad (8)$$

No friction was used in subsequent runs, except in the upper mesosphere. An example of a mask that worked well is shown in Figure 5, with a typical profile of body force at northern winter solstice. Values of  $f_m$  are identically zero in the tropical lower stratosphere but unity outside  $30^\circ$  latitude and unity throughout the troposphere and mesosphere. Forces increase rapidly with latitude in the subtropics.

The reason for using a tropical mask is that any nonzero force at the equator, even if small by extratropical standards, would interfere with the evolution of the QBO. Forces in the equatorial lower stratosphere of the control run are of the order of  $\pm 0.1 \text{ ms}^{-1} \text{ per day}$ . The whole point is to model the QBO without specifying equatorial forces a priori. This proce-

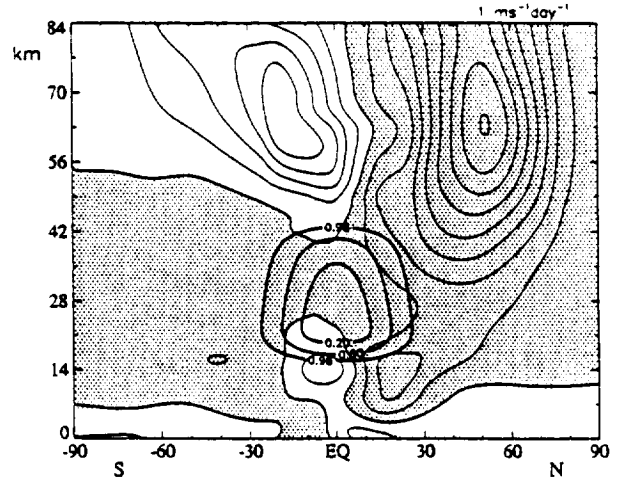


Figure 5. Climatological body force  $G(y, z, t)$  at northern winter solstice. Contours:  $1 \text{ ms}^{-1} \text{ d}^{-1}$ , with negative values shaded. Tropical mask is shown by thick lines.

cedure, incidentally, assumes that the tropical QBO has no effect on extratropical wave driving, despite observational evidence to the contrary [Holton and Tan, 1980; Dunkerton and Baldwin, 1991]. A simple modification would allow the body-force profile to be perturbed slightly by the extratropical QBO.

Frictional relaxation to  $\bar{u}^M$  was included in the upper mesosphere with rate coefficient

$$\alpha_M(z) = \alpha_{M1} \left[ 1 + \tanh \left( \frac{z - z_r}{D_r} \right) \right] / 2 \quad (9)$$

where

$$\alpha_{M1} = 0.5 \text{ per day} \quad (10a)$$

$$z_r = 63 \text{ km} \quad (10b)$$

$$D_r = 7 \text{ km.} \quad (10c)$$

The timescale for friction in the lower stratosphere is  $\sim 6000$ – $900,000$  days and can be safely ignored. The coefficient of vertical eddy diffusion  $K_{zz}$  was  $2.0 \text{ m}^2 \text{ s}^{-1}$  in the troposphere, decreasing rapidly to  $\sim 0.8 \text{ m}^2 \text{ s}^{-1}$  near 21 km and maintained near this value in the middle stratosphere, increasing rapidly to  $30 \text{ m}^2 \text{ s}^{-1}$  in the middle mesosphere. The coefficient of horizontal eddy diffusion  $K_{yy}$  was set to a negligibly small value ( $10^4 \text{ m}^2 \text{ s}^{-1}$ ) everywhere. Model values of  $K_{zz}$  in the lower stratosphere, required for realistic QBO shear, are 2–3 times as large as that of HL72 ( $0.3 \text{ m}^2 \text{ s}^{-1}$ ). Their value is consistent with observations of turbulence at Arecibo [Woodman and Rastogi, 1984]. No measurements of vertical diffusion are available in the equatorial lower stratosphere. Recent observations of enhanced gravity-wave activity at the equator [Allen and Vincent, 1995; Ogino *et al.*, 1995] may imply enhanced diffusion there; this matter is left for further study. Model experience (with realistic upwelling and wave flux) suggests that values of  $K_{zz}$  in the range  $0.3$ – $1.0 \text{ m}^2 \text{ s}^{-1}$  are appropriate at the equator, mainly in the vicinity of QBO shear zones. The possibility that this indicates some defect in the wave-transport parameterization cannot be ruled out. Larger values of  $K_{zz}$  are required just above the tropopause (D85), consistent with occasional penetration by deep tropical convection, or breakdown of vertically propagating waves. A mixed layer at 18–19 km was observed by

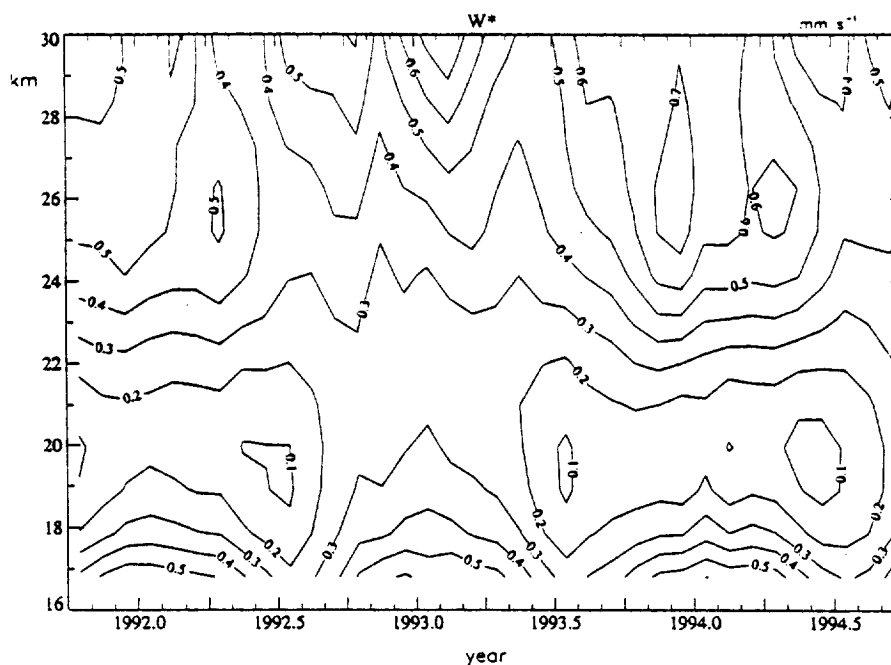


Figure 6. Residual vertical velocity averaged within  $10^\circ$  of the equator, derived by Rosenlof [1995] from a radiative code using UKMO temperatures and UARS constituent observations as input. Contours:  $0.1 \text{ mm s}^{-1}$ .

Vömel *et al.* [1995] in water vapor soundings over the western Pacific during the Central Equatorial Pacific Experiment (CEPEX).

### 3. Observational Constraints

Holton and Lindzen [1972] demonstrated that a fairly realistic QBO could be obtained in a one-dimensional model using equatorial-wave fluxes similar to those inferred from the observed Kelvin and Rossby-gravity waves [Wallace and Kousky, 1968; Yanai and Maruyama, 1966]. Unfortunately, HL72 did not include climatological upwelling, nor did LH68. (Although LH68 used a two-dimensional model, their radiative equilibrium temperature was independent of latitude.) The theory is adequate only if additional fluxes can be found. Modelers may increase the flux in order to produce an oscillation [Gray and Pyle, 1989; D91; Kinnersley and Pawson, 1995], but they need an observational basis for doing so. To gain a better understanding of fluxes that are required, the mean vertical motion of the tropical lower stratosphere must be known.

#### 3.1. Estimates of Upwelling

For many years it has been thought that air enters the middle atmosphere through the tropical tropopause, a "cold trap" in which parcels are dehydrated to lower stratospheric mixing ratios, after which they move upward, poleward, and downward, reentering the troposphere in tropopause folds [Brewer, 1949; Dobson, 1956; Dunkerton, 1978; Holton *et al.*, 1995].

Theoretical calculations of radiative heating predict slow but nonzero ascent in the tropical lower stratosphere. According to Dopplnick [1979] the heating rate  $\bar{Q}$  in this region is about  $0.3 \text{ K/d}$ . Balanced by adiabatic cooling,  $\bar{Q}$  is equivalent to upwelling of about  $0.3 \text{ mm/s}$ , or  $0.8 \text{ km per month}$ . The ascent is comparable but opposite in sign to the rate of QBO shear-zone descent.

Similar upwelling is implied by contemporary radiative transfer models [Olague *et al.*, 1992; Rosenlof, 1995]. These calculations have become rather precise. Rosenlof used United Kingdom Meteorological Office (UKMO) temperatures and constituent data from the Upper Atmosphere Research Satellite (UARS) together with the radiative code of Olague *et al.* to obtain upwelling of  $0.1\text{--}0.6 \text{ mm s}^{-1}$ , within  $10^\circ$  of the equator, at altitudes 17–30 km. Her calculated  $\bar{w}^*$  for the UARS period is shown in Figure 6. Residual vertical velocity ( $\bar{w}^*$ ) decreases rapidly with height above the tropopause to a minimum near 19–20 km and increases more gradually with height above this level. The annual variation indicates stronger upwelling in northern hemisphere winter, consistent with the annual cycle of temperature in this region [Reed and Vlcek, 1969; van Loon and Jenne, 1970; Yulaeva *et al.*, 1994]. Interannual variability is also observed, due to the QBO and other effects.

Unfortunately, the radiative balance is delicate in this region. Direct measurement of  $\bar{w}^*$  is impossible, and estimates of this quantity (from radiative or mass balances) are imprecise, leaving considerable uncertainty in the momentum balance of the QBO (D91). Recent satellite observations provide indirect evidence of upwelling for comparison to radiatively derived  $\bar{w}^*$ .

#### 3.2. Observations of Apparent Upwelling

Apparent upwelling in the tropical lower stratosphere has been observed in satellite measurements of water vapor [Mote *et al.*, 1995, 1996] from the Microwave Limb Sounder (MLS) and Halogen Occultation Experiment (HALOE), both aboard UARS, and from the Stratospheric Aerosol and Gas Experiment (SAGE II) aboard the Earth Radiation Budget Satellite (ERBS).

Among conservative tracers, water vapor is affected to an unusual degree by its time-varying source/sink at the tropical



tropopause. Because of the annual cycle of temperature and the sensitivity of saturation mixing ratio to small variations of  $T$ , significant annual variation of  $H_2O$  mixing ratio is observed ( $\sim 30\%$ ). The annual variation becomes imprinted on air slowly ascending into the tropical lower stratosphere, making it possible to observe the rate of ascent in the altitude range 15–35 km over a period of 1–2 years [Mote *et al.*, 1996, Plate 1]. Mote *et al.* liken this effect to that of an atmospheric “tape recorder.”

Radiative estimates of  $\bar{w}^*$  agree with the water vapor observations, at least qualitatively. Bands of high/low  $H_2O$  mixing ratio ascend at a rate of  $\sim 0.25$ – $0.60 \text{ mm s}^{-1}$  although there is some variability due to the annual cycle, QBO, and other effects. The time-averaged apparent upwelling derived by the author from Plate 1 of Mote *et al.* [1996], plus or minus one standard deviation, is shown in Figure 7 together with January and July profiles of  $\bar{w}^*$  derived from Figure 6. There is an increase with height of apparent vertical velocity above  $\sim 25$  km. Larger velocity near the tropopause (15–18 km) compared with that immediately above (19–22 km) is also seen. On closer examination the radiatively derived  $\bar{w}^*$  below 20 km is somewhat smaller and has its minimum value at a slightly lower altitude. It is uncertain whether the ascent of water vapor anomalies is due entirely to vertical advection; for example, vertical diffusion may also be important. It can be safely assumed that the observed ascent provides an upper limit on the upwelling rate. The annual variation does not explain the entire range of observed upwelling, due to interannual variability (e.g., QBO). Vertical diffusion in a quasi-compressible atmosphere introduces an effective upward vertical velocity  $K_{zz}/H$ , which is approximately  $0.1 \text{ mm s}^{-1}$  if model values of  $K_{zz}$  are adopted, and it is assumed that vertical diffusion of momentum and of constituents is equivalent, i.e., a turbulent Prandtl number of order unity. Compared to the Brewer-Dobson circulation, the effective velocity is small but not negligible; it is smaller still if (1) the damping of QBO regimes can be attributed in part to other processes, for example, lateral mixing, alleviating the need for such large  $K_{zz}$ , and (2) the turbulent Prandtl number is substantially greater than unity, as expected for convectively unstable gravity waves. These issues are fundamental to transport in the equatorial lower stratosphere and deserve further study.

In a recent study of ozone in the equatorial lower stratosphere using a simple photochemical model, Avallone and Prather [1996] suggest that upwelling rates of 1/25 to 1/60 km per day are consistent with the observed ozone profile. Their estimates agree with the apparent upwelling and radiatively derived values of  $\bar{w}^*$ .

### 3.3. Equatorial-Wave Fluxes

“Equatorial waves” in this context will refer to large-scale disturbances observable by rawinsondes and satellites, having periods greater than  $\sim 2$  days, and zonal wavelengths greater than  $\sim 2000 \text{ km}$  ( $s \leq 20$ ), for example, Kelvin, Rossby-gravity, and equatorially trapped Rossby waves. By such criteria, inertia-gravity waves (IGWs) may or may not be included, depending on their spatial and temporal scale. Mesoscale gravity waves are discussed in the following subsection. The structure, amplitude, and characteristic scale of Kelvin and Rossby-gravity waves [Wallace and Kousky, 1968; Yanai and Maruyama, 1966] were summarized by Holton [1975], Wallace [1973], and Andrews *et al.* [1987]. From Table 4.1 of Andrews *et al.* it is possible to estimate the vertical component of Eliassen-Palm

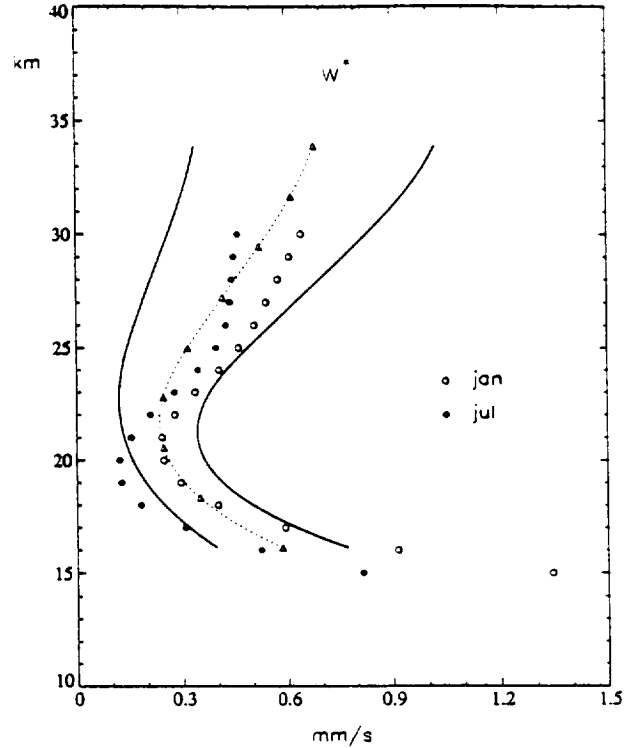


Figure 7. Estimate of time-mean apparent upwelling derived from water vapor anomalies in Plate 1 of Mote *et al.* [1996] (dashed line) plus or minus one standard deviation (thick lines). Radiative values of  $\bar{w}^*$  from Figure 6 are also shown (symbols).

flux due to each wave. For long-period ( $\sim 15$  days) Kelvin waves the vertical flux of zonal momentum during active periods is approximately

$$\overline{u'w'} \sim \frac{1}{2} (8 \text{ ms}^{-1}) (1.5 \times 10^{-3} \text{ ms}^{-1}) = 6 \times 10^{-3} \text{ m}^2 \text{ s}^{-2} \quad (11)$$

at the latitude ( $\sim 7^\circ\text{N}$ ) and altitude ( $\sim 20$ – $25 \text{ km}$ ) of observation. The amplitude of Kelvin waves should be largest at the equator, however. Using high-quality rawinsonde data from Singapore ( $1.3^\circ\text{N}$ ), Maruyama [1994] obtained  $\overline{u'w'} \sim 2$ – $8 \times 10^{-3} \text{ m}^2 \text{ s}^{-2}$  in descending QBO westerlies and at lower levels (near 17 km) at all times for disturbances in the period range 7.4–32 days. (Note that the contour interval in his Figures 7 and 8 was erroneously listed as  $2 \times 10^{-2} \text{ m}^2 \text{ s}^{-2}$  rather than the correct value,  $2 \times 10^{-3} \text{ m}^2 \text{ s}^{-2}$ .) Fluxes near 17 km contain a significant contribution from long-period waves that are trapped or easily damped in the immediate vicinity of the tropopause [Parker, 1973; Tsuda *et al.*, 1994]. For Rossby-gravity waves it is necessary to include (in addition to the vertical flux of zonal momentum) the meridional heat flux in the evaluation of  $F_{(z)}$ . The total Eliassen-Palm flux is theoretically equivalent to vertical energy flux divided by intrinsic phase speed:

$$\overline{u'w'} \sim 1.9 \times 10^{-3} \text{ m}^2 \text{ s}^{-2} \quad (12a)$$

$$-\frac{\overline{fv'\phi'_z}}{N^2} \sim -2.3 \times 10^{-3} \text{ m}^2 \text{ s}^{-2} \quad (12b)$$

$$\frac{\overline{w'\phi'_z}}{c - \bar{u}} \sim -1.0 \times 10^{-3} \text{ m}^2 \text{ s}^{-2} \quad (12c)$$

(see *Andrews and McIntyre* [1976] for discussion of the conditions required for this approximation). Our estimate is imprecise, but the Rossby-gravity flux is evidently smaller than assumed in HL72 by a factor of  $\sim 2$ –4. During transient wave events when meridional velocity approaches  $4$ – $6 \text{ ms}^{-1}$  [*Dunkerton*, 1991b], the flux may be larger than (12) by a factor of  $\sim 4$ . It will be assumed that on the average the vertical component of Eliassen-Palm flux at the tropopause due to Rossby-gravity waves is in the range  $-(1.0\text{--}2.5) \times 10^{-3} \text{ m}^2 \text{ s}^{-2}$ .

In order to use these estimates in a two-dimensional model, an overbar should refer to the zonal mean, which cannot be determined accurately from rawinsonde data. Most stations in the equatorial zone are located in or near regions of intense convection. If such measurements are biased, it can be safely assumed that the bias is in the direction of overestimating rather than underestimating the zonally averaged Eliassen-Palm flux due to vertically propagating waves excited by tropical convection. Additional flux could originate in regions of suppressed convection, due to lateral forcing of Rossby-gravity waves [*Randel*, 1992; *Dunkerton*, 1993; *Dunkerton and Baldwin*, 1995; *Magaña and Yanai*, 1994]. Rossby-gravity waves originating in the upper troposphere over the eastern tropical Pacific have slightly lower frequencies and do not seem to propagate vertically into the lower stratosphere as efficiently as higher-frequency waves of convective origin [*Dunkerton*, 1993]. Convectively coupled Rossby-gravity waves in the troposphere were discussed by *Hendon and Liebmann* [1991].

Identification of short-period disturbances in Singapore rawinsonde data was the subject of two interesting studies by *Maruyama* [1994] and *Sato et al.* [1994]. Applying high-pass filters to the data prior to calculating the covariance of zonal wind and temperature tendency fluctuations, Maruyama estimated that disturbances in the period range  $\sim 1$ –3 days have a vertical flux of zonal momentum comparable to that of long-period (7.4–32 days) Kelvin waves. Fluxes in both frequency bands are amplified in descending QBO westerlies. Sato et al. discovered that the cospectrum of zonal wind and temperature is more significant for short-period waves than the quadrature spectrum and that the cospectrum of these waves alternates sign with the QBO, having the same sign as the vertical shear. Long-period waves also have a nonzero cospectrum but are amplified only in descending westerlies. An interpretation of their result is that both eastward and westward waves are present, interacting with QBO shear zones [*Dunkerton*, 1995]. Equatorial inertia-gravity waves may therefore explain the short-period disturbances in addition to Kelvin waves. (For further discussion of tropical and subtropical IGWs, see *Hirota and Niki* [1985], *Hamilton* [1991], *Hostetler and Gardner* [1994], *Riggin et al.* [1995], *Karoly et al.* [1996].) There is a hint in Figure 7 of *Maruyama* [1994] that the vertical flux of zonal momentum in short-period disturbances alternates sign with the QBO shear, but the data are noisy, and it is unclear whether this result is significant. An indirect estimate of momentum flux using equation (2.21) of *Dunkerton* [1995] was obtained by *Sato and Dunkerton* [this issue]: for short-period waves,  $|\overline{u'w'}| \sim 10\text{--}50 \times 10^{-3} \text{ m}^2 \text{ s}^{-2}$  at QBO altitudes. The flux in long-period waves  $|\overline{u'w'}| \sim 5\text{--}15 \times 10^{-3} \text{ m}^2 \text{ s}^{-2}$  is smaller, as expected from the direct estimate.

Relatively little attention has been given to equatorially trapped Rossby waves, an obvious candidate for easterly acceleration [*Andrews and McIntyre*, 1976] if it can be demonstrated that such waves exist with a significant vertical flux and are absorbed, rather than reflected, in the descending QBO

easterly shear zone. Rossby waves were included in the interpretation of rawinsonde measurements over the tropical Pacific [*Yanai et al.*, 1968] along with Rossby-gravity waves. *Ziemke and Stanford* [1994] found evidence of equatorial Rossby (ER) waves in 13 years of total ozone mapping spectrometer (TOMS) ozone data. The stronger ER events in their data tend to coincide with westerly QBO winds rather than forcing the QBO easterly phase, although some evidence of forcing was seen in weaker events. From a theoretical calculation of wave spectra using cloud imagery, *Bergman and Salby* [1994] obtained a significant vertical flux in very slow Rossby waves. Unfortunately, the theoretical implications are unclear, so this aspect of the QBO problem must be left for future study. In order for Rossby waves to escape damping, their vertical wavelength must be large compared to other equatorial waves. The WKB approximation is therefore invalid. Their phase speed relative to the ground is small, suggesting that any deceleration or lateral mixing would occur primarily in the vicinity of the zero-wind line.

### 3.4. Gravity-Wave Fluxes

"Gravity waves" in this context will refer to small-scale disturbances difficult to observe by rawinsondes or satellites, having periods less than 2 days and zonal wavelengths less than  $\sim 2000 \text{ km}$  ( $s \geq 20$ ). Mesoscale gravity waves were examined by *Pfister et al.* [1993a, b] with horizontal scales of several hundred kilometers or less and periods of a few hours or less. Using cloud imagery, *Bergman and Salby* [1994] calculated a theoretical spectrum of waves excited by tropical convection with periods  $\geq 6$  hours and horizontal wavenumbers  $s \leq 256$ . They distinguish "gravity waves" from slower equatorial modes such as Kelvin, Rossby, and Rossby-gravity waves, although the resolution of cloud imagery would imply that their gravity waves are necessarily longer and slower than those considered by *Pfister et al.* At the equator there is no dynamical distinction to be made between gravity or inertia-gravity waves at different scales. Unique to the equatorial waveguide is the ability of IGWs to propagate vertically at any intrinsic frequency  $\hat{\omega}$  with absolute value greater than zero.

There is presently no consensus on how the vertical Eliassen-Palm flux or momentum flux is distributed among waves as a function of zonal wavenumber. However, it is clear from simple theoretical considerations that even though the energy contained in small-scale waves is small relative to that of large-scale waves, a disproportionate amount of momentum flux is attributable to waves of small horizontal scale or large intrinsic frequency:

$$\overline{u'w'} \sim \frac{k}{m} \overline{u'^2} \sim \frac{\hat{\omega}}{N} \overline{u'^2} \quad (13)$$

Consistent with this, the frequency spectrum of  $F_{(z)}$  calculated by *Bergman and Salby* [1994] is very broad compared to that of geopotential, emphasizing waves with periods less than 2 days.

According to those authors, planetary-scale Kelvin, Rossby, and Rossby-gravity waves account for only  $\sim 40\%$  of the Eliassen-Palm flux within  $15^\circ$  of the equator; the remainder is carried by gravity waves. Their phase-speed spectra of  $F_{(z)}$ , for various zonal wavenumber truncations, show that while low wavenumbers ( $s < 20$ ) are responsible for most of the Eliassen-Palm flux at slow ( $|c| < 12 \text{ ms}^{-1}$ ) and fast ( $|c| > 50 \text{ ms}^{-1}$ ) phase speeds, these wavenumbers seriously underestimate the flux at intermediate speeds. For  $|c| = 12\text{--}20 \text{ ms}^{-1}$ ,

approximately 75% of the Eliassen-Palm flux is contained in waves with  $s > 20$ . It appears from Figure 16 of Bergman and Salby that in this range of phase speeds, roughly equal amounts of flux are found in wavenumber bands 1–20, 20–40, 40–60, and 60–256. With a little imagination it could be supposed that unresolved disturbances ( $s > 256$ ) contribute about as much flux as one of these bands. By extrapolation of the frequency spectrum, Bergman and Salby claim that 80–90% of  $F_{(z)}$  is contained in frequencies resolved by the cloud imagery.

Although it is difficult to obtain a dimensional estimate of  $F_{(z)}$  from Bergman and Salby's analysis, since the heating variance is unknown, some useful guidelines are as follows: (1) The total Eliassen-Palm flux in the equatorial zone may be  $\sim 2.5$  times as large as that associated with planetary-scale equatorial modes. As shown in section 4, this total flux is adequate to resolve the "QBO problem" with Brewer-Dobson upwelling, if the observed large-scale fluxes are adopted. (2) Small zonal wavenumbers  $s < 20$  are almost entirely responsible for the flux in fast ( $|c| > 20 \text{ ms}^{-1}$ ) waves that are required to drive the QBO according to the theory of HL72. (3) Slower phase speeds account for most of the integrated Eliassen-Palm flux, but (except for very slow Rossby waves) most of the flux in these waves is attributable to large zonal wavenumbers  $s \gg 20$ . (4) The slower waves will encounter critical levels in the QBO; if absorbed, they will contribute to shear-zone descent. (5) For these waves the shape of the phase-speed spectrum of  $F_{(z)}$  is similar to that inferred theoretically by Pfister *et al.* [1993a, b], a mathematical model of which (equation (6)) was introduced earlier. (6) The spectrum of  $F_{(z)}$  is sensitive to zonal wind in the tropical upper troposphere. Easterlies shift the spectrum toward positive phase speeds and vice versa.

In summary, the analysis of Bergman and Salby [1994] provides theoretical and (indirect) observational support for the hypothesis that large-scale Kelvin and Rossby-gravity waves are responsible for the formation of QBO shear zones (HL72) but are unable to cause realistic shear-zone descent in the presence of Brewer-Dobson upwelling (D91). Absorption of gravity waves enables QBO shear zones to descend at a reasonable rate, producing the observed oscillation.

This statement may appear at odds with Pfister *et al.* [1993a] who suggest that mesoscale gravity waves account for only  $\sim 10\%$  of the observed QBO acceleration in the middle stratosphere. Taking into account upwelling, the fraction of wave-induced acceleration attributable to mesoscale waves would be much smaller than 10%. For several reasons, however, the role of gravity waves in the QBO is more significant than implied by Pfister *et al.* [1993a]. (1) In the sequel, Pfister *et al.* [1993b, p. 8634] suggest that the flux attributable to mesoscale waves may be twice as large, due to larger vertical displacement of isentropic surfaces in the Stratosphere-Troposphere Exchange Project (STEP) 1987 campaign compared with those observed in the Panama experiment. (2) The profile of mean wind over Panama [Pfister *et al.*, 1993a, Figure 8] underestimates the equatorial vertical shear by a factor of  $\sim 2$ . From the discussion of section 2.5 it may be supposed that larger acceleration occurs in larger vertical shear. (3) This type of analysis cannot resolve all gravity waves excited by tropical convection. Activity interpreted as observational noise may have a nonzero momentum flux associated with it (J. Alexander, personal communication, 1995). (4) Numerical simulations of a two-dimensional midlatitude squall line show a much larger momentum flux emerging from the storm [Alexander and Pfis-

ter, 1995]. (5) Most important, the analysis of Pfister *et al.* considers only the "topographic" effect of convection impinging on the tropopause at spatial and temporal scales resolved by the ER-2 aircraft. Larger scales and lower frequencies are not resolved, nor is excitation associated with large-scale convective heating taken into account. Bergman and Salby emphasized the role of intermediate waves in the range  $s = 20$ –256, the importance of which was also recognized by Pfister *et al.* [1993a].

To lend some quantitative insight to this discussion, we note from Figure 7 of Pfister *et al.* [1993a] that the absolute value of momentum flux  $M(c)$  due to mesoscale waves with phase speeds near  $\pm 10 \text{ ms}^{-1}$  (with zero mean wind at the tropopause) is about  $1.2 \times 10^{10} \text{ kg}$ , or larger by a factor of 2 according to Pfister *et al.* [1993b]. This number may be translated into something useful as follows:

$$\mathcal{B}_0(c) = \frac{M(c)}{\rho_0 A T} \quad (14)$$

where  $\rho_0$  is atmospheric density at the tropopause and  $AT$  is the "area-time" occupied by an individual storm. Taking  $A = 30,000 \text{ km}^2$  and  $T = 5$  hours (J. Alexander, personal communication, 1995), we obtain a maximum value of  $\mathcal{B}_0(c) = 0.178 \text{ mm/s}$  (or  $0.356 \text{ mm s}^{-1}$ ). By itself, this "velocity" (i.e., of shear-zone descent, section 2.5) is significant for the QBO, especially with  $\exp z/H$  factor included. However, it must be multiplied by a number representing the fractional area covered by deep tropical convection, which is  $\sim 0.015$ – $0.13$  according to Pfister *et al.* [1993a]. Using the larger of the two estimates of  $\mathcal{B}_0(c)$  and imagining that the entire flux is absorbed in descending QBO shear zones, the effect of mesoscale waves on the QBO appears insignificant when a small fractional coverage is assumed. Evidently, all scales of gravity-wave motion must be considered, from planetary scale to mesoscale [Pfister *et al.*, 1993a; Bergman and Salby, 1994]. Another possibility is that local mesoscale fluxes are substantially larger [Alexander and Pfister, 1995]. It is unlikely, however, that the momentum flux of convectively generated mesoscale gravity waves is adequate for the QBO, especially the easterly phase. The spectrum of mesoscale waves is likely shifted toward westerly phase speeds, because easterly mean winds tend to accompany deep convection in the tropical upper troposphere.

#### 4. Numerical Results

Two-dimensional simulations of the QBO were performed with equatorial and gravity-wave momentum transport parameterized as in sections 2.4 and 2.5, inserting the masked body-force profiles ( $G_m$ ) of a control run as explained in section 2.6. Two sets of  $G(y, z, t)$  were obtained with thermal relaxation and MIDRAD, respectively. These profiles were saved every 10 days. In control runs, the timescale for relaxation to observed winds was set to 5 days ( $\alpha_{w0} = 0.2$  per day). Mechanical relaxation determines the magnitude, distribution, and seasonal variation of body force  $G(y, z, t)$ . Upwelling in the tropical lower stratosphere is determined, in part, by extratropical body forces [D91; Yulaeva *et al.*, 1994] and the QBO [Plumb and Bell, 1982; D85, D91]. The time-mean upwelling and its seasonal variation should be realistic prior to adding a QBO. This aspect of the simulation is discussed first, followed by QBO integrations.

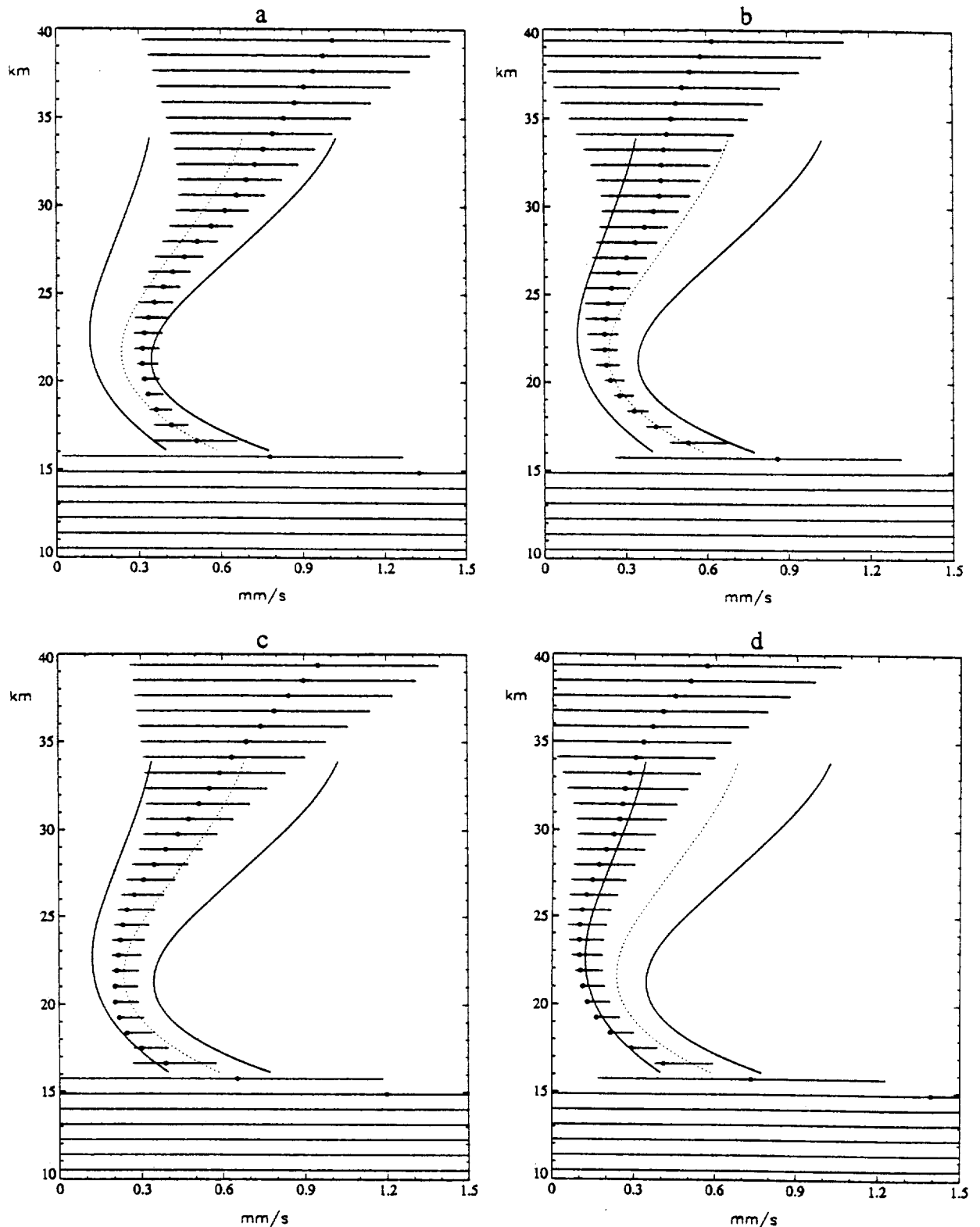


**Figure 8.** Simulated upwelling at equator (dots) and range of  $\bar{w}^*$  within  $10^\circ$  of equator (horizontal lines) at (a, c) northern winter solstice and (b, d) northern summer solstice. A modified profile of  $\bar{T}^E$  was used in Figures 8c and 8d (see text). Apparent upwelling of Figure 7 is shown for comparison.

#### 4.1. Upwelling in the Tropical Lower Stratosphere

Figures 8a and 8b show vertical velocity at the equator, and its range within  $10^\circ$  of the equator, at northern and southern winter solstices, obtained from a control run with thermal

relaxation. Vertical velocities in the tropospheric Hadley cell are much larger and generally fall outside the range plotted. The simulated upwelling has a minimum at 20–21 km and increases with height above this altitude. Values of  $\bar{w}^*$  agree

with *More et al.* [1996], including the altitude of minimum upwelling. This agreement is by design, the apparent upwelling having been used to determine acceptable combinations of  $\alpha_T(z)$  and  $\alpha_{M0}$ . There is strong annual variation with greater upwelling in northern winter, enhanced relative to southern winter by 50% or more at altitudes above 20 km. The simulated annual variation is smaller at lower levels, considerably less than Rosenlof's (Figure 7), although the time mean is reasonable. Model simulations were designed to produce a Hadley cell in the southern winter troposphere approximately equal and opposite that of northern winter. No attempt was made to reproduce the seasonal asymmetry of the tropospheric Hadley circulation [Oort, 1983] other than that due to the asymmetry of  $G(y, z, t)$ . The maximum height of the Hadley circulation is essentially fixed at 100 mbar by the cumulus parameterization (section 2.3) without any seasonal variation of tropopause height, unlike in observations [Gage and Reid, 1987; Zhang, 1993]. Rosenlof's variation of  $\bar{w}^*$  is consistent with a higher, colder tropopause in northern winter. Body forces exerted mainly in extratropical latitudes are responsible for the annual cycle of temperature at the base of the tropical stratosphere [Gray and Dunkerton, 1990; Yulaeva et al., 1994; Holton et al., 1995]. It seems unlikely that the annual variation of tropopause height and temperature is important to the QBO; it will be ignored here.

Profiles of  $\bar{w}^*$  at altitudes 17–25 km obtained with MIDRAD are similar to those of Figures 8a and 8b, and the tropospheric Hadley cell is almost identical (not shown). Upwelling above 25 km is shifted somewhat farther from the equator, resulting in smaller equatorial  $\bar{w}^*$  at these altitudes. MIDRAD heating rates above 21 km are more sensitive to QBO temperature perturbations, as discussed in section 4.3.

A key parameter for the simulated time-mean upwelling and its seasonal variation is the mechanical relaxation rate  $\alpha_{M0}$ . In the winter hemisphere, radiative cooling by itself produces very cold temperatures and strong zonal winds [Shine, 1987]. Body forces are required to prevent unrealistic winds and to maintain the observed departure from radiative equilibrium. The magnitude of force required depends on the strength of the radiative "spring." Thermal forcing is largely responsible for the mean meridional circulation, but mechanical forcing is largely responsible for the departure from radiative equilibrium. (A caveat is that radiative equilibrium is impossible in the tropics, and the circulation does not vanish in the limit of zero body force; see Dunkerton [1989] and D91.) The connection between mechanical forcing and induced mean meridional circulation is expressed in the "downward (or nonlocal) control principle" [Haynes et al., 1991] derived under steady state conditions with nonzero meridional angular momentum gradient. This principle works best in extratropical latitudes where the position of an angular momentum isopleth is approximately known and varies little with time. In the tropics the angular momentum gradient is weak, and angular momentum responds to the induced circulation [Held and Phillips, 1990; D91] so that the distribution of upwelling cannot be obtained from nonlocal control. At the solstices, however, the net tropical upwelling (not necessarily equal to the total upwelling) can be determined accurately if the angular momentum distribution and relevant body forces are known [Rosenlof, 1995].

The interplay between thermal drive and body force is tantalizing; a complete discussion of factors that determine tropical upwelling is beyond the scope of this paper. "Nonlocal control" should not obscure the role of thermal forcing, in

particular, the sensitivity of induced circulation to the meridional gradient and curvature of  $\bar{T}^E$  [Held and Hou, 1980; Lindzen and Hou, 1988; D89]. This sensitivity remains when body forces are included in the problem, as demonstrated by a simple example. In Figures 8c and 8d the radiative equilibrium at 20–30 km was reduced by approximately 5 K at the equator, adding a small positive curvature to  $\bar{T}^E$  while keeping the same value of  $\alpha_{M0}$ . The minimum upwelling in this case is reduced by 40–60% from its "observed" value (compare to Figures 8a and 8b). Flattening the meridional profile of  $\bar{T}^E$  in the tropics has a smaller but similar effect. The change in  $\bar{w}^*$  is significant for the momentum balance of the QBO and exposes the difficulty of estimating the required vertical wave flux with any degree of precision.

#### 4.2. Simple QBO Simulation

Several economical QBO simulations were performed with the two-dimensional model using thermal relaxation (section 2.2) and the simple gravity-wave parameterization of LH68 (section 2.5) together with one or two Kelvin waves and a Rossby-gravity wave (section 2.4). The LH68 scheme cannot accelerate the mean flow beyond the range of speeds already achieved as a result of other momentum transport processes. The amplitude of the QBO in this case is limited by the phase speeds of Kelvin and Rossby-gravity waves (HL72). These waves have phase speeds consistent with the observed QBO [Yanai and Maruyama, 1966; Yanai et al., 1968; Wallace and Kousky, 1968; Andrews et al., 1987; Maruyama, 1991; Dunkerton, 1991b, 1993; Ziemke and Stanford, 1994]. Reasonable values of zonal wavenumber  $k$ , ground-based phase speed  $c$ , and Eliassen-Palm flux  $B(z_0)$  for a simple simulation of the QBO (three equatorial waves plus gravity-wave spectrum) are, for the first Kelvin wave:

$$k_{KQ1}a = 2 \quad (15a)$$

$$c_{KQ1} = 30 \text{ ms}^{-1} \quad (15b)$$

$$B_{KQ1}(z_0) = 2.5 \times 10^{-3} \text{ m}^2 \text{ s}^{-2}, \quad (15c)$$

for the second Kelvin wave:

$$k_{KQ2}a = 2 \quad (16a)$$

$$c_{KQ2} = 20 \text{ ms}^{-1} \quad (16b)$$

$$B_{KQ2}(z_0) = 5.0 \times 10^{-3} \text{ m}^2 \text{ s}^{-2}, \quad (16c)$$

and for the Rossby-gravity wave:

$$k_{RG}a = 4 \quad (17a)$$

$$c_{RG} = -40 \text{ ms}^{-1} \quad (17b)$$

$$B_{RG}(z_0) = -2.5 \times 10^{-3} \text{ m}^2 \text{ s}^{-2} \quad (17c)$$

where  $z_0$  is the tropical tropopause height (17 km) and  $a$  is the radius of the Earth. The flux attributable to slower Kelvin waves may be significantly larger than in (16c), but because of their slow phase speed, such waves play only a minor role in the QBO. Fluxes attributable to faster Kelvin (KQ) and Rossby-gravity (RG) waves were estimated in section 3.3; model values (15c–17c) lie at the high end of an acceptable range (section 3.3). The two Kelvin waves are intended to represent disturbances in the period range ~7–12 days, corresponding to those observed by Maruyama [1991] but excluding the lower-frequency end. Results are rather insensitive to how the

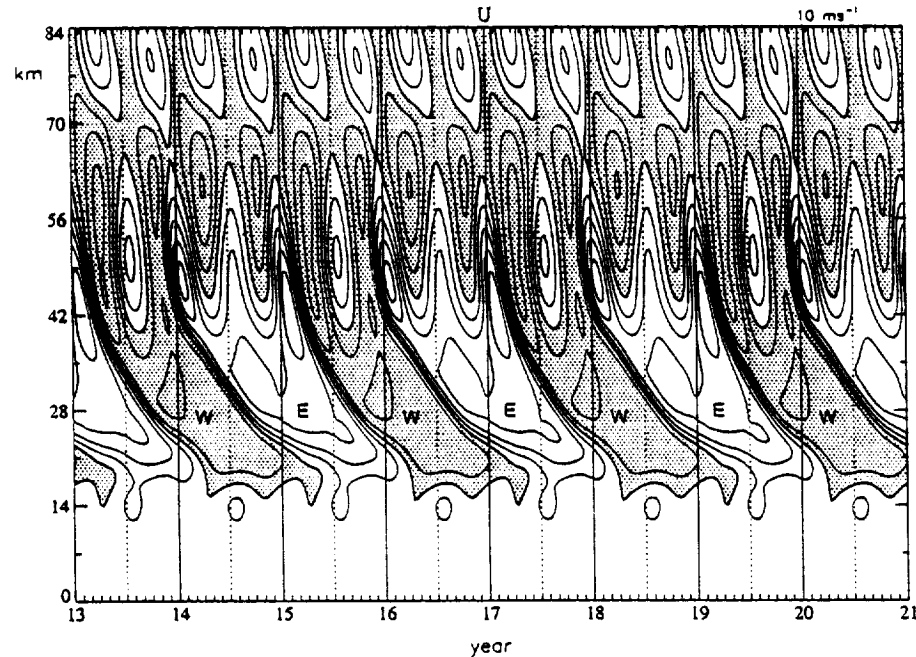


**Figure 9.** Time-height section of mean zonal wind at equator, from simple two-dimensional quasi-biennial oscillation (QBO) integration with two Kelvin waves, one Rossby-gravity wave, and continuous gravity-wave spectrum. Contours:  $10 \text{ ms}^{-1}$ , with westerlies shaded.

Kelvin-wave flux is partitioned, but a slightly “red” spectrum of flux is reasonable and produces a more realistic QBO westerly phase. For gravity waves the phase-speed spectrum of (6) was assumed, with magnitude  $B_{GW}(z_0)$  at the tropopause. The meridional profile of gravity-wave momentum flux was set equal to the cosine of latitude and held constant in time. Gravity waves are expected to follow the seasonal march of tropical convection, some evidence of which is seen in Figure 7 of *Allen and Vincent* [1995] (top panel). The gravity-wave scheme was applied only up to 63 km (tapered to zero at that level); it was used as a QBO remedy only and is inappropriate for the mesosphere.

When  $B_{GW}(z_0) = 0$  and equatorial wave parameters are given by (15)–(17), the model asymptotes to a steady state with easterlies overlying westerlies (not shown). Without upwelling, the equatorial waves alone produce a realistic QBO (D85); but with apparent upwelling, additional fluxes are necessary. In Figure 9,

$$B_{GW}(z_0) = 25 \times 10^{-3} \text{ m}^2 \text{ s}^{-2} \quad (18)$$

This value is equivalent to *Pfister et al.*’s [1993b] local momentum flux assuming 125% coverage by convection in the equatorial zone (obviously impossible!) or 12% coverage with local fluxes 10 times as large. The second alternative is also unrealistic: although large local fluxes are possible [*Alexander and Pfister*, 1995], they are associated with only the most vigorous storms occupying a small surface area. There is no need for mesoscale waves to supply all of the momentum required for the QBO, however. The numerical simulation indicates the total flux required to produce a realistic QBO in this model configuration, with thermal relaxation to climatological  $\bar{T}^E$ .

The cross section of mean zonal wind in Figure 9 is impressively realistic. The QBO amplitude, vertical shear, and mean flow acceleration are close to observed values, including the vertical profiles of these quantities. The period is relatively

short (720 days). With other parameters fixed, the gravity-wave flux  $B_{GW}(z_0)$  can be adjusted to produce virtually any QBO period (apart from the effect of seasonal synchronization, as noted below, which may restrict the average QBO period to certain “quantized” values). This parameter also affects the vertical profile of QBO amplitude, tending to bring the maximum amplitude down to a lower altitude as  $B_{GW}(z_0)$  is increased. The LH68 scheme cannot, however, cause the amplitude of the QBO to exceed the peak-to-peak range  $|c_{KQ} - c_{RG}|$  attributable to equatorial waves alone.

A few interesting features of the simulation may be noted. (1) Because of the large gravity-wave flux in this model run, the simulated QBO is synchronized with the seasonal cycle. There is exactly one QBO cycle every 2 years. The stratopause semi-annual oscillation is responsible for synchronization in the model. The QBO westerly phase in each cycle is triggered by the westerly phase of the “first” SAO cycle in a calendar year, as often observed south of the equator [LH68; *Dunkerton and Delisi*, this issue]. Downward influence is attributable to the mathematical form of the LH68 parameterization (advection) and is expected of continuous gravity-wave spectra under more general circumstances (see Appendix). (2) Selective transmission of waves, due to QBO filtering, affects stratopause and mesopause SAOs although these oscillations are strongly constrained by body forces and mechanical relaxation to match the climatology. Westerlies in the stratopause SAO descend farther as the QBO westerly phase wanes (as observed; e.g., *Dunkerton and Delisi* [this issue]) and easterlies in the mesopause SAO connect with stratopause easterlies only at the onset of a new QBO easterly phase. Interannual variability of the observed SAOs is discussed by *Garcia et al.* [this issue]. The observed mesopause SAO is apparently modulated by the QBO to a greater degree than in our frictionally controlled simulation of the mesosphere.

When the gravity-wave forcing is reduced, the simulated

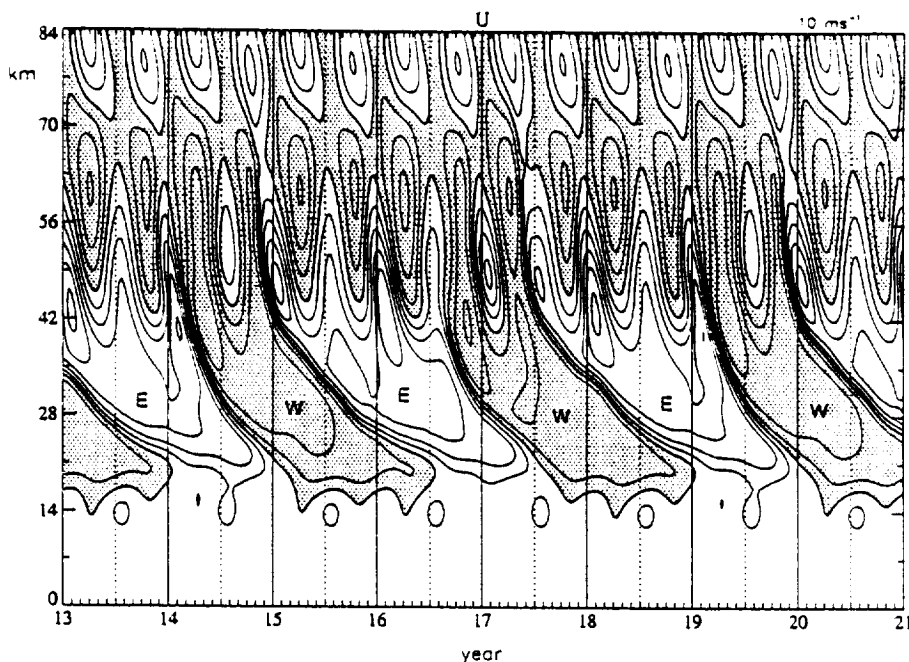


Figure 10. Time-height section of mean zonal wind at equator, as in Figure 9 but with slightly reduced gravity-wave flux.

QBO period lengthens in a series of jumps, evidently so as to maintain synchronization with the seasonal cycle. In Figure 10,  $B_{GW}(z_0) = 20 \text{ m}^2 \text{ s}^{-2}$ ; the average QBO period is 2.5 years. The length of individual cycles is slightly different from this, but each adjacent pair requires exactly 5 years. Another view of this simulation is shown in Figure 11a. The distribution of phase onsets in a calendar year forms a “binary cluster” as described by Dunkerton [1990]. Trinary clusters are also simulated, an example of which is discussed in section 4.4. In Figure 10 it is interesting to note that alternating QBO westerly phases begin as in Figure 9, triggered by the westerly phase of the first SAO cycle, while other westerly phases are initiated by a combination of first and second SAO cycles. In the latter case, a new QBO westerly shear zone temporarily stalls at 35–42 km in the middle of a calendar year [e.g., at 16.5 years]. This behavior is sometimes observed in the real QBO [Dunkerton and Delisi, this issue].

Upwelling in the equatorial lower stratosphere varies significantly on account of the QBO, as shown in Figure 12. The variation of  $\bar{w}^*$  is greatly enhanced relative to that of the control run (annual cycle only) and agrees better with the observed range of apparent upwelling and radiatively determined  $\bar{w}^*$ . In reality, the annual variation of  $\bar{w}^*$  may be larger than simulated here, possibly affecting the timing of QBO onsets in a calendar year [Dunkerton, 1990; Kinnarsley and Pawson, 1995]. The equatorial annual cycle can be increased by magnifying the difference in extratropical body force between northern and southern hemisphere winters. Seasonal variations of equatorial wave flux [Maruyama, 1991; Dunkerton, 1991b] also modulate the QBO [Dunkerton, 1990].

The latitudinal structure of the 2.5-year simulated QBO at 24.5 km is shown in Figure 13. Note that easterlies are shaded here. When the annual cycle is included, the easterly phase appears broad compared to the westerly phase. The westerly phase wobbles about the equator with the annual cycle. When the annual cycle is removed, as in Figure 14, the two phases

have equal width. Onset of the westerly phase begins at the equator, as first noted by Hamilton [1984]. This feature and the latitudinal extent of the simulated QBO agree well with a composite of the observed QBO derived by Dunkerton and Delisi [1985]. Figure 14 suggests that QBO phases are pulled slightly off the equator by the annual cycle, even though the seasonal cycle was removed from the figure. Also, deseasonalized westerlies (easterlies) tend to maximize near the equinox (solstice). The latitude of maximum wave driving is determined by the total wind (QBO plus seasonal cycle), and meridional advection of angular momentum is important in the QBO westerly phase (D91).

#### 4.3. Damping of QBO Temperature Anomalies

Although thermal relaxation adequately describes the damping of small ( $\leq 4 \text{ K}$ ) QBO temperature anomalies by radiative transfer, these anomalies are shallow and depend on wave driving, advection, and vertical diffusion in a complicated way. It is difficult to predict the damping rate of QBO temperature anomalies because their vertical scale is not known a priori, and their shape is not sinusoidal as required by the Fels [1982] parameterization. For thermal relaxation the profile of  $\alpha_T(z)$  was designed to reproduce MIDRAD heating rates (section 2.2) and climatological upwelling (Figures 8a and 8b), but no attempt was made to adjust  $\alpha_T$  for shallow QBO perturbations.

Simulations were performed using the MIDRAD algorithm for middle atmosphere heating rates instead of thermal relaxation. Overall, the results were similar to those obtained with thermal relaxation, because of our effort to calibrate  $\alpha_T(z)$  in the first place. A MIDRAD simulation is shown in Figure 11b, using the same wave flux as in Figure 11a. Minor differences are observed in the behavior of the QBO. (1) The period is exactly 2 years; the QBO “clock” is reset in every cycle by the westerly onset of the SAO. (2) Westerlies descend more rapidly, and easterlies more slowly, than in Figure 11a, due to the enhanced radiative damping of QBO temperature anomalies.



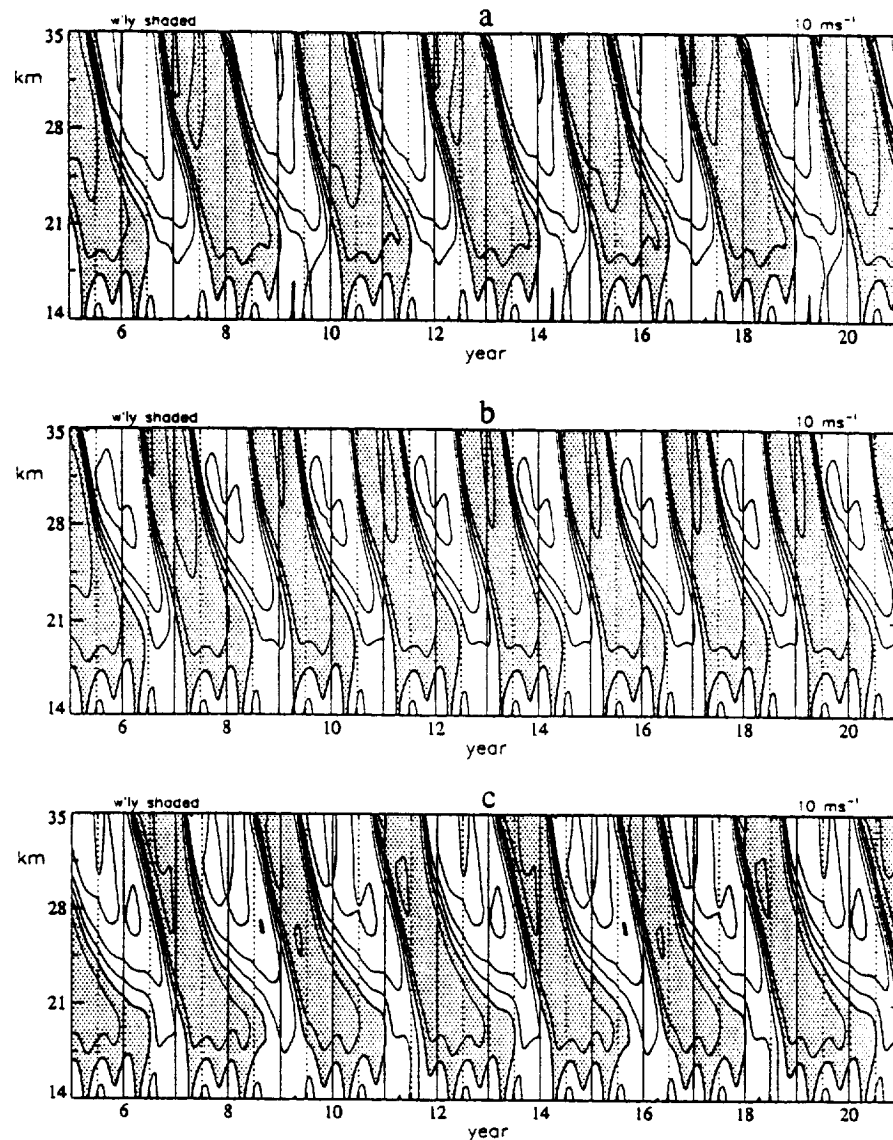


Figure 11. (a) Mean zonal wind as in Figure 10. (b) As in Figure 11a but for MIDRAD run. (c) As in Figure 11a but for multiwave run. Contours:  $10 \text{ ms}^{-1}$ , with westerlies shaded.

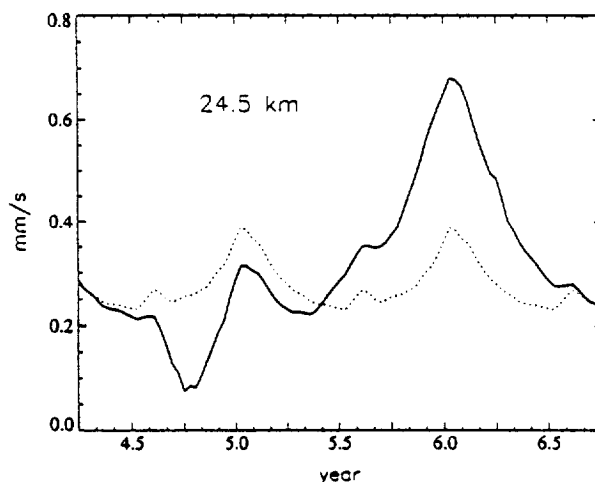


Figure 12. Equatorial vertical velocity at 24.5 km, comparing QBO run of Figure 10 (solid line) and control run (dotted line).

Related to this, absolute downwelling occurs in SAO westerly shear. (3) The asymmetry of QBO phases is obvious: westerlies last longer than easterlies at lower levels, as observed. (4) Amplitude of the QBO easterly phase is slightly weaker at 21–25 km. (5) Realistic QBO periods are obtained with a smaller gravity-wave flux;  $B_{GW}(z_0) = 12 \times 10^{-3} \text{ m}^2 \text{ s}^{-2}$  is adequate in this case (not shown).

Because the numerical model integrates the zonal momentum equation, differences in the MIDRAD simulation are due entirely to residual advection. There is a change in climatological upwelling at the equator, and a change in the response of  $\bar{w}^*$  to the QBO. To illustrate these differences, it is instructive to correlate the equatorial  $\bar{w}^*$  with mean vertical shear at the equator, at each vertical level:

$$\bar{w}^* = a(z) + b(z) \frac{\partial \bar{u}}{\partial z} + \dots \quad (19)$$

For simplicity the annual cycle is ignored (e.g., a pair of regression coefficients could be defined in each calendar month). Climatological upwelling is contained in  $a(z)$ , and the effect of



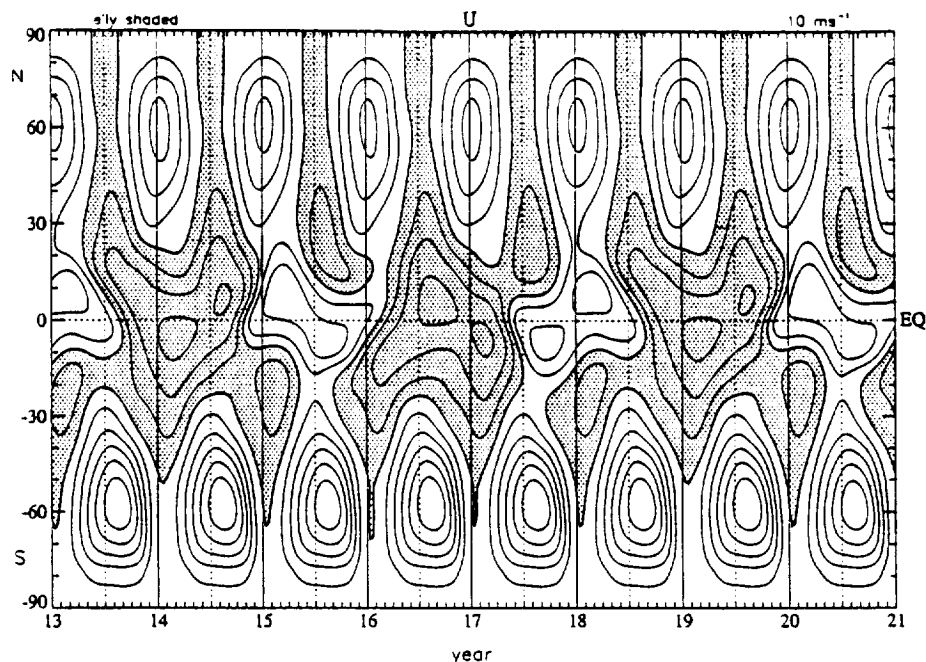


Figure 13. Time-latitude section of mean zonal wind at 24.5 km, from simulation of Figure 10. Contours: 10  $\text{ms}^{-1}$ , with easterlies shaded.

the QBO is represented by  $b(z)$ , as can be seen by differentiating the thermal wind equation with respect to  $y$  at the equator (D91). Profiles of  $a(z)$  and  $b(z)$  obtained with thermal relaxation and MIDRAD are compared in Figure 15a, 15b, respectively. Climatological upwelling in both runs is approximately the same below 25 km but is reduced in the MIDRAD simulation above 25 km. The QBO variation above 21 km is substantially stronger with MIDRAD. This means that for a given QBO shear, the  $\bar{w}^*$  anomaly is larger, so that

westerlies descend more rapidly, and vice versa. Note that  $b(z)$  is everywhere negative; the advective acceleration is positive in both shear zones as expected (LH68). Assuming a fixed latitudinal scale of the QBO, the coefficient  $-b(z)$  is proportional to the effective thermal damping rate, which is enhanced by 50–100% in the QBO region.

MIDRAD heating rates were obtained with climatological ozone, tending to exaggerate  $b(z)$ . Ozone advection raises (lowers) the equilibrium temperature in westerly (easterly)

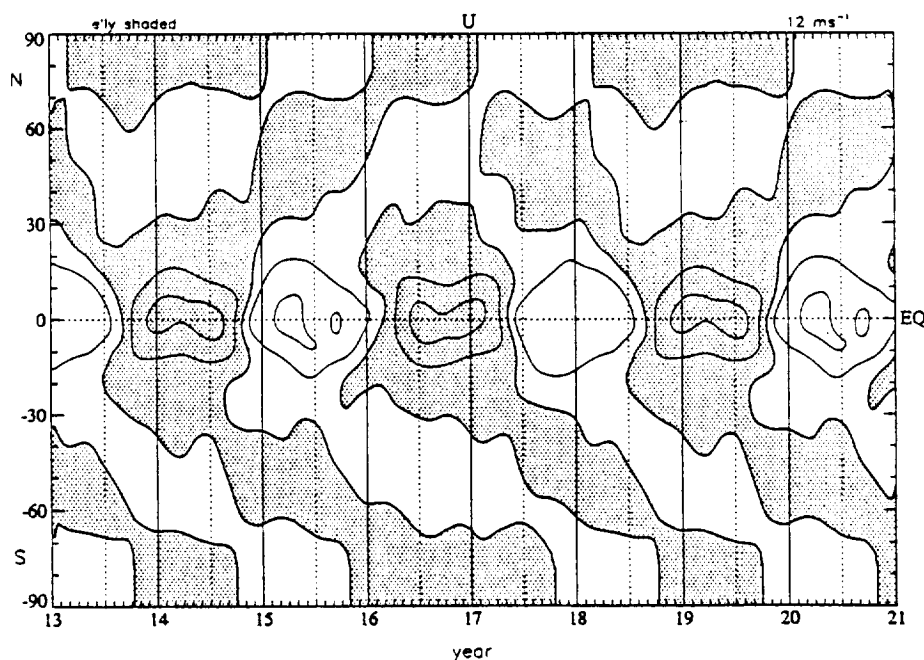


Figure 14. Time-latitude section of mean zonal wind at 24.5 km as in Figure 13 but with seasonal cycle removed. Contours: 12  $\text{ms}^{-1}$ , with easterlies shaded.

shear [Hasebe, 1994; Li et al., 1995; Kinnersley and Pawson, 1995], which has a buffering effect on the induced QBO mean meridional circulation [Kinne et al., 1992] because the departure from radiative equilibrium is reduced.

#### 4.4. Multiwave Experiment

Simple QBO integrations, like those described above, suffice to demonstrate that a realistic QBO is possible with Brewer-Dobson upwelling if the total wave flux is increased (relative to HL72) to account for vertical transport by waves with higher frequencies and shorter horizontal wavelengths. In these experiments the parameterization of additional waves was based entirely on the LH68 formula. All waves experience breaking or damping (section 2.4), however, especially those with slower vertical group velocity.

Modeling the acceleration due to a continuous spectrum of saturated or damped waves may be possible (see Appendix), but it is unlikely that all inertia-gravity waves can be embraced by a single scheme. More likely, parameterizations of this sort will be developed for high-frequency waves propagating vertically at a single latitude. Low-frequency IGWs propagate meridionally as well as vertically, rendering a local parameterization meaningless. Equatorially trapped modes are a case in point. A discrete multiwave model (e.g., section 3.3), used in conjunction with a continuous parameterization of high-frequency waves, represents a practical interim solution for modeling vertical transport by an entire spectrum of waves.

Without extensive observations of intermediate waves it is impossible to simulate their role in the QBO precisely. Nevertheless, it is easy to show that realistic QBOs can be obtained if the flux in  $B_{GW}(z_0)$  is spread among a large number of discrete intermediate waves, leaving a smaller part of the flux in the continuous mesoscale spectrum [Pfister et al., 1993a, b]. In other words,

$$B_{GW}(z_0) \rightarrow \sum_i B_{IG}(z_0) + B_{GW}(z_0) \quad (20)$$

where IG signifies the planetary and intermediate-scale inertia-gravity waves. The challenge is to specify IGW properties. Three arbitrary assumptions simplify the problem: (1) IGWs are assigned slower phase speeds than the planetary-scale Kelvin and Rossby-gravity waves; that is,

$$c_{RG} \leq c \leq c_{KQ} \quad (21)$$

so that all intermediate waves are completely absorbed in descending QBO shear zones. (2) The vertical group velocity of intermediate waves in a resting basic state is set to a constant. This simplification determines  $c$  as a function of  $k$ . (3) The vertical group velocity, dissipation rate and latitudinal profile of acceleration are approximated by those of Kelvin and "anti-Kelvin" waves for eastward and westward waves, respectively. This device places all of the momentum flux at the diagonal edges  $k = \pm \varepsilon^{1/2} \omega$  of the dispersion diagram, which form an envelope for the inertia-gravity manifold in the  $(k, \omega)$  plane. It can be shown that vertical group velocity varies by only a factor of 2 (with  $\omega$  and  $m$  held constant) going from  $k = 0$  to  $k = \pm \varepsilon^{1/2} \omega$ . In the "Kelvin/anti-Kelvin" approximation, rotation is effectively ignored, and the latitudinal profile of  $\bar{u}$ , constrained to maximize on the equator [Gray and Pyle, 1989; Saravanan, 1990; D91; Kinnersley and Pawson, 1995]. A refinement of this technique would incorporate a few discrete inertia-gravity modes near the lower boundary of the IGW mani-

fold, preserving some asymmetry of eastward versus westward waves due to rotation.

Multiwave QBO integrations were performed with thermal relaxation. Figure 11c shows an example, using the same planetary-scale equatorial modes (equations (15)–(17)), together with 15 eastward and 15 westward waves uniformly spaced in  $\log(k)$  between  $ka = 4$  and  $ka = 64$ , with phase speeds ranging from  $c = 30 \text{ ms}^{-1}$  to  $c = 7.5 \text{ ms}^{-1}$ , such that in a resting basic state

$$\frac{kc^2}{N} = W_g = \text{constant}. \quad (22)$$

Wave periods range from  $\sim 1$ –4 days. Each wave was assigned a flux  $B_{IG}(z_0) = 1 \times 10^{-3} \text{ m}^2 \text{ s}^{-2}$ . This choice cannot be justified except to note that the indirect estimate of momentum flux in short-period waves at Singapore (with geopotential symmetric about the equator) is about half as large as that assumed here (section 3.3). The ratio of intermediate to planetary-scale flux is  $\sim 3:1$ , in approximate agreement with Bergman and Salby [1994]. For the continuous spectrum,  $B_{GW}(z_0) = 7.5 \times 10^{-3} \text{ m}^2 \text{ s}^{-2}$ , approximately one fourth of its previous value.

As it turns out, the results are insensitive to how the flux is distributed among intermediate waves having the same vertical group velocity. Most important are (1) the total flux  $\Sigma B_{IG}(z_0) + B_{GW}(z_0)$ , (2) the vertical group velocity  $W_g$  of damped waves, and (3) the fact that QBO amplitude is limited by the phase speeds of planetary-scale modes as implied by (21). Increasing the total flux reduces the QBO period, as expected. Different behavior is observed when only eastward (or westward) fluxes are increased. With small asymmetry of forcing, the QBO period is reduced, but when the asymmetry passes a certain threshold, the period begins to increase rapidly until a steady state is reached. This behavior is also seen in idealized two-wave models of the QBO.

The simulation in Figure 11c resembles that of Figure 11a but with slightly weaker easterlies and somewhat weaker shear zones. Good east-west asymmetry of the QBO is obtained as in Figure 11b. There are three QBO cycles in 7 years, corresponding to a "trinary cluster" of phase onsets in the calendar year. Century-long simulations demonstrate that exact synchronization with the seasonal cycle is robust (even in a complicated form such as this) when wave forcings are held constant in time. Similar behavior was noted by Dunkerton [1990] when wave forcings contained a sufficiently large annual variation. QBO synchronization as modeled here evidently does not require seasonal variation of wave fluxes at the tropopause.

## 5. One-Dimensional Model

Quasi-biennial oscillations in the two-dimensional model depend on tropical upwelling and the Eliassen-Palm flux of vertically propagating waves near the equator. Upwelling is determined, in part, by the radiative drive and body forces of the extratropical middle atmosphere, which are related. In the two-dimensional model, upwelling can be regulated via  $\alpha_T(z)$  and  $\alpha_{M0}$  but in a somewhat awkward way.

Recognizing that the basic QBO dynamics are captured in a one-dimensional model [HL72; Plumb, 1977], it is easier to study the effect of upwelling by inserting a profile of  $\bar{w}^*$  in such a model. This was done by Saravanan [1990] and Dunkerton [1982a] for the climatological Hadley circulation and QBO circulation, respectively. Making use of the regression (19), the

two components of  $\bar{w}^*$  ( $= a + b\bar{u}_z$ ) can be incorporated in a one-dimensional model simultaneously. Likewise, the effective  $\beta$  ( $= \beta_M$  of D85) used in the Rossby-gravity parameterization scheme can be regressed against equatorial  $\bar{u}$ . With  $\beta_M$  and  $\bar{w}^*$  parameterized in terms of equatorial  $\bar{u}$  and  $\bar{u}_z$ , respectively, the one-dimensional model should reproduce the equatorial time-height section of  $\bar{u}$  from the two-dimensional model if horizontal advection, horizontal diffusion, and climatological body forces are unimportant at the equator. Fortunately, this requirement is met in the QBO region, at least approximately, so that a one-dimensional representation is possible. Horizontal advection displaces the westerly phase into the winter hemisphere by a few degrees but has almost no effect on the easterly phase with its small angular momentum gradient (D91). (The consequences of ignoring horizontal advection in the troposphere and upper stratosphere will become apparent, however.) Horizontal diffusion was set to a negligibly small value in two-dimensional simulations. Climatological body forces in the equatorial zone were masked out between 21 and 35 km (section 2.6).

A one-dimensional model with parameterized vertical advection is useful for exploration. After a QBO is obtained in the two-dimensional model, regression coefficients are calculated, and the one-dimensional model is integrated to obtain a similar oscillation. Small variations can be anticipated quickly with the one-dimensional model, for example, due to changes in the configuration of the wave spectrum. This technique is especially useful for multiwave calculations involving many tunable parameters.

Using the one-dimensional model, the gravity-wave flux required for an 840-day QBO was determined as the upwelling rate is systematically varied from its original two-dimensional model value back to zero. Observations of the "tape recorder" effect [Mote *et al.*, 1995, 1996] presumably indicate upwelling, but the derived values of  $\bar{w}^*$  are uncertain (Figure 7). It is too early to say, for example, whether the ascent of water vapor anomalies is due entirely to vertical advection, as vertical diffusion and isentropic mixing may also be important, depending on altitude. Upwelling may be smaller at  $\sim 20$  km, especially in northern summer (Figure 7), in which case the vertical wave fluxes required for the QBO are less than those of section 4.

To keep the calculation as simple as possible, the configuration of section 4.2 was used (three equatorial waves plus gravity-wave spectrum) so that only  $B_{GW}(z_0)$  is varied, while equatorial-wave fluxes were fixed as in (15)–(17). Figure 16 shows the one-dimensional version of the original two-dimensional simulation. Compared with Figure 9, the agreement is quite good. The QBO period is 836 days in the one-dimensional model, compared with 720 days in the two-dimensional model. Presumably, this represents the natural period in the absence of SAO or seasonal synchronization. Another difference is that the one-dimensional oscillation penetrates below the tropopause, demonstrating the importance of horizontal advection in the upper tropical troposphere for preventing the QBO from penetrating the troposphere, along with vertical advection as discussed by Saravanan [1990]. The oscillation period in one dimension is lengthened slightly as a result of the more "slippery" lower boundary condition on the QBO [cf. Plumb, 1977]. This underscores an indirect role of the tropospheric Hadley circulation in the QBO, namely, in eliminating any tendency for QBO regimes to penetrate the troposphere, thereby hastening the QBO switching mechanism above the tropopause. Other two-dimensional simulations (not

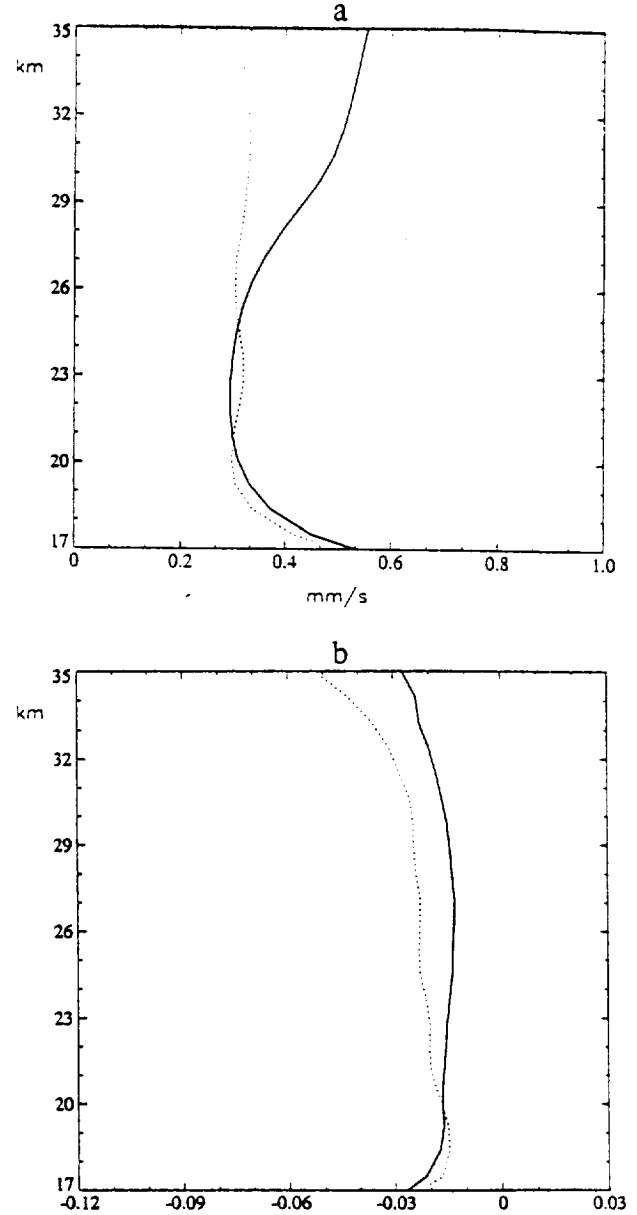


Figure 15. Regression coefficients for residual vertical velocity in equation (19), comparing thermal relaxation (solid line) with MIDRAD (dotted line). (a)  $a(z)$ ; (b)  $b(z)$ .

reported here) demonstrate that the QBO period depends weakly on the strength of the tropospheric Hadley circulation. For this reason, the model Hadley circulation was calibrated to match the observed [Oort, 1983].

Figure 17 shows the gravity-wave flux required for an 840-day QBO in the one-dimensional model, displayed as a function of the fraction of  $\bar{w}^*$  retained; that is,

$$a(z) \rightarrow \varepsilon_w a(z) \quad (23a)$$

$$b(z) \rightarrow \varepsilon_w b(z) \quad (23b)$$

at  $z > 17.5$  km. Vertical velocity in the troposphere was unaltered. Three variations are shown in the figure: reduced  $a(z)$  with original  $b(z)$ ; reduced  $b(z)$  with original  $a(z)$ ; and  $a(z)$ ,  $b(z)$  both reduced. The required flux is approximately linear in  $\varepsilon_w$ . The greatest diminution of  $B_{GW}(z_0)$  is obtained

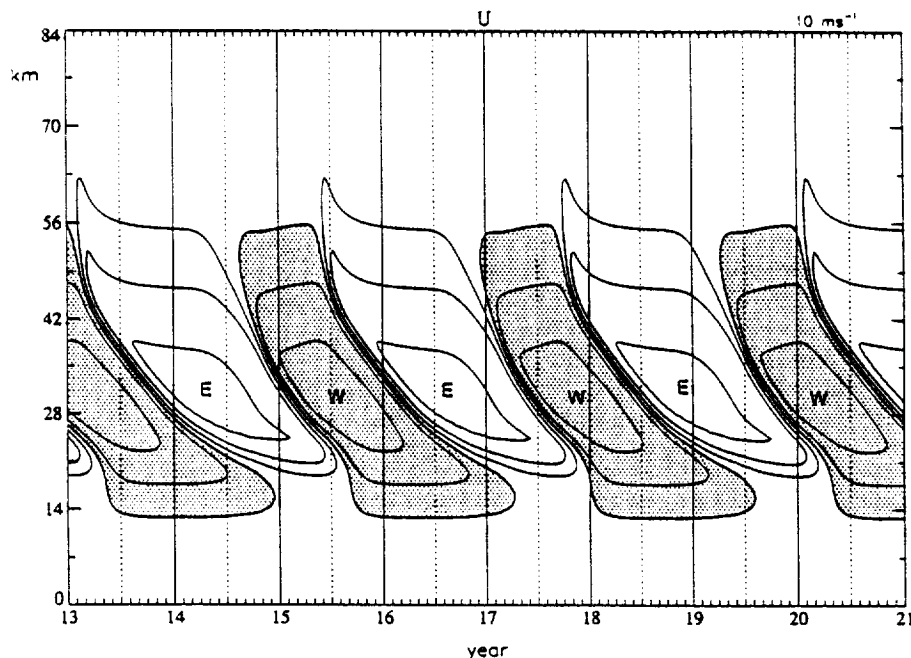


Figure 16. Time-height section of mean zonal wind at equator, from one-dimensional QBO integration with two Kelvin waves, one Rossby-gravity wave, and continuous gravity-wave spectrum. Contours:  $10 \text{ ms}^{-1}$ , with westerlies shaded.

when both regression coefficients are reduced. The flux is approximately linear in  $\varepsilon_w$  due to the mathematical nature of the LH68 formula. There is an effective downward "advection" of QBO shear zones due to gravity-wave absorption that overcomes upward advection due to the residual mean meridional circulation.

Without upwelling, planetary-scale waves alone are adequate for a realistic QBO (D85). In fact, the simulated period is 881 days. With only  $a(z)$  reduced, results are similar. Reduction of  $b(z)$  alone has little effect on QBO period. Asymmetric descent of shear zones is more realistic, however, with larger  $b(z)$  as noted in section 4.3. Heating anomalies due to the ozone QBO are therefore expected to alter the descent of easterly and westerly phases without having much effect on the QBO period as a whole. Of course the total upwelling, hence the QBO period, are determined in part by solar heating, which depends on ozone mixing ratio. Thus ozone advection is indirectly important to the dynamical QBO. From the discussion of sections 3.1 and 3.2 it is unlikely that  $\varepsilon_w < 0.5$ , i.e., that the climatological  $\bar{w}^*$  is less than half as large as that simulated in the two-dimensional model. Gravity-wave fluxes (due to planetary, intermediate, and/or mesoscale waves) in the range  $10\text{--}30 \times 10^{-3} \text{ m}^2 \text{ s}^{-2}$  are evidently required for a realistic QBO in addition to the fluxes associated with large-scale Kelvin and Rossby-gravity waves. The lower end of this range is adequate if climatological upwelling resembles Figures 8c and 8d rather than Figures 8a and 8b. In the two-dimensional model with modified  $T^E$  (as described in section 4.1) the QBO period is 720 days if  $B_{GW}(z_0) = 8\text{--}12 \times 10^{-3} \text{ m}^2 \text{ s}^{-2}$ .

## 6. Conclusion

The role of gravity-wave momentum transport in the quasi-biennial oscillation (QBO) was investigated using a two-dimensional numerical model. In order to obtain an oscillation

with realistic vertical structure and period, vertical momentum transport in addition to that of large-scale, long-period Kelvin and Rossby-gravity waves [Holton and Lindzen, 1972] is necessary. The total wave flux required for the QBO is sensitive to the rate of upwelling, due to the Brewer-Dobson circulation [Dunkerton, 1991a], which can be estimated from the observed ascent of water vapor anomalies in the tropical lower stratosphere [Mote et al., 1995, 1996]. Although mesoscale gravity waves contribute to mean flow acceleration, it is unlikely that the momentum flux in these waves is adequate for the QBO,

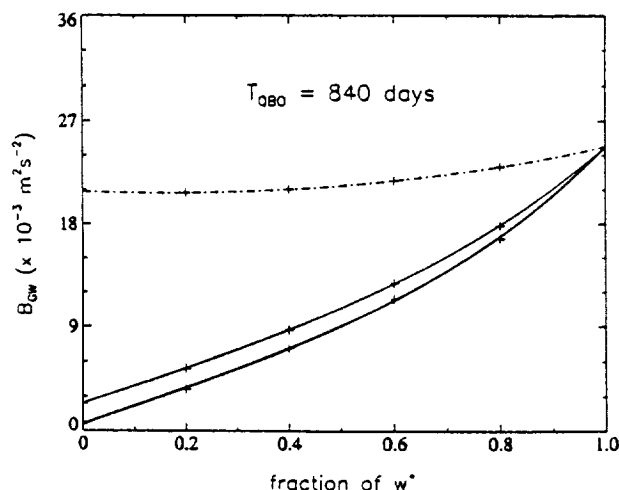


Figure 17. Gravity-wave flux required for an 840-day QBO in the one-dimensional model, as a function of the nondimensional parameter  $\varepsilon_w$  representing the fraction of upwelling coefficient [ $a(z)$ ,  $b(z)$ ] retained above 17.5 km. Three variations are shown, reducing  $a(z)$  and  $b(z)$  (thick line),  $a(z)$  only (thin line),  $b(z)$  only (dotted-dashed line).

especially if their spectrum is shifted toward westerly phase speeds. Short-period Kelvin and inertia-gravity waves at planetary and intermediate scales also transport momentum [Maruyama, 1994; Sato *et al.*, 1994; Bergman and Salby, 1994; Dunkerton, 1995; Sato and Dunkerton, this issue] and play an important role in the QBO. Numerical results suggest that the flux in all vertically propagating waves (planetary-scale equatorial modes, intermediate inertia-gravity waves, and mesoscale gravity waves), in combination, is sufficient to obtain a QBO with realistic Brewer-Dobson upwelling if the total wave flux is 2–4 times as large as that of the observed large-scale, long-period Kelvin and Rossby-gravity waves. Lateral propagation of Rossby waves from the winter hemisphere is unnecessary in this case, although it may be important in upper and lowermost levels of the QBO and subtropics [Andrews and McIntyre, 1976; Dunkerton, 1983, 1985].

The apparent upwelling of water vapor anomalies near the equator [Mote *et al.*, 1995, 1996] agrees reasonably well with the profile of residual vertical velocity derived from a radiative code [Rosenlof, 1995]. On closer examination the radiatively derived  $\bar{w}^*$  below 20 km is somewhat smaller and has its minimum value at a slightly lower altitude, perhaps on account of vertical diffusion or isentropic mixing. Given the uncertainty in  $\bar{w}^*$ , it is impossible to determine with any precision the total flux in vertically propagating waves required for a realistic QBO. It is useful to note, however, that the required flux varies (approximately) linearly with respect to upwelling rate in the QBO region. Fluxes attributable to intermediate and mesoscale waves are not well known, and large-scale Rossby-gravity fluxes remain uncertain. Assuming “classical” values of planetary-wave flux [Andrews *et al.*, 1987] and that mesoscale fluxes are in the ballpark implied by Pfister *et al.* [1993a, b], there is obviously a need for additional fluxes associated with intermediate inertia-gravity waves [Bergman and Salby, 1994]. Bergman and Salby estimate that the ratio of total Eliassen-Palm flux to that of planetary-scale equatorial modes is  $\sim 2.5:1$ . This ratio, and their implied suggestion that most of the additional flux is contained in waves having critical levels in the QBO, agrees well with the numerical analysis presented here if planetary-wave fluxes are assumed known. Evidence of momentum flux in short-period ( $\sim 1$ –3 days) waves is encouraging [Maruyama, 1994; Sato *et al.*, 1994; Sato and Dunkerton, this issue], but additional observations of waves in this frequency range are desperately needed. Further study of mesoscale waves and their effect on the tropical lower stratosphere would also be timely.

The role of gravity waves in the equatorial middle atmosphere becomes more important with increasing height. It is thought that these waves are primarily responsible for the stratopause and mesopause semiannual oscillations [Hitchman and Leovy, 1988; Hamilton and Mahlman, 1988; Dunkerton, 1982c]. That gravity waves also have an important role to play in the QBO is not surprising, since the majority of these waves have critical levels in descending QBO shear zones (D91). At certain phases of the QBO, when winds are westerly or easterly over a deep layer, waves with phase speeds of opposite sign escape to greater altitudes and contribute to shear-zone descent in the overlying SAO. This effect is clearly seen in observations and in the model as well, providing strong evidence that the local spectrum of gravity-wave phase speeds in the middle atmosphere is modulated by the mean flow at underlying levels.

Recent attempts to model the QBO in three-dimensional

general circulation models (GCMs) highlight the need for additional fluxes [Takahashi and Boville, 1992; Hayashi and Golder, 1994; Takahashi and Shiobara, 1995; Takahashi, 1996; Takahashi and Kumakura, 1995; Takahashi *et al.*, 1996]. In GCM studies, an important question arises concerning the horizontal and vertical resolution required for three-dimensional simulation of the QBO. The role of gravity waves in the QBO must be taken into account in order to answer this question. With finer horizontal resolution, a broader spectrum of gravity waves can be represented numerically, capturing a larger percentage of the total flux attributable to deep tropical convection. Finer vertical resolution allows the process of wave, mean-flow interaction to be simulated more faithfully, e.g., without spurious critical-level reflection. Both aspects are important for the QBO: it is necessary that the total flux and its local convergence be sufficient to overcome Brewer-Dobson upwelling.

The role of laterally propagating planetary Rossby waves from the winter stratosphere was downplayed in this paper for two reasons. (1) Observations of a semipermeable transport barrier in the subtropical lower stratosphere suggest that (for the most part) surf-zone mixing does not extend farther equatorward at these altitudes [McIntyre and Palmer, 1983, 1984]. (2) Available evidence suggests that the equatorial QBO can be modeled successfully without laterally propagating Rossby waves. With regard to the first point, although isentropic mixing in the equatorial lower stratosphere is weaker than in midlatitudes, we should not regard this region as completely isolated from lateral propagation and detrainment. Lateral propagation is important in the middle and upper stratosphere and near the tropopause but (from time to time) may also affect the QBO. When QBO and midlatitude westerlies connect, as sometimes observed [Dunkerton and Delisi, 1985], quasi-stationary Rossby waves and associated surf-zone disturbances are expected to enter the tropics, contributing to horizontal mixing and deceleration.

In a QBO model there is no need to exclude lateral propagation entirely [cf. Takahashi *et al.*, 1996], but several qualifications should be made. (1) Meridional mixing, as a rule, is quite “toxic” to the QBO, having an adverse effect on oscillation amplitude and descent of the narrow westerly “nose” [Hamilton, 1984; Dunkerton and Delisi, 1985; Dunkerton, 1985, 1991a]. It is extremely unlikely that significant meridional mixing could occur at the tip of the nose, since this region is isolated from midlatitude westerlies, and narrow westerlies at the equator would be easily erased by horizontal diffusion. (2) Deceleration due to quasi-stationary waves and associated surf-zone disturbances might help the zero-wind line descend in the easterly acceleration phase, but it is not immediately obvious why strong easterlies should be produced as a result of this process, unless westward disturbances were also excited in the surf zone. (3) If the locus of wavebreaking and mixing is a narrow critical layer, it could very well be that during the westerly phase of the QBO, laterally propagating Rossby waves affect the summer subtropics [O’Sullivan and Chen, 1996; Chen, 1995] rather than the equator. It is expected that equatorial westerlies are shielded from breakdown of quasi-stationary waves by a belt of weak winds in the winter subtropics [O’Sullivan, 1996]. As a result, equatorial westerlies are able to persist irrespective of lateral propagation of Rossby waves from midlatitudes.

Lateral propagation may nevertheless be important, particularly in upper levels of the QBO and in the lowermost strato-

sphere. The possibility that lateral mixing may contribute to the destruction of QBO regimes just above the tropopause has not been explored; it is conceivable that in such a model the role of vertical diffusion could be minimized, and estimates of required wave flux might be altered.

In conclusion, it can be said that the quasi-biennial oscillation of the equatorial lower stratosphere is fundamentally simple in its mechanism [Lindzen and Holton, 1968; Holton and Lindzen, 1972; Plumb, 1977; Plumb and McEwan, 1978] but complicated in detail. The sensitivity to climatological upwelling, modulation of upwelling by the QBO, dependence of the QBO on vertical wave transport over a wide range of spatial and temporal scales, and possible effects of lateral propagation make the QBO problem an intricate one. Individual aspects of the problem are challenging by themselves. For example: (1) Climatological upwelling is attributable to body forces of tropical and extratropical origin, integrated along angular momentum surfaces above the level in question [Haynes *et al.*, 1991; Rosenlof, 1995]. In the tropics, angular momentum surfaces are determined in part by extratropical body forces [Dunkerton, 1989, 1991a]. (2) Transport of ozone by the QBO alters the radiative balance locally [Kinne *et al.*, 1992; Hasebe, 1994; Li *et al.*, 1995; Kinnarsley and Pawson, 1995]. Ozone advection creates a heating anomaly consistent with the temperature tendency in the dynamical QBO, buffering the induced circulation. (3) Estimation of momentum flux in short-period disturbances is problematic [Sato *et al.*, 1994; Bergman and Salby, 1994]. A novel method for determining the flux in vertical shear utilizes the cospectrum of zonal wind and temperature [Dunkerton, 1995] which is prominent in short-period waves. Application of this formula to Singapore rawinsonde data suggests that the momentum flux in short-period disturbances is significant relative to that of long-period Kelvin waves [Sato and Dunkerton, this issue]. (4) Representation of a continuous gravity-wave spectrum is necessary for QBO modeling, but the method of LH68 could be improved considerably as discussed in the Appendix. Our interim solution of dividing the spectrum into an ensemble of discrete equatorial modes [Saravanan, 1990] and a continuous spectrum of smaller-scale waves is a practical approach, but an objective distinction between the discrete and the continuous spectrum is lacking.

As GCM resolution improves, the problem of parameterization will gradually recede until all scales of motion relevant to the QBO are explicitly simulated. For now, intermediate IGWs and mesoscale gravity waves must be parameterized. Effects of lateral Rossby-wave propagation, on the other hand, can be investigated in current models with a modest increase in horizontal resolution.

## Appendix: Gravity-Wave Spectrum

If it is assumed that waves are steady and conservative beneath their critical level but completely absorbed at that level, as implied by Booker and Bretherton's [1967] analytic solution at large Richardson number, then

$$\mathcal{B}(c, z) = \mathcal{B}(c, z_0) \quad \text{in } z_0 < z < z_c \quad (\text{A1})$$

where  $z_c$  is the first critical level encountered by a wave with phase speed  $c$ , above the forcing level  $z_0$ . According to the theorem of Eliassen and Palm [1961] the quantity  $\mathcal{B}$  is invariant with height below the critical level. The change of  $\rho_0 B$  between two adjacent levels  $z_1, z_2$  is due entirely to critical-level absorption of waves having phase speeds in the range

$$\bar{u}(z_1) < c < \bar{u}(z_2) \quad (\text{A2})$$

so that

$$\rho_0^*(z) B(z) = \int_{-\infty}^{\infty} \mathcal{B}_0(c) H(z_c - z) dc \quad (\text{A3})$$

where  $\mathcal{B}_0(c) = \mathcal{B}(c, z_0)$ ,  $\rho_0^* = \exp - (z - z_0)/H$ , and

$$\begin{aligned} -\frac{\partial}{\partial z} \rho_0^*(z) B(z) &= \int_{-\infty}^{\infty} \mathcal{B}_0(c) \delta(z_c - z) dc \\ &\approx \int_{-\infty}^{\infty} \mathcal{B}_0(c) |\bar{u}_z(z_c)| \delta\left[\frac{c - \bar{u}}{\bar{u}_z(z_c)}\right] d\left[\frac{c - \bar{u}}{\bar{u}_z(z_c)}\right] \\ &= \mathcal{B}_0(\bar{u}) \cdot |\bar{u}_z| = |\mathcal{B}_0(\bar{u})| \cdot \bar{u}_z. \end{aligned} \quad (\text{A4})$$

In the second equality of (A4) the mean flow was expanded in a Taylor series about the critical level  $\bar{u}(z_c) = c$ . The absolute value of  $\bar{u}_z(z_c)$  was used to avoid reversing the direction of integration, and the delta function was assumed symmetric about the origin, consistent with (A3). The last equality follows, as explained by LH68 in connection with their equations (8) and (9), from the expectation that only waves with positive (negative) momentum flux contribute to the local acceleration in positive (negative) shear. The wave-induced acceleration is then

$$\frac{\partial \bar{u}}{\partial t} = |\mathcal{B}_0(\bar{u})| \cdot \bar{u}_z \exp [(z - z_0)/H] \quad (\text{A5})$$

subject to the "nonlocal" condition that  $\bar{u}$  must be outside the range of mean-flow speeds already encountered between  $z_0$  and  $z$ . If this condition is met, the effect of critical-level absorption of a continuous spectrum of waves is to cause a shear zone to move downward as if it were advected by a mean vertical velocity of magnitude  $|\mathcal{B}_0(\bar{u})| \exp [(z - z_0)/H]$ . The column-integrated acceleration (weighted by nondimensional density) attributable to eastward waves, for example, is

$$\int_{z_0}^{\infty} \rho_0^* \frac{\partial \bar{u}}{\partial t} dz = \int_{z_0}^{\infty} \mathcal{B}_0(\bar{u}) \bar{u}_z dz = \int_{\bar{u}_0}^{\bar{u}_\infty} \mathcal{B}_0(\bar{u}) d\bar{u} \quad (\text{A6})$$

where  $\bar{u}_\infty$  is the maximum value of  $\bar{u}$ ; the acceleration is due only to waves having critical levels above  $z_0$ , while other waves "radiate to space." This representation of gravity waves was advanced by Lindzen and Holton [1968] and is central to their theory of the QBO.

Several features of their theory may be noted. (1) The range of attainable mean-flow speeds in the QBO is determined either by the range of speeds at some upper level (due to the SAO) or by the range of phase speeds in the gravity-wave spectrum, whichever is less. (2) The rate of shear zone descent, hence the period of the QBO, is determined in part by the amplitude of waves forced from below. (3) Descent is faster at upper levels because the density is lower there. (4) Waves of one sign are completely absorbed in their shear zone (the shielding effect), leaving the flow at upper levels free to accelerate in the opposite direction when waves of the opposite sign no longer encounter a critical level at lower altitudes. (5) The wave-induced acceleration is determined locally as a function of the vertical shear  $\bar{u}_z$  and momentum flux density  $\mathcal{B}(c = \bar{u})$ .

together with a nonlocal condition that  $\bar{u}$  must be outside the range of mean flows already encountered below the level in question. (6) Downward influence is possible due to the mathematical form (advection). (7) Other parameters such as the horizontal wavenumber, damping rate, and static stability do not appear. The acceleration is independent of these quantities so that no particular model of wave absorption need be adopted.

Several problems of the theory may also be noted. (1) The timing and magnitude of simulated QBOs is determined in part by the overlying SAO, without which an oscillation would be impossible. In contrast, the *Holton and Lindzen* [1972] theory, using two discrete (damped) waves, admits no downward influence apart from diffusion [*Plumb*, 1977] and does not require an SAO to initiate QBO shear zones. (2) Zonal perturbation velocity at the critical level is singular in the *Booker and Bretherton* [1967] solution, and the kinetic energy density is infinite [*Fritts and Lu*, 1993]. (3) Regardless of how small, real waves tend to break or be absorbed a short distance ahead of their critical level, as the integrand of (1b) becomes singular. (4) Vertically discontinuous mean flows and/or accelerations are implied by (A5); an example was shown in LH68. This is also a feature of discrete models [*Dunkerton*, 1981, 1982b].

In a QBO model, the first problem is easily avoided by using two or more discrete (damped) equatorial waves as the primary momentum source [HL72, *Plumb*, 1997]. Formation of internal shear zones, without overlying shear, is then possible. In this paper, a continuous spectrum of waves is superposed on the discrete spectrum in order to obtain the correct rate of shear-zone descent in the presence of Brewer-Dobson upwelling. The fourth problem is avoided, as in discrete models, by vertical diffusion of momentum. The second and third problems require further comment: Is (A5) adequate?

The absorption of a spectrum of noninteracting, steady, damped waves is obtained by combining (1a), (1b) and (4) [*Saravanan*, 1990]:

$$\rho_0^*(z) B(z) = \int_{-\infty}^{\infty} \mathcal{B}_0(c) \exp - \int_{z_0}^z D(c, z') dz' dc \quad (\text{A7})$$

For waves governed by (A12), assuming that the damping rate is nonsingular at the critical level, it can be shown (see below) that

$$\rho_0^*(z) B(z) \approx \int_{-\infty}^{\infty} \mathcal{B}_0(c) \exp - \frac{\varepsilon}{z_c^* - z^*} dc \quad (\text{A8})$$

where  $z^* = z/H$  and

$$\varepsilon = \frac{\alpha(z_c) N(z_c)}{k \bar{u}_{zc}(z_c)^2 H} \quad (\text{A9})$$

for suitably small values of  $\varepsilon$ , requiring in effect that the integral over  $z'$  in (A7) is dominated by the singularity of  $D$  at the critical level. It can also be shown that

$$-\frac{\partial}{\partial z} \rho_0^*(z) B(z) \approx \int_{-\infty}^{\infty} \mathcal{B}_0(c) (H\varepsilon)^{-1} \xi^2 \exp - \xi dc \quad (\text{A10})$$

where

$$\xi = \frac{\varepsilon}{z_c^* - z^*}. \quad (\text{A11})$$

The quantity  $\varepsilon^{-1} \xi^2 \exp - \xi$  may be likened to an asymmetric delta function in the limit  $\varepsilon \rightarrow 0$ , with maximum amplitude at  $\xi = 2$  and constant area with respect to the  $z$  axis. The function is identically zero at the critical level ( $\xi = \infty$ ) and at any finite distance below ( $\xi = 0$ ).

To keep the algebra reasonably simple, we set [*Saravanan*, 1990]

$$D = \frac{\alpha N}{k(c - \bar{u})^2} \quad (\text{A12})$$

where  $\alpha$  is the temporal damping rate,  $N$  is static stability, and  $k$  is zonal wavenumber. When  $\alpha$  is small or  $k$  is large, the momentum flux of each component  $\mathcal{B}(c)$  is approximately invariant with height [*Eliassen and Palm*, 1961; *Andrews and McIntyre*, 1976] until  $\bar{u}$  approaches  $c$  at the critical level. In this case,

$$\begin{aligned} P(c, z) &= \int_{z_0}^z D(c, \bar{u}') \left( \frac{\partial \bar{u}'}{\partial z'} \right)^{-1} d\bar{u}' \approx \frac{\alpha_c N_c}{k \bar{u}_{zc}} \int_{z_0}^z \frac{d\bar{u}'}{(c - \bar{u}')^2} \\ &= \frac{\alpha_c N_c}{k \bar{u}_{zc}} \left[ \frac{1}{c - \bar{u}} - \frac{1}{c - \bar{u}_0} \right] \approx \frac{\alpha_c N_c}{k \bar{u}_{zc}(c - \bar{u})} = \xi. \end{aligned} \quad (\text{A13})$$

The subscript  $c$  denotes evaluation at the critical level  $\bar{u}(z_c) = c$ . In general,  $\alpha$  is a function of  $(c - \bar{u})$ , which requires a slight modification of (A13).

The mean-flow acceleration (weighted by nondimensional density) is

$$\rho_0^* \bar{u}_t = - \frac{\partial}{\partial z} \rho_0^* B = - \int_{-\infty}^{\infty} \frac{\partial \mathcal{B}}{\partial z} dc = \int_{-\infty}^{\infty} \mathcal{A} dc \quad (\text{A14})$$

where

$$\mathcal{A} = - \frac{\partial \mathcal{B}}{\partial z} = D \mathcal{B}. \quad (\text{A15})$$

Now

$$\lim_{z \rightarrow z_c} D = \frac{\alpha_c N_c}{k(c - \bar{u})^2} = \frac{\alpha_c^2 N_c^2}{k^2 \bar{u}_{zc}^2 (c - \bar{u})^2} \cdot \frac{k \bar{u}_{zc}^2}{\alpha_c N_c} = \xi^2 (\varepsilon H)^{-1}. \quad (\text{A16})$$

Also,

$$\xi = \frac{\alpha_c N_c}{k \bar{u}_{zc}(c - \bar{u})} = \frac{\alpha_c N_c}{k \bar{u}_{zc}(z_c - z)} = \frac{\varepsilon}{z_c^* - z^*} \quad (\text{A17})$$

where  $z^* = z/H$ . The acceleration per unit phase speed is approximately

$$\mathcal{A} \approx \mathcal{B}_0(\varepsilon H)^{-1} \xi^2 \exp - \xi. \quad (\text{A18})$$

Approaching a critical level, the acceleration (initially small) rises to a maximum at  $\xi = 2$  and then decays rapidly to zero at  $z_c$ . Similar behavior is observed when  $\alpha$  is a function of  $(c - \bar{u})$ , but the definition of  $\xi$ , exponent of  $\xi$ , and altitude of maximum acceleration are different. In the limit  $\varepsilon \rightarrow 0$ , the acceleration per unit phase speed may be likened to an asymmetric delta function centered at an infinitesimal distance beneath the critical level. The vertically integrated acceleration per unit phase speed is finite regardless of  $\varepsilon$ :

$$\int_{z_0}^{z^*} \mathcal{A} dz' = \mathcal{B}(z_0) - \mathcal{B}(z^*). \quad (\text{A19})$$



This formula ensures conservation of zonal momentum in the vertical column bounded by  $z_0$  and  $z_T$ . The total acceleration (weighted by nondimensional density) is obtained by substituting (A18) in (A14):

$$\rho_0^* \bar{u}_z = -\frac{\partial}{\partial z} \rho_0^* B \approx \int_{-\infty}^{\infty} \mathcal{B}_0(\varepsilon H)^{-1} \xi^2 \exp -\xi \, d\xi. \quad (\text{A20})$$

This quantity is finite and well behaved if the integral over  $c$  is evaluated prior to the limit  $\varepsilon \rightarrow 0$ . For any  $\varepsilon$ , there is a certain minimum spectral resolution  $\Delta c$  required for a smooth acceleration profile.

(Determining the integrated momentum flux or its divergence due to a continuous spectrum of nearly undamped waves involves two limits:  $\varepsilon \rightarrow 0$  and  $\Delta c \rightarrow 0$ . The result obtained evidently depends on the order in which the limits are taken. If the integral over  $c$  is approximated by a set of discrete phase speeds, and  $\varepsilon$  approaches zero first, we obtain several infinitely narrow, infinite spikes of acceleration at discrete levels (just below each wave's critical level). Adding more waves (such that the total momentum flux at the lower boundary remains constant) simply increases the number of spikes while reducing their individual amplitude. Each wave is completely unaffected by the mean flow above the critical level, as in the work of Plumb [1977]. On the other hand, if  $\varepsilon$  is initially finite and held constant while adding more waves, the profile of acceleration remains smooth as  $\Delta c \rightarrow 0$ . Repeating the exercise with a reduced value of  $\varepsilon$  generates another smooth profile, assuming that  $\Delta c$  is adequately small to begin with. The succession of smooth profiles as  $\varepsilon \rightarrow 0$  presumably asymptotes to that of LH68; numerical calculations (not shown) support this conjecture.)

Lindzen and Holton [1968] simplified matters by assuming that the waves are exactly conservative until  $z = z_c$ . This assumption is no longer tenable, for reasons discussed above, although the LH68 formula provides a "quick fix" for QBO models with Brewer-Dobson upwelling (section 4). Their formula actually belongs to a general class of simplified profiles

$$\mathcal{A} \propto \mathcal{B}_0 \delta(z - z_b) \quad (\text{A21})$$

where  $z_b = z_b(c)$  is the altitude (not necessarily the critical level) where a wave of phase speed  $c$  accelerates the mean flow. The approximation in (A21) is to concentrate each wave's acceleration in an infinitesimal layer. In the exact formula, the acceleration per unit phase speed is spread over a finite range of altitudes. The location of  $z_b$  might correspond to  $\xi = 2$  in the example outlined above, or perhaps the "breaking level" of Lindzen [1981]. Another choice would equate  $z_b$  with the altitude at which the intrinsic phase speed matches the "characteristic" intrinsic phase speed  $c_*$  of Fritts and Lu [1993]. In the latter case, there would be only two values of  $i$  corresponding to positive and negative, respectively, intrinsic phase speeds. Inserting (A21) in (A14), the mean-flow acceleration (weighted by nondimensional density) at altitude  $z$  is

$$\rho_0^* \bar{u}_z = \sum_i \frac{\mathcal{B}_0(c_i)}{(\partial z_b / \partial c)_i} \quad (\text{A22})$$

where  $z = z_b(c_i)$ . A preliminary test, assigning  $z_b$  to the altitude of maximum acceleration  $\mathcal{A}$  (due to steady, damped, nonsaturated waves), demonstrates that (A22) gives better agreement with the exact acceleration in Figure 4 than the

formula of LH68. Acceleration is increased above and below the center of the shear zone.

In order for the gravity-wave spectrum to decelerate a jet, it is essential that waves break or be absorbed below their critical level. Otherwise, the effect of wave absorption would be simply to advect the bottom half of the jet downward (LH68). In general, a combination of deceleration above the jet maximum and downward 'advection' below may be expected if the jet is free to accelerate in this manner.

**Acknowledgments.** Discussions and correspondence with Joan Alexander, John Bergman, Ping Chen, Peter Haynes, Jim Holton, Phil Mote, Donal O'Sullivan, Karen Rosenlof, and Kaoru Sato were helpful to this study. Keith Shine kindly provided a working version of his radiation scheme. This research was supported by the National Science Foundation, grants ATM-9123797 and ATM-9500613, and the National Aeronautics and Space Administration, contract NASW-4844.

## References

- Alexander, M. J., and L. Pfister, Gravity wave momentum flux in the lower stratosphere over convection, *Geophys. Res. Lett.*, 22, 2029–2032, 1995.
- Allen, S. J., and R. A. Vincent, Gravity wave activity in the lower atmosphere: Seasonal and latitudinal variations, *J. Geophys. Res.*, 100, 1327–1350, 1995.
- Andrews, D. G., and M. E. McIntyre, Planetary waves in horizontal and vertical shear: The generalized Eliassen-Palm relation and the mean zonal acceleration, *J. Atmos. Sci.*, 33, 2031–2048, 1976.
- Andrews, D. G., J. R. Holton, and C. B. Leovy, *Middle Atmosphere Dynamics*, 489 pp., Academic, San Diego, Calif., 1987.
- Avallone, L. M., and M. J. Prather, Photochemical evolution of ozone in the lower tropical stratosphere, *J. Geophys. Res.*, 101, 1457–1461, 1996.
- Bergman, J. W., and M. L. Salby, Equatorial wave activity derived from fluctuations in observed convection, *J. Atmos. Sci.*, 51, 3791–3806, 1994.
- Booker, J. R., and F. P. Bretherton, The critical layer for internal gravity waves in a shear flow, *J. Fluid Mech.*, 27, 513–539, 1967.
- Brewer, A. W., Evidence for a world circulation provided by the measurements of helium and water vapor distribution in the stratosphere, *Q. J. R. Meteorol. Soc.*, 75, 351–363, 1949.
- Cadet, D., and H. Teitelbaum, Observational evidence of internal inertia-gravity waves in the tropical stratosphere, *J. Atmos. Sci.*, 35, 892–907, 1979.
- Chen, P., The influences of zonal flow on wavebreaking and tropical/extratropical interaction in the lower stratosphere, *J. Geophys. Res.*, in press, 1995.
- Dickinson, R. E., Method of parameterization for infrared cooling between altitudes of 30 and 70 km, *J. Geophys. Res.*, 78, 4451–4457, 1973.
- Dobson, G. M. B., Origin and distribution of the polyatomic molecules in the atmosphere, *Proc. R. Soc. London A*, 236, 187–192, 1956.
- Dopplnick, T. G., Radiative heating of the global atmosphere: Corrigendum, *J. Atmos. Sci.*, 36, 1812–1817, 1979.
- Dunkerton, T. J., On the mean meridional mass motions of the stratosphere and mesosphere, *J. Atmos. Sci.*, 35, 2325–2333, 1978.
- Dunkerton, T. J., Wave transience in a compressible atmosphere, 1. Transient internal wave, mean-flow interaction, *J. Atmos. Sci.*, 38, 281–297, 1981.
- Dunkerton, T. J., Shear zone asymmetry in the observed and simulated quasi-biennial oscillations, *J. Atmos. Sci.*, 39, 461–469, 1982a.
- Dunkerton, T. J., Wave transience in a compressible atmosphere, Part 3: the saturation of internal gravity waves in the mesosphere, *J. Atmos. Sci.*, 39, 1042–1051, 1982b.
- Dunkerton, T. J., Theory of the mesopause semiannual oscillation, *J. Atmos. Sci.*, 39, 2681–2690, 1982c.
- Dunkerton, T. J., Laterally-propagating Rossby waves in the easterly acceleration phase of the quasi-biennial oscillation, *Atmos.-Ocean*, 21, 55–68, 1983.
- Dunkerton, T. J., A two-dimensional model of the quasi-biennial oscillation, *J. Atmos. Sci.*, 42, 1151–1160, 1985.



- Dunkerton, T. J., Nonlinear Hadley circulation driven by asymmetric differential heating, *J. Atmos. Sci.*, **46**, 956–974, 1989.
- Dunkerton, T. J., Annual variation of deseasonalized mean flow acceleration in the equatorial lower stratosphere, *J. Meteorol. Soc. Jpn.*, **68**, 499–508, 1990.
- Dunkerton, T. J., Nonlinear propagation of zonal winds in an atmosphere with Newtonian cooling and equatorial wave driving, *J. Atmos. Sci.*, **48**, 236–263, 1991a.
- Dunkerton, T. J., Intensity variation and coherence of 3–6 day equatorial waves, *Geophys. Res. Lett.*, **18**, 1469–1472, 1991b.
- Dunkerton, T. J., Observation of 3–6 day meridional wind oscillations over the tropical Pacific, 1973–1992: Vertical structure and interannual variability, *J. Atmos. Sci.*, **50**, 3292–3307, 1993.
- Dunkerton, T. J., Horizontal buoyancy flux of internal gravity waves in vertical shear, *J. Meteorol. Soc. Jpn.*, **73**, 747–755, 1995.
- Dunkerton, T. J., and M. P. Baldwin, Quasi-biennial modulation of planetary wave fluxes in the northern hemisphere winter, *J. Atmos. Sci.*, **48**, 1043–1061, 1991.
- Dunkerton, T. J., and M. P. Baldwin, Observation of 3–6 day meridional wind oscillations over the tropical Pacific, 1973–1992: Horizontal structure and propagation, *J. Atmos. Sci.*, **52**, 1585–1601, 1995.
- Dunkerton, T. J., and D. P. Delisi, Climatology of the equatorial lower stratosphere, *J. Atmos. Sci.*, **42**, 376–396, 1985.
- Dunkerton, T. J., and D. P. Delisi, Interaction of the quasi-biennial oscillation and stratopause semiannual oscillation, *J. Geophys. Res.*, this issue.
- Dunkerton, T. J., and D. J. O'Sullivan, Mixing zone in the tropical stratosphere above 10 mb, *Geophys. Res. Lett.*, **23**, 2497–2500, 1996.
- Eliassen, A., and E. Palm, On the transfer of energy in stationary mountain waves, *Geophys. Publ.*, **22**(3), 1960.
- Fels, S. B., A parameterization of scale-dependent radiative damping rates in the middle atmosphere, *J. Atmos. Sci.*, **39**, 1141–1152, 1982.
- Fritts, D. C., and W. Lu, Spectral estimates of gravity wave energy and momentum fluxes, II, Parameterization of wave forcing and variability, *J. Atmos. Sci.*, **50**, 3695–3713, 1993.
- Gage, K. S., and G. C. Reid, Longitudinal variations in tropical tropopause properties in relation to tropical convection and El Niño–Southern Oscillation events, *J. Geophys. Res.*, **92**, 14,197–14,203, 1987.
- Garcia, R. R., Parameterization of planetary wave breaking in the middle atmosphere, *J. Atmos. Sci.*, **48**, 1405–1419, 1991.
- Garcia, R. R., T. J. Dunkerton, R. S. Lieberman, and R. A. Vincent, Climatology of the semiannual oscillation of the tropical middle atmosphere, *J. Geophys. Res.*, this issue.
- Gille, J. C., and L. V. Lyjak, Radiative heating and cooling rates in the middle atmosphere, *J. Atmos. Sci.*, **43**, 2215–2229, 1986.
- Grant, W. B., et al., Aerosol-associated changes in tropical stratospheric ozone following the eruption of Mount Pinatubo, *J. Geophys. Res.*, **99**, 8197–8211, 1994.
- Gray, L. J., and T. J. Dunkerton, The role of the seasonal cycle in the quasi-biennial oscillation of ozone, *J. Atmos. Sci.*, **47**, 2429–2451, 1990.
- Gray, L. J., and J. A. Pyle, A two dimensional model of the quasi-biennial oscillation of ozone, *J. Atmos. Sci.*, **46**, 203–220, 1989.
- Hamilton, K., The vertical structure of the quasi-biennial oscillation: Observations and theory, *Atmos. Ocean*, **19**, 236–250, 1981.
- Hamilton, K., Mean wind evolution in the tropical lower stratosphere, *J. Atmos. Sci.*, **41**, 2113–2125, 1984.
- Hamilton, K. P., Climatological statistics of stratospheric inertia-gravity waves deduced from historical rocketsonde wind and temperature data, *J. Geophys. Res.*, **96**, 20,831–20,840, 1991.
- Hamilton, K., and J. D. Mahlman, General circulation model simulation of the semiannual oscillation of the tropical middle atmosphere, *J. Atmos. Sci.*, **45**, 3212–3235, 1988.
- Hasebe, F., Quasi-biennial oscillations of ozone and diabatic circulation in the equatorial stratosphere, *J. Atmos. Sci.*, **51**, 729–745, 1994.
- Hayashi, Y., and D. G. Golder, Kelvin and mixed Rossby-gravity waves appearing in the GFDL 'SKYHI' general circulation model and the FGGE data set: Implications for their generation mechanism and role in the QBO, *J. Meteorol. Soc. Jpn.*, **72**, 901–935, 1994.
- Haynes, P. H., C. J. Marks, M. E. McIntyre, T. G. Shepherd, and K. P. Shine, On the 'downward control' of extratropical diabatic circulations by eddy-induced mean zonal forces, *J. Atmos. Sci.*, **48**, 651–678, 1991.
- Held, I. M., and A. Y. Hou, Nonlinear axially symmetric circulations in a nearly inviscid atmosphere, *J. Atmos. Sci.*, **37**, 515–533, 1980.
- Held, I. M., and P. J. Phillips, A barotropic model of the interaction between the Hadley cell and a Rossby wave, *J. Atmos. Sci.*, **47**, 856–869, 1990.
- Hendon, H. H., and B. Liebmann, The structure and annual variation of antisymmetric fluctuations of tropical convection and their association with Rossby-gravity waves, *J. Atmos. Sci.*, **48**, 2127–2140, 1991.
- Hirota, I., and T. Niki, A statistical study of inertia-gravity waves in the middle atmosphere, *J. Meteorol. Soc. Jpn.*, **63**, 1055–1066, 1985.
- Hitchman, M. H., and G. Brasseur, Rossby wave activity in a two-dimensional model: Closure for wave driving and meridional eddy diffusivity, *J. Geophys. Res.*, **93**, 9405–9417, 1988.
- Hitchman, M. H., and C. B. Leovy, Estimation of the Kelvin wave contribution to the semiannual oscillation, *J. Atmos. Sci.*, **45**, 1462–1475, 1988.
- Holton, J. R., *The Dynamic Meteorology of the Stratosphere and Mesosphere*, 319 pp., Am. Meteorol. Soc., Boston, Mass., 1975.
- Holton, J. R., and R. S. Lindzen, An updated theory for the quasi-biennial cycle of the tropical stratosphere, *J. Atmos. Sci.*, **29**, 1076–1080, 1972.
- Holton, J. R., and H.-C. Tan, The influence of the equatorial quasi-biennial oscillation on the global circulation at 50 mb, *J. Atmos. Sci.*, **37**, 2200–2208, 1980.
- Holton, J. R., P. H. Haynes, M. E. McIntyre, A. R. Douglass, R. B. Rood, and L. Pfister, Stratosphere-troposphere exchange, *Rev. Geophys.*, **33**, 403–439, 1995.
- Hostetler, C. A., and C. S. Gardner, Observations of horizontal and vertical wavenumber spectra of gravity wave motions in the stratosphere and mesosphere over the mid-Pacific, *J. Geophys. Res.*, **99**, 1283–1302, 1994.
- Karoly, D. J., G. L. Roff, and M. J. Reeder, Gravity wave activity associated with tropical convection detected in TOGA COARE sounding data, *Geophys. Res. Lett.*, **23**, 261–264, 1996.
- King, J. C., W. H. Brune, D. W. Toohey, J. M. Rodriguez, W. L. Starr, and J. F. Vedder, Measurements of ClO and O<sub>3</sub> from 21°N to 61°N in the lower stratosphere during February 1988: Implications for heterogeneous chemistry, *Geophys. Res. Lett.*, **18**, 2273–2276, 1991.
- Kinne, S., O. B. Toon, and M. J. Prather, Buffering of stratospheric circulation by changing amounts of tropical ozone: A Pinatubo case study, *Geophys. Res. Lett.*, **19**, 1927–1930, 1992.
- Kinnersley, J. S., A realistic three-component planetary wave model, with a wave-breaking parameterization, *Q. J. R. Meteorol. Soc.*, **121**, 853–881, 1995.
- Kinnersley, J. S., and S. Pawson, The descent rates of the shear zones of the equatorial QBO, *J. Atmos. Sci.*, **53**, 1937–1949, 1996.
- Leroy, S., and A. P. Ingersoll, Convective generation of gravity waves in Venus's atmosphere: Gravity wave spectrum and momentum transport, *J. Atmos. Sci.*, **52**, 3717–3737, 1995.
- Li, D., K. P. Shine, and L. J. Gray, The role of ozone-induced diabatic heating anomalies in the quasi-biennial oscillation, *Q. J. R. Meteorol. Soc.*, **121**, 937–943, 1995.
- Lindzen, R. S., Turbulence and stress due to gravity wave and tidal breakdown, *J. Geophys. Res.*, **86C**, 9707–9714, 1981.
- Lindzen, R. S., and J. R. Holton, A theory of the quasi-biennial oscillation, *J. Atmos. Sci.*, **25**, 1095–1107, 1968.
- Lindzen, R. S., and A. Y. Hou, Hadley circulations for zonally averaged heating centered off the equator, *J. Atmos. Sci.*, **45**, 2416–2427, 1988.
- Lindzen, R. S., and C.-Y. Tsay, Wave structure of the tropical stratosphere over the Marshall Islands area during 1 April–1 July 1958, *J. Atmos. Sci.*, **32**, 2008–2021, 1975.
- Magaña, V., and M. Yanai, Mixed Rossby-gravity waves triggered by lateral forcing, *J. Atmos. Sci.*, **52**, 1473–1486, 1994.
- Maruyama, T., Annual variations and QBO-synchronized variations of the equatorial wave intensity in the lower stratosphere at Singapore during 1961–1989, *J. Meteorol. Soc. Jpn.*, **69**, 219–232, 1991.
- Maruyama, T., Upward transport of westerly momentum due to disturbances of the equatorial lower stratosphere in the period range of about 2 days—A Singapore data analysis for 1983–1993, *J. Meteorol. Soc. Jpn.*, **72**, 423–432, 1994.
- McIntyre, M. E., and T. N. Palmer, Breaking planetary waves in the stratosphere, *Nature*, **305**, 593–600, 1983.
- McIntyre, M. E., and T. N. Palmer, The 'surf zone' in the stratosphere, *J. Atmos. Terr. Phys.*, **46**, 825–849, 1984.

- Mengel, J. G., H. G. Mayr, K. L. Chan, C. O. Hines, C. A. Reddy, N. F. Arnold, and H. S. Porter, Equatorial oscillations in the middle atmosphere generated by small-scale gravity waves, *Geophys. Res. Lett.*, 22, 3027–3030, 1995.
- Mote, P. W., K. H. Rosenlof, J. R. Holton, R. S. Harwood, and J. W. Waters, Seasonal variations of water vapor in the tropical lower stratosphere, *Geophys. Res. Lett.*, 22, 1093–1096, 1995.
- Mote, P. W., K. H. Rosenlof, M. E. McIntyre, E. S. Carr, J. C. Gille, J. R. Holton, J. S. Kinnery, H. C. Pumphrey, J. M. Russell III, and J. W. Waters, An atmospheric tape recorder: The imprint of tropical tropopause temperatures on stratospheric water vapor, *J. Geophys. Res.*, 101, 3989–4006, 1996.
- Murphy, D. M., D. W. Fahey, M. H. Proffitt, S. C. Liu, K. R. Chan, C. S. Eubank, S. R. Kawa, and K. K. Kelly, Reactive nitrogen and its correlation with ozone in the lower stratosphere and upper troposphere, *J. Geophys. Res.*, 98, 8751–8773, 1993.
- Naujokat, B., An update of the observed quasi-biennial oscillation of the stratospheric winds over the tropics, *J. Atmos. Sci.*, 43, 1873–1877, 1986.
- Ogino, S., M. D. Yamanaka, and S. Fukao, Meridional variation of lower stratospheric gravity wave activity: A quick look at Hakuho-Maru J-COARE cruise rawinsonde data, *J. Meteorol. Soc. Jpn.*, 73, 407–413, 1995.
- Olague, E. P., H. Yang, and K. K. Tung, A reexamination of the radiative balance of the stratosphere, *J. Atmos. Sci.*, 49, 1242–1263, 1992.
- Oort, A. H., Global atmospheric circulation statistics, 1958–1973, *NOAA Prof. Pap.* 14, 180 pp., U.S. Govt. Print. Off., Washington, D. C., 1983.
- O'Sullivan, D. J., The interaction of extratropical Rossby waves with westerly QBO winds, *J. Geophys. Res.*, in press, 1996.
- O'Sullivan, D., and P. Chen, Modeling QBO influence on isentropic tracer transport in the subtropics, *J. Geophys. Res.*, 101, 6811–6821, 1996.
- Parker, D. E., Equatorial Kelvin waves at 100 millibars, *Q. J. R. Meteorol. Soc.*, 99, 116–129, 1973.
- Pfister, L., S. Scott, M. Loewenstein, S. Bowen, and M. Legg, Mesoscale disturbances in the tropical stratosphere excited by convection: Observations and effects on the stratospheric momentum budget, *J. Atmos. Sci.*, 50, 1058–1075, 1993a.
- Pfister, L., K. R. Chan, T. P. Bui, S. Bowen, M. Legg, B. Gary, K. Kelly, M. Proffitt, and W. Starr, Gravity waves generated by a tropical cyclone during the STEP tropical field program: A case study, *J. Geophys. Res.*, 98, 8611–8638, 1993b.
- Plumb, R. A., The interaction of two internal waves with the mean flow: Implications for the theory of the quasi-biennial oscillation, *J. Atmos. Sci.*, 34, 1847–1858, 1977.
- Plumb, R. A., A "tropical pipe" model of stratospheric transport, *J. Geophys. Res.*, 101, 3957–3972, 1996.
- Plumb, R. A., and R. C. Bell, A model of the quasi-biennial oscillation on an equatorial beta-plane, *Q. J. R. Meteorol. Soc.*, 108, 335–352, 1982.
- Plumb, R. A., and A. Y. Hou, The response of a zonally symmetric atmosphere to subtropical thermal forcing: Threshold behavior, *J. Atmos. Sci.*, 49, 1790–1799, 1992.
- Plumb, R. A., and A. D. McEwan, The instability of a forced standing wave in a viscous stratified fluid: A laboratory analog of the quasi-biennial oscillation, *J. Atmos. Sci.*, 35, 1827–1839, 1978.
- Randel, W. J., Upper tropospheric equatorial waves in ECMWF analyses, *Q. J. R. Meteorol. Soc.*, 118, 365–394, 1992.
- Randel, W. J., B. A. Boville, J. C. Gille, P. L. Bailey, S. T. Massie, J. B. Kumer, J. L. Mergenthaler, and A. E. Roche, Simulation of stratospheric N<sub>2</sub>O in the NCAR CCM2: Comparison with CLAES data and global budget analyses, *J. Atmos. Sci.*, 51, 2834–2845, 1994.
- Reed, R. J., and C. L. Vilek, The annual temperature variation in the lower tropical stratosphere, *J. Atmos. Sci.*, 26, 163–167, 1969.
- Riggin, D., D. C. Fritts, C. D. Fawcett, and E. Kudeki, Observations of inertia-gravity wave motions in the stratosphere over Jicamarca, Peru, *Geophys. Res. Lett.*, 22, 3239–3242, 1995.
- Rosenlof, K. H., Seasonal cycle of the residual mean meridional circulation in the stratosphere, *J. Geophys. Res.*, 100, 5173–5191, 1995.
- Saravanan, R., A multiwave model of the quasi-biennial oscillation, *J. Atmos. Sci.*, 47, 2465–2474, 1990.
- Sato, K., and T. J. Dunkerton, Estimates of momentum flux associated with equatorial Kelvin and gravity waves, *J. Geophys. Res.*, this issue.
- Sato, K., F. Hasegawa, and I. Hirota, Short-period disturbances in the equatorial lower stratosphere, *J. Meteorol. Soc. Jpn.*, 72, 859–872, 1994.
- Shine, K. P., The middle atmosphere in the absence of dynamical heat fluxes, *Q. J. R. Meteorol. Soc.*, 113, 603–633, 1987.
- Stevens, D. E., On symmetric stability and instability of zonal mean flows near the equator, *J. Atmos. Sci.*, 40, 882–893, 1983.
- Takahashi, M., Simulation of the stratospheric quasi-biennial oscillation using a general circulation model, *Geophys. Res. Lett.*, 23, 661–664, 1996.
- Takahashi, M., and B. A. Boville, A three-dimensional simulation of the equatorial quasi-biennial oscillation, *J. Atmos. Sci.*, 49, 1020–1035, 1992.
- Takahashi, M., and T. Kumakura, Equatorial wave behavior in a three-dimensional sector model: Relation to the simulated QBO-like oscillation and comparison with a T21 general circulation model, *J. Meteorol. Soc. Jpn.*, 73, 1011–1027, 1995.
- Takahashi, M., and M. Shiobara, A note on a QBO-like oscillation in a 1/5 sector three-dimensional model derived from a GCM, *J. Meteorol. Soc. Jpn.*, 73, 131–137, 1995.
- Takahashi, M., N. Zhao, and T. Kumakura, Equatorial waves in a general circulation model simulating a quasi-biennial oscillation, *J. Meteorol. Soc. Jpn.*, in press, 1996.
- Tsuda, T., Y. Murayama, H. Wiryosumarto, S. W. B. Harijono, and S. Kato, Radiosonde observations of equatorial atmospheric dynamics over Indonesia. 1. Equatorial waves and diurnal tides, *J. Geophys. Res.*, 99, 10,491–10,506, 1994.
- van Loon, H., and R. L. Jenne, The annual wave in the temperature of the low stratosphere, *J. Atmos. Sci.*, 27, 701–705, 1970.
- Vijayan, L., and C. A. Reddy, Radiative damping of equatorial waves in the middle atmosphere, *Q. J. R. Meteorol. Soc.*, 120, 1323–1343, 1994.
- Vömel, H., S. J. Oltmans, D. Kley, and P. J. Crutzen, New evidence for the stratospheric dehydration mechanism in the equatorial Pacific, *Geophys. Res. Lett.*, 22, 3235–3238, 1995.
- Wallace, J. M., General circulation of the tropical lower stratosphere, *Rev. Geophys.*, 11, 191–222, 1973.
- Wallace, J. M., and V. E. Kousky, Observational evidence of Kelvin waves in the tropical stratosphere, *J. Atmos. Sci.*, 25, 900–907, 1968.
- Waugh, D. W., Seasonal variation of transport out of the tropical stratosphere, *J. Geophys. Res.*, 101, 4007–4023, 1996.
- Woodman, R. F., and P. K. Rastogi, Evaluation of effective eddy diffusive coefficients using radar observations of turbulence in the stratosphere, *Geophys. Res. Lett.*, 11, 243–246, 1984.
- Yanai, M., and T. Maruyama, Stratospheric wave disturbances propagating over the equatorial Pacific, *J. Meteorol. Soc. Jpn.*, 44, 291–294, 1966.
- Yanai, M., T. Maruyama, T. Nitta, and Y. Hayashi, Power spectra of large-scale disturbances over the tropical Pacific, *J. Meteorol. Soc. Jpn.*, 46, 308–323, 1968.
- Yulaeva, E., J. R. Holton, J. M. Wallace, On the cause of the annual cycle in tropical lower-stratospheric temperatures, *J. Atmos. Sci.*, 51, 169–174, 1994.
- Zhang, C., On the annual cycle in highest, coldest clouds in the tropics, *J. Clim.*, 6, 1987–1990, 1993.
- Ziemke, J. R., and J. L. Stanford, Quasi-biennial oscillation and tropical waves in total ozone, *J. Geophys. Res.*, 99, 23,041–23,056, 1994.

T. J. Dunkerton, Northwest Research Associates, P.O. Box 3027, Bellevue, WA 98009. (email: tim@nwra.com)

(Received March 12, 1996; revised September 17, 1996; accepted September 17, 1996.)



